**Sensor Devices, Sensor Networks
and its Applications I**

# Sensors & Transducers

**International Official Journal of the International Frequency Sensor Association (IFSA) Devoted to Research and Development of Sensors and Transducers**

## Volume 180, Issue 10, October 2014

# Contents

### Research Articles

Authors are encouraged to submit article in MS Word (doc) and Acrobat (pdf) formats
by e-mail: editor@sensorsportal.com. Please visit journal's webpage with preparation instructions:
http://www.sensorsportal.com/HTML/DIGEST/Submition.htm

International Frequency Sensor Association (IFSA).

www.sensorsportal.com

# Computer-Aided Diagnosis Sensor and System of Breast Sonography: A Clinical Study

\* **Jong-Ha Lee and Eun-Jin Lee**

Keimyung University, School of Medicine, Medical Imaging and Biosignals Laboratory,
Daegu, South Korea
Tel.: 053-580-3736, fax: 053-580-3746
\* E-mail: segeberg@kmu.ac.kr

**Abstract:** Early detection of breast cancer is critical in determining the best possible treatment approach. Ultrasound imaging has become an important modality in breast tumor detection and classification owing to its superiority to mammography in its ability to detect focal abnormalities in dense breast tissue. This paper discusses novel Fourier-based shape feature extraction techniques that provide enhanced classification accuracy for breast tumors in the computer-aided B-mode ultrasound diagnosis system. To verify the effectiveness of the proposed technique, experiments were performed using 4,107 ultrasound images containing 2,508 malignancy cases. Experimental results showed that the breast tumor classification accuracy has specificity of 95.8 %, sensitivity of 94.1 %, precision and recall of 95.7 %, and accuracy of 94.9 %. *Copyright © 2014 IFSA Publishing, S. L.*

**Keywords:** Computer-aided diagnosis, Ultrasound, Big data, Breast cancer, Early detection.

## 1. Research Background

### 1.1. The Need for Breast Ultrasonography

The incidence of breast cancer in women worldwide has been on the rise for 30 years. In particular, the incidence of breast cancer has increased by 2.5 fold of that of other cancers. In 2010 alone, 1.6 million women worldwide were diagnosed with breast cancer, while 425,000 people died of it, 68,000 of who were women between the ages 15 and 49 years living in developing countries [1]. In addition, breast cancer has the highest incidence rate among all cancers in females in Korea, and the World Health Organization reported that the rate of increase in breast cancer patients was the highest in Korea globally during the past 10 years. In order to curb the rate of breast cancer mortality, early diagnosis is essential, and regular check-ups are necessary starting at the age of 35 at the latest due to the high number of breast cancer patients in their 40s in Korea.

Mammography is the standard imaging technique for breast cancer diagnosis [2]. Mammography is used to identify abnormal lesions or tumors in the breasts and takes 2 images of each breast using the craniocaudal (CC) and mediolateral oblique (MLO) imaging techniques [3]. In CC, the patient stands facing the X-ray tube with feet apart and lifts the breast so that the angle between the breast and the chest becomes 90°. The technique requires matching the height of the cassette holder to that of the breast, pulling breast to the front of the chest, and compressing it until it is tight and the profile of the nipple is located at the center of the image. In MLO, the direction of the X-ray tube is set at 40–60°,

depending on the physique of the patient, and the height of the film tray is adjusted while the patient is holding onto a handle on the equipment with the hand on the side being examined. The patient places the other hand toward the ribs on the other breast in order to stretch the breast tissues, as well as the front and inside chest muscles, while pressure is gradually applied to the patient who is leaning against the equipment with the breast and chest muscles facing forward on the tray.

In mammography, breast cancer appears as masses or patterns of microcalcifications; however, most are identified as irregular masses with ragged borders. Approximately 1/4 of cases show patterns of microcalcifications, while early-phase breast cancer shows only microcalcifications without masses. The examination results are either normal or require further examinations which include breast ultrasonography or zoom imaging of suspected areas. However, such breast imaging techniques have limitations for early diagnosis [4]. The average size of a tumor detectable by mammography is 1 cm and is often discovered in the 1B phase; in addition, the cost of equipment is approximately 200 to 300 million KRW, and the imaging process causes discomfort and pain in women. Furthermore, young Korean women (mostly single women in their 30 s or those with firm breasts) tend to have tight breast form with dense fibrous tissues and less fat tissues, which makes the detection of calcification or masses difficult because the images appear cloudy or blurry. Therefore, the U.S. is increasingly mandating the notification of breast density to breast cancer patients, and a statute was enacted in 2010 requiring ultrasound examination to be performed in parallel to mammography for women with dense breast tissues.

In contrast, breast ultrasonography is more effective for imaging dense breasts and is being increasingly preferred by specialists because it achieves higher resolution enabling a better-quality diagnosis. However, despite its advantage of real-time examination, diagnosis results vary greatly depending on the device used for ultrasonography and the experience of the physician, which has prevented the technique from being recognized as a standard and objective method among all tests. In addition, there is a high possibility of fatigue-induced misdiagnosis in general hospitals with a large number of patients because the physician must identify the presence of lesions while conducting the ultrasonography directly. Moreover, the same imaging may yield different readings depending on physicians because it involves subjective interpretation by physicians. Cancer diagnosis by breast ultrasonography is achieved by identifying specific lesions in the imaging, which are then categorized as malignant or benign. However, for inexperienced physicians, it is not easy to identify and categorize lesions. In addition to such difficulty arising from the varying skills of physicians, other factors that may cause error in diagnosis include (1) dissimilarity among images in the imaging device

and (2) noise within the digital image. Noise is the major cause of diagnostic error. Ultrasonography by nature has considerable image noise, and imaging processing techniques are critical. These factors pose serious difficulties in detecting a certain lesion. Breast ultrasonography, unlike mammography, cannot produce an image of the entire breast, it requires a long examination time, and it cannot diagnose the microcalcifications within breasts.

## 1.2. The Need for a Computer-aided Diagnosis System

Therefore, in order to overcome such difficulties, a computer-aided diagnosis (CAD) system is needed to assist with diagnosis by automatically processing the acquired breast ultrasonography imaging to detect lesions and analyze patterns [5, 6]. With such a technique, the subjectivity among physicians can be minimized while enhancing the overall sensitivity, accuracy, and detection rate in the diagnostic procedures performed by physicians. This study examined a CAD system for diagnosing lesions in breast ultrasonography by recording and analyzing abnormal findings in an image by interpreting, digitalizing, and automatically calculating the image according to the Breast Imaging-Reporting and Data System (BI-RADS) categorization method as specified by the U.S. Radiological Society [7]. BI-RADS is a lexicon for organizing interpretation items to ensure consistency in ultrasonography terminology and includes definitions for tumors, structural distortion of breasts, asymmetry, density, and calcification [8]. BI-RADS results quantified by various algorithms are provided to physicians as secondary findings to supplement overall lesion discovery and diagnostic procedures, while CAD acts as a supplementary diagnostic system for inexperienced physicians by digitalizing the subtle differences between malignant and benign lesions that are difficult to detect by gross examination only.

## 2. Methods

### 2.1. Meaning and Mechanism of CAD

Fig. 1 shows the CAD system diagram of breast ultrasonography suggested in this study. Breast ultrasonography CAD is divided into CADe, which indicates suspected areas of lesions, and CADx, which indicates the malignancy of the lesions. Suspected areas are first identified with CADe, and the lesions are then described and diagnosed according to BI-RADS in CADx. The BI-RADS items of CADx are used not only for the physician's diagnosis but also for calculating the malignancy of the lesions. In order to diagnose the malignancy of the lesions, an automated diagnostic model created in advance is required. This model is created from the

BI-RADS result of each image from a large database of breast ultrasonography called the Picture Archiving and Communication System (PACS).

First, suspected areas of lesions are marked in the breast ultrasonography, and results are classified according to the BI-RADS lexicon by radiologists.
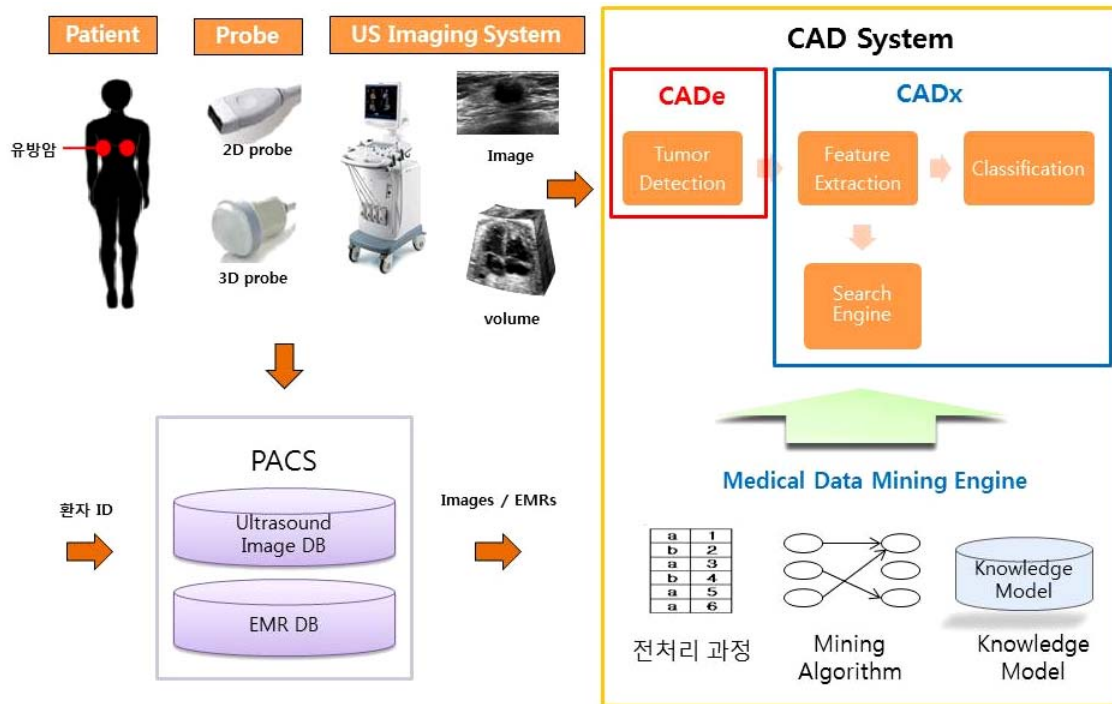


**Fig. 1.** Configuration of breast ultrasonography CAD system. CAD consists of CADe and CADx. The automatic breast cancer diagnosis model is generated from the large database of ultrasonography images in PACS.

## 2.2. BI-RADS

BI-RADS lexicon items include shape, orientation, margin, echo pattern, and posterior; particularly, the shape of the lesion acts as the most important factor in diagnosing breast cancer [9]. Fig. 2 is the example of ultrasonography. Shape is determined as oval when it is ellipsoidal or there are 2 or 3 curves, as round when it is circular, and as irregular when neither description applies. Benign tumors are usually oval or round with smooth edges because they do not metastasize, while malignant tumors are irregular with ragged edges due to invasive metastasis and irregular growth.
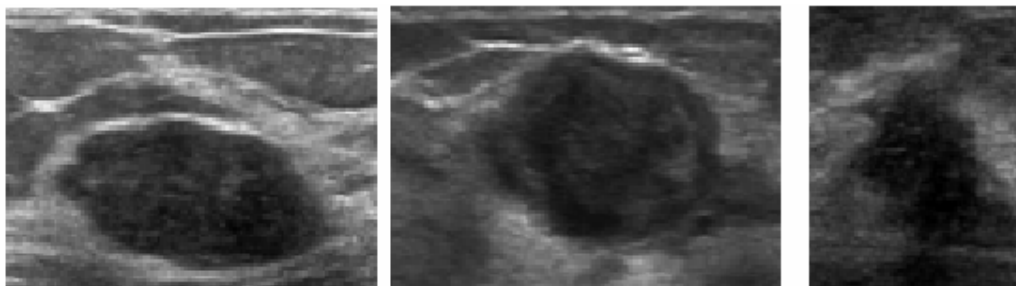


**Fig. 2.** Examples oval, round, and irregular lesions in ultrasonography.

This study used a Fourier-conversion-based lesion shape calculator which quantifies irregularity by Fourier-converting the border of the lesions in order to express the irregularity quantitatively [10]. Orientation is described as parallel when the long axis of the tumor is parallel to skin wrinkles and when the horizontal axis is longer than the vertical axis, or as nonparallel when the long axis is not aligned with the skin wrinkles and when the vertical axis is longer than the horizontal axis. Benign tumors are more flexible compared with malignant tumors; they become distorted or displaced when pressure is applied, while malignant tumors tend to retain their shape. Fig. 3. Shows the examples of parallel and nonparallel lesions in ultrasonography.
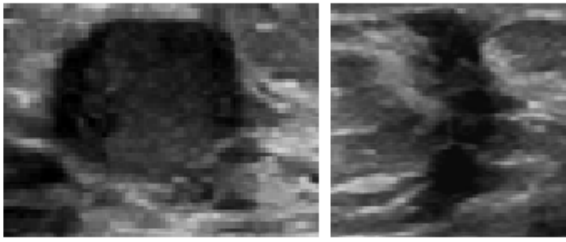
**Fig. 3.** Examples of parallel and nonparallel lesions
in ultrasonography.

A margin is defined as the border between a lesion and the surrounding tissues; it is described as circumscribed when the border is clearly visible or noncircumscribed if it is not. Noncircumscribed cases are further classified into indistinct (indistinct border between the mass and surrounding tissues), angular (several or all edges of the borders are clear and contain acute angles), microlobulated (showing fan shapes in short cycles along the border of the mass), and spiculated (having a needle-shaped border). Benign tumors are separated from surrounding tissues and are wrapped in fibrous film, while malignant tumors are not covered in film; therefore, circumscribed borders usually indicate benign tumors while noncircumscribed cases are most often malignant.

Lesion boundaries are divided into abrupt interface and echogenic halo types. In an abrupt interface, a clear border between the lesion and the surrounding tissues is very narrow, and the echo around the edges is clearly visible regardless of the thickness of the surrounding tissues. Conversely, in an echogenic halo, the border between the lesion and the surrounding tissues is not clear, and it appears to be continuous with the reflected areas. Fig. 4. Shows the examples of ultrasonography.
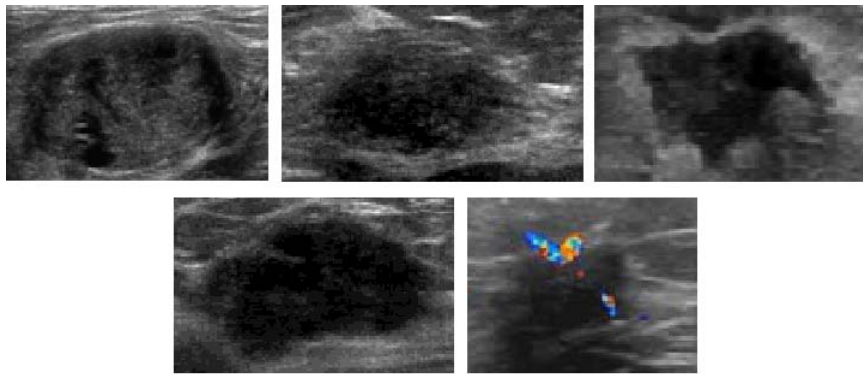


**Fig. 4.** Examples of (a) circumscribed; (b) indistinct; (c) angular; (d) microlobulated,
and (e) spiculated lesions in ultrasonography.

Echo patterns are categorized into anechoic (no internal reflection), hyperechoic (internal reflectivity is higher compared to fat and similar to that of fibrous tissues), hypoechoic (showing low echo in fat tissues), complex (having the characteristics of both anechoic and echogenic) and isoechoic (difficult to distinguish due to a similar degree of reflection as fat tissues in other tissues).

Fig. 5. Shows the examples of an abrupt interface and echogenic halos in ultrasonography.
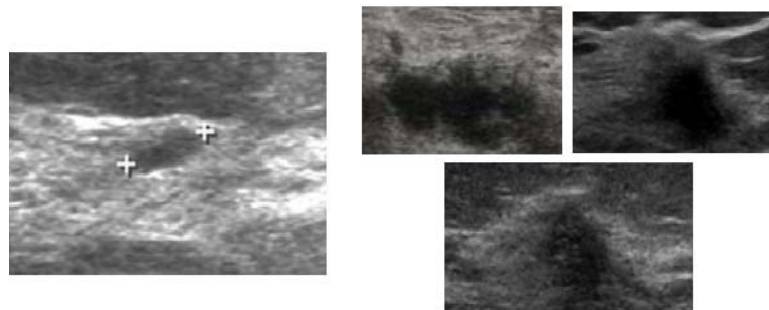


**Fig. 5.** Example of an (a) abrupt interface, and (b) echogenic halos in ultrasonography.

Posterior acoustic features are divided into enhancement (increased echo in the posterior of the tumor), shadowing (reduced echo, excluding the shadow of the border), no posterior acoustic feature

(without enhancement or shadowing), and combined pattern (showing both enhancement and shadowing or damping in the posterior). Fig. 6 shows the examples of ultrasonography patterns. Fig. 7 shows the examples of enhancement and shadowing in ultrasonography.

In addition to the shape of the lesions, a characteristic extractor was created to suite the purpose of each item in order to determine the BI-RADS categories such as posterior acoustic, orientation, margin, and echo pattern as characteristics in the image. In order to create an automatic lesion diagnosis model, a supplementary breast cancer diagnosis model was generated by determining the characteristics of each BI-RADS category from a large database of PACS breast ultrasonography images using a characteristic extractor, and then using a pattern-recognition algorithm and data mining technique. The supplementary breast cancer diagnosis model created by this method was able to identify the location of the lesions and identify benign or malignant tumors automatically when a new breast ultrasonography image was input into the CAD system.
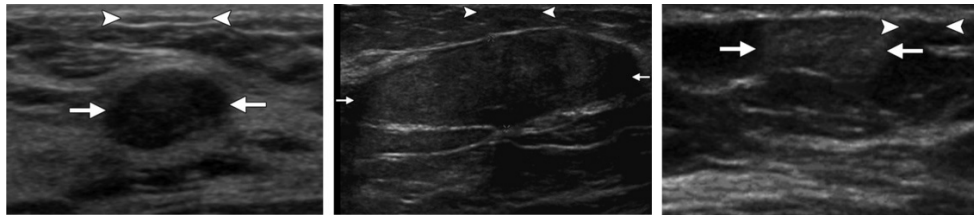


**Fig. 6.** Examples of (a) hypoechoic; (b) isoechoic, and (c) hyperechoic patterns in ultrasonography.
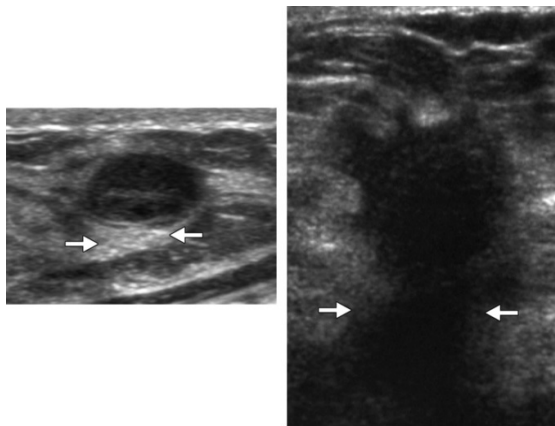


**Fig. 7.** Examples of (a) enhancement, and (b) shadowing in ultrasonography.

glandular tissue, retromammary fat, and pectoralis muscle. Fat layers and lesions appear dark, while breast tissues appear white. Therefore, the characteristics of lesions include a dark interior compared to surroundings with a circular or oval shape. In addition, the location of lesions is generally in the mammary glandular tissue. Therefore, lesion detection may be higher when looking for lesions in the mammary glandular tissue area rather than in the entire image. Therefore, this study examines the algorithm for detecting lesions in the mammary glandular tissue area using morphological information of the lesion and the structural information of the breasts. Fig. 8 shows the mammary glandular tissue area in breast ultrasonography.

### 2.3. Image Segmentation and Detection

The CAD system suggested in this study extracts lesions from breast ultrasonography images, describes extracted lesion areas based on their BI-RADS classification, and processes the information using a lesion diagnostic modeling categorizer [11]. The identification of tumors includes three steps: 1) detection of lesion areas, 2) extraction of the lesion boundaries, and 3) determination of lesion malignancy.

### 2.3.1. Lesion Area Detection Using the Morphological Information of Lesions and Structural Information of Breasts

The characteristics of breast ultrasonography include speckle noise and the appearance distinguishing skin, subcutaneous fat, mammary

### 2.3.2. Extraction of Lesion Boundaries Using the Canny Algorithm

Once a lesion area has been detected, the boundaries of the lesion must be extracted. In general, the lesion area in breast ultrasonography is darker than the surrounding tissues, and the pixel value abruptly changes in the image. In this study, the boundaries of the lesion are extracted using the gradient information of the pixel value. First, the image is convoluted through a Gaussian mask which is a blurring technique that smoothens the image by removing fine details. Then, the gradient magnitude and direction is calculated for each resulting pixel. The second derivative is then calculated along the gradient direction, and a point with a value of 0 is categorized as a lesion boundary. The lesion boundaries are extracted by connecting all such points.
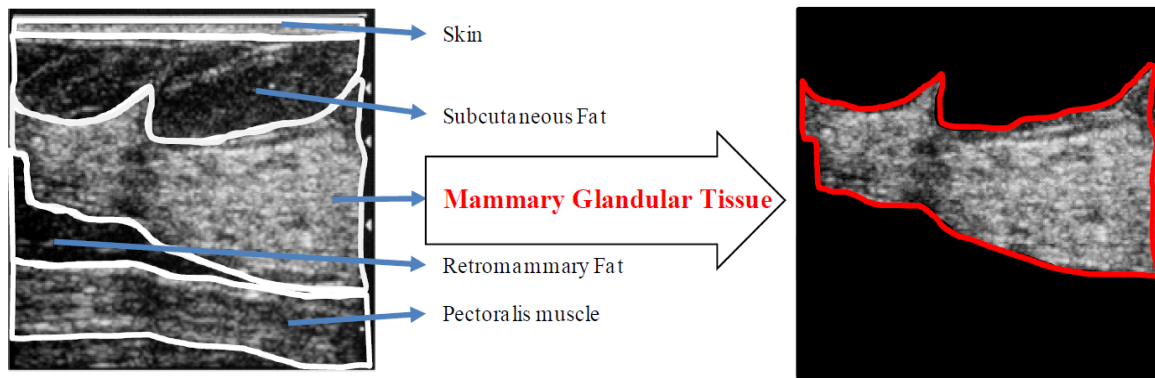
**Fig. 8.** Example of morphological information in breast ultrasonography and the area of mammary glandular tissue separated from the image.

### 2.3.3. Determining the Malignancy of a Tumor Using BI-RADS Category Information

An algorithm that analyzes lesions using the extracted lesion outline was studied. In this study, the malignancy of lesions in breast ultrasonography is calculated using five types of BI-RADS category information. The BI-RADS categories to be calculated include Shape (Regular/Irregular), Orientation (Parallel/Nonparallel), Margin (Circumscribed/Noncircumscribed), Echo pattern (Anechoic/Hyperechoic) and Posterior (No posterior/Shadowing). These BI-RADS categories are part of the mass categories and are essential to the diagnosis of lesions. In order to extract each BI-RADS category, the morphological characteristics and texture characteristics of lesions are used. In particular, the morphology of the lesion is the most important factor in determining its malignancy. In order to express the morphology of the lesion clearly, the study suggests Fourier conversion based a lesion morphology description algorithm. The Fourier-conversion-based lesion morphology description algorithm first calculates a morphology histogram from the lesion outline and converts this histogram into a one-dimensional signal. The morphology histogram is generated by a log–polar bin histogram generator [12]. The Fourier coefficient is obtained by Fourier transforming the one-dimensional signal. The Fourier coefficient is used as a characteristic for determining the morphology of the lesion. In general, a greater malignancy of the lesion results in greater irregularity of lesion shape, and the change in the Fourier coefficient is expected to differ greatly from benign to malignant. Fig. 9 shows the location of malignant lesion in breast ultrasonography of breast cancer patient.

Fig. 10 shows the histogram calculated using the lesion histogram from lesion outline in Fig. 9 with the one-dimensional signal from it.

In order to determine the malignancy of lesions, an automatic breast cancer diagnosis model was created from a large database of PACS breast ultrasonography images using a data mining technique. Data mining calculates all BI-RADS characteristics by analyzing ultrasonography of previous breast cancer patients saved in PACS and then creates a model. The model created in such a manner extracts the BI-RADS characteristics in an image when a new breast ultrasonography is input and determines whether the lesion is benign or malignant based on the values. Table 1 shows the BI-RADS feature lists.
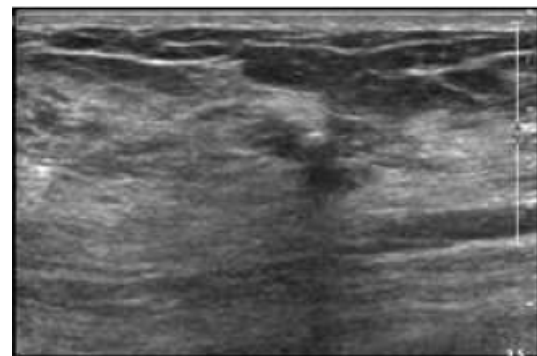


(a) Breast ultrasonography of breast cancer patient.



(b) Location of malignant lesion in breast ultrasonography (red border)

**Fig. 9.** Location of malignant lesion in breast ultrasonography of breast cancer patient. (Samsung Medical Center, 2012).

(a)  (b)  (c)
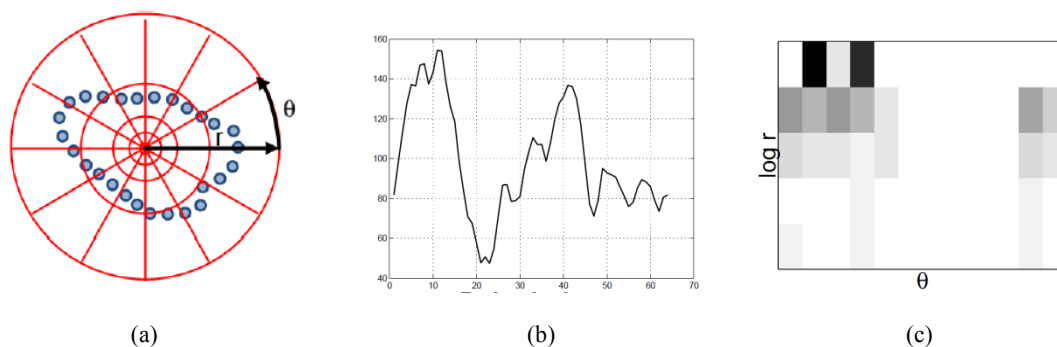
**Fig. 10.** (a) log-polar diagram. (b) 2-dimensional boundary histogram contained in per bin unit.
(c) Histogram transformed into 1-D.

## 2.4. Feature List

**Table 1.** BI-RADS Feature List.

| Extractor | Feature No. | Feature Name |
|---|---|---|
| 1 | F1–F140 | Spatial gray-level dependence (SGLD) matrix |
| 2 | F141–F203 | Fourier with shape context |
| 3 | F204–234 | Fourier with centroid distance (Magnitude) |
| 4 | F235–F265 | Fourier with centroid distance (Phase) |
| 5 | F266 | Intensity in the mass area |
| 6 | F267 | Gradient magnitude in the mass area |
| 7 | F268 | Orientation |
| 8 | F269 | Depth–width ratio |
| 9, 10, 11 | F270–F272 | Distance between mass shape and best-fit ellipse |
| 12, 13, 14, 15, 16, 17 | F273–F278 | The average gray changes between tissue area and mass area |
| 18 | F279 | The average gray changes between posterior and mass area |
| 19, 20, 21, 22 | F280–F283 | The histogram changes between tissue and mass (bin 0–3) |
| 23 | F284 | Compare the gray value of left, post, and right under lesion |
| 24 | F285 | The number of lobulate areas |
| 25 | F286 | The number of protuberances |
| 26 | F287 | The number of depressions |
| 27 | F288 | Lobulation index |
| 28, 29 | F289–F290 | Elliptic-normalized circumference |
| 30, 31, 32, 33, 34, 35 | F291–F296 | Histogram (mean, variance, skewness, kurtosis, energy, entropy) |
| 36, 37 | F297–F298 | Fourier power spectrum (annular-ring and wedge sampling geometries) |
| 38, 39, 40, 41, 42, 43, 44, 45, 46 | F299 | Circularity |
| | F300 | Norm. radial length standard dev. |
| | F301 | Area ratio |
| | F302 | Roughness index |
| | F303 | Spiculation index ratio (CCW) |
| | F304 | Spiculation ratio (CCW) |
| | F305 | D-W Ratio (density gradient) |
| | F306 | D-W Ratio (interclass variance) |
| | F307 | D-W Ratio (variance) |

## 2.5. Machine Learning Algorithm

In order to create an automatic lesion diagnostic model, an automatic breast cancer diagnostic model was created using a pattern recognition algorithm and big data mining technique after calculating the characteristics of BI-RADS from a large database of PACS breast cancer ultrasonography images using the characteristics extractor. In order to create this model, learning was performed using the five representative machine learning algorithms (Aadaboost, J48, Logitboost, NaïveBayes, J48). A machine learning algorithm inputs data into the computer, performs learning based on a specific algorithm, establishes criteria for categorization, and predicts the category of the data when new data are input. Data mining refers to the process of discovering useful correlations hidden in large quantities data and extracting information which can be used in future decision-making. The five algorithms used in model creation are described below.

### 2.5.1. Support Vector Machine (SVM)

A machine learning algorithm refers to an algorithm which inputs given data into the computer, performs learning based on a specific algorithm, establishes criteria for categorization, and predicts the category of the data when new data are input. Data mining refers to the process of discovering useful correlations hidden in large quantities data and extracting information which can be used in future decision-making.

In order to create an automatic lesion diagnostic model, an automatic breast cancer diagnostic model was created using a pattern recognition algorithm and big data mining technique after calculating the characteristics of BI-RADS from a large database of PACS breast cancer ultrasonography images using a characteristics extractor. This paper will describe in detail the SVM algorithm which is most frequently used with an elevated accuracy.

$C_i$ refers to the variable having the value of 1 or −1 and is the class $x_i$ belongs to, while $x_i$ is the real vector in the $p$-dimension. $H_3$ does not properly sort the points in the 2 classes. $H_1$ and $H_2$ classify the points in the 2 classes, and it can be see that $H_2$ classifies them with a larger margin than $H_1$ does. Many learning algorithms, including neural networks, have the common goal of identifying the hyperplane which separates the $c_i = 1$ points from the $c_i = −1$ points when such learning data were given. What differentiates SVM from other algorithms is that it identifies the maximum-margin hyperplane among many potential planes which may separate the points. Here, margin refers to the minimum value for the distance from the hyperplane to each point. In order to maximize the margin while classifying points into 2 classes, the hyperplane must be located so that the minimum value among the distances belonging to class 1 and the minimum value among the distances belonging to class −1 must be the same. Such a hyperplane is known as the maximum-margin hyperplane. In conclusion, SVM is an algorithm that identifies how to maximize the distance between the points of the 2 classes among the countless hyperplanes which separate the points belonging to the 2 classes.

### 2.5.2. Adaboost

Adaboost is an algorithm that creates a strong classifier by combining weak classifiers. Here, a weak classifier generally uses a threshold classifier of a specific dimension.

### 2.5.3. J48 (Decision Tree)

A decision tree is a graphic representation of procedures for categorizing or assessing items of interest.

### 2.5.4. Logitboost

While Adaboost is an algorithm that can minimize exponential loss, Logitboost is an algorithm that can minimize logistics damage.

### 2.5.5. Naïve Bayes

Naïve Bayesian classification is a simple probabilistic categorization. The probabilistic model can be induced using the Bayes' Theorem and includes a strong independent assumption which cannot be derived in reality.

## 3. Experimental

A total of 4,107 breast cancer tumor images were obtained from Samsung Medical Center which were taken between 2006 and 2010. Among the images obtained, 1,599 images were of benign tumors taken from patients aged 11–81 ($M = 45$); the remaining 2,508 images were of malignant tumors taken from patients aged 24–86 ($M = 49$). All images were taken using the Philips ATL iU22 ultrasound device under the supervision of Samsung Medical Center. The scanner was mounted with a 6-cm linear probe set at 5–12 MHz. The image size in B-mode was 1024 × 768 pixels with a spatial resolution of 0.23 mm/pixel. The generated algorithm was applied to the obtained images according to the BI-RADS categorization method in order to interpret and calculate images to identify benign or malignant tumors.

[Breast ultrasonography imaging ⇒ BI-RADS characteristics extracted and calculated ⇒ Pattern recognition algorithm + data mining technique ⇒ Breast cancer diagnosis model creation]

Five types of algorithm learning were performed using "Weka," a java-based data mining software application. In addition, each algorithm was applied using the filtered classifier.

When using SVM, options such as Gamma and Nu values, which affect the formation of the classifier, as well as Kernel type and Normalize, were varied. A more accurate diagnosis model could be identified by comparing the values for Specificity, Sensitivity, Accuracy, Precision, and Recall obtained as results.

From individual images, a total of 290 BI-RADS-based characteristics were extracted, and a total of 5 types of algorithms, namely, J48, Adaboost, Logitboost, NaïveBayes, and SVM, were used in order to determine whether the lesion was benign or malignant using the distribution of characteristic values. The category performance measured by each algorithm was compared using Specificity, Sensitivity, Precision, Recall, and Accuracy, and the results are shown in Fig. 11. According to the experiment, the performance of SVM was the highest with specificity of 95.8 %, sensitivity of 94.1 %, precision and recall of 95.7 %, and accuracy of 94.9 %. Therefore, the provided characteristics and SVM algorithm could categorize benign and malignant lesions with the highest probability in all 5 categories. Table 2 outlines the performances of the 5 algorithms.
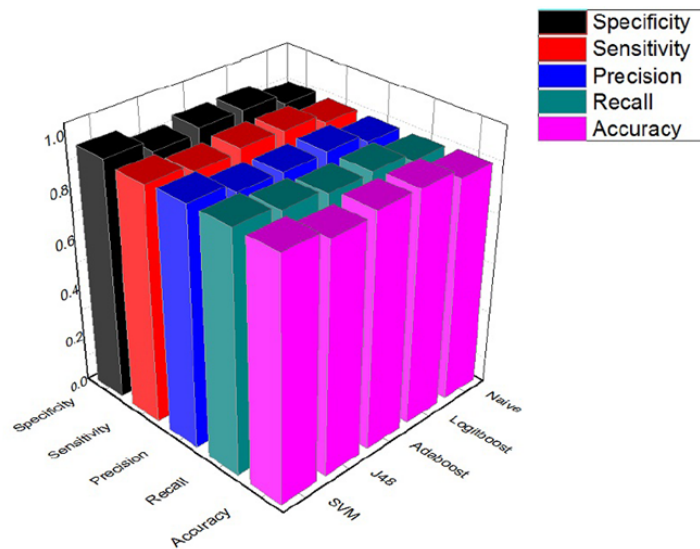


**Fig. 11.** Comparison of specificity, sensitivity, precision, recall, and accuracy of lesion categorization algorithms.

**Table 2.** Results of algorithm execution.

|             | SVM        | Adaboost    | Logitboost  | J48         | Naïve Bayes |
|-------------|------------|-------------|-------------|-------------|-------------|
| Specificity | 0.958      | 0.921       | 0.92        | 0.917       | 0.891       |
| Sensitivity | 0.944      | 0.901       | 0.912       | 0.909       | 0.875       |
| Accuracy    | 95.066 %   | 91.1272 %   | 91.6222 %   | 91.3366 %   | 88.3283 %   |
| Precision   | 0.951      | 0.911       | 0.916       | 0.913       | 0.883       |
| Recall      | 0.951      | 0.911       | 0.916       | 0.913       | 0.883       |

Experiments showed that the best results are obtained when SVM is applied to the filtered classifier. This diagnostic model is therefore expected to diagnose breast cancer with the highest accuracy.

## 4. Results

This study examined an automatic analysis system for breast ultrasonography images. In order to describe the lesions detected in ultrasonography, images were interpreted, digitalized, and automatically calculated according to the BI-RADS categorization method to study a CAD system for breast ultrasonography examination that records radiological findings and analyzes them to diagnose lesions. As a result, the suggested system could categorize a total of 4,107 breast cancer images taken between 2006 and 2010 at the Samsung Medical Center with specificity of 95.8 %, sensitivity of 94.1 %, precision and recall of 95.7 %, and accuracy of 94.9 %. The automatic ultrasonography analysis system proposed in this paper is an essential system contributing to forestalling the fatigue of physicians and enhancing diagnostic accuracy.

## References

[1]. A. Jemal, R. Siegel, E. Ward, Y. Hao, J. Xu, M. J. Thun, Cancer statistics, 2011, *CA: A Cancer Journal for Clinicians*, Vol. 61, Issue 2, 2011, pp. 225-249.

[2]. S. A. Feig, Effect of service screening mammography on population mortality from breast carcinoma, *Cancer,* Vol. 95, 2002, pp. 451–457.

[3]. V. Jackson, R. Hendrick, S. Feig, D. Kopans, Imaging of the radiographically dense breast, *Radiology*, Vol. 188, 1993, pp. 297-301.

[4]. K. Doi, H. MacMahon, M. L. Giger, K. R. Hoffman, Computer aided diagnosis in medical imaging, Computer-aided diagnosis and its potential impact on diagnostic radiology, *Elsevier Science B V*, 1999, pp. 57-59.

[5]. K. Horsch, M. L. Giger, C. J. Vyborny, L. A. Venta, Performance of computer-aided diagnosis in the interpretation of lesions on breast sonography, *Acad Radiol,* Vol. 11, 2004, pp. 272–280.

[6]. E. Lazarus, M. B. Mainiero, B. Schepps, S. L. Koelliker, L. S. Livingston, BI-RADS lexicon for US and mammography: interobsever variability and positive predictive value, *Radiology,* Vol. 239, 2006, pp. 385-391.

[7]. C.-M. Chen, Y.-H. Chou, K.-C. Han, C.-M. Tiu, H.-J. Chiou, S.-Y. Chiou, Breast lesions on sonograms: Computer-aided diagnosis with nearly setting-independent features and artificial neural networks, *Radiology*, Vol. 226, Issue 2, 2003, pp. 504-514.

[8]. C. T. Zhan, and R. Z. Roskies, Fourier descriptors for plane closed curves, *IEEE Trans. Computers*, C-21, 1972, pp. 269-281.

[9]. S. Belongie, J. Malik, J. Puzicha. Shape Matching and Object Recognition Using Shape Contexts, *IEEE Trans. Pattern Anal. Mach. Intell.*, Vol. 24, Issue 24, 2002, pp. 509-521.

[10]. J. Otero, L. Sánchez, Induction of descriptive fuzzy classifiers with the Logitboost algorithm, *Soft Computing,* Vol. 10, Issue 9, pp. 825-835.

[11]. Liangxiao Jiang, Learning Instance Weighted Naïve Bayes from labeled and unlabeled data, Materials, Vol. 38, No. 1, pp. 257–268.

[12]. E. Frank, M. Hall, L. Trigg, G. Holmes, I. H. Witten, Data mining in bioinformatics using Weka, *Bioinformatics Applications Note,* Vol. 20, Issue 15, 2004, pp. 2479-2481.

------------------------

# Sensors & Transducers

# Design of Reflective Intensity Modulated Fiber-Optic Sensor Based on TracePro and Taguchi Method

**[1] Junjie Yang, [2] Zhihe Fu, [2] Yibiao Fan, [1] Wenxiang Chen, [1] Zhiping Xie, [1] Wei Wu, [1] Xiaoyu Shan**

[1] Department of Mechanical and Electrical Engineering, Xiamen University,
Xiamen, Fujian 361005, China
[2] Department of Mechanical and Electrical Engineering, Longyan College,
Longyan, Fujian 364012, China
[1] Tel.: 13606932279, fax: +86 592 2186383
E-mail: jjyang022076@163.com

**Abstract:** Compare with traditional way of numerical simulation by establishing the mathematical model through geometry optic, we design a TracePro model to analyze the sensing process of reflective intensity-modulated fiber optic sensor base on ray tracing. This type of sensor has advantages over other fiber optic sensor, including simple structure, flexible design, reliable perform, low cost etc. In this paper, to design the reflective intensity modulated fiber optic sensor with concave reflected surface, TracePro software is used for modeling, TP modeling results are consistent with the existing conclusions show that the method is reasonably effectively, can improve the design efficiency. Meanwhile the Taguchi method is used to optimize coupling efficiency of receiving fiber in fiber optic displacement sensor design. Through optimizing three controllable factors the optimization configuration of A1B1C1 combinations is gain, presents a viable solution for the design of this sensor type. *Copyright © 2014 IFSA Publishing, S. L.*

**Keywords:** Fiber optic sensor, Intensity modulated, Reflective surface, TracePro, Taguchi method.

## 1. Introduction

Reflective intensity-modulated fiber optic sensor (RIM-FOS) are widely used for such physical parameters measurements as distance, vibration, sound, pressure, temperature and acceleration because of their advantages over other fiber sensor, including simple structure, flexible design, reliable perform, low cost etc. [1]. Most works focus on the plane reflector [2-5], however such type of sensor with concave reflector which is seen frequently in mechanical circumstance could cause major differences in modulation property [6-9]. Such as the

blind region of the sensor, having concave reflector is small as compare to the blind region of the sensor having plane reflector. Such type of sensor can be used, where the space required for the measurement is the major limitation.

So far the research of this kind of sensor is based on numerical simulation by establishing the mathematical model through geometry optic. The more complex the reflecting surface is, the more difficult to establish the mathematical model which is suit for qualitative discussions. With the change of the structural parameters, the corresponding mathematical models may need to re-establish. This

is unfavorable for application of this type of sensor. In addition in the design process multi-parameter configuration optimization has been a major trouble for designers.

To better understand the working principle and improve the performance of the sensor, the ray - tracing simulation was carried out by using optical analysis software TracePro (TP), which provides the sensing process for us. Meanwhile Taguchi method was used to optimize the configurations.

## 2. TracePro Model

A typical two-fiber RIM-FDS configuration is shown in Fig. 1. It consists of a transmitting fiber (TF), concave reflector, receiving fiber (RF), an optical source (LED) and a photo detector (PD). The fiber tips and concave reflector are separated by a distance d. The mathematical models for optical fiber sensors with concave reflector were presented [6-9]. This paper focuses on the TP model of optical fiber sensor with concave reflector.
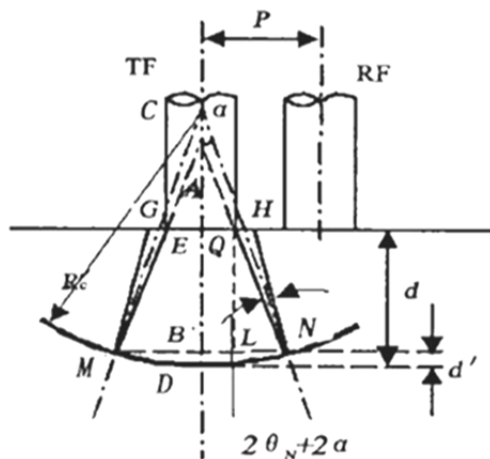


**Fig. 1.** Concave reflective surface.

Following assumptions are being considered for the TP model:

1. The transmitting fiber and receiving fiber have perfectly circular cross sections with radius of 0.1 mm.

2. The transmitting fiber is placed on the focal axis of the concave reflector.

3. Both the fibers are straight parallel, with no space left between them and having the same numerical aperture NA of 0.56. So the beam divergence angle can be described as

$$\theta = \sin^{-1}\frac{NA}{n_0} \qquad (1)$$

$n_0$ was the refractive index of the medium present in between the fiber tips and the concave reflector. Here was zero, then $\theta = 34^0$. A hollow thin round

table structure shown in Fig. 2 was built to compensate the light loss caused by NA, where S1 and S2 plane is set to be completely absorbed in TP.
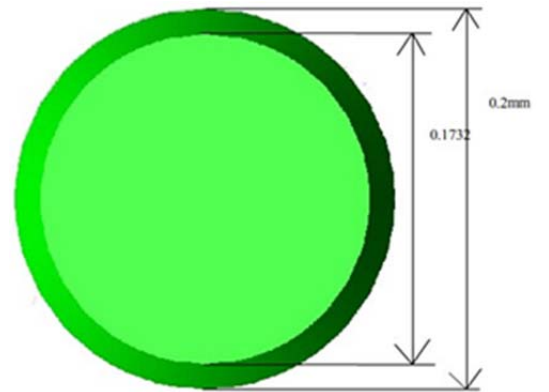


(a)
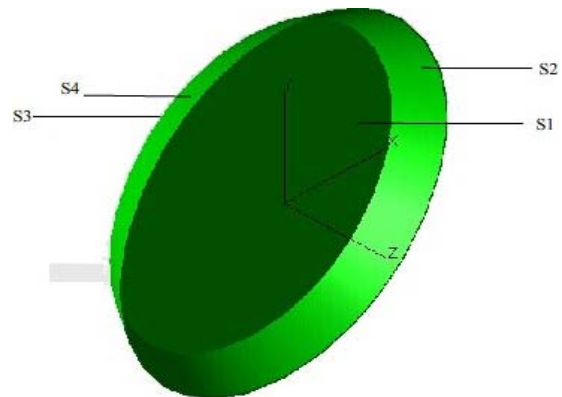


(b)

**Fig. 2.** Thin round table structure (a) Bottom view (b) three-dimensional view.

4. Light source: The light emitting characteristics of transmitting fiber (TF) tip was generally recognized as Gaussian distribution [10]. For this reason a grid light was set with an outer diameter of 0.1 mm and divergence angle 34°, the angular distribution was set to be Gaussian density distribution.

The amount of the light collected by the receiving fibers is directly correlated to the distance between the fibers tips and the reflector. Therefore, the distance variation can be measured by monitoring the intensity change of the collected light. However, most of the light representing useful sensing information is lost at the transduction region between the fiber tips and the reflector. Only a small portion of the light is reflected to the receiving fiber for collecting. Thus, much work has been done to improve the collecting efficiency. In order to analyze the distribution of light intensity in the receiving side (XY plane), which is conducive to reasonable arrangements for TF and RF position, a rectangular receiving surface structure was constructed in Fig. 3.
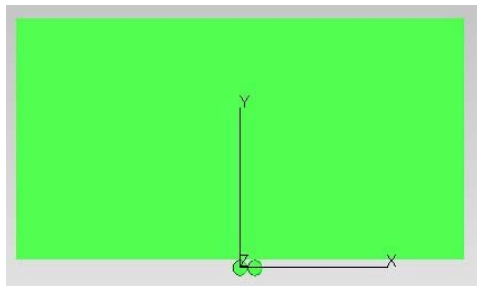
**Fig. 3.** Rectangular receiving surface.

By now the TP model was constructed as shown in Fig. 4.

In the configuration with radius of curvature R = 6 mm, distance d=0.3 mm, the irradiance of the receiving surface was gain as shown in Fig. 5, the light intensity distribution appear to be the ladder distribution. The cross-sectional view of the right figure shows corresponding areas of the horizontal light intensity distribution of and vertical direction.
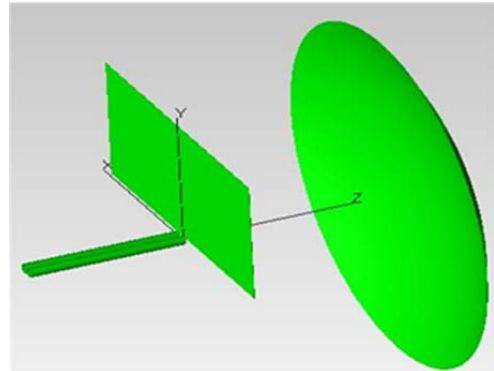


**Fig. 4.** TP model.
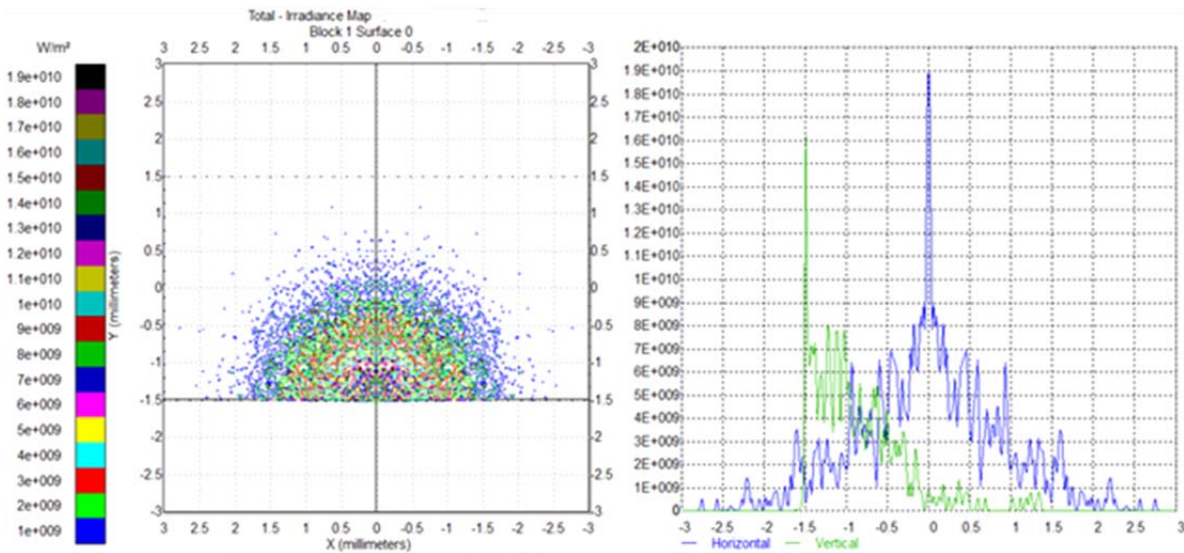


**Fig. 5.** Irradiance chart of receiving surface.

Here light intensity function M could be expressed as

$$M = \frac{N}{N_{Total}}, \qquad (2)$$

where N represents the light intensity collected from S1 surface, $N_{Total}$ represent the total light number of light source from TF. In this case coupling efficiency of the light intensity could replace with M.

By changing the radius of curvature R and the distance d which was between reflecting surface center and RF tip (with spacing of 0.05 mm) we obtain light intensity values of different radii of curvature, their modulation curves were shown in Fig. 6 by Origin software process.

In Fig. 6 the distance between two optical fibers p was set to be 0.3 mm and the radius of curvature R were taken by 3 mm, 6 mm, 9 mm respectively.
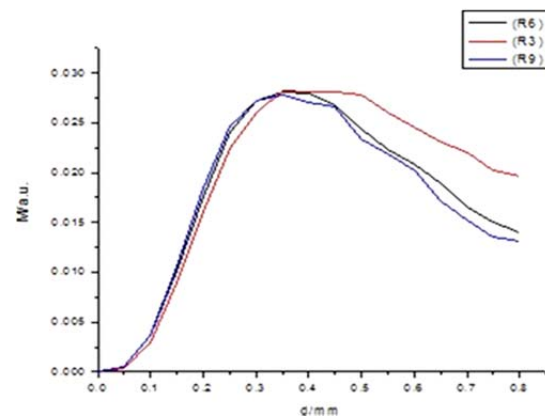


**Fig. 6.** Light intensity curve of Concave reflective surfaces with different R.

As the concave radius of curvature becomes large, the dead zone of the characteristic curve

becomes smaller, the linear range of the front slope decreases and the sensitivity increases, the linear range of the back slope decreases and the curve slope increases. The property of low signal loss in optical fibers permits long distance optical data transmission, enabling remote physical quantity measurements to be conducted without losing significant sensing accuracy. As there is a deviation between mathematical modeling and the actual situation, tp modeling method also has its difference. This work was aimed at providing designers with a cost-effective methodology to enhance the fiber coupling efficiency compare with numerical simulation approach. For now these conclusions are consistent with the numerical simulation results, showing that this method is reasonable.

## 3. Taguchi Method

The Taguchi method combined with principal component analysis can use in the extended optimization of non-image optics, because this method does not depend on the number of ray tracings [11]. Most commercial optical software performs well in analysis work; however, during optimization, ray tracing numbers are used.

In the Taguchi method, experiments are conducted to determine the best levels based on an orthogonal array (OA) [12]. An orthogonal array is a fractional factorial matrix that assures a balanced comparison of levels for any factor or interaction of factors. Assuming an orthogonal array of strength t is expressed by a matrix of j rows and i columns that makes $a_i^j$

$$\text{Each } a_i^j \in \{0, 1, \dots, q-1\}.$$

When setting $t \leqslant i$ in each j by t sub-matrix of all $q^t$ possible rows occur the same number of $\lambda$ times, so $\lambda q^t = j$ [13]. Such an array is denoted by OA (j, i, q, t), in which all possible combinations of symbols in any array of strength t appear with equal frequency [14]. The orthogonal array is to set up experiments that require only a fraction of the full factorial combinations. The treatment combinations are chosen to provide sufficient information to determine the factor effects using the analysis of means (ANOM). Orthogonal refers to the balance between the various combinations of factors so that no one factor is given more or less weight in the experiment than the other factors. Orthogonal also refers to the fact that the effect of each factor can be mathematically assessed independently of the effect of the other factors.

With negligible interactions between the control factors, the S/N effects can be modeled by simply adding the main effects from each control factor. This is referred to as an additive model, which takes on the following form [12].

$$M_{predict} = \overline{M} + (\overline{M}_A - \overline{M}) + (\overline{M}_B - \overline{M}) + \cdots + \text{error}, \tag{3}$$

where $\overline{M}$ is the overall average response for the entire OA and $\overline{M}_A$, $\overline{M}_B$ are the response average for factors A, B, C, respectively. The error term is the difference between the actual response on the left and the predicted response based on the additive model.

To use TP software for simulation, first we should define the sensitivity of coupling for each parameter. There are some factors that could affect the efficiency of RF receiver:

1) Theoretically the radius of curvature of the reflecting surface R could range from 0 to infinity. In fact when the R value exceeds a certain range, the result is close to the plane reflector of the case. To highlight the characteristics of a concave reflector, the values of R were given in 0 ~ 8 mm.

2) Based on longitudinal sectional view of the right in Fig. 5, the configuration with distance p between TF and RF is obtained reasonable in 0.2 mm to 0.6 mm.

3) By the light intensity modulation curve in Fig. 6, the characteristic area is 0 ~ 0.8 mm.

4) Other variables, including the selection of the light source, the reflective surface, the optical fiber type, in order to better control variable values were set to be constant values.

According to the above principles, controllable factor table was design (Table 1).

**Table 1.** Controllable factor table.

|      | Level 1 | Level 2 | Level 3 | Level 4 |
|------|---------|---------|---------|---------|
| A(R) | 2 mm    | 4 mm    | 6 mm    | 8 mm    |
| B(p) | 0.2 mm  | 0.3 mm  | 0.4 mm  | 0.5 mm  |
| C(d) | 0.2 mm  | 0.4 mm  | 0.6 mm  | 0.8 mm  |

According to Table 1, there are three factors and four levels, thus we could selected $L_{16}$ orthogonal table to plan the simulation experiments. The results were shown in Table 2.

**Table 2.** Coupling efficiency test table.

| No. | Configuration | M |
|-----|---------------|---|
| 1 | A1B1C1 | 0.063165 |
| 2 | A1B2C2 | 0.029224 |
| 3 | A1B3C3 | 0.01617 |
| 4 | A1B4C4 | 0.0096883 |
| 5 | A2B1C2 | 0.044618 |
| 6 | A2B2C1 | 0.01685 |
| 7 | A2B3C4 | 0.014221 |
| 8 | A2B4C3 | 0.0096876 |
| 9 | A3B1C3 | 0.026546 |
| 10 | A3B2C4 | 0.014007 |
| 11 | A3B3C1 | 0.0035795 |
| 12 | A3B4C2 | 0.0071622 |
| 13 | A4B1C4 | 0.01859 |
| 14 | A4B2C3 | 0.020013 |
| 15 | A4B3C2 | 0.014741 |
| 16 | A4B4C1 | 0.0013687 |

Table 2 shows that, the optimal configuration can be get from A1B1C1 configuration. According to Eq. (3), the predictive result is 0.057329 compare with the simulation result which is 0.063165.

Convert to coupling efficiency, the predictive and simulate value are 5.73 % and 6.31 % respectively, the difference which is reasonable between them can be used to predict the impact of the overlapping effect of factors.

At the meantime

$$y_k = \frac{sum\ of\ y_k\ in\ tab.2}{4} \tag{4}$$
$$y=A, B, C; k=1, 2, 3, 4$$

The coupling efficiency of each factor can be calculated by Eq. (4) (Shown in Fig. 7). Fig. 7 shows the smaller the radius of curvature R, the higher the coupling efficiency is obtained, indicating the good light gathering ability and of high coupling efficiency concave reflector compare with the plane reflector. Decreasing fibers distance p could help to improve the coupling efficiency.
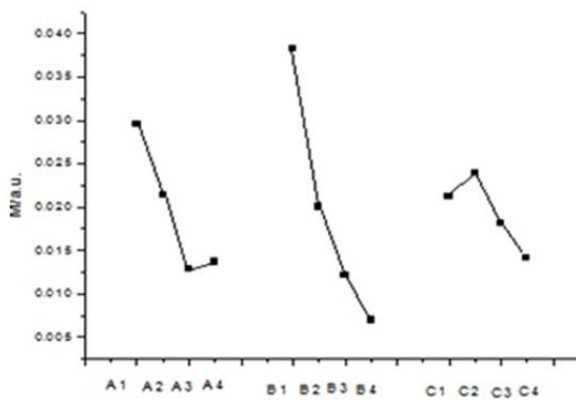


**Fig. 7.** Coupling efficiency of each factor.

## 4. Conclusions

For the analysis of complex reflective surfaces, the introduction of TP model can effectively improve the efficiency of this type of sensor design. The results show that the proposed model can simulate the output response in an effective way. Using the Taguchi method to obtain optimized configuration A1B1C1 whose coupling efficiency can reach 6.31 %. While the smaller the radius of curvature R and fibers distance p, the higher the coupling efficiency. As the numerical analysis method has certain defects, tp modeling in the specific design of the sensor also needs to be calibrated. Further work should be focus on that.

## Acknowledgements

## References

[1]. Chengqi Li, Xiaodong Zhang, Ping Zhang, Study on the Compensation Technology for the Intensity Modulated Two-Circle Coaxial Fiber Optic Displacement Sensor, in *Proceedings of the IEEE International Conference on Mechatronics and Automation*, Beijing, China, 7 – 10 August 2011.

[2]. P. Puangmali, K. Althoefer, Mathematical modeling of intensity-modulated Bent-tip optical fiber displacement sensors, *IEEE Trans. Instrum. Meas.*, 59, 2010, pp. 283–291.

[3]. J. B. Faria, A theoretical analysis of the bifurcated fiberbundle displacement sensor, *IEEE Trans. Instrum. Meas.*, 47, 3, 1998, pp. 742–747.

[4]. P. B. Buchade, A. D. Shaligram, Influence of fiber geometry on the performance of two-fiber displacement sensor, *Sens. Actuators A*, 136, 2007, pp. 199–204.

[5]. S. Hadjiloucas, J. Irvine, J. Bowen, Radiometric analysis of the light coupled by optimally cut plastic optical fiber amplitude modulating reflectance displacement sensors, *Rev. Sci. Instrum.*, 71, 2000, pp. 3007–3009.

[6]. Yang Huayong, Research on the Mathematical Model and Key Technologies of the Reflective Intensity Modulated Fiber-Optic Sensor, *Changsha: National University of Defense Technology*, 2002, pp. 35-39.

[7]. Yang Huayong, Lu Haibao, Influence on the intensity modulation of a reflective fiber optic displacement sensor induced by reflector shape, *Optics and Precision Engineering*, 10, 4, 2002, pp. 379-382.

[8]. A. D. Gaikwad, J. P. Gawande, A. K. Joshi, *et al.*, An intensity-modulated optical fiber sensor with concave mirror for measurement of displacement, *Optical Society of India*, 42, 4, 2013, pp. 300–306.

[9]. Shan Ming-Guang, Peng Huan, Zhong Zhi, *et al.*, Influence of Reflector Shape on the Intensity Modulation of Fiber Optical Distance Sensors, *Acta Photonica Sinica*, 39, 12, 2010.

[10]. Li Y. F., Study on a New Reflective Optical Fiber Sensor, *Chinese Journal of Scientific Instrument*, 26, 10, 2005, pp. 1097-1100.

[11]. Yi-Chin Fang, Yih-Fong Tzeng, Kuo-Ying Wu, A Study of Integrated Optical Design and Optimization for LED Backlight Module with Prism Patterns, *Journal of Display Technology*, 10, 10, 2014, pp. 840-846.

[12]. Jr-Yun Hua, Che-Ping Linb, Shih-Yu Hungb, *et al.*, Semi-ellipsoid microlens simulation and fabrication for enhancing optical fiber coupling efficiency, *Sensors and Actuators A: Physical*, 147, 2008, pp. 93–98.

[13]. C. T. Su, C. C. Chiu, H. H. Chang, Parameter design optimization via neural networks and the genetic algorithm, *J. Ind. Eng. Int.*, 7, 2000, pp. 224–231.

[14]. G. J. Wang, J. C. Tsai, P. C. Tseng, T. C. Chen, Neural-Taguchi method for robust design analysis, *J. CSME*, 19, 1998, pp. 223–230.

# Optic Fiber Sensing IOT Technology and Application Research

## Wenjuan Zeng, Haibo Gao

School of Information Science and Engineering, Hunan International Economics University,
Changsha, 410205, China
Tel.: 86-0731-88140728
E-mail: matlab_wjf@126.com

**Abstract:** The growth of the Internet of Things (IOT) industry has become a new mark of the communication domain. As the development of the technology of the IOT and the fiber-optical sensor, the combination of the both is a big question to be discussed, and the fiber-optical IOT also has a good development prospect. This article first introduces IOT's current status, the key technology, the theoretical frame and the applications. Then, it discusses the classification of the optical fiber sensor as well as the development and its application's situation. Lastly, it puts the optical fiber sensing technology into the IOT, and introduces a specific application which is used in the mine safety based on the fiber-optical IOT. *Copyright © 2014 IFSA Publishing, S. L.*

**Keywords:** Fiber-optical sensor, Internet of Things (IOT), Fiber-optical IOT, Machine to Machine (M2M), Mine Safety Monitoring.

## 1. Introduction

Internet of Things (IOT) is an important part of China's strategic emerging industries, it is a new round revolution in information technology after the computer, the Internet and mobile communications, it is driving a new round of information wave on information technology, and it has deeper applications in all walks of life. On the basis of the computer Internet, through radio frequency identification, infrared sensors, global positioning systems, laser scanners and other information sensing device, according to the agreed protocol, anything are connected with the Internet, information exchange and communication are realized to achieve intelligent identify, locate, track, monitor and manage in a network, the Internet is still the core and foundation, but for an extension and expansion of the Internet, it is possible to interconnect with a variety of networks and communicate seamlessly with multi-networks.

Optical fiber sensing technology is developed rapidly in recent years, it is new technology, and it has been widely applied in the fields of energy, health care, aerospace, chemicals, environment, etc. Compared to traditional detection technology, optical fiber sensing technology is with remote transmission, multi-parameter, multiplexing capability, ease of networking, real-time online, interference, intrinsic safety, etc., it is facilitated to analyze comprehensively all aspects of the information, it can greatly enhance the existing security monitoring and production automation. In recent years, various special features of fiber, active devices, passive devices have come out in the international community, and it has been greatly improved in terms of performance, the price is reduced accordingly, thus the fiber optic sensor technology is greatly promoted

in the information transmission and sensing aspects, and it has a wide range of applications.

In the development of the Internet of Things (IOT), the fiber-optic communications network is capable of carrying higher bandwidth, and t is suitable for long distance transmission, it is very suitable for expanding IOT applications, it has been applied in network layer of IOT (the Internet of Things). A large variety of sensors are used in the bottom layer of IOT, initial information is provided for IOT perception layer, the rapid rise of the optical fiber sensor has integrated a great achievement which has achieved in many fields, such as fiber optic technology, laser technology and optical detection, the optical fiber sensor has many advantages in promoting the development of IOT, it is widely used in various fields of national economy and people's lives.

## 2. Things Technology

IOT is defined by radio frequency identification (RFID), infrared sensors, global positioning systems, laser scanners and other information sensing device, according to the agreed protocol, anything is connected with the Internet, information exchange and communication are realized to achieve intelligent identification, positioning, tracking, monitoring and management in a network [1].

### 2.1. Architecture of Things

In the system study, the system architecture is a primary premiseto guide specific design, the architecture design is also expected to decide on the technical details, application patterns and trends of things. At present, when the domestic researchers describe the architecture of things, USN high-level architecture will described as a basis in ITU-T recommendations, which is divided into five levels for bottom-up, such as sensor networks, access network, backbone network, middleware and application platforms. In addition to ITU, other international standardization organizations describe and research IOT architecture from different sides, such as the European Telecommunications Standards Institute and the Technical Committee of the machine, they present a simple M2M framework from the perspective of end-to-end, network domain is formed by M2M core network, the M2M application domain will be is connected with the M2M devices domain. This is a simplified architecture of USN.

M2M is machine-to-machine abbreviation, i.e. "machine to machine" abbreviation, it was understood that human-to-machine (man-to-machine), machine-to-human (machine-to-man), etc., communication technology is used to achieve intelligent and interactive link seamlessly between human, machine and system. M2M device is able to answer the data request in some equipment or apparatus to automatically transfer the data contained in these devices. M2M communication is consistent with the core idea of things, the difference is the concept of things, technology and applications which are used in a broader scene. And then M2M focus on wireless communication network applications, it is a major way of IOT applications. Things architecture is now widely considered to be divided into three things, such as the perception layer, network layer and application layer [2]. As is shown in Fig. 1.
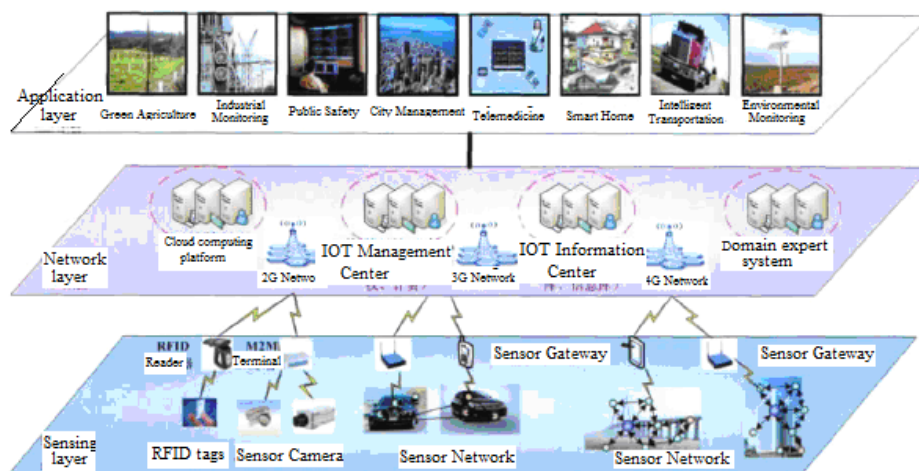


**Fig. 1**. Architecture of Things.

Sensing layer consists of various types of acquisition and control modules, such as RFID tags and readers, sensor networks, temperature, sound, vibration sensor, two-dimensional bar code, a variety of terminals. The underlying information is mainly collected in the perception layer, the data acquisition and device control functions is completed in IOT applications. it is the basis of IOT applications and

development. Sensing layer typically comprises a data acquisition and short-distance transmission, information and data are collected by sensing devices, they are passed to the gateway via bus or short-distance wireless transmission technology, the information is submitted to the upper layer.

Network layer is built on the basis of existing networks, the existing network integration and expansion are made, a network is the formed by which multiple heterogeneous networks coexist with a variety of organic integration networks, the functions of data transmission are primarily assumed, there is the ability to transmit data in the perceived layer with accessibility, high reliability, high security, especially long-distance transmission. Meanwhile perception layer also includes part of the perception of data management and processing techniques [3].

Application layer is the driving force and purpose of the development of things. The main function of the application layer is the perception and transmission information to be analyzed and processed, the correct control and decision-making, intelligent management, applications and services are made. This layer solve the problem of information processing and human-machine interface. Specifically, the data coming from the network layer is to be processed by various information systems, and they interact with people through a variety of devices. It can be divided generally into two sub-layers: the application layer and the layer of the terminal devices.

## 2.2. The Key Technology of Things

IOT is a comprehensive body of information technology, communications, sensors and automatic control and other technologies, IOT technology can be divided into three levels with the application layer, network layer and perception layer. In the perception layer, the key technologies involve in sensor technology, RFID technology, wireless communication, self-organizing networks, middleware and embedded systems. At the network layer, it mainly includes heterogeneous network convergence, M2M, cognitive radio technology and network context-aware technology. At the application layer, according to the architecture, the main techniques have to take into account the massive data storage, data sharing, data mining, cloud computing, resource virtualization, software architecture, etc. [4]. Things technology architecture is shown in Fig. 2.

In the perception layer, the perception layer technology includes data collection techniques, short-distance communication and collaborative information processing technology [5]. In data acquisition techniques, sensor can feel the measured information, and according to certain rules, the detect information can be converted into electrical signal or other forms of the required information, which are output to meet the information transmission, processing, storage, display, recording and control requirements. RFID technology achieves non-contact transmission of information by the radio frequency signals and space electromagnetic coupling, and the object is identified by the information conveyed. RFID technology can be seen as device identification technology and can also be seen as one of short-range communications technology. In the short-range communication technology, a common ZigBee technology is a short-range and low-power wireless transmission technology, it is suitable for carrying data traffic in small business.
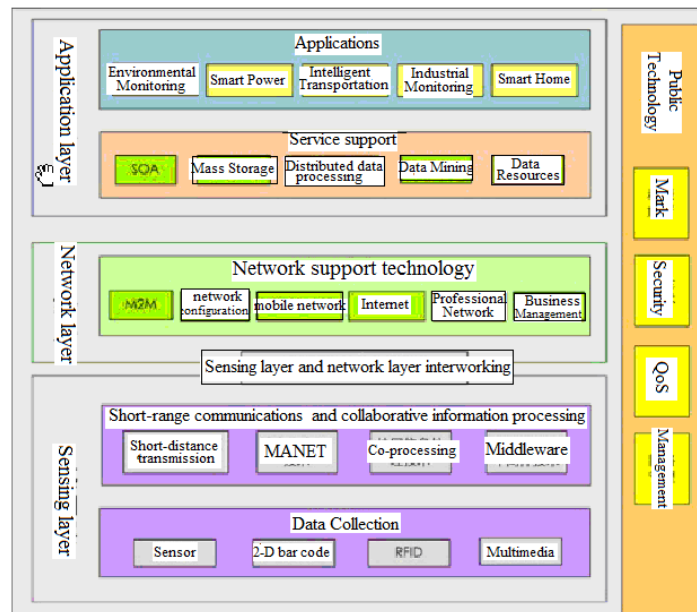


**Fig. 2.** Things technology architecture.

At the network layer, we mainly consider the networking and communications technology. Network is infrastructure of the IOT information transmission and support services, through ubiquitous connectivity features, perceptive Informatics is achieved and transferred in high reliability and high security. In addition to considering traditional mobile communication networks, the Internet and other technologies, our main consideration is heterogeneous network convergence technology, a variety of wireless and wired networks are organically fused to form a unified information exchange network, the information silos are excluded, a global information is integrated.

In the application layer, compared with the general network, there is massive computing and processing sensory information, a major problem is considered after the application of large-scale development of things, data fusion, efficient storage, semantic analysis, parallel processing and data mining and other functions are realized in the mass information [6].

In addition, IOT public administration and support technology is the most important issue, which are considered in the construction of things, because things have openness, inclusiveness and autonomy, so we have to study the new management model and key technologies of IOT, as well as security technology is more optimized to ensure the normal development of IOT [7-13].

## 3. Development and Application of Optical Fiber Sensing Technology

### 3.1. Fiber Optic Sensor Characteristics and Classification

Fiber optic sensor not only has the basic technology with traditional sensors, but also has many unique advantages. When the optical fiber sensor uses the light transmission through the optical fiber, its phase, polarization, wavelength and other parameters change with external factors, the corresponding changes are sensed in the external physical quantity, the sensing measurements are realized. The basic working principle of the optical fiber sensor is that the light from the light source is fed to the modulator via an optical fiber, after the measured parameter is interacted with the light which enters modulation region, the optical properties of light (e.g., light intensity, wavelength, frequency, phase, Modifier state, etc.) are resulted in change, it is referred to as the modulated signal light, then which is fed to the light detector through the optical fiber, after demodulation, the measured parameters are obtained [14]. Fiber optic gyro sensor principle is shown in Fig. 3.

Compared with the conventional sensor, optical fiber sensor has many advantages, such as that the

broadcast information is transmitted, electromagnetic interference is immuned, corrosion resistance, anti-hypertension (high pressure). By using a phase-coherent technology, it has high sensitivity, and light weight, small size, and applicability. And its frequency is bandwidth, there is the wide dynamic range, the reliability and accuracy are improved on the measurements, in addition, fiber optic sensors can also detect various physical quantities, this research is a major breakthrough within the range of the sensor.
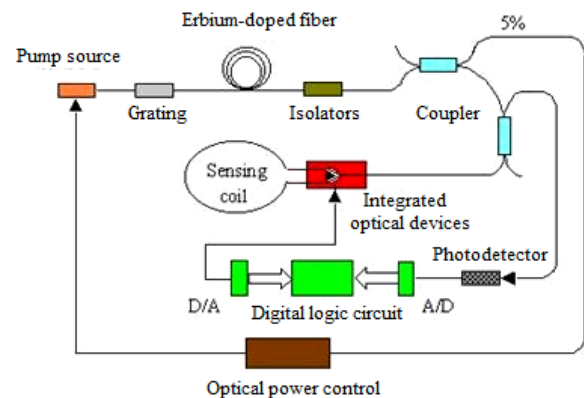


**Fig. 3.** Fiber optic gyro sensor principle.

Fiber optic sensor can be divided into two categories by sensing principle, one is called as functional sensors, the optical fiber role are both the signal transmission and its sensitive, it has a unity of sense and mass characteristics. Another is known as non-functional sensors, which only serves as an optical fiber transmission, and the feeling of the signal is to use the other to complete the optical sensor. By modulation principle of light in the fiber, fiber optic sensors can be divided into several forms, such as light intensity, phase modulation, polarization modulation and wavelength modulation, etc.

### 3.2. Applications and Developments of Optical Fiber Sensors

Fiber optic sensor is used to measure the magnetic, acoustic, pressure, temperature, acceleration, gyroscope, displacement, surface, torque, photoacoustic, current, physical strain [15]. It has wide range of applications, it is mainly in the following areas.

1) Interferometer gyroscopes and Grating Pressure Sensors applications in urban construction, such as bridges, dams, oil fields. Fiber optic sensors can be embedded in the concrete, carbon fiber reinforced plastic and various composite materials for testing stress relaxation, stress of construction and dynamic load stress, in order to assess the performance of the bridge structure of short-term

construction phase and long-term operation state. FBG settlement sensor application is shown in Fig. 4.



**Fig. 4.** FBG settlement sensor application.

2) The temperature, current and other parameters need to be determined in the power system, such as the inside detection of high-voltage transformer and large motor stator and rotor temperature, because electromagnetic type sensors is susceptible to electrical interference, which can't be used in such occasions, only fiber optic sensors can be used. Distributed fiber optic temperature sensors are developed in recent years, it is a high-tech for real-time measurement of space temperature field distribution. Optical fiber temperature sensor application in on-line monitoring of power high-voltage switch  is shown in Fig. 5.
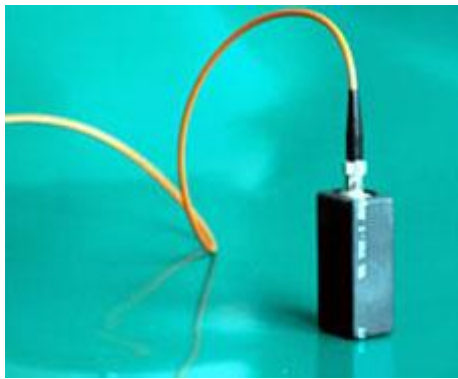


**Fig. 5.** Optical fiber temperature sensor application in on-line monitoring of power high-voltage switch.

3) Fiber optic sensors can be used to temperature measurement on flammable materials production processes and equipment. Fiber optic sensor is essentially a anti-fire and anti-explosion device, it does not require the use of explosion-proof measures, and it is very safe and reliable. Compared with electrical sensors, both costs are reduced and the sensitivity can be improved [16].

In addition, fiber optic sensor is also possible to monitor the railway, rocket propulsion systems, and application of well testing, etc., fiber optic sensors have a variety of the application, it can be applied to all sectors of our country, we believe that optical fiber sensing technology has great market potential.

## 4. To Investigate the Optical Fiber Sensing Technology in the Internet of Things

### 4.1. Optical Fiber Sensing Technology Application in Sensing Layer

A wide variety of sensors are used in the Internet of Things, fiber optic sensors are different from the traditional sensors and has a lot of advantages, the application of the Internet of Things will be unparalleled. In the application of Things perception layer, on the one hand, fiber optic sensors can be used to detect a wide variety of environments, they bring things more timely detection information, and they are not impacted by the detect environment. On the other hand, the entire network can be brought to a higher detection sensitivity, the accuracy and the reliability of the network information are ensured. Also, its sense unity characteristics is suitable for a distributed sensing system, the continuous sensing detection and transmission are realized over long distance lines, which is very necessary in IOT network, it is suitable to build network architecture of things [16].

### 4.2. Application Case Study

In the connectivity platform cloud technology research of the mine fiber IOT, we focus on mine safety detection problem, we propose a universal fiber optic sensor IOT interfaces, a fiber-optic sensor IOT is built [17]. System is connected by the user, the Internet, cloud platform, and fiber optic sensors, wherein the optical fiber sensor is a main way to collect information for monitoring mine gas concentration, temperature, level, vibration, humidity, dust concentration, harmful gases, etc. In the cloud connected platform, the collected information is acquired with a wide range of the optical fiber sensors and its different parameters, and through signal conversion, unified transport protocol and data format are uploaded ultimately to the control room or the Internet on Inoue, but also the terminal control command is accessed, the command is converted to the instruction format, which can be identified in terminal device, that is sent to the device control terminal for device to be controlled. Internet function is to transmit information. This system of coal mine safety provides a more effective solution, the ability and level of coal mine safety testing have been to greatly enhanced [17]. Fiber optic ring network transmission of security monitoring system is shown in Fig. 6.
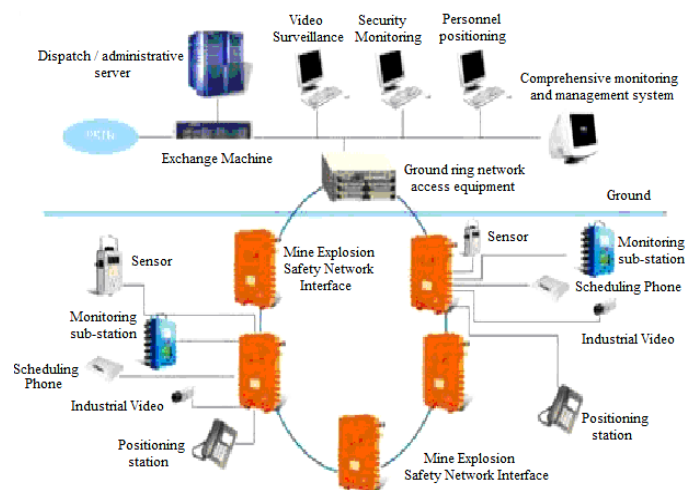
**Fig. 6.** Fiber optic ring network transmission of security monitoring system.

## 5. Conclusions and Outlook

IOT framework technology and fiber optic sensing technology has been studied in this paper, the optical fiber sensing technology applications are analyzed in IOT perception layer, and the specific applications of the optical fiber sensing things are studied in mine safety testing, that fiber-optic sensor network is found to provide greater protection for mine safety, based on this, we can predict that the fiber-optic sensing things will have the greater development and application space in the future.

## Acknowledgements

## References

[1]. Wu Bende, Summary about The Internet of Things (Part 1), *Cable Television Technology*, 18, 1, 2011, pp. 107-110.

[2]. Wu He Quan, Review on Internet of Things: application and challenges, *Journal of Chongqing University of Posts and Telecommunications (Natural Science Edition)*, 22, 5, 2010, pp. 526-531.

[3]. Fan Xuemei, A Survey on Development of Internet of Things, *Computer Measurement & Control*, 19, 5, 2011, pp. 1002-1004.

[4]. Zhao Haixia, Analysis and Development of IOT key technologies, *Science and Technology of West China*, 09, 14, 2010, pp. 25-26.

[5]. Liu Huajun, Research on Key Technology for Internet of Things, *Computer Era*, 7, 2010, pp. 4-6.

[6]. L. Schmidtobreick, S. Bagnulo, IOT Overview: Optical Multi-Object Spectrographs, in *Proceedings of the ESO Instrument Calibration Workshop, ESO Astrophysics Symposia European Southern Observatory,* 2008, pp 75-80.

[7]. Ding Lu, Jia Ni, The Overview of Internet of Things and Sensor Technology Development, *China Instrumentation*, 9, 2013.

[8]. Conti P., The Internet of Things, *Communications Engineer*, 06, 2006, pp. 20-25.

[9]. Rolf H. W., Romana W., Internet of Things, *Springer-Verlag*, Berlin Heidelberg New York, 2010, pp. 1-4.

[10]. Welbourne E., Battle L., Cole G., Building the Internet of Things Using RFID: The RFID Ecosystem Experience, *Internet Computing*, 03, 2009, pp. 48-55.

[11]. Kortuem G., Kawsar F., Fitton D., Smart objects as building blocks for the Internet of things, *Internet Computing*, 01, 2010, pp. 44-51.

[12]. Koshizuka N., Sakamura K., Ubiquitous ID: Standards for Ubiquitous Computing and the Internet of Things, *Pervasive Computing*, 04, 2010, pp. 98-101.

[13]. Michahelles F., Karpischek S., Schmidt A., What Can the Internet of Things Do for the Citizen? in *Proceedings of the Workshop at Pervasive Computing*, 04, 2010, pp. 102-104.

[14]. Wu Jie, Xue Lingling, Research and development of optical fiber sensor, *Laser Journal*, 28, 5, 2007, pp. 4-5.

[15]. Wang Pengyu, Optical fiber sensors application of the key technology in the internet of things, *Electronic Design Engineering*, 20, 22, 2012.

[16]. Qi Haifeng, Liu Tongyu, etc., Accelerometers Based on Fiber Optic Interferometer, *Shandong Science*, 21, 6, 2008, pp. 23-26.

[17]. Hou Peihu, Fu Xiaoning, etc., Research on coal mine cloud connection platform of fiber internet of things, *Shandong Science*, 24, 2, 2011, pp. 41-46.

---

# The Low-frequency Compensation of the Vibration Sensor's Amplitude-frequency Characteristics

**Lifeng Pan**

School of Electrical & Information Engineering, Hunan International Economics University,
Changsha, 410205, China
Tel.: 86-0731-88760386
E-mail: matlab_wjf@126.com

**Abstract:** The hydropower generating units' vibration parameter is an important indicator to monitor its roll-stabilization. To measure the low-frequency vibration of the large and middle scale of hydropower generating units, according to frequency characteristic compensation principle of the vibration sensor, a low-frequency compensating circuit was designed to extend the frequency characteristic to the low frequency region. The mathematical model of the magnetoelectric drommeter vibration sensor and the design of the compensation circuit were detailed. The amplitude-frequency characteristics of the sensor and its mathematical model were comparatively analyzed before and after compensation respectively. The experimental result shows that the design could extend the amplitude-frequency characteristics to the low frequency region, and have good sensitivity and linearity. *Copyright © 2014 IFSA Publishing, S. L.*

## 1. Introduction

Hydro accident showed vibration fault [1]. Medium-sized hydro group transfer frequency is low, about 1-2 Hz, and unit water vortex-induced vibration which hydro draft Tube produces is lower, about 1/5 to 1/3 of rotation frequency. In addition, once the accident occurred during hydropower units operation, which load shedding and load rejection transition process, vibration signal frequency will be lower [2]. In magnetic vibration velocity sensors, smaller natural frequency, the greater the volume. Considering the ease of installation of the sensor, the magnetic vibration velocity sensor is widely used in engineering, and its natural frequency limit of is about 2.5 Hz, but also the measurement frequency is higher and 2 to 3 times than the natural frequency of

vibration sensor [3]. If the sensor is without compensation, and the direct the measurement is operated, the measurement is not accurate. How to design compensation circuit, and the vibration frequency characteristics is allowed to expand the low-frequency or to meet the requirements of the low-frequency test, it is the focus of the study.

## 2. Establish and Validate of the Vibration Sensor Model

### 2.1. Operating Principle of the Oscillation Sensor

Magnetic vibration velocity sensors have been widely applied in low-frequency sensor, because of

these advantages which their output signal is large, the follow-up circuit is simple, anti-jamming capability is strong. As shown in Fig. 1, the vibration sensor is fixed with a permanent magnet inside, and in the outer casing, the magnetic circuit of the magnet is enclosed within the housing. Two circular spring upper and lower is fixed between the magnet and the housing. They support the coil, and are surrounded by the coil with mass m and without touching the magnet. When the external action of the vibration sensor, the relative motion is made between the magnet and the coil, the coil is cutting magnetic induction line, and is generating a voltage signal.
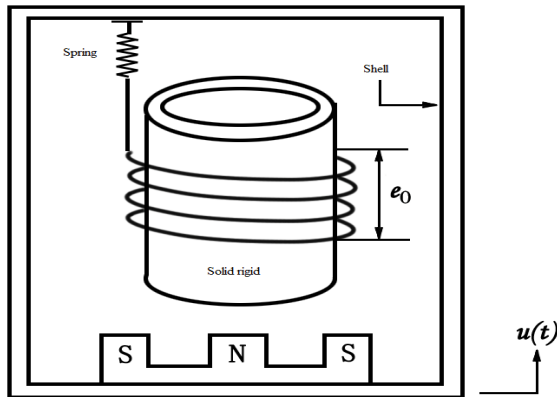


**Fig. 1.** Magnetic vibration sensor structure diagram.

## 2.2. Model Building

It is an inertial sensor, the mechanical model can be simplified as a single system with the degree of freedom, which is composed of three-part system of a spring with elastic coefficient k, inertial mass m and damping C [4] as shown in Fig. 2.
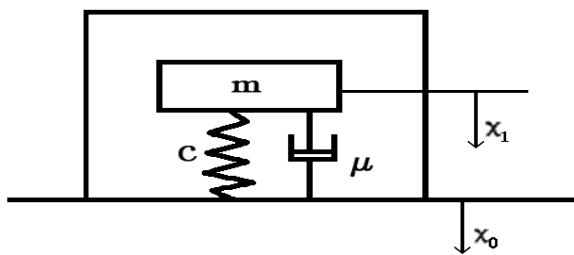


**Fig. 2.** Mechanical model.

The motion equation is

$$mx_1'' + \mu(x_1' - x_0') + c(x_1 - x_0) = F(t), \qquad (1)$$

where m is the inertial body mass (coil);

C is the spring stiffness;

$\mu$ is the Damping;

$x_0$ is the absolute displacement of the base housing;

$x_1$ is the absolute displacement of the inertial body;

$x_0'$ is the speed of the base housing;

$x_1'$ is the speed of the inertia body;

$x_1''$ is the acceleration of the inertial body;

$F(t)$ is the forces acting on the inertial body;

Take $F(t) = 0$;

$\omega_0^2 = c/m$, $\omega_0$ is the characteristic angular frequency;

$2\xi_0\omega_0 = \mu/m$, $\xi_0$ is the damping ratio;

$x_r = x_1 - x_0$, Mass displacement is relative to vibration sensor housing. (1) by the Laplace transform as follows:

$$H(s) = \frac{X_r(s)}{X_0(s)} = \frac{s^2}{s^2 + 2\varsigma_0\omega_0 s + \omega_0^2} \qquad (2)$$

Vibration sensors coil is are cutting magnetic induction line, the output voltage is:

$$u_0 = Blx_r' \qquad (3)$$

By Laplace transform as follows:

$$U_0(s) = BlsX_r(s) = k_0 sX_r(s), \qquad (4)$$

which B is the magnetic field strength;

$l$ is the length of the coil which is cutting magnetic field lines;

$k_0$ is the sensor sensitivity coefficient.

By the Formula (2), (4), a vibration sensor output response:

$$\begin{aligned} U_0(s) &= k_0 H(s) sX_0(s) \\ &= \frac{-k_0 s^2}{s^2 + 2\xi_0\omega_0 s + \omega_0^2} sX_0(s) \end{aligned} \qquad (5)$$

Vibration sensor transfer function is:

$$G_1(s) = \frac{-k_0 s^2}{s^2 + 2\xi_0\omega_0 s + \omega_0^2} \qquad (6)$$

In CDJ-Z2.5C vibration sensor as a reference, to establish the mathematical model. Natural frequency $f_0$=2.5±10 % Hz, take value 2.5. Damping is $\xi_0 = 0.7 \pm 10\%$, take value 0.75. $\omega_0^2 = (2\pi f_0)^2$ =246.74, $2\xi_0\omega_0 =$ 23.56. If $k_0$ =1800, the Formula (6) can be written as:

$$G_1(s) = \frac{-1800 s^2}{s^2 + 23.56 s + 246.74} \qquad (7)$$

Matlab simulating curve with the amplitude-frequency characteristic, as shown in Fig. 3, curve B is the simulation results.
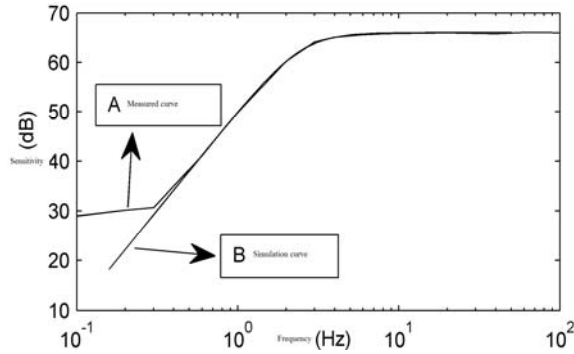


**Fig. 3.** Amplitude-frequency characteristic curve.

### 2.3. Verify Model

Equipment used in the experiment: one CDJ-Z2.5C vibration sensor, an integrated vibration tester. The vibration sensor is put vertically on the vibration generator, the output of the sensor is directly connected to the tester's input. Set the output vibration level, vibration level is 0.5 cm/s. Table 1 shows the raw data which is collected by the vibration.

**Table 1.** Original vibration data.

| 0.5 Vibration level data (before compensation) | | | |
|---|---|---|---|
| Frequency (Hz) | Voltage (mV) | the measured vibration level (cm/s) | Sensitivity (mV/cm·s⁻¹) |
| 0.1 | 0.01288 | 0.465 | 28 |
| 0.2 | 0.01088 | 0.485 | 32 |
| 0.3 | 0.01641 | 0.483 | 34 |
| 0.4 | 0.02689 | 0.483 | 56 |
| 0.6 | 0.05101 | 0.452 | 113 |
| 0.8 | 0.10522 | 0.522 | 201 |
| 1 | 0.15651 | 0.507 | 308 |
| 2 | 0.53186 | 0.519 | 1023 |
| 4 | 0.87278 | 0.487 | 1793 |
| 6 | 2.47287 | 1.292 | 1913 |
| 8 | 1.47976 | 0.759 | 1949 |
| 10 | 1.1035 | 0.562 | 1962 |
| 20 | 0.90408 | 0.453 | 1993 |
| 40 | 0.92791 | 0.476 | 1948 |
| 60 | 0.96076 | 0.479 | 2007 |
| 80 | 0.96471 | 0.482 | 2001 |
| 100 | 0.96373 | 0.484 | 1992 |

**Note:** Sensitivity = voltage / vibration level, the unit is mV/cm·s⁻¹.

In Table 1, the sensitivity is the voltage which is normalized by dividing the vibration level, unit is mV·cm⁻¹. The measured amplitude-frequency characteristic curve is curve A which is shown in Fig. 3. Comparison of the curves A, B in Fig. 3, it

can be seen that the simulation and measured curve are same when frequency is larger than 0.3 Hz, almost exactly. The vibration frequency is less than 0.3 Hz, output of the sensor itself is small, and because of the floor and all noise, the relative output is high. The lower the frequency, the larger the error. Comprehensive assessment is that model is feasible.

## 3. Design of Compensation Aspects

### 3.1. Compensation Principle

In order to extend the frequency response of the low-frequency magnetic vibration velocity sensors, the circuit compensation method is required. There are two compensation forms in the circuit compensates, which are feedback compensation and series compensation, and the feedback compensation is with lower natural frequency, while the damping ratio is reduced, stability is poor, but also it is easy to produce oscillations [5]. It is used in series compensation. The sensor output voltage is in series with a compensation network C(s), so that the pole of the original transfer function G1(s) is eliminated by the C(s) zero point, C(s)'s pole becomes the pole of the transfer function G(s) after passing compensation, so the low-frequency output characteristics of the sensor can been changed by changing the compensation network's poles. The transfer function of the compensation aspects were given in Literature [5-8], equation (8) below, this transfer function can be decomposed by three parallel filtering part, namely all-pass, low-pass, band-pass filtering links.

$$C(s) = \frac{s^2 + 2\xi_0\omega_0 s + \omega_0^2}{s^2 + 2\xi_1\omega_1 s + \omega_1^2}$$

$$= 1 + \frac{\omega_0^2 - \omega_1^2}{s^2 + 2\xi_1\omega_1 s + \omega_1^2} + \frac{2(\xi_0\omega_0 - \xi_1\omega_1)s}{s^2 + 2\xi_1\omega_1 s + \omega_1^2}, \quad (8)$$

where $\xi_1$ is the damping ratio of compensation aspects, which reflects the frequency characteristic in the oscillation links, and does not directly reflect the frequency response of the filter circuit. So in this paper, the damping ratio $\xi_1$ is replaced by the equivalent quality factor Q, Q is a parameter which reflects the frequency response of the filter circuit. As shown in Formula (9):

$$C(s) = \frac{s^2 + 2\xi_0\omega_0 s + \omega_0^2}{s^2 + \frac{\omega_1}{Q}s + \omega_1^2}, \quad (9)$$

where $\omega_1 = 2\pi f_1$ is the characteristic angular frequency which is compensated. After the compensation, transfer function G(s) of the vibration sensor is:

$$G(s) = G_1(s) \bullet C(s)$$

$$= \frac{-k_0 s^2}{s^2 + \dfrac{\omega_1}{Q}s + \omega_1^2} \qquad (10)$$

Compensation circuit C(s) is designed, so that $\omega_1 < \omega_0$, and Q is the best equivalent quality factor. Compensated system maintains the original vibration sensor high mechanical properties unchanged, and the natural frequency depends entirely on the compensation circuit which is connected in series, thus in compensated sensor system, the original sensor volume is small, and performance characteristics is good, but also low-frequency output characteristics is improved.

### 3.2. Vibration Sensor Compensation Circuit Design

To meet the measurement requirements of hydroelectric generating low-frequency vibration, the natural frequency of the sensor is needed to expand from 2.5 Hz to the low-frequency 0.2 Hz, to maintain the best quality factor. That is $f_1 = 0.2$ Hz, Q = 0.7. The compensation link C(s) is divided into:

$$C(s) = 1 + \frac{k_1 A_{VF} \omega_1^2}{s^2 + \dfrac{\omega_1}{Q}s + \omega_1^2} + \frac{k_2 A_{VF} \omega_1 s}{s^2 + \dfrac{\omega_1}{Q}s + \omega_1^2}, \qquad (11)$$

in the formula,

$$k_1 = \frac{\omega_0^2 - \omega_1^2}{\omega_1^2 A_{VF}}, k_2 = \frac{2\xi_0 \omega_0 - \omega_1/Q}{\omega_1 A_{VF}}$$

Among them, $A_{VF}$ for the same phase scaling circuit voltage gain.

By Formula (11), it can be seen that the compensation aspect is the parallel together with all-pass, low-pass, band-pass three aspects, the structure is shown in Fig. 4.
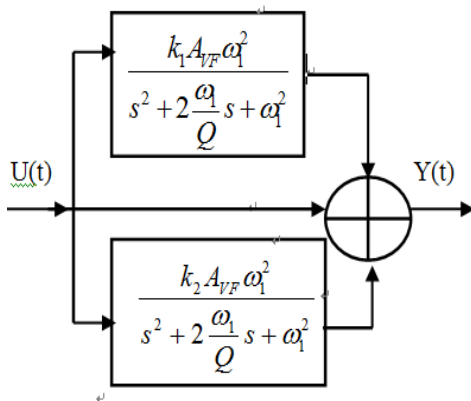


**Fig. 4**. Compensation link structure figure.

The ratio between these three gains is adjusted, zerosof the compensation link and poles of the original system are made offset, allowing the system to achieve the desired frequency characteristics. Because of the integrated operational amplifier module features itself, little DC offset will been produced, after amplification, this can't be ignored, so after the filter circuit, the DC offset is removed in series with a first-order high-pass filter circuit. The cutoff frequency should be much less than 0.1 Hz. Fig. 5 is compensation circuit wiring diagram.
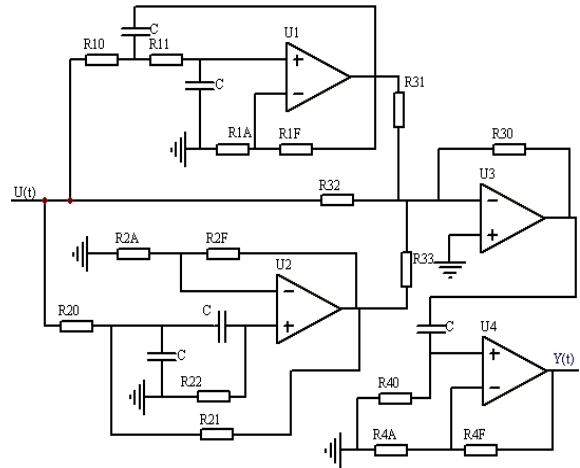


**Fig. 5**. Compensation circuit wiring diagram.

Wherein: $R_{10}$, $R_{11}$, $R_{1A}$, $R_{1F}$, C, $U_1$ constitutes a second-order low-pass filter circuit; $R_{20}$, $R_{21}$, $R_{22}$, $R_{2A}$, $R_{2F}$, C, $U_2$ constitutes a second order band-pass filter circuit; **$R_{32}$** is an all-pass circuit; $R_{30}$, $R_{31}$, $R_{32}$, $R_{33}$, $U_3$ constitute an addition circuit; $R_{40}$, $R_{4A}$, $R_{4F}$, C, U4 form a first order high pass filter. To reduce system circuit noise, each resistor in the circuit should be trillion level and below, so the capacitance value C = 10 uF to simplify the calculation, so that $R_{10}=R_{11}=R_{20}=R_{22}=R$; $R_{22}=2R$; $R_{30}=R_{32}=100$ kΩ. The design requirements were: $R_{1A}=R_{2A}=R_A$; $R_{1F}=R_{2F}=R_F$. And $V_{AF} = 1 + \dfrac{R_F}{R_A} = \dfrac{3Q-1}{Q}$, $R_A$ ‖ $R_F = 2R$, $\omega=2\pi f =1/RC$, $R_{31} = R_{30}/k_1$, $R_{33} = R_{30}/k_2$, so the parameter values of the circuit is about R = 80 kΩ, $R_A = 440$ kΩ, $R_F = 250$ KΩ, $R_{31} = 1$ kΩ, $R_{33} = 9$ kΩ. For a first-order high-pass filter, parameter is not strictly required to achieve the blocking effect. Due to the low signal to noise ratio of low frequency sensor output voltage, low-frequency amplitude of the original system is bigger than the theoretical value. $R_{20}$, $R_{21}$, $R_{22}$ resistance can be increased, so that the amplitude-frequency characteristic of the band rejection filter circuit is translated to the high frequency. In order to increase the output voltage of the sensor system, the voltage drop of the circuit is compensated. The measured data is showed in Table 2 after compensation.

**Table 2.** Measured data after compensated.

| 0.5 vibration level data (after compensation) | | | |
|---|---|---|---|
| Frequency (Hz) | Voltage (mV) | Measured vibration level (cm/s) | Sensitivity (mV/cm·s⁻¹) |
| 0.1 | 472 | 0.6 | 788 |
| 0.2 | 800 | 0.531 | 1508 |
| 0.3 | 856 | 0.510 | 1679 |
| 0.4 | 796 | 0.462 | 1725 |
| 0.6 | 864 | 0.480 | 1789 |
| 0.8 | 1031 | 0.563 | 1833 |
| 1 | 916 | 0.496 | 1846 |
| 2 | 970 | 0.504 | 1924 |
| 4 | 907 | 0.467 | 1942 |
| 6 | 2516 | 1.295 | 1942 |
| 8 | 1472 | 0.758 | 1943 |
| 10 | 1473 | 0.760 | 1943 |
| 20 | 885 | 0.455 | 1945 |
| 40 | 916 | 0.481 | 1905 |
| 60 | 943 | 0.487 | 1937 |
| 80 | 942 | 0.484 | 1946 |
| 100 | 936 | 0.487 | 1922 |

**Table 3.** Linearity relative error.

| Frequency (Hz) | Before compensation | After compensation |
|---|---|---|
| 0.1 | -0.986 | -0.595 |
| 0.2 | -0.984 | -0.225 |
| 0.3 | -0.983 | -0.137 |
| 0.4 | 0.972 | -0.113 |
| 0.6 | -0.943 | -0.080 |
| 0.8 | -0.899 | -0.058 |
| 1 | -0.845 | 0.051 |
| 2 | -0.487 | -0.011 |
| 4 | -0.100 | -0.002 |
| 6 | -0..040 | -0.002 |
| 8 | -0.022 | -0.001 |
| 10 | -0.016 | -0.001 |
| 20 | 0 | 0 |
| 40 | -0.023 | -0.020 |
| 60 | -0.007 | -0.004 |
| 80 | -0.004 | 0.0005 |
| 100 | -0.0005 | -0.012 |

## 4. Analysis

### 4.1. Development of Low-frequency

The amplitude-frequency characteristic curve before and after the system compensation can be drawn from Tables 1 and 2, as shown in Fig. 6. The curves A, B is respectively the amplitude-frequency characteristic curve before and after the system compensation [9-11]. The linearity relative errors are shown in Table 3. And generally, the-3dB frequency corresponding about 70 % of the flat area is the natural frequency of the system. For example, the compensation is not increased in circuit, if frequency is equal to 20Hz, the sensitivity is 1993, and its 70 % is 1395. From the data in the table, the natural frequencies are showed between 2-3 Hz, about 2.5 Hz, and it is the actual match. After adding the compensation circuit, if frequency is equal to 20 Hz, the sensitivity is 1945 and its 70 % is 1361, its natural frequency should be between 0.1-0.2 Hz which is seen from Table 2, approximately 0.18 Hz. It can be seen in Fig. 6 that curve A natural frequency is about 2.5 Hz, the natural frequency of curve B is about 0.18 Hz, thus the system is expanded to 13.8 times of low frequency, that is 0.18 Hz, the design requirements are meet.

### 4.3. Sensitivity

Vibration data 0.5 cm/s is for a standard vibration level, the relative error of the sensitivity is calculated by a vibration data acquisition another 0.8 cm/s vibration level, so the sensitivity stability of the compensated system is the assessed. Table 4 shows that the relative error is 0.005 or less in the sensitivity, a sensitivity of the system remains stable after compensation.

**Table 4.** Sensitivity relative error.

| Frequency (Hz) | 0.5 cm/s | 0.8 cm/s | Relative error |
|---|---|---|---|
| 0.1 | 788 | 793 | -0.006 |
| 0.2 | 1508 | 1506 | 0.001 |
| 0.3 | 1679 | 1687 | -0.005 |
| 0.4 | 1725 | 1727 | -0.001 |
| 0.6 | 1789 | 1782 | 0.004 |
| 0.8 | 1833 | 1825 | 0.004 |
| 1 | 1846 | 1850 | -0.002 |
| 2 | 1907 | 1906 | 0.0005 |
| 4 | 1942 | 1946 | -0.002 |
| 6 | 1942 | 1940 | 0.001 |
| 8 | 1943 | 1941 | 0.001 |
| 10 | 1943 | 1940 | 0.002 |
| 20 | 1945 | 1942 | 0.002 |
| 40 | 1905 | 1895 | -0.005 |
| 60 | 1937 | 1936 | 0.0005 |
| 80 | 1946 | 1949 | -0.002 |
| 100 | 1922 | 1922 | 0 |

## 5. Conclusion and Outlook

In the design of the compensation aspects, the equivalent quality factor is cited by Q, so that the compensation circuit design of the magnetic vibration velocity sensor is simple and straight victory. The low-frequency system is developed to low-frequency after compensated, there are



**Fig. 6.** Compensated amplitude-frequency characteristic curve.

sensitivity, linearity, more comprehensive analysis, these are indicating that the sensor system performance is good after compensating, the design of the compensation aspects is proved reasonably practicable.
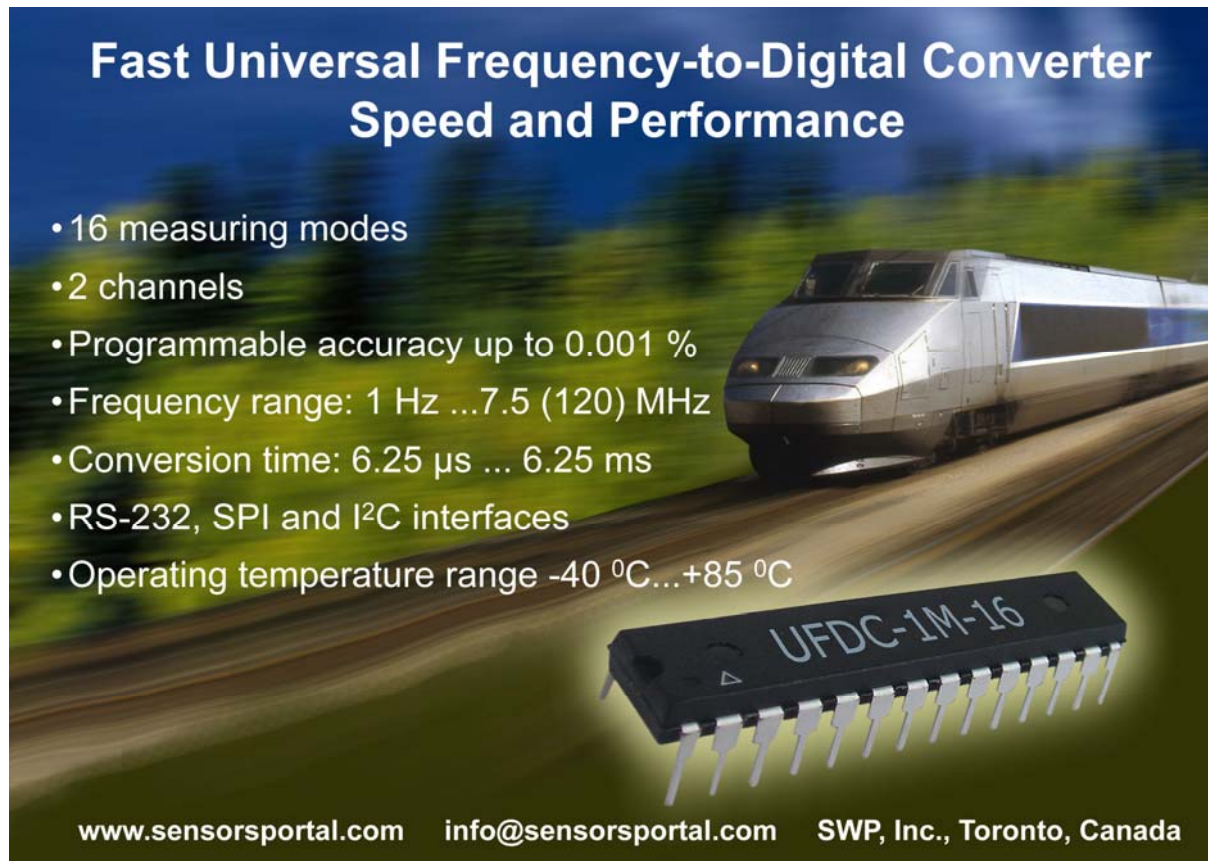
## Acknowledgements

## References

[1]. Shen Dong, Chu Fu-Tao, Chen Si, Diagnosis and Identification of Vibration Accident for Hydrogenerator Unit, *Journal of Hydrodynamics*, 15, 1, 2000, pp. 129-133.

[2]. Zheng Jinju, Yu Shuibao, Sun Xiaoqin, A New Magnetic Sensor, *Chinese Journal of Scientific Instrument*, 26, 8, 2005, pp. 40-44.

[3]. Xiao Mingwei, Yang Yongming, Zhong Yulin, Research on the measurement of low-frequency vibration of water turbine generators, *Transducer and Microsystem Technologies*, 30, 5, 2011.

[4]. Liu Yu, The Establishment of Vibration Sensor Verification Device, *Metrology & Measurement Technique*, 39, 11, 2012.

[5]. Yunxiao Fan, Hua Liu, Nong Wang, Study on Ultra-Low Frequency Vibration Sensor by Using Magnetoelectric Speedometer, *Journal of University of Science and Technology*, 20, 3, 2001, pp. 41-43.

[6]. Li Ming-Guo, Sun Rong-Xiang, Li Yong, Research on Vibration Sensor of Ultra Low Frequency, *Colliery Mechanical & Electrical Technology*, 3, 2008, pp. 37-39

[7]. Along Yu, Weiyi Huag, Research on Methods of Improvement for Amplitude/Frequency Characteristic of Vibration Velocity Transducer, *Process Automation Instrumentation*, 3, 4, 2004, pp. 289-291, 295.

[8]. Yu Shuibao, Study on optimizing technique for transfer function of the ULF absolute vibration sensor, *Chinese Journal of Scientific Instrument*, 27, 8, 2006, pp. 940-942.

[9]. Yang X. S., Low-frequency characteristic extension technique research for velocity vibration sensor, *Earthquake Engineering and Engineering Vibration*, 02, 2004, pp. 139-146.

[10]. A1 Bedoor B. O., Blade Vibration Measurement in Turbo-machinery: Current Status, *Shock and Vibration Digest*, 06, 2002, pp. 455-461.

[11]. Wang Chao, Tang Huang, Xiao Qian, The Application of Wide Spectrum Laser in Noncontact Vibration Measurement, *Microwave and Optical Technology Letters*, 12, 2009, pp. 2858-2861.

---

# Sensors & Transducers

# Challenge of the Process Variation on Designing the On-Chip EMI Sensor Array

**[1] Zixin Wang, [2] Yehua Yang, [1] Dihu Chen, [1] Min Chen, [1,] \* Tao Su**

[1] School of Physics and Engineering, Sun Yat-Sen University, Guangzhou,
Guangdong, 510275, China
[2] Guangzhou Institute of Measuring and Testing Technology, Guangzhou, Guangdong, 510030, China
[1] Tel.: 86-13418092804
\* E-mail: sutao@mail.sysu.edu.cn

**Abstract:** This paper presents our first design of the on-chip EMI sensor array. The feedback signal from the sensor array helps to determine the location of the failed circuit on the chip of an integrated circuit (IC) when external electromagnetic interference (EMI) is applied to the IC. The array structure, the feedback signal and the corresponding circuit of the sensor cell is developed. The design is implemented with a FPGA. The functionality of the design is checked through measuring the generated feedback signal of the FPGA. The feedback signal suffers instability problems due to the on-chip process variation. A set of equations are developed to describe the performance limitation that current IC technology put on the sensor array. The trade-off between the timing and the spatial resolutions of the array is analyzed. The conclusion of the paper shows the necessary conditions to make the measurement method practical. *Copyright © 2014 IFSA Publishing, S. L.*

**Keywords:** IC, EMI, Sensor, FPGA, Process Variation.

## 1. Introduction

When EMI is applied on an IC, the EMI signal is spread in the on-chip power distribution network (PDN). Some locations of the chip will be hot-spots [1]. At those hot-spots, the transistor circuits suffer great disturbance and even fail. To optimize the immunity of the IC, it is important to find the distribution of the hotspots. Therefore, it is interesting to measure the two-dimension (2D) EMI distribution in the PDN.

The most popular method to study EMI of ICs in a laboratory environment is the direct power injection method [2], which is sketched in Fig. 1. Under that environment, the on-chip EMI distribution has several important properties:

- The EMI signal comes from external sources.
- Monitoring locations are spread on the chip.

- The response of the IC to EMI is in real time.
- The IC is forced to fail in the immunity test.

The 2D EMI measurement method should match the aforementioned properties of EMI. Moreover the measurement itself should bring modification on the PDN as less as possible.
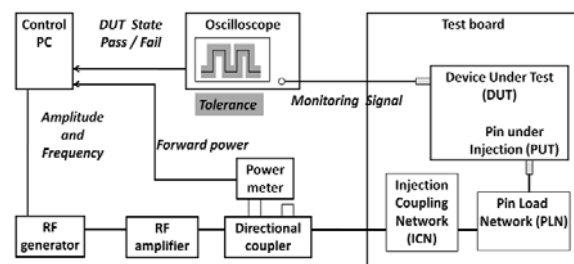


**Fig. 1.** Immunity Measurement Setup.

Measuring signals in PDN is difficult because the PDN is embedded on the chip inside the package. Several on-chip probing systems have been reported since 1990s [3-21]. However, when applying those systems to measure the 2D on-chip EMI in immunity test environment, following problems appear:

- The measured signals have to be stored first and then read out afterwards [3-8]. They are not suitable for real-time monitoring.

- There are control, switching, storage, buffering and other associative circuits [5-6, 9-19]. If those circuits fail due to their local EMI, the measured signals at target location cannot be properly read out. The location of the EMI hotspot cannot be determined.

- The target signal has to be internally generated in a repeated way [5-8]. They are not suitable to measure external signal with unpredicted waveform.

- Additional PDNs are inserted for probing circuits [8, 10-11, 20-21]. The measure fixture may modify the host PDN considerably.

- Multiple pins are required to measure and read the target signal of single location [8]. Appling that probing circuit in a massive way required too many pins and is thereby impractical.

The solution we propose in this paper is an on-chip EMI sensor array (EMISA). The array contains sensor cells distributed uniformly on the chip. The cells can send feedback signals indicating the cells' status. Sensor cells generate their feedback signals independently from each other. During the operation, the cells sense their local supply voltage. If the EMI shifts the local supply voltage by a certain threshold, the corresponding cell on that location fails and can no longer generate the correct feedback signal. By reading the feedback signals of the cell array, the failed cells can be identified. The location of the failed cells corresponds to the location in the PDN where severe EMI are presented. The EMISA performs the following operation mechanism:

- An EMISA has multiple sensor cells distributed on the chip.

- The operation status of cell is determined by only its local supply voltage.

- The cell status is presented by the feedback signal generated from the cell.

- The feedback signal of a cell can be accessed in real time.

- The propagation of the feedback signal from the target cell to off-chip circuit does not rely on circuit at any other location.

- The combination of the feedback signals of whole array form a feedback pattern.

- Sensor cells at the EMI hotspots fail during the immunity test.

- The feedback pattern implies locations of the failed cells.

- The locations of the failed cell show the distribution of the on-chip EMI hotpots.

Obviously, the EMISA has no storage circuits, no center control circuits, and no switch circuits.

Watching the EMI at one location does not rely on the operation of any circuits at other locations. It is suitable to measure the on-chip EMI distribution in the immunity test environment.

This paper is organized as the following. The second section introduces the circuit structure and the operational mechanism of the proposed EMISA. The third section implements the sensor array with a FPGA. The feedback signals generated by the FPGA are presented. Based on the obtained pattern of feedback signals, problems of EMISA are pointed out. The fourth section discusses the origins of the problem. The limitation factors on the performance of EMISA are analyzed. The final section is the conclusion.

## 2. Principle and Design

The EMISA presented in this paper is called TSCI EMISA for the following reasons: the feedback signals are designed and analyzed in Time domain; the feedback signals from cells are assembled in Series and share a common output channel; the feedback signals are connected to the detector in a Conducted way; and the feedback signals from all cells have the Identical waveform.

### 2.1. Feedback Signal

The structure of the TSCI EMISA is shown in Fig. 2. The parameters of the array are given in Table 1. Each row (column) has a signal propagation path and a port. A signal propagation path starts with the port and ends at the last cell on the other side of a row (column). Outputs of sensor cells of the same row (column) are directly connected to the same signal propagation path. A signal propagation path for a row of cells is a row path. Its port is a row port. The signal propagation path for a column of cells is a column path. Its port is a column port.

A sensor cell contains a pulse generator and two delayers. All sensor cells have the same pulse generator. However, their delayers are different from each other. The generator produces periodical pulses. The pulse to the row path is delayed by a time proportional to the column index of the cell. The pulse to the column path is delayed by a time proportional to the row index of the cell.

Pulses of different cells on a row (column) arrive at the port at different time. Their arrivals are uniformly spaced in time domain. A pulse sequence thereby appears on the port. The signal seen on a port is called monitoring signals (MS). The expected regular pattern of MS in the normal operation is sketched in Fig. 2c. The pattern is repeated for every $T_{CLK}$.
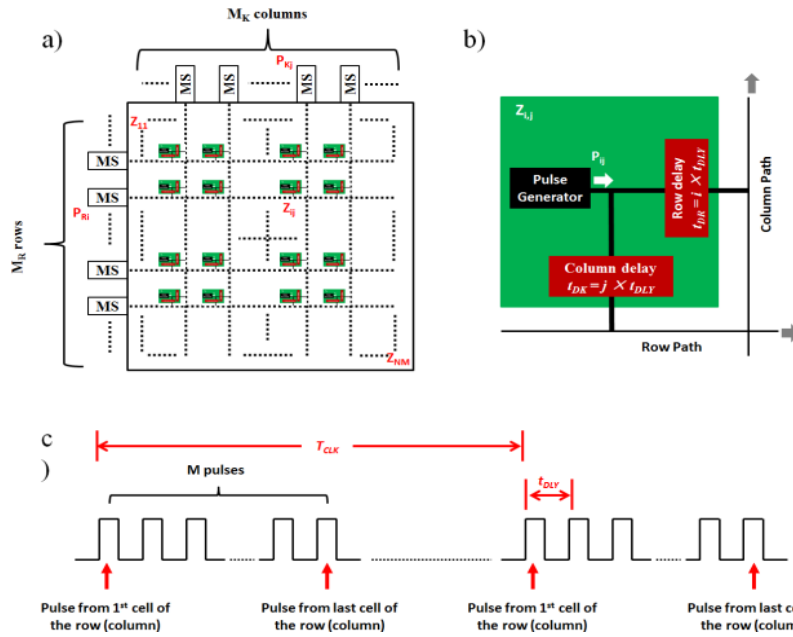
**Fig. 2.** The TSCI OCEMISA: a) array organization; b) Feedback signal generation; c) Expected feedback pattern.

**Table 1.** Parameters of the TSCI EMISA.

| Parameters | Meaning |
|---|---|
| $M_R$ | Number of the rows |
| $M_K$ | Number of the columns |
| $Z_{ij}$ | Sensor cell at (i, j) |
| $P_{ij}$ | Pulse generated by $Z_{ij}$ |
| $t_{DLY}$ | Unit delay |
| $T_{CLK}$ | Period of the cell pulse |
| $t_{DK\_ij}$ | Column delay time of $Z_{ij}$, $t_{DK\_ij} = j \times t_{DLY}$ |
| $t_{DR\_ij}$ | Row delay time of $Z_{ij}$, $t_{DR\_ij} = i \times t_{DLY}$ |

The location of the failed cells is determined by the following mechanism: If cell $Z_{ij}$ fails, the shape or the arrival time of its pulse will be modified. Consequently, waveforms of the monitoring signals on ports of the $i^{th}$ row and the $j^{th}$ column will be irregular. A port where the MS is irregular is called an error port. With the indices of the error ports, the location of the failed cells, which is at the $i^{th}$ row and the $j^{th}$ column, can be identified. The indices of the error ports form a vector called EPIV (error port index vector). For cases of single-cell failures, the EPIV uniquely determines the location of the failed cell.

## 2.2. Circuit of the Sensor Cell

The function of a sensor cell is to generate an output signal which is dependent on its supply voltage. A simple solution for the sensor circuit is shown in Fig. 3. The cell contains a ring oscillator and a counter with parameters defined in Table 2. The ring oscillator generates a clock whose period ($T_{CLK\_ij}$ for $Z_{ij}$) depends on the supply voltage. The clock is fed to a counter and produces a pulse, which is $P_{ij}$. By setting the parameter of the counter, the

duration and the position of the pulse can be controlled in such a way that pulses of cells from a row (a column) form a required pattern like the one in Fig. 2c. The supply voltage at $Z_{ij}$ is denoted with $V_{ij}$. When $V_{ij}$ is changed by the EMI, $T_{CLK\_ij}$ will change, and the waveform of $P_{ij}$ will change accordingly. Thus monitoring signals at the $i^{th}$ row and the $j^{th}$ column will be irregular. From the EPIV, the location of the corresponding $V_{ij}$ is determined. In the circuit shown in Fig. 3, each cell has its own ring oscillator and counter, therefore cell signals are generated independently, and $P_{ij}$ responds only to $V_{ij}$.
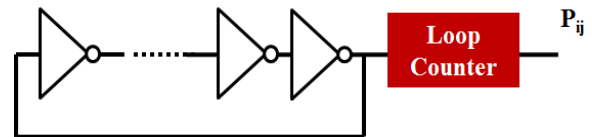


**Fig. 3.** Circuit of a sensor cell.

**Table 2.** Parameters of the Sensor Cell.

| Parameters | Meaning |
|---|---|
| $N_{RN}$ | Number of the cascaded NOT gates in the ring oscillator |
| $N_{DIV}$ | Modulus of the counter |

There are various methods to build the ring oscillator using CMOS logic gates. In this paper, the ring oscillator is composed of a chain of NOT gates of an odd number $N_R$. The period of an $N_{RN}$ stage ring oscillator is $2N_{RN}$ times as long as the delay time of a NOT gate: $T_{RN} = 2N_{RN} \times t_{NOT}$. The $t_{INV}$ stands for the delay time of NOT gate, which is affected by the local supply voltage.

The frequency divider module is designed as a loop counter. A $N_{DIV}$-modulus counter can divide the frequency of clock signal by $2N_{DIV}$. A pulse is generated for every $2N_{DIV} \times T_{RN}$. By increasing or reducing the modulus of the loop counter, we can adjust the pulse period. Also we can adjust the pulse width of the feedback signals. In this test design, $N_{DIV}$ equals 64 and the pulse width is one $T_{RN}$. The pulse width is smaller than $t_{DLY}$. And $t_{DLY}$ is much smaller than $t_{CLK}$.

## 3. FPGA Implementation of the TSCI EMISA

The Field Programmable Gate Array (FPGA) contains basic logic gates that can form NOT gate, counter, and delayer. The interconnections between gates are programmed. Moreover, the locations of the routed gates are selectable. The sensor cells can be easily implemented and positioned in a FPGA. The FPGA, when programmed as an EMISA, is called a FPGA EMISA. The FPGA EMISA can be applied to perform the initial function verification on the sensor circuit designed in the section 3. After the FPGA verification, a customized IC design procedure will be conducted to put the sensor design into an ASIC (application specified IC) chip in future. In this paper, a FPGA from [22] is utilized to implement the EMISA.

As the first step, a single cell is built in the FPGA to check the response of the cell to the EMI. In the original design, see Fig. 2, the cell drives the monitoring port directly. However, that is not possible in FPGA. Therefore the output of the sensor cell is connected to an input/output cell (I/O) of the FPGA. The monitoring port is driven by the I/O cell. The signal generated by the single cell is shown in Fig. 4. The cell generates pulses with period $T_{CLK}$ as expected.
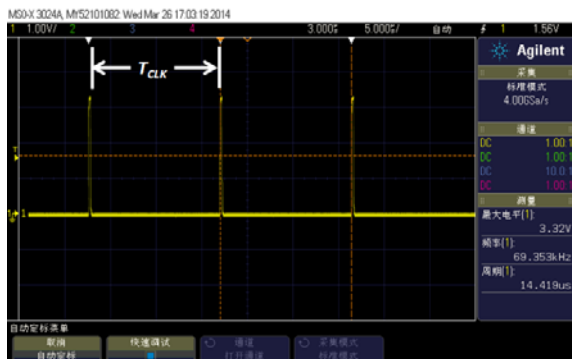


**Fig. 4.** Pulses generated by a single cell without EMI.

A radio frequency signal generator, as the EMI source, is connected to the supply pin of the FPGA. The frequency of EMI is set to be 940 MHz, which is much higher than the frequency of the ring oscillator.

Refer to Fig. 5, applying EMI cause the duration of the pulse to be wider than the normal case. An increase in $T_{CLK}$ is observed. The relationship between $\Delta T_{CLK}$ and $V_{EMI}$ is relatively linear. Here $V_{EMI}$ is the amplitude of the EMI at the source. The sensor do reacts with the EMI. Therefore, it can be utilized to detect the EMI.

After verifying the functionality of a single sensor cell, an 8-row and 8-column sensor array is implemented. The locations of cells and their indices are shown in Fig. 6. A necessary modification should be made here. In the original design, outputs of cells of the same row (or column) are connected to the same signal propagation path. That is not realizable with FPGA. Therefore, the feedback signals from the cells of the same row (or column) are connected to an OR gate. Noting that delayers of different lengths are inserted between the output of the counters and the inputs of the OR gate.

The MS are displayed with an oscilloscope. Snapshots of two typical waveforms of the MS at a row port are shown in Fig. 7. We do observe repeated eight-pulse sequences on the oscilloscope, as expected. However there are two negative behaviors on the MS waveform.

The first negative behavior is the phase difference. In Fig. 7a or Fig. 7b, each snapshot contains two cycles and each cycle has a sequence of eight pulses. The spaces between two neighboring pulses are not uniform. The cause of the problem is the phase difference between the ring oscillators and delayers of the different cells. The problem makes it difficult to recognize the pulse from the first cell of a row (or column).

The second negative behavior is the frequency difference. Comparing the sequence waveforms in Fig. 7a or Fig. 7b, we can find that the spaces of pulses in a sequence are changing with time. The cause of the problem is the frequency difference between the ring oscillators of different cells. If the oscillators of cells operate with different frequencies, then the pulse pattern on the MS will not be a fixed pattern. Without a fixed regular pattern, it is very difficult to judge the operation status of a MS. Moreover, it is impossible to recognize the location of the corresponding cell for a specific pulse.

The phase difference problem is bad but still solvable. Due to the phase problem, the exact position of pulse of a cell in the feedback pattern is unknown. However, a cell is monitored with a column port and a row port. If a cell fails, a distorted pulse appears on both the column port and the row port of the cell. Recoding the EPIV gives the location of the failed cell.

The frequency difference problem is fatal. The origin of the problem is the process variation on a chip. The geometry and chemical components of a circuit element like transistors vary with location on a chip. Consequently, the electrical properties of the circuits of the same type but at different locations are different.
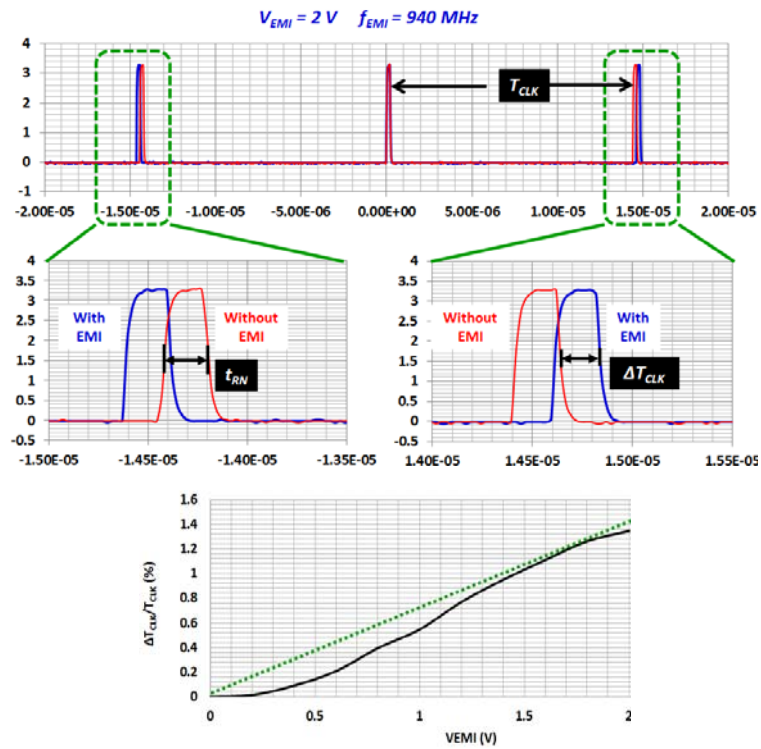
**Fig. 5.** Response of a single cell to EMI.
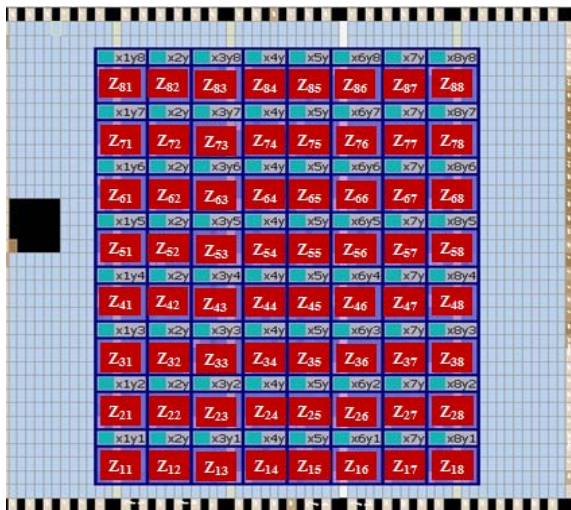


**Fig. 6.** Distribution of the sensor cell in FPGA.
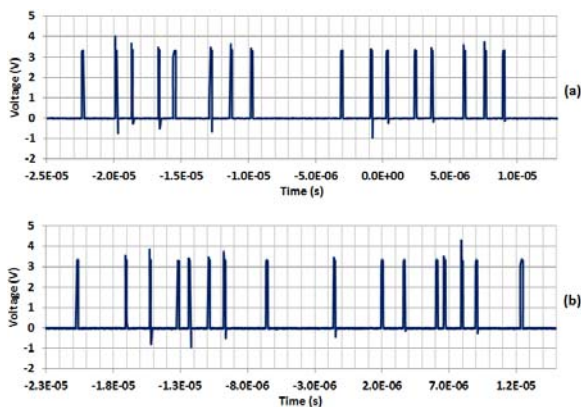


**Fig. 7.** Measured monitoring signals.

The process variation in FPGA will also happen in ASIC. The phase and frequency variation problems will appear when the sensor array is implemented with ASIC.

## 4. Discussion

The above experiment shows the difficulty in implementing the TSCI EMISA. It is a problem due to the process technology. It is interesting to see whether we can overcome the difficulty and apply the TSCI EMISA for voltage distribution measurement or not. The question is addressed through three aspects:

1) What is the up limit of the stability performance?

2) How to optimize the sensor circuits?

3) How to adapt the voltage distribution measurement procedure?

### 4.1. Arrival Jittering ($\Delta t_{ij}$)

With the parameters defined in Table 3, the arrival time of the $(N_{CLK}+1)^{th}$ pulse generated by cell at $(i,j)$ at the row port is rewritten as (1). The second term of the right side is the accumulation of the clock periods; the third term is the delayer's delays. By inserting the expression of $T_{CLK}$ (2), (1) can be converted into (3).

**Table 3.** Parameters of the cell pulse.

| Parameters | Meaning |
|---|---|
| $t_s$ | Occurrence time of the first pulse of a cell |
| $t_{DIV}$ | Delay of the counter |
| $N_{CLK}$ | Number of the past clock cycles |
| $t_{ij}$ | Actual arrival time of a pulse from $Z_{ij}$ |
| $t_{ij0}$ | Average arrival time of a pulse from $Z_{ij}$ |
| $\Delta t_{ij}$ | Arrival jittering, $\Delta t_{ij} = t_{ij} - t_{ij0}$ |

$$t_{ij} = t_{s\_ij} + \sum_{k=0}^{N_{CLK}} T_{CLK\_ij} + it_{DLY}, \quad (1)$$

$$T_{CLK\_ij} = (2N_{RN})t_{NOT\_ij}(2N_{DIV}) + t_{DVI\_ij}, \quad (2)$$

$$t_{ij} = t_{S\_ij} + 4N_{RN}N_{DIV}\sum_{k=0}^{N_{CLK}} t_{NOT\_ij}$$
$$+ \sum_{k=0}^{N_{CLK}} t_{DIV\_ij} + it_{DLY\_ij} \quad (3)$$

(3) shows that the actual pulse arrival time is determined by $t_S$, $t_{NOT}$, $t_{DIV}$, $t_{DLY}$. Variations of those parameters with time cause the pattern instability problem. Variations of those parameters with location cause the phase difference problem.

Table 4 defines a few processing parameters. With those parameters a few equations can be established as (4) – (7). With the definition of the ideal arrival time (8), the shift of the arrival time can be calculated with (9). For simplicity in writing, the shift of the arrival time is called the arrival jittering. Fig. 8 depicts the timing parameters on the waveform of the feedback signal.

**Table 4.** Process Parameters of FPGA.

| Parameters | Meaning |
|---|---|
| $t_{S0}$ | Average starting time of first pulse of a cell |
| $t_{DLY0}$ | Average propagation delay of a delayer |
| $t_{NOT0}$ | Average propagation delay of a NOT gate |
| $t_{DIV0}$ | Average delay of a counter |
| $\beta$ | Spatial variation of ($t_S$, $t_{DLY}$, $t_{NOT}$, $t_{DIV}$) |
| $\Delta\beta$ | Range of the spatial Variation in the temporal evolution of ($t_S$, $t_{DLY}$, $t_{NOT}$, $t_{DIV}$) |
| $\gamma$ | Temporal variation of ($t_S$, $t_{DLY}$, $t_{NOT}$, $t_{DIV}$), $\gamma = \gamma_{AVE} + \gamma_{VAR}$ |
| $\Delta\gamma$ | Range of the temporal variation in the temporal evolution of ($t_S$, $t_{DLY}$, $t_{NOT}$, $t_{DIV}$) |

$$t_{S\_ij} = t_{S0}[1 + \beta_S(i,j)], \quad (4)$$

$$t_{DLY\_ij} = t_{DLY0}[1 + \beta_{DLY}(i,j) + \gamma_{DLY}(t,i,j)], \quad (5)$$

$$t_{N0T\_ij} = t_{N0T0}[1 + \beta_{N0T}(i,j) + \gamma_{N0T}(t,i,j)], \quad (6)$$

$$t_{DIV\_ij} = t_{DIV0}[1 + \beta_{DIV}(i,j) + \gamma_{DIV}(t,i,j)], \quad (7)$$

$$t_{ij0} = t_{S0} + 4N_{RN}N_{DIV}\sum_{k=0}^{N_{CLK}} t_{NOT0}$$
$$+ \sum_{k=0}^{N_{CLK}} t_{DIV0} + it_{DLY0}, \quad (8)$$

$$\Delta t_{ij} = \Delta t_{S0} + 4N_{RN}N_{DIV0}\sum_{k=0}^{N_{CLK}} \Delta t_{N0Tij}$$
$$+ \sum_{k=0}^{N_{CLK}} \Delta t_{DIV\_ij} + i\Delta t_{DLY\_ij}, \quad (9)$$
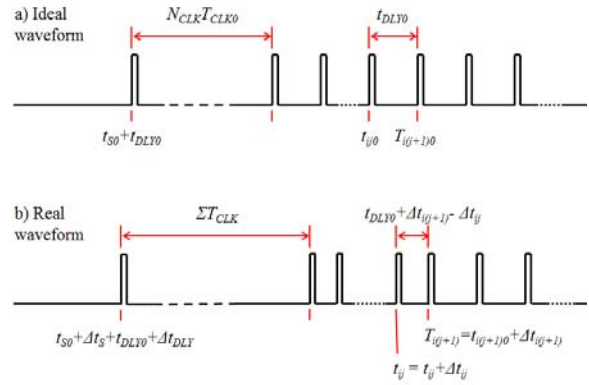


**Fig. 8.** Waveform parameters.

### 4.2. Spatial Variation in the Arrival Jittering Due to β

The arrival jittering due to the spatial variation of the process parameters alone is given in (10).

$$\Delta_S(t_{ij}) = t_{S0}\beta_S(i,j)$$
$$+ 4N_{RN}N_{DIV}N_{CLK}t_{N0T0}\beta_{NOT}(i,j) \quad (10)$$
$$+ t_{DIV0}N_{CLK}\beta_{DIV}(i,j) + t_{DLY0}i\beta_{DIV}(k,j)$$

The second and third terms of the right side in (10) shows that $\Delta S(t_{ij})$ changes with time ($N_{CLK}$). Because β varies with the cell location, the change in $\Delta S(t_{ij\_L})$ is not uniform. That means the space of the pulses from different cells change with time. Consequently, the pulse pattern is broken. The difference in the shifts of the two neighbor pulses is called the relative shift. Suppose the maximal difference of β is Δβ, the worst-case relative shift is estimated with (11).

$$\delta_S(t_{ZP}) = 4N_{RN}N_{DIV}t_{N0T0}N_{CLK}\Delta\beta_{NOT}$$
$$+ t_{DIV0}N_{CLK}\Delta\beta_{DIV} \quad (11)$$

Fig. 9 shows a pattern mask on the oscilloscope, with which the feedback signal can be checked. If the feedback signal does not fit the mask, the circuit is considered to be wrong. If the relative shift exceeds $t_{DLY0}$, the feedback pattern will not fit the mask. The circuit will be considered wrong even in absence of the external EMI. Therefore, to measure the voltage distribution on the chip, (12) must be satisfied for the entire duration of the measurement
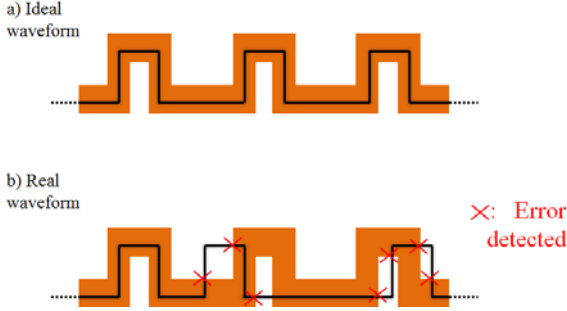


**Fig. 9.** Criterion for detecting the intolerable EMI.

$$\delta_S(t_{ZP}) < t_{DLY0} \tag{12}$$

If the spatial variation alone is considered, we can use (11) and (12) to calculate the maximal number of clock periods in the measurement duration, as shown in (13). $t_{DVI0}$ is roughly the order of $N_{DIV}t_{NOT0}$. For large $N_{RN}$, the denominator of the second term in the right side of (13) is neglectful. The expression of the maximal number clock period can be simplified as (14). The corresponding measurement time is given in (15).

$$N_{CLK} < \frac{t_{DLY0}}{T_{CLK0}\Delta\beta_{NOT}} \frac{1}{1 + \dfrac{1}{4N_{RN}N_{DIV}} \dfrac{t_{DIV0}}{t_{NOTO}} \dfrac{\Delta\beta_{DIV}}{\Delta\beta_{NOT}}}, \tag{13}$$

$$N_{CLK\_\max\_S} = \frac{t_{DLY0}}{T_{CLK0}\Delta\beta_{NOT}}, \tag{14}$$

$$t_{MT\_S} = N_{CLK\_\max}T_{CLK0} = \frac{t_{DLY0}}{\Delta\beta_{NOT}} \tag{15}$$

### 4.3. Spatial Variation in the Arrival Jittering Due to γ

Same analysis can be made on the effect of γ. The arrival jittering due to the temporal variation of the process parameters alone is given in (16).

$$\Delta_T(t_{ij}) = 4N_{RN}N_{DIV}t_{NOT0}\sum_{k=0}^{N_{CLK}}\gamma_{NOT} \tag{16}$$

$$+ t_{DIV0}\sum_{k=0}^{N_{CLK}}\gamma_{DIV} + it_{DLY0}\gamma_{DIV}$$

The worst-case relative shift can be estimated with (17).

$$\delta_T(t_{ZP}) = 4N_{RN}N_{DIV}t_{NOT\ 0}N_{CLK}\Delta\gamma_{NOT}$$
$$+ t_{DIV0}N_{CLK}\Delta\gamma_{DIV} + t_{DLY0}\Delta\gamma_{DIV} \tag{17}$$

If the temporal variation alone is considered, we can use (17) and (18) to calculate the maximal number of clock cycles in the measurement duration. The formula is given in (19) and simplified as (20). The corresponding measurement duration in time scale is given in (21).

$$\delta_T(t_{ZP}) < t_{DLY0}, \tag{18}$$

$$N_{CLK} < \frac{t_{DLY0}(1-\Delta\gamma_{DIV})}{T_{CLK0}\Delta\gamma_{NOT}} \frac{1}{1 + \dfrac{1}{4N_{RN}N_{DIV}t_{NOT0}} \dfrac{t_{DIV0}\Delta\gamma_{DIV}}{\Delta\gamma_{NOT}}} \tag{19}$$

$$N_{CLK\_\max\_T} = \frac{t_{DLY0}(1-\Delta\gamma_{DIV})}{T_{CLK0}\Delta\gamma_{NOT}}, \tag{20}$$

$$t_{MT\_T} = N_{CLK}T_{CLK0} = \frac{t_{DLY0}(1-\Delta\gamma_{DIV})}{\Delta\gamma_{NOT}} \tag{21}$$

### 4.4. Overall Spatial Variation in the Arrival Jittering

The total amount of the relative shift is the sum of effects due to β and γ, see (22). If ΔγDIV is sufficient small, the maximal duration allowed to complete an immunity measurement is given in (23) and (24). The duration is inversely proportional to the process variation parameters.

$$\delta(t_{ZP}) = \delta_S(t_{ZP}) + \delta_T(t_{ZP}), \tag{22}$$

$$N_{CLK\_\max} = \frac{t_{DLY0}}{T_{CLK0}(\Delta\beta_{NOT} + \Delta\gamma_{NOT})}, \tag{23}$$

$$t_{MT} = \frac{t_{DLY0}}{\Delta\beta_{NOT} + \Delta\gamma_{NOT}} \tag{24}$$

To observe how serious the process variation is, a special experiment is done: the repetition rate of the pulses of 64 cells are measured and compared. The pulse rate of a cell is averaged by 10000 times. The measurement results are presented in a frequency distribution map in Fig. 10. The map is draw with 8 by 8 mono-color gray blocks. Each block corresponds to a sensor cell in Fig. 6. The gray scale

of block gives the pulse rate. The right bar in the figure gives the scale of the frequency.

In Fig. 10, the pulse rate ranges from 67.2 kHz to 69.0 kHz. The frequency distribution map gives a variation in the pulse frequency of 2.7 %. That is the rough value of $\Delta\beta_{NOT} + \Delta\gamma_{NOT}$. In Fig. 7, $t_{DLY0}$ is 2 µs and $T_{CLK0}$ is 20 µs. According to (24), $N_{CLK\_max}$ is 3.7. That means a feedback pattern can be hold only for 4 cycles and the measurement should be completed within 74 µs. It is impractical.
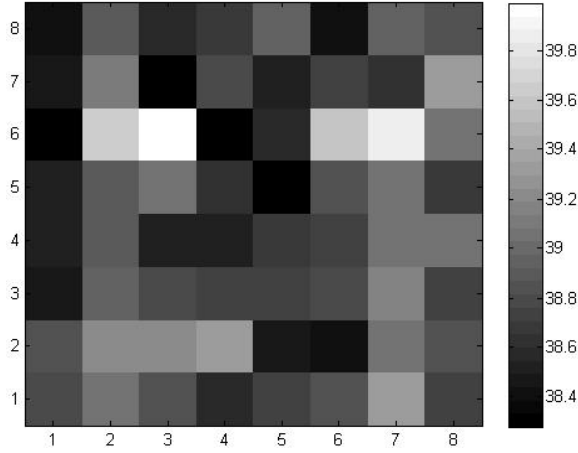


**Fig. 10.** Pulse rate (in kHz) of cells at different location.

### 4.5. Array Optimization

The instability limit causes the tradeoff between the timing and the spatial resolution of the measurement. $t_{DLY0}$ and $T_{CLK0}$ are not completely independent. All pulses of cells from the same row (or column) should appear within one clock cycle. Relationship (25) must be hold. Inserting (26) into (24), we obtain (26).

$$M_{R,K} t_{DLY0} = \alpha T_{CLK0}$$
$$0 < \alpha < 1, \tag{25}$$

$$N_{CLK\_max} M_{R,K} = \frac{\alpha}{\Delta\beta_{NOT} + \Delta\gamma_{NOT}} \tag{26}$$

$N_{CLK\_max}$ corresponds to the timing resolution of the measurement. $M_{R,K}$ corresponds to spatial resolution of the measurement. (26) shows that for a given process, the product of those two resolutions is a constant. Fig. 11 shows the up-limit of the timing and spatial resolutions for various process uniformity.

If 100 $T_{CLK0}$ measurement time is desired on a 10 * 10 array, the spatial process variation should be less than 0.1 %. The requirement is far beyond what can be offered in the current state of art [23].

As the IC technology approaches nano-meter scale, the process variation increases. Under that technology, it is almost impossible to get a stable pattern of pulses from independent cells. The time-domain feedback scheme does not work. Another approach should be developed so that independent feedback signals form a stable pattern under the current process variation. A possible solution is to set $T_{CLK}$ of the cells different from each other and monitor the MS in frequency domain. In frequency domain, the spectrums of the cell pulse are stable and are separated from each other. The process variation may broaden of the spectrum of the cell pulses thus cause overlap between the signals of two cells. However, the problem can be solved by selecting proper value of the difference in $T_{CLK}$.
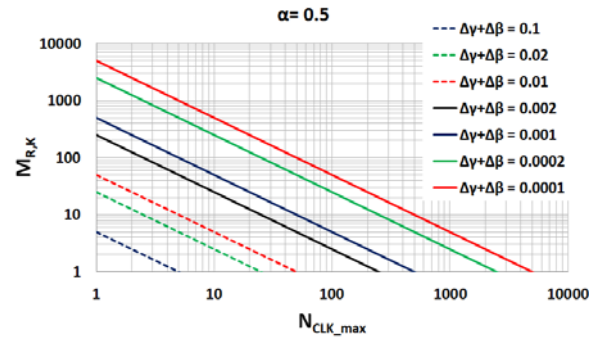


**Fig. 11.** Tradeoff between spatial and timing resolutions.

### 5. Conclusions

It is interesting to see a two-dimension distribution of the EMI voltage in the power distribution network on an IC chip. There is a wide range of possible schemes of OCEMISA for measuring the distribution. The TSCI is an intuitively simple approach to perform the measurement. The process variation causes instability problem on the feedback signals and thereby limits the application of the feedback pattern to monitor the EMI voltage. The limitation is expressed in an analytical way by relating the process variation parameter to the spatial and the timing resolutions of the measurement. Under current processing technology, the TSCI scheme cannot measure two-dimension distribution of the EMI voltage with reasonable spatial and timing resolution. Looking for a solution in frequency domain might be the right direction to realize EMISA.

### Acknowledgement

## References

[1]. A. Boyer, S. Bendhia, E. Sicard, Characterisation of electromagnetic susceptibility of integrated circuits using near-field scan, *Electronics Letters*, Vol. 43, No. 1, January 2007, pp. 15–16.

[2]. M. Joester, F. Klotz, W. Pfaff, T. Steinecke, Generic IC EMC Test Specification, *German Electrical and Electronic Manufactures' Association*, Frankfurt, Germany, 2010.

[3]. Takamiya M., M. Mizuno, K. Nakamura, An on-chip 100 GHz-sampling rate 8-channel sampling oscilloscope with embedded sampling clock generator, *ISSCC Digest of Technical Paper*, February 2002, pp. 182-183.

[4]. Zheng Y., K. L. Shepard, On-chip oscilloscopes for noninvasive time-domain measurement of waveforms in digital integrated circuits, *IEEE Transactions on Very Large Scale Integration (VLSI) Systems*, Vol. 11, June 2003, pp. 336-344.

[5]. Alon E., V. Stojanovic, M. A. Horowitz, Circuits and techniques for high-resolution measurement of on-chip power supply noise, *IEEE Journal of Solid-State Circuits*, Vol. 40, April 2005, pp. 820-827.

[6]. Milosevic P., J. E. S. Aine, On-chip oscilloscope for signal integrity characterization of interconnects in 130 nm CMOS technology, *IEEE Electrical Performance of Electronic Packaging*, October 2008, pp. 65-68.

[7]. Alon E., V. Abramzon, B. Nezamfar, M. Horowitz, On-die power supply noise measurement techniques, *IEEE Transactions on Advanced Packaging*, Vol. 32, May 2009, pp. 248-258.

[8]. Dhia S. B., A. Boyer, B. Vrignon, M. Deobarro, T. V. Dinh, On-chip noise sensor for integrated circuit susceptibility investigations, *IEEE Transactions on Instrumentation and Measurement*, Vol. 61, March 2012, pp. 696-707.

[9]. Hideyuki A., M. Ikeda, K. Asada, On-chip voltage noise monitor for measuring voltage bounce in power supply lines using a digital tester, in *Proceedings of the International Conference on Microelectronic Test Structures*, 2000, pp. 112–117.

[10]. Okumoto T., M. Nagata, K. Taki, A built-in technique for probing power-supply noise distribution within large-scale digital integrated circuits, in *Proceedings of the Symposium on VLSI Circuits Digest of Technical Papers*, 2004, pp. 98-101.

[11]. Shimazaki K., M. Nagata, T. Okumoto, S. Hirano, H. Tsujikawa, Dynamic power-supply and well noise measurements and analysis for low power body biased circuits, *The Institute of Electronics, Information and Communication Engineers*, Vol. E88-C, April 2005, pp. 589-596.

[12]. Kanno Y., Y. Kondoh, T. Irita, K. Hirose, R. Mori, Y. Yasu, S. Komatsu, H. Mizuno, In-situ measurement of supply-noise maps with millivolt accuracy and nanosecond-order time resolution, *IEEE Journal of Solid-State Circuits*, Vol. 42, April 2007, pp. 784-789.

[13]. Bando Y., S. Takaya, M. Nagata, An on-chip continuous time power supply noise monitoring technique, in *Proceedings of the IEEE Asian Solid-State Circuits Conference*, Taipei, November 2009, pp. 97-100.

[14]. Hashida T., M. Nagata, On-chip waveform capture and diagnosis of power delivery in SoC integration, in *Proceedings of the Symposium on VLSI Circuits/Technical Digest of Technical Papers*, 2010, pp. 121-122.

[15]. Zhang X., K. Ishida, H. Fuketa, M. Takamiya, T. Sakurai, On-chip measurement system for within-die delay variation of individual standard cells in 65-nm CMOS, *IEEE Transactions on Very Large Scale Integration (VLSI) Systems*, Vol. 20, October 2012, pp. 1876-1880.

[16]. Yuan S. Y., Y. L. Wu, R. Perdriau, S. S. Liao, Detection of electromagnetic interference in microcontrollers using the instability of an embedded phase-lock loop, *IEEE Transactions on Electromagnetic Compatibility*, Vol. 55, April 2013, pp. 299-306.

[17]. Noguchi K., M. Nagata, An on-chip multichannel waveform monitor for diagnosis of systems-on-a-chip integration, *IEEE Transactions on Very Large Scale Integration (VLSI) Systems*, Vol. 15, October 2007, pp. 1101-1110.

[18]. Ogasahara Y., M. Hashimoto, T. Onoye, All-digital ring-oscillator-based macro for sensing dynamic supply noise waveform, *IEEE Journal of Solid-State Circuits*, Vol. 44, June 2009, pp. 1745-1755.

[19]. Muhtaroglu A., G. Taylor, T. R. Arabi, On-die droop detector for analog sensing of power supply noise, *IEEE Journal of Solid-State Circuits*, Vol. 39, April 2004, pp. 651-660.

[20]. C. Bona, F. Fiori, A New Front-End for Binary Data Recovery in EM Polluted Environment, *IEEE Transactions on Circuits and Systems I: Regular Papers*, Vol. 59, No. 10, Oct. 2012, pp. 2232–2243.

[21]. F. Caignet, N. Nolhiera, M. Bafleur, A. Wangb, N. Mauran, On-chip measurement to analyze failure mechanisms of ICs under system level ESD stress, *Microelectronics Reliability*, Vol. 53, No. 9-11, Sept. 2013, pp. 1278-1283.

[22]. FPGA (EP2C35F672C6N), Altera, Datasheet, 2004.

[23]. K.-J. Kuhn, M.-D. Giles, D. Becher, P. Kolar, A. Kornfeld, R. Kotlyar, S.-T. Ma, A. Maheshwari, S. Mudanai, Process technology variation, *IEEE Transactions on Electron Devices*, Vol. 58, August 2011, pp. 2197-2208.

---

# Optimal Sensor Placement in Bridge Structure Based on Immune Genetic Algorithm

**Zhen-Rui PENG, Hong YIN, Yu ZHAO, An PAN**

School of Mechatronics Engineering, Lanzhou Jiaotong University, 730070, Lanzhou, China
Tel.: 86-0931-4956436, fax: 86-0931-4956439
E-mail: pzrui@163.com

**Abstract:** For the problem of optimal sensor placement (OSP), this paper introduces immune genetic algorithm (IGA), which combines the advantages of genetic algorithm (GA) and immune algorithm (IA), to minimize sensors placed in the structure and to obtain more information of structural characteristics. The OSP mode is formulated and integer coding method is proposed to code an antibody to reduce the computational complexity of affinity. Additionally, taking an arch bridge as an example, the results indicate that the problem can be achieved based on IGA method, and IGA has the ability to guarantee the higher calculation accuracy, compared with genetic algorithm (GA). *Copyright © 2014 IFSA Publishing, S. L.*

**Keywords:** Optimal sensor placement, Immune genetic algorithm, Structural health monitoring.

## 1. Introduction

Large-scale civil infrastructures may cause damage during long service period, extreme loads, harsh environment or natural calamities, such as winds and earthquakes. In severe cases, these factors can lead to major accident and have disastrous effects on human life [1]. In order to guarantee the safety, integrity and durability of structures, effective methods employed to monitor the security situation. Structural health monitoring (SHM) system is developed to detect anomalies in loading and response, and possible damage at an early stage, to provide the real-time information for safety assessment, in the long term, to obtain the massive amount data for the leading edge research in structure engineering guide for future similar structures [2].

A typical SHM system includes three major components: a sensor system, a data processing system (including the data acquisition, transmission, and storage), and a health evaluation system [3]. The

health status of structures can be surveilled, evaluated, assessed by the overall system. Sensor system plays a key part in the SHM system. Owing to the limitation of financial conditions, it is impossible to place sensors in all candidate positions. Deploying fewer sensors on the bridge structures and acquiring more health information is the focus of the study. How to place sensors reasonably has become one of the most importantly problems, which is known as optimal sensor placement (OSP). Kammer developed the effective independence (EFI) method which played close attention to the contribution of each sensor position to the linear independence of the identified modes [4]. Lim employed the method based on a given rank for the system observability matrix that satisfy modal test constraints to determine sensor locations [5]. Carne and Dohmann [6] proposed to use modal assurance criterion (MAC) matrix as a measure of the utility of a sensor configuration. Heo and Wang presented the modal kinetic energy (MKE) method and optimized the

transducer placement of a long span bridge for identification and control purposes [7]. Miller introduced an approach to compute a Gaussian quadrature formula to give the optimal locations for sensors, and to illustrate the approach by a slewing beam [8]. Park *et al.* utilized modal controllability and observability defined in balanced coordinate system to select the location s of sensors and actuators [9]. Meo and Zumpano modified the EFI method, and posed the effective independence driving-point residue (EFI-DPR) method for OSP to identify the vibration characteristics of the bridge [10]. Li *et al.* combined the EFI method and MKE method, raised a quick EFI method through QR decomposition, and demonstrated the connections between EFI and MKE on the I-40 Bridge [11]. With the development of intelligence algorithms, some approaches rely on intelligence algorithms, such as genetic algorithm (GA), were used to solve the OSP. For the modal identification of a large space structure, Yao *et al.* took the GA to place sensors, the simulated results more accurately than EFI method [12]. Guo *et al.* presented some strategies (crossover based on identification code, mutation based on two gene bits) to improve the convergence speed of simple GA [13]. Work by Liu *et al.* [14] introduced a method based on GA to find the optimal placement of sensors, used the decimal two-dimension array coding method to overcome the low computational efficiency of traditional approaches. Another improved genetic algorithm called generalized genetic algorithm (GGA) is adopt to get the optimal placement of sensors. The placement scheme obtained by the GGA showed better feasibility and effectiveness compared with exiting genetic algorithm [15]. GA is a great method to optimization problems like OSP, but some faults, for instance degenerative phenomena, need to be improved further [16]. In the later research, virus evolutionary theory was emerged into GA to enhance the speed of convergence [17]. Especially, in recent years, the successful application of the new intelligence algorithms in combinatorial optimization problems, such as traveling salesman problem (TSP), knapsack problem (KP) [18-19], bring fresh ideas to the problem of OSP. Immune algorithm (IA) to solve these problems is also illustrated in some case studies [20]. On this base, a study based on immunity for OSP is presented.

In this paper, Immune genetic algorithm (IGA) is used to determine the location and the quantity of sensors. The mathematic mode of OSP is established, and an arch bridge is presented to verify the effectiveness of the algorithm.

## 2. Arch Bridge Structure

### 2.1. Description of Arch Bridge

Fig. 1 shows the diagram of an arch bridge. The main span is 3350.98 cm. And two side spans are both 2113.34 cm. The main structure is composed of beams and plate materials. Elastic modulus of bridge floor is $E = 1.6 \times 10^5 \, \text{MPa}$. Poisson ration is 0.35. Elastic modulus of materials for other beams is $E = 2.06 \times 10^5 \, \text{MPa}$.
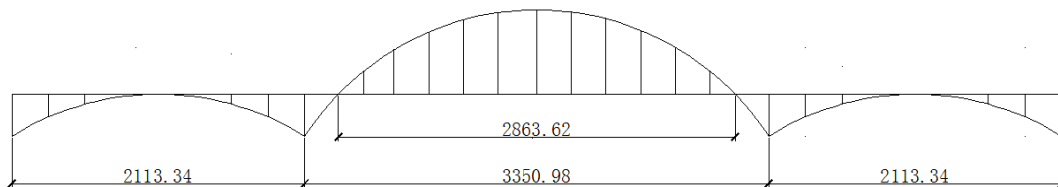


**Fig. 1.** Diagram of bridge structure (unit: cm).

### 2.2. Finite Element Model of the Bridge

To obtain input data for OSP problem, a finite element (FE) model of the arch bridge is built by software ANSYS (ANSYS, Pittsburgh, PA, USA) [21]. The truss and the deck are simulated using beam elements and shell elements in the ANSYS element library. The model has 12631 frame elements and 11332 node elements. The three-dimension FE model developed is shown in Fig. 2.

A modal analysis is performed to gain the vibration properties. Considering the low order modal has greater participation coefficient, the first 6 modal frequency of arch bridge is calculated. The frequencies are given in Table 1.
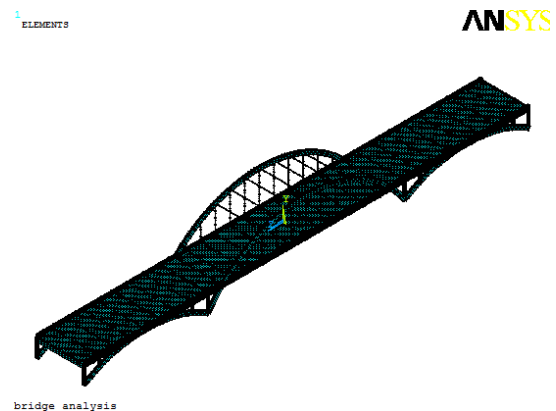


**Fig. 2.** FE model of arch bridge.

**Table 1.** The first 6 modal frequency of arch bridge.

| Order number | 1 | 2 | 3 |
|---|---|---|---|
| Frequency/Hz | 0.0568 | 0.1545 | 0.1789 |
| Order number | 4 | 5 | 6 |
| Frequency/Hz | 0.2240 | 0.2283 | 0.2290 |

## 2.3. Mathematic Model of OSP

A matrix $\Phi_{n \times l}$ is defined as the modal matrix which is made of the data from modal analysis, where $n$ is the degrees of freedom (DOFs), namely, DOFs of candidate sensor positions (every node has 2 DOFs, translation $x, y, z$ and rotation $Ux$, $Uy$, $Uz$); $l$ denotes the order number of modal. We need select $m$ DOFs from the $n$ DOFs as the final sensor locations. In order to guarantee the linear independency of the measured modal vectors, modal assurance criterion (MAC) is applied to distinguish measured modal vectors [6]. The mathematic mode can be expressed as

$$\begin{cases} min & \max_{i \neq j} \{MAC_{ij}\} \\ s.t. & m < n \end{cases}, \qquad (1)$$

where $MAC_{ij} = \dfrac{\left(\varphi_i^T \varphi_j\right)^2}{\left(\varphi_i^T \varphi_i\right)\left(\varphi_j^T \varphi_j\right)}$, $\phi_i$ and $\phi_j$ are the

$i^{th}$ and $j^{th}$ column vectors in matrix $\Phi$, respectively, and the superscript $T$ denotes the transpose of the vector. In Equation (1), if the element values of $MAC$ tend to zero, it indicates that there is little correlation between the off-diagonal element $MAC_{ij}$ $(i \neq j)$, that is to say, the modal vector can be distinguished easily. Otherwise the modal vector fairly to be identified. In this paper, the fitness function is established according to the mathematic mode and OSP intelligence methods.

## 3. Description of Algorithms

### 3.1. Immune Genetic Algorithm

Generally, Immune genetic algorithm (IGA) is regarded as a modified immune algorithm that combines the advantages of IA and GA. IA is a kind of population-based algorithm inspired by biological immune system. IGA is a heuristic search and optimization technique combined genetic operator (selection, crossover and mutation operators) and immune system. Immunity-based algorithm was widely applied in many fields, such as fault detection [22], pattern recognition [23], shop scheduling [24] and other engineering problems [25-26].

In the natural immune system, the lymphocytes recognize invading antigens and produce antibodies

to exclude the foreign antigens [27]. Relevantly, the antigen is equivalent to the optimization problem, after making a detailed analysis of the problem, the objective function is established, and the antibody is the feasible solution of the problem in the artificial immune system. In coping with real optimization problem, variable is coded into a string as an antibody which is similar to a chromosome in GA, which is a globally optimal method. Variable parameters are coded into a genetic string called a chromosome (individual). Different antibody composes a population which produces new individuals by selection, crossover and mutation operators, and the better antibodies are stored in memory bank to maintain the superiority of population, the fitness antibody corresponds to optimal value. The main components of an IGA are calculation of affinity and genetic operators, thus, to increase the diversity of antibody population and to prevent the premature convergence the algorithm.

### 3.2. Coding Method

The first important problem to be solved in IGA is coding, taking the OSP problem into account, the result is the locations of sensors, that is, the number of nodes on the FE modal. The integer coding method is adopted to overcome the difficulty from binary coding. For instance, the candidate sensor positions are coded as an antibody (1, 2, 3, 4, 5, 6, 7, 8, 9, 10). That denotes that sensors are placed on these nodes. The method avoids decoding of binary variables and enhances efficiency to some degree [28].

### 3.3. Fitness Function

On the basis of IGA and OSP problem, the fitness function is defined as

$$f(s) = 1 - \max_{i \neq j} \{MAC_{ij}\}, \qquad (2)$$

where $s$ means an antibody. In the problem of OSP, demanding the largest value of off-diagonal element in the $MAC$ matrix is to be minimum run up to zero, and the variable parameters in the antibody are as less as possible.

### 3.4. Affinity Calculation

In consideration of IGA and fitness function, the affinity between antigens and antibodies is defined as

$$A_V = f(s) = 1 - \max_{i \neq j} \{MAC_{ij}\}, \qquad (3)$$

where $f(s)$ is fitness function. $A_V$ expresses the identification degree of the antibody to the antigen.

### 3.5. Antibody Concentration

The concentration of antibody can be calculated by

$$C_V = \frac{1}{N} \sum S_{V,S} , \qquad (4)$$

where $N$ is the number of antibody; $S_{V,S}$ is the affinity between antibody and antibody, which reflects the similarity between antibodies; $S_{V,S} = \begin{cases} 1, & S_{V,S} > T \\ 0, & otherwise \end{cases}$ . $T$ is the certain threshold, here, $T = 0.2$ .

### 3.6. Selection Probability

In the IGA, the selection probability can be calculated according to the following equation

$$P = \alpha \frac{A_V}{\sum A_V} + (1 - \alpha) \frac{C_V}{\sum C_V} , \qquad (5)$$

where $A_V$ and $C_V$ are given in Equation (3) and (4), respectively. $\alpha$ represents diversity evaluation parameters, $0 \le \alpha \le 1$ . Adjust $A_V$ and $C_V$ to ensure the diversity of population. Here, $\alpha$ is set to 0.98. From the Equation (5), it can be noticed that the antibody with high value is more likely to be selected.

### 3.7. Genetic Operator

By calculating the fitness of each individual, the fittest antibodies pass to successive generation. Selection probability can be used to implement the selection procedure in accordance with Equation (5), the individual with higher fitness value have the greater probability to be selected. Then the crossover operator is employed to produce new individuals by exchanging some bits in antibodies, randomly.

In this work, take two-point crossover to choose new offspring. The two parent individuals are divided into three parts by the cutting, and swapping the middle part to generate two offspring. Assuming the cutting position chosen at random are 4 and 7, the two-point crossover operation is shown.

```
 9   5   1 | 3   7   4   2 |10   8   6
10   5   4 | 6   3   8   7 | 2   1   9
```

After cross

```
 9   5   1 | 6   3   8   7 |10   *   *
10   5   * | 3   8   4   2 | *   1   9
```

The number in the individual may repeat (the positions are showed with *). By now, keep the no repeat figures, and use part mapping method to eliminate the conflict position.

After this, mutation operator is executed with a small probability, here, two bits are chosen from the antibody at random, then exchange the two bits. For an antibody $(9, 5, 1, 6, 3, 8, 7, 10, 4, 2)$ , for the case of the two bits are 4 and 7, respectively.

```
9   5   1 | 6   3   8 | 7 |10   4   2
```

Then the antibody is changed into

```
9   5   1 | 7 | 3   8 | 6 |10   4   2
```

That is the basic theory (selection, crossover and mutation operators) of genetic operation.

### 3.8. Steps of IGA Methods

The whole process of IGA for OSP of the arch bridge is summarized as following steps:

**Step 1.** Initialize the antibody population randomly, set related parameters, population size $N1$ , memory capacity $N2$ , the number of iterations $M$, crossover probability $p_c$ and mutation probability $p_m$ .

**Step 2.** Antibody evaluation, calculate the selection probability values of the antibodies in the population using Equation (5).

**Step 3.** Generate parent population, and descend sort the values calculated in Step 2, and then select $N1$ antibodies to form parent population the individuals. The elitist strategy is used to update memory, the antibody with high affinity $A_V$ and selection probability $P$ are stored in memory bank.

**Step 4.** Genetic operators, apply the crossover operation by two-point crossover, and execute the mutation operation using two bits mutation method, and then take out the antibody in the memory bank to make up new antibodies group.

**Step 5.** Repeat Step 2 to Step 4 until meeting the maximum iterations.

The flowchart of IGA for OSP is shown in Fig. 3.

## 4. OSP for Arch Bridge

### 4.1. OSP Based on IGA

Considering the symmetry of the arch bridge, only a quarter of bridge structure is selected as the research object to achieve OSP. A number of 78 translational DOFs in 26 nodes are possible sensor installation in the case. The candidate nodes are shown in Fig. 4.

The flowchart for OSP shows in Fig. 3 can be implemented with the software MATLAB. The relative parameters are listed in Table 2. The change curve of the maximum off-diagonal element of the *MAC* matrix is showed in Fig. 5.

From Fig. 5, it can be easily found that when the sensor number is set between 1 and 5, the maximum value of the off-diagonal elements in the *MAC*

matrix decreases rapidly with sensor added, and the sensor number is set to 10, the maximum value of the off-diagonal elements reaches its minimum, then the values increase slowly. Obviously, to select 10 DOFs as the sensor quantity, the final sensor placement result of the arch bridge is given in Table 3.
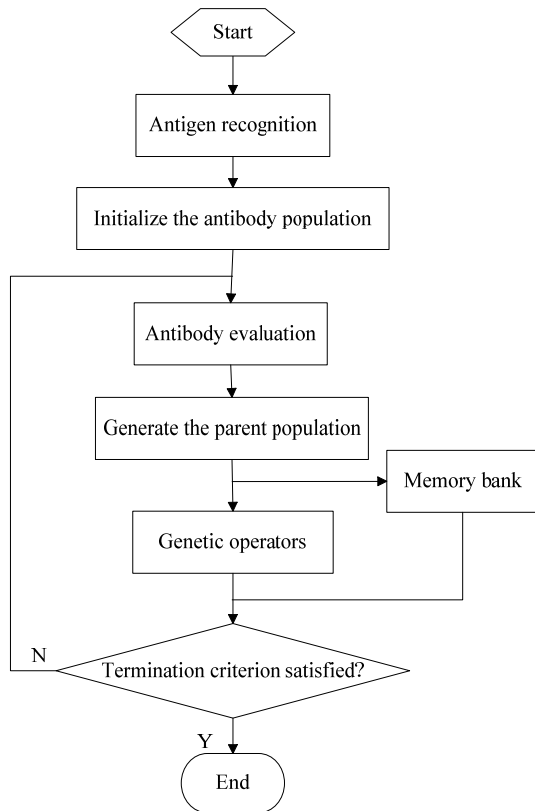


**Fig. 3.** Flowchart of the IGA for OSP.
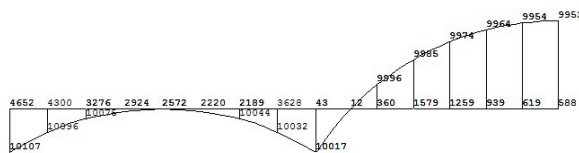


**Fig. 4.** Diagram of sensor candidate nodes.
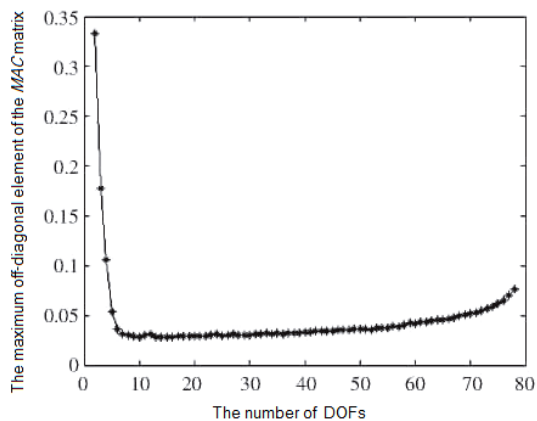


**Fig. 5.** The change curve of the maximum off-diagonal element of the *MAC* matrix.

## 4.2. Comparison of the Methods

To show the effectiveness performance of IGA for OSP, GA and IGA are carried out to compare their performances. The parameters (Population size, Iterations, Crossover probability and Mutation probability) of GA are the same as IGA.

As shown in Fig. 6, maximum fitness values of IGA and GA tend to 1, thus, both methods are effective to OSP of bridge, but fitness value by the IGA is larger than that by GA, the value by IGA is 0.972, that means, the maximum value of the off-diagonal elements in the *MAC* matrix obtained by IGA is 0.028, and from Fig. 6, the convergence speed of the IGA is also higher than that of GA method.

**Table 2.** Parameters of IGA for OSP.

| Parameters | Values |
|---|---|
| Population size | 90 |
| Memory capacity | 30 |
| Iterations | 100 |
| Crossover probability | 0.99 |
| Mutation probability | 0.4 |

**Table 3.** Sensor placement of the arch bridge.

| Sensor number | Node | Direction |
|---|---|---|
| 1 | 4300 | $z$ |
| 2 | 619 | $x$ |
| 3 | 588 | $y$ |
| 4 | 9985 | $x$ |
| 5 | 588 | $x$ |
| 6 | 10075 | $z$ |
| 7 | 9953 | $y$ |
| 8 | 4652 | $x$ |
| 9 | 9953 | $x$ |
| 10 | 939 | $x$ |
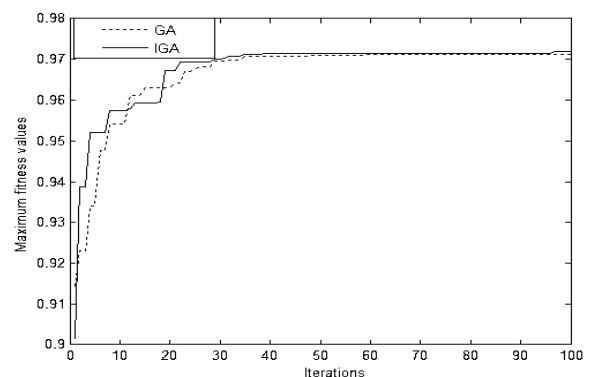


**Fig. 6.** Comparison of convergence curve between IGA and GA.

## 5. Conclusions

In this paper, IGA is outlined for OSP of arch bridge SHM sensor system. To solve the problem of

OSP, integrating the advantages of GA and IA to increase the diversity of population and the speed of convergence, and combing the characteristic of the mathematic mode of OSP and IGA to establish the fitness function to make the solution more perfect. And, in order to reduce the complexity of the algorithm, integer coding method is used in the calculation. Finally, by the analysis of OSP for an arch bridge, results suggest compared with GA, the IGA method can better solve the problem, and has an advantage of high-precision.

## Acknowledgements

## References

[1]. B. Li, D. Li, X. Zhao, *et al*., Optimal sensor placement in health monitoring of suspension bridge, *Science China Technological Sciences*, Vol. 55, Issue 12, 2012, pp. 2039-2047.

[2]. J. M. Ko, Y. Q. Ni, Technology developments in structural health monitoring of large-scale bridges, *Engineering Structures*, Vol. 27, Issue 12, 2005, pp. 1715-1725.

[3]. G. W. Housner, L. A. Bergman, T. K. Caughey, *et al*., Structural control: past, present, and future, *Journal of Engineering Mechanics*, Vol. 123, Issue 9, 1997, pp. 897-971.

[4]. D. C. Kammer, Sensor placement for on-orbit modal identification and correlation of large space structures, *Journal of Guidance, Control and Dynamics*, Vol. 14, Issue 2, 1991, pp. 251-259.

[5]. K. B. Kim, Method for optimal actuator and sensor placement for large flexible structures, *Journal of Guidance, Control and Dynamics*, Vol. 15, Issue 1, 1992, pp. 49-57.

[6]. G. C. Thomas, R. D. Clark, A modal test design strategy for modal correlation, in *Proceedings of the 13th International Modal Analysis Conference*, Nashville, Tennessee, 1995, pp. 927-933.

[7]. G. Heo, M. L. Wang, D. Satpathi, Optimal transducer placement for health monitoring of long span bridge, *Soil Dynamics and Earthquake Engineering*, Vol. 16, Issue 7, 1997, pp. 495-502.

[8]. R. E. Miller, Optimal sensor placement via Gaussian quadrature, *Applied Mathematics and Computation*, Vol. 97, Issue 1, 1998, pp. 71-79.

[9]. U. S. Park, J. W. Choi, W.-S. Yoo, Optimal placement of sensors and actuators using measures of modal controllability and observability in a balanced coordinate, *Journal of Mechanical Science and Technology*, Vol. 17, Issue 1, 2003, pp. 11-22.

[10]. M. Meo, G. Zumpano, On the optimal sensor placement techniques for a bridge structure, *Engineering Structures*, Vol. 27, Issue 10, 2005, pp. 1488-1497.

[11]. D. Li, H. Li, C. P. Fritzen, The connection between effective independence and modal kinetic energy methods for sensor placement, *Journal of Sound and Vibration*, Vol. 305, Issue 4-5, 2007, pp. 945-955.

[12]. Y. Yao, W. A. Sethares, D. C. Kammer, Sensor placement for on-orbit modal identification via genetic algorithm, *American Institute of Aeronautics and Astronautics*, Vol. 1, Issue 10, 1993, pp. 1922-1928.

[13]. H. Guo, L. hang, L. Zhang, *et al*., Optimal placement of sensors for structural health monitoring using improved genetic algorithms, *Smart Materials and Structures*, Vol. 13, Issue 3, 2004, pp. 528-534.

[14]. W. Liu, W. Gao, Y. Sun, *et al*., Optimal sensor placement for spatial lattice structure based on genetic algorithms, *Journal of Sound and Vibration*, Vol. 317, Issue 1-2, 2008, pp. 175-189.

[15]. T. Yi, H. Li, M. Gu, Optimal sensor placement for health monitoring of high-rise structure based on genetic algorithm, *Mathematical Problems in Engineering*, Vol. 2011, 2011, pp. 1-12.

[16]. L. Jiao, L. Wang, A novel genetic algorithm based on immunity, *IEEE Transactions on System, Man and Cybernetics. Part A: System and Humans*, Vol. 30, Issue 5, 2000, pp. 552-561.

[17]. F. Kang, J. Liu, Q. Xu, Virus coevolution partheno-genetic algorithms for optimal sensor placement, *Advanced Engineering Informatics*, Vol. 22, Issue 3, 2008, pp. 362-370.

[18]. Y. Liao Y, D. Yau, C. Chen, Evolutionary algorithm to travelling salesman problems, *Computers & Mathematics with Applications*, Vol. 64, Issue 5, 2012, pp. 788-797.

[19]. C. B. Jagdish, D. Kusum, A modified binary particle swarm optimization for knapsack problems, *Applied Mathematics and Computation*, Vol. 218, Issue 22, 2012, pp. 11042-11061.

[20]. Z. Jun, Q. Liu, W. Wang, *et al*., A parallel immune algorithm for traveling salesman problem and its application on cold rolling scheduling, Information *Sciences*, Vol. 181, Issue 7, 2011, pp. 1212-1223.

[21]. ANSYS, ANSYS, Inc. Pittsburgh, PA, USA (http://www.ansys.com).

[22]. D. Bradley, A. Tyrell, Immunotronics: Hardware fault tolerance inspired by the immune system, in *Proceedings of the 3rd International Conference on Evolvable Systems: From Biology to Hardware (ICES2000)*, Springer, 2000, pp. 11-20.

[23]. W. Wang, S. Gao, Z. Tang, Improved pattern recognition with complex artificial immune system, *Soft Computing: A Fusion of Foundations, Methodologies and Applications*, Vol. 13, Issue 12, 2009, pp. 1209-1217.

[24]. B. Naderi, M. Mousakhani, M. Khalili, Scheduling multi-objective open shop scheduling using a hybrid immune algorithm, The International *Journal of Advanced Manufacturing Technology*, Vol. 66, Issue 5-8, 2013, pp. 895-905.

[25]. Y. C. Wong Eugene, Y. K. Lau Henry, K. L. Mark, Immunity-based evolutionary algorithm for optimal global container repositioning in liner shipping, *OR Spectrum*, Vol. 32, Issue 3, 2010, pp. 739-763.

[26]. C. Chen, D. Pi, Z. Fang, Artificial immune algorithm applied to short-term prediction for mobile object location, *Electronics Letters*, Vol. 48, Issue 17, 2012, pp. 1061-1062.

[27]. J. Farmer, N. Packard, A. Perelson, The immune system, adaptation and machine learning, *Physica. D:*

*Nonlinear Phenomena*, Vol. 22, Issue 1-3, 1986, pp. 187-204.

[28]. H. Guo, L. Zhang, L. Zhang, *et al*., Optimal placement of sensors for structural health monitoring using improved genetic algorithms, *Smart Materials and Structures*, Vol. 13, Issue 3, 2004, pp. 528-534.

---

I²MTC 2015 spans research, development and applications in the field of instrumentation and measurement science and technology. This includes Industrial Tracks, where research merges with practical applications in industrial technology used every day. The Conference fosters the exchange of know-how between industry and academia. Paper contests will include a Conference Best Paper Award and Student Best Poster Awards. In addition to papers, the conference will also have Tutorials and Exhibits covering the entire range of Instrumentation and Measurement Technology. The Conference focuses on all aspects of instrumentation and measurement science and technology-research, development and applications. The program topics include:

- Advances in Instrumentation and Measurement Developments and Techniques
- Biomedical Systems
- Data Acquisition Systems and Techniques
- Energy and Power Systems
- Industrial Process Control
- Measurement and Instrumentation for Industrial Applications
- Measurement Applications
- Measurement of Electric and Magnetic Quantities
- Measurement of Materials and Mechanical Quantities
- Measurement, Instrumentation and Methodologies Related to Healthcare Systems
- Measurement Systems and Theory
- Non-invasive Measurement Techniques and Instrumentation
- Real-Time Measurement
- Robotics and Controls
- Sensors and Sensor Fusion
- Signal & Image Processing Techniques
- Software Development for Measurement and Instrumentation Support
- Techniques related to Instrumentation
- Transducers
- Virtual Measurement Systems
- Wireless Sensors and Systems

## IMPORTANT DATES

**September 15, 2014** - Submission of FULL PAPERS (**HARD Deadline**)
**December 05, 2014** - Notification of paper acceptance, rejection or revision
**January 12, 2015** - Submission of final version (**HARD Deadline**)
**February 9, 2015** - Final notification of paper acceptance

# State Estimation for Sensor Monitoring System with Uncertainty and Disturbance

**[1] Jianhong Sun, [2] Xiaoying Yu, [2] Jiangwei Qiu, [3] Pengfei Guo**

[1] School of Electronic Engineering and Optoelectronic Techniques, Nanjing University of Science and Technology, Nanjing, 210094, China

[2] Changjiangrunfa Machinery Co., Ltd., Suzhou, 215633, China

[3] School of Automation, Nanjing University of Science and Technology, Nanjing, 210094, China

[1] Tel.: +86-025-84303086

[1] E-mail: sunjh@njust.edu.cn

**Abstract:** This paper considers the state estimation problem for the sensor monitoring system which contains system uncertainty and nonlinear disturbance. In the sensor monitoring system, states of each inner sensor node usually contains system uncertainty, and external noise often works as nonlinear item. Besides, information transmission in the system is also time consuming. All mentioned above may arouse in unstable of the monitoring system. In this case, states of sensors could be wrongly sampled. Under this circumstance, a proper mathematical model is proposed and by the use of Lipschitz condition, the nonlinear item is transformed to linear one. In addition, we suppose that all sensor nodes are distributed arranged, no interface occurs with each other. By establishing proper Lyapunov–Krasovskii functional, sufficient conditions are acquired by solving linear matrix inequality to make the error augmented system stable, and the gains of observers are also derived. Finally, an illustrated example is given to show that system observed value tracks system states well, which fully demonstrate the effectiveness of our result. *Copyright © 2014 IFSA Publishing, S. L.*

**Keywords:** State estimation, Sensor monitoring system, System uncertainty, Nonlinear disturbance, Linear matrix inequality.

## 1. Introduction

During last decades, states estimation and other related problems are hot issues in the scholar field due to the increasing demand of sensor monitoring system, which is a distributed system composed of sensor nodes [1-3]. Because of its convenience for use and low cost, sensor monitoring system aroused much attention both from theoretical researches and practical occasions, such as in industry, agriculture, military and some other occasions [4]. Sensors collect data from the field and also control the operating parameters. By running a dedicated data collection procedure to achieve field data collection,

in addition, control operating parameters are transferred to sensors via data bus to achieve automatic control. However, many problems are resulted in for its special system structure. Information flow between sensor nodes is time consuming, which reflects as time-delay in system model. In addition, outer environment, take temperature, pressure, moist for example, can greatly affect sensors' working condition, so system uncertainties and disturbances are inevitable when modeling for sensor monitoring system. Take all mentioned above, states estimation is quite important for the stability analysis of sensor monitoring system.

Still now, great effort has been done to deal with states estimation problem [5-7]. Reference [8] studied the spread of subsurface contaminants, proposed a dual estimation strategy for data assimilation into a one-way coupled system by treating the flow and the contaminant models separately. This strategy didn't only deals with states estimation, but also could be used for parameter estimation. Reference [9] considered a fuzzy-integral model of a fuzzy process. Sufficient conditions were established for the existence of an optimal estimating fuzzy process. Reference [10] researched estimation problem around human environment. A Human motion map was proposed which incorporating human states information into results of conventional SLAM.

Motivated by previous research stated above, our target is to make state estimation for sensor monitoring system, which contains uncertainty and nonlinear disturbance. By establishing proper Lyapunov-Krasovskii functional, sufficient conditions are proposed to make system stable, and observe gains are also acquired.

## 2. Problem Formulation

Consider a type of sensor monitoring system, which is composed of several sensor nodes, and the dynamic system with uncertainty and disturbance can be described as shown in (1):

$$\begin{cases} x_i(k+1) = (A+\Delta A)x_i(k) \\ \qquad + A_d x_i(k-\tau) \\ \qquad + Bu(k) + E_g g(x_i(k)) \\ y_i(k) = Cx_i(k) \end{cases}, \qquad (1)$$

where $x_i(k) \in R^n$ denotes the state of $i^{th}$ node, $x_i(k-\tau) \in R^n$ denotes the state delay of the node, $g(x_i(k)) \in R^n$ denotes the nonlinear disturbance, $u(k) \in R^{n_u}$ is the system input, $y_i(k) \in R^n$ denotes system output, $\Delta A$ is internal perturbation arising from uncertain factors, $A$, $A_d$, $E_g$, $B$ and $C$ are constant matrices with appropriate dimensions.

Here we make the following assumption for system model (1).

**Assumption 1.**
Perturbation parameter of the model satisfies:

$$\Delta A = GD(k)H \qquad (2)$$

Respectively, $G$ and $H$ are known constant matrix, $D(k)$ is time delay uncertain matrix, yet Lebesgue-measurable, and $D^T(k)D(k) \le I$.

**Assumption 2.**
State delay has an upper bound, which satisfies $0 \le \tau \le d$.

**Assumption 3.**
System nonlinear factor g(·) satisfies the following Lipschitz condition:

$$\left\| g(x_1) - g(x_2) \right\| \le \left\| \Sigma(x_1 - x_2) \right\|,$$

where $\Sigma$ is the constant matrix with proper dimensions, and $g(0)=0$.

Next, a state observer for the $i^{th}$ node is constructed.

$$\begin{cases} \hat{x}_i(k+1) = A\hat{x}_i(k) \\ \qquad + \sum_{j=1}^{N} k_{ij} C[x_i(k) - \hat{x}_i(k)], \\ \qquad + Bu(k) + E_g g(\hat{x}_i(k)) \\ \hat{y}_i(k) = C\hat{x}_i(k) \end{cases} \qquad (3)$$

where $\hat{x}_i(k)$ and $\hat{y}_i(k)$ are the observed value of $x_i(k)$ and $y_i(k)$, respectively. $K_{ij} \in R^n$ is the gain of observer to be designed.

In this case, the states error and output error are defined as:

$$\begin{cases} e_{xi}(k) = x_i(k) - \hat{x}_i(k) \\ e_{yi}(k) = y_i(k) - \hat{y}_i(k) \end{cases}, \qquad (4)$$

where

$$\begin{aligned} e_{xi}(k+1) &= (A - \sum_{j=1}^{N} k_{ij} C)e_i(k) \\ &+ \Delta A x_i(k) + A_d x_i(k-\tau) \\ &+ E_g g(e_{xi}(k)) \end{aligned} \qquad (5)$$

By utilizing the Kronecker product, the error dynamics governed by (5) can be rewritten as:

$$\begin{aligned} e(k+1) &= (\tilde{A} - K\tilde{C})e(k) \\ &+ \Delta\tilde{A}x(k) + \tilde{A}_d x(k-\tau) \\ &+ \tilde{E}_g g(e_x(k)) + \tilde{E}_f f(k), \end{aligned} \qquad (6)$$

where $\tilde{A} = I_N \otimes A$, $K = (k_{ij})_{n \times n}$, $\tilde{C} = I_N \otimes C$, $\Delta\tilde{A} = I_N \otimes \Delta A$, $\tilde{A}_d = I_N \otimes A_d$, $\tilde{E}_g = I_N \otimes E_g$, $\tilde{E}_f = I_N \otimes E_f$. By employing an augmented vector $Z(k) = \begin{bmatrix} x^T(k) & e^T(k) \end{bmatrix}^T$, so we have augmented system:

$$\begin{aligned} Z(k+1) &= \bar{A}Z(k) + \Delta\bar{A}Z(k) \\ &+ \bar{A}_d Z(k-\tau) \\ &+ \bar{E}_g g(Z(k)) + \bar{E}_f f(k), \end{aligned} \qquad (7)$$

where

$$\overline{A}=\begin{bmatrix} \tilde{A} & 0 \\ 0 & \tilde{A}-K\tilde{C} \end{bmatrix}, \quad \overline{A}_d=\begin{bmatrix} \tilde{A}_d & 0 \\ \tilde{A}_d & 0 \end{bmatrix}$$

$$\Delta\overline{A}=\begin{bmatrix} \Delta\tilde{A} & 0 \\ \Delta\tilde{A} & 0 \end{bmatrix}, \quad \overline{E}_g=\begin{bmatrix} \tilde{E}_g & 0 \\ 0 & \tilde{E}_g \end{bmatrix}$$

$$\overline{E}_f = \begin{bmatrix} \tilde{E}_f \\ \tilde{E}_f \end{bmatrix}$$

Furthermore, some important lemmas will be used in this paper are listed below.

**Lemma 1.** For any $x, y \in R^n$, $\mu > 0$, the following equation holds.

$$2x^T y \le \mu x^T x + \frac{1}{\mu} y^T y$$

**Lemma 2.** Let $Y=Y^T$, $M$, $N$, and $D(t)$ be real matrix of proper dimensions, and $D^T(t)D(t) \le I$, then inequality $Y+MDN+(MDN)^T < 0$ holds if there exists a constant $\varepsilon$, which makes the following inequality holds.

$$Y + \varepsilon NN^T + \varepsilon^{-1}M^T M < 0$$

## 3. Main Results

In this part, two sufficient conditions are proposed to make augmented system (7) stable, in addition, the gains of observer can also be acquired.

**Theorem 1.** For the augmented system as shown in (7), it is said to be asymptotically stable if there exists positive definite matrix $P = diag\{P_1, P_2\}$, $Q$ and a constant $\varepsilon$, make the following inequality holds.

$$\begin{bmatrix} \Omega & 0 & \Gamma & 0 & 0 & 0 \\ * & -Q & 0 & 0 & 2\overline{A}_d^T P & 0 \\ * & * & -P & 0 & 0 & 0 \\ * & * & * & -P & 0 & \tilde{G}^T \overline{P} \\ * & * & * & * & -P & 0 \\ * & * & * & * & * & -\varepsilon I \end{bmatrix} < 0$$

where

$$\Omega = -P + (1+d)Q + 4\lambda \sum^T \sum + \varepsilon \overline{H}^T \overline{H}$$

$$\overline{H} = \begin{bmatrix} \tilde{H} & 0 \end{bmatrix}$$

$$\overline{P} = \begin{bmatrix} P_1^T & P_2^T \end{bmatrix}^T$$

$$\tilde{G} = I_N \otimes G$$

Proof: By constructing the following Lyapunov-Krasovslii functional

$$V(k) = V_1(k) + V_2(k), \tag{8}$$

where

$$V_1(k) = Z^T(k)PZ(k)$$

$$V_2(k) = \sum_{i=k-\tau}^{k-1} Z^T(i)QZ(i)$$

$$+ \sum_{j=1-d}^{0} \sum_{i=k+j}^{k-1} Z^T(i)QZ(i)$$

So the forward difference of $V(k)$ along (7) is:

$$\begin{aligned}
&E\Delta V_1 \\
&= E\{Z^T(k+1)PZ(k+1) \\
&\quad -Z^T(k)PZ(k)\} \\
&= Z^T(k)\overline{A}^T P\overline{A}Z(k) \\
&\quad +2Z^T\overline{A}^T P\Delta\overline{A}Z(k) \\
&\quad +2Z^T(k)\overline{A}^T P\overline{A}_d Z(k-\tau) \\
&\quad +2Z^T(k)\overline{A}^T P\overline{E}_g g(Z(k)) \\
&\quad +Z^T\Delta\overline{A}^T P\Delta\overline{A}Z(k) \\
&\quad +2Z^T\Delta\overline{A}^T P\overline{A}_d Z(k-\tau) \\
&\quad +2Z^T\Delta\overline{A}^T P\overline{E}_g g(Z(k)) \\
&\quad +Z^T(k-\tau)\overline{A}_d^T P\overline{A}_d Z(k-\tau) \\
&\quad +2Z^T(k-\tau)\overline{A}_d^T P\overline{E}_g g(Z(k)) \\
&\quad +g^T(Z(k))\overline{E}_g^T P\overline{E}_g g(Z(k)) \\
&\quad -Z^T(k)PZ(k)
\end{aligned} \tag{9}$$

By the use of **Lemma 1**, we can obtain:

$$\begin{aligned}
&2Z^T(k)\overline{A}^T P\overline{A}_d Z(k-\tau) \\
&\le Z^T(k)\overline{A}^T P\overline{A}Z(k) \\
&\quad +Z^T(k-\tau)\overline{A}_d^T P\overline{A}_d^T Z(k-\tau)
\end{aligned} \tag{10}$$

$$\begin{aligned}
&2Z^T(k)\overline{A}^T P\overline{A}_d Z(k-\tau) \\
&\le Z^T(k)\overline{A}^T P\overline{A}Z(k) \\
&\quad +Z^T(k-\tau)\overline{A}_d^T P\overline{A}_d^T Z(k-\tau)
\end{aligned} \tag{11}$$

$$\begin{aligned}
&2Z^T(k)\overline{A}^T P\overline{E}_g g(Z(k)) \\
&\le Z^T(k)\overline{A}^T P\overline{A}Z(k) \\
&\quad +g^T(Z(k))\overline{E}_g^T P\overline{E}_g g(Z(k))
\end{aligned} \tag{12}$$

$$2Z^T(k)\Delta\overline{A}^T P\overline{A}_d Z(k-\tau)$$

$$\leq Z^T(k)\Delta\overline{A}^T P\Delta\overline{A}Z(k) \tag{13}$$

$$+ Z^T(k-\tau)\overline{A}_d^T P\overline{A}_d Z(k-\tau)$$

$$2Z^T(k)\Delta\overline{A}^T P\overline{E}_g g(Z(k))$$

$$\leq Z^T(k)\Delta\overline{A}^T P\Delta\overline{A}Z(k) \tag{14}$$

$$+ g^T(Z(k))\overline{E}_g^T P\overline{E}_g g(Z(k))$$

$$2Z^T(k-\tau)\overline{A}_d^T P\overline{E}_g g(Z(k))$$

$$\leq Z^T(k-\tau)\overline{A}_d^T P\overline{A}_d Z(k-\tau) \tag{15}$$

$$+ g^T(Z(k))\overline{E}_g^T P\overline{E}_g g(Z(k))$$

According to assumption 3, nonlinear disturbance can be rewritten into the form:

$$g^T(Z(k))\overline{E}_g^T P\overline{E}_g g(Z(k))$$

$$\leq \lambda_{\max}(\overline{E}_g^T P\overline{E}_g)g^T(Z(k))g(Z(k)) \tag{16}$$

$$\leq \lambda Z^T(k)\sum{}^T\sum Z(k)$$

$$E\Delta V_2$$

$$= \sum_{i=k+1-\tau}^{k} Z^T(i)QZ(i) - \sum_{i=k-\tau}^{k-1} Z^T(i)QZ(i)$$

$$+ \sum_{j=1-d}^{0}\sum_{i=k+1+j}^{k} Z^T(i)QZ(i)$$

$$- \sum_{j=1-d}^{0}\sum_{i=k+j}^{k-1} Z^T(i)QZ(i)$$

$$\leq Z^T(k)QZ(k) - Z^T(k-\tau)QZ(k-\tau)$$

$$+ \sum_{i=k+1-\tau}^{k-1} Z^T(i)QZ(i)$$

$$+ \sum_{j=1-d}^{0}\{Z^T(k)QZ(k) \tag{17}$$

$$- Z^T(k+j)QZ(k+j)\}$$

$$= Z^T(k)QZ(k) - Z^T(k-\tau)QZ(k-\tau)$$

$$+ \sum_{i=k+1-\tau}^{k} Z^T(i)QZ(i)$$

$$+ dZ^T(k)QZ(k) - \sum_{i=k+1-\tau}^{k} Z^T(i)QZ(i)$$

$$= (1+d)Z^T(k)QZ(k)$$

$$- Z^T(k-\tau)QZ(k-\tau)$$

By substituting (9) to (17) into (8), we have:

$$E\Delta V = E\{\Delta V_1 + \Delta V_2\}$$

$$= X^T(k)YX(k) \quad,$$

where

$$X(k) = \begin{bmatrix} Z^T(k) & Z^T(k-\tau) \end{bmatrix}^T$$

$$Y = \begin{bmatrix} Y_{11} & 0 \\ 0 & Y_{22} \end{bmatrix}$$

$$Y_{11} = 4\overline{A}^T P\overline{A} + 4\Delta\overline{A}^T P\Delta\overline{A} + 4\lambda\sum{}^T\sum$$

$$- P + (1+d)Q$$

$$Y_{22} = 4\overline{A}_d^T P\overline{A}_d - Q$$

According to Schur complement, $Y < 0$ equals to:

$$\begin{bmatrix} Y_1 & 0 & 2\overline{A}^T & 2\Delta\overline{A}^T & 0 \\ * & -Q & 0 & 0 & 2\overline{A}_d^T \\ * & * & -P^{-1} & 0 & 0 \\ * & * & * & -P^{-1} & 0 \\ * & * & * & * & -P^{-1} \end{bmatrix} < 0,$$

where

$$Y_1 = -P + (1+d)Q + 4\lambda\sum{}^T\sum$$

Multiply $diag\{I, I, P, P, P\}$ on both sides of the inequality, the following inequality can be acquired.

$$\begin{bmatrix} Y_1 & 0 & 2\overline{A}^T P & 2\Delta\overline{A}^T P & 0 \\ * & -Q & 0 & 0 & 2\overline{A}_d^T P \\ * & * & -P & 0 & 0 \\ * & * & * & -P & 0 \\ * & * & * & * & -P \end{bmatrix} < 0 \tag{18}$$

According to Lemma 2 and the notation defined in the theorem, result can be easily acquired, so the proof of Theorem 1 is complete.

Theorem 1 only demonstrate the stability of error system (7), however, observer gains can't be acquired, so the following theorem is given.

**Theorem 2.** For the augmented system as shown in (7), it is said to be asymptotically stable if there exists positive definite matrix $P = diag\{P_1, P_2\}$, $Q$ and a constant $\varepsilon$, make the following inequality holds.

$$\begin{bmatrix} \Omega & 0 & 2\overline{A}^T P & 0 & 0 & 0 \\ * & -Q & 0 & 0 & 2\overline{A}_d^T P & 0 \\ * & * & -P & 0 & 0 & 0 \\ * & * & * & -P & 0 & \tilde{G}^T\overline{P} \\ * & * & * & * & -P & 0 \\ * & * & * & * & * & -\varepsilon I \end{bmatrix} < 0,$$

where

$$\Omega = -P + (1+d)Q + 4\lambda \sum^T \sum + \varepsilon \bar{H}^T \bar{H}$$

$$\bar{H} = \begin{bmatrix} \tilde{H} & 0 \end{bmatrix}$$

$$\bar{P} = \begin{bmatrix} P_1^T & P_2^T \end{bmatrix}^T$$

$$\tilde{G} = I_N \otimes G$$

$$\Gamma = 2 \begin{bmatrix} \tilde{A}P_1 & 0 \\ 0 & \tilde{A}P_2 - \tilde{C}^T S \end{bmatrix}$$

$\Omega$, $\bar{H}$, $\bar{P}$, $\tilde{G}$ have the same meaning as defined in Theorem 1, and the gain of observe is:

$$K = P_2^{-1} S^T$$

Proof: Setting $K^T P_2 = S$, so $K = P_2^{-1} S^T$, by substituting $K^T P_2 = S$ into Theorem 1, we can get the result easily.

## 4. Numerical Example

In this part, a numerical example is given to show the effectiveness of proposed method. Transform the case on [11], parameters in (1) are given as:

$$A = \begin{bmatrix} 0.2546 & 0.2472 \\ 0.2323 & 0.2268 \end{bmatrix},$$

$$A_d = \begin{bmatrix} -0.1434 & 0.0061 \\ -0.0118 & 0.0384 \end{bmatrix}, B = \begin{bmatrix} 0.1669 \\ 0.1174 \end{bmatrix},$$

$$E_g = \begin{bmatrix} -0.0130 \\ 0.0742 \end{bmatrix}$$

$$C = \begin{bmatrix} 1.1866 & 0.4552 \\ 0.5395 & 0.3164 \end{bmatrix}$$

$$G = \begin{bmatrix} 0.0618 & 0.1236 \\ 0 & 0.1422 \end{bmatrix},$$

$$D(k) = \begin{bmatrix} 0.2\sin(0.6k) & 0 \\ 0 & 0.2\sin(0.6k) \end{bmatrix},$$

$$H = \begin{bmatrix} 0.4450 & 0.3214 \\ 0.2596 & -0.4326 \end{bmatrix},$$

$$g_i(x(k)) = \begin{bmatrix} 0.12\cos x_{i1}(k) & 0.41x_{i2} \end{bmatrix}^T$$

$$u(k) = 5e^{-0.01k}\sin(k)$$

The initial states of each sensor nodes are:

$$x_1 = \begin{bmatrix} 3.2 \\ -3.5 \end{bmatrix}, x_2 = \begin{bmatrix} 2.2 \\ -1.6 \end{bmatrix}, x_3 = \begin{bmatrix} 2.72 \\ 3.25 \end{bmatrix}$$

Observer gain can be obtained based on Theorem 1 and Theorem 2, we have:

$$k_{11} = k_{22} = k_{33} = \begin{bmatrix} -0.4067 & 1.3663 \\ -0.3762 & 1.2581 \end{bmatrix}$$

Simulation results are given in Fig. 1, where red lines denotes for real system state, blue dashed line denotes for observed value. From the result, we can see that observed value tracks system states well, which can fully demonstrate the effectiveness of proposed method. Estimation error is shown in Fig. 2, which is much smaller than the method proposed in [12], compared with Fig. 3.
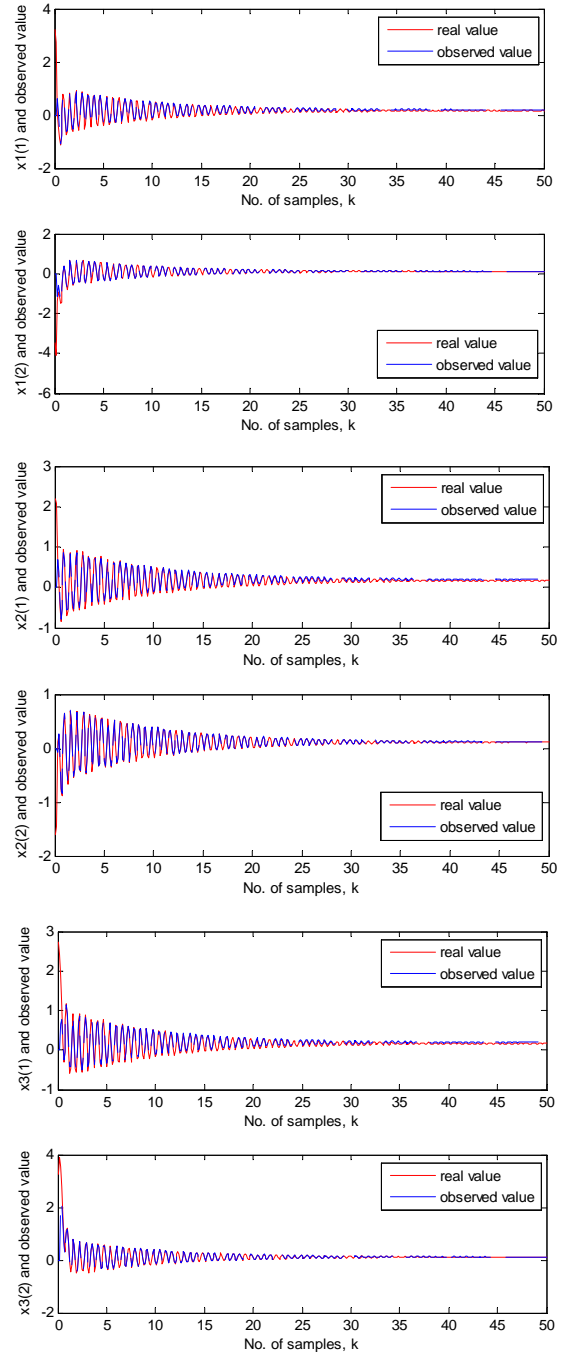


**Fig. 1.** System states and observed value.
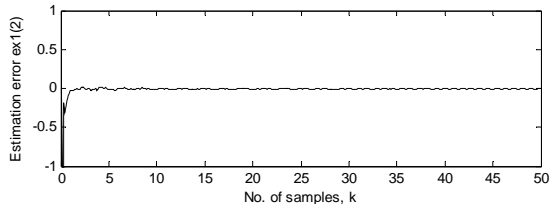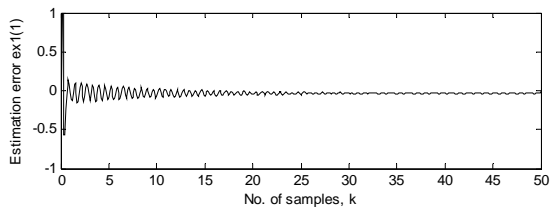
(a) Estimation error $e_{x1}$
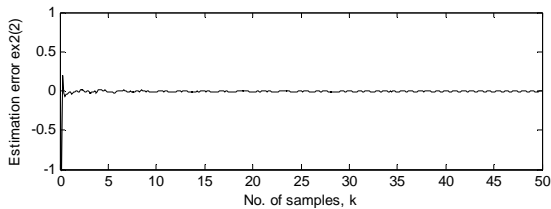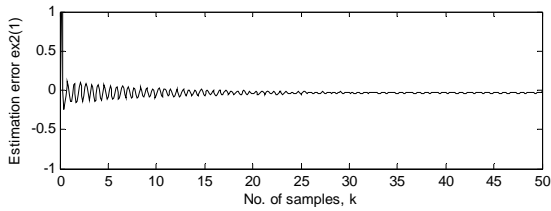


(b) Estimation error $e_{x2}$
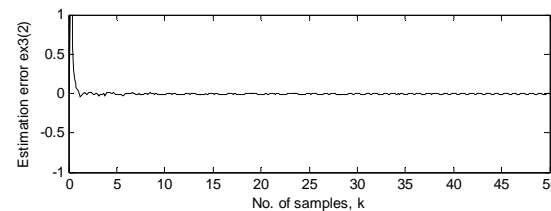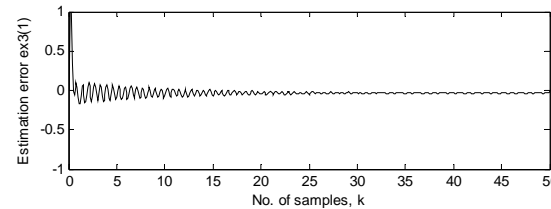


(c) Estimation error $e_{x3}$

**Fig. 2.** Estimation error for system states.
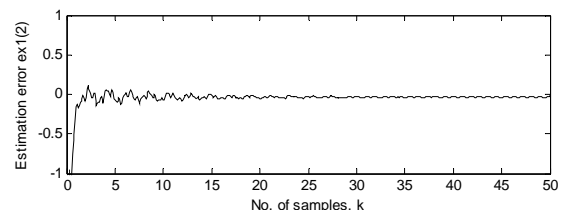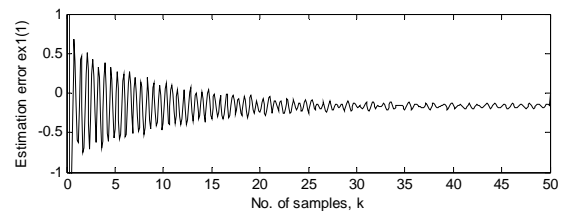


(a) Estimation error $e_{x1}$
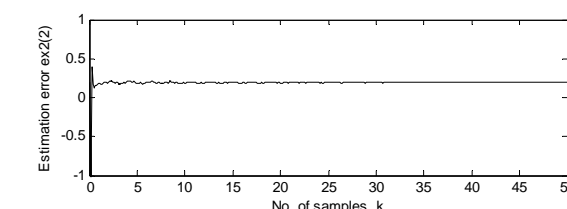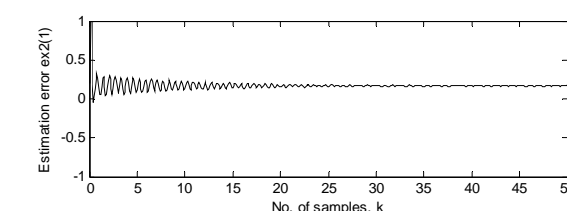


(b) Estimation error $e_{x2}$
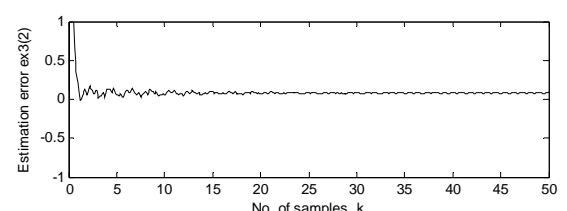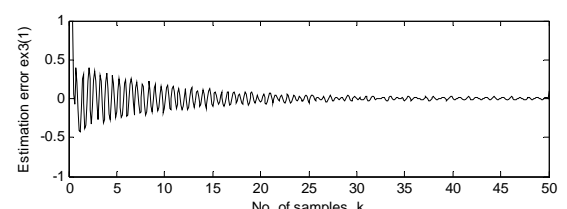


(c) Estimation error $e_{x3}$

**Fig. 3.** Method proposed in [12].

## 5. Conclusions

This paper deals with the state estimation problem for a class of sensor monitoring system, which contains system uncertainty and nonlinear disturbance. By establishing proper Lyapunov–Krasovskii functional, sufficient conditions are proposed to guarantee the stability of error system, and the gains of observes are also acquired. Finally, an illustrated example shows the effectiveness of proposed method.

## Acknowledgements

## References

[1]. Yurish S. Y., Smart sensors systems design: new curricula based on Marie Curie Chairs Excellence

(EXC) project's results, *Measurement*, Vol. 43, Issue 1, 2010, pp. 21-30.

[2]. Wu L., Shi P., Gao H., State estimation and sliding-mode control of Markovian jump singular systems, *IEEE Transactions on Automatic Control,* Vol. 55, Issue 5, 2010, pp. 1213-1219.

[3]. Rubinov M., Sporns O., Complex network measures of brain connectivity: uses and interpretations, *Neuroimage,* Vol. 52, Issue 3, 2010, pp. 1059-1069.

[4]. Yurish S. Y., Smart and Intelligent Optoelectronic Sensor Systems: OEM Design Approach, in *Proceedings of the 2nd International Conference on Sensor Device Technologies and Applications (SENSORDEVICES'11)*, 2011, pp. 38-43.

[5]. Kandepu R., Foss B., Imsland L., Applying the unscented Kalman filter for nonlinear state estimation, *Journal of Process Control,* Vol. 18, Issue 7, 2008, pp. 753-768.

[6]. Singh R., Pal B. C., Jabr R. A., Choice of estimator for distribution system state estimation, *IET Generation, Transmission & Distribution,* Vol. 3, Issue 7, 2009, pp. 666-678.

[7]. Fridman L., Shtessel Y., Edwards C., *et al*., Higher-order sliding-mode observer for state estimation and input reconstruction in nonlinear systems, *International Journal of Robust and Nonlinear Control,* Vol. 18, Issue 4-5, 2008, pp. 399-412.

[8]. Gharamti M. E., Hoteit I., Valstar J., Dual states estimation of a subsurface flow-transport coupled model using ensemble Kalman filtering, *Advances in Water Resources*, Issue 60, 2013, pp. 75-88.

[9]. Sirbiladze G., Problems of States Estimation (Filtration) of Extremal Fuzzy Processes, *Extremal Fuzzy Dynamic Systems. Springer New York,* 2013, pp. 255-288.

[10]. Ogawa Y., Wang Z., Wada T., *et al*., Building Human Motion Map with human states estimation in indoor dynamic environments, in *Proceedings of the IEEE International Conference on Robotics and Biomimetics (ROBIO),* 2011, pp. 1090-1095.

[11]. F. Gouaisbaut, M. Dambrine, J. Richard, Robust control of delay systems: a sliding mode control design via LMI, *Systems & Control Letters*, Vol. 46, Issue 4, 2002, pp. 219-230.

[12]. Chen W., Mehrdad S., Observer design for linear switched control systems, in *Proceedings of the American Control Conference,* 2004, pp. 5796-5801.

_____

# Research on Ground Penetrating Radar Migration Imaging Technology

**[1] Yao QIN, [2] Qi-Fu WANG, [1] Li-Hong QIAO, [1] Xiao-Zhen REN**

[1] College of Information Science and Engineering, Henan University of Technology, Zhengzhou, Henan 450001, China
[2] Henan Academy of Science, Applied Physics Institute Co., Ltd, Zhengzhou, Henan, 450001, China
[1] Tel.: 86-037163296259, fax: 86-037163392656
[1] E-mail: eqinyao@163.com

**Abstract:** The ability of Ground penetrating radar (GPR) to estimate the shape and position of objects in target area is depends on the imaging technology. Migration image method was popular used in seismic wave detection technology, and now it is used in GPR electromagnetic wave detection technology. In this paper, three migration image methods: Finite Difference Time Domain (FDTD), Frequency Wave number, and Kirchhoff migration method are been discussed separately. By dealing with GPR simulation and experiment data, it shows that the seismic wave migration method used in GPR imaging is effectiveness and stability. At last, compare the imaging results of three migration methods, several useful conclusions are been given. *Copyright © 2014 IFSA Publishing, S. L.*

**Keywords:** Ground penetrating radar, Migration imaging, FDTD, Frequency Wave number, Kirchhoff.

## 1. Introduction

Ground penetrating radar (GPR) is a mature remote sensing technique employed by engineers and scientists to obtain information from subsurface structures. Image technology is an important subject of ground penetrating radar signal processing technology. The images of subsurface objects are different with actual location because the antenna has limited lobe width and bandwidth. There is one of the most important problems that how to extract the information such as the location and shape of subsurface objects from GPR output images. Different methods have been put forward by overseas and domestic scholars. Migration method is been widely used in seismic data processing. This paper chooses Finite Difference Time Domain (FDTD), Frequency Wave-number, and Kirchhoff migration method to deal with GPR imaging. Simulation and experiment results show that the seismic wave migration method used in GPR imaging is effectiveness and stability.

## 2. Migration Theory

Migration is a tool used in GPR processing to get an accurate picture of underground targets. It involves geometric repositioning of return signals to show an event where it is being hit by the electromagnetic wave rather than where it is picked up.

Migration principle can be explained by Fig. 1. In Fig. 1, GPR detects on the surface of medium. There is a metal point target in the medium. O is the true position of the target. O' is the detected position

from $x_i$. Assuming $\Delta x_i = |x_i - x_0|$, the travel time from $x_i$ to O' is $\dfrac{t_i}{2}$, and from $x$ to O' is $\dfrac{t}{2}$. According to the geometric repositioning, the relationship of travel time from different position can be written as:

$$\left(\frac{t}{2}\right)^2 = \left(\frac{t_i}{2}\right)^2 + \left(\frac{\Delta x_i}{v}\right)^2 \qquad (1)$$

Hence:

$$t_i = \left[t^2 - 4(\Delta x_i/v)^2\right]^{1/2} \qquad (2)$$
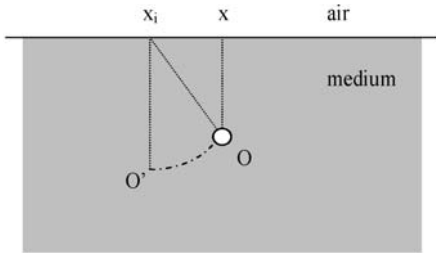


**Fig. 1.** Migration principle.

Migration process can be summarized as: GPR ground receiving point is considered as the center. Put reflection arrival time of different detect position to the arc, and the radius depth of the arc is $z = \dfrac{1}{2} vt$. Plus all the value together on the same point, then, the migration section is been built up.

## 3. FDTD Migration Method

According to explode reflection model (ERM) used in GPR data processing, the propagation path of electromagnetic wave under ground can be considered to be vertical if reflecting angle is less than $30°$. Then using $15°$ finite difference time domain method to solve electromagnetic wave equation can get the satisfied results. $15°$ FDTD is a recursive method，and it is sensitive with different horizontal velocity and vertical velocity of electromagnetic wave.

Under ground electromagnetic wave $\varphi(x, z, t)$ can satisfied with two-dimensional wave equation:

$$\varphi_{xx} + \varphi_{zz} - \frac{4}{c^2(x,z)} \varphi_{tt} = 0 \qquad (3)$$

Assuming $D = \dfrac{1}{2} ct + z$, $d = z$, the above can be written as:

$$\phi_{xx} + \phi_{dd} + 2\phi_{dD} = 0 \qquad (4)$$

By variable substitution, the wave filed $\phi(x, 0, D)$ can be transformed to $\phi(x, D, D)$. Migration of the point is been finished. If the incident direction of electromagnetic wave is nearly perpendicular, reflect wave inclination angle is also smaller then $15°$, $\phi_{xx} \gg \phi_{dd}$, $\phi_{dd}$ can be neglected, the reflect wave function can be written as

$$\phi_{xx} + 2\phi_{dD} = 0 \qquad (5)$$

Discrete variable, assuming $D_j = j\Delta D$ and $d_k = k\Delta d$, note $\phi(x)_j^k \equiv \phi(x, d_k, D_j)$. Symmetry implicit difference grid is been used to do the iterative compute. The difference grid is shown in Fig. 2. Here, horizontal and vertical axes are representation $x$ and $d$ direction, respectively. The calculated direction with $d$ is from top to down. The direction perpendicular to the paper is D, which is extension direction.
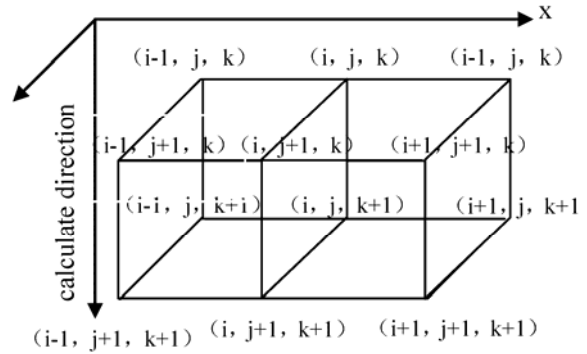


**Fig. 2.** Finite difference time domain grid.

Differential expression for the wave equation is:

$$(1-T)\phi_j^{k+1} = -(1-T)\phi_{j+1}^k + (1+T)\left(\phi_{j+1}^{k+1} + \phi_j^k\right), \qquad (6)$$

where $T = \dfrac{\Delta D \Delta d}{8} \dfrac{d^2}{dx^2}$, derive that:

$$\phi_j^{k+1} = -\phi_{j+1}^k + (1+2T)\left(\phi_{j+1}^{k+1} + \phi_j^k\right) \qquad (7)$$

Equation (7) is the iterative function of FDTD migration.

## 4. Frequency Wave-number Migration Theory

The electromagnetic pulse, radiated from GPR transmitting antenna, impinges on the objects and is scattered back towards the received antenna.

According to Huygens' principle, the reflected field, supposed the propagation velocity in the medium is half of the true value, it can be thought originated from the scatters and propagating towards the antenna. The problem is to reconstruct the wavefield existed at $t = 0$ from the wavefield observed at $z = 0$.

Supposed that the recorded profile is $e(x, z = 0, t)$, x and z are horizontal and vertical coordinates respectively, t is time, the migrated profile is $e(x, z, t = 0)$, Let $E(k_x, z = 0, \omega)$ be the 2-D Fourier transform of $e(x, z = 0, t)$

$$E(k_x, z = 0, \omega) = \int \int e(x, z = 0, t) e^{-j(k_x x + \omega t)} dx dt \quad (8)$$

In the F-K domain, wavefield at the depth of z can be expressed as

$$E(k_x, z, \omega) = E(k_x, z = 0, \omega) e^{jk_z z}, \quad (9)$$

where $k_x$, $k_z$ and $\omega$ are constrained by the dispersion relation for scalar waves

$$\frac{\omega^2}{(v/2)^2} = k^2 = k_x^2 + k_z^2 \quad (10)$$

Let $e(x, z, t)$ be the 2-D inverse Fourier transform of $E(k_x, z, \omega)$ with respect to $k_x$ and $\omega$

$$e(x, z, t) = \frac{1}{(2\pi)^2} \int \int E(k_x, z, \omega) e^{j(k_x x + \omega t)} dk_x d\omega \quad (11)$$

Using (10) and let $t = 0$, then

$$e(x, z, t = 0) = \frac{1}{(2\pi)^2} \int \int E\left(k_x, z = 0, \frac{v}{2}\sqrt{k_x^2 + k_z^2}\right) \cdot \left(v / (2\sqrt{1 + k_x^2 / k_z^2})\right) e^{jk_x x} e^{jk_z z} dk_x dk_z \quad (12)$$

This is the migrated profile. Let

$$A(k_x, k_z) = E(k_x, z = 0, \frac{v}{2}\sqrt{k_x^2 + k_z^2}) \cdot (v / (2\sqrt{1 + k_x^2 / k_z^2}))$$

F-K migration can be described as the flowing steps:
$$e(x, z = 0, t) \overset{FFT}{\rightarrow} E(k_x, z = 0, \omega) \rightarrow A(k_x, k_z) \overset{IFFT}{\rightarrow} e(x, z, t = 0)$$
The F-K migration is the fasted known migration techniques. In the transforms of $E(k_x, z = 0, \omega) \rightarrow A(k_x, k_z)$, we need properly choice the interpolation method. The F-K migration is also very sensitive with the variation of velocity in the medium, so it is relatively suitable for the homogeneous medium.

## 5. Kirchhoff Migration Method

Kirchhoff migration method uses diffraction integral formula to collect different traces energy from the same diffraction point, and forces the hyperbola focus to the reflection point.

Assuming the underground medium is uniformity and isotropy, the scalar quantity electric field equation can be written as:

$$\nabla^2 E(\bar{x}, t) = k^2 \frac{\partial^2 E(\bar{x}, t)}{\partial t^2}, \quad (13)$$

where $k^2 = 1/v_0^2$, $v_0$ is the velocity of electromagnetic wave in the medium.

According to Green theorem and point source Green formula, we can get the integral equation:

$$E(\bar{x}_0, t) = \int_{\partial V} \begin{bmatrix} \frac{1}{r}\left[\frac{\partial E}{\partial n}\right]_{t+r/v_0} - \frac{1}{v_0 r}\frac{\partial r}{\partial n}\left[\frac{\partial E}{\partial t}\right]_{t+r/v_0} \\ + \frac{1}{r^2}\frac{\partial r}{\partial n}[E]_t \end{bmatrix} d_{surf}, \quad (14)$$

here $v_0$ is the velocity, it can be a constant or a matrix. $r$ is the distance from transmition point to the reflection point, $r = \sqrt{(x - x_0)^2 + (y - y_0)^2 + (z - z_0)^2}$ $n$ is stands for the outside normal direction of integration plane, and the direction of z axis is pointing down, so $\partial_n = -\partial_z$.

The traditional selection of integral surface is to choose infinite ground plane and the lower hemisphere. In practical problems, the observation surface and reflection points cylindrical surface is often used as integral surface. Ignore the boundary effect and the near-field term, the integral equation can be expressed as:

$$E(\bar{x}_0, t) = \int \left[ -\frac{1}{r}\left[\frac{\partial E}{\partial z}\right]_{t+r/v_0} + \frac{1}{v_0 r}\frac{\partial r}{\partial z}\left[\frac{\partial E}{\partial t}\right]_{t+r/v_0} \right] dsurf \quad (15)$$

## 6. Simulation Results

Fig. 3a is a simulation image of GPR by GprMaxV2.0 software. The width and depth of simulation area is 1.21 m and 0.75 m separately. There are three perfect metal pipes 0.45 m up to the bottom. The transmitting and receiving antenna move on the ground, and detect every 1cm distance. The sample interval is 0.001 ns. There are totally 121 traces which contain 2050 samples of each trace. The actual electromagnetic wave velocity is 17.3 cm/ns.

Fig. 3b-3d are FDTD migration, FK migration and Kirchhoff migration results respectively with the same velocity 16.6 cm/ns, which is lower by 4 % with the actual value.

Even through, from the results of three different migration methods, there can be clearly recognized the point targets. The simulation results represent that migration methods to dealing with the GPR image is effective and the error between estimated velocity and actual velocity is acceptable.

## 7. Experiment Results

Fig. 4a is a GPR data profile. The horizontal and vertical coordinates are trace and sample point respectively. Fig. 4b-4d are FDTD migration, FK migration and Kirchhoff migration results respectively with the same velocity 8.1 cm/ns. From the result, we can see that the hyperbola focuses its vertex. And the position and shape of the target can be seen clearly.
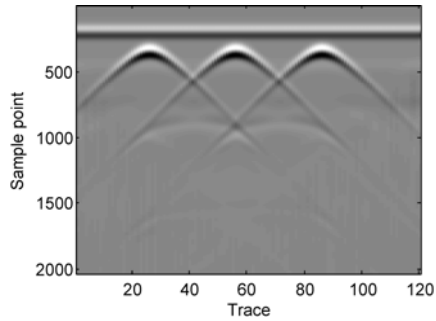


**Fig. 3a.** Point scatter image.



**Fig. 4a.** Image get from GPR.
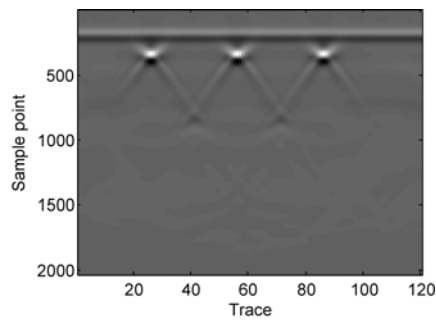


**Fig. 3b.** FDTD Migration of Fig. 3a.



**Fig. 4b.** FDTD Migration of Fig.4a.



**Fig. 3c.** FK Migration of Fig. 3a.
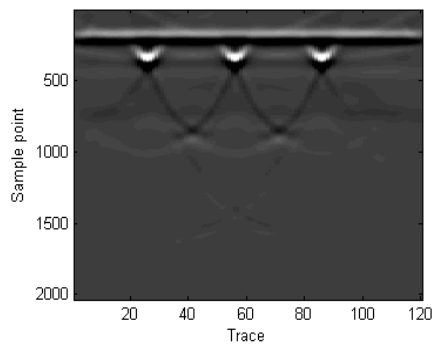


**Fig. 4c.** FK Migration of Fig.4a.
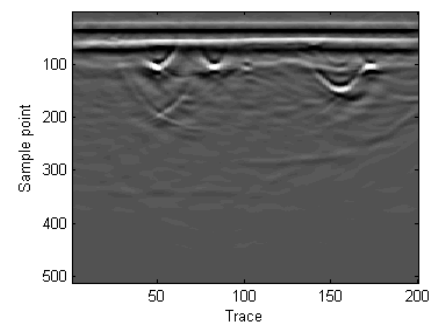


**Fig. 3d.** Kirchhoff Migration of Fig. 3a.
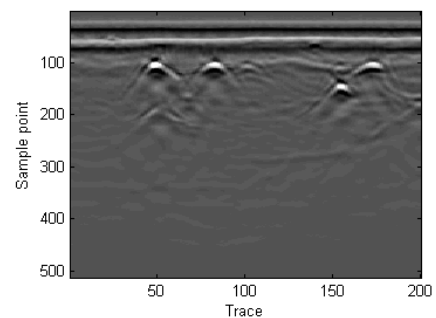


**Fig. 4d.** Kirchhoff Migration of Fig.4a.

## 8. Conclusions

The simulation and experiment results show that FDTD, FK and Kirchhoff Migration methods have strong ability to image the multiple objects in GPR output images. But there are some differences between the three methods. FDTD is an iterative method, it saves memory but costs longer time. FK migration method is sensitively by wave velocity. It only can be used in well proportioned medium. Kirchhoff migration method needs some transcendental knowledge of the medium, otherwise it is hard to confirm the migration parameters.

In summary, using migration methods to dealing with the GPR image is effective. The position and the shape of the objects can be easily obtained, and the velocity of electromagnetic wave in the detect medium can be estimated. According to the specifically application situation, we can choose the proper migration method.

## Acknowledgements

## References

[1]. Abma R., Sun J., Bernitsas N., Antialiasing methods in Kirchhoff migration, *Geophysics*, Vol. 64, 1999, pp. 1783-1792.

[2]. Bevc D., Imaging complex structures with semirecursive Kirchhoff migration, *Geophysics*, Vol. 62, 1997, pp. 577-588.

[3]. Dai Q. W., Feng D. S., He J. S., Finite difference time domain method forward simulation of complex geoelectricity ground penetrating radar model, *Journal of Central South University of Technology*, Vol. 12, 2005, pp. 478-482.

[4]. Daniels D. J., Ground penetrating radar, 2nd ed., *The Institute of Electrical Engineers*, Beijing, 2004.

[5]. Deng W., Wang X. B., Li W. C., The FDTD forward modeling of two dimension geoelectricity based on UWB signal, *Chinese Journal of Engineering Geophysics*, Vol. 3, 2006, pp. 419-426.

[6]. Leuschen C. J., Plumb R. G., A matched filter based reverse time migration algorithm for Ground Penetrating Radar data, *IEEE Transactions on Geosciences and Remote Sensing*, Vol. 39, 2001, pp. 929-936.

[7]. Li W. C., Wang X. B., Deng W., The FDTD Forward Mordeling and Migration Based on UWB Signal, *Control & Automation*, Vol. 3, 2008, pp. 169-172.

[8]. Margrave G. F., Numerical Methods of Exploration Seismology with algorithms in Matlab, *CREWES*, January 2001.

[9]. Michael H. P., Charles P. O., Migration of Dispersive GPR Data, in *Proceedings of the 10th International Conference on Ground Penetrating Radar*, June 2004.

[10]. Plumb R. G., Leuschen C. J., A class of migration algorithms for ground penetrating radar data, *Geoscience and Remote Sensing Symposium*, Vol. 5, 1999, pp. 2519-2521.

[11]. Qin Y., Wang Q. F., Ground Penetrating Radar Imaging based on FDTD Migration Method, *Advanced Materials Research*, Vol. 490-495, 2012, pp. 1261-1264.

[12]. Qin Y., Wang Q. F., Kirchhoff Migration Algorithm for Ground Penetrating Radar Data, *ICCSEE*, Hangzhou, 2012, pp. 396-398.

[13]. Qin Y., Wang Q. F., Using GPR Spectrum Inversion Method to Improve Recognition Ability of Thin-layer, *International Journal of Digital Content Technology and its Applications*, Vol. 6, 2012, pp. 136-143.

[14]. Ruthenberg I. A., Migration is a tool used in GPR processing to get an accurate picture of underground targets, *Department of Computer Science and Electrical Engineering, University of Queensland*, 1998.

[15]. Stolt R. H., Migration by Fourier transform, *Geophysics*, Vol. 43, No. 1, February 1978, pp. 23-48.

[16]. Vardy M. E., Henstock T. J., A frequency approximated approach to Kirchhoff migration, *Geophysics*, Vol. 75, November 2010, pp. S211-S218.

[17]. Zheludev V. A., Ragoza E., Kosloff D. D., Fast Kirchhoff migration in the wavelet domain, *Exploration Geophysics*, Vol. 33, 2002, pp. 23-27.

# Desgin of On-line Monitoring Device for MOA (Metal Oxide Arrestor) Based on FPGA and C8051F

**[1] Xiaotong YAO, [1] Jirong WANG, [2] Jinyang XU**

[1] Institute of Telecommunications, Lanzhou Jiaotong University, 730070, China
[1] Tel.: 086-13893252022
[1] E-mail: lzjt12@163.com

**Abstract:** Monitoring of metal oxide surge arresters (MOA) due to aging, moisture and other components cause increased resistive current. Through a lot of practices, it has been proved that in the early days, MOA insulation damage and current increase is not obvious. The accurate working conditions of the MOA are also not obvious but it can reflect the aging or moisture of MOA. When the resistive current of the fundamental component increases, there is no increment in the harmonic components that is the general performance of a serious or moisture contamination. In the same way when the resistive current of harmonic components increases, the fundamental component is not increased and it is the general performance of aging. Therefore, this paper designed an experiment-based FPGA and C8051F-line monitoring device. This device uses resistive current as a detection target. The main monitoring parameters are the fundamental and peak value of resistive current, third harmonic content of the leakage current, phase angle difference and power consumption. Through laboratory tests, the device can be used with a network arrester line monitoring, maintenance, reduce the economic losses caused by power outages and improve the distribution network reliability. *Copyright © 2014 IFSA Publishing, S. L.*

**Keywords:** (MOA) metal oxide surge arrester, On-line monitoring, FPGA, C8051F, Resistive current.

## 1. Introduction

The MOA with non-linear characteristics like the large flow capacity, no series gaps, small size, light weight and excellent features gradually replaced the traditional SiC arrester, so it is used in power plants, substations and transmission lines that can protect the equipments of electrical power system from over voltage. Its main role is to absorb over-voltage, operating the energy impact of over-voltage and prevent over-voltage substation to damage the electrical equipments. Under normal operating voltage, the current flowing through the arrester is few micro amps, when applied over-voltage the flow of current through the arrestor reached thousand of amps due to the non-linearity of zinc oxide varistor

while surge arresters is in the conduction state [1-3]. The release of over-voltage energy, while limiting the amplitude, which badly violates the over-voltage power transmission equipment, after than we resumed the zinc oxide varistor in impedance state, so that the power system will back to normal operation. Due to continuous operating voltage arrester long-term effects, if the product has too high chargeability arrester beyond capacity, it will accelerate the aging of resistors, resistive current and subsequent increase in the power consumption that cause a crash, subsequent heat lightning breakdown or explosion. Internal moisture is caused by a lightning arrester which is important factor in accident.

According to the "preventive test code equipment DL/T-596-1996 provisions of China" [2] electricity distribution network detection system is used for preventive methods: light prevention trial period is one time in a year. There are large number of distribution arresters networks, each test consumes a lot of manpower, material resources and power outages but cannot control the light damage, so many departments have to run the test period 3 ~ 7 times in a year. In recent years, some research institutes and manufacturers launched an online monitoring system that monitor the total leakage current of MOA [4-6]. Some results show that in the early MOA insulation damage and there is not increment in the current value, it also not properly shows the working condition of MOA but it reflects the resistive current aging and moisture for MOA. The MOA is under the appropriate chargeability conditions like 10 % to 20 % of the total current, so we need to separate the resistive current from the total current in order to clearly understand its different behaviour.

In this paper, the status quo of China distribution network arrester monitoring system presents a FPGA and C8051F based on line monitoring device that monitor the distribution network of the arrester. The device uses resistive leakage current component as a detection object. By the lab experiments, we observe the operation of the online monitoring system fulfil the requirements of the arrester.

## 2. The Leakage Current of MOA

MOA leakage current monitoring main purpose is to monitor the MOA due to aging, moisture and other meritorious that causes increase in power consumption, heat and other parameters. The equivalent circuit of MOA is shown in Fig. 1.
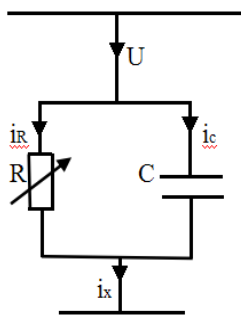


**Fig. 1.** The equivalent circuit of MOA.

In Fig. 1, R is the equivalent nonlinear resistance; C is a constant equivalent capacitance; $i_R$ is resistive leakage current; $i_c$ is capacitive leakage currents; $i_x$ is the total leakage current; U is the operating voltage of MOA.

The main purpose of this modelling is to calculate the resistance of nonlinear resistor that is given in Fig. 1. The volt-ampere characteristics of MOA explain that the application of five polynomial fitting methods can create mathematical models for MOA under normal conditions. The equation for the resistive leakage current is given below:

$$i_R = 0.8756\ u^5 - 1.949\ u^4 + 1.601\ u^3 - 0.5401\ u^2 + 0.0894\ u \tag{1}$$

On the basis of above equation (1) and from the experimental data of [7] it has been proved that MOA aging is five times current polynomial fitting characteristics to calculate the equivalent resistance R during the nonlinear mathematical model. The equation for resistive leakage current during the MOA aging is given below:

$$i_R = 0.02082\ u^5 + 0.1108\ u^4 + 0.234721\ u^3 + 0.076\ u^2 + 0.0291\ u \tag{2}$$

On the basis of above Equations (1), (2) and by using MATLAB R2010B we can plot the average nonlinear voltage characteristics of MOA that is shown in Fig. 2. In Fig. 2, the u (u=U/UN, the unit is pu) is represents by vertical axis and $i_R$ (resistive leakage current) is represents by horizontal axis. The results of the average nonlinear voltage characteristics for MOA are given below:
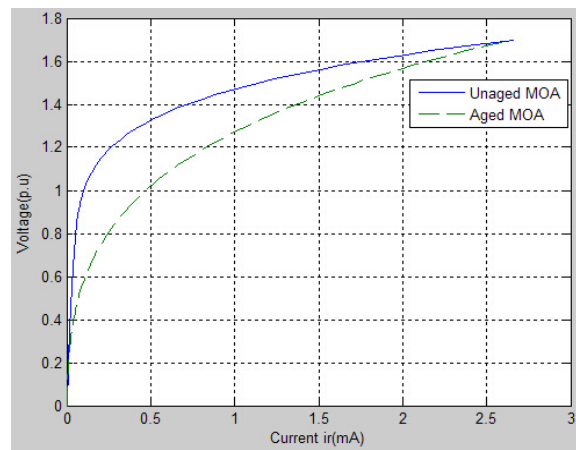


**Fig. 2**. The graph for MOA resistive current average voltage characteristic.

From Fig. 1, the value of $i_x$ as follows:

$$i_x = i_R + i_c \tag{3}$$

We can set the grid voltage as follows:

$$u = U_1 \sin(\omega_1 t) + \sum U_n (t + \varphi_n) \tag{4}$$
$$n=3, 5, 7$$

$$i_c = i_{c1} + \sum i_{cn}, \tag{5}$$

where $i_{c1}$ is the capacitive fundamental current and $i_{cn}$ is the capacitive harmonic currents and these currents are created in the grain boundary capacitor of C by applying the fundamental and harmonic voltage. Because $i_{5r}$ and $i_{7r}$ are very small so ignore them. The values of $i_R$, $i_r$ and $i_{3r}$ can be calculated by the following equations:

$$i_R = i_r + i_{3r}, \tag{6}$$

$$i_r = i_r' + i_r'', \tag{7}$$

$$i_{3r} = i_{3r}' + i_{3r}'', \tag{8}$$

$i_r'$ and $i_{3r}'$ are obtained by the fundamental voltage that is applied to the resulting nonlinear resistor R. In the same way, $i_r''$ and $i_{3r}''$ are obtained by the harmonic voltage that is applied to the resulting nonlinear resistor R. $i_r'$ and $i_{3r}'$ can be used to judge the MOA's operating conditions, so it is very important for operating conditions of MOA.

We divided the resistive current in two parts that is given in Fig. 3. The $R_0$ and $C_0$ are the electrical parameters of MOA. The $R$ and $C$ are selected from the monitoring device.
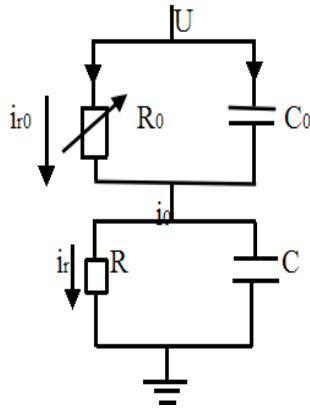


**Fig. 3.** Resistive current separation principle.

In Fig. 3, the frequency current flowing through the arrester is $i_0$, the resistive component $i_{r0}$ and the current $i_r$ flowing through a small resistor can be obtained:

$$i_{r0} = \frac{1/j\omega C_0}{R_0 + 1/j\omega C_0} i_0 = \frac{1}{1/j\omega R_0 C_0 + 1} i_0 \tag{9}$$

$$i_r = \frac{1/j\omega C}{R + 1/j\omega C} i_0 = \frac{1}{1/j\omega R\ C + 1} i_0 \tag{10}$$

The $i_{r0}$ is the true resistive current and in this case its value should be calculated but the actual measured current is $i_r$, if $i_{r0} = i_r$, it means that $R_0 C_0 = RC$. The measured value of the current flowing through the resistive arresters has equal amplitude and same phase.

There is also need to determine whether there is a change in the access RC parallel branch after passing through the arrester leakage current and resistive components.

$$i_x = U(j\omega C_0 R_0 + 1)/R_0, \tag{11}$$

$$i_0 = \frac{U(j\omega C_0 R_0 + 1)(j\omega CR + 1)}{j\omega R_0 R(C + C_0) + R + R_0}, \tag{12}$$

where $i_x$ and $i_0$ both are the leakage currents as $i_0$ is connected to the RC branch but $i_x$ is not. Because $R_0 C_0 = RC$, $R_0 \gg R$, we can be know that $i_0' \approx i_0$. There is very small change after accessing RC leakage current because the frequency equivalent impedance of MOA is greater then RC parallel impedance within a certain voltage range, as $i_0$ is substantially constant, so after accessing the RC circuit resistive current flowing through the arrester there will be a little change in the current that is flowing through the resistor R and it may be considered on the leakage current of the surge arrester that is the resistive component.

During the decline of the MOA characteristics, the initial resistive current changed but the whole current change is relatively small. At this point surge arresters electrical parameters remain unchanged. While $R_0$ becomes smaller but its frequency equivalent shunt impedance is still much larger than RC. $i_0$ basically unchanged.

After the MOA electrical parameters change, some parameters changed like $R_0'$ and $C_0'$, the current flowing through the MOA resistive component is $i_{r1}$ and calculated value of $i_r$ remains constant. The equations for calculating the $i_{r1}$ and $i_r$ are given below:

$$i_{r1} = \frac{1/j\omega C_0'}{R_0' + 1/j\omega C_0'} i_0 = \frac{1}{j\omega R_0' C_0' + 1} i_0 \tag{13}$$

$$i_r = \frac{1/j\omega C_0}{R + 1/j\omega C} i_0 = \frac{1}{j\omega RC + 1} i_0 \tag{14}$$

The error exists and equation for this error is as following:

$$\Delta i_r = i_{r1} - i_r = \left( \frac{1}{j\omega R_0' C_0' + 1} - \frac{1}{j\omega RC + 1} \right) i_0 \qquad (15)$$

Suppose normal detecting $i_r = i_{r0} = 0.1 i_0$, the parameter changed then set $i_{r0}' = 0.2 i_0$, and the measured value $i_r' = 0.1 i_0$. According to the above equation the error is $\Delta i_r = 0.1 i_0$ which is acceptable. During MOA critical aging, the leakage current will increase then the errors will also increase and this error is much low as compared to the full current detection method. Our main goal is to monitor the resistive current.

## 3. The Design of Arrester on Line Monitoring Device

For MOA automatic monitoring and testing equipment the budget is a main thing. In addition to the distribution network, some MOA are installed in more places. We also need some person who can give supply to self-test devices and timely inspect our system. So in this design i choose FGPA and

C8051F to control external components and we also set up a power detection device charge section for monitoring patrol officers.

During normal operation the leakage current of 10 kV arrester is very small. When MOA insulation damage is not critical, the resistive current increases several times but there is not much increment in the full current and it can't timely detect of an accident. Resistive current can be used to detect hidden arrester insulation, so the self-monitoring device uses resistive current as a detection target. We used some digital waveform analysis techniques like harmonic analysis and digital filtering software interference method that measure very accurate and stable results. It can also analyse the component of the fundamental and harmonic for 3~7 times, overcome interference and correctly measure the resistive current of arrester. You can also determine the resistive current percentage over total current and in this way you can judge the MOA's initial operating conditions. The vertical comparison method can be used historical data to better reflect the operation of the tin oxide surge arresters. MOA-line monitoring device principle block diagram in Fig. 4.
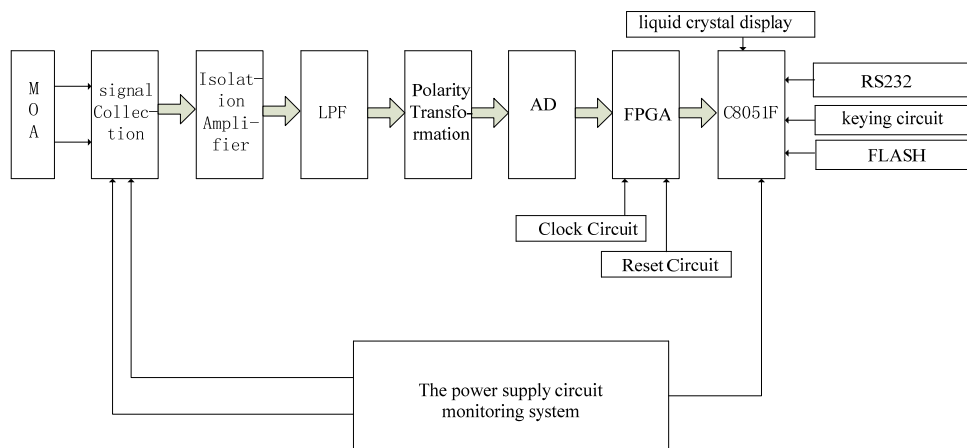


**Fig. 4.** MOA-on line monitoring device.

The Hardware system consists of three parts: signal conditioning circuits, signal processing circuit and system power circuit. A signal sampling circuit and a voltage transformer have a small current and they connected the sensor to obtain the voltage and current of MOA. Isolation amplifier circuit is to filter the signal and the internal circuit is to isolate MOA monitoring system, so that no interference and the current signal amplification system is using active filter. It can remove the high frequency noise and prevent aliasing but after filtering a small part of the harmonic components of the signal also exist that can be eliminated by digital filtering and interference method. We used an external 16-bit AD converter for converting the analog signal into digital and then passed through FPGA [8] control and handling. We

can get good data processed by the incoming C8051F120 processor. This processor sends the date to the resultant data storage and we can see the current measured data on the LCD with the help of button. Monitoring the final results and by using the RS232 uploaded all data to the main control room of the host computer.

## 4. The Results of MOA-line Monitoring

We used the MOA of 10 kV (HY5WS-17/50 type) for our laboratory test, this device can test the effectiveness and motion effects, the wiring of laboratory is shown in Fig. 5.
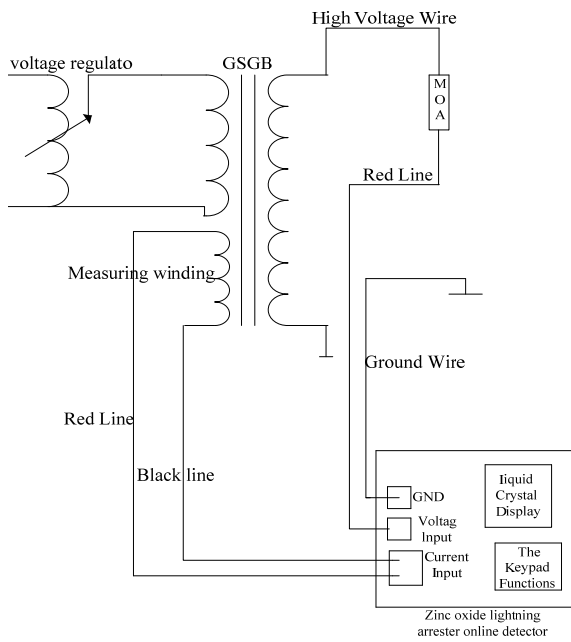
**Fig. 5**. The circuit of MOA-line monitoring in the laboratory tests.

Through testing transformer can adjust the voltage on the arrester; the testing transformer variable ratio is 500:1. The data of MOA in the laboratory of MOA is shown in Table 1. This data is an average and shows the relationship between the voltage waveform, full current, resistive current that is shown in Fig. 6.

**Table 1.** The results for different voltages.

|  | The results for different voltage | | |
|---|---|---|---|
| U (KV) | 7.60 | 8.40 | 9.20 |
| P (W) | 0.05 | 0.06 | 0.07 |
| $i_x$ (mA) | 0.078 | 0.085 | 0.093 |
| $\vartheta$ (ºC) | 85.4 | 85.4 | 85.4 |
| $i_R$ (mA) | 0.006 | 0.007 | 0.007 |
| $i_c$ (mA) | 0.078 | 0.084 | 0.093 |
| $I_R$ (mA) | 0.114 | 0.123 | 0.133 |
| $i_{3R}$ (mA) | 0.000 | 0.001 | 0.000 |
| $i_{5R}$ (mA) | 0.001 | 0.001 | 0.001 |

Depend on the above tests, we obtained some results that are as follow:

1) In the system voltage, the full current is 0.078 mA and the resistive current component is 0.006 mA. We can see that the resistive current is only 13 % of full current. Some researchers explained that the resistance current is about 10 % ~ 20 % of the total current under the normal conditions, if the test values will be in this range then it shows that MOA is working well. If resistance

current is about 25 % ~ 40 % of all current then that will increase the testing frequency and pay close attention to transformation, do data analysis and judgment. If resistance current is more than 40 % of all current, it is consider out of operation.

2) Through above data we observed that the value of the resistive current for current is very small and the total content of capacitive current is very large.

3) By testing we observed that the performance of MOA is good, so in this case the $i_{3R}$, $i_{5R}$ and $i_{7R}$ are consider 0.

4) Interphase interference affects the result of the test but didn't affect the validity of the test results. We can use the historical data of the longitudinal comparison method that can better reflect the working status of MOA.
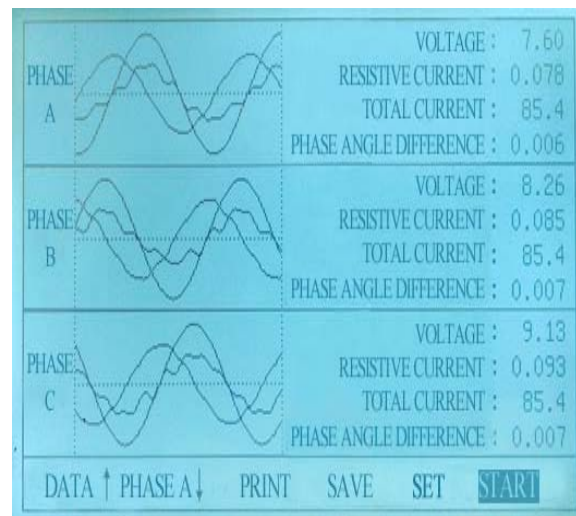


**Fig. 6**. The relationship between voltage, full current and resistance.

## 5. Conclusions

The MOA of 10 KV is used in the laboratory for on-line monitoring testing, it can be detected during MOA aging, moisture and resistive current component that can be used to detect hidden arrester insulation in time. The resistive current component is consider as detection target for auto-monitoring device, using a digital waveform analysis technique, such as harmonic analysis and digital filtering software anti-interference methods to make the measurement results accurate and stable. It can accurate analysis the fundamental wave and harmonic content for 3 ~ 7 times, overcome the interphase interference effects and correctly measure the resistance of arrester current. Based on these values of longitudinal and transverse comparison, we concluded that the arrester is in aging or may be affected with damp. This can determine whether or not to stop the working of MOA and reduce the damage for electric power system.

## Acknowledgements

## References

[1]. Zhang Zhenhong, Zang Dianhong, Study on the On-line Monitoring Method of Metal Oxide Surge Arrester, *High Voltage Apparatus*, Vol. 45, No. 5, 2009, pp. 126-129.

[2]. Yuan Wu, Jianjun Qiang, Xinbo Huang, Design of a Remote-Monitoring System of MOA Based on GPRS, in *Proceedings of the 9th International Conference on Electronic Measurement & Instruments (ICEMI'09),* 2009, pp. 1-675 - 1-679.

[3]. Wang Yongqiang, Lu Fangcheng, Shang Jing, Li Heming, Influence of Power System's Harmonic Voltage and Interphase Interference to On-line Resistive Leakage Current monitoring of MOA, in *Proceedings of the 4th Asia-Pacific Conference on Environmental Electromagnetics (CEEM'06),* Dalian*, 2006, pp. 620-623.

[4]. Xiong Pengcheng, Zhou Wenjun, Su Xueyuan, Yi Xiao, Li Xiaolu, Yang Xia, Design of On-line Monitoring Device for MOA Used in 10 kV Distribution Network, *High Voltage Engineering,* Vol. 33, No. 8, 2007, pp. 174-177.

[5]. Liu Huijia, Li Ning, Research on Detection Method of MOA Resistence Leakage Current Based on Harmonic Analysis, *Three Gorges Univ (Natural Sciences)*, Vol. 23, No. 2, 2003, pp. 144-147.

[6]. Xu Zhiniu, Zhao Lijuan, Ding Ao, Lu Fangcheng, Calculation of MOA resistive current, *Electric Power Automation Equipment*, Vol. 30, No. 12, 2010, pp. 47-50.

[7]. Zhu Hanxin, Raghuveer M. R., Influence of representation model and voltage harmonics on metal oxide surge arrester diagnostics, *IEEE Transactions on Power Dilivery*, Vol. 16, No. 4, 2001, pp. 599-603.

[8]. Fabao Yan, Jianxin Liu, Shaoheng Chun, Study of the Way to Firmware Program Upgrade in FPGA Reconfiguration of Distributed Geophysical Instruments, *Sensors & Transducers Journal*, Vol. 172, Issue 6, June 2014, pp. 130-138.

_____

# Design and Fabricate the Remote Monitor on the Scenic Spot Based on Integrated Sensor System

**[1, 2] Xiaohui Wang, [3] Lei Tian, [2] Kewei Lei, [2] Xiaoning Dou**

[1] College of Tourism and Environment, Shaanxi Normal University, Xi'an 710119, China
[2] Management College, Xi'an Eurasia University, Xi'an 710065, China
[3] School of Electronic Engineering, Xi'an University of Posts and Telecommunications,
Xi'an 710121, China
[1, *] Tel.: +086-13389243081, fax: +086-029-8166266
[1] E-mail: tianlei@xupt.edu.cn

**Abstract:** Based on the embedded Linux system, established the integrated sensing system to monitor the scenic spot and transmit the collected data to the users. The platform based on the ARM11 development board as the hardware of the system. Used the sensors to collect the different data and pictures and then they were transmitted by the wired and wireless mode. Set up the small Web server by the Boa (small Web server) and realized the integrated Web technology and CGI (Common Gateway Interface) program. According to the difference information of the scenic spot, the mobile platform collected the needed data and transmitted it to the control platform by the ZigBee wireless module and displayed in the embedded platform. The administrator can realize monitoring all the spots of the scenic and control the terminal equipments in the whole day. *Copyright © 2014 IFSA Publishing, S. L.*

**Keywords:** Sensor system, Embedded Linux, Remote monitoring, B/S mode.

## 1. Introduction

Today, all kinds of remote monitoring alarm system with its convenience, intuitive and variable attracted more and more people [1-3]. Especially with the rapid development of sensor technology, the remote monitoring system based on embedded device emerged, and has been widely used in all walks of life [4]. In this paper, a new B/S (browser and server) embedded remote monitoring system was developed and used in the scenic spot. Used the terminal equipment to monitor all aspects of spots. At the same time, user can through the browser to control the terminal equipment. It reflected the human-computer interaction perfectly and greatly reduces the cost of the system development.

## 2. System Structure and Function Design

### 2.1. The Integrated Design of the System

The remote monitoring system was divided into three layers: the equipment layer, the transmission layer and the interface layer. The architecture of the system was showed in Fig. 1.

In the terminal equipment layer, the ARM11 embedded board connected with USB camera [5], infrared sensor, sound sensor, light sensor and the temperature (humidity) sensor to monitor the spot information. Using the TCP/IP protocol [6], the information transmission layer sends the data which came from the terminal equipment layer through CGI

interface to the user interface layer [7]. In the interface layer, the user login in and view the real-time data from the transport layer through the browser. The user can input the control information from the interface and control the terminal sensor. Through the three layers' complete information, the system realized the purpose of the display and control the monitoring spots in real-time.
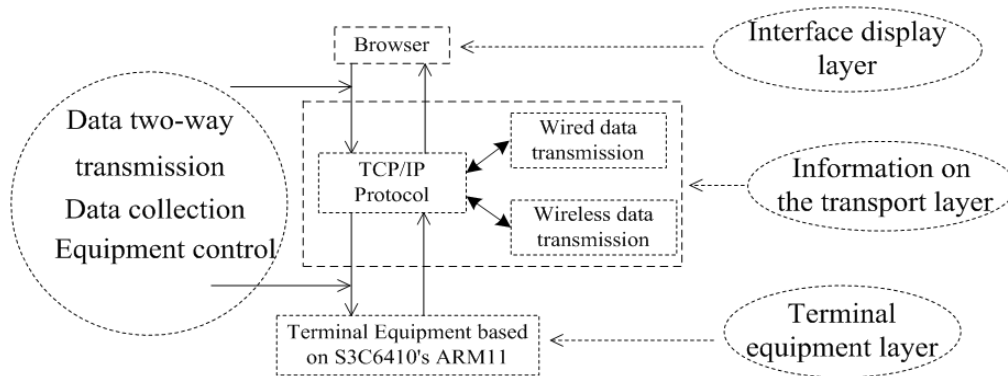


**Fig. 1.** Structure diagram of the whole system.

## 2.2. Hardware Structure of the Monitoring System

For the various considerations of safety, stable and transmission distance, the system transmitted the data in two ways; the wire transmission and the wireless transmission [8-9]. Different transmission modes corresponding to the different hardware and the hardware design as shown in Fig. 2.
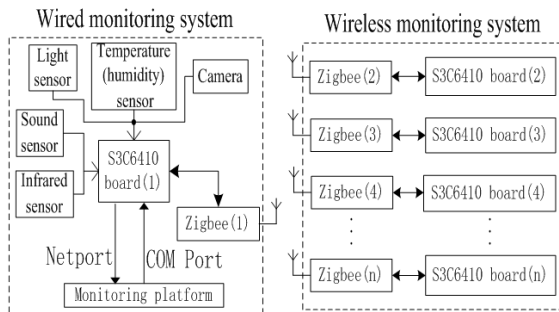


**Fig. 2.** Hardware structure of the system.

## 2.2.1. Hardware Design of the Wire Transmission

In the wired data transmission, using the No. 1 S3C6410 embedded board as the core board, through the SDIO extended port connected with the human body infrared sensor, the sound sensor, the light sensor and the temperature (humidity) sensor. Using the USB camera acquire the spot information of monitoring site. The embedded board connected to the PC and builds the LAN (local area network) through the network interface. The embedded board was controlled and programmed through serial port COM1.

## 2.2.2. Hardware Design of the Wireless Transmission

During the period of the wireless transmission, the system can virtual the same S3C6410 development board as a mobile platform named No. 2, 3, 4 … and etc. Because they have the same configurations with No. 1 embedded board, so the collected data can be send through the ZigBee module in real-time [10-11]. At the same time, the ZigBee module in No. 1 embedded board can be a receiver, the received data can be transmitted to monitoring platform.

## 2.3. Software Structure of the Monitoring System

### 2.3.1. Design of the Data Transmission Interface

In order to send the collected data to the user by a simple way and the user can view it directly [12-13]. The most ideal method is using Web Server based on the Boa, through the CGI public interface, to implement the data exchange interface, as shown in Fig. 3:
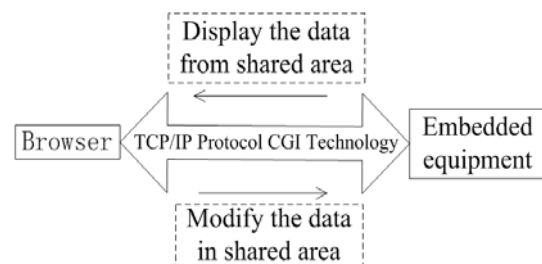


**Fig. 3.** Data transmission interface diagram.

In order to establish the Web server, the development environment was established on the PC platform through the Boa. In this process, several steps should be done: modify the configure files, modify the source code and compile the Boa program. After transplant the program to the development board, in the process of configure the Boa permissions, set the domain name, set the file storage directory, set the Web server. And then the data should be transmitted through the CGI coding technology.

### 2.3.2. Design the Software Program

The software of this monitoring system was developed and operated based on the Linux platform.

The control information can be viewed through the Windows or Linux platform. The system based on the B/S structure, using the TCP/IP protocol to transmit the data, to save the collected information through the established data sharing area and transmitted the sharing data to the monitoring platform. The sharing area is the database of the system with the function of the data control and maintenance. On the one hand, the collected data would be stored in shared area, and on the other hand, the system would determine the data whether abnormal or not. When the data is abnormal, the buzzer would alarm, when the data is normal, the alarm would be relieve. The specific process of software system as shown in Fig. 4.
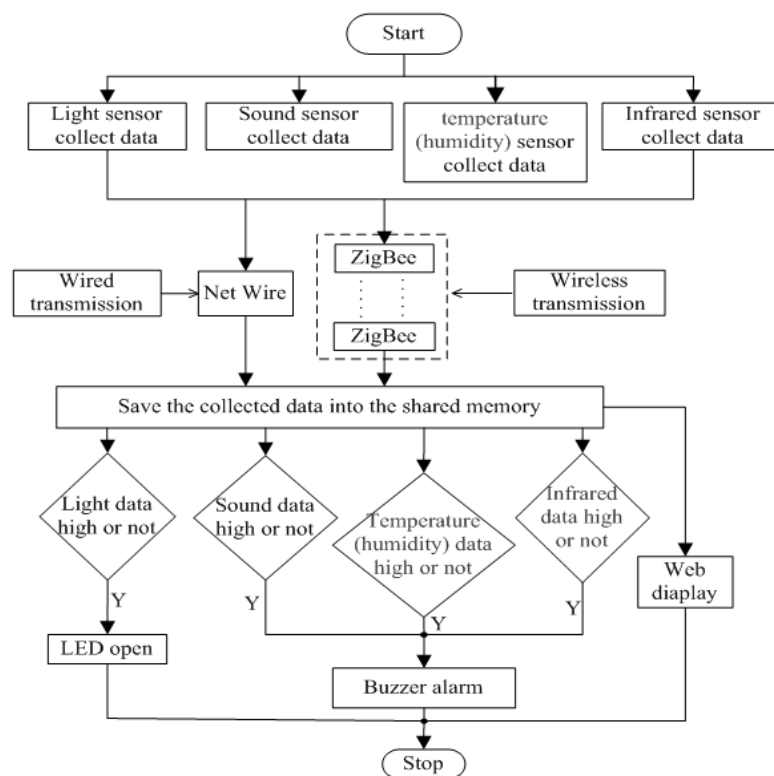


**Fig. 4.** Structure of the software architecture.

In order to obtain the data from the range of the monitored spot, the development board connected the USB camera, the temperature (humidity) sensor, the infrared sensor, the sound sensor and the light sensor with the SDIO port. Due to all the sensors need store the collected data constantly into the sharing area, the multi-thread coding technology based on Linux system would be needed.

Using sharing memory in the Linux system, created the shared database to store the collected data. And established the configuration files to save the system login account information and the value of each sensor and the upper and lower limits of the temperature (humidity). Programed the CGI with the

C language, displayed in the web page by reading the sharing area. Whenever refresh the web page, the data would be acquired from the sharing area. At the same time, read the input data configuration files from the web page and control the system.

## 3. Simulation Results

### 3.1. Terminal Setting

In this system, set up the web page interface, users can easily control the terminal equipment; terminal settings interface as shown in Fig. 5.
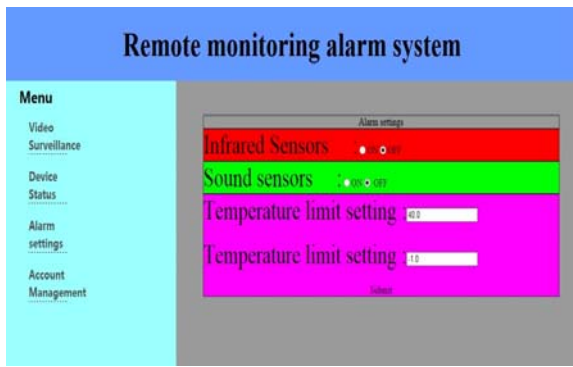
**Fig. 5.** Terminal setting interface.

The user can regulate the switch of the infrared sensor and the sound sensor to control the sensors in the monitoring spots, and the upper and lower limits of the temperature can be manually set.

### 3.2. Terminal Display

In the reality test mode, the system got the environmental data through the variable sensors. Form the human body infrared sensor, if someone located in the monitoring spot, the interface display "somebody", or display "nobody". From the sound sensor, if the environment sound exceed the upper limits, the interface display "YES", or display "NO". From the light sensor, if the obtained ambient light bigger than the setting value, the interface display "bright", or display "weak". The temperature (humidity) sensors display the true value of the current environment in Fig. 6:
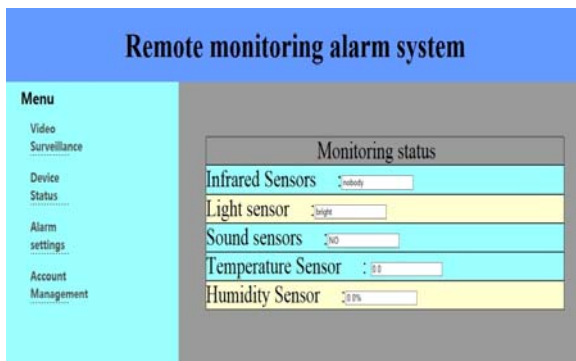


**Fig. 6.** Display interface.

Fig. 7 shows the various monitoring value in the acquisition monitoring area by each sensor.

### 4. Test Results

From the simulation results, the integrated sensor system can work very well in the monitoring spot. In this paper, the system was tested in the Huashan Mountain. The collected data was transmitted by the ZigBee wireless module in the situation without wireless signal. The picture was showed in the touch screen in the embedded platform and told other users the scene of the situation.
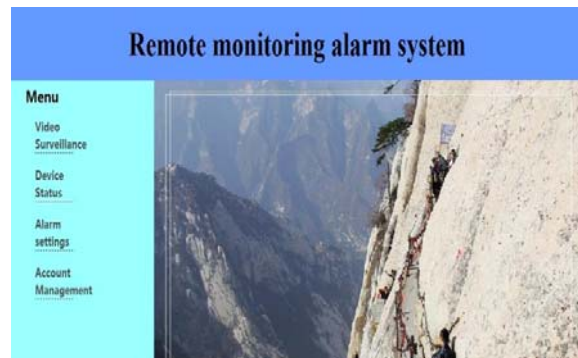


**Fig. 7.** Feedback test status data.

In the reality mountain spots, the wireless signals do not exist, so the mobile phone and the function of the mobile station will not be used. In this extreme situation, this integrated sensor system will help users to know the reality topography in time.

### 5. Conclusions

The remote monitoring system in this paper utilized the B/S mode, reduced the development cost and the maintenance is convenient. The integrated sensor system collected all the data and transmitted to the main control platform. The multi-thread data transmission mode guaranteed the wired transmission system safety and stable. For the wider mobility, the wireless data transmission system was developed. In this system, take the advantages of both transmission modes, protect the normal operation of the monitoring system and extended the mobile area and saving the resources.

### Acknowledgements

### References

[1]. Wu Mingxin, Study of 3D Wireless Sensor Network Based on Overlap Method, *Sensors & Transducers*, Vol. 159, Issue 11, November 2013, pp. 431-439.

[2]. Guifang Qiao, Guangming Song, Yali Wang, Jun Zhang, Weiguo Wang, Autonomous Network

Repairing of a Home Security System Using Modular Self-Reconfigurable Robots, *IEEE Transactions on Consumer Electronics*, Vol. 59, Issue 3, 2013, pp. 562-570.

[3]. Janusz Kaczmarek, Wiesław Miczulski, Mirosław Kozioł, Albin Czubla, Integrated System for Monitoring and Control of the National Time and Frequency Standard, *IEEE Transactions on Instrumentation and Measurement*, Vol. 62, Issue 10, 2013, pp. 2828-2838.

[4]. Pesola Aki, Serkkola Ari, Lahdelma Risto, Salminen Pekka, Multicriteria evaluation of alternatives for remote monitoring systems of municipal buildings, *Energy and Buildings*, Vol. 72, April, 2014, pp. 229-237.

[5]. Yuan Jian, Yin Dongsheng, Wireless camera based on ARM11, in *Proceedings of the International Conference on Computer Science and Service System (CSSS' 11)*, 2011, pp. 1887-1890.

[6]. M. Abrishamkar, M. Hussein, K. Zakaria, H. Maleki, TCP/IP-based control and monitoring of manufacturing system, *Advanced Materials Research,* Vol. 845, 2014, pp. 975-979.

[7]. Magdaleno Eduardo, Rodríguez Manuel, Pérez Fernando, Hernández David, García Enrique, A FPGA embedded web server for remote monitoring and control of smart sensors networks, *Sensors,* Vol. 14, Issue 1, 2013, pp. 416-430.

[8]. Calcante Aldo, Mazzetto Fabrizio, Design, development and evaluation of a wireless system for the automatic identification of implements, *Computers and Electronics in Agriculture*, Vol. 101, February 2014, pp. 118-127.

[9]. Dawei He, Weixuan Lin, Nan Liu, Ronald G. Harley, Thomas G. Habetler, Incorporating Non-Intrusive Load Monitoring into Building Level Demand Response, *IEEE Transactions on Smart Grid*, Vol. 4, Issue 4, 2013, pp. 1870-1877.

[10]. Zhiyang Jin, Zhongxing Li, Hong Jiang, Liqin Sun, Wen Xiao, The software design of natural rubber plantation temperature and humidity monitoring system based on ZigBee, *Open Automation and Control Systems Journal*, Vol. 6, Issue 1, 2014, pp. 9-16.

[11]. Chen Zhicong, Casciati Fabio, A low-noise, real-time, wireless data acquisition system for structural monitoring applications, *Structural Control and Health Monitoring*, Vol. 21, Issue 7, 2014, pp. 1118-1136.

[12]. A. D. Spacek, O. H. Ando Junior, J. Mota Neto, V. L. Coelho, M. O. Oliveira, V. Gruber, L. Schaeffer, Management of Mechanical Vibration and Temperature in Small Wind Turbines Using ZigBee Wireless Network, *IEEE Latin America Transactions*, Vol. 11, Issue 1, 2013, pp. 512-517.

[13]. Huanhuan Bian, Yuduo Wang, The design of wireless data acquisition and remote transmission interface in micro-seismic signals, *Sensors &Transducers*, Vol. 164, Issue 2, February 2014, pp. 114-119.

_____

# Correlation Analysis of Urban Land Surface Temperature and Fluxes Based on Remote Sensing Technology

**Wen-Xia QIU**

College of Mechanical and Electrical Engineering, Northeast Forest University,
Harbin, 150040, China
College of Information and Computer Engineering, Northeast Forest University,
Harbin, 150040, China
Tel.: 86-13633610309
E-mail: nefuzyf@126.com

**Abstract:** Land surface temperature and fluxes (soil heat flux, sensible heat flux and latent heat flux) of the Nanchong city in Sichuan Province on September 20, 2007, were retrieved using Landsat ETM+ images. Then based on sampling points in study area, surface temperature and each flux were compared with scatter diagram, and simulated the function to explore their correlation. The research results are the following:
1) Land surface temperature had positively correlation with both soil heat flux and sensible heat flux, but negatively correlation with latent heat flux. 2) Surface temperature was absolutely affected by sensible heat flux. *Copyright © 2014 IFSA Publishing, S. L.*

**Keywords:** Land surface temperature, Soil heat flux, Sensible heat flux, Latent heat flux, Correlation analysis.

## 1. Introduction

In recent years, with the development of urbanization, the scale of city has expanded continuously, the population of which has increased sharply, and large amount of natural surface, for example, woodland, farmland and grassland, etc, have changed into building, road, etc., which uses cement as main materials, in addition a lot of heat, which is from cars, computers, air conditionings, refrigerators, mobile phones, and IPADs, etc., has discharged into air. Theses have caused obvious Heat Island Effects, which is seriously affecting city people's quality of life.

At present, there are two methods of urban heat island research using remote sensing technology. The first is retrieving land surface temperature, the second is retrieving land surface fluxes. But the relationship between surface temperature and heat fluxes has not yet been studied specially. Based on this, taking the Nanchong city in Sichuan Province as an example, the correlation between surface temperature and heat fluxes, which was retrieved respectively using remote sensing technology, was explored to provide basis for research work of Urban Heat Island.

## 2. Research Region and Data Source

The Nanchong City lies in the northeast of Sichuan Basin, and locates in the middle reaches of the Jialing River (see Fig. 1). The topography is mainly hilly, and the altitude is from 26 to 480 meters. The research region is the urban area of the Nanchong city, which locates in the west of the

Jialing River and the east of the Xi River, including the Shunqing District, the Jialing District and the Gaoping District. The Shunqing District and the Jialing District lies in the west of the Jialing River, and the Gaoping District lies in the east of the Jialing River. The Jialing River flows through the east side of the urban from north to south. The urban area is surrounded by the highway. The highway from Chengdu to Nanchong runs across the south of urban area.
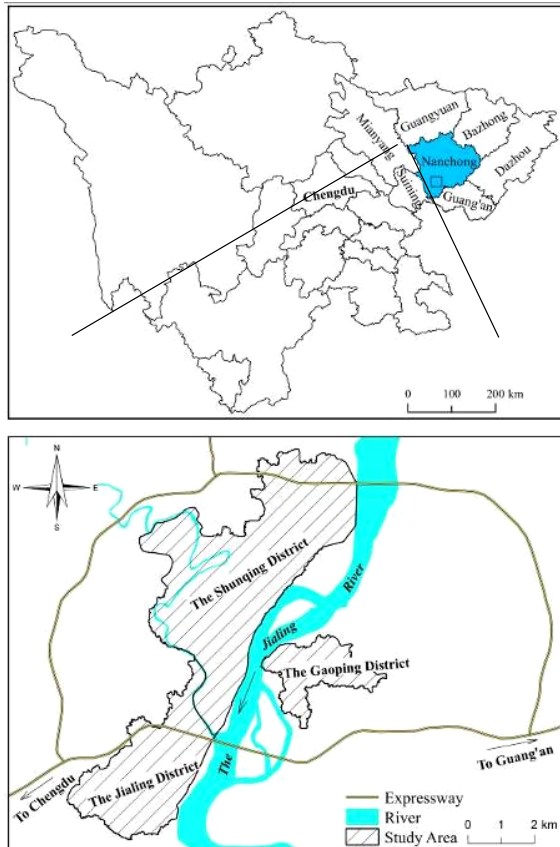


**Fig. 1.** General situation of research region.

This research used Landsat-7 ETM+ data obtained on September 20, 2007, DEM and atmosphere temperature. The projection of the ETM+ images was UTM 48N, the ellipsoid and reduced plane of which was WGS84, the spatial resolution of which was 30 m. The quality of images was good. DEM was downloaded from Global Mapper, and its projection and resolution was same as ETM+ images.

# 3. Retrieving Land Surface Temperature

## 3.1. Radiation Calibration

Radiation calibration is a process of converting the digital value of remote sensing data into spectral radiance value of sensor. The model is Formula (1) [1].

$$L_\lambda = \frac{L_{\max_\lambda} - L_{\min_\lambda}}{Q_{\max} - Q_{\min}}(Q_\lambda - Q_{\min}) + L_{\min_\lambda}, \qquad (1)$$

where $\lambda$ is the band value, $L_\lambda$ is the spectral radiance by the sensor ($W \cdot m^{-2} \cdot sr^{-1} \cdot \mu m^{-1}$), $Q_\lambda$ is the digital number of analyzed pixel, $Q_{\max}$ is the maximum recorded (255), $Q_{\min}$ is the minimum recorded, $L_{\max_\lambda}$ and $L_{\min_\lambda}$ are the maximum and minimum spectral radiance, detected for $Q_{\min}$ and $Q_{\max}$.

## 3.2. Radiation Calibration

1) Retrieving brightness temperature (BT).
Based on spectral radiation value of pixels on sensor, BT can be calculated directly by Planck's radiation function or an approximation Formula (2) [2-3].

$$T=K_2/\ln(1+K_1/L_\lambda), \qquad (2)$$

where T is the BT of pixels and its unit is K, $K_1$ and $K_2$ are the pre-launch calibration constants, as for ETM+ band62, $K_1$ is $666.093 W \cdot m^{-2} \cdot ster^{-1} \cdot \mu m^{-1}$, and $K_2$ is 1282.708 K.
2) Retrieving land surface temperature (LST).
LST can be calculated according to Formula (3) [4].

$$T_s = \frac{T_{rad}}{1 + (\lambda \cdot T_{rad}/\rho)\ln\varepsilon}, \qquad (3)$$

where $T_s$ is the LST and its unit is K; $T_{rad}$ is the BT; $\lambda$ is the center wavelength (11.4 $\mu m$); $\rho = h \cdot c / \sigma$, where h is the Planck constant ($6.626 \times 10^{-34} J \cdot s$), c is the velocity of light ($2.998 \times 10^8 m/s$), $\sigma$ is the Boltzmann constant ($1.38 \times 10^{-23} J/K$); $\varepsilon$ is the surface emissivity, when NDVI<0.05, $\varepsilon$=0.973, when NDVI>0.7, $\varepsilon$=0.99, when 0.05≤NDVI≤0.7, $\varepsilon = 0.004 P_v + 0.986$, where $P_v$ is the vegetation proportion in pixel, $P_v = (NDVI - NDVI_s)/(NDVI_v - NDVI_s)$, $NDVI = (\rho_4 - \rho_3)/(\rho_4 + \rho_3)$, $\rho_3$ and $\rho_4$ are the surface reflectance acquired in the visible (red) and near-infrared band, respectively [5-6]. $NDVI_v$ (0.7) and $NDVI_s$ (0.05) stand for the NDVI value of vegetation and bare land.

# 4. Retrieving Land Surface Fluxes

This research is mainly based on the surface energy balance Equation (4) [7].

$$R_n = LE + H + G + PH, \qquad (4)$$

where $R_n$ is the net radiation, LE is the latent heat flux, H is the sensible heat flux, G is the soil heat flux, and the unit is $w/m^2$. PH is the energy for plant photosynthesis and biomass increased, and can be neglected in actual calculation because its value is very small.
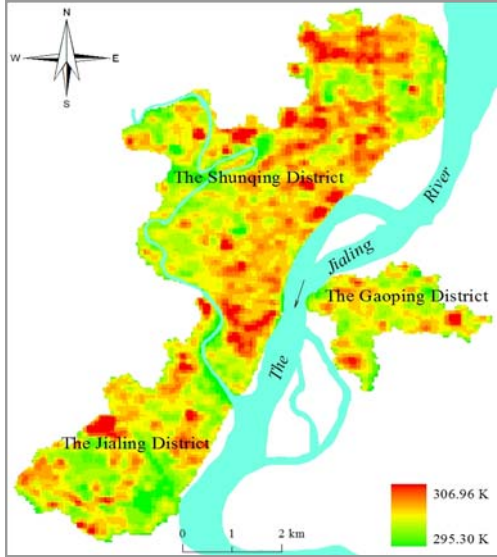


**Fig. 2.** Land surface temperature distribution on September 20, 2007.

1) Estimating surface net radiation (Rn).

The surface net radiation (Rn) is obtained according to the Formula (5) [8].

$$R_n = Q(1-\alpha) + \varepsilon_\alpha \sigma T_\alpha^4 - \varepsilon_s \sigma T_s^4, \qquad (5)$$

where Q is the total solar radiation, $Q = Gd\tau_{sw}\cos\theta$, G is the solar constant ($1367 w/m^2$), d is the sun-earth distance, $\theta$ is the zenith angle, $\theta = 90° - \beta$, $\beta$ is the solar elevation, $\alpha$ is the surface albedo, $\alpha = 0.356 R_s(1) + 0.130 R_s(3) + 0.373 R_s(4) + 0.085 R_s(5) + 0.072 R_s(7) - 0.0018$ [9], $R_s(i)$ is the band surface reflectance, $\sigma$ is the Stefan-Boltzmann constant, and its value is $5.67 \times 10^{-8} W \cdot m^2 \cdot K^4$, $\varepsilon_\alpha \sigma T_\alpha^4$ is the atmospheric long wave radiation, $\varepsilon_\alpha$ is the atmospheric emissivity, $\varepsilon_\alpha = 1.08(-\ln\tau_{sw})^{0.265}$ [10] $\tau_{sw}$ is the atmospheric transmittance, $\tau_{sw} = 0.75 + 2\times10^{-5}\times Z$ [11], $\varepsilon_s \sigma T_s^4$ is the surface long wave radiation, $\varepsilon_s$ is the surface emissivity, $T_\alpha$ is the near surface air temperature, $T_s$ is the land surface temperature, Z is the altitude at the measurement point and its value is from DEM.

2) Estimating soil heat flux (G).

The soil heat flux is the heat stored in the soil layer, and often estimated using the empirical formula. In this paper, the soil heat flux is calculated based on the Formula (6) [12] proposed by Bastiaanssen in 2000.

$$G = R_n \cdot T_s (0.0038\alpha + 0.0074\alpha^2) \cdot (1 - 0.98NDVI^4)/\alpha, \qquad (6)$$

where $R_n$ is the surface net radiation, $T_S$ is the surface temperature, $\alpha$ is the surface albedo.

3) Estimating sensible heat flux (H).

The sensible heat flux is the exchange energy between land surface and atmosphere, and is determined by the surface temperature, are temperature and air resistance. The model is Formula (7) [12].

$$H = \frac{\rho_{air} \cdot C_p \cdot dT}{r_{ah}}, \qquad (7)$$

$$\rho_{air} = 349.635 \times ((T - 0.0065Z)/T)^{5.26}/T, \qquad (8)$$

where $\rho_{air}$ is the air density ($kg \cdot m^{-3}$), and is calculated by Formula (8) [13-14], $C_p$ is the air specific heat at constant pressure ($1004 J \cdot kg^{-1} \cdot K^{-1}$), $dT$ is the temperature difference at the height of $Z_1$ and $Z_2$, $Z_1$ (0.01 m) is the bare land roughness length, $Z_2$ (2m) is the reference height of meteorological data, $dT = a(T_s - 0.0065 Z) + b$, a and b are constants, and their values are obtained by selecting the "cold point" and "hot point" from remote sensing image; $r_{ah}$ is the corrected aerodynamic resistance, unstable, and can be calculated through multiple recursive calculation.

4) Estimating Latent heat flux (LE).

The latent heat flux is the heat energy of evaporation or condensation water, can be calculated by the surface heat balance Equation (9).

$$LE = R_n - H - G \qquad (9)$$

## 5. Correlation Analysis of Land Surface Temperature and Fluxes

To analyze the correlation between surface temperature and heat fluxes, 163 sampling points were uniformly selected in study area. Then, the values of land surface temperature, soil heat flux, sensible heat flux, and latent heat flux of sampling points were obtained through spatial analysis between sampling points data and surface temperature, soil heat flux, sensible heat flux, latent heat flux, respectively. Finally, surface temperature and soil heat flux, sensible heat flux, latent heat flux of each sampling point were compared with scatter diagram respectively, and least square method was used to simulate the function (Fig. 4~6).
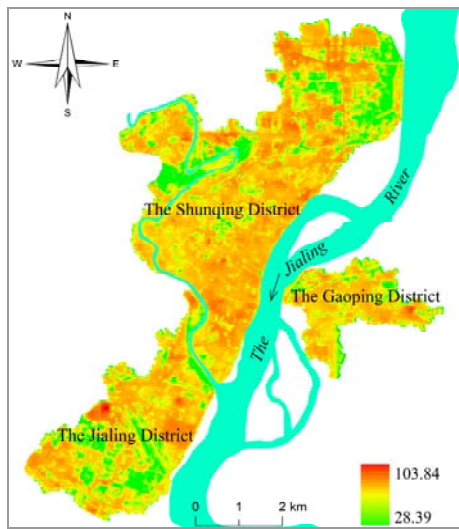
a) Soil heat flux (G)
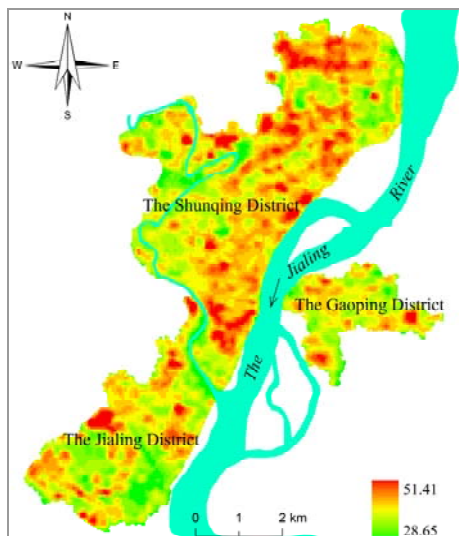


b) Sensible heat flux (H)
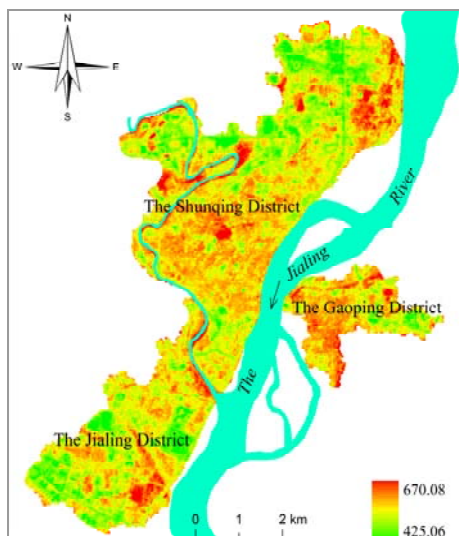


c) Latent heat flux (LE)

**Fig. 3.** Land surface heat fluxes distribution on September 20, 2007.
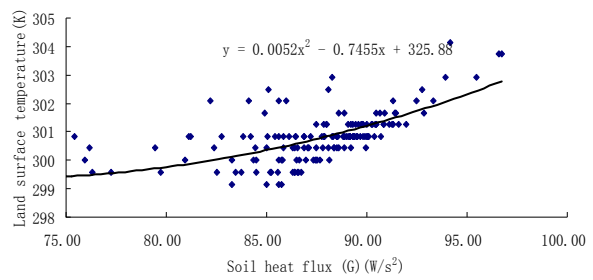


**Fig. 4.** Correlation diagram between land surface temperature and soil heat flux.
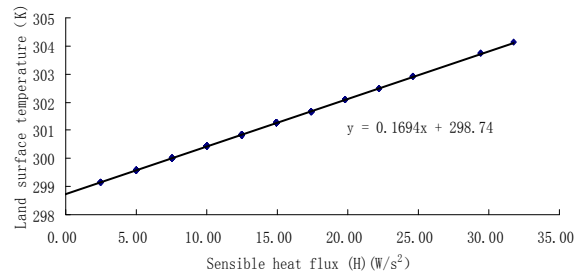


**Fig. 5.** Correlation diagram between land surface temperature and sensible heat flux.
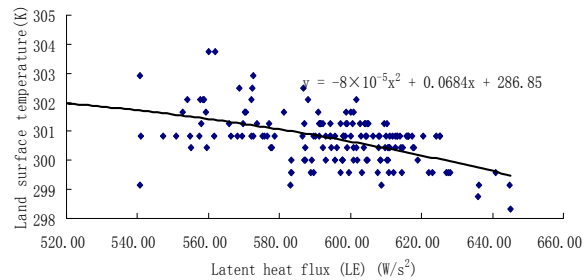


**Fig. 6.** Correlation diagram between land surface temperature and latent heat flux.

The analysis results showed that,

1) Land surface temperature (y) and soil heat flux (x) was positively related, the fitting relationship: $y=0.0052x^2-0.7455x+325.88$, and the correlation coefficient was 0.66. All data distributed in the right part of the function symmetry axis, so land surface temperature was increased smoothly with increasing soil heat flux.

2) Land surface temperature (y) had absolutely linear positive correlation with sensible heat flux (x), the fit function was: $y = 0.1694x + 298.74$, and the correlation coefficient was 1. So land surface temperature was increased linearly with increasing sensible heat flux.

3) Land surface temperature (y) was negatively correlated with latent heat flux (x), the fit function was $y=-8\times10^{-5}x^2+0.0684x+286.85$, and the correlation coefficient was 0.55. All data distributed in the right part of the function symmetry axis, so land surface temperature was decreased smoothly with increasing latent heat flux.

## 6. Conclusion and Discussion

The Nanchong city in Sichuan Province was taken as an example, the correlation between land surface temperature and heat fluxes were researched. The main conclusions are the following:

1) Land surface temperature had positively correlation with both soil heat flux and sensible heat flux, but negatively correlation with latent heat flux.

2) Land Surface temperature was absolutely effected by sensible heat flux.

3) Influence mechanism of heat island effect is that the impervious surface area has higher soil heat flux, lower latent heat flux, because it cuts off the soil-atmosphere heat exchange, its evapotranspiration is small, energy conservation ability is weak, speed of absorbing or releasing energy is high, and higher sensible heat flux, because its roughness is lower, and its albedo is higher, most of solar radiation is reflected to the atmosphere, more heat in life is discharged in addition, and conversely, the natural surface or vegetation cover area has lower soil heat flux, higher latent heat flux, and lower sensible heat flux. So the land surface temperature of impervious surface area is higher, which of natural surface or vegetation cover area is lower.

## Acknowledgements

## References

[1]. Xu Hanqiu, Image-based Normalization Technique Used for Landsat TM/ETM+ Imagery, *Geomatics and Information Science of Wuhan University,* Vol. 32, No. 1, 2007, pp. 62-67.

[2]. Gyanesh Chander and Brian Markham, Revised Landsat-5 TM Radiometric Calibration Procedures and Post-calibration Dynamic Ranges, IEEE Transactions on Geoscience and Remote Sensing, Vol. 41, No. 11, November, 2003.

[3]. J. F. Mustard, M. A. Camey, A. Sen, The use of satellite data to quantify thermal effluent impacts, *Estuarine Coastal and Shelf Science*, 49, 1999, pp. 509-524.

[4]. Artis D. A., Carnahan W. H., Survey of emissivity variability in thermography of urban areas, *Remote Sensing of Environment*, Vol. 12, No. 4, 1982, p. 313-329.

[5]. Goward S. N., Markham B., Dye D. G., Dulaney W., Yang J., Normalized difference vegetation index measurements from the advanced very high resolution radiometer, *Remote Sensing of Environment*, Vol. 35, 1991, pp. 257–277.

[6]. Santos P., Negri A. J., A comparison of the normalized difference vegetation index and rainfall for the Amazon and Northeastern Brazil, *Journal of Applied Meteorology and Climatology,* Vol. 36, 1997, pp. 958-965.

[7]. Zhao Yingshi, Analysis theory and method of remote sensing application, *Science Press*, Beijing, 2003.

[8]. Liebe H. J., Hufford G. A., Cotton M. C., Propagation Modeling of Moist air and suspended water/ice particles at frequencies below 1000 GHz, in *Proceedings of the AGARD 52nd Special Meeting of the Electromagnetic Wave Propagation Pand*, Vol. 3. 1993, pp. 1-10.

[9]. Liang Shunlin, Narrowband to broadband conversions of land surface albedo I algorithms, *Remote Sensing of Environment*, Vol. 76, 2000, pp. 213-238.

[10]. Bastiaanssen W. G. M, Menenti M., Feddes R. A., *et al.*, A remote sensing surface energy balance algorithm for land (SEBAL) formulation, *Journal of Hydrology*, 1998, pp. 212-213.

[11]. Tasumi M., Allen R. G., Application of the SEBAL methodology for estimating consumptive use of water and stream flow depletion in the Bear River Basin of L daho through remote sensing, *Final Report Submitted to the Raytheon Systems Company, Earth Observation System Data and Information System Project*, 2000.

[12]. Bastiaanseen W. G. M., SEBAL-based sensible and latent heat fluxes in the irrigated Gediz Basin, *Journal of Hydrology*, Turkey, Vol. 229, 2000, pp. 87-100.

[13]. Burman R. D., Jensen M. E., Allen R. G., Thermodynamic factors in evapotranspiration, *in Proceedings of the Irrigation Systems for the 21st Century Conference*, 1987, pp. 140-148.

[14]. Smith M., Allen R. G., Monteith J. L., *et al.*, Report on the expert consultation on procedures for revision of FAO guidelines for prediction of crop water requirements, *Land and Water Development Division, United Nations Food and Agriculture Service*, Rome, Italy, 1992.

---

# Study on the Thermal Resistance of Multi-chip Module High Power LED Packaging Heat Dissipation System

[1, 2] **Kailin Pan,** [1] **Hua Lin,** [1] **Yu Guo,** [1] **Na Wei,** [2] **Tao Lu,** [2] **Bin Zhou**

[1] School of Mechanical and Electrical Engineering, Guilin University of Electronic Technology,
1 Jinji Road, Guilin, 541004, China
[2] Science and Technology on Reliability Physics and Application of Electronic Component
Laboratory, CEPREI 110, Dongguanzhuang Road, Tianhe District, Guangzhou, 510000, China
E-mail: panklphd@gmail.com, gxnnezbjnl11@sina.cn, zhoubin722@163.com

**Abstract:** Thermal resistance is a key technical index which indicates the thermal management of multi-chip module high power LED (MCM-LED) packaging heat dissipation system. In this paper, the prototype structure of MCM-LED packaging heat dissipation system is proposed to study the reliable thermal resistance calculation method. In order to analyze the total thermal resistance of the MCM-LED packaging heat dissipation system, three kinds of thermal resistance calculation method including theoretical calculation, experimental testing and finite element simulation are developed respectively. Firstly, based on the thermal resistance network model and the principle of steady state heat transfer, the theoretical value of total thermal resistance is 6.111 K/W through sum of the thermal resistance of every material layer in the major direction of heat flow. Secondly, the thermal resistance experiment is carried out by T3Ster to obtain the experimental result of total thermal resistance, and the value is 6.729 K/W. Thirdly, a three-dimensional finite element model of MCM-LED packaging heat dissipation system is established, and the junction temperature experiment is also performed to calculated the finite element simulated result of total thermal resistance, the value is 6.99 K/W. Finally, by comparing the error of all the three kinds of result, the error of total thermal resistance between the theoretical value and experimental result is 9.2 %, and the error of total thermal resistance between the experimental result and finite element simulation is only about -3.9 %, meanwhile, the main reason of each error is discussed respectively. *Copyright © 2014 IFSA Publishing, S. L.*

**Keywords:** High power LED, Thermal resistance, Heat dissipation system, T3Ster, Finite element simulation.

## 1. Introduction

According to DOE's Solid-State Lighting (SSL) Research & Development (R&D) Multi-Year Program Plan (MYPP) [1], High power light emitting diode (LED) is identified as typical green lighting source with penetrating into illumination planning and application, such as road lighting, interior lighting and special lighting, and so on. However, on the current market, the electro-optical conversion efficiency of high power LED chip is less than 30 % at the normal drive current. Inevitably, the problem exerts much of excess input power and redundant heat and ultimately enhances the junction temperature which affects the lifetime of LED lamp [2]. Thermal management is the key technology to the development of the reliable LED lamp. In order to evaluate the level of thermal management and optimize the heat dissipation system, most of designers attach the importance of thermal resistance

of LED lamp. Meanwhile, due to the complex heat transfer path of multi-chip module high power LED (MCM-LED) packaging heat dissipation system, it is necessary to develop the research on the thermal resistance calculation method.

There are some reports on the thermal resistance analysis of single-chip and multi-chip LED packaging. Lan Kim and Woong Joon Hwang presented and discussed the thermal transient management of one-chip, two-chip and four-chip high power LED packaging to analyze thermal resistance with the structure function theory [3]. Aiming at a LED street lamp prototype, S. Liu and co-workers established the multi-chip spreading resistance model [4]. Huanting Chen and co-workers developed a method for creating compact thermal models of single-chip and multi-chip LED packaging and evaluated with good agreement between the finite volume simulation and experimental data [5]. Henning Dieker compared thermal resistance of simulations of various substrate materials and packaging technologies by FLOTHERMAL software, and determined the thermal path using the T3Ster analyzer [6]. However, there have been no reports on the comparison analysis of the thermal resistance calculation method of MCM-LED packaging heat dissipation system of all the best knowledge authors.

In this paper, the prototype structure of MCM-LED packaging heat dissipation system is proposed to study the reliable thermal resistance calculation method. Then aiming at the prototype structure, three kinds of thermal resistance calculation method including theoretical calculation, experimental testing and finite element simulation are developed respectively. Finally, by comparing the three kinds of result, the cause of the errors is discussed.

## 2. Research Methods

### 2.1. Prototype Structure of MCM-LED Packaging Heat Dissipation System

In order to study the thermal resistance of high power LED lamps, the light source of the LED lamp is composed by the two same MCM-LED modules, and each module includes a 2×2 GaN-based flip chip LED (FC-LED) array which is bonded on the same silicon substrate by the gold bumps [7]. The structure of MCM-LED module is shown in Fig. 1. Lc and Wc are the size of LED chip, and the size of GaN-based FC-LED is set with 35 mm × 35 mm × 0.889 mm in this paper.

Thermal management of high power electronic packaging is necessary to design a heat dissipation system which can control the junction temperature of the chip and enhance the reliability of electronic system. The lower junction temperature of LED chip is not only improves its life time, but also improves light output at the same input power.
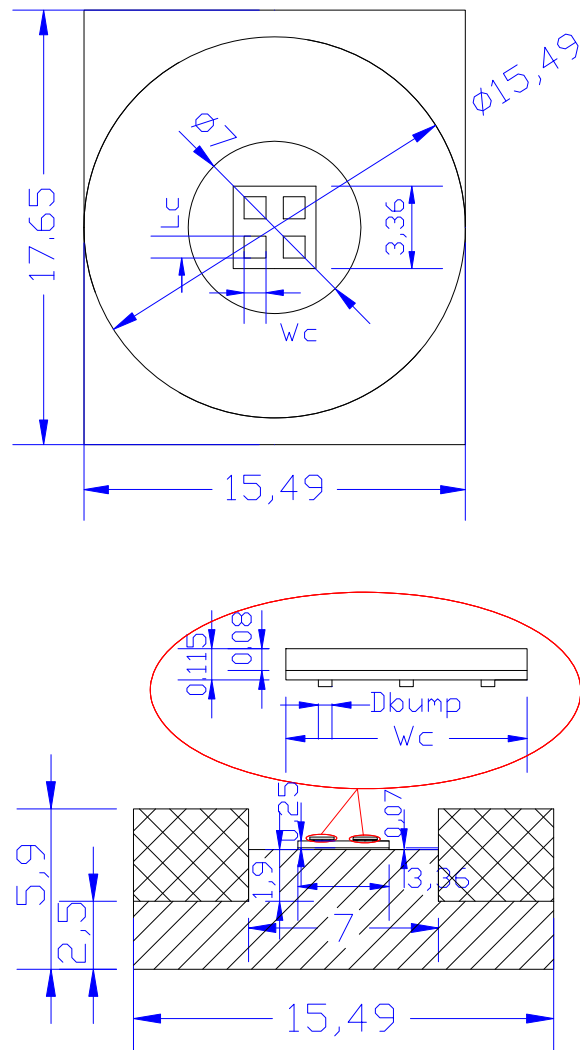


**Fig. 1.** Structure of MCM-LED module.

Therefore, the structure of MCM-LED packaging heat dissipation system is proposed to reduce the junction temperature of LED chip and enhance the reliability of LED lamp, as shown in Fig. 2. The MCM-LED Packaging Heat Dissipation System includes two MCM-LED modules, thermal interface material (TIM) layer, metal core printed circuit board (MCPCB) layer and heat sink. The dimension of aluminum heat sink board is 75 mm×75 mm×5 mm, and the height, thickness and number of heat sink fin are 33 mm, 3 mm and 11 respectively. Meanwhile, the thickness of TIM1 layer, TIM2 layer and PCB are 0.25 mm, 0.1 mm and 1.5 mm respectively. Aiming at the structure of MCM-LED packaging heat dissipation system, the materials in the major direction of heat flow are illustrated in Fig. 3. The heat which is generated by LED chip is transferred to the MCPCB by heat conduction, and then the heat dissipated to the surrounding environment by the heat convection of heat sink. In order to analyze the thermal resistance of MCM-LED Packaging Heat Dissipation System, all the materials parameters related to the heat transfer are listed in Table 1.
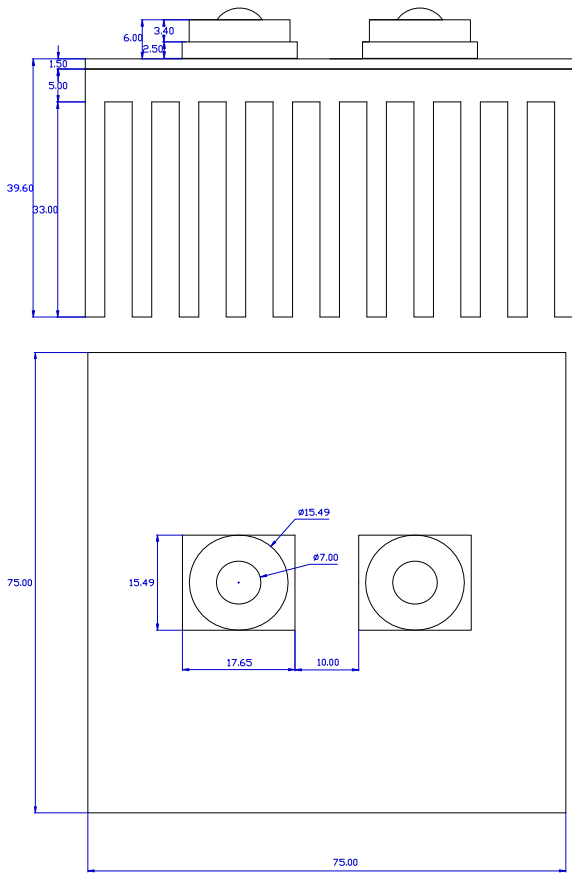
**Fig. 2.** Structure of MCM-LED packaging heat dissipation system.
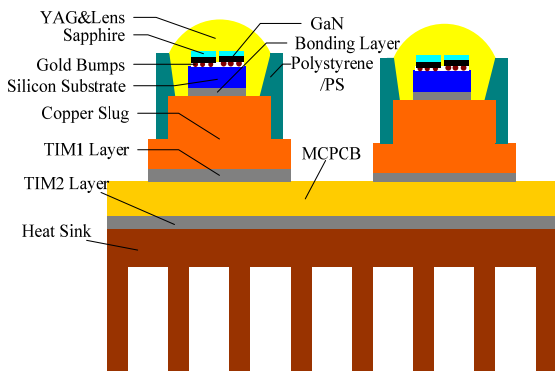


**Fig. 3.** Materials in the major heat flow direction.

**Table 1.** Heat transfer related materials parameters.

| Material | k (W·m⁻¹·k⁻¹) | C (J·kg⁻¹·k⁻¹) | ρ(kg·m⁻³) |
|---|---|---|---|
| Sapphire | 41.9 | 730 | 3965 |
| GaN | 130 | 40 | 6095 |
| Gold | 300 | 132 | 19320 |
| Silicon | 124 | 700 | 2330 |
| Copper | 385 | 385 | 8930 |
| Sn63Pb37 | 59 | 150 | 8400 |
| MCPCB | 2 | 800 | 2700 |
| Aluminum | 237 | 875 | 2710 |
| Silver colloid | 2.45 | 250 | 3800 |
| TIM | 0.98 | 711 | 1120 |

In this paper, the two MCM-LED modules are assumed completely identical and the electric power of each MCM-LED module is 4.53 W. Therefore, the electric power of each FC-LED chip is 1.133 W, and the electro-optical conversion efficiency of high power LED chip is about 27 %.

### 2.2. Theoretically Calculated of Thermal Resistance

Aiming at the prototype structure of MCM-LED packaging heat dissipation system, the thermal resistance network which helps to solve the complex heat transfer problems is established in the major direction of the heat flow to analyze the theoretical thermal resistance, is as shown in Fig. 4.
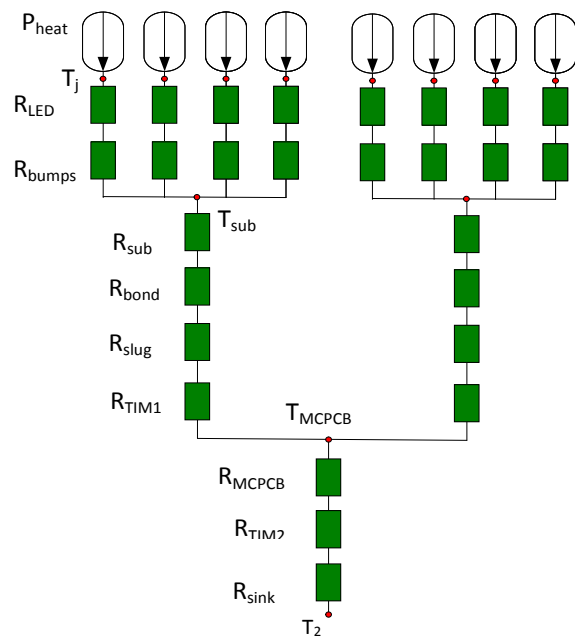


**Fig. 4.** Thermal resistance network of MCM-LED packaging heat dissipation system.

In the theoretical calculated of thermal resistance, some material layers in the secondary direction of heat flow are neglected, such as polystyrence layer, YAG&lens layer, and the thermal contact resistance is neglected in the interface between two layers.

The total thermal resistance of MCM-LED packaging heat dissipation system is written as Eq. (1).

$$R_{total} = \Delta T_{total} \Big/ 8P_{heat}, \qquad (1)$$

where $R_{total}$ is the total thermal resistance of MCM-LED packaging heat dissipation system, and $P_{heat}$ is the thermal power of LED chip, and $\Delta T_{total}$ is the temperature difference between junction temperature and ambient temperature, is as shown in Eq. (2).

$$\Delta T_{total} = T_j - T_a$$
$$= (T_j - T_{sub}) + (T_{sub} - T_{MCPCB}) + (T_{MCPCB} - T_a)$$
$$= P_{heat}(R_{LED} + R_{bumps}) + 4P_{heat}(R_{sub} + R_{bond}$$
$$+ R_{slug} + R_{TIM1}) + 8P_{heat}(R_{MCPCB} + R_{TIM2} + R_{sink}), \quad (2)$$

where $T_j$, $T_a$, $T_{sub}$ and $T_{MCPCB}$ are the junction temperature, ambient temperature, silicon substrate surface temperature and MCPCB surface temperature respectively, and $R_{LED}$, $R_{bumps}$, $R_{sub}$, $R_{bond}$, $R_{slug}$, $R_{TIM1}$, $R_{MCPCB}$, $R_{TIM2}$ and $R_{sink}$ are the thermal resistance of LED chip, bumps of FC-LED layer, silicon substrate, bonding layer, heat slug layer, TIM1 layer, MCPCB layer, TIM2 layer and heat sink respectively. The total thermal resistance $R_{total}$ is shown as Eq. (3).

$$R_{total} = \frac{R_{LED} + R_{bumps}}{8} + \frac{R_{sub} + R_{bond} + R_{slug} + R_{TIM1}}{2}$$
$$+ R_{MCPCB} + R_{TIM2} + R_{sink} \quad (3)$$

The thermal resistance of heat sink ($R_{sink}$) is composed by $R_{board}$, $R_{fins}$, $R_{air}$ which is the outside convection resistance of heat sink, and $R_s$ which is the spreading resistance of the board, is as shown in Eq. (4).

$$R_{sink} = R_{board} + R_{fins} + R_{air} + R_s$$
$$= \frac{h_{board}}{k_{Al}A_{board}} + \frac{h_{fin}}{11 \times k_{Al}A_{fin}} + \frac{1}{hA_0} + R_s \quad (4)$$

where $h_{board}$ is the thickness of the heat sink board, $A_{board}$ is the area of the heat sink board, $h_{fin}$ is the height of fins, $A_{fin}$ is the cross-sectional area of fin, $A_0$ is the area of heat sink in the convective environment, $k_{Al}$ is the thermal conductivity of heat sink, $h$ is the nature convection coefficient, and the number of fin is 11.

The spreading resistance of the board of heat sink $R_s$ is written as Eq. (5) and Eq. (6) [8].

$$R_s = \frac{\psi_{avg}}{\sqrt{\pi}k_{Al}A} = \frac{\sqrt{A_{board}} - \sqrt{A_{MCM-LED}}}{k_{Al}\sqrt{\pi A_{MCM-LED}A_{board}}}$$
$$\times \frac{\lambda k_{Al}A_{board}R_0 + \tanh(\lambda h_{board})}{1 + \lambda k_{Al}A_{board}R_0 \tanh(\lambda h_{board})} \quad (5)$$

$$\lambda = \frac{\pi^{3/2}}{\sqrt{A_{board}}} + \frac{1}{\sqrt{A_{MCM-LED}}}, \quad (6)$$

where $A_{MCM-LED}$ is the cross-sectional area sum of the two MCM-LED modules bottom surface, and $R_0$ is the average thermal resistance of the heat sink board. Therefore, according to Eq. (3), (4), (5), (6), the $R_{total}$ is the total thermal resistance of MCM-LED

packaging heat dissipation system in Eq. (3) can be obtained by theoretical calculation.

$$R_{total} = 6.111 \, K\!\!\Big/\!\!W$$

Assuming that the value of h is 5 W/(m²k), and ambient temperature is 25 ºC. The junction temperature of LED is estimated by Eq. (7).

$$T_j = 8P_{heat}R_{total} + T_a$$
$$= 8 \times 1.133 \times (1 - 0.27) \times 6.111 + 25 = 65.435°C \quad (7)$$

### 2.3. Experimental Value of Thermal Resistance

Aiming at the prototype structure of MCM-LED packaging heat dissipation system, the thermal resistance experiment is carried out by T3Ster which is a thermal transient tester, and the experimental materials are shown in Fig. 5. The theoretical framework of the evaluation of the T3Ster is based on a representation of the distributed RC networks [9, 10].
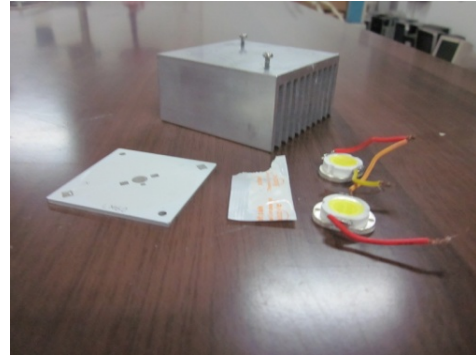


**Fig. 5.** Experimental materials.

Firstly, the K factor is test by the integrating sphere. Sensor current is used to detect the forward voltage of the MCM-LED module. Based on the JESD51-1 standards [11], considering the environment temperature of the lab is 11 ºC, the test temperature of the test chamber is set with 10 ºC, 30 ºC, 50 ºC, 70 ºC and 90 ºC. Fig. 6 is the forward voltage versus temperature plot. The linearity between the voltage and temperature is K factor, and the value of K factor is -5.615 mV/K when the sensor current is 2 mA.

Secondly, Fig. 7 shows that the luminous power of the two MCM-LED modules is about 2450 mW when the drive current is 750 mA. Fig. 8 shows that the electric power of the two MCM-LED modules is 9.059 W when the drive current is 750 mA. Therefore, the electro-optical conversion efficiency of high power LED chip is about 27 % at the drive current. The experimental results of the electric power and the electro-optical conversion efficiency

of LED chip stay the same level as the assuming condition which is applied in the theoretically calculated of thermal resistance.

Finally, the total thermal resistance of the MCM-LED packaging heat dissipation system is obtained by the T3Ster experiment which is shown in Fig. 9. Fig. 10 represents the derivative of thermal capacitance as a function of thermal resistance for the MCM-LED packaging heat dissipation system, and the total thermal resistance is about 6.729 K/W.
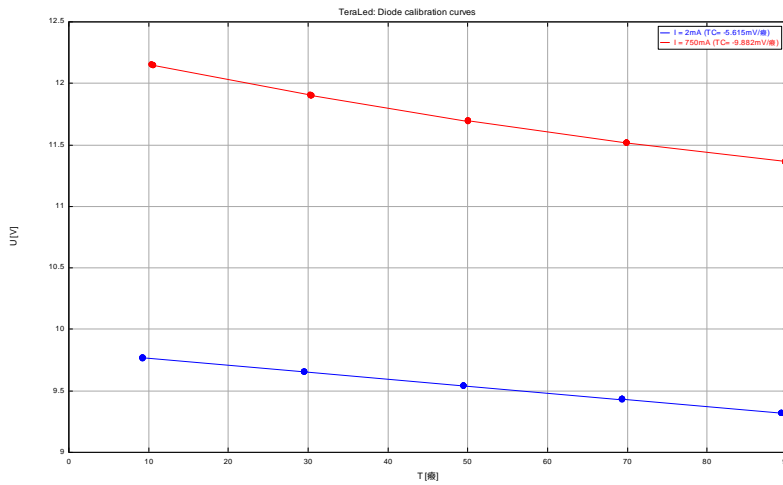


**Fig. 6.** Forward voltage versus temperature plot showing the K factor.
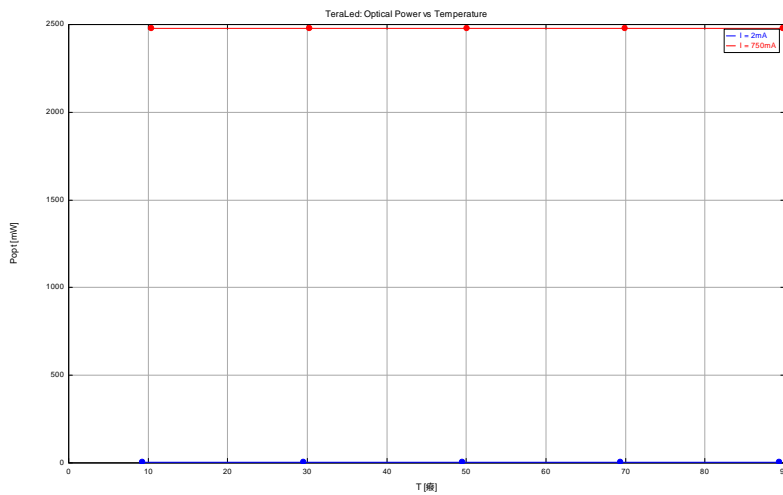


**Fig. 7.** Luminous power of the two MCM-LED modules at the drive current of 750 mA.
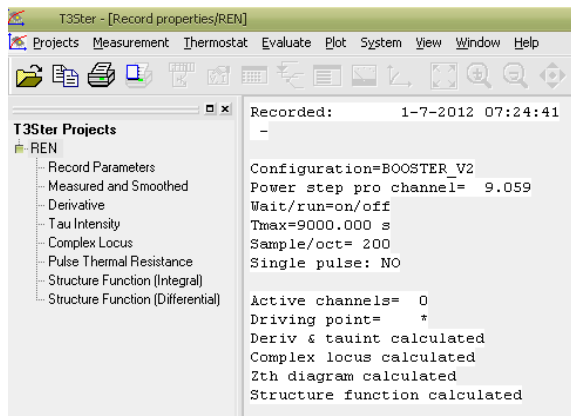


**Fig. 8.** Electric power of the two MCM-LED modules at the drive current of 750 mA.



**Fig. 9.** T3Ster experiment.
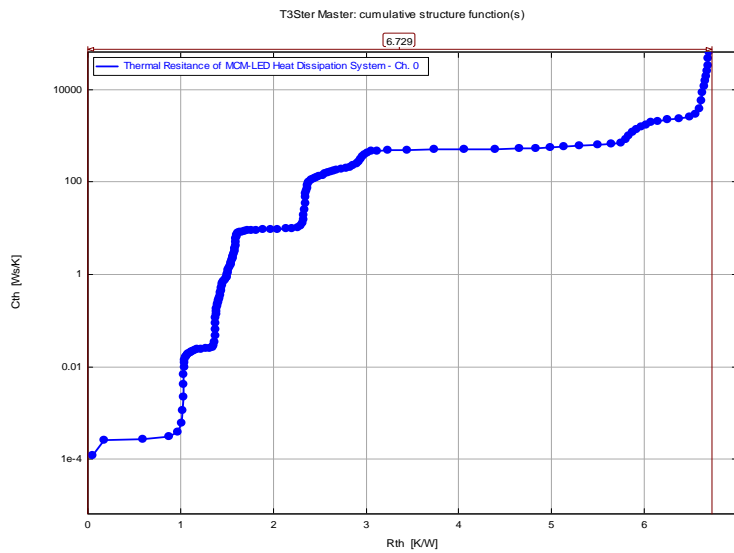
**Fig. 10.** Cumulative structure functions of the MCM-LED packaging heat dissipation system.

### 2.4. Finite Element Simulation of Thermal Resistance

In order to facilitate the complex of finite element model and improve the calculation speed of computer, some structures are neglected, such as the pins of MCM-LED module, bonding wires. Based on the numerical analysis method and MCM-LED packaging heat dissipation system, a 3-D finite element model (FEM) is developed by the software ANSYS, which is shown in Fig. 11. The element type is SOLID 70.





**Fig. 11.** FEM of MCM-LED packaging heat dissipation system.

The electric power of each FC-LED chip is 1.133 W and the electro-optical conversion efficiency of high power LED chip is about 27 %. The GaN-base active layer of LED chip is known as a heat source, and the heat generating is $2.99 \times 1010$ W/m$^3$. The ambient temperature is set to 25ºC, and the nature convection coefficient is 5 W/(m$^2$·k).

The temperature distribution of MCM-LED packaging heat dissipation system is shown in Fig. 12. The simulation result reveals that the junction temperature of LED is 71.225ºC. The total thermal resistance of finite element simulation is calculated by the Eq. (8), and the value of Rtotal is 6.99 K/W.

$$R_{total} = \frac{T_j - T_a}{P_h} = 6.99\,K\!\!\diagup\!\!_W, \tag{8}$$

where Ph is the total heat power dissipation in the two MCM-LED modules.

### 3. Results and Discussion

The total thermal resistance and junction temperature of theoretical value, experimental result and finite element simulation are compared, which is shown in Table 2. The results indicate that the order of total thermal resistance is theoretical value (6.111 K/W) < experimental result (6.729 K/W) < finite element simulation (6.99 K/W).

By comparing the three kinds of result, the cause of errors is discussed. Firstly, at the theoretical value and experimental result aspects, the error of total thermal resistance and junction temperature are 9.2 % and 5.8 %, respectively. The main reason of the error is that the calculation cross-sectional area of material layer is bigger than the actual application area in the
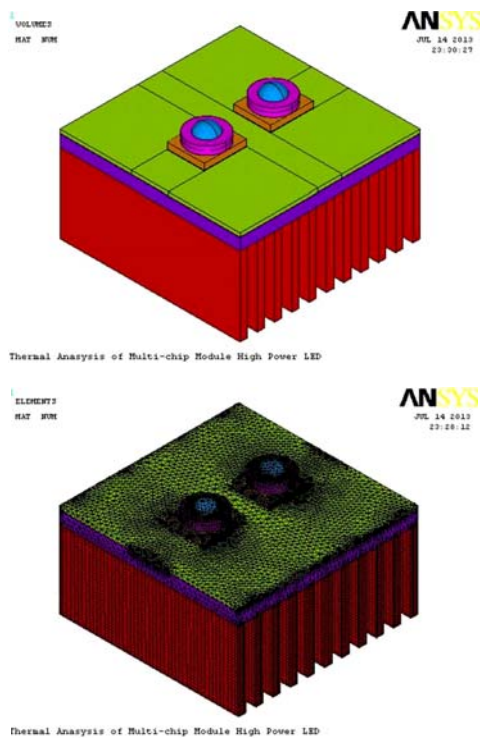
theoretical calculation of thermal resistance. Therefore, the theoretical value is less than the experimental result, and the suitable cross-sectional area of material layer should be selected by experience in the theoretical calculation of thermal resistance to improve the accuracy of theoretical calculation. Secondly, at the experimental result and finite element simulation aspects, the error of total thermal resistance and junction temperature are only about -3.9 % and -2.5 %. The main reason of the error is that the nature convection which should be loaded in some outside surface of MCM-LED packaging heat dissipation system is neglected in the finite element simulation. Due to only consider the nature convection on the surface of fins, so the finite element simulation result is a little more than the experimental result.

## 4. Conclusions

In this research, aiming at the designed prototype structure of MCM-LED packaging heat dissipation system, the total thermal resistance is analyzed by theoretical calculation, experimental testing and finite element simulation, respectively. Firstly, with establishing thermal resistance network model of the MCM-LED packaging heat dissipation system and using the principle of steady state heat transfer, the material layer thermal resistance and total thermal resistance (6.111 K/W) are theoretically calculated. Secondly, the thermal resistance experiment is carried out by T3Ster to obtain the experimental result of total thermal resistance, which is 6.729 K/W. Thirdly, a detail FEM of MCM-LED packaging heat dissipation system is established, and the junction temperature experiment is also performed to calculated the finite element simulated result of total thermal resistance, which is 6.99 K/W. Finally, by comparing the error of the three kinds of result, the cause of errors is discussed.

## Acknowledgements

(a)                                    (b)
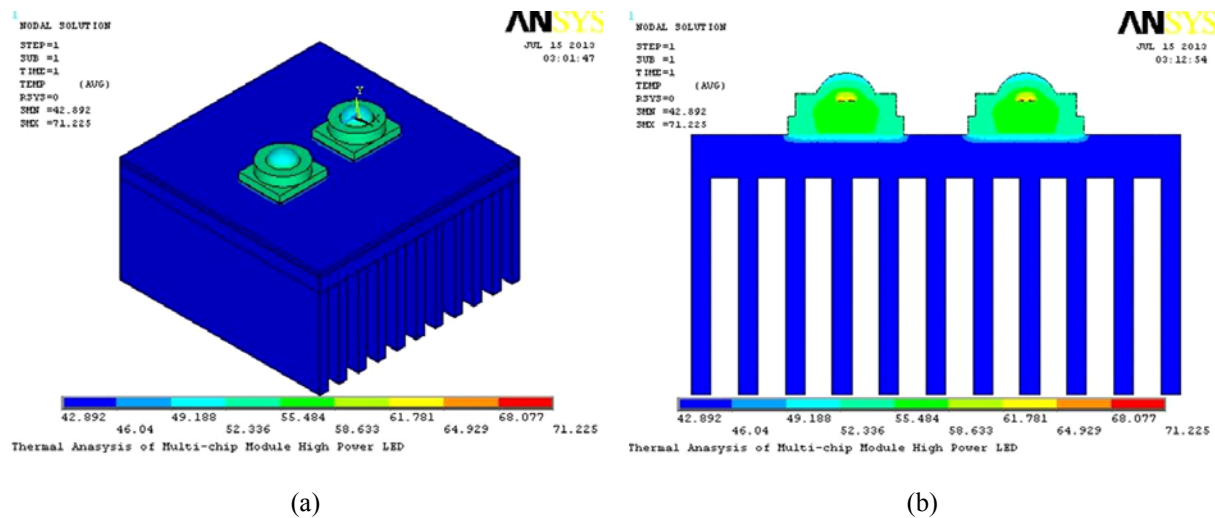
**Fig. 12.** Temperature distribution of finite element simulation.

**Table 2.** Compare results of total thermal resistance and junction temperature.

| | | **Theoretical Value** | | **Finite Element Simulation** | |
|---|---|---|---|---|---|
| **Experimental Result** | Total Thermal Resistance (K/W) | Total Thermal Resistance (K/W) | Error | Total Thermal Resistance (K/W) | Error |
| | 6.729 | 6.111 | 9.2 % | 6.99 | -3.9 % |
| | Junction Temperature (°C) | Junction Temperature (°C) | Error | Junction Temperature (°C) | Error |
| | 69.5 | 65.435 | 5.8 % | 71.225 | -2.5 % |

## References

[1]. DOE: Solid-State Lighting Research & Development Multi-Year Program Plan, March 2010.

[2]. Pan Kailin, Jiaopin Wang, *et al*., Numerical Analysis for Thermal Performance of High Power Multi-chip LED Packaging, *Advanced Materials Research*, Vol. 139-141, 2010, pp. 1433-1437.

[3]. Lan Kim, Woong Joon Hwang, Moo Whan Shin, Thermal Resistance Analysis of High Power LEDs with Multi-chip Package, in *Proceedings of the Electronic Components and Technology Conference*, 2006, pp. 1076-7081.

[4]. Luo X., Liu S., *et al.*, Temperature estimation of high-power light emitting diode street lamp by a multi-chip analytical solution, *IET Optoelectronics*, Vol. 3, No. 5, 2009, pp. 225-232.

[5]. Huanting Chen, Yijun Lu, *et al*., The performance of compact thermal models for LED package, *Thermochimica Acta*, Vol. 488, 2009, pp. 33-38.

[6]. Henning Dieker, Christian Miesner, *et al.*, Comparison of different LED Packages, *in Proceedings of the SPIE*, Vol. 6797, 2007, pp. 1-12.

[7]. Pan Kailin, Ren Guotao, *et al*., Thermal Analysis of Multi-chip Module High Power LED Packaging, in *Proceedings of the International Conference on Electronic Packaging Technology & High Density Packaging*, 2011, pp. 1124-1127.

[8]. Song S., Lee S., Au V., Closed-Form Equation for Thermal Constriction/Spreading Resistances with Variable Resistance Boundary Conditions, in *Proceedings of the IEPS Conference*, 1994, pp. 111-121.

[9]. Yu Guo, Kai-Lin Pan, *et al.*, Research on LED Temperature Characteristic and Thermal Analysis at Low Temperatures, in *Proceedings of the IEEE International Conference on Electronic Packaging Technology & High Density Packaging*, Guilin, China, 2012, pp. 1411-1415.

[10]. Lan Kim, Jong Hwa Choi, *et al.,* Thermal analysis of LED array system with heat pipe, *Thermochimica Acta*, Vol. 455, 2007, pp. 21-25.

[11]. EIA/JESD51-1, Integrated Circuit Thermal Measurement Method - Electrical Test Method (Single Semiconductor Device), December 1995.

_____

# Field Effect Devices Sensitive to CO at Room Temperature

**[1, 2] Ricardo ARAGÓN, [1] Rina LOMBARDI**

[1] Laboratorio de Películas Delgadas, Depto. Física, Facultad de Ingeniería, Universidad de Buenos Aires, Paseo Colón 850, C. P. 1063, Buenos Aires, Argentina
[2] DEINSO (Solid State Research Dept.) – CITIDEF– UNIDEF (MINDEF-CONICET) San Juan Bautista de La Salle 4397 (B1603ALO) Villa Martelli, Argentina
[1] Tel.: (54 11) 4343 0891, fax: (54 11) 4331 0129
E-mail: raragon@fi.uba.ar

**Abstract:** [5,10,15-Tris(2,6-dichlorophenyl)corrolate] cobalt(III) was used to chemisorb CO selectively, on the gap-gate of MOS capacitors and the state of charge monitored by voltage shifts of the photocurrent induced by pulsed illumination under constant D. C. bias, proportionally to CO concentration in air. Negative chemically induced charges at room temperature induce positive responses above and negative shifts below the threshold voltage, conforming to acceptor behavior, and the dynamic range (125 ppm) is limited by the silicon doping concentration. The linear proportionality between CO concentration and surface charge ($6.46[ppm.m^2.\mu C^{-1}]$) corresponds to the low concentration limit of the Langmuir isotherm. Sluggish CO desorption can be compensated by photo stimulation at 395 nm. *Copyright © 2014 IFSA Publishing, S. L.*

**Keywords:** CO, FET sensor, Room temperature, Co-corrole, Photodesorption.

## 1. Introduction

Carbon monoxide is toxic, because its affinity for hemoglobin is more than 200 times that of oxygen, resulting in the formation of carboxyhemoglobin, with even relatively low amounts of inhaled carbon monoxide, under extended exposure [1]. This sluggish release of CO from the active heme group (Fig. 1a) discourages its possible use as a sensing probe, whereas cobalt (III) corroles (Fig. 1b) have shown strong reversible chemisorption of CO [2], even in the presence of $O_2$ and $N_2$, due to increased electron density of the central metal. Two alternative strategies are possible to take advantage of the high resulting selectivity for their potential use in gas sensors [3]: either functionalize these compounds [4] to obtain continuous thin films suitable for conductimetric probes, or resort to sensing techniques independent of compound resistivity or state of aggregation, such as SAW [5-7].
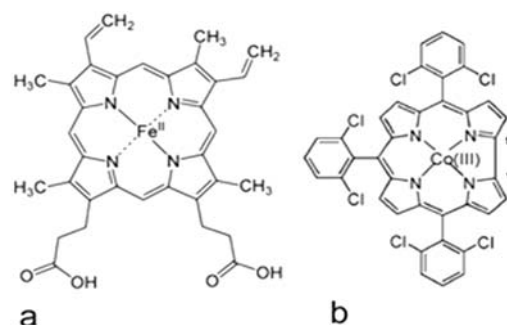


**Fig. 1.** Heme and Co-corrole structures. a) Heme B, b) 5,10,15-Tris(2,6-dichlorophenyl)corrolate] cobalt(III).

FET devices have been employed with organometallic sensing films at room temperature in a conductimetric mode [8], which monitors compound resistivity changes in response to chemical stimulation at very low concentration (<15 ppm), whereas gap-gate devices interrogated by pulsed illumination techniques extend the dynamic range beyond 100 ppm [9]. This work addresses the application of the latter method to CO detection, at room temperature, with Co-corrole active films.

## 2. Materials and Methods

Gap-gate MOS capacitors [9] were fabricated with 4-40 $\Omega$.cm, p-type, boron doped silicon wafers, thermally oxidized to 130 nm. Circular (2.5 mm O. D.) magnetron sputtered chromium gates were masked, leaving a 250 micron gap, to allow the inversion layer to extend continuously beneath it under positive polarization (Fig. 2), thus relieving the chemically sensitive material of any electrical functionality. The capacitors were mounted on hybrid alumina substrates and enclosed in an air tight chamber, for pulsed illumination measurements [10], with previously described instrumentation [11]. All devices were cycled repeatedly, biased from deep-inversion to depletion, until reproducible dependence of the photocurrent (u) with bias voltage ($V_A$) was verified.
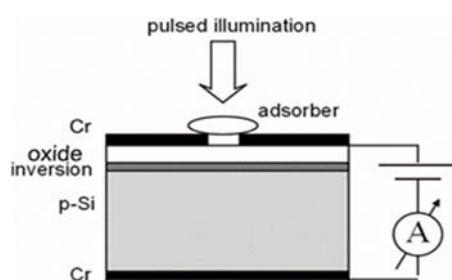


**Fig. 2.** Schematic sensor cross section, represented under forward applied bias, which induces a continuous inversion layer across the gap of the gate electrode, over which a Co-corrole dichloromethane solution is seeded, for detection by the phase sensitive amperometric circuit.

A KEITHLEY Source and Measure Model 2400 unit supplied constant applied bias, and allowed monitoring of the polarization current. Pulsed illumination with a HITACHI HL6501MG, 658 nm, 35 mW laser diode, thermally stabilized and driven by a THORLABS LTC-100-B unit, modulated at 1 kHz, induced a photocurrent (u), which was monitored phase sensitively with the HL6501 photodiode reference, on a SIGNAL RECOVERY Model 1265 lock-in amplifier operated in external mode, after pre-amplification by an ad-hoc transimpedance current to voltage converter [11], through calibrated 10 k$\Omega$ load resistors and the respective signals were displayed on a Tektronix TDS 220 dual channel oscilloscope. Constant flow of synthetic air and 1000 ppm CO in $N_2$

gas mixtures, totaling 100 cm$^3$/min, was secured with independent MKS 1259 mass flow controllers.

5,10,15-Tris[(2,6-dichlorophenyl)corrolate] cobalt(III), synthesized at DQIAQF-UBA by previously described methods [12], yielded UV-Vis and 1H NMR spectra coincident with those reported in [4]. 20 $\mu$L of a $10^{-3}$ molar solution of this compound in dichloromethane were delivered directly to the gap window, with a micropipette, before each measurement. Consistently with prior reports [8], it was found beneficial to expose the device to 50 ppm CO in nitrogen or air carrier to activate the corrole deposit. Although long term exposure to light and air is known to induce oligomerization [13] in analogue Co-corroles, no perceptible CO sensitivity changes were found, for dichloromethane solutions stored in caramel bottles, even after three months.

## 3. Results and Discussion

The response to chemical stimulation by mass flow controlled mixtures of 100 ppm CO, in nitrogen or dry-air indistinctly, with a constant 100 cm$^3$/min total flow, defined by the shift in bias tension at constant photocurrent, is negative in the depletion regime below the threshold voltage ($V_T = 2.5$ V, Fig. 3a) and positive under full inversion above this limit (Fig. 3b), consistently with an acceptor character, associated with negatively charged chemisorbed species [14].
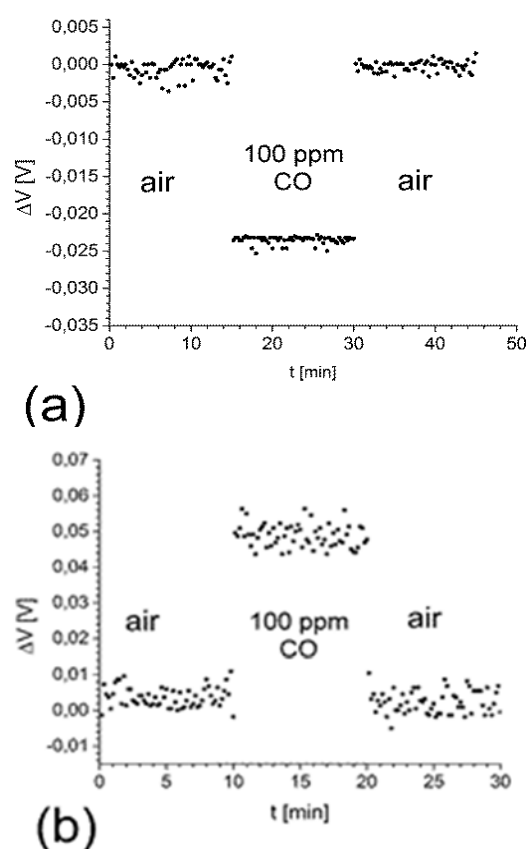


**Fig. 3.** Temporal dependence of responses to 100 ppm CO in air, 20 ºC (a) biased at 2.2 V < $V_T$; (b) 3.5 V > $V_T$.

Room temperature operation narrows the difference between threshold and flat band voltages, rendering the photocurrent voltage dependence steeper [15], such that if device geometry is increased to allow for inverse response in the depletion mode, the normal response in full inversion mode exceeds the dynamic range of the detection circuitry.

A representative example of the temporal response to increasing CO stimulation in dry air, at 20 °C, monitored in full inversion, under 3.9 V polarization, is illustrated in Fig. 4.
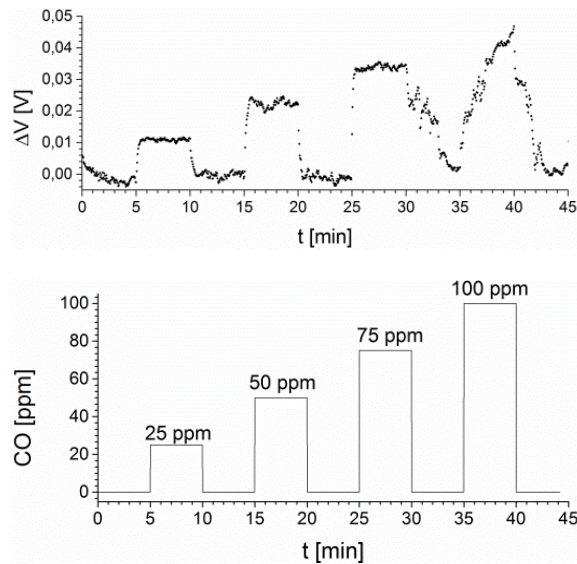


**Fig. 4.** Temporal response to increasing 5 minute CO stimulation in air, at 20 °C, biased at 3.9 V, illustrating the influence incomplete CO desorption.

Initial response and relaxation are commensurate with the sampling interval (3 s), consistently with fast charge transfer processes, but the third stimulation at 75 ppm displays a relaxation transient, disclosing a kinetic barrier for CO desorption, which subsequently hampers adsorption as well, in the fourth stimulation at 100 ppm. Upon further chemical stimulation (Fig. 5), no return to base line is observed and ultimately, sensitivity is lost, unless CO desorption is stimulated, either thermally or by cycling in vacuum [7].

Since capacitors are charge transducers, the strong dependence of the measured $\Delta V$ response on operating conditions may be eliminated by computation of the chemically induced charge, through the product of the high frequency capacitance at the bias of interest and $\Delta V$, to obtain a surface charge density uniquely dependent on stimulus concentration [15] (Fig. 6).

The dynamic range of these devices is limited by the maximum sustainable charge at the dielectric interface, which is a function of the doping level of the semiconductor ($N_A^{2/3}$) [16], corresponding to 23.5 $\mu C/m^2$ for the wafers employed in this work; consequently, only the low concentration regime of

the Langmuir adsorption isotherm is accessible for measurement, which yields the linear dependence of surface charge on concentration apparent in Fig. 6.
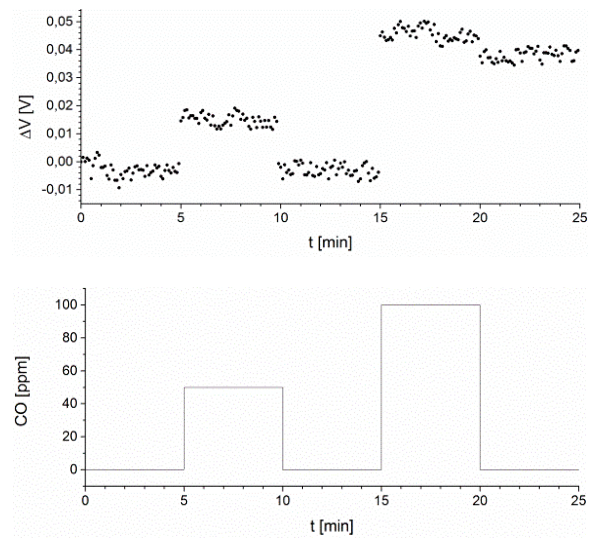


**Fig. 5.** Response relaxation from 100 ppm stimulus is inhibited by un-desorbed CO ($V_{bias} = 7.0$ V).
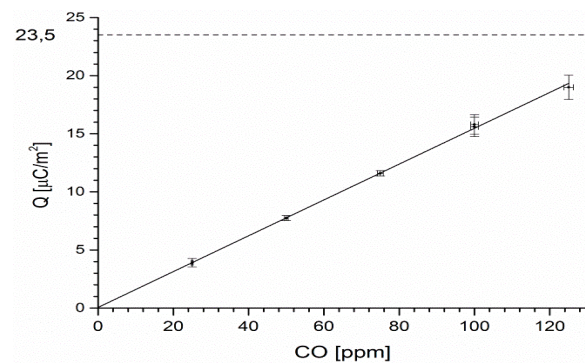


**Fig. 6.** Chemically induced surface charge as a function of CO concentration in air (6.46[ppm.m$^2$.$\mu$C$^{-1}$]) (full line), at 20 °C, and the upper limit of the dynamic range (dashed line), corresponding to $N_A^{2/3} = 23.5$ $\mu$C/m$^2$, for 4 Ohm.cm boron doped wafers. Error bars are standard deviations of 100 measurements.

The sensitivity slope of the fitted straight line (6.46[ppm.m$^2$.$\mu$C$^{-1}$]) corresponds to the product of the chemisorbed complex ionic surface charge and the Langmuir equilibrium constant.

Whenever a common mechanism mediates the chemisorption of different analytes, interference cannot be avoided. Such is the case of $NO_2$ and $SO_2$ on gold, where sensitivity doubles for the latter, consistently with doubly charged chemisorbed species, thus halving the effective dynamic range [11, 17]. At higher concentrations, in the case of donor stimuli, such as hydrogen on Pd or Pt gates, the excess positive charge is swept to ground and maintained at the maximum, consistently with electrical saturation, whereas with acceptor stimuli, the negative

chemically induced charge is completely drained by forward bias, yielding an apparent null response [11].

The CO pressure for half occupancy of the Co-corrole adsorption sites, measured by gas uptake [2], yields a very low 0.37 torr, compared to an oxygen equivalent of 946 torr, with a ratio of 2557, which is evidence for highly selective chemisorption of CO and chemical saturation, at almost 500 ppm, well in excess of the electrical capacitive limit. This high affinity for CO hampers its ready release after repeated stimulation, consistently with prior reports [7] in which vacuum was used to promote desorption. Heating to 80ºC, in 1 atm of air, can likewise restore the initial base line but the ensuing delay to stabilize the measurement disrupts continuous operation. Photodesorption provides a convenient alternative. Continuous illumination at 395 nm, coincident with the B band of Co-corrole (Fig. 7), with an EPITEX L395-06 LED, rated at 3.0 mW total radiated power, over 9º solid angle, operated at 20 mA, for one hour, is sufficient to restore sensitivity. The B or Soret absorption band corresponds to a spin allowed triplet ($S = 1$) to quintuplet transition ($S = 2$), by contrast with the spin forbidden Q band [18]. DFT calculations [19] show that the electron configuration of the quintuplet state, $(dxy)^2 (dz^2)^2 (d\pi1)^1 (d\pi2)^1 (\phi cor')^1 (\phi cor)^1$ for S=2, results from excitation of a filled bonding corrole orbital ($\phi cor'$), to an unfilled corrole orbital ($\phi cor$) of antibonding character, associated with an extension of the C9-C12 bond (Fig. 1b). Hence, comparatively modest constant illumination intensities, which do not interfere with the pulsed illumination at 658 nm, are sufficient to promote CO desorption.
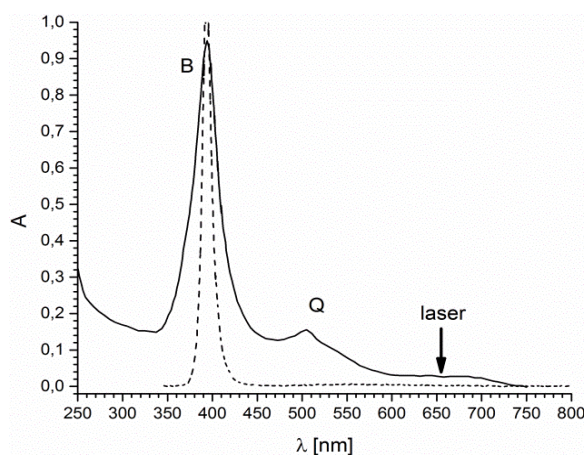


**Fig. 7.** Absorption spectrum of a [5,10,15-Tris(2,6-dichlorophenyl)corrolate] cobalt(III) in dichloromethane (full line) displaying the B and Q bands, superposed on the normalized emission spectrum (dashed line) of the EPITEX L395-06 LED used for photodesorption. The arrow indicates the wavelength of the HITACHI HL6501MG laser used for pulsed illumination, beyond the corrole absorption range.

The early work on chemically sensitive field effect devices [20] was dominated by metallic chemisorbers,

such as Pd, Pt, Au and their alloys, in which comparatively low adsorption enthalpies ($\approx$20 kCal/mol) favored chemical saturation of available adsorption sites, which required high operating temperature ($\approx$150ºC) to release their occupancy, albeit much lower than semiconducting conductimetric alternatives. It has become apparent [21] that organic and organometallic compounds can overcome this limitation, particularly if additional requirements such as favorable electrical properties can be avoided. Field effect devices are suitable, whenever chemisorption is associated with the formation of an electrically charged chemisorbed complex.

Cobalt corroles configure planar molecules [22], with 4-fold coordinated Co(III), for which changes in oxidation state are unlikely, due to lack of flexibility to accommodate the ensuing ionic radii changes, consistently with electronic structure computations [19]. Nonetheless, their redox cycles confirm one electron oxidation [23], unassociated to the central cation, which preserves its gyromagnetic factor under ESR monitoring, thus confining charge transfer to the macrocycle.

## 4. Conclusions

The chemisorption of CO on 5,10,15-[Tris(2,6-dichlorophenyl)corrolate] cobalt(III) yields a negatively charged complex, which renders detection by field effect devices possible at room temperature. Based on its oxidation behavior [23], it can be inferred that the pertinent charge transfer is located on the macrocycle, rather than the central metal. Only the low concentration limit of the pertinent Langmuir adsorption isotherm is accessible for measurement, because the dynamic range is limited by the two thirds power law on silicon doping concentration [16], which restricts the maximum accumulated charge. The high affinity of the corrole for CO, which promotes selective sensitivity, can also hamper desorption, which can be conveniently photo stimulated by illumination at 395 nm.

## Acknowledgements

## References

[1]. L. Weaver, Carbon Monoxide Poisoning, *New England Journal of Medicine*, Vol. 360, 2009, pp. 1217-1225.

[2]. J. M. Barbe, G. Canard, S. Brandès, F. Jerôme, G. Guilard, Metallocorroles as sensing components

for gas sensors: remarkable affinity and selectivity of cobalt(III) corroles for CO vs. $O_2$ and $N_2$, *Dalton Transactions*, 2004, pp. 1208-1214.

[3]. J. M. Barbe, G. Canard, S. Brandès, R. Guilard, Synthesis and Physicochemical Characterization of meso-Functionalized Corroles: Precursors of Organic–Inorganic Hybrid Materials, *European Journal of Organic Chemistry*, 2005, pp. 4601-4611.

[4]. J. M. Barbe, G. Canard, S. Brandès, R. Guilard, Organic–Inorganic Hybrid Sol–Gel Materials Incorporating Functionalized Cobalt(III) Corroles for the Selective Detection of CO, *Angewandte Chemie International Edition*, Vol. 44, 2005, pp. 3103-3106.

[5]. M. Vanotti, V. Blondeau-Patissier, S. Ballandras, Love Wave Sensors Functionalized with Cobalt Corroles or Metalloporphyrines Applied to the Detection of Carbon Monoxide, in *Proceedings of the Second International Conference on Sensor Device Technologies and Applications (SENSORDEVICES'11)*, 2011, pp. 54-57.

[6]. V. Blondeau-Patissier, M. Vanotti, T. Prêtre, D. Rabus, L. Tortora, J. M. Barbe, S. Ballandras, Detection and monitoring of carbon monoxide using cobalt corroles film on Love wave devices with delay line configuration, *Procedia Engineering*, Vol. 25, 2011, pp. 1085-1088.

[7]. M. Vanotti, V. Blondeau-Pattissier, D. Rabus, J. Y. Rauch, J. M. Barbe, S. Ballandras, Development of Acoustic Devices Functionalized with Cobalt Corroles or Metalloporphyrines for the Detection of Carbon Monoxide at Low Concentration, *Sensors and Transducers Journal*, Vol. 14, 2012, pp. 197-211.

[8]. P. S. Barker, M. C. Petty, A. P. Monkman, J. McMurdo, M. J. Cook, R. Pride, A hybrid phthalocyanine/siilicon field-effect transistor sensor for $NO_2$, *Thin Solid Films*, Vol. 284, 1996, pp. 94-97.

[9]. D. Filippini, I. Lundstöm, H. Uchida, Gap-gate field effect gas sensing device for chemical image generation, *Applied Physics Letters*, Vol. 84, 2004, pp. 2946-2947.

[10]. O. Engstrom, A. Carlsson, Scanned Light Pulse Technique for the Investigation of Insulator-Semiconductor Interfaces, *Journal of Applied Physics*, Vol. 54, 1983, pp. 5245-5251.

[11]. R. Lombardi, R. Aragón, H.A. Medina, MOS Device Chemical Response to Acceptor Stimuli, *Sensors and. Transducers Journal*, Vol. 147, 2012, pp. 143-150.

[12]. B. Koszarna, D. T. Gryko, Efficient Synthesis of meso-Substituted Corroles in a H2O−MeOH Mixture, *Journal of Organic Chemistry*, Vol. 71 2006, pp. 3707–3717.

[13]. J. F. B. Barata, M. G. P. M. S. Neves, A. C. Tomé, M. A. F. Faustino, A. M. S. Silva, J. A. S. Cavaleiro, How light affects 5,10,15-tris(pentafluorophenyl) corrole, *Tetrahedron Letters*, Vol. 51, 2010, pp. 1537-1540.

[14]. R. Lombardi, R. Aragón, Bias dependent response reversal in chemically sensitive metal oxide semiconductor capacitors, *Journal of Applied Physics*, Vol. 103, 2008.

[15]. R. Lombardi, R. Aragón, MOS Chemical Response Reversal with Temperature, *Sensors and Actuators B*, Vol. 144, 2010, pp. 457-461.

[16]. R. S. Muller, T. J. Kamins, Device Electronics for Integrated Circuits Second Edition. *Wiley*, New York, 1986, p. 399.

[17]. R. Lombardi, R. Aragón $SO_2$ sensitivity of Au gate MOS capacitors, *Procedia Engineering*, Vol. 25, 2011, pp. 1061–1064.

[18]. T. Rio, Y. Rodrııguez-Morgade, S. Torres, Modulating the electronic properties of porphyrinoids: a voyage from the violet to the infrared regions of the electromagnetic spectrum, Organic Biomolecular Chemistru, Vol. 6, 2008, pp. 1877–1894.

[19]. C. Rovira, K. Kunc, J. Hutter, M. Parrinello, Structural and Electronic Properties of Co-corrole, Co-corrin, and Co-porphyrin, *Inorganic Chemistry*. Vol. 40, 2001, pp. 11-17.

[20]. I. Lundström, T. Ederth, H. Kariis, H. Sundgren, A. Spetz, F. Winquist, Recent developments in field-effect gas sensors, *Sensors and Actuators B*, Vol. 23, 1995, pp. 127-133.

[21]. M. C. Petty, R. Casalini, Gas sensing for the 21st century: the case for organic thin films, *Engineering Science and Education Journal*, Vol. 6, 2001, pp. 99-105.

[22]. K. E. Thomas, A. B. Alemayehu, J. Conradie, C. M. Beavers, A. Ghosh, The Structural Chemistry of Metallocorroles: Combined X-ray Crystallography and Quantum Chemistry Studies Afford Unique Insights, *Accounts Chemical Research*, Vol. 12, 2011, pp. 1-12.

[23]. K. M. Kadish, J. Shen, L. Frémond, P. Chen, M. El Ojaimi, M. Chkounda, C. P. Gros, J. M. Barbe, K. Ohkubo, S. Fukuzumi, R. Guilard, Clarification of the oxidation state of cobalt corroles in heterogeneous and homogeneous catalytic reduction of dioxygen, *Inorganic Chemistry*, Vol. 47, 2008, pp. 6726-6737.

---

# White Blood Cell Nucleus Segmentation Based on Canny Level Set

**[1] Qiu Wenhua, [2] Wang Liang, [3] Qiu Zhenzhen**

[1] Guangdong Mechanical & Electrical College, Guangzhou, 510515, China
[2] Guangdong post, 510515, China
[3] Zengcheng College of South China Normal University, Guangzhou, 510515, China
[1] Tel.: 13560248550
E-mail: qiuwhua@126.com

**Abstract:** Cell image segmentation is an important study direction and white blood cell composition reveals important diagnostic information about the patients. Manually counting of white blood cells is a tiresome, time-consuming and susceptible to error procedure. Due to the tedious nature of this process, an automatic system is preferable. In this automatic process, segmentation of white blood cells is one of the most important stages. In order to solve problems of the traditional method for cell segmentation, a method of level-set 3D segmentation for White blood cells was proposed using canny. The Level-set segmentation was based on geometric active contour models instead of parameter active contour models. The method overcame the obscurity of white blood cells' boundary by taking advantage of the structure of conforming anatomic arrange of threshold. Further, the initial segmented results preprocessed were applied using anisotropic diffusion and the real border of cell was detected using canny. Finally, the cell was finely segmented using the level-set method. Thus, the segmentation of white blood cells could be done more accurately. *Copyright © 2014 IFSA Publishing, S. L.*

## 1. Introduction

White blood cell nucleus segmentation is a key technology in medical image processing, its task is to extract interesting objects from the medical image in order to serve the clinician computer-aided diagnosis. Substituting automatic detection of white blood cells for manually locating, identifying and counting different classes of cells is an important topic in the domain of cancer diagnosis. Automatic recognition of white blood cells in hematological can be divided into four major parts: preprocessing, image segmentation, feature extraction and classification. Segmentation of white blood cells is one of the most important stages in this process [1].

At present, many researchers study the variation level set method applied in medical image segmentation. Variation level set method widely used in tracking and modeling, and it flourishes in the past decade research both in theoretical and practical. From the references we can see that the variation level set methods become very popular in image processing methods, therefore, the variation level set is well suited for complex topologies strong noise and low contrast areas of medical image analysis. In this paper, we introduce a novel method of level-set 3D segmentation for white blood cells using canny. The Level-set segmentation was based on geometric active contour models instead of parameter active contour models. The method overcame the obscurity

of white blood cells' boundary by taking advantage of the structure of conforming anatomic arrange of threshold [2]. Further, the initial segmented results preprocessed were applied using anisotropic diffusion and the real border of cell was detected using canny. Finally, the cell was finely segmented using the level-set method. Thus, the segmentation of white blood cells could be done more accurately.

## 2. Level Set Method

The level set method was first proposed by Osher and Sethian (1988). It describes the propagating fronts by a PDE (Malladi *et al.*, 1995; Museth *et al.*, 2002), and it can solve the topological change of the interface robustly. Some numerical methods proposed to accelerate the solution (Sethian, 1999), such as narrow band method, fast marching method, higher order difference schemes. Now, the level set method has become popular in many disciplines, such as image processing, computer graphics, computational geometry, optimization, and computational fluid dynamics.

The level set method is a numerical technique for tracking interfaces and shapes. The advantage of the level set method is that one can perform numerical computations involving curves and surfaces on a fixed Cartesian grid without having to parameterize these objects (this is called the Eulerian approach). Also, the level set method makes very easy to follow shapes which change topology, for example when a shape splits in two, develops holes, or the reverse of these operations. All these make the level set method a great tool for modeling time-varying objects, like inflation of an airbag, or a drop of oil floating in water.

The original idea behind the level set method was a simple one. Given an interface $\Gamma$ in $R^n$ of codimension one, bounding an (perhaps multiply connected) open region $\Omega$, we wish to analyze and compute its subsequent motion under a velocity field $\vec{v}$. This velocity can depend on position, time, the geometry of the interface (e.g. its normal or its mean curvature) and the external physics. The idea, as devised in 1987 by S. Osher and J. A. Sethianis merely to define a smooth (at least Lipschitz continuous) function $\varphi(x,t)$, that represents the interface as the set where $\varphi(x,t) = 0$. Here $x = x(x_1,......,x_n) \in R^n$. The level set function $\phi$ has the following properties [3]:

$$\varphi(x,t) > 0 \text{ for } x \in \Omega$$
$$\varphi(x,t) < 0 \text{ for } x \notin \Omega \quad (1)$$
$$\varphi(x,t) = 0 \text{ for } x \in \partial\Omega = \Gamma(t)$$

Thus, the interface is to be captured for all later time, by merely locating the set $\Gamma(t)$ for which $\varphi$ vanishes. This deceptively trivial statement is of great significance for numerical computation, primarily because topological changes such as breaking and merging are well defined and performed "without emotional involvement".

The motion is analyzed by connecting the $\varphi$ values (levels) with the velocity field $\vec{v}$. This elementary equation is

$$\frac{\partial \varphi}{\partial t} + \vec{v} \bullet \nabla \varphi = 0 \quad (2)$$

Here $\vec{v}$ is the desired velocity on the interface, and is arbitrary elsewhere. Actually, only the normal component of $v$ is needed：$v_N = \vec{v} \bullet \dfrac{\nabla \varphi}{|\nabla \varphi|}$, so (2) becomes

$$\frac{\partial \varphi}{\partial t} + v_N \bullet |\nabla \varphi| = 0 \quad (3)$$

Here we give simple and computationally fast prescriptions for reinitializing the function $\varphi$ to be signed distance to $\Gamma$, at least near the boundary [4], smoothly extending the velocity field $v_N$ off of the front $\Gamma$ [5] and solving equation (3) only locally near the interface $\Gamma$, thus lowering the complexity of this calculation by an order of magnitude [6]. This makes the cost of level set methods competitive with boundary integral methods, in cases when the latter are applicable, e.g. see [7]. We emphasize that all this is easy to implement in the presence of boundary singularities, topological changes, and in 2 or 3 dimensions. Moreover, in the case which $v_N$ is a function of the direction of the unit normal (as in kinetic crystal growth [8], and Uniform Density Island Dynamics [9-10]) then equation (3) becomes the first order Hamilton-Jacobi equation

$$\frac{\partial \varphi}{\partial t} + |\nabla \varphi| \gamma(\vec{N}) = 0, \quad (4)$$

where $\gamma = \gamma(\vec{N})$ a given function of the normal, $\overline{N} = \dfrac{\nabla \varphi}{|\nabla \varphi|}$.

High order accurate, essentially non-oscillatory discretizations to general Hamilton-Jacobi equations including (4) were obtained in [11], see also [12] and [13].

## 3. Edge-detection Method Based on the Canny Operator

Canny brought out the rule that excellent edge-detection method should pleased in 1986 [14]:

1) Fine SNR (Signal-to-Noise), is that the probability of the edge-point to be mistaked must be low;

2) Good performance of positioning, is that the detected edge-point should be at the center of real edge to its best possibility;

3) Single edge response, is that the single edge has only one response, and the false edge should be restrained mostly.

The course of edge-detection by canny operator includes: the first step, noise reduction by Gaussian smoothing function, for the late process to prepare; the second step, first-order difference convolution template is used to calculate ladder degree of amplitude and direction; the third step, for the maximum inhibition of gradient amplitude.

## 4. The Proposed Algorithm

As mentioned above, the canny can detect the approximate contour quickly, and the level set method can pick up the edge exactly. This paper takes advantage of both the canny and level set method. First, using level-set method to overcome the obscurity of white blood cells' boundary by taking advantage of the structure of conforming anatomic arrange of threshold. Further, the initial segmented results preprocessed were applied using anisotropic diffusion and the real border of cell was detected using canny. Finally, the cell was finely segmented using the level-set method. The method would reduce the iteration times effectively. At the same time, it can make level set method avoid across boundary or astringing local. The availability of the new algorithm is well proved in the cell image detection. The algorithm flow chart is shown in Fig. 1.
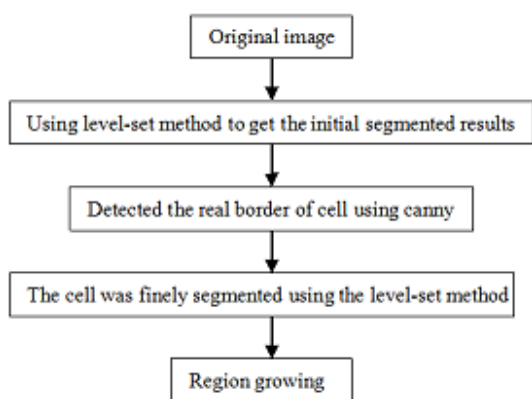


**Fig. 1.** Algorithm flow chart.

## 5. Experiment Result

The white blood cell detection is very important in the medical image processing. The proposed segmentation method is carried out on a Pentium IV, CPU 2.4 GHz, EMS memory 1G computer.

Fig. 2 (a, c, e) are three original white blood cell images. We could get the cell approximate contour as the level set method initial evolvement curve. During the evolvement process, the curve closes upon the cell contour step by step. Further, using canny to detect the real border of cell. Finally, the cell was finely segmented using the level-set method. So we can pick up the cell contour accurately as shown respectively in Fig. 2 (b, d, f). The experimental results indicate that the algorithm can pick up the object contour exactly and effectively.



| (a) Original image | (b) The cell nucleus contour picked up |



| (c) Original image | (d) The cell nucleus contour picked up |



| (e) Original image | (f) The cell nucleus contour picked up |
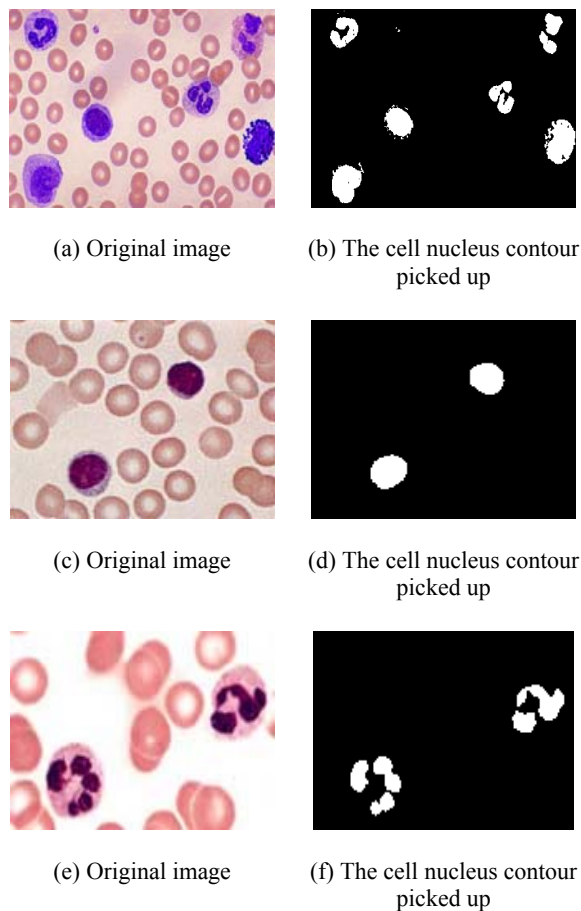
**Fig. 2** White blood cell images**.**

## 6. Conclusions

This paper puts forward a segmentation algorithm which combines canny with level set method. Its main characteristic is that making use of level-set to get the object approximate contour. It as the level set initial evolvement curve can avoid striding over boundary or constringency local. Weighting the edge detection function of the level set function equation can improve picking up weak edge object veracity and reduce the level set method iterations. The new algorithm is effective in the experiment of picking up cell nucleus image contour.

## References

[1]. S. H. Rezatofighi, H. Soltanian-Zadeh, R. Sharifian, R. A. Zoroofi, A New Approach to White Blood Cell Nucleus Segmentation Based on Gram-Schmidt Orthogonalization, in *Proceedings of the International Conference on Digital Image Processing*, 2009, pp. 107-111.

[2]. Gao Qi-Xin, Yang Jin-Zhu, Zhao Da-Zhe, Liu Ji-Ren, Pulmonary Vessel for X-RAY CT Images Segmented Through Canny Level-Set, *Journal of System Simulation*, Vol. 20, No. 20, 2008.

[3]. Stanley Osher, Ronald P. Fedkiw, Level Set Methods: An Overview and Some Recent Results, *IPAM GBM Tutorials*, 27 March – 6 April 2001.

[4]. Sussman M., Smereka P., Osher S., A Level Set Approach for Computing Solutions to Incompressible Two-Phase Flow, *J. Comput. Phys.*, 114, 1, 1994, pp. 146-159.

[5]. Chen S., Merriman B., Osher S., Smereka P., A simple level set method for solving Stefan problems, *J. Comput. Phys.*, 135, 1997, pp. 8-29.

[6]. Peng D., Merriman B., Osher S., Zhao H.-K., Kang M., A PDE-Based Fast Local Level Set Method, *J. Comput. Phys.*, 155, 1999, pp. 410-438.

[7]. Hou T., Li Z., Osher S., Zhao H.-K., A Hybrid Method for Moving Interface Problems with Application to the Hele-Shaw Flow, *J. Comput. Phys.*, 134, 1997, pp. 236-252.

[8]. Osher S., Merriman B., The Wulff Shape as the Asymptotic Limit of a Growing Crystalline Interface, *Asian J. Math.*, 1, 3, 1997, pp. 560-571.

[9]. Caflisch R. E., Gyure M., Merriman B., Osher S., Ratsch C., Vvedensky D., Zinck J., Island Dynamics and the Level Set Method for Epitaxial Growth, *Appl. Math. Lett.*, 12, 1999, pp. 13-22.

[10]. Gyure M., Ratsch C., Merriman B., Caflisch R. E., Osher S., Zinck J., Vvedensky D., Level Set Methods for the Simulation of Epitaxial Phenomena, *Phys. Rev. E*, 59, 1998, pp. 6927-6930.

[11]. Osher S., Sethian J. A., Fronts Propagating with Curvature Dependent Speed: Algorithms Based on Hamilton-Jacobi Formulations, *J. Comput. Phys.*, 79, 1988, pp. 12-49.

[12]. Osher S., Shu C. W., High Order Essentially Non-Oscillatory Schemes for Hamilton-Jacobi Equations, *SIAM J. Numer. Anal.*, 28, 4, 1991, pp. 907-922.

[13]. Jiang G.-S., Peng D., Weighted ENO Schemes for Hamilton Jacobi Equations, *SIAM J. Sci. Comput.*, 21, 6, 2000, pp. 2126-2143.

[14]. Li Er-Sen, Zhu Shu-Long, An Adaptive Edge-detection Method Based on the Canny Operator, in *Proceedings of the International Conference on Environmental Science and Information Application Technology,* 2009, pp. 465–469.

_____

# An Improved Green Energy Granary Monitoring System Based on Wireless Sensor Network

## [1] Bin Wang, [1] Jun Guo, [2] Dong Su

[1] College of Electronic Engineering, Chongqing University of Post and Telecommunications,
Chongqing 400065, P. R. China
[2] 26th Institute of Electronics Technology Group Corporation, Chongqing 400065, P. R. China
[1] Tel.: +86-18602328202
E-mail: wangbin1@cqupt.edu.cn

**Abstract:** In the study of granary monitoring, many research projects are involved in environmental monitoring in recent years. However, most existing studies are interested in the outdoor natural environment monitoring. Few of them focus on the indoor monitoring. This paper presents a system based on wireless sensor network (WSN) for granary monitoring including grain temperature and humidity. The whole system adopts sensors DS18B20 to measure the granary temperature, DHT11 to measure humidity, and the data is processed by transceiver CC2530, which is a true system-on-chip (SoC) solution for IEEE 802.15.4 applications. To deal with energy consumption problems effectively, the scheme of solar battery board is proposed in order to produce a kind of clean and renewable energy. In addition to showing the temperature and humidity monitoring and alarm mechanism, the system can set up or modify the working parameters through keywords at control terminals. The overall system architecture is described in detail. What is more, the network deployment and wireless communication protocol etc. are introduced. Experimental results in actual granary show that the proposed new system is convenient, efficient, and correct. *Copyright © 2014 IFSA Publishing, S. L.*

**Keywords:** WSN, DS18B20, DHT11, CC2530, IEEE 802.15.4, Solar battery board.

## 1. Introduction

With the rapid growth of population and improvement of person's life quality in china, the grain storage plays an important role in current society, and its requirements are also gradually improving. The granary type of our country could be divided three types: The first one is the old granary which is simulated the Soviet Union-type structure position for the main body. Their storage capability is so large, more than billion kilograms. As they built for a long time, part of the environment of granaries is poor and lack of supporting of some mechanization facilities, at that time, they usually used artificial monitoring and natural ventilation.

Then the next category is built in the 80's and 90's. These storehouses are divided into the simple room type granary, the round brickwork granary, the underground storehouse and the mountain storage cavern primarily. As the underground storehouse and the mountain storage cavern are at low temperature the whole year, the food deterioration is slower and the keeping cost is lower.

Since then, the granaries' structure have been changed, which the main type is warehouse, and the other categories are shallow silos and vertical silos. We have the abundant granary construction history more than 50 years, accumulate rich experience in the positions, and there are also many painful lessons. Granary construction should be fully guaranteed the grain storage safety in the first place.

However, in the process of the grain storage, the quality of grain is directly affected by the change of temperature and humidity in granary. Consequently, the veracity and reliability of the grain monitoring system is immediately concerned about the application of grain storage and the quality and safety of the grain.

In recent years, researchers have done a lot of efforts about the environment monitoring, from manpower to automation, from wire to wireless. The conventional way is outdated, for example, sampling data by artificial consumes a lot of labor force and low efficiency, poor accuracy. In addition, the complex wiring type has low anti-interference capacity and poor maintenance, which restrain its application and popularization. Comparing the traditional way, the Wireless Sensor Network (WSN) technology appeared on the scene, especially in the agriculture (such as the granary monitoring). Wireless Sensor Network is a specific network consisting of an increasing number of low-power sensor nodes with a self-organizing way which can gather environment information and transmit the data by wireless. [1]

In order to effectively monitor the granary environment and enhance the efficiency, a simple and intelligent granary measurement and control system based on ZigBee wireless sensor network is proposed in this paper, which the core is radio frequency chip CC2530 connecting with temperature sensors, humidity sensors and the executive devices, and the object of controlling and monitoring temperature and humidity is complemented, at the same time, the temperature and humidity parameters can be real-time displayed on the computer.

## 2. Base Theory

### 2.1. What is ZigBee

ZigBee is a standard that defines a set of communication protocols for low-data-rate short-range wireless network [2]. Short-range wireless networking methods are divided into two main categories: wireless local area networks (WLANs) and wireless personal area networks (WPANs). WLAN is a replacement or extension for wired local area networks (LANs) such as Ethernet (IEEE 802.3). A WLAN device can be integrated with a wired LAN network, and once the WLAN device becomes part of the network, the network treats the wireless device the same as any other wired device within the network [3]. The goal of a WLAN is to maximize the range and data rate. WPANs, in contrast, are not developed to replace any existing wired LANs. WPANs are created to provide the means for power-efficient wireless communication within the personal operating space (POS) without the need for any infrastructure. POS is the spherical region that surrounds a wireless device and has a radius of 10 meters (33 feet) [4]. WPANs are divided into

three classes (see Fig. 1): high-rate (HR) WPANs, medium-rate (MR) WPANs, and low-rate (LR) WPANs [5]. An example of an HR-WPAN is IEEE 802.15.3 with a data rate of 11 to 55 Mbps [6]. This high data rate helps in applications such as real-time wireless video transmission from a camera to a nearby TV. Bluetooth, with a data rate of 1 to 3Mbps, is an example of an MR-WLAN and can be used in high quality voice transmission in wireless headsets. ZigBee, with a maximum data rate of 250 kbps, is classified as an LR-WPAN.
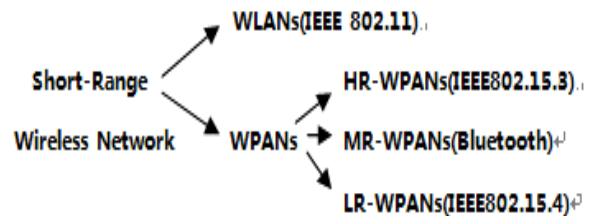


**Fig. 1.** Short-range wireless networking classes.

While most wireless standards are striving to go faster, ZigBee aims for low data rates. While other wireless protocols add more and more features, ZigBee aims for a tiny stack that fits on 8-bit microcontrollers. While other wireless technologies look to provide the last mile to the Internet or deliver streaming high-definition media, ZigBee looks to control a light or send temperature data to a thermostat. While other wireless technologies are designed to run for hours or perhaps days on batteries, ZigBee is designed to run for years. And while other wireless technologies provide 12 to 24 months of shelf life for a product, ZigBee products can typically provide decades or more of use. The market category ZigBee serves is called "wireless sensor networking and control" or simply, "wireless control". In fact, the slogan for ZigBee is, "Wireless Control That Simply Works".

### 2.2. Working Principle of ZigBee Technique

ZigBee is synonymous with IEEE 802.15.4 protocol. ZigBee-based wireless devices operate in 868 MHz, 915 MHz, and 2.4 GHz frequency bands. In the 2.4 GHz frequency band, it has 16 channels which are global standards, free of charge, non-application. ZigBee is targeted mainly for battery-powered applications where low data rate, low cost, and long battery life are main requirements. In many ZigBee applications, the total time wireless device is engaged in any type of activity is very limited; the device spends most of its time in a power-saving mode, also known as sleep mode. As a result, ZigBee enabled devices are capable of being operational for several years before their batteries need to be replaced.

Since the late 90 s, a lot of scientists in America, Europe and China have devoted themselves to the

study of wireless measurement and control system, in which ZigBee technology with high reliability and lower consumption is applied, not the other short-range wireless networking methods, Bluetooth or IEEE 802.11b. As shown in Fig. 2 and Table 1, we compare the power consumption, complexity, cost and data rate. So, we can conclude ZigBee is a candidate for wireless communication technology of WSN.
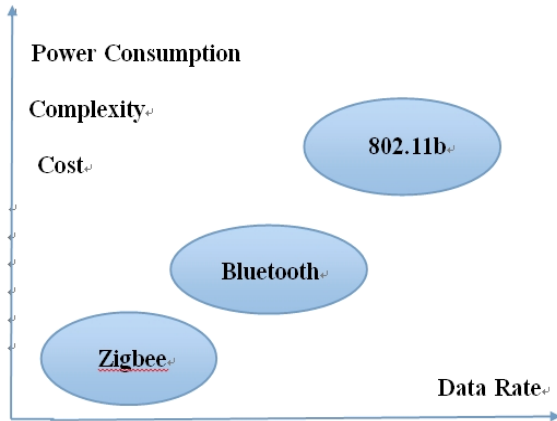


**Fig. 2.** Comparing the ZigBee standard with Bluetooth and IEEE 802.11b.

**Table 1.** Analysis the specific features of ZigBee, Bluetooth and IEEE 802.11b.

| Target Type | Data Rate | Typical Range | Application Examples |
|---|---|---|---|
| ZigBee | 20 to 250 kbs | 10-100 m | Wireless Sensor Networks |
| Bluetooth | 1 to 3 Mbps | 2-10 m | Wireless Headset Wireless Mouse |
| IEEE 802.11b | 1 to 11 Mbps | 30-100 m | Wireless Internet Connection |

## 2.3. ZigBee Network Topology Structure

In order to enable suppliers to offer the lowest possible power equipment, IEEE (Institute of Electrical and Electronics Engineers) defines two different types of equipment: one is the full function device (FFD), the other is reduced function device (RFD). In Fig. 3, we can see that ZigBee networking can support three main wireless networks: star network, net network, and clusters network. FFD can support any kind of topological structures, which can be used as a network negotiator and the general coordinator, and it can communicate with any kinds of equipment. RFD only supports star structure, which can't to be any negotiator. But it can communicate with network negotiator, and the process is very simple.
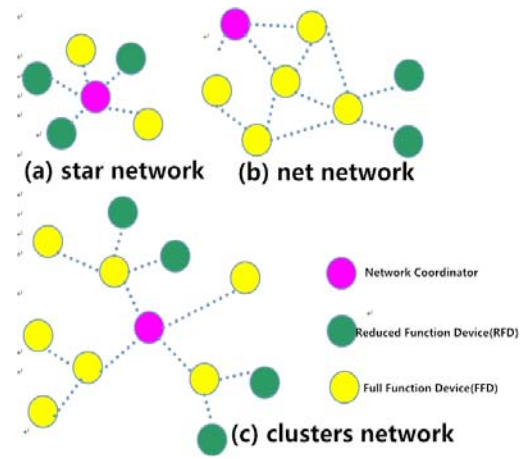


**Fig. 3.** Three main types of wireless network.

## 3. Design the Green Granary Monitoring System

### 3.1. Description of the Granary Location

The barn we have monitored is located in Chongqing, China. It is well known that Chongqing is a mountainous area with the subtropical inland climate. In summer, we can hardly breathe because the highest temperature can reach to 43.8 °C. However, autumn and winter are often accompanied by the rainy weather, and the lowest limit temperature can reach to minus 3.8 °C. Especially from July to August, the highest temperature is mostly between 27 °C and 38 °C. Therefore, the drop temperature is large, saving the grain is even more important.

### 3.2. Wireless Sensor Network Architecture

In this system we proposed here, the star network topologies (see in Fig. 4) are used by us to monitor and control the granary. The average size of a granary holding in the region is around 11232 m³, which the length, width and height are 78 m, 24 m, 6 m. The distance from the granary to controlling core is about 100 m, and it means that the ZigBee network can transmit the data effectively. In the granary, we use the sensor node DS18B20 to monitor the temperature, the DHT11 to measure the temperature and humidity. Compared with the traditional sensor network of sensor pattern, we introduced a new sensor network of temperature measurement cables pattern. The new sensor network architecture is shown in Fig. 4, the granary monitoring network by a "sink node" and tens to hundreds of cables with temperature and humidity sensor nodes. "Sink nodes" can be placed anywhere in the barn, mainly responsible for receiving all the uploading data of sensor nodes. Sensor nodes with temperature measurement cables can be placed over the surface of grain, but the temperature cables

should be buried in grain. Since the top of grain surface is a barrier-free space transmission and the transmission distance is large, sensor nodes collect data from temperature measurement cables by cycle or timing type, and report to "sink node" through the way of self-organizing network.

Combining with the wired monitoring structure analysis of medium-sized barn, it shows that more than 50 cables installed sensor nodes and a "sink node" can be composed of grain temperature and humidity measurement system. The advantages of this network are obvious, which temperature measurement cables installation and removal are more convenient than the current bus-type grain monitoring system. Due to the existence of wireless ad hoc network in granary, you can always maintain the failed nodes or cables without affecting the other nodes, but also saving maintenance costs. Thus we solve some problems fundamentally of

electromagnetic interference, lightning stroke etc., causing the system to crash through the introduction of transmission bus. However, the disadvantage is that domestic specialists and abroad ones don not conduct a comprehensive study for this application mode, network topology and feasibility may need to assess in a long time.

As Fig. 4 shows, there will be two-way communication between the sensor nodes and the monitoring software at the base station (BS), by means of the corresponding gateway. With this implementation, large areas can be covered, even if scattered, avoiding the difficulty of developing and implementing mesh/cluster topologies (a smaller number of devices is required) and reducing the energy consumption of the devices that perform sensory functions (since they do not perform data routing functions).
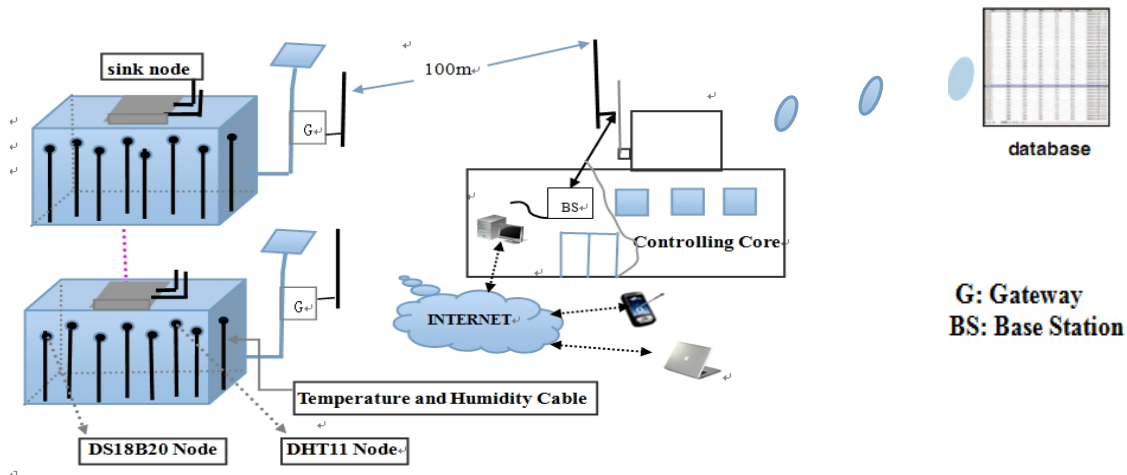


**Fig. 4.** Architecture proposed for the monitoring of granary.

## 4. Simulation for the WSN Design

### 4.1. Selection of the Software, Hardware and Communication Protocol

In order to establish the basic components (temperature node, temperature and humidity node and gateway) of WSN architecture, a number of physical devices (radio module and sensor elements) were selected: CC2530 radio transceiver (Texas Instruments, USA), DS18B20 digital temperature sensor (DALLAS company, USA), DHT11 digital temperature and relative humidity sensor (domestic electron company, China), and temperature measurement cable or called hotspot detector.

Another important component of the architecture is to select the communication protocol. The standard of the field of wireless sensor network is IEEE 802.15.4, which presented the greatest commercial development, and the ZigBee system is composed with these services [7]. It is a appreciate technology that implementing communications between wireless

devices and the gateway due to the low cost and little energy consumption. In order to complete this standard, a whole mechanism has been listed to provide even the lower consumption. A B-MAC mechanism was selected as the medium access control protocol to arbitrate the communication of multiple sensors over the radio channel [8]. As we know, IEEE802.15.4 has its own medium access control protocol called slotted Carrier Sense Multiple Access with Collision Avoidance (CSMA-CA), however, a specific system which features Low Power Listening (LPL) specifically designed for low power consumption. Therefore, the B-MAC mechanism exploits a scheduled scheme operation that nodes know the reasonable interval in which they must be awaken for receiving information. But the nodes are always awakened until they receive data in the active period of a slotted CSMA-CA protocol, so that it wasted more energy. The data frame formats of the standard IEEE 802.15.4 have been used, but B-MAC was used as the protocol for accessing to the radio channel.

## 4.2. Experiment Environments and Simulation Results

In order to test the performance of designed node, we built a simple temperature and humidity test environment based on two terminals, one router and one coordinator. After a period of debugging, the wireless communication of the system is realized. Fig. 5(a) and (b) show the topology structures of single hop and multi-hop between end device and coordinator, and the red, blue, yellow knots present coordinators, routers, terminals.
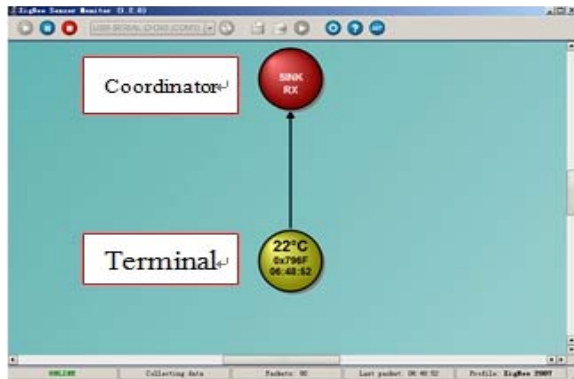


(a) Single hop
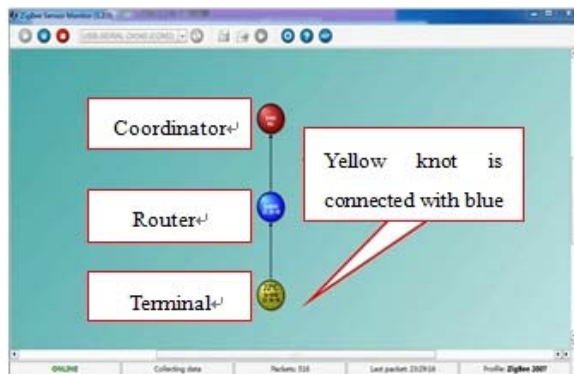


(b) Multi-hop

**Fig. 5.** Communication between terminal device and coordinator.

Simulation of the sensor network is a necessary first step prior to the actual implementation. It was carried out using the software of ZigBee Sensor Monitor, and we can see that blue knot has been started as a router. At the same time, it is obviously that the blue one has already connected to the red node, and starts to send data to the red node.

## 5. Design of the Hardware Node

The main elements of the hardware nodes (see Fig. 6(a) are sensors and the CC2530 transceiver. CC2530 is a true system-on-chip (SoC) solution for IEEE 802.15.4 applications. It combines the excellent performance of a leading RF transceiver with an industry standard enhanced 8051 CPU, the memory arbiter, the 8-KB SRAM, the IEEE 802.15.4-compliant radio transceiver, and some other powerful features. It also has in increasing number of operating modes, making it perfectly suited for systems where low power consumption is required.

The battery consisted of 5 V alkaline battery can supply energy for sensor node, or to deal with energy consumption problems effectively, the scheme of solar battery board is proposed in order to produce a kind of clean and renewable energy. A 3.3 V low-dropout DC/DC converter has been added to adjust the battery voltage (over 4 V when charged). The DS18b20 sensor node and DHT11 sensor node, which are connected to the I/O interface, are both fitted on the wall and in the grain by cable.

In addition to the CC2530 transceiver, the gateway includes a long-range radio module to provide two-way communication between the sink nodes and the farm offices. What is more, this device has no output interface for connecting sensors. The device is set on the 5 m high wall which is also fitted with a photovoltaic solar panel to supply power. At the same time, this solar panel charges a 12 V/6.5 Ah lead-acid battery. The device is further equipped with two antenna, one gain is 8dBi and the other one is 4 dBi.

As Fig. 6 (b) shows, the main peripheral circuits of central node are given.

The wireless sensor network nodes are composed of processor module, wireless communication module, power module and sensor module. As we know, the processor module and wireless communication module are integrated on CC2530 chip, which greatly simplify the RF circuit design. The temperature sensor DS18b20 and temperature humidity sensor DHT11 are used in the sensor module.

The single-wire digital temperature sensor DS18b20 is produced by American DALLAS semiconductor company, which is in 3-pined TO-92 small volume seal form. The temperature measurement range is from -55 to +125 °C, programmable for 9-12 bits conversion accuracy and temperature measurement resolution reaches 0.0625 °C. And the sign-extended 16 bits digital value serial output is used for the measured temperature. It requires only one report wire for DS18b20 CPU to communicate with numerous DS18b20, which occupies less microprocessor port so that it can save plenty of leads and logic circuits.

The DHT11 is a very widely used digital interface temperature and humidity sensors, which measure the humidity range of 20 % to 90 %, temperature measure range of 0~50 °C, measurement accuracy of 5 %, and it is consistent with the needs of the measuring system. DHT11 uses a single bus data transfer structure, which is easy to connect with a variety of MCU and the signal transmission distance up to 20 m or more, as well as ultra-low power consumption.
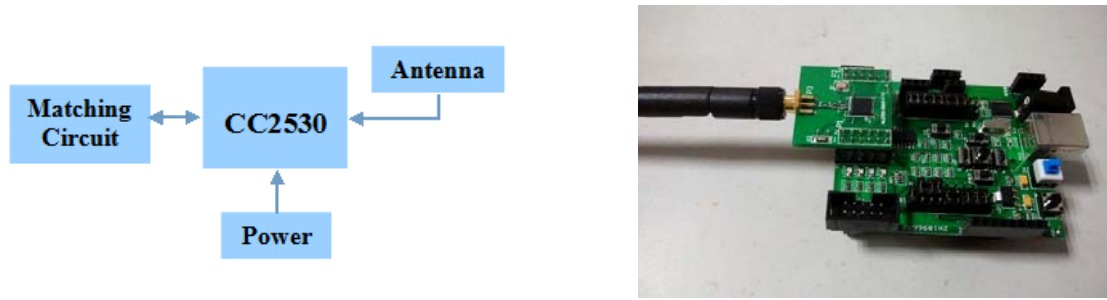
**Fig. 6 (a).** The manufactured sensor node picture.
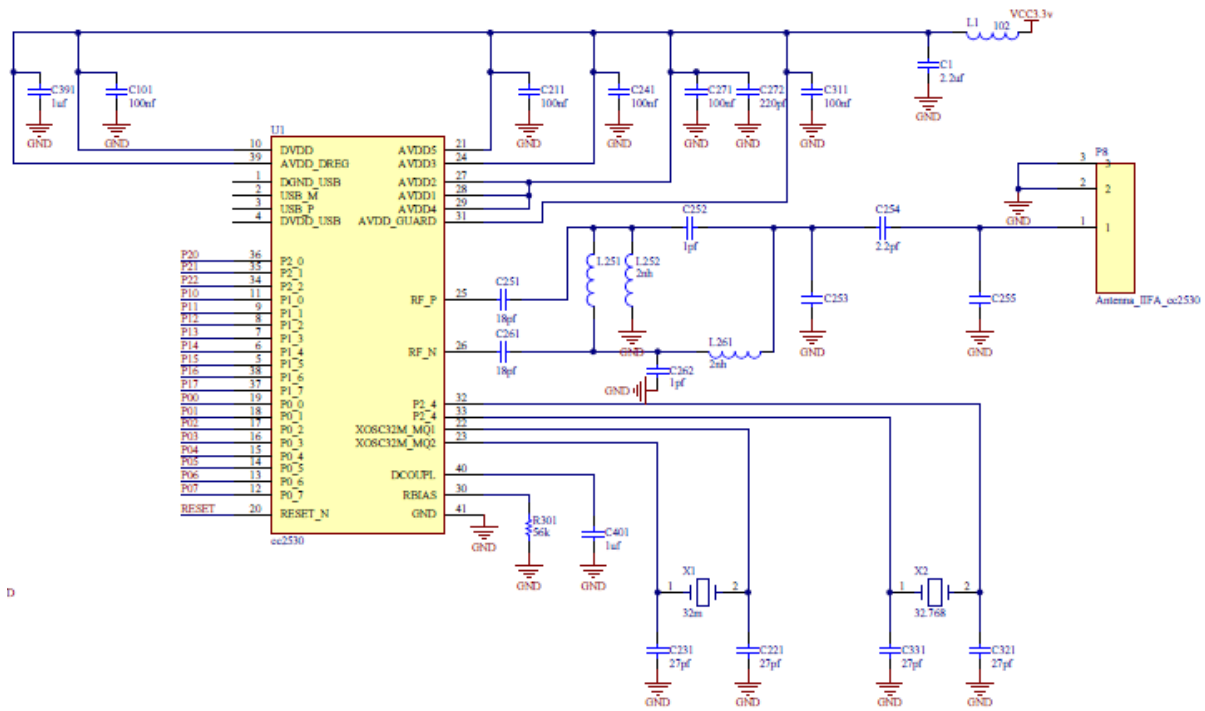


**Fig. 6 (b).** Main peripheral circuits of central node.

The commonly used antennas of wireless sensor network node include dipole antenna, PIFA antenna and integrated ceramic antenna. They have omnidirectional radiation pattern, simple structure, low production cost etc., and it is particularly suitable for use in the sensor nodes. After the analysis of the three types of antennas, based on cost and two important indicators of the signal attenuation, we conclude that a PIFA antenna may be the best choice, which the center frequency can reach 2.4 GHz.

## 6. Experimental Results in the Grain

To illustrate the advantage compared the traditional way, when the design of wireless granary monitoring system is completed, it is necessary to verify its performance in real granary. The overall layout of the testing granary is shown in Fig. 7.

The gateway (G) was connected with two antennas (one is 4.2 dBi monopole antenna and the other is 8 dBi omni-directional antenna), and the first one is placed on a wall 6 m high. As to guarantee line-of-sight between the gateway and the offices, the 8 dBi omni-directional antenna was placed on the office roof 9 m high. Wireless communication between the Base Station (BS) and the rooftop antenna was achieved by means of repeater.

These nodes were installed in the first week of December and we began to gather experimental data. During this time the cumulative rainfall was 40 mm, moderately strong winds of up to 60 km/h and low temperatures (4 °C in average).

As we know, before this technology was introduced, the workers monitored their grains in the traditional way, which wasted a lot of time and time. But now, with the technology that has been developed, grain variables can be ascertained in real time. Fig. 8 shows that this system could monitor the granary in real time that the optimum conditions for the grain storage were preserved (temperature between 10-28 °C, and relative humidity in the range 30 % - 80 %), and can use the stored information for future analysis and statistics purpose.
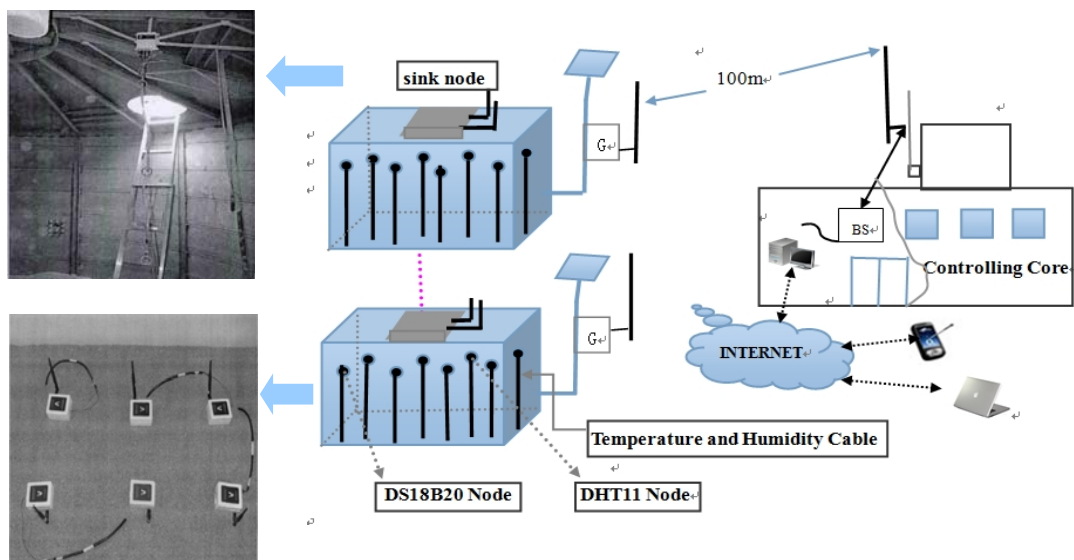
**Fig. 7.** The overall layout of actual testing granary.
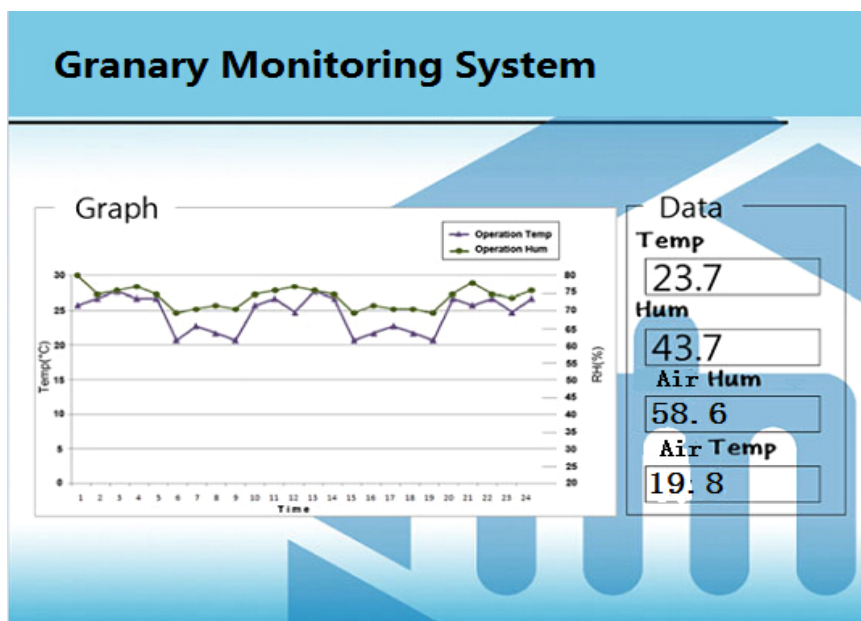


**Fig. 8.** The real-time monitoring system.

## 7. Conclusion

An innovative system which can achieve temperature and humidity monitoring and alarming is proposed. Meanwhile, we can deal with energy consumption problems effectively, and the scheme of solar battery board is proposed in order to produce a kind of clean and renewable energy. Then we introduce that gateway is one of the most important parts to connect wireless sensor network with internet. Experimental results of actual granary show that the proposed method not only overcome the lack of traditional wire network, but also can monitor the granary efficiently, conveniently and accurately. So we can believe that it is essential to research grain storage based on wireless sensor network.

## References

[1]. Karl H., Willing A., Protocols and architectures for wireless sensor networks, *IEEE Press–Wiley Interscience*, New York, 2011.

[2]. ARM Microcontrollers, available at http://www.ARM.com

[3]. HCS08 microcontroller families, available at http://www.freescale.com

[4]. Grebennikov A., RF and Microwave Power Amplifier, *Design, McGraw-Hill Professional*, 25 August 2009.

[5]. Inter-IC Sound (I²S) Bus Specifications, available at http://www.nxp.com

[6]. IEEE Standard Association, http://www.ieee.org

[7]. Baronti P., Pillai P., Chook V., Chessa S., Gotta A., Wireless sensor networks: a survey on the state of the art and the 802.15.4 and ZigBee standards, *Computer Communications*, 30, March 2012, pp. 1655–1695.

[8]. Polastre J., Hill J., Culler D., Versatile low power media access for wireless sensor networks, in *Proceedings of the 2nd ACM International Conference on Embedded Networked Sensor Systems*, Baltimore, America, MD: Association for Computing Machinery, March 2004, pp. 95–107.

_____

SAS provides a forum for sensor users and developers to meet and exchange information about novel and emergent applications in smart sensors, homeland security, biology, medicine, system health management, and related areas. The main purpose of SAS is to collaborate and network with scientists, engineers, developers, and customers through formal technical presentations, workshops, and informal interface meetings.

## Suggested topics for SAS 2015 include:

### Sensors
* New sensors (e.g. Biological, Magnetic, Optical)
* Smart and Virtual Sensors and Standards
* MEMS and Nano-sensors
* Sensor Arrays and Multi-sensor Data Fusion
* Sensor Networks (Wireless, Optical, and Ethernet)
* Non-destructive Evaluation and Remote Sensing

### Sensor Applications
* Building and Home Automation and Security
* Agriculture, Environment and Health Monitoring
* Integrated System Health Management (ISHM)
* Robotics and Automation
* Commercial Development
* Education

Additional topics for workshops and new sessions are especially welcome - please  contact the organizers. Papers presented at SAS  2015 will be eligible  for consideration for publication in a Special Issue of the IEEE Transactions on Instrumentation & Measurement.

### Important Dates:

**Paper Submission Deadline**
October 24, 2014
**Acceptance/Rejection/Revision Notification**
January 16, 2015
**Final Paper Submission**
February 6, 2015
**Final Acceptance/Rejection Notification**
February 27, 2015

### General Chairs:
Vedran Bilas
University of Zagreb, Croatia

Alessandra Flammini
University of Brescia, Italy

Organized and Sponsored by:

http://sensorapps.org

# Data Aggregation with Sequential Detection in Wireless Sensors Network

**Song Xiao-Ou**

Engineer University of CAPF, Xi'an, 710086, China
Tel.: 0086+18691566981, fax: 0086+029-84563833
E-mail: e_miracle@163.com

**Abstract:** As the advanced information acquiring technology, wireless sensor networks are being applied in more and more areas. Data aggregation is the effective information processing to solve the energy saving problem of WSN (Wireless Sensor Network). Most existing data aggregation algorithm discuss fusion problem in the scene that the number of nodes is fixed. However, the amount of data transmitted is directly proportional to the number of nodes. Hence the appropriate strategy should be that the number of nodes is alterable under the satisfaction of performance. In this paper, sequential detection is applied in data aggregation for wireless sensor network. And the mathematical model is established. Considering the fading problem of wireless channel and the characters of physical layer, WSN data aggregation with sequential detection (WDASD) is proposed. The characters of WDASD are tested by simulations. In the end, a cross-layer scheme is proposed and simulation test is made to validate it. *Copyright © 2014 IFSA Publishing, S. L.*

**Keywords:** Wireless Sensor Network, Data Aggregation, Sequential Detection, Cross-layer design, Energy consumption.

## 1. Introduction

In order to increase the sensing performance and the robustness, more redundant nodes are arranged in Wireless Sensors Network (WSN), which cause that the network load increases. Hence it is necessary to adopt data aggregation algorithm, to guarantee the energy consumption effective [1]. The data aggregation in Wireless Sensors Network is quite different from that in Wired Sensors Network, because wireless channel fading may cause serious affect to the transmitting data. The representative research results of data aggregation in WSN are illustrated as follow. The optimal decision fusion rule is researched in document [2], to propose a suboptimal algorithm with a compromise among performance, energy consumption and complexity.

Utilizing the conditional probability density function, suboptimal data aggregation algorithms are proposed under different SNR conditions in document [3], which reduce the channel estimation complexity. Under the condition that transmitting bandwidth is limited, distributed aggregation in the cluster network is analyzed in document [4], which averages the received data at the leader node to make a decision. Supposing the wireless channel as Binary Symmetric Channel, distributed aggregation algorithm based on Weighted average is proposed in document [5]. Under the hypothesis that the number of nodes participating in the aggregation algorithm is constant, the above aggregation algorithms can gain some optimal performance indexes, in specified application scenarios.

When the number of nodes participating in the aggregation algorithm achieves a certain number, the

data aggregation system can meet the expected performance. In order to save energy consumption in WSN, the remaining nodes, not participating in the aggregation algorithm, should enter the sleep state and stop transmitting, which introduces sequential detection method of signal detection into the data aggregation algorithm. In this paper, data aggregation model based on sequential detection in WSN is constructed in the fading channel, which makes the number of nodes participating in the aggregation algorithm unfixed. Considering the modulation and demodulation characteristics of physical layer, WSN Data Aggregation base on Sequential Detection (WDASD) is further proposed. And its performance is proved by simulations. Then combining the thought of cross-layer scheduling, WDASD general scheme is finally proposed and tested by simulations.

## 2. Data Aggregation System Model

According to network topology structure, data fusion can be distinguished into cluster based data fusion, tree based data fusion, and cluster and tree based data fusion [6]. Whichever network topology structure are adopted, the elementary unite can come down to star network. It is supposed that there are one sink node and $N*$ sensor nodes in the elementary unite. Every sensor node doesn't communicate with other sensor nodes. At the sink node, the sensor data transmitted from different sensor nodes are collected and aggregated. Supposing that the node communication model is half-duplex communication, then communication between the sensor node and the sink node is established in turn. In order to specify the working mode of the elementary unite, it is supposed that TDMA is adopted as the network access mode, which means that the sink node allocates a time slot to every sensor node for sensor data transmission. The data transmitted from sensor node to sink node in turn can be described as $\{x_1, x_2, \ldots x_N\}$.

Decision fusion [1] is adopted in this paper, which means that the binary decision results, "0" or "1", are transmitted from sensor nodes and aggregated at the sink node to get the global decision hypothesis $H_0$ or hypothesis $H_1$, described as follow:

1) $H_0$: There is no specified event happening.
2) $H_1$: There is the specified event happening.

The performance of data aggregation algorithm is evaluated by false alarm probability $P(H_1 | H_0)$ and detection probability $P(H_1 | H_1)$. Considering that WSN is energy limited network [7], energy consumption of the data aggregation system is also an important performance index under the satisfied false alarm probability and detection probability. It is illustrated in document [8] that energy consumption of the data aggregation system is proportional to the transmitting amount of data, when the transmitting power of node is fixed. Under the condition that the data packets transmitted by sensor node possess the

same length, the transmitting amount of data is proportional to the number of sensor nodes participating in the aggregation algorithm, denoted by $N$. Hence $N$ is described as the performance index of energy consumption in this paper.

## 3. Aggregation Algorithm Based on Sequential Detection

Sequential detection belongs to statistic detection, which is usually used in signal detection. It is proved by Wold and Wolfwitz that sequential detection needs the least average number of observations to get a decision, with the fixed false alarm probability and missing detection probability [9]. It is supposed that all the sensor nodes work under ideal conditions without any noise interference. When the decision results transmitted from multiple sensor nodes through wireless channel, converge into a data sequence $\{x_1, x_2, \ldots x_N\}$ at the sink node, the noise introduced to the data aggregation system is just the noise of wireless channel. Then the decision process can be modeled as sequential detection, considering the number of data packets received by the sink node as the observation number. Hence the decision process of data aggregation based on sequential detection needs the least average number of participating nodes with the least energy consumption. The decision process of data aggregation based on sequential detection is specifically illustrated as follow.

Supposing that the data transmission between the $N^{th}$ sensor node and the sink node is completed, we can get an observation sequence with $N$ decision results, described by $(x_1, x_2, \ldots, x_N)^T$. The $N$ dimensional random vector is then mapped to one point in the observation space $\Phi$. As shown in Fig. 1, the observation space $\Phi$ is divided into three decision domains [10], which satisfy the follow requirements:

$$\Phi = \bigcup_{j=0}^{2} \Phi_j, \ \Phi_i \bigcap \Phi_j = \varphi \ i, j = 0, 1, 2, \quad (1)$$

where $\phi$ denotes empty set.
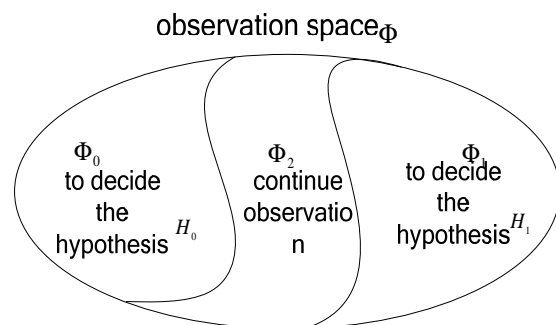


**Fig. 1.** Decision domain of sequential detection.

If the observation vector $\vec{x}_N = (x_1, x_2, \ldots x_N)^T$ is mapped into decision domain $\Phi_0$, we decide the hypothesis $H_0$. If the observation vector is mapped into decision domain $\Phi_1$, we decide the hypothesis $H_1$. And If the observation vector is mapped into decision domain $\Phi_2$, it indicates that the decision satisfying performance requirement cannot be made. At this moment, we must continue observation to receive the next sensor data $x_{N+1}$. It is known from above analysis that there are two likelihood ratio detection thresholds, shown by $\eta_0$ and $\eta_1$, even $\eta_1 > \eta_0$. Hence the likelihood ratio detection can be expressed by

$$\lambda(\vec{x}_N) = \frac{p(\vec{x}_N|H_1)}{p(\vec{x}_N|H_0)} \overset{H_1}{\geq} \eta_1 \qquad (2)$$

$$\lambda(\vec{x}_N) = \frac{p(\vec{x}_N|H_1)}{p(\vec{x}_N|H_0)} \overset{H_0}{\leq} \eta_0 \qquad (3)$$

## 4. Decision Method with the Characteristics of Physical Layer and Wireless Channel

### 4.1. Problem Description and Decision Method

Adopting 2FSK as the physical layer modulation mode, synchronization detection is chosen as the demodulation method, shown in Fig. 2.
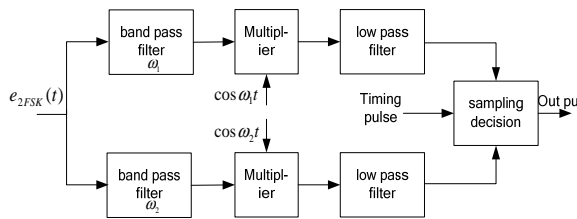


**Fig. 2.** 2FSK performance analysis using synchronization detection.

As shown in Fig. 2, at the receiver two band pass filters are used to distinguish between two signals with the central frequencies $f_1$ and $f_1$. After the coherent demodulation, the output signal of two band pass filters are sent to the sampling decision device.

Supposing that the transmitting symbol is "1", the input waveform of the two branches in Fig. 2 are separately denoted by

the upper branch $x_1(t) = a + n_{1c}(t)$, (4)

the lower branch $x_2(t) = n_{2c}(t)$, (5)

where a is the signal component, $n_{1c}(t)$ and $n_{2c}(t)$ are low pass Gauss White Noise with the mean value 0 and the variance value $\sigma_n^2$.

Supposing that the transmitting symbol is "0", the input waveform of the two branches are separately denoted by

the upper branch $x_1(t) = n_{1c}(t)$ (6)

the lower branch $x_2(t) = a + n_{2c}(t)$ (7)

As shown in Fig. 2, the output of the sampling decision device is the synchronization detection result, denoted by z.

$$z = x_1 - x_2, \qquad (8)$$

where z is Gaussian random variable. If the receiving signal is "1", the random variable z possesses the mean value a and the variance value $2\sigma_n^2$. If the receiving signal is "0", the random variable z possesses the mean value -a and the variance value $2\sigma_n^2$. The receiver SNR value is $r = a^2/2\sigma_n^2$. Considering wireless channel fading, we define $a_i$ by

$$a_i = \sqrt{P_r} = \sqrt{P_t/P_{loss}}, \qquad (9)$$

where $P_{loss}$ is the path loss ratio of the $i^{th}$ channel, $P_t$ is the transmitting power, and $P_r$ is the receiving power. Supposing that the path loss between every sensor node and the sink node is constant, then the wireless channel can be considered as constant channel, which indicates that with the unchanged transmitting power of the $i^{th}$ sensor node, the parameter $a_i$ is always constant.

According to the characters of physical layer, the receiving signal $x_k$ at the sink node under the two hypotheses $H_0$ and $H_1$ is separately described by

$$H_0 : x_k = -a_k + n_k, \quad k = 1, 2, \cdots, \qquad (10)$$

$$H_1 : x_k = a_k + n_k, \quad k = 1, 2, \cdots, \qquad (11)$$

where $n_k$ is the Gauss noise with the mean value 0 and the variance value $2\sigma_n^2$; $a_k \in \{a_1, a_2, \cdots, a_{N^*}\}$, and $N^*$ is the number of the transmitting sensor nodes.

After the Nth reception from sensor node, the likelihood ratio function is

$$\lambda(x) = \frac{p(\vec{x}_N | H_1)}{p(\vec{x}_N | H_0)} = \frac{\prod_{k=1}^{N} p(x_k | H_1)}{\prod_{k=1}^{N} p(x_k | H_0)}$$

$$= \exp\left(\sum_{k=1}^{N} \frac{x_k a_k}{\sigma_n^2}\right) \qquad (12)$$

Then the log likelihood ratio function is

$$\ln \lambda(\vec{x}_N) = \sum_{k=1}^{N} \frac{x_k a_k}{\sigma_n^2} \qquad (13)$$

Hence the decision expression is denoted by

$$\sum_{k=1}^{N} \frac{x_k a_k}{\sigma_n^2} \overset{H_1}{\geq} \ln \eta_1 \qquad (14)$$

$$\sum_{k=1}^{N} \frac{x_k a_k}{\sigma_n^2} \overset{H_0}{\leq} \ln \eta_0 \qquad (15)$$

The above decision method is WSN Data Aggregation base on Sequential Detection (WDASD).

## 4.2. Threshold Evaluation

It is supposed that the constraint value of $P(H_1 | H_0)$ and $P(H_0 | H_1)$ is separately $\alpha$ and $\beta$.

$$\alpha = \int_{R_1} p(\vec{x}_N | H_0) d\vec{x}_N \qquad (16)$$

$$1 - \beta = \int_{R_1} p(\vec{x}_N | H_1) d\vec{x}_N$$
$$= \int_{R_1} p(\vec{x}_N | H_0) \lambda(\vec{x}_N) d\vec{x}_N \qquad (17)$$

Under the hypothesis $H_1$, if the decision is $H_1$, it must be satisfied that $\lambda(x_N) \geq \eta_1$, which is brought into Eq. (17) to conclude

$$1 - \beta \geq \eta_1 \int_{R_1} p(\vec{x}_N | H_0) d\vec{x}_N = \eta_1 \alpha \qquad (18)$$

Hence

$$\eta_1 \leq (1 - \beta) / \alpha \qquad (19)$$

According to the sequential detection requirement that the decision is $H_1$ under the condition $\lambda(x_N) \geq \eta_1$, the theory upper limit of $\eta_1$ is chosen to guarantee enough observation data to get the decision satisfying the performance index. Hence the threshold $\eta_1$ is denoted by

$$\eta_1 = (1 - \beta) / \alpha \qquad (20)$$

Similarly

$$\eta_0 = \beta / (1 - \alpha)$$

When $\ln \eta_0 < \ln \lambda(x_n) < \ln \eta_1$, the sink node does not make any decision. But it is supposed that there

are only $N^*$ sensor nodes in the Wireless Sensor Network. When number of the sensor nodes participating in the aggregation algorithm comes to $N^*$, the compulsory decision result is made.

## 4.3. Simulation

It is supposed that the AWGN channel parameters from different sensor nodes to sink node are the same; $a$ sequence is the all "1" sequence; SNR value is $a^2 / 2\sigma_n^2 = 0.5$, i.e. 0dB; there are 100 sensor nodes in the elementary unite; and the constraint values of $P(H_1 | H_0)$ and $P(H_0 | H_1)$ are all 0.01. The simulation results are shown in Fig. 3.



(a) decision results



(b) number of participating nodes
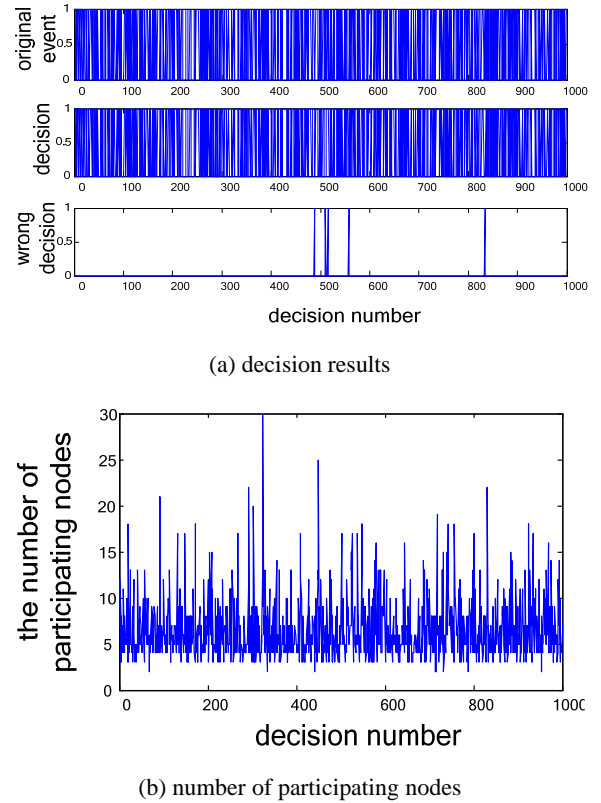
**Fig. 3.** WDASD performance under the same channel condition.

As shown in Fig. 3(a), in 1000 decision processes, there are five wrong decision processes, which satisfy the constraint of false alarm. It is illustrated in Fig. 3(b) that the number of nodes participating in the aggregation algorithm is not confirmed in the range of 2 to 30, with the mean value 6.5610. The larger the noise variance is, the wider the fluctuation range of the participating node number is, with a larger mean value.

In the realistic environment, the channel parameters from different sensor nodes to sink node are always different. Hence it is supposed that the receiving signal strength is distributed evenly in the

range of [0, 1]; at the sink node the noise variance is $\sigma_z^2 = 2\sigma_n^2 = 2$. Then the simulation result is shown in Fig. 4.
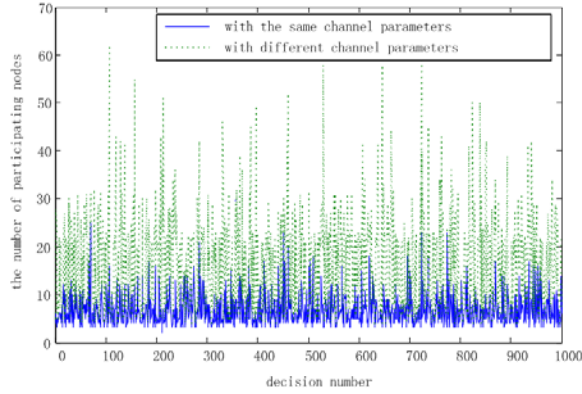


**Fig. 4.** WDASD performance with different channel parameters.

As shown in Fig. 4, with different channel parameters, the number of participating nodes is larger than the number of participating nodes with the same channel parameters. And the curve fluctuation is also larger when the channel parameters are different.

On this basis, the effect of different channel parameter arrangements to the average number of participating nodes is researched as follow. In the simulation, 50 *a* sequences are randomly generated; and 1000 fusion decision processes are carried on according to every *a* sequence to get the average number of nodes participating in the aggregation algorithm. As shown in Fig. 5, under the condition of different channel parameters arrangements, the average numbers of participating nodes are different.
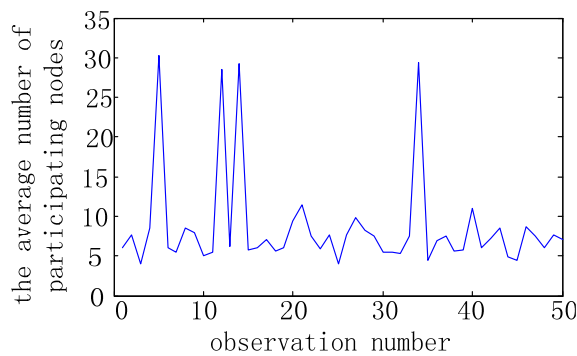


**Fig. 5.** WDASD performance with random channel arrangement.

Because different channel parameters arrangements cause the SNR value different at the sink node in the same receiving order, which means that the receiving order of signals with different SNR values has a big affect on the algorithm performance.

# 5. Data Aggregation Cross-layer Design Scheme Based on WDASD

## 5.1. Data Aggregation Scheme

From the above discussion, it is known that if the sensor node with high SNR value transmits the sensor data first, namely in the descending order of receiving SNR value at the sink node, the performance of data aggregation algorithm can be optimized to reduce the number of anticipating nodes. And in WSN, SNR value of the receiving signal can be tested by RSSI in the physical layer. Considering that TDMA is adopted in the data aggregation system, the sink node can allocate the time slots to sensor nodes in the descending order of SNR value. Then the data aggregation cross-layer design scheme is illustrated as follow:

1) The data packets are transmitted by sensor nodes with the same fixed power, which denotes the signal strength by $i_0$. At the sink node, the RSSI values of the receiving signals transmitted through different channels are measured, which is indicated by $i_k (n = 1, 2, \cdots, N^*)$. Then the background noise is measured, indicated by $i_{noise}$. $i_k$ is denoted by

$$i_k = a_k^2 \qquad (22)$$

2) The transmission order of the sensor nodes, i.e. {MID1, MID2, …, MIDn}, are sorted by the sink node in the descending order of receiving SNR value. Namely the sensor node with good link quality transmits first. First the sink node transmits the communication order information. Then every sensor node confirms its distributed communication time slot and measures environmental parameters. Lastly some strategy is adopted to wait for the communication time slot.

3) The sensor nodes transmit the data packets in order to the sink node. And the sink node receives the data packets and measures the RSSI values of the receiving signals. Meanwhile, WDASD is carried on to get a satisfied decision result. And then transmits a stopping fusion signal which makes the remaining nodes stop this data packets transmission.

4) The next data aggregation process is started. Then the above procedures are repeated.

## 5.2. Simulation

The simulation conditions are the same as that described in 3.3. Two cases are considered in this section:

1) Case 1: cross-layer scheduling is not adopted, which means that the sensor nodes transmit the data packets randomly;

2) Case 2: cross-layer scheduling is adopted, which means that the sensor nodes transmit the data

packets in the descending order of receiving SNR value. The simulation results are shown in Fig. 6.
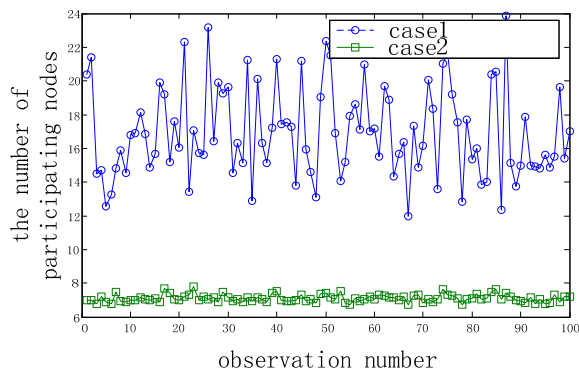


**Fig. 6.** WDASD performance adopting and not adopting cross-layer scheduling.

As shown in Fig. 6, when cross-layer scheduling is adopted, the number of participating nodes is much decreased. Under the condition that there are 100 sensor nodes in the elementary unite, the performance of Median fusion algorithm [5] and WDASD algorithm with cross-layer scheduling is compared as the follow. It is supposed that through the AWGN channel the signals transmitted from 100 sensor nodes are distributed evenly in the range of [0, 1]. The noise variance increase progressively from one observation to the next. In one observation, 100000 fusion simulations are carried out to get the false decision probability and the average number of participating nodes, shown by Fig. 7.

As shown in Fig. 7(a), when the noise variance is less than 2, the performance of WDASD algorithm is worse than the performance of Median fusion algorithm in the aspect of false alarm decision probability. But with the noise variance larger than 2, the performance of WDASD algorithm is better than the performance of Median fusion algorithm. It is illustrated by Fig. 7(b) that the average numbers of participating number in WDASD algorithm with different noise variance are also different, which can reduces the number of participating nodes.

## 6. Conclusions

In order to reduce the number of nodes participating in the aggregation algorithm in the elementary unite of WSN, sequential detection method is applied into data aggregation, to propose WSN Data Aggregation base on Sequential Detection (WDASD) algorithm and prove its performance by simulations. To further improve the performance of WDASD algorithm, cross-layer scheduling scheme suitable for WDASD is proposed. The WDASD algorithm adopting cross-layer scheduling is simulated, which indicates that the number of participating nodes can be further reduced with lower energy consumption than that of WDASD algorithm not adopting cross-layer scheduling.
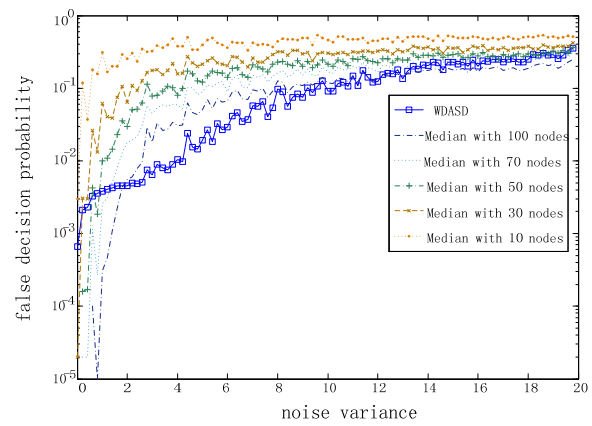


(a) false decision probability.
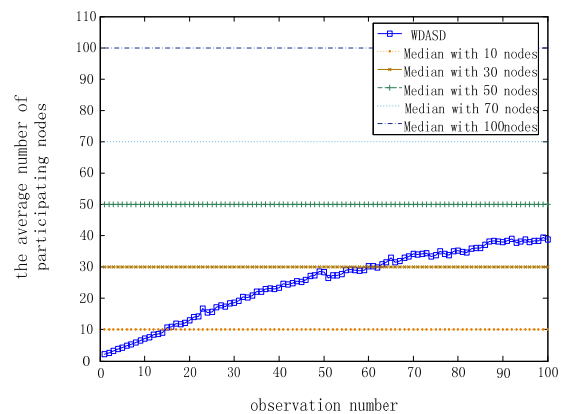


(b) the average number of participating nodes.

**Fig. 7.** Performance comparison.

## Acknowledgements

## References

[1]. Bhasker L., Genetically derived secure cluster based data aggregation in wireless sensor networks, *IET Information Security*, Vol. 8, Issue 1, 2014, pp. 1-7.

[2]. Mathapati B. S., Patil S. R., Mytri V. D., Energy Efficient Reliable Data Aggregation Technique for Wireless Sensor Networks, in *Proceedings of the Conference on Computing Sciences (ICCS'12)*, Phagwara, Sept. 2012, pp. 153-158.

[3]. Rong Zhou, Wang Suoping, Sub-optimal decision fusion under channels in wireless sensor networks, *Chinese Journal of Scientific Instrument*, Vol. 31, Issue 11, 2010, pp. 2622-2628.

[4]. Z. Q. Luo, Universal Decentralized Detection in a Bandwidth Constrained Sensor Network, *IEEE Transactions on Signal Processing*, Vol. 53, Issue 8, 2005, pp. 2617-2624.

[5]. Q. Tian, E. J. Coyle, Optimal Distributed Detection in Clustered Wireless Sensor Network: The Weight median, in *Proceedings of the IEEE Conference INFOCOM'06*, 2006, pp. 562-568.

[6]. Lu Z., Wen Y., Distribution Algorithm for Tree Structure Data Aggregation Service Placement in Smart Grid, *IEEE Systems Journal*, Vol. 8, Issue 2, 2014, pp. 553-561.

[7]. Jian Xu, Geng Yang, Zheng-Yu Chen, Lei Chen, Performance analysis of data aggregation algorithms in wireless sensor networks, in *Proceedings of the Conference on Electrical Control Engineering (ICECE'11)*, Yichang, September 2011, pp. 4619-4622.

[8]. Din W. I. S. W., Yahya S., Taib M. N., Yassin A. I. M., Energy efficient of WSN using two parameters selection, in *Proceedings of the Conference on Systems, Process & Control (ICSPC'13)*, Kuala Lumpur Malaysia, Dec. 2013, pp. 181-185.

[9]. J. G. Proakis, Tang Jun, Statistic Signal Processing Algorithm, *Qinghua University Publisher*, Beijing, 2006, pp. 250-267.

[10]. A. A. Amini, Xua Long Nguyen, Sequential Detection of Multiple Change Point in Networks: A Graphical Model Approach, *IEEE Transactions on Information Theory*, Vol. 59, Issue 9, 2013, pp. 5824-5841.

———————————————

# A Wildlife Monitoring System Based on Wireless Image Sensor Networks

**[1] Junguo Zhang, [1] Xin Luo, [2] Chen Chen, [3] Zhen Liu, [4] Shuai Cao**

[1] School of Technology, Beijing Forestry University, Beijing 100083, China
[2] Department of Electrical Engineering, University of Texas at Dallas, Richardson 75080, USA
[3] Neusoft, Beijing 100193, China
[4] Beijing Wisdom Industrial Park of Science & Technology Co., LTD, Beijing 100091, China
E-mail: zhangjunguo@bjfu.edu.cn, luoxinstudy@126.com, chenchen870713@gmail.com,
zhen-liu@neusoft.com, drshuai1218@126.com

**Abstract:** Survival and development of wildlife sustains the balance and stability of the entire ecosystem. Wildlife monitoring can provide lots of information such as wildlife species, quantity, habits, quality of life and habitat conditions, to help researchers grasp the status and dynamics of wildlife resources, and to provide basis for the effective protection, sustainable use, and scientific management of wildlife resources. Wildlife monitoring is the foundation of wildlife protection and management. Wireless Sensor Networks (WSN) technology has become the most popular technology in the field of information. With advance of the CMOS image sensor technology, wireless sensor networks combined with image sensors, namely Wireless Image Sensor Networks (WISN) technology, has emerged as an alternative in monitoring applications. Monitoring wildlife is one of its most promising applications. In this paper, system architecture of the wildlife monitoring system based on the wireless image sensor networks was presented to overcome the shortcomings of the traditional monitoring methods. Specifically, some key issues including design of wireless image sensor nodes and software process design have been studied and presented. A self-powered rotatable wireless infrared image sensor node based on ARM and an aggregation node designed for large amounts of data were developed. In addition, their corresponding software was designed. The proposed system is able to monitor wildlife accurately, automatically, and remotely in all-weather condition, which lays foundations for applications of wireless image sensor networks in wildlife monitoring. *Copyright © 2014 IFSA Publishing, S. L.*

**Keywords:** Wildlife monitoring system, Wireless image sensor networks, System architecture, Node design, Software process design.

## 1. Introduction

Survival and development of wildlife sustains the balance and stability of the entire ecosystem. Wildlife monitoring can provide a wealth of information such as wildlife species, quantity, habits, quality of life and habitat conditions, to help researchers grasp the status and dynamics of wildlife resources, and to provide basis for effective protection, sustainable use as well as scientific management of wildlife resources. Traditional wildlife monitoring methods (e.g., [1-5]) have been extensively explored in monitoring applications. However, they all have limitations.

Here, we overview some of the traditional wildlife monitoring methods.

First is artificial field survey including linear intercept method, fixed-point notation, meet rate method, and questionnaire [1]. It is limited in scope of monitoring, labor-intensive, high-risk and cannot achieve all-weather monitoring. Second is a global positioning system (GPS) collar. Compared with traditional radio collars, GPS collars can provide better spatial resolution and determine the location in broader temporal and spatial conditions [2-3]. However, this monitoring method is not able to obtain image information of animals. The third method employs infrared cameras. The image data taken from infrared cameras are stored in the local large-capacity SD memory card. At a certain time interval, researchers have to go to the scene to remove the SD card and read the data [4]. This approach has many drawbacks such as lagged data collection, long monitoring cycle, high labor intensity, high risk, etc. Some infrared cameras connected with 3G networks can send the image data to the user's mobile phone through 3G networks. This method relies on the coverage of 3G mobile phone signal, and the core area of some national nature reserves is not covered by mobile phone signal. The fourth method uses wireless cameras to transmit images through wireless broadband microwave. Due to the necessity of power supply and high deployment, obtaining images of wildlife forest activities is difficult and the equipment cost is relatively high. The fifth method is satellite remote sensing [5]. Satellite remote sensing integrated monitoring is difficult to accurately measure the local microscopic information due to the spatial resolution. In addition, satellite remote sensing cannot provide real-time monitoring since it has scan cycle.

Wireless sensor networks (WSNs) consist of thousands of cost-effective miniature sensor nodes capable of computation, communication and sensing [6]. WSNs can overcome the shortcomings of the traditional monitoring methods and have provided tremendous benefit for applications such as forest fire monitoring, nature biodiversity monitoring, timber detection and forest ecology [7-12]. With the advancement in CMOS image sensor technology, wireless sensor networks combined with image sensors, namely wireless image sensor networks (WISNs), have recently come into prominence since they can provide visual monitoring of effects in the environment. In this paper, we propose a wildlife monitoring system based on WISNs. In essence, the major contribution of this paper involves general system architecture of the wildlife monitoring system based on WISNs and the hardware and software design of the system. The proposed system is able to monitor wildlife accurately, automatically, and remotely in all-weather condition.

The rest of the paper is organized as follows. In Section 2, an overview of WISNs is presented. In Section 3, the proposed wildlife monitoring system based on WISNs is stated. The hardware and software design of the monitoring system is described in Section 4 and Section 5, respectively. Finally, some conclusion remarks are made in Section 6.

## 2. Wireless Image Sensor Networks

WSNs, combine sensors, embedded systems and wireless communication technology, have a wide range of potential applications due to their advantages including self-organization, adaptive capacity, data-centric, application-specific, small size, low cost and wide area monitoring capability. WSN technology is also an important branch of the Internet of Things [13]. WSNs have increasingly being used in the military, space exploration, environmental monitoring, home health care, disaster prevention and other areas [14]. WSNs mainly collect simple physical information such as light and temperature leading to a small amount of data. However, with the advancement of the CMOS image sensor technology, it is possible to integrate small, low power, and cost-effective image sensors to WSNs. The resulted WISNs are able to collect valuable visual information of the target object and its surroundings. Wildlife monitoring is one of the most promising applications of WISNs [15]. WISNs can collect image information and realize wireless remote transmission to achieve real-time, fine-grained, and precise wildlife monitoring [16].

## 3. Wildlife Monitoring System Based on WISNs

Cervus elaphus is a second class national-level protected animal due to excessive cubs hunting and habitat loss. Inner Mongolia is one of the main Cervus elaphus distribution areas. This paper chooses wild Cervus elaphus in Inner Mongolia Saihanwula as the object to carry out the research of wildlife monitoring using WISNs. The monitoring system based on WISNs includes a wireless infrared image sensor network, a base station and a wildlife monitoring center. The overall architecture of the wildlife monitoring system based on WISNs is shown in Fig. 1.

A WISN consists of many infrared image sensor nodes deployed in wildlife activity areas or nearby areas and a sink node. Infrared image sensor nodes usually lie dormant. Once a wild animal enters the detection zone, the pyroelectric infrared sensor is triggered and infrared image sensor nodes start immediately for capturing images. Light sensors will determine whether the light is adequate or not. If the light is adequate, color photographs will be taken. If the light is not adequate, infrared LEDs start automatically for lighting and black and white photographs will be taken. Meanwhile, GPS positioning module starts automatically for obtaining positioning data. Infrared image sensor nodes will process the data locally and transfer the processed

data to the sink node. The sink node is deployed in locations with 3G networks coverage and sends data to the base station through 3G networks. Base station connected to the internet is responsible for transmitting the received data to the wildlife monitoring center over the internet. Wildlife monitoring center is equipped with 3D GIS system and a wild animal image information database. Researchers can store and analyze the collected data.
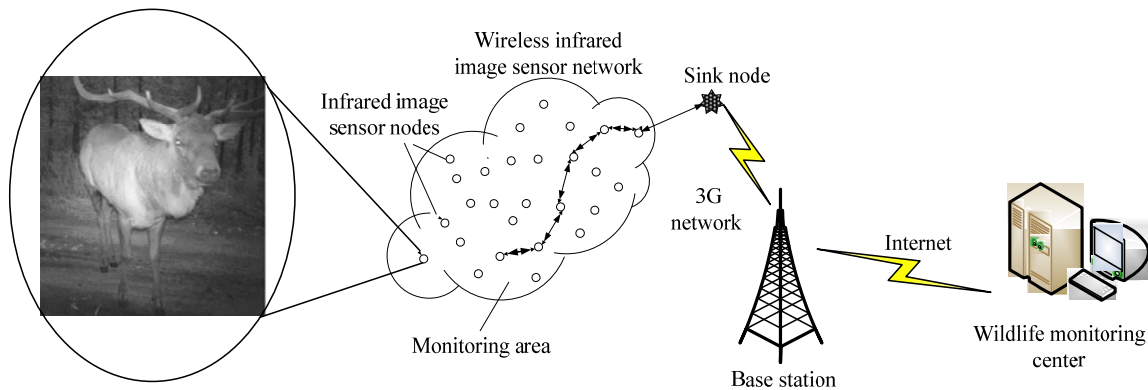


**Fig. 1.** The architecture of wildlife monitoring system based on wireless image sensor network.

## 4. Hardware Design

Nodes are the basic units of the wildlife monitoring system based on WISNs. Nodes include wireless infrared image sensor nodes and a sink node. Wireless infrared image sensor nodes are responsible for obtaining monitoring information and are the basic units of the monitoring system. The sink node is the hardware infrastructure connected to WISNs and the access network. The hardware design for these nodes is critical for functionality and performance of the entire system. Next, we present the detailed design of a wireless infrared image sensor node and a sink node.

### 4.1. Design of Rotatable and Self-powered Wireless Infrared Image Sensor Nodes

Wireless infrared image sensor nodes are the basic units of a WISN. To build a ZigBee protocol-based wireless infrared image sensor network system, the main task is to develop low-power wireless infrared image sensor network nodes for power efficiency.

The structure of a wireless infrared image sensor node designed in this paper is shown in Fig. 2. As can be seen in Fig. 2, the structure is equipped with three pyroelectric infrared sensors, infrared LEDs, light sensors and two servos. The sensing angle of the pyroelectric infrared sensor is 120°. Three pyroelectric infrared sensors are facing three directions, and the corresponding sensing ranges do not overlap. Infrared image sensor nodes usually lie dormant. Once a wild animal enters the detection zone, infrared image sensor nodes start immediately to capture images by controlling the rotation angles of the two servos and adjusting the camera lens to the

direction faced by the pyroelectric infrared sensor detects the wildlife. Light sensors will determine the lighting condition. If the light is sufficient, color photographs will be taken, otherwise, infrared LEDs start automatically for lighting and black and white photographs will be taken. A wireless infrared image sensor node can achieve all-weather acquisition, compression and transmission of infrared image data of wildlife. It can communicate with other infrared image sensor nodes and achieve the GPS positioning function.
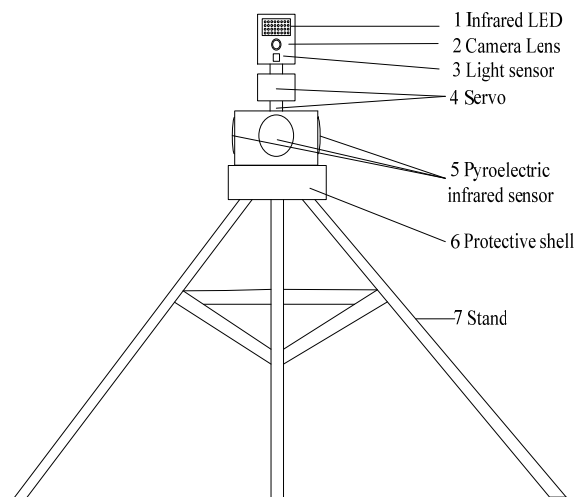


**Fig. 2.** The structure diagram of a wireless infrared image sensor node.

Given the characteristics of image data processing and energy consumption, wireless infrared image sensor nodes based on ARM7 are designed in this paper. A wireless infrared image sensor node includes

an image acquisition module, an image processing module, a ZigBee transceiver, a GPS module, and a solar energy supply module. The specific hardware architecture is shown in Fig. 3.
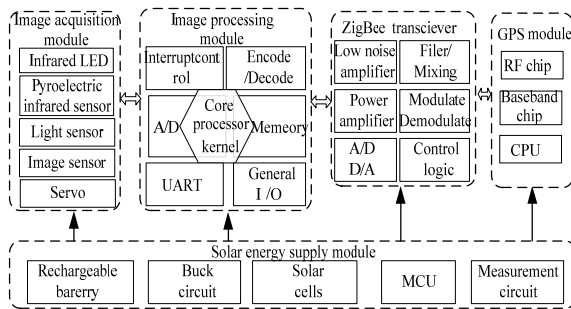


**Fig. 3.** Specific hardware architecture of a wireless infrared image sensor node/module block diagram.

The processor used in our sensor nodes is the Atmel AT91SAM7X512, which is based on ARM7TDMI (a 32-bit RISC architecture). It operates at a maximum speed of 55 MHz and features 512 kB of flash and 128 kB of SRAM. Typical core supply is 1.8 V. I/Os are supplied at 1.8 V or 3.3 V and are 5 V tolerant. It can set the parameters of the imager, instructs the imager to capture a frame and run local computation on the image to produce an inference. We adopt TI CC2520 as the ZigBee transceiver. The CC2520 is TI's second generation ZigBee/IEEE 802.15.4 RF transceiver for the 2.4 GHz unlicensed ISM band. This chip enables industrial grade applications by offering state-of-the-art selectivity/co-existence, excellent link budget, hardware support for frame handling and low voltage operation, thus reducing the load on the host controller. It connects to the processor through SPI. The image sensor module for our platform is OmniVision OV7670 combined with embedded DSP OV529. The OV7670 image sensor is a low voltage CMOS sensor that provides the full functionality of a single-chip VGA camera and an image processor. The OV7670 provides full-frame, sub-sampled or windowed 8-bit images in a wide range of formats, operating at up to 30 frames per second (fps). It is controlled through the serial camera control bus (SCCB) interface. The OV529 serial bridge contains an embedded JPEG CODEC and a controller chip that can compress and transfer image data from the camera sensor to an external device. The image sensor module connects to the processor through UART. HC-SR501 sensor module, as the pyroelectric infrared sensor, is cheap, high sensitivity and its detection distance is 7 meters. Its working voltage is 4.5-20 V, and the output level is 3.3 V or 0 V. In addition, a solar energy module is developed, which consists of a microcontroller MSP430, solar cells, rechargeable battery, measurement circuits, BUCK circuits, etc, to supply power to the node efficiently.

## 4.2. Design of the Sink Node

The sink node aims at connecting the wireless image sensor network with 3G telecommunication network. It establishes a reliable connection and two-way data transmission between a remote server or mobile users and a wireless image sensor network to meet the practical needs. The specific hardware architecture is shown in Fig. 4.
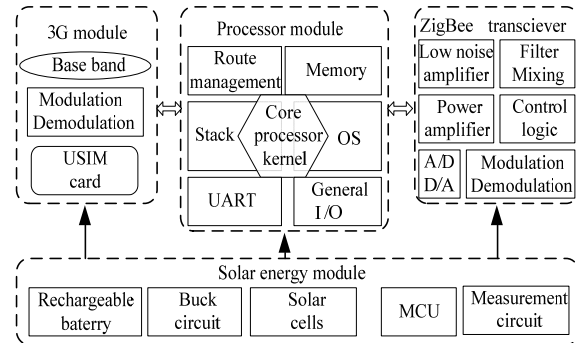


**Fig. 4.** Specific hardware architecture of the sink node.

The sink node consists of processor, memory, a ZigBee transceiver, a 3G communication module and other expanded interfaces. Considering the large amount of data of the sink node received, PXA270 from Marvell has been chosen as the core processor module. It incorporates the Intel XScale technology which complies with the ARM* version 5TE instruction set (excluding floating-point instructions) and works at 520 MHz. To work with the PXA270, two chips of HY57V561620 from Hynix have been selected as 64 MB SDRAM, and two chips of TE28F128J3C-150 from Intel have been selected as 64 MB Flash. CC2520 has been adopted as the aforementioned ZigBee transceiver. We choose SIMCom SIM5218 as the 3G module. The SIM5218 series is a Tri-Band/Single-Band HSPA/WCDMA and Quad-Band GSM/GPRS/EDGE module solution which supports up to 7.2 Mbps downlink speed and 5.76 Mbps uplink speed services. It connects to the processor through UART.

## 5. Equations Software Design

System software design mainly includes the programming of ZigBee protocol stack, 3G protocol stack, and software design of wireless infrared image sensor nodes and the sink node. Since the ZigBee technology and 3G technology are more mature, the existing protocol stack program is used by the system. The study focuses on the software design of the wireless infrared image sensor node and the sink node. Since the features and tasks of the wireless infrared image sensor node and the sink node are different, they are discussed separately.

### 5.1. Programming of the Wireless Infrared Image Sensor Nodes

Wireless infrared image sensor nodes formed a self-organizing network are the sink node's children and grassroots links of a WISN. Wireless infrared image sensor nodes are directly associated with capturing wildlife image and passing compression-encoded image data. The main tasks of wireless infrared image sensor nodes are node wake, wildlife image acquisition, image compression, data transmission, and returning to dormancy. The specific workflow is presented in Fig. 5.
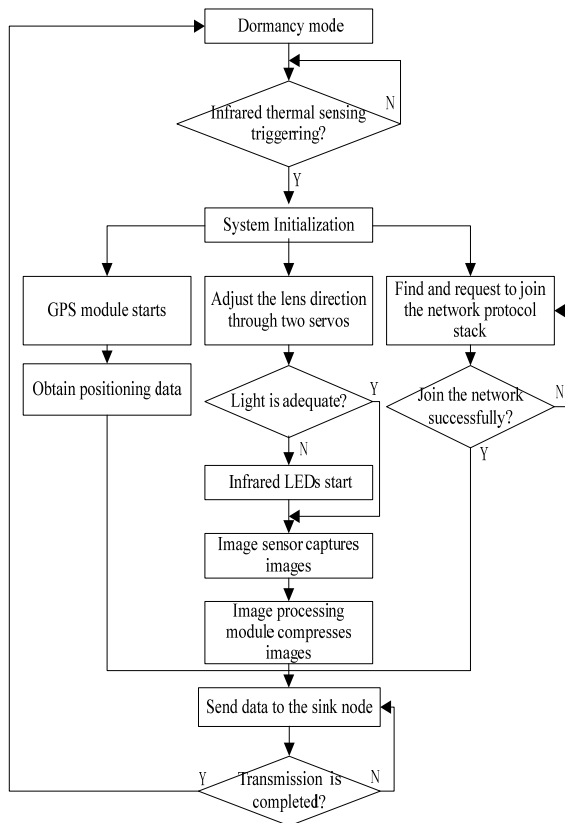


**Fig. 5.** Program flow chart of the wireless infrared image sensor node.

Infrared image sensor nodes usually lie dormant. Once pyroelectric infrared sensors are triggered, infrared image sensor nodes start immediately and capture images by controlling the rotation angles of the two servos and adjusting the camera lens to the direction that faced by pyroelectric infrared sensor detects the wildlife. Light sensors will determine the lighting condition. If the light is not sufficient, infrared LEDs start automatically for lighting. GPS module starts to obtain positioning data. Meanwhile, a request is sent to join the network. After the sink node responses, the infrared image sensor nodes successfully join the network and start transmitting the compressed image data and location data to the upper nodes. The upper nodes send the acknowledge bit after determining successful reception. The

wireless infrared image sensor nodes return to the dormancy mode, so on ad infinitum.

### 5.2. Programming of the Sink Node

The sink node is responsible for building and managing a network. It allows or denies any sensor node to join the network. It collects data of the wireless infrared image sensor nodes and sends them to the base station via 3G networks. Its work process includes node wake, building network, joining node, receiving data, sending data, and returning to dormancy. The specific workflow is presented in Fig. 6.
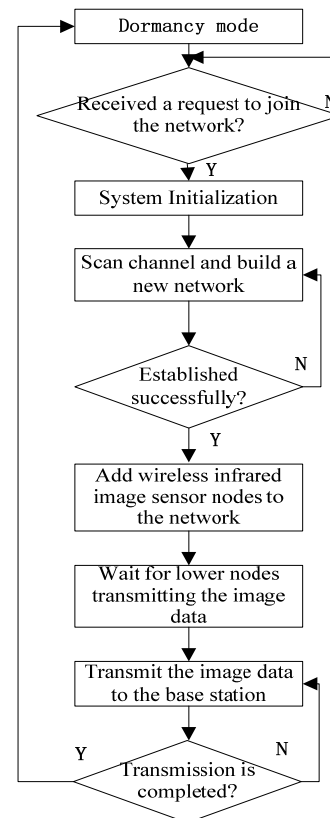


**Fig. 6**. Program flow chart of the sink node.

The sink node usually lies dormant. Once it receives a request signal to join the network, the system is initialized and begins to establish a network. When building the network, the sink node will continue to search for an empty channel. If a searched channel is occupied by another sink, then the search continues until an empty channel is found. When an empty channel is found, it immediately performs the appropriate identification to build its own network. According to the resource need, the sink node decides whether to allow this wireless infrared image sensor node to join. If this node is allowed to join, it is assigned a network address to build a new network. At the same time, the sink node waits for the image data and location data. Then the

sink node transmits the received data to the base station via 3G networks.

## 6. Conclusions

Wildlife monitoring is important for effective protection, sustainable use, and scientific management of wildlife resources. Compared to the traditional wildlife monitoring methods, wildlife monitoring based on wireless image sensor networks is able to meet the new requirements, such as remote, real-time, all-weather monitoring, and capturing image information. This paper proposed a wildlife monitoring system based on the wireless image sensor networks to overcome the shortcomings of traditional monitoring methods. System architecture, design of wireless image sensor nodes and software design have been studied and presented. However, there are still many issues to be resolved in wildlife monitoring applications using wireless image sensor networks. For example, how to reduce the image compression algorithm complexity while maintaining the quality of images, how to achieve low-power local image recognition, and how to deploy image nodes to maximize the coverage of monitoring area. In our future research, we will tackle these issues.

## Acknowledgements

## References

[1]. E. Gao, B. Liang, Y. Song, Wildlife monitoring at home and abroad, *Forest Resources Management*, Vol. 3, 2001, pp. 27-30.

[2]. J. Frair, S. Nielsen, E. Merrill, S. Lele, M. Boyce, R. Munro, G. Stenhouse, H. Beyer, Removing GPS collar bias in habitat selection studies, *Journal of Applied Ecology*, Vol. 41, No. 2, 2004, pp. 201-212.

[3]. N. Tomkins, P. O'Reagain, Global positioning systems indicate landscape preferences of cattle in the subtropical savannas, *The Rangeland Journal*, Vol. 29, No. 2, 2007, pp. 217-222.

[4]. L. Feng, L. Lin, L. Zhang, Evidence of wild tigers in southwest China - a preliminary survey of the Xishuangbanna National Nature Reserve, *Cat News*, Vol. 48, 2008, pp. 4-6.

[5]. T. Wark, C. Crossman, P. Valencia, D. Swain, G. Hishop-Hurley, R. Handcock, Sensor and actuator networks: protecting environmentally sensitive areas, *IEEE Pervasive Computing*, Vol. 8, No. 1, 2009, pp. 30-36.

[6]. J. Zhang, W. Li, X. Zhao, X. Bai, C. Chen, Simulation and Research on Data Fusion Algorithm of the Wireless Sensor Network Based on NS2, in *Proceedings of the WRI World Congress on Computer Science and Information Engineering*, Los Angeles, CA, March 2009, pp. 66-70.

[7]. J. Zhang, Study on Techniques of Wireless Sensor Network oriented to Forest Fire Detection, Doctoral Dissertation, *Beijing Forestry University*, 2009.

[8]. J. Zhang, W. Li, N. Han, J. Kan, Forest fire detection system based on ZigBee wireless sensor network, *Frontiers of Forestry in China*, Vol. 3, No. 3, 2008, pp. 369-374.

[9]. G. Li, J. Zhao, Z. Wang, Forest Fire Detection System Based on Wireless Sensor Network, *Chinese Journal of Sensors and Actuators*, Vol. 19, No. 6, 2006, pp. 2760-2764.

[10]. D. Liu, Application of Localization Algorithm for Internet of Things Based on Forest Fire Monitoring, *Journal of Northeast Forestry University*, Vol. 39, No. 8, 2011, pp. 131-133.

[11]. Y. Zheng, Study on Forest Fire Auto-inspecting System Base on Wireless Sensor Network, Master's thesis, *Nanjing Forestry University*, 2007.

[12]. C. Chen, N. Han, C. Yao, Y. Li, A Novel Fast Inter Mode Decision Algorithm in H.264/AVC for Forest Fire Prevention Surveillance, in *Proceedings of the 5th International Conference on Active Media Technology*, Beijing, China, October 2009, pp. 397-408.

[13]. J. Zhang, W. Li, Z. Fu, Research and Construction of a Sensing Forest System based on the Internet of Things, *Measuring Technology and Mechatronics Automation in Electrical Engineering*, Springer US, 2012, pp. 407-414.

[14]. L. Cui, H. Ju, Y. Miao, T. Li, W. Liu, Z. Zhao, Overview of Wireless Sensor Networks, *Journal of Computer Research and Development*, Vol. 42, No. 1, 2005, pp. 163-174.

[15]. R. Bagree, V. Jain, A. Kumar, P. Ranjan, TigerCENSE: wireless image sensor network to monitor tiger movement, *Real-World Wireless Sensor Networks*, Springer Berlin Heidelberg, 2010, pp. 13-24.

[16]. I. Downes, L. Rad, H. Aghajan, Development of a mote for wireless image sensor networks, in *Proceedings of the Cognitive Systems and Interactive Sensors (COGIS)*, Paris, France, March 2006.

---

# Sensors & Transducers

# A Traffic Flow Based Clustering Scheme for VANETs

**[1] Fan Yang, [2] Zhijian Lin, [3] Yuliang Tang**

Department of Communication Engineering, Xiamen University, Xiamen 361005, China
E-mail: yfh1101@126.com, tyl@xmu.edu.cn

**Abstract:** Recently, vehicular ad hoc networks (VANET) have attracted great interests from both academia and industry. As an extreme case of mobile ad hoc networks (MANET), VANETs have some unique features, such as high node mobility, frequent topology changes and breakages of wireless links. In this paper, we propose a novel traffic flow based (TFB) clustering scheme, aiming to construct stable clusters for urban scenarios. This scheme takes traffic flow, speed difference and node position into consideration, in order to select the most stable cluster head. In addition, only vehicles within the predefined speed difference with the cluster head is allowed to join the cluster. Simulations are conducted to evaluate the performance of this proposed scheme. The results show that the proposed scheme imparts a significant performance improvement in terms of average cluster lifetime and average number of clusters changed per vehicle. *Copyright © 2014 IFSA Publishing, S. L.*

## 1. Introduction

With the rapid development of communication, sensor, and other related technologies, vehicular ad hoc networks are emerging to provide various services to drivers, including safety applications (e.g., emergency or incident warning, lane change assistance, and intersection management), traffic management (e.g., toll collection and intersection management), and user infotainment services (e.g. the Internet access) [1]. Generally, communications in VANETs can be classified into two categories: vehicle-to-vehicle (V2V) and vehicle-to-roadside unit (V2R) communications. Each vehicle in VANETs is equipped with an on-board unit (OBU), which is a wireless interface to communicate with other vehicles as well as roadside units (RSU). Roadside units are stationary network nodes distributed along the road, and they provide the access to the Internet.

The U.S. Federal Communications Commission (FCC) has approved 75 MHz for Intelligent Transportation System (ITS). The licensed 75 MHz (5.850-5.925 GHz) is divided into seven channels. CH178 is designated as the control channel (CCH), which is used for safety-related applications and system management. The other six channels are service channels (SCH) for delivering non-safety messages. Compared to other MANETs, vehicular ad hoc networks are characterized by high node mobility, frequent topology changes and breakages of wireless links. In addition, different applications have different QoS requirements. Generally, safety applications demand the quick and reliable message delivery, while non-safety applications require the high throughput and fair access to the channel [2]. Therefore, it is very challenging to efficiently utilize the resources in VANETs to meet QoS demands of different applications.

Clustering in VANETs is an effective method to simplify some important functions, such as node management, routing, medium access management, resource management and bandwidth allocation. Some clustering-based schemes in VANETs, such as MAC protocols and routing algorithms, have been proposed in the literature. However, it is a key

problem for all these schemes to keep the stability of clusters, due to the high mobility of vehicles in VANETs. In this paper, we propose a novel clustering scheme, aiming to construct stable clusters in urban scenarios. This scheme takes traffic flow, speed difference and node position into consideration, in order to select the most stable cluster head. In addition, only vehicles within the predefined speed difference with the cluster head is allowed to join the cluster.

The rest of this paper is organized as follows: Section 2 presents related works on the clustering algorithm. Section 3 presents the proposed TFB clustering scheme. Section 4 evaluates the proposed scheme through extensive simulations. This paper concludes with Section 5.

## 2. Related Works

The clustering algorithm has been studied in MANETs, and many schemes have been proposed in the literature. However, these schemes are not suitable for VANETs, due to the unique features of VANETs, such as the movement pattern of vehicles, sufficient energy and etc. Therefore, the clustering scheme for VANETs should be designed specifically.

A common clustering scheme in MANETs is the lowest-ID algorithm [3]. In this algorithm, each node is assigned a unique ID, and the node with the lowest ID in its neighborhood is selected as the cluster head. The lowest-ID algorithm proposes a basic method to group nodes into clusters. However, this algorithm does not consider the mobility of nodes. The cluster head needs to be reselected, when the topology of network changes. In an effort to reduce the frequent reselecting of cluster heads, the least cluster change (LCC) scheme is proposed in [4]. In LCC scheme, reselecting of cluster heads only occurs when two cluster heads come into each other's transmission range. Therefore, the stability of clusters is improved.

In order to represent the mobility of nodes, different metrics have been proposed in the literature. One of the most frequently mentioned mobility based algorithm is MOBIC [5]. It is based on the lowest-ID algorithm, and the mobility metric for selecting a cluster head is based on the ratio between successive measurements of the received power at any node from its neighbors. In [6], a new aggregate local mobility (ALM) metric is proposed. In this algorithm, the distance between a node and its neighbors, instead of signal strength, is used to calculate the relative mobility of vehicles. Both of the aforementioned algorithms produce one-hop clusters. A multi-hop clustering algorithm is presented in [7]. It is based on the beacon delay on each node. However, these metrics can't reflect the mobility of vehicles accurately, because the realistic situation of wireless channels is more complex than the ideal model used in these algorithms. Further, these algorithms are not suitable for the urban scenario. They can only work well in the highway scenario.

Currently, most cars on the road are equipped with GPS devices, which can provide the instant movement information, such as direction, speed, position, and etc. Thus, A few algorithms based on the movement information are proposed in the literature. In [8], a direction based algorithm is proposed for the urban scenario. According to the predefined path and the position of vehicles, clusters are formed before the road intersection. However, this algorithm can only be used in some special situations of VANETs, and does not consider the mobility of vehicles. In [9], the authors present an affinity propagation based clustering algorithm. Affinity algorithm is originally used for data clustering. Vehicles exchange the availability and responsibility information with their neighbors, and the cluster head is selected based on the information. However, this algorithm does not take the speed difference of vehicles into consideration. In [10], the authors propose a modified distributed and mobility adaptive clustering algorithm for VANETs. In this scheme, a weight is assigned to each node. The weight of a node is calculated based on a set of parameters, including connectivity, mobility, and etc. As a result, the node with the biggest weight is selected as the cluster node. To increase the stability of clusters, the reclustering process is not performed, when two clusters of vehicles with different directions move into each other's range. In [11], the authors propose a laned-based clustering (LBC) algorithm for the urban scenario. In this algorithm, the metric for a node to be selected as the cluster head is based on the number of lanes in its traffic flow. However, this algorithm does not consider the exact number of vehicles for each flow. In order to improve the stability of clusters, we propose a novel traffic flow based algorithm for the urban scenario. This algorithm takes the number of vehicles for each flow, speed difference, and vehicle position into consideration.

## 3. TFB Scheme

In this section, we discuss the detail operation of the TFB algorithm, including the scenario and system model we consider, the cluster head election algorithm, and the clustering process.

### 3.1. Scenario and Assumptions

We consider the urban scenario with intersections. The traffic flow splits at each intersection. Each intersection has at most three traffic flows: left turn, right turn and straight-going flows [11]. Vehicles in the flow with more vehicles should be given a higher priority to be selected as the cluster head, in order to increase the stability of the cluster. Fig. 1 shows a road with 4 lanes. Lane 1 is the left-turn lane with 3 cars. Lane 2 and 3 are straight-going lanes with 9 cars in total. Lane 4 is the

right-turn lane with 2 cars. Obviously, the cluster head should be selected from the cars on Lane 2 or 3, so that fewer cars leave the cluster after crossing the intersection.

Each vehicle on the road is equipped with a GPS device, by which it knows its instant movement information, such as position, speed and direction. However, GPS has a 5 meters error which is larger than the distance between lanes [11]. Several other techniques have been proposed in the literature to help detect lanes on the road. One method is to adopt the GPS combined with a wheel odometer [12]. The wheel odometer can detect the vehicle's movement on the order of tenths of millimeters [11]. Besides, the methods that do not use GPS can also detect lanes on the road [13-15]. Through the aforementioned methods, every vehicle in the system knows its lane number.
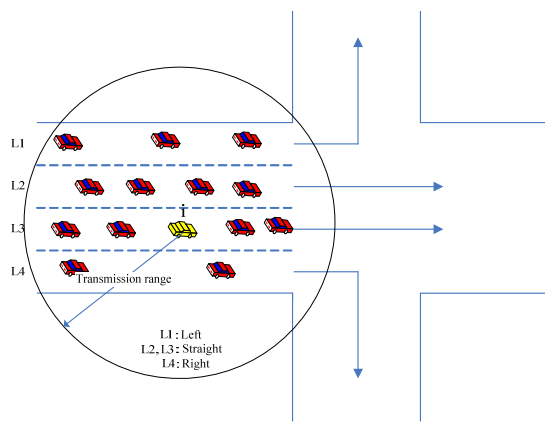


**Fig. 1.** Application scenario.

Each vehicle in the system is assigned a distinct ID, and periodically broadcasts its current movement information, including its speed, position direction, and lane number, to other vehicles within its transmission range. These vehicles in the transmission range are neighbors of this node (the terms "node" and "vehicle" are used interchangeably throughout this paper). The interval between two consecutive broadcasts is $T$. The priority of a node to be selected as the cluster head is calculated based on the movement information of its neighbors. In each cluster, a node is selected to be the cluster head (CH) and the other nodes are cluster members (CM). Nodes in the system can operate on the following states: cluster head, cluster member, isolation node, and temporary member. The state transition diagram is shown in Fig. 2.

1) Cluster head: a node that is selected to manage a cluster.

2) Cluster member: a node that belongs to a cluster.

3) Isolation node: a node that does not belong to any cluster.

4) Temporary member: a node that does not receive a packet from the cluster head for once.
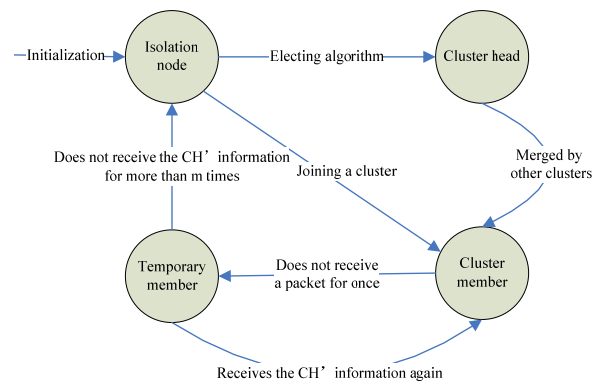


**Fig. 2.** State transition diagram.

### 3.2. Cluster Head Election Algorithm

Each node in the network periodically broadcasts its movement information, including the speed, position, lane number and direction to its neighbors. The cluster head is selected based on the information. In order to increase the stability of a cluster, nodes with different directions form different clusters. Only the nodes with the same direction can join a cluster. In the following, we only discuss the neighbors with the same direction with node $i$. For node $i$, let $v_i$ denote its speed, $p_i$ its position, and $l_i$ its lane number. Then, a function $pr_i = g(v_i, p_i, l_i)$ is defined to compute the priority that node $i$ is selected as the cluster head. Every node computes its priority, and broadcasts the priority with the movement information. The node $i$ with the smallest $pr_i$ in the neighborhood is selected as the cluster head.

### 3.2.1. Traffic Weight

Different traffic flows lead to different directions, and they will split after the intersection. In order to reduce the number of vehicles that leave the cluster, vehicles in different traffic flows should be given different weights to be selected as the cluster head. Here, we divide the neighbors with the same direction of node $i$ into three sets: set $S_L$ of the left-turn nodes, set $S_R$ of the right-turn nodes, and set $S_S$ of the straight-going nodes. The number of nodes in each set is denoted as $N_L$, $N_R$ and $N_S$ respectively. The total number of neighbors with the same direction of node $i$ is denoted as $N$. The flow where node $i$ resides should be given the most weight. The weight for any other traffic flow is determined by the number of neighbors in this flow and the total number of its neighbors. Let $j$ denote the flow where node $i$ resides. Then, the weight for each flow can be calculated as

$$W_i^k = \begin{cases} 1, & k = j \\ \dfrac{N_k}{N}, & k \neq j \end{cases}, k \in (L, R, S), \qquad (1)$$

where $k$ is the index of flows, $k \in (L, R, S)$. For example, we have a road of 4 lanes as illustrated in Fig. 1. Lane 1 is the left-turn lane, Lane 2 and 3 the straight-going lanes, and Lane 4 the right-turn lane. For node $i$, its transmission range covers all the other nodes in Fig. 1. Then, the weight for each flow is $\frac{3}{14}$, 1 and $\frac{2}{14}$ respectively.

### 3.2.2. Speed Difference

Speed difference is a key factor that determines the stability of a cluster. The node with the closer speed to its neighbors should be given the higher priority to be selected as the cluster head. When node $i$ receives its neighbors' movement information, it calculates the average speed of each traffic flow as follows

$$u_i^k = \frac{\sum_{j=1}^{N_k} v_j}{N_k}, k \in (L, R, S),\qquad(2)$$

where $N_k$ is the number of nodes in traffic flow $k$, $u_i^k$ is the average speed of traffic flow $k$, and $v_j$ is the speed of node $j$. Then, node $i$ calculates the speed difference between itself and the average speed of each flow, and the normalization technique is used to avoid that one parameter dominates the result of calculation. Let $v_{\max}^k$ denote the maximum speed of flow $k$. Then, the normalized speed difference $v_i^{k_{norm}}$ with each flow is computed by

$$v_i^{k_{norm}} = \left| \frac{v_i - u_i^k}{v_i - v_i^{k_{\max}}} \right|, k \in (L, R, S)\qquad(3)$$

For node $i$, the weight of speed difference with each flow is different, because the vehicles in different flow split after crossing the intersection. The flow where node $i$ resides should be given the most weight. Then, for node $i$, the overall speed difference with its neighbors is

$$v_i^{norm} = \sum W_i^k v_i^{k_{norm}}, k \in (L, R, S)\qquad(4)$$

### 3.2.3. Position

Node position is another factor we consider when selecting the cluster head. The node with a closer distance to the mean position of its neighbors should be given the higher priority to be selected as the cluster head. Let $(x_j, y_j)$ denote the position coordinate of node $j$. Then, the mean position of each flow is

$$x_i^{k_u} = \frac{\sum_{j=1}^{N_k} x_j}{N_k}, y_i^{k_u} = \frac{\sum_{j=1}^{N_k} y_j}{N_k}, k \in (L, R, S)\qquad(5)$$

Let $(x_i^{k_{\max}}, y_i^{k_{\max}})$ denote the node position that has the longest distance with the mean position $(x_i^{k_u}, y_i^{k_u})$. Then, the normalized distance with the mean position of each flow is

$$d_i^{k_{norm}} = \frac{\sqrt{(x_i - x_i^{k_u})^2 + (y_i - y_i^{k_u})^2}}{\sqrt{(x_i^{k_{\max}} - x_i^{k_u})^2 + (y_i^{k_{\max}} - y_i^{k_u})^2}}, k \in (L, R, S)\qquad(6)$$

Then, for node $i$, the distance with its neighbors is

$$d_i^{norm} = \sum W_i^k d_i^{k_{norm}}, k \in (L, R, S)\qquad(7)$$

Therefore, the priority $pr_i$ of node $i$ can be calculated as

$$pr_i = v_i^{norm} + d_i^{norm}\qquad(8)$$

### 3.3. Clustering Process

The clustering scheme consists of 6 processes: initialization, joining process, cluster head electing process, losing contact with the CH temporarily, leaving process and merging process.

1) Initialization: When a vehicle enters the road, it is initialized as the isolation node.

2) Joining process: Every CH broadcasts the *invite-to-join* message (ITJ) together with its movement information every $T$ period. Once an isolation node receives an ITJ message, it checks whether the CH's direction is the same with itself. Then, it checks whether the speed difference between the CH and itself is within $\pm \Delta V_{th}$. If the direction is the same and the difference is within $\pm \Delta V_{th}$, it sends a *request-to-join* message (RTJ) to the CH. After the CH receives the RTJ message, it sends back an acknowledge (ACK) and accepts the node as a cluster member. If a node receives more than one ITJ, it sends the RTJ to the CH with the smallest speed difference.

3) Cluster head electing process: If an isolation node does not receive any ITJ message during $T$ period, it starts the cluster head electing process. It gathers the information of its neighboring isolation nodes and the proposed algorithm is used to select the cluster head as described in Section 3.2. The isolation node within a CH' transmission range $R_T$ is not allowed to start the head electing process, in order to reduce the number of clusters on the road.

4) Losing contact with the CH temporarily: When a CM does not receive the information broadcasted by the CH every $T$ period, the state of this node changes from cluster member to temporary member.

It does not leave the cluster immediately, because this disconnection may be due to the poor quality of the wireless link. If the temporary member receives the information broadcasted by the CH again in the next $mT$ period, the state changes to CM again.

5) Leaving process: When a temporary member does not receive the CH' information consecutively for $m$ times, the state of this node changes to the isolation node. Meanwhile, the CH will delete this member from the member list.

6) Merging process: When two cluster heads come into each other's transmission range, the cluster merging process holds. The cluster head with less members gives up the role of cluster head and joins the cluster with more members. The other members of the cluster head either join the neighboring clusters or form new clusters.

## 4. Simulation Results

Simulations were conducted in NS-2 simulator (version 2.35), to evaluate the performance of the proposed clustering scheme. In addition, Simulation of Urban Mobilty (SUMO) was used to produce the simulation scenario and the traffic flow. SUMO is an open source, microscopic and continuous road traffic simulation package designed to handle large road networks. It is developed by the Institute of Transportation Systems at the German Aerospace Center. There are 400 cars on the road, and the speed of cars ranges from 0-80 km/h. We compare the simulation results with the LBC algorithm proposed in [11], because it considers the same scenario with the proposed TFB algorithm. Two metrics are defined as follows to evaluate the stability of the proposed algorithm.

1) *Average cluster head lifetime* ( *ACHL* ): the average time period from the moment when a vehicle becomes a cluster head to the time when it is merged by anther cluster head. Long cluster head time implies the high stability of the cluster.

$$ACHL = \frac{\sum_{i=1}^{n}(t_i^m - t_i^b)}{n},$$

where $n$ is the number of clusters formed during the simulation time, $t_i^b$ is the time when cluster $i$ is built, and $t_i^m$ the time when cluster $i$ is merged.

2) Average number of clusters changed per vehicle ( *ANCC* ): the average number of clusters changed per vehicle during the simulation.

$$ANCC = \frac{\sum_{i=1}^{m} c_i}{m}$$

where $m$ is the number of vehicles, and $c_i$ the number of cluster changes of vehicle $i$ during the simulation.

Fig. 3 and Fig. 4 illustrate the average cluster head lifetime of the proposed algorithm and TFB algorithm. The results show that the average cluster head lifetime is significantly increased, when the proposed algorithm is adopted. This is because the probability that a CH leaves its cluster decreases, when the proposed algorithm is adopted. The vehicles in the major traffic flow have higher probability to be selected as the CH. Thus, the CH is more stable, after crossing the intersection. In addition, with the increase of transmission range, the average cluster head time increases. This is because more members can join a cluster, when the transmission range increases. Thus, the probability that the cluster is dismissed decreases.
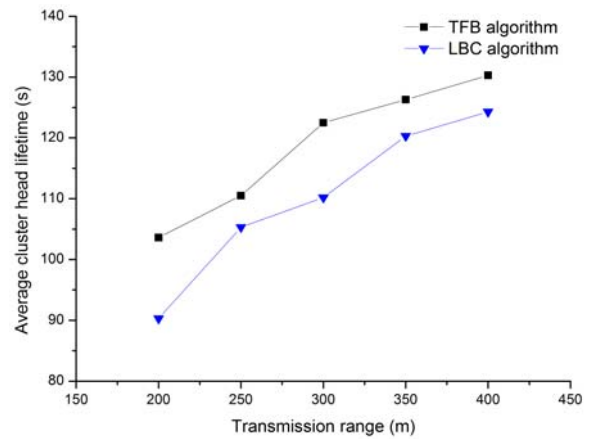


**Fig. 3.** Average cluster head lifetime vs. transmission range, with $\Delta v_{th} = 20 km/h$ .
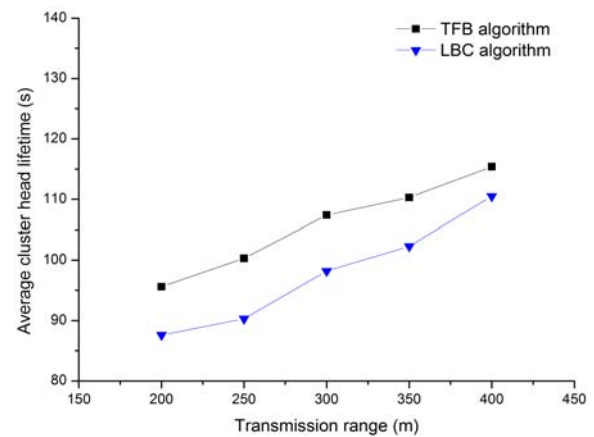


**Fig. 4.** Average cluster head lifetime vs. transmission range, with $\Delta v_{th} = 30 km/h$ .

Fig. 5 and Fig. 6 compare the average number of clusters per vehicle of the proposed algorithm and TFB algorithm. The average number of clusters per vehicle is decreased, when the proposed algorithm is adopted. This is because the probability that a cluster is dismissed decreases, when the proposed algorithm is adopted. Thus, the time when a CM stays in the same cluster is longer than that of TFB. In addition,

114

with the increase of transmission range, the average number of cluster changes becomes smaller. This is because the probability that a cluster member leaves its cluster decreases, when the transmission range becomes bigger.
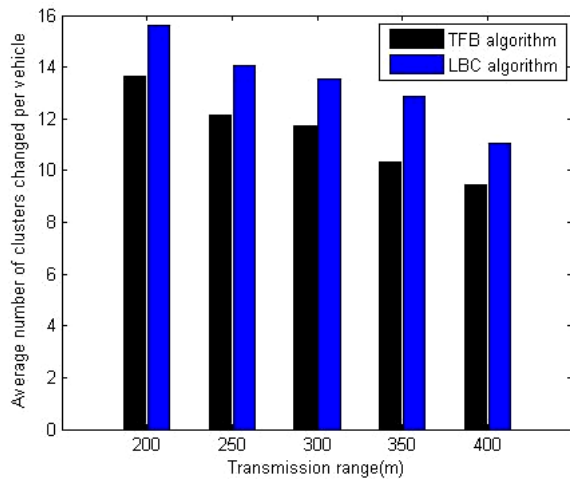


**Fig. 5.** Average number of clusters changed per vehicle vs. transmission range, with $\Delta v_{th} = 20km/h$ .
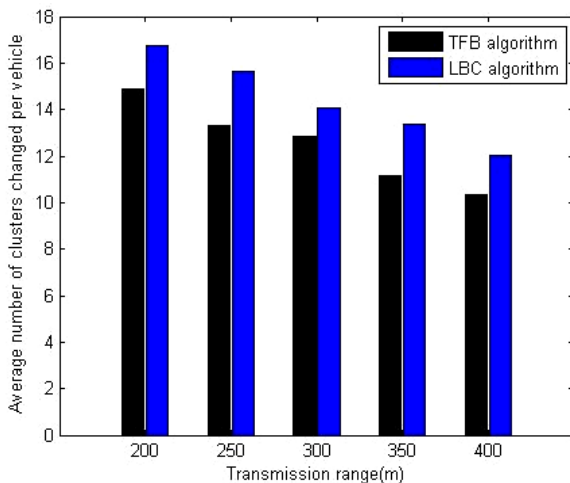


**Fig. 6.** Average number of clusters changed per vehicle vs. transmission range with $\Delta v_{th} = 30km/h$ .

## 5. Conclusions

In this paper, we propose a traffic flow based clustering algorithm, aiming to form stable clusters in urban scenarios. Traffic flow, speed difference and position of vehicles are taken into consideration in this algorithm. Vehicles in the major traffic flow are given higher priority to be selected as the cluster head. The simulation results show that the proposed algorithm significantly increases the stability of a cluster, compared to the existing algorithms.

## Acknowledgements

## References

[1]. M. J. Booysen, S. Zeadally, G. J. van Rooyen, Survey of media access control protocols for vehicular ad hoc networks, *IET Communications*, Vol. 5, 2011, pp. 1619-1631.

[2]. Y. Bi, K. Liu, L. X. Cai, X. Shen, A multi-channel token ring protocol for QoS provisioning in inter-vehicle communications, *IEEE Transaction on Wireless Communications*, Vol. 8, 2009, pp. 5621-5631.

[3]. C. Lin, M. Gerla, Adaptive clustering for mobile wireless networks, *IEEE Journal on Selected Areas in Communications*, Vol. 15, 1997, pp. 1265-1275.

[4]. C.-C. C. Hsiao-Kuang, C. Chan Chiang, H. Kuang Wu, W. Liu, M. Gerla, Routing in clustered multihop mobile wireless networks with fading channel, in *Proceedings of the IEEE Singapore International Conference on Networks*, 1997.

[5]. P. Basu, N. Khan, T. D. C. Little, A mobility based metric for clustering in mobile ad hoc networks, in *Proceedings of the International Conference on Distributed Computing Systems Workshop*, 2001, pp. 413-418.

[6]. E. Souza, A new aggregate local mobility clustering algorithm for VANETs, in *Proceedings of the International Conference on Communications (ICC)*, 2010, pp. 1-5.

[7]. Z. Zhang, A novel multi-hop clustering scheme for vehicular ad-hoc networks, in *Proceedings of the 9th ACM International Symposium on Mobility Management and Wireless Access*, 2011, pp. 19-26.

[8]. N. Maslekar, M. Boussedjra, J. Mouzna, H. Labiod, A stable clustering algorithm for efficiency applications in VANETs, in *Proceedings of the 7th International Wireless Communications and Mobile Computing Conference (IWCMC)*, 2011, pp. 1188-1193.

[9]. C. Shea, B. Hassanabadi, S. Valaee, Mobility-based clustering in VANETs using affinity propagation, in *Proceedings of the IEEE Telecommunications Conference (GLOBECOM)*, 2009, pp. 1-6.

[10]. G. Wolny, Modified DMAC clustering algorithm for VANETs, in *Proceedings of the 3rd International Conference on Systems and Networks Communications*, 2008, pp. 268-273.

[11]. M. S. Almalag, M. C. Weigle, Using traffic flow for cluster formation in vehicular ad-hoc networks, in *Proceedings of the 35th Annual IEEE Conference on Local Computer Networks*, 2010, pp. 631-636.

[12]. A. J. Dean, S. N. Brennan, Terrain-based road vehicle localization on multi-lane highways, in *Proceedings of the American Control Conference*, 2009, pp. 707–712.

[13]. M. Jabbour, P. Bonnifait, V. Cherfaoui, Enhanced local maps in a GIS for a precise localisation in urban area, in *Proceedings of the 9th IEEE Conference on Intelligent Transportation Systems (ITSC)*, 2006, pp. 468 - 473.

[14]. C. D. McGillem, T. S. Rappaport, A beacon navigation method for autonomous vehicles, *IEEE*

*Transactions on Vehicular Technology*, Vol. 38, 1989, pp. 132–139.

[15]. T. Oskiper, Z. Zhu, S. Samarasekera, R. Kumar, Visual odometry system using multiple stereo cameras and inertial measurement unit, in *Proceedings of the Computer Vision and Pattern Recognition*, 2007, pp. 1 - 8.

_____

# Multi-Agent Based Microscopic Simulation Modeling for Urban Traffic Flow

[1, 2, *] **Xianyan Kuang**, [1] **Lunhui Xu**, [1, 2] **Cuiqin Wu**, [1] **Yinfeng Wu**

[1] School of Electrical Engineering and Automation, Jiangxi University of Science and Technology, Ganzhou, Jiangxi, 341000, China
[2] School of Civil Engineering and Transportation, South China University of Technology, Guangzhou, Guangdong, 510640, China
[*] E-mail: xianyankuang@163.com

**Abstract:** Traffic simulation plays an important role in the evaluation of traffic decisions. The movement of vehicles essentially is the operating process of drivers, in order to reproduce the urban traffic flow from the micro-aspect on computer, this paper establishes an urban traffic flow microscopic simulation system (UTFSim) based on multi-agent. The system is seen as an intelligent virtual environment system (IVES), and the four-layer structure of it is built. The road agent, vehicle agent and signal agent are modeled. The concept of driving trajectory which is divided into LDT (Lane Driving Trajectory) and VDDT (Vehicle Dynamic Driving Trajectory) is introduced. The "Link-Node" road network model is improved. The driving behaviors including free driving, following driving, lane changing, slowing down, vehicle stop, etc. are analyzed. The results of the signal control experiments utilizing the UTFSim developed in the platform of Visual Studio. NET indicates that it plays a good performance and can be used in the evaluation of traffic management and control. *Copyright © 2014 IFSA Publishing, S. L.*

## 1. Introduction

The traffic system simulation is to reproduce the spatiotemporal evolution of traffic flow using the system simulation and system modeling technologies, and to investigate the traffic behavior. The traffic flow state variables changed with time and space, the relationship between the traffic flow state variables and the traffic control variables can be achieved through the traffic system simulation research. The traffic system simulation can provide technical supports for the traffic design and traffic management as well as the evaluation of the traffic influence on the environment.

According to the different levels of traffic simulation models in describing traffic systems, traffic simulation models can be divided into macroscopic, mesoscopic, and microscopic models [1]. The macroscopic simulation models investigate the relationship between velocity, density and volume by observing road network traffic flow characteristics, and describe some clustering phenomenon of traffic flow. But the description about elements, entity, behavior and their interactions in traffic system is very rough. The microscopic simulation models combine some aspects of the macroscopic models and describe the traffic various elements in great detail. In the microscopic traffic

simulation, the basic unit is a single vehicle, and the vehicle microscopic behaviors such as following, overtaking and lane changing can be reproduced particularly and factually by means of computer animation. The description of mesoscopic models is between the macroscopic and microscopic models.

In recent years, the modeling and using of the microscopic traffic simulation have become more and more popular in transportation modeling [2]. An open-source microscopic traffic simulator [3] is presented which focuses on investigating fundamental issues of traffic dynamics. A microscopic simulation model (named as MITSIMLab) is developed in [4]. Burghout [5] presents a hybrid mesoscopic-microscopic model that applies microscopic simulation to areas of specific interest while simulating a large surrounding network in less detail with a mesoscopic model. Cai [6] presents the microscopic traffic simulation models by integrating the geographic information system (GIS) and microscopic traffic simulation. Chen [7] analyzes the capacity impact of weaving sections caused by exclusive bus lanes (XBLs) on urban expressways with a microscopic traffic simulation approach. A microscopic model for the study of operations at public transport stops is built in [8]. Liu [9] proposes a microscopic traffic model which is composed of a road model and a vehicle behavior model.

Traffic system is composed of people, vehicles, road and traffic environment. The traffic simulation system is a typical multi-agent-based system (MABS) [10]. Paper [11] builds a multi-agent behavioral model and designs a road traffic simulation tool able to deal realistically with road junctions. A continuous microscopic traffic simulation approach with activity-based agent behavior is introduced in [12]. Fujii [13] develops a traffic simulator named MATES based on intelligent multi-agent model and coordinative behavior model. A framework with three-level Petri net for urban traffic systems microscopic simulation based on agent is presented in [14].

In this paper, we attempt to establish a multi-agent based urban traffic flow microscopic simulation system (MAB-UTFSim). Firstly, the structure of this system including four layers is built. Then the agents in this system are modeled. We introduce the concept of driving trajectory, improve the "Link-Node" road network model, and analyze in detail the driving behaviors of drivers on the urban traffic road. Finally, we develop the UTFSim and do some experiments which reveal the good performance of this system.

## 2. Structure of the Multi-agent Based Traffic Simulation System

The structure of the traffic simulation system based on multi-agent is shown in Fig. 1.

The structure is divided into four layers:

Layer 1 is the bottom called computer environment layer, which provides the software and hardware supports for the operation of the simulation system, including the operating system, database, graphics card, etc. This layer is the carrier of the simulation system.

Layer 2 is the visual layer of simulation. The real-time running states of traffic simulation are shown in the form of 2D or 3D dynamic images. In this layer, the mapping relationship between the coordinate systems of simulation system and computer display system will be built, and the graphics and image technologies such as GDI (Graphics Device Interface), DirectX, OpenGL etc. will be used to show the running process of traffic flow simulation.

Layer 3 is the agent layer: This layer is the core of the traffic simulation system which contains all kinds of agent entities such as management agent, road agent, vehicle agent, signal agent, etc. Agents interacte with the specific communication mechanism.

Layer 4 is the human-computer interface layer. In this layer, user can customize the environment of simulation system and set the simulation parameters, the results can be provided.
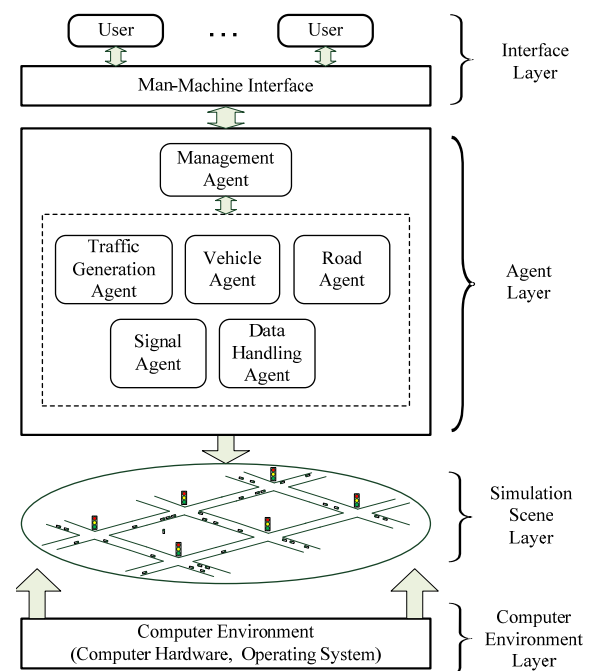


**Fig. 1.** Structure of multi-agent based traffic simulation system.

## 3. Multi-agent-based Traffic Simulation Modeling

### 3.1. Road Agent

The road is composed of nodes and links (Roads between the adjacent nodes). Node usually is a junction or intersection in the urban road. Link is

composed of one or more segments which consist of several lanes. The traffic signs and markings which indicate the functions and traffic rules of each node and link attach in the road. The nodes and links as well as their traffic rules can be abstracted as the road model named classically as Node-Link model. This road model is detailed in Fig. 2.

Road agent can be composed of node agent and segment agent for the road consists of one or more nodes and segments.
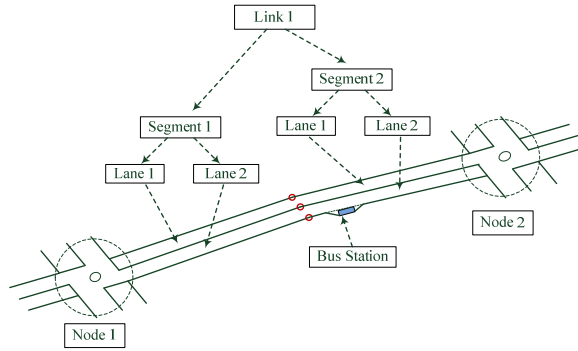


**Fig. 2.** Road model.

### 3.1.1. Driving Trajectory

In order to express the driving behavior and the constraint relationship between vehicles in the simulation road, we introduce the concept of driving trajectory (DT) which is the moving trajectory of the center projection point of the vehicle on the road. Driving trajectory can be divided into lane driving trajectory (LDT) and vehicle dynamic driving trajectory (VDDT), shown as Fig. 3.
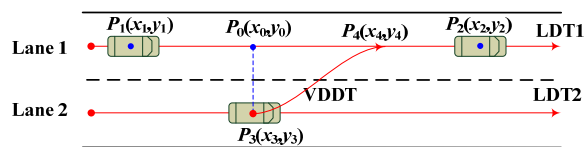


**Fig. 3.** Driving trajectory.

LDT: LDT belongs to a lane or a node and can be used to drive by the vehicles. The virtual center line of each lane is identified as LDT. The center projection point of the simulation vehicle is in the LDT. LDT is determined by the road geometry. If two lanes that belong to different node or segment are connected, the LDT of these two lanes will be end to end. Each LDT have one or more upstream LDT and downstream LDT, the end point of upstream LDT and the starting point of downstream LDT are overlapping. In Fig. 3, the LDT of Lane 1 is LDT1, and the LDT of Lane 2 is LDT2.

VDDT: The VDDT of vehicle is temporarily dynamically generated according to the driving

conditions when the vehicle needs to change lane. The VDDT is a curve which joins the LDT of current lane and the LDT of neighbouring target lane. The starting point of VDDT is the vehicle's position in the LDT of current lane when vehicle starts to change lane. The end point of VDDT is in the LDT of the neighbouring target lane, and is related to vehicle speed and lane changing time.

### 3.1.2. Node

The node in the road model usually is the plane intersection which can have three-leg, four-leg or five-leg. The structure model of a typical four-leg intersection is depicted in Fig. 4.
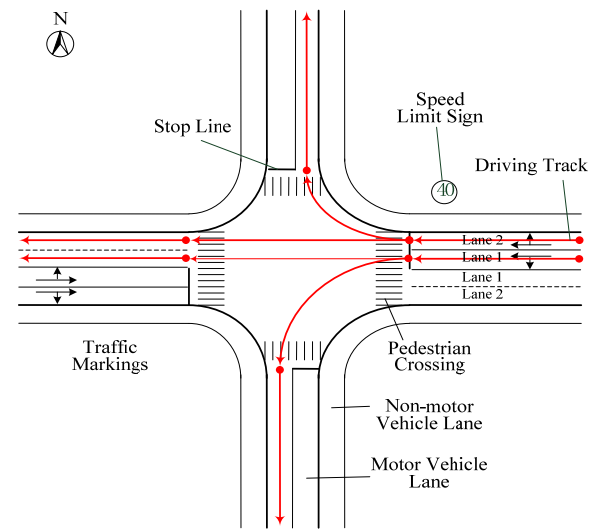


**Fig. 4.** The four-leg intersection node.

The intersection node consists of several legs and the weaving area. The leg of intersection usually is a segment from the stop line to the upstream somewhere. The vehicles come from upstream can't change lane when drive into this segment. Each lane of this segment has one LDT, as an example, the LDT of the east import lane is shown with an arrow line in Fig. 4.

The weaving area of the intersection is an area surrounded by the stop lines of all legs and the road edge. There are three traffics which come from each import lane to pass the intersection: through, left-turn and right-turn traffic. In the weaving area of the intersection, there are multiple LDT, of which the starting point is the end point of the import lane LDT on an approach to the intersection, and the end point is the starting point of the export lane LDT on another approach to the intersection.

The total number of LDT in the 4-leg intersection is as following:

$$N = N_{leg} + N_{weaving}, \tag{1}$$

$$N_{leg} = \sum_i n^i , \qquad (2)$$

$$N_{weaving} = \sum_i (n^i_{through} + n^i_{left} + n^i_{right}) , \qquad (3)$$

where $i=1, 2, 3, 4$, represent the four legs: east, south, west and north respectively. $N_{leg}$ is the total number of LDT of all lanes on all legs, and is equal to the total number of all import and export lanes on all legs. $N_{weaving}$ is the number of LDT in weaving area. $n^i_{through}$ is the number of lanes of through traffic. Correspondingly, $n^i_{left}$ and $n^i_{right}$ are respectively the numbers of lanes of left-turn and right-turn traffic.

### 3.1.3. Link

The link is the road between two adjacent nodes, consists of one or more segment. The segment has three types according to the segment structure: linear, curve, and linear with bus stops. The LDT of each lane on linear segment is the center line. The LDT of each lane on curve segment is also the center curve.

### 3.2. Traffic Generating Agent

The traffic on the simulation road network is generated by the traffic generating agent according to the traffic volume of each road entry. When the vehicle is generated, the parameters, such as vehicle type, geometric parameters, speed, maximum acceleration, travel route, and so on, need to be initialized. The travel route of vehicles in the simulation road network is an important parameter. If the OD trips or the destinations of each vehicle are given, the travel route can be achieved using the shortest path algorithm such as Dijkstra algorithm.

### 3.3. Vehicle Agent

The vehicle on the road is controlled by the driver, so each vehicle in the simulation system is a driver-vehicle-agent-unit (DVAU). The structure of vehicle agent is shown in Fig. 5.

Each DVAU has the following features:

1) Attributes: There are two types of attributes: static attributes and dynamic attributes. The static attributes of DVAU consist of the type, geometry, maximum speed, maximum acceleration of vehicles, and the age, driving experience, personality types (radical or steady), degree of travel emergency, reaction time of drivers, and so on. Dynamic attributes of DVAU consist of the position, speed and acceleration of vehicles.

2) Perception: The DVAU can percept the situations around such as road, other vehicles, and environment. The perception ensures the driving safety.

3) Behaviors: The behaviors of DVAU can be divided into internal behaviors and external behaviors. The internal behaviors are to adjust the changes of dynamic driving attributes which mainly include free driving, following driving, lane changing, slowing down and vehicle stop et. The external behaviors are usually the communication behaviors and interaction behaviors with other agents and the traffic environment.
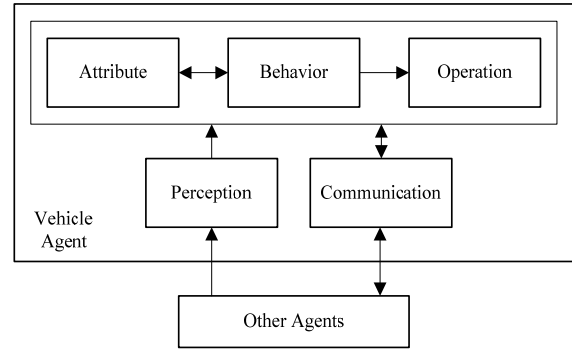


**Fig. 5.** The structure of vehicle agent.

### 3.4. Driving Behavior Model

The driving behaviors conclude free driving, following driving, lane changing, slowing down, vehicle stop, etc.

### 3.4.1. Free Driving

When the distance between the vehicle and the vehicle in front $\Delta D$ is greater than a certain threshold $\Delta D_0$, the vehicle is not affected by the vehicle in front, the free speed $V_f$ is a desired speed of drivers in free driving, and is restricted only by the structure of the road and the legal speed, influenced by the driver's driving habits and the degree of travel emergency. In the simulation system, the probability density function of $V_f$ which is a random variable is determined by the Gaussian function:

$$f(V_f) = \frac{1}{\sqrt{2\pi}\sigma} \exp(-\frac{(V_f - V_{f0})^2}{2\sigma^2}) , \qquad (4)$$

where $V_f$ is the free speed of vehicle, $V_{f0}$ is the average free speed, $\sigma$ is the standard deviation.

In order to achieve the $V_f$ from Gaussian function, Eq. (4) needs to be transformed by the following equation:

$$V_f = V_{f0} + \sqrt{\sigma(-2\ln u_1)} \cos 2\pi u_2 , \qquad (5)$$

where $u_1$ and $u_2$ are the independent standard uniform random number between 0 and 1 respectively.

When the speed $V$ of the vehicle is less than $V_f$, it will accelerate to the free speed $V_f$ with the acceleration $a$. Generally the acceleration is larger at low speed and is smaller at high speed that can use the following model [15]:

$$a = \begin{cases} 1.1 m/s^2, & V < 12.19 \text{m/s} \\ 0.37 m/s^2, & V \geq 12.19 \text{m/s} \end{cases} \quad (6)$$

### 3.4.2. Following Driving

When $\Delta D$ is less than $\Delta D_0$, the vehicle will be restricted by the vehicle in front in the case of no overtaking, the vehicle is in the following driving. The stimulus-response model is the typical representative of the following driving and is expressed as following:

$$a(t+T) = \frac{cV^m(t+T)}{\Delta D^l(t)} \Delta V(t), \quad (7)$$

where the $c, m, l$ are the constant; $T$ is the reaction time of driver; $\Delta V(t)$ is the speed difference between the leader vehicle and following vehicle at the time $t$; $\Delta D(t)$ is the distance between the leader vehicle and following vehicle at the time $t$; $V(t+T)$ is the speed of the following vehicle at the time $t+T$.

### 3.4.3. Lane Changing

Lane changing is an important behavior in vehicle driving [16]. According to the requirements of drivers, there are two types of lane changing: "Essential" and "Desirable". "Essential" is that the vehicle has to change lane to the determined target lane in a certain site. "Desirable" is that the lane changing behavior is based on the driver individual desire.

The process of lane changing is illustrated in Fig. 3. Assume $d_{ij}$ is the distance between the point $P_i$ and $P_j$, if the driving direction of LDT2 is the same as the positive direction of $X$ axis, the curvilinear equation of VDDT of vehicle 3 is as following:

$$y = \frac{d_{03}}{2} \sin(\frac{\pi}{d_{04}} x + x_3 + \frac{d_{04}}{2}) + y_3 + \frac{d_{03}}{2} \quad (8)$$

### 3.4.4. Slowing Down

Lane changing is an important behavior in vehicle.

The behavior of slowing down has three situations on non-following status: slowing down for conflict, slowing down for speed limit, and slowing down for vehicle stop.

1) Slowing down for conflict.

The conflict usually occurs in the intersection. If the two or more driving trajectories are crossed, the vehicles will conflict passing through this site. The deceleration of the vehicle before the conflict point in the driving trajectory without priority is expressed as

$$a = \frac{(v - v_{low})^2}{d_c - d_0}, \quad d_c = vT_b + d_0, \quad (9)$$

where $d_c$ is the distance to the conflict point, $d_0$ is the minimum safe stopping distance to the conflict point, $d_0 = 2m$, $T_b$ is the buffer time from the higher speed to lower, $T_b = 3.0s$, $v_{low}$ is the desired low speed in $d_0$ away from the conflict point, $v_{low} = 0s$ for the non-priority vehicles.

2) Slowing down for speed limit.

The urban road usually has the provisions of speed limit, especially on the site with bend, slope or traffic incident. If the speed $v$ of a vehicle is higher than the limit speed $v_{limit}$ of the road ahead, the vehicle needs to start slow down at the distance $d$ away from the road ahead, $d = vT_b$. The deceleration $a$ of the vehicle is described as following:

$$a = (v - v_{limit})^2 / d \quad (10)$$

3) Slowing down for vehicle stop.

The vehicle, which is the first one before the stop line at the signalized intersection during the red signal, or in front of which there is stop sign or queue, needs to start slow down to stop at the distance $d$ away from stop point, also, $d = vT_b$. The deceleration $a$ is described as following

$$a = v / T_b \quad (11)$$

### 3.5. Signal Agent

In the traffic signal control system, the signal of each intersection is seen as an agent named signal agent. The signal parameters, such as cycle, phase and so on, are adjusted through the perception of traffic flow at the intersection as well as the coordination and cooperation with the adjacent signal agents.

### 3.6. Communication and Coordination of Multi-Agent System

The group way is used in this traffic simulation system (shown in Fig. 6).

An agent group consists of a node agent or a segment agent, vehicle agents and signal agent in the node or segment. A group management agent is

created to provide the service of communication for those agents in the agent group.
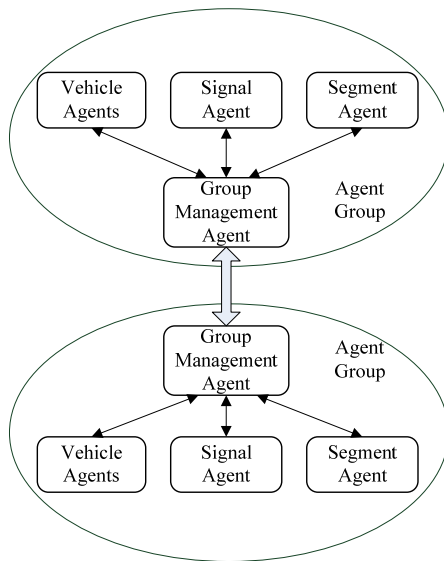


**Fig. 6.** Communication mode between agents.

## 4. Simulation Procedure

The simulation procedure (shown in Fig. 7) includes simulation parameters configuration, simulation running and analysis and output of results.
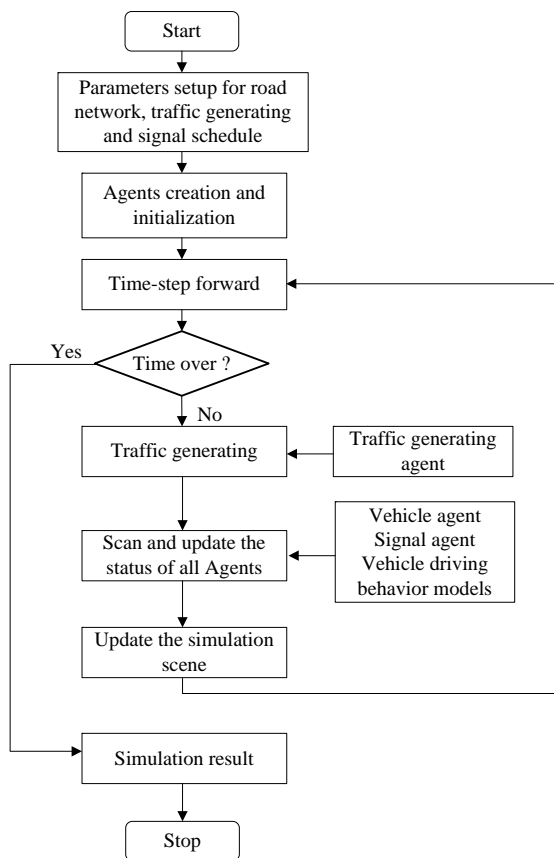


**Fig. 7**. Simulation procedure.

## 5. Experiments

The UTFSim is developed in the platform of Visual Studio. NET, a sample screen shot of UTFSim system is shown in Fig. 8.



**Fig. 8.** A sample screen shot of UTFSim.

### 5.1. Signal Control Experiments of Single Intersection

The intersection for experiment is a typical four-legs signalized intersection. On each approach of this intersection, there are two through lanes, one left-turn lane and one right-turn lane, the width of each lane is 3.2 m and the length is 150 m. Lane changing which should be accomplished far away from the stop line is prohibited before the stop line of 50 m. In the signal control scheme, there are four phases, that are east west through phase, east west left-turn phase, south north through phase and south north left-turn phase.

The experiments of capacity and delay are accomplished to the intersection using the UTFSim. In the experiments of capacity, the Webster method is adopted for the signal timing, the signal cycle increases gradually from the shortest cycle. The experiments test the maximum number of vehicles passing through in various cycles, and the results are shown as Fig. 9. In the experiments of delay, the total volume of the intersection is fixed (assume 3000 $vh/h$, large vehicles accounted for 10 %, cars 90 %), the signal cycle increases similarly from the shortest cycle. The experiments test the mean delays of the intersection with different cycle, and the results are shown as Fig. 10.

From the simulation system, we can observe that the movement behaviors of simulation vehicles such as following, stop, accelerating and lane changing, etc., are consistent with the actual, the vehicle driving is smooth and nature. The results of capacity in Fig. 9 indicate that, in the anterior part of the curve, capacity increases more obviously with the increasing of cycle, however, in the hinder part, capacity increases very slowly. The results of delay in Fig. 10 indicate that, the delay decreases first and

then increases as cycle increase, especially when the cycle is small, the delay will be very large for the capacity is less than the arrival volume. When the cycle is large, the delay increases for the long green time causes the long waiting time of the vehicles in the red phase.
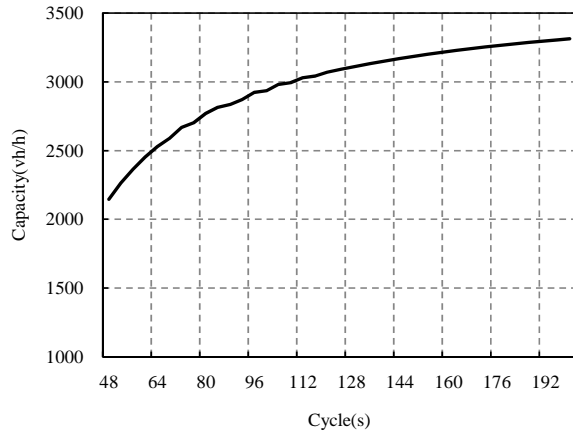


**Fig. 9.** Results of capacity.
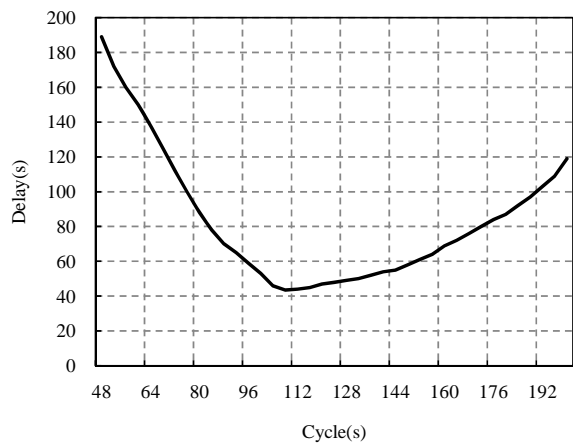


**Fig. 10.** Results of delay.

### 5.2. Signal Control Experiments of Multi Intersections

The signal control experiments of multi intersections are shown in Fig. 8. The road includes three intersections. The main road is east-west direction. In the case of three coordination control modes which are no coordination, one-way coordination and two-way coordination, the experiments are accomplished with the UTFSim. The results are shown in Table 1.

The results indicate that the mean delays of the main road with coordination control are less obviously than without coordination control, meanwhile, the mean delays of whole road decline. The two-way coordination is better than the one-way coordination in declining the mean delay of the main road.

**Table 1.** Delay in the simulation for multi intersection.

| Coordination control mode | The mean delay of the main road (s) | The mean delay of whole road (s) |
|---|---|---|
| Without coordination | 106.8 | 71.5 |
| One-way coordination | 76.3 | 62.8 |
| Two-way coordination | 66.9 | 56.7 |

## 6. Conclusions

An urban traffic flow microscopic simulation system (UTFSim) is established based on multi-agent which can describe the relationships and interactions between vehicles, vehicles and traffic facilities. The urban traffic simulation system consists of four layers: computer environment layer, visual layer, agent layer and human-computer interface layer. This paper presents an improved Node- Link road network model which the driving trajectory is introduced and divided into LDT and VDDT. The vehicle agent model is built based on the analysis of driving behaviors such as free driving, following driving, lane changing, slowing down, vehicle stop, etc. The UTFSim is developed in the platform of Visual Studio. NET. The experiments of signal control at single and multi intersections are performed using UTFSim, and achieve good performance.

## Acknowledgments
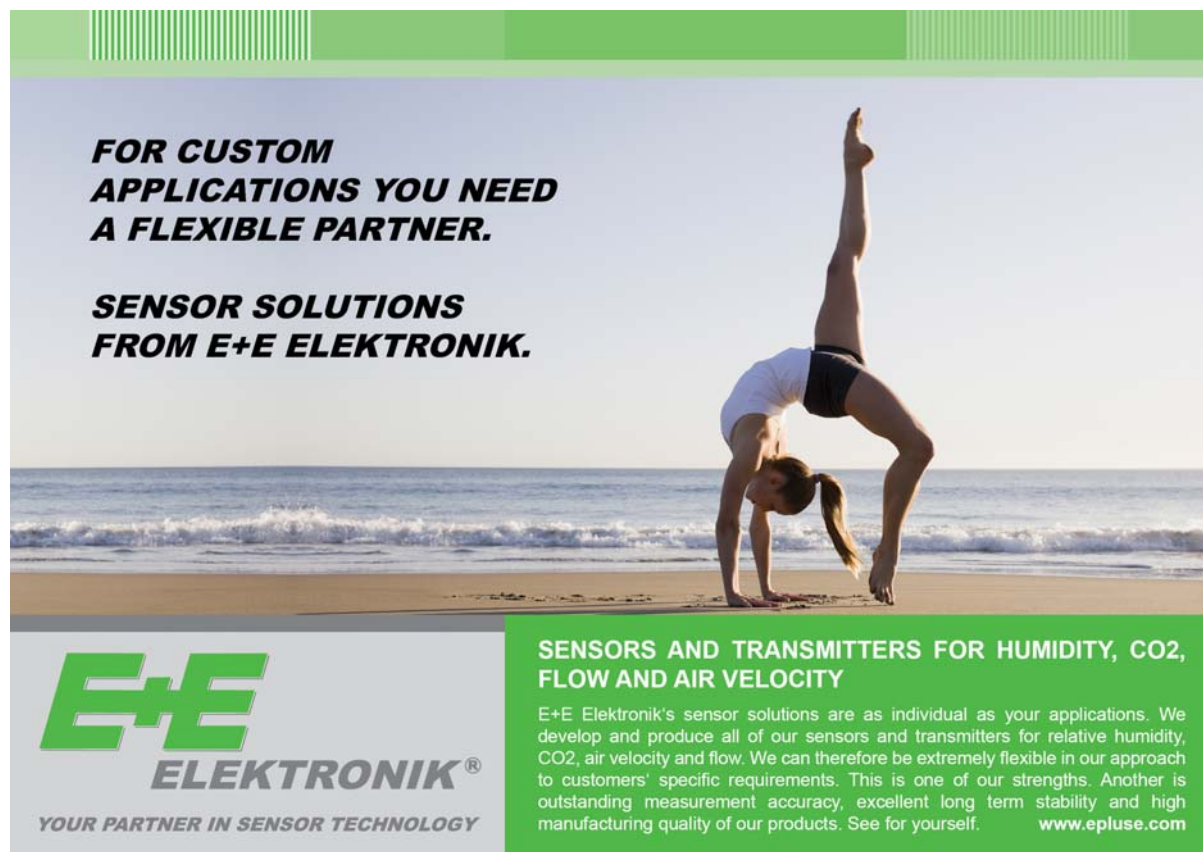
## References

[1]. J. Barceló, Models, Traffic Models, Simulation, and Traffic Simulation, Fundamentals of Traffic Simulation, *Springer*, New York (NY), Vol. 145, 2010, pp. 1-62.

[2]. S. Huang, A. W. Sadek, Artificial Intelligence and Microscopic Traffic Simulation Models: Applications to Parameter Calibration and Origin–Destination Estimation, *Transportation Research E-Circular*, Issue E-C168, pp. 65-69, 2012.

[3]. M. Treiber, A. Kesting, An Open-Source Microscopic Traffic Simulator, *IEEE Intelligent Transportation Systems Magazine*, Vol. 2, Issue 3, 2010, pp. 6-13.

[4]. M. Jha, K. Moore, B. Pashaie, Emergency Evacuation Planning with Microscopic Traffic Simulation, *Transportation Research Record: Journal of the Transportation Research Board*, Vol. 1886, 2004, pp. 40-48.

[5]. W. Burghout, H. N. Koutsopoulos, I. Andréasson, Hybrid Mesoscopic-Microscopic Traffic Simulation, *Transportation Research Record: Journal of the*

*Transportation Research Board*, Vol. 1934, 2005, pp. 218-255.

[6]. H. Cai, J. S. Oh, C. Y. David Yang, Integrating GIS and Microscopic Traffic Simulation to Analyze Impacts of Transportation Infrastructure Construction, *Journal of Computing in Civil Engineering*, Vol. 26, No. 4, 2012, pp. 478-487.

[7]. X. Chen, L. Yu, L. Zhu, *et al*., Microscopic Traffic Simulation Approach to the Capacity Impact Analysis of Weaving Sections for the Exclusive Bus Lanes on an Urban Expressway, *Journal of Transportation Engineering*, Vol. 136, No. 10, 2010, pp. 895–902.

[8]. R. Fernández, Modelling public transport stops by microscopic simulation, *Transportation Research Part C*, Vol. 18, No. 6, 2010, pp. 856–868.

[9]. D. H. Liu, H. Su, Microscopic Traffic Model in Virtual Environment, *Journal of Southwest Jiaotong University*, Vol. 48, No. 1, 2013, pp. 165-172.

[10]. M. Wooldridge, N. R. Jennings, Intelligent agents: theory and practice, *The Knowledge Engineering Review*, Vol. 10, No. 02, 1995, pp. 115-152.

[11]. A. Doniec, R. Mandiau, S. Piechowiak, S. Espié, A behavioral multi-agent model for road traffic simulation, *Engineering Applications of Artificial Intelligence*, Vol. 21, No. 8, 2008, pp. 1443-1454.

[12]. F. Marki, D. Charypar, K. W. Axhausen, Continuous Activity Planning for Continuous Traffic Simulation, *Journal Transportation Research Record: Journal of the Transportation Research Board*, No. 2230, 2011, pp. 29-37.

[13]. H. Fujii, S. Yoshimura, K. Seki, Multi-agent based traffic simulation at merging section using coordinative behavior model, *Computer Modeling in Engineering and Sciences*, Vol. 63, No. 3, 2010, pp. 265-282.

[14]. E. López-Neri, A. Ramírez-Treviño, E. López-Mellado, A modeling framework for urban traffic systems microscopic simulation, *Simulation Modelling Practice and Theory*, Vol. 18, No. 8, 2010, pp. 1145-1161.

[15]. G. H. Bham, R. F. Benekohal, A high fidelity traffic simulation model based on cellular automata and car following concepts, *Transportation Research Part C*, Vol. 12, No. 1, 2004, pp. 1-32.

[16]. P. Hidas, Modelling lane changing and merging in microscopic traffic simulation, *Transportation Research Part C*, Vol. 10, No. 5-6, 2002, pp. 351–371.

_____

# Research on Wireless Signal Coverage in Metro Station

**Linna He, Haiyang Yu, Xiaodong Chai**
Shanghai University of Engineering Science, 201620, China
Tel.: +86-21-67791420, fax: +86-21-67791163
E-mail: hln-gcd@163.com

**Abstract:** In this paper, Firstly, we analyzed metro platform types and the basic principle of radio frequency (RF) technology. Secondly, we proposed an application method of radio frequency technology in metro. Then, by studying the wireless signal coverage in metro station, we got results of relationships of reflection coefficient $\Gamma$ with angle $\theta$, and with phase shift $\zeta$. Finally, we studied an example of signal coverage for wireless network in metro station, three kinds of path difference $\Delta L_i$ ($i = 2, 3, 4$) between the reflected wave and incident wave are calculated. This work could provide certain theoretical and practical research value for studying the security transmission of wireless signal in metro station. *Copyright © 2014 IFSA Publishing, S. L.*

**Keywords:** Metro station, Electromagnetic waves, Wireless signal, Propagation, Coverage.

## 1. Introduction

With the development of society, metro construction showing a rapid development trend. As an important technology in metro - wireless signal coverage is to get a great deal of attention to us. Wireless signal coverage in metro can effectively ensure the safe operation of the train and improve the operating efficiency of the train, and facilitate the general public to travel.

Metro station not only provides the basic functions for passengers to get on and off, but also accommodates the major technical equipment and operations management systems, in order to protect the safe operation of metro. Metro station has an internal wireless dispatch system, and the normal public wireless communications network is essential [1-3].

The study of propagation conditions and coverage solutions for tunnel environments have been studied in several previous publications [4-6], whereas not

much attention has been given to understand the wireless signal coverage in metro stations. An example of studying the covering type of electromagnetic wave field strength in the concourse from the theory to reduce the blind spot of signal and guide the design antenna arrangement is given in [7], the paper studied design of antenna arrangement. The study of discussing the modelling and analyzing of the initial radio coverage design in underground stations of the New Copenhagen metro system by way of a commercial ray-tracing tool is given in [8]. Instead, in this paper our aim is to discuss the wireless signal coverage in metro station and calculate path difference of electromagnetic waves between the reflection waves and the incident wave by the way of studying reflected wave and transmitted wave of electromagnetic field at interface of two media.

In order to improve the operational efficiency and operational safety for metro system, the modern train control system is moving in the direction of

automation, intelligent, systematic, network and information technology. Communication based train control (CBTC) technology is currently the most advanced train control technology. The CBTC system using wireless communication technology to achieve real-time and bi-directional communication between train and trackside equipment through an open data communication network [9-14].

We will analyze metro platform types in the following Section 2 and basic principle of radio frequency (RF) technology that we have analyzed in Section 3. In Section 4, we propose a method of radio frequency technology application in metro. Wireless signal coverage in metro station that we have analyzed in Section 5. Based on this we select an example of analyzing the signal coverage for wireless network in metro station in Section 6. Finally, section 7 concludes this paper.

## 2. Metro Platform Types

Metro station is divided into several types, such as island platform station and side platform station, as well as station hall. According to different needs, there are a variety of categories that can be classified according to the operations nature, the platform forms and transfer mode.

According to station's operations nature, metro station can be divided into intermediate stations, regional stations, transfer stations, hub stations, transport stations and terminal stations.

According to station's platform, metro station can be divided into island platform, side platform as well as island and side hybrid platform.

Island platform station is located between the upper and downlink. Island platform station is a common platform form, with a platform area of high utilization, improve facilities are shared, flexible passengers transfer, easy to use, more concentrated management, generally used in large passenger stations.

Side Platform station is located on both sides of uplink and downlink. Side platform station is also a common platform form, although its platform area utilization is low, and adjusts the uplink and downlink passenger traffic and other aspects do not like island platform station, but the elevated station of side platform enables more reasonable range.

Island and side hybrid platform is island platform and side platform co-located in a station.

Island platform station is located between two tunnels and narrow shape, so generally shared leaky cables with tunnels to meet the needs of coverage for wireless signal. If strength of wireless signal is not enough in metro platform station, an omni-directional antenna will be installed, meanwhile can provide signal handoff and updated positions.

Side platform station is located on the both sides of rail line area, the station hall and side platform station are at the same level, in most cases,

omni-directional antenna is used for wireless signal coverage.

Generally station hall uses the antenna system with RF cable, if strength of wireless signal is not strong enough in some places, we can use fiber optic repeater or repeater to enhance the wireless signal.

## 3. The Basic Principle of Radio Frequency Technology

The propagation mechanism of electromagnetic waves is very complex, usually with incident propagation, reflection propagation, transmission propagation. In any types of wireless far field, the radiated waves are a spherical waves, and the electric and magnetic fields can be shown by the following two formulas (1) and (2)

$$\vec{E} = \vec{a}_E ZI \frac{e^{-jkt}}{r} f(\theta, \phi), \qquad (1)$$

$$\vec{H} = \frac{1}{\eta} \vec{a}_r \times \vec{E}, \qquad (2)$$

where $\vec{a}_r$ is the unit vector of $\vec{H}$ direction; $\vec{a}_E$ is the unit vector of $\vec{E}$ direction; r is the radius of sphere; I is the current on the antenna; Z is the reactance; k is the coefficient, $k = \omega/\lambda f$ ( $\omega$ is the angular frequency, $\lambda$ is wavelength, $f$ is frequency); $\eta$ is the coefficient, $\eta \approx 377$.

Therefore, the radiation power density is

$$p = \frac{1}{2} R_e |\vec{E} \times \vec{H}| = \vec{a}_r \frac{1|ZI|}{2\eta r^2} |f(\theta, \phi)|^2, \qquad (3)$$

Meanwhile, the total power of the spherical surface is

$$p_r = \oiint_S \vec{p} \times \vec{a}_r dA, \qquad (4)$$

$$p_r = \int_{-\pi}^{\pi} \int_0^{\pi} \frac{|ZI|}{2\eta r^2} |f(\theta, \phi)|^2 r^2 \sin\theta n d\phi, \qquad (5)$$

For purposes of calculation and analysis, assuming antenna considered a point source, and within the range considered, every direction of the antenna is the same nature. Then, in the free space, sine wave emitted by a point source will propagate radially, for the isotropic antenna, if the power delivered to the antenna is $p_t$, antenna gain is $G_t$, then the antenna transmitting power is

$$P_{r \wedge d} = P_t G_t, \qquad (6)$$

The wave power per unit area from the point source at r is

$$P_{fs} = \frac{P_{r \wedge d}}{4\pi r^2}, \qquad (7)$$

In order to derive the desired, using electric field strength of root mean square can be written

$$E_{fs} = \sqrt{Z_{fs} P_{fs}}, \qquad (8)$$

where $Z_{fs}$ is the impedance of free space, it can be shown as

$$Z_{fs} = \sqrt{\mu_{fs} \varepsilon_{fs}} = 120\pi \approx 377\Omega, \qquad (9)$$

where $\mu_{fs}$ is the permeability of free space, $\mu_{fs} = 4\pi \times 10^{-7} H/m = 4\pi \times 10^{-7} V_{-s}/A_{-m}$; $\varepsilon_{fs}$ is the permittivity of free space, $\varepsilon_{fs} = (10^{-9}/36\pi)F/m = (10^{-9}/36\pi)A_{-sec}/V_{-m}$

## 4. The Applications of Radio Frequency Technology in Metro

Due to the limited space in metro station, the metro station hall is generally no longer than 200 m, and its width is about 40 m. In process of wireless signal propagation, apart from the incident wave of electromagnetic waves from the antenna to the receiver, the power of reflected wave is also very large. Metro is composed of station and tunnel. Most metro station reinforced concrete structure, which is generally divided into two parts of the concourse level and platform layer. Concourse level is mainly composed of the station control room, equipment room, as well as Sale and check tickets area. Platform layer is mainly waiting area and equipment rooms. Tunnels of metro typically use concrete structure, tunnels of metro with respect to the road and rail tunnels are to narrow. The narrow space makes the incident angle of wireless signal is small, uneven distribution of signals inside the tunnel. When a train through the tunnel in metro, the tunnel remaining space becomes smaller, at this time there is a great difference between the wireless signal propagation through the train body with no, the wireless signal is blocked very easily and create shadow effects. Train itself also has a greater impact on the wireless signal propagation in metro, because the train body is metal, the wireless signal can only be injected into the train from the window section. At the same time, windows also have some signal attenuation. There are a lot of columns supporting at the platform layer, which also formed a wireless signal propagation block. Meanwhile, concrete materials and aluminum

construction of the body on the sites with the absorption of the signal loss and penetration loss. In order to improve operational efficiency and operational safety of metro system, studying on wireless signal coverage in metro station is particularly important.

## 5. Research on Wireless Signal Coverage in Metro Station

In metro station, electromagnetic waves propagation from the transmitting antenna to the receiver antenna is incident wave, reflected wave and transmitted wave. When the electromagnetic waves incident upon the walls of the metro station hall, because permittivity and conductivity of the walls are not same in free space, therefore, there are reflected wave and transmitted wave at the interface of two media. The schematic diagram of reflected wave and transmitted wave for electromagnetic field is shown in Fig. 1.

In Fig. 1, $\mu_1$, $\varepsilon_1$, $\delta_1$ and $\mu_2$, $\delta_2$, $\varepsilon_2$ represent the permittivity and conductivity of the two substances, respectively.
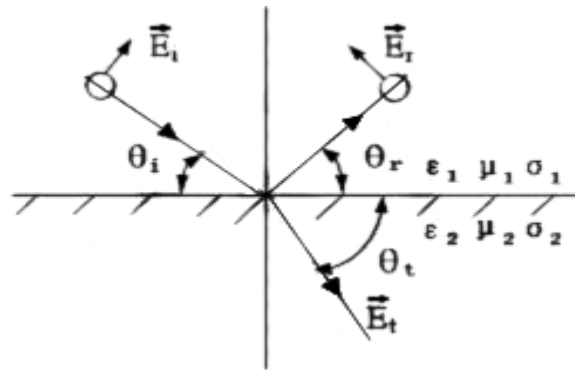


**Fig. 1.** The schematic diagram of reflected wave and transmitted wave for electromagnetic field.

If the reflection coefficient vector is $\Gamma$, relationships between incident wave and reflected wave, incident wave and transmitted wave can be expressed as below

$$E_r = \Gamma E_i, \qquad (10)$$

$$E_t = (1 - \Gamma) E_i, \qquad (11)$$

$$\Gamma = \frac{\sin\theta_i - Z}{\sin\theta_i - Z} = |\Gamma| e^{j\varsigma}, \qquad (12)$$

$$Z = \sqrt{\varepsilon_g - \cos^2\theta_i}, \qquad (13)$$

(Horizontal polarization)

$$Z = \sqrt{\varepsilon_g - \cos^2 \theta_i / \varepsilon_g} , \qquad (14)$$

(Vertical polarization)

Outside the walls of metro is the soil, the typical parameter values of walls are taken as follows: $\varepsilon$ =10(F/m), $\delta$ =0.01(S/m),

$$\varepsilon_g = 10 - j\frac{179.8}{f(MHz)} , \qquad (15)$$

If it is assumed frequency of mobile communication is 900 MHz, then the above equation (15) can be written as

$$\varepsilon_g = 10 - j0.19981 , \qquad (16)$$

Equation (15) is substituted into equation (13), and then substituted into the equation (12), we can obtain function of reflection coefficient $\Gamma$.

$$\Gamma = |\Gamma(\theta)| e^{j\varsigma} , \qquad (17)$$

We made a curve of reflection coefficient $\Gamma$ of horizontally polarized changing with $\theta$, as shown in Fig. 2.
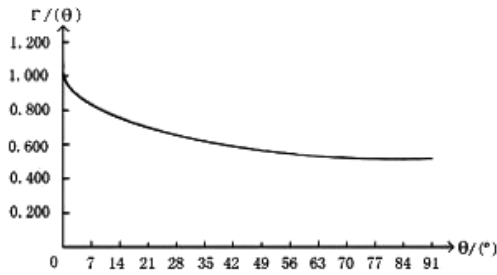


**Fig. 2.** Curve of reflection coefficient $\Gamma$ of horizontally polarized changing with $\theta$.

We made a curve of phase shift $\varsigma$ of $\Gamma$ changing with $\theta$, as shown in Fig. 3. From Fig. 2 and Fig. 3, We can get results that the amplitude of $\Gamma$ varies between 0.6 and 1, the phase shift of $\Gamma$ varies between 0 and $-0.35^0$.
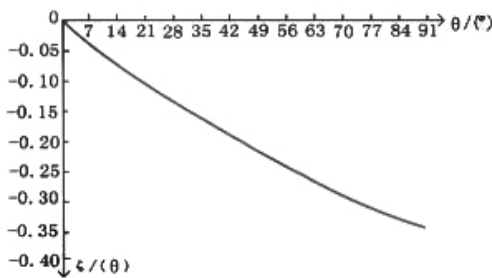


**Fig. 3.** Curve of phase shift $\varsigma$ of $\Gamma$ changing with $\theta$.

## 6. Research on Signal Coverage for Wireless Network in Metro Station

A metro station hall is shown in Fig. 4. An antenna is installed on the roof, a mobile phone is located at $L$ from the antenna.
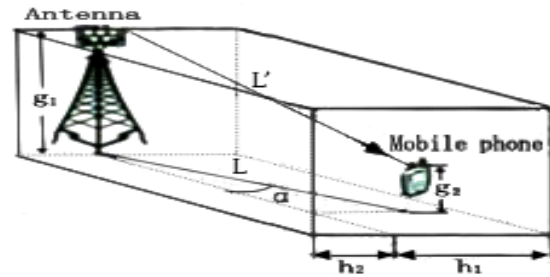


**Fig. 4.** Three-dimensional graphics of metro station hall.

Wireless signals are received by the mobile phone, not only incident wave from the antenna, but also reflected wave from wall and ground. There are three main ways of reflected wave, the first way is reflected wave from the ground as shown in Fig. 5, the second way is reflected wave from the right wall as shown in Fig. 6, the third way is reflected wave from the left wall.
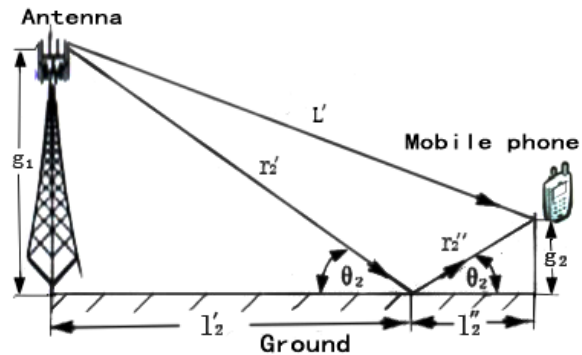


**Fig. 5.** Schematic diagram of reflected wave from the ground.
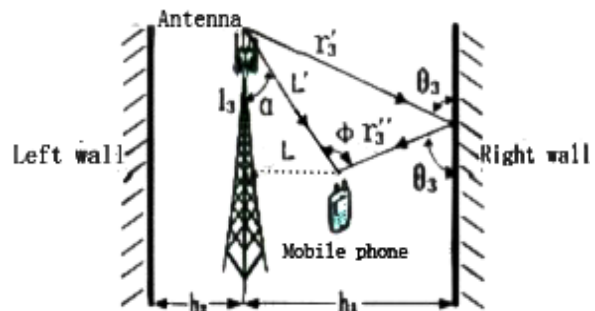


**Fig. 6.** Schematic diagram of reflected wave from the right wall.

Each path length of the reflected wave is different, amplitude and phase shift of Γ are not the same, thus resulting in the multipath effects generated at the receiving point are not same. Here, three kinds of path difference $\Delta L_i$ ( $i = 2, 3, 4$) between the reflected wave and the incident wave are calculated.

For reflected wave from the ground

$$\sin \theta_2 = \frac{g_1}{r_2'} = \frac{g_2}{r_2''},\qquad (18)$$

We can obtain

$$g_1 = \sin \theta_2 r_2',\qquad (19)$$

$$g_2 = \sin \theta_2 r_2'',\qquad (20)$$

$$\therefore tg\theta_2 = \frac{g_1}{l_2'} = \frac{g_2}{l_2''} = \frac{g_1 + g_2}{l_2' + l_2''} = \frac{g_1 + g_2}{L},\qquad (21)$$

Then

$$\Delta L_2 = (r_2' + r_2'') - L$$

$$\Delta L_2 = g_1\sqrt{1 + \frac{L^2 - (g_1 - g_2)^2}{(g_1 + g_2)^2}} + g_2\sqrt{1 + \frac{L^2}{(g_1 + g_2)^2}} - L,\qquad (22)$$

The reflected wave from right wall

$$l_3 = r'\cos\theta_3 + r_3''\cos\theta_3,\qquad (23)$$

$$l_3 = (r_3' + r_3'')\cos\theta_3 = L'\cos\alpha,\qquad (24)$$

$$r_3' + r_3'' = \frac{\cos\alpha}{\cos\theta_3}L',\qquad (25)$$

$$\sin\theta_3 = \frac{h_1}{r_3'} = \frac{h_1}{L'} \bullet \frac{2\sin\theta_3\cos\theta_3}{\sin(\theta_3 + \alpha)},\qquad (26)$$

$$\cos\theta_3 = \frac{\cos\alpha}{\sqrt{(\frac{2h_1}{L'})^2 - 2(\frac{2h_1}{L'})\sin\alpha + 1}},\qquad (27)$$

Therefore

$$\Delta L_3 = (r_3' + r_3'') - L' = L'(\frac{\cos\alpha}{\cos\theta_3} - 1),\qquad (28)$$

$$\Delta L_3 = L'[\sqrt{(\frac{2h_1}{L'} - \sin\alpha)^2 + \cos^2\alpha} - 1],\qquad (29)$$

The reflected wave from left wall, similar as reflected wave from right wall

$$r_4' + r_4'' = L' \bullet [\frac{\cos\alpha}{\cos\theta_4}],\qquad (30)$$

Then

$$\cos\theta_4(\frac{2h_1}{L'} + \sin\alpha) = \sin\theta_4\cos\alpha,\qquad (31)$$

$$tg\theta_4 = \frac{\sin\theta_4}{\cos\theta_4} = \frac{[\frac{2h_1}{L'} + \sin\alpha]}{\cos\alpha},\qquad (32)$$

We can obtain

$$\Delta L_4 = L' \bullet [\frac{\cos\alpha}{\cos\theta_4} - 1],\qquad (33)$$

$$\Delta L_4 = L' \bullet [\cos\alpha\sqrt{tg^2\theta_4 + 1} - 1],\qquad (34)$$

$$\Delta L_4 = L' \bullet [\sqrt{(\frac{2h_1}{L'} + \sin\alpha)^2 + \cos^2\alpha} - 1],\qquad (35)$$

## 6. Conclusions

This paper presents a method of studying wireless signal coverage in metro by the way of studying incident wave, reflected wave and transmitted wave of electromagnetic waves at the interface of two media. This work could provide certain theoretical and practical research value for studying wireless signal coverage in metro station. With the popularity of communications technology applications in metro, the issue of security transmission for wireless signal has been caused concern [15]. In the future, we will focus on research the security transmission of wireless signal in metro.

## Acknowledgements

## References

[1]. Zhaofeng Wu, Jun Zhou, Biyi Lin. Study on Metro Wireless Communication Technology, *Modern Urban Transit,* Vol. 5, Issue 2, 1995, pp. 10-15.
[2]. Zongheng Li, Wen Liu, Coexist Interference Analysis for mobile communication systems in Metro Scene,

*Mobile Communications,* Vol. 36, Issue 1, 2012, pp. 25-29.

[3]. Y. Zhang, G. Zheng, and J. Sheng, Radio Propagation at 900 MHz in Underground Coal Mines, *IEEE Transactions on Antennas and Propagation*, Vol. 49, Issue 5, 2001, pp. 757-762.

[4]. M. Boutin, A. Benzakour, C. Despins, and S. Affes, Radio Wave Characterization and Modeling in Underground Mine Tunnels, *IEEE Transactions on Antennas and Propagation*, Vol. 56, Issue 2, 2008, pp. 540-549.

[5]. F. Marti, F. Ponce, and L. Juan-Lacer, Analysis of Path Loss and Delay Spread at 900 MHz and 2.1 GHz While Entering Tunnels, *IEEE Transactions on Vehicular Technology*, Vol. 50, Issue 3, 2001, pp. 767-776.

[6]. Y. Zhang, G. Zheng, and J. Sheng, Radio Propagation at 900 MHz in Underground Coal Mines, *IEEE Transactions on Antennas and Propagation*, Vol. 49, Issue 5, 2001, pp. 757-762.

[7]. Meng-Hua Tao, Analysis and Calculation of Mobile Communication Signal in Metro Station, *Journal of Railway Engineering Society*, Vol. 25, Issue 8, 2008, pp. 84-88.

[8]. Carmen de la O Millán, Troels B. Sørensen and Niels Michael Mikkelsen, A Study on the Radio Coverage in Underground Stations of the New Copenhagen Metro System, in *Proceedings of the 8th ACM Workshop on Performance Monitoring and Measurement of Heterogeneous Wireless and Wired Networks,* Barcelona, Spain, 03-08 November 2013, pp. 99-106.

[9]. He Linna, Application of wireless communication technology in the train control system. *Communication Technology*, Vol. 41, Issue 10, 2008, pp. 201-203.

[10]. Heddebaut, Inst M. F. N., Leaky Waveguide for Train-to-Wayside Communication-Based Train Control, *IEEE Transactions on Vehicular Technology*, Vol. 58, Issue 3, 2009, pp. 1068 - 10762.

[11]. IEEE Standard for Communication Based Train Control System (CBTC) Performance and Functional Requirements, *IEEE,* Std 1474. pp. 1-1999.

[12]. Chen Fenghua, Liu Ling, Xu Song, Communication based train control CBTC system, *Railway Signal and Communication Engineering,* Vol. 14, Issue 1, 2005, pp.40-42.

[13]. Fu Song, Meng Fanjiang, Wang Zhongfeng, Study on Data Communication Subsystem in Urban Mass Transit CBTC System, *Modern Urban Transit,* Vol. 47, Issue 3, 2012, pp. 3-6.

[14]. Tang Lu-Jie, Qian Jian-Min, Liang Jian-Ru, CBTC signaling system based on mobile communication technology, *Journal of Shanghai University of Engineering Science*, Vol. 25, Issue 3, 2011, pp. 217-220.

[15]. Linna He, Wei Yin, The Research of Electromagnetic Interference in Metro Signal System, *Applied Mechanics and Materials*, Vol. 40-41, 2011, pp. 478-481.

---

# Sensors & Transducers

# Single Allocation Hub-and-spoke Networks Design Based on Ant Colony Optimization Algorithm

**\* Yang Pingle, Zhang Qinge**

Jiangsu University of Science and Technology, Zhangjiagang 215600, Jiangsu, China
\* Tel.: 15151570809, fax: 051256731103
E-mail: plyoung@126.com

**Abstract:** Capacitated single allocation hub-and-spoke networks can be abstracted as a mixed integer linear programming model equation with three variables. Introducing an improved ant colony algorithm, which has six local search operators. Meanwhile, introducing the "Solution Pair" concept to decompose and optimize the composition of the problem, the problem can become more specific and effectively meet the premise and advantages of using ant colony algorithm. Finally, location simulation experiment is made according to Australia Post data to demonstrate this algorithm has good efficiency and stability for solving this problem. *Copyright © 2014 IFSA Publishing, S. L.*

**Keywords:** Hub-and-spoke network, Ant Colony Optimization Algorithm, Solution pair, Capacitated hub location, Local search.

## 1. Introduction

Hub-and-spoke networks are usually used to describe this sort of question: a graph contains more than one node and these nodes send and receive the commodities [1]. In one of the subgraphs, all the flow of goods must go through a number of special nodes which will be called hubs in this paper [2]. Hub-and-spoke networks are being increasingly used in postal services, aviation and telecommunications and other fields. The existence of hub nodes makes it possible to re-find the path selection in the process of cargo transportation and lower the cost of network construction as well [3-4]. The capacity of hub-and-spoke networks is often limited in practical applications, thus introducing hub-and-spoke networks with capacity limits is of more practical significance [5-7]. This paper deals with the solution

to Capacitated Single Allocation Hub Location Problems (CSAHLP). (Each node can only be allocated to one hub, as shown in Fig. 1).

Ant colony optimization algorithm is optimized on the basis of ant system proposed by the Italian scholars M. Dorigo, V. Maniezz and A. Colorni in the early 1990s [8]. Ant colony optimization algorithm is a new kind of intelligent optimization algorithm which has been used to solve the famous Traveling Salesman Problem [9-11]. In recent years, this algorithm has been more and more used in combinatorial optimization, function optimization, robot path planning, data mining and other fields [12-15]. In this paper, ant colony optimization algorithm will be used to solve CSAHLP problem, using the CSAHLP problem whose optimal variable is $O(n^3)$ for validation.
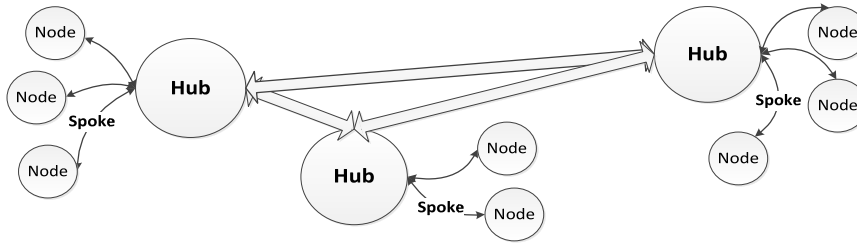
**Fig. 1.** Single allocation hub-and-spoke network.

## 2. Design Model for the Capacitated Single Allocation hub-and-spoke Networks

Formulation 1 can be used to describe CSAHLP. Hub node p here is still not sure, and one of the goals of this paper is to determine hub node p. Model equations are as follows:

$$L = min \sum_i \sum_k C_{ik} X_{ik} (\chi O_i + \delta D_i) + \sum_i \sum_k \sum_l \alpha C_{kl} Y_{kl}^i + \sum_k F_k X_{kk}, \tag{1}$$

$$s.t. \sum_k X_{ik} = 1 \; \forall i \in N, \tag{2}$$

$$X_{ij} \le X_{jj} \quad \forall i,j \in N \tag{3}$$

$$\sum_{i \in N} O_i X_{ik} \le \Gamma_k X_{kk} \; \forall k \in N, \tag{4}$$

$$\sum_l Y_{kl}^i - \sum_l Y_{lk}^i = O_i X_{ik} - \sum_j W_{ij} X_{jk} \; \forall i,k \in N, \tag{5}$$

$$X_{ik} \in \{0,1\} \; Y_{kl}^i \ge 0 \quad \forall i,k,l \in N \tag{6}$$

The objective function 1 minimizes the transportation costs of the network. The fees include the fixed costs of hub facilities and the sum of the total transportation costs. We assume that the network has n nodes. $N = \{1,2,\dots,n\}, i \in N$ represents the set of all nodes. We will choose p nodes from it as hubs and any two of them can be used as the origin and destination of the traffic flow (OD). $W_{ij}$ represents the traffic flow from node $i$ to node $j$, $O_i = \sum_j W_{ij}$, $D_i = \sum_i W_{ij}$. $C_{ij}$ represents the standards of transportation cost in traffic flow from node $i$ to node $j$, $\alpha$ represents the discount factor of the standards of transportation cost of traffic flow from in node $k$ to node $l$, generally $\alpha \le 1.0$, $\chi$ represents the discount factor of the transportation cost from node to hub, $\delta$ represents the discount factor from hub to node. They are all set according to the data from Australia Post (AP). We assume that the fixed construction cost for changing node j to hub is $F_j$. $Y_{kl}^i$ represent all the traffic flow that go through node $i$ and node $l$. $X_{ij}$ represents integer variables $\{0,1\}$. When node $i$ is the branch node of hub $X_{ij}$, the value is 1, otherwise, the

value is 0. $X_{kk} = 1$ shows that node k is a hub and $\Gamma_k$ is the collection capacity of hub $k$. Any node will be constrained by single allocation, namely each can only be allocated to one hub (as the constraint conditions shown in equation 2). Meanwhile, $e$ is not a hub and can only be allocated to hubs (as the constraint conditions shown in equation 3). The capacity of the hub also has certain constraints (as the constraint conditions shown in equation 4). The flow conservation equality $i$ at node $k$ is constrained by equation 5, and the demand and supply is decided by the allocation $X_{ik}$ at node $k$.

Due attention should be paid to the equation:

1. A node or hub may have reached their own flow, namely $W_{ii} > 0$.

2. Any two hubs can be directly connected to each other, namely there are no other hubs between hub $k$ and hub $l$.

3. Any two nodes belonging to one hub can be simply connected to each other by common hub.

4. Considering the capacity limits, only the lowest overall cost remains to be solved, namely the minimum of objective function.

## 3. Ant Colony Optimization Algorithm Model

Ant colony optimization algorithm can be seen as a search algorithm framework based on the parametric probability distribution model of solution space. In this algorithm, pheromones are parameters of the model when solving the parametric probability of solution space, thus pheromone model is the parametric probability distribution model. In this model-based search algorithm, feasible solutions can be generated by searching the parametric probability distribution model of solution space. We use the generated solutions to update the parameters of this model and make the search in new models gather in high-quality search space of solutions.

When solving general problems, ant colony optimization algorithm is divided into the following steps:

1. In each iteration, when solving the problem every ant in the ant colony form their own solution as they move until they constitute all the solutions.

2. After every ant completing its solution, the pheromone will be updated according to the composition of the solution. The pheromone update

makes the solution space to optimized region. The moving direction of the next ant, the probability of the direction, and the path the ant choose later are decided by the updated pheromone.

The formula used in the update is:

$$\tau_{\text{gh}}(i,j) \leftarrow (1-\rho) \cdot \tau_{\text{gh}}(i,j) + \rho \cdot \tau_{\text{g0}}, \qquad (7)$$

$\rho \in (0,1)$ is a constant representing the volatilizing factor of local pheromones.

3. Each ant will face the problem of path selection in its moving process. It follows pseudo random choice rule and the following transfer probability formula:

$$s = \begin{cases} \arg\, max_{(i,j)\in J_{gh}(r)}[\tau_{gh}(i,j)]^{\alpha}[\eta_g(i,j)]^{\beta} \,, if\, q \le q_0 \\ \qquad \text{(Formulation 9)} \qquad\qquad \text{otherwise} \end{cases}$$
$$(8)$$

$$P_{\text{gh}}(s)$$
$$= \begin{cases} \dfrac{[\tau_{\text{gh}}(i,j)]^{\alpha} \cdot [\eta_g(i,j)]^{\beta}}{\sum_{(i,j)\in J_{\text{gh}}(r)}[\tau_{\text{gh}}(i,j)]^{\alpha}[\eta_g(i,j)]^{\beta}}, if\, s \in J_{\text{gh}}(r), \\ \qquad\qquad 0\,, \qquad\qquad\qquad \text{otherwise} \end{cases}$$
$$(9)$$

where $q_0 \in (0,1)$ is the constant, $q \in (0,1)$ is the random number, $\tau_{gh}(i,j)$ is the pheromone of solution composition $(i,j)$, $\eta_g(i,j)$ is the heuristic factor of solution composition $(i, j)$, $\alpha$ represents the importance of information quantity the ants accumulated in their moving process, $\beta$ is the relative strength of heuristic factor. $q$ will have been generated randomly before the next step. If $q \le q_0$, we need to find the maximum solution composition $[\tau_{gh}(i,j)]^{\alpha} \cdot [\eta_g(i,j)]^{\beta}$ from all the rest feasible solution compositions. And $[\tau_{gh}(i,j)]^{\alpha} \cdot [\eta_g(i,j)]^{\beta}$ is the solution composition that will be selected next; if $q > q_0$, we need to select the next solution composition according to the probability calculated in the equation 9.

4. In each iteration, we need to find the ant that has reached the optimal value of objective function and update the global pheromone about solution composition according to it, using the formula as follows:

$$\tau_g(i,j) \leftarrow (1-\gamma) \cdot \tau_g(i,j) + \gamma \cdot \Delta\tau_g(i,j)$$
$$\Delta\tau_g(i,j) =$$
$$\begin{cases} L_g^{-1}, \; if\,(i,j) \in the-best-solution \\ \quad 0, \qquad\qquad \text{otherwise} \end{cases} \qquad (10)$$

## 4. The Strategy of ant Colony Optimization Algorithm for Solving CSAHLP

### 4.1. The Design of ant Colony Optimization Algorithm

The method Tabu List Search was used to solve the problem TSP in ant colony optimization

algorithm. This algorithm obviously contracts allocation of solution space in every step, accelerates convergence and gets optimal solution in finite iterations. This paper introduces the concept of solution pair (SP) when using ant colony optimization algorithm.

In this paper, solution pair is defined like this: In the CSAHLP, node i and its corresponding hub k is a solution pair. Considering the order of solutions, hub node k and hub k itself is also called a solution pair.

With the concept of solution pair, the solutions to CSAHLP are decomposed into discrete solutions pairs in this paper. The example is as follows (as shown in Fig. 2): in general cases, solution compositions i, m deliver freights to j via k, l .

After processing the models of solution pair, we got the following solution pair(as shown in Fig. 3).
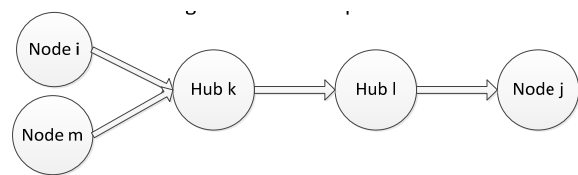


**Fig. 2.** Solution composition.
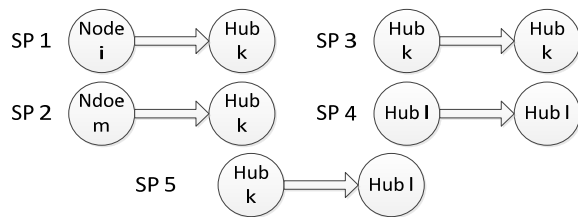


**Fig. 3.** Solution Pair.

It's not difficult to see that in CSAHLP the number of solution pairs equals that of cities. Ant colony optimization algorithm will turn the problem into deterministic problem after the solutions are decomposed into solution pairs.

The steps of ant colony optimization algorithm for solving CSAHLP are as follows:

1. Initialization.

1) Confirming the number g of ants in each iteration ( $1 \le g \le \sqrt{1.44n}$, n represents the number of cities).

2) Setting the maximum iteration number called MaxiItcount. MaxiItcount is general constraint condition helping the program avoid getting into endless loop when falling into local optimal solutions. Randomly ranking n cities, the serial numbers of each city are: $k_1, k_2, ..., k_n$ . After randomization, it forms arrays to g*MaxiItcount in total, like $k_{j1}, k_{j2}, ... k_{jn}$ ($j \in random(n)$), ensuring that every ant will get different collating sequence, also ensuring the diversity and uniqueness of solution.

3) When initializing CSAHLP, we calculate the distance distance$(k_i, k_j)$ between two cities first and then initialize the pheromone m_dTrial$(k_i, k_j)$ between two cities. According to the ACS theory of M. Dorigo [16], the initial non-zero pheromone between any two points is very small. The purpose is to facilitate the operation of local pheromone updating. Initializing every city capacity Cap$(k_i)$ and logistics quantity Weight$(k_i)$ that every city needs to distribute.

2. Finding solution pairs.

Each ant chooses a randomized sequence of cities and begins to build solution pair from the first city. In every city, ant $k_j$ uses pseudo random choice rule to calculate and uses equation 8, 9 to find the city which has the strongest relationship with it to form $k_{sp}$. $k_{sp}$ is labeled as comba[ $k_j$ ] = $k_{j_{sp}}$ with array link. After that, the comba[$k_{j_{sp}}$] of k$_{sp}$ needs to be labeled as comba[$k_{j_{sp}}$] = $k_{j_{sp}}$ in case that k$_{sp}$ points to other cities later, namely hubs won't form any solution pair with unknown nodes any more. After finding solution pair, Cap$(k_{sp})$ minus Weight$(k_j)$ is Cap$(k_{sp})$, namely Cap$(k_{sp})$=Cap$(k_{sp})$-Weight$(k_j)$. It reflects the constraints of capacity limit. Every ant builds their own solution following these steps.

3. Calculating the value of objective function. After each ant completing crawling all the nodes, we will deal with solutions. We then calculate the value $L$ of objective function according to equation 11 and update the local pheromone of $L's$ solution according to $L$.

$$L = min \sum_i \sum_k C_{ik} X_{ik} (\chi O_i + \delta D_i) \sum_i \sum_k \sum_l \alpha C_{kl} Y_{kl}^i + \sum_k F_k X_{kk}, \quad (11)$$

4. Global pheromone updating.

In each MaxiItcount, the ant who has the minimal value $L$ of objective function will update the global pheromone according to its own solution pair.

5. Calculating the optimal solution in finite MaxiItcount and solution saving solution.

## 4.2. Local Search Strategy

Ant colony algorithm needs to be combined with local search strategy. This paper introduces local search algorithm to accelerate the convergence speed. In this paper, with reference to the six kinds of local search operator proposed by literature [16-18] to calculate with ant colony algorithm. We define the concept of group before introducing the six kinds of local search operator. Group refers to node group containing a hub node and the nodes allocated to the hub. Each hub node is allocated to itself. Here are the six kinds of local search operator:

1. Resetting the hub: changing the hub node in any of the groups into another randomly selected node in the group. The transformation is applied to those groups containing at least one node.

2. Resetting the node: allocating a node in any of the groups to another randomly selected group, especially when a group contains only one hub node. Allocating this node to other group will reduce the number of groups or hubs.

3. Setting new hubs: setting a randomly selected node as hub node to establish a new group containing only one node.

4. Combining groups: allocating all the nodes in a group to a hub node in another randomly selected group and combining these two groups as a whole.

5. Splitting groups: allocating part of the nodes in a group to another randomly selected node to split them in two groups.

6. Switching node: switching the nodes in two groups and allocating these nodes to the hub node in each other's group.

All these local search operator cannot violate weight limit in operation. And as to every ant colony system, the global update of its own ant colony algorithm should come after completing local search. The operation of the six local search operators first follows criterion [17]. As long as a local search operator generates more reasonable objective function values, it will update solutions. If there are more than one search operators to generate more reasonable objective function values, then we randomly choose the result of a search operator to update solutions.

## 5. Experimental Result

This paper verifies this method using data from Australia Post (AP) [18]. Through repeated simulation operation, we got the following solutions (Table 1, Table 2): It is relatively obvious that the ant colony algorithm for solving CSAHLP cannot avoid the inherent shortcoming of falling into local optimums.

Compared with TSP, in CSAHLP, the production of solution pairs and the diversity of path selection make it easy to fall into local optimums. Combined with six local search operators to avoid falling into local optimums, the data below 25TT are all optimal solutions generated after several operations and are the same as proven optimal solutions.

This algorithm adds some methods of combining groups in the process of design to reduce the number of solutions.

In the experimental result, we can see the allocation of every node and the confirmation hub nodes. Compared with the proven optimal results, its deviation is 0, well proving the feasibility and reliability of the solution.

In solving practical engineering, combined with optimal solutions, we find that the solutions of this paper generate too many hub nodes, and optimal solutions were gotten after using the method of merging groups to merge some hub nodes randomly.

**Table 1.** Calculation results.

| Problem | Hubs | Allocation |
|---|---|---|
| **Problem 10LL** | 2, 3, 6 | 2 3 2 3 6 3 6 6 6 6 |
| **Problem 10LT** | 0,3,4,9 | 0 3 4 3 4 3 9 9 9 9 |
| **Problem 10TL** | 3, 4, 9 | 4 3 4 3 4 3 9 9 9 9 |
| **Problem 10TT** | 3, 4, 9 | 4 3 4 3 4 3 9 9 9 9 |
| **Problem 20LL** | 6,13 | 6 6 6 6 6 6 6 13 6 6 6 13 13 13 13 13 13 13 13 |
| **Problem 20LT** | 9,13 | 9 9 9 9 9 9 9 9 9 9 9 9 9 13 13 9 9 13 13 13 |
| **Problem 20TL** | 6,18 | 6 6 6 6 6 6 6 18 6 6 6 18 18 18 18 18 18 18 18 |
| **Problem 20TT** | 0, 9,18 | 0 0 9 9 9 9 9 9 9 9 9 9 9 18 9 9 18 18 18 18 |
| **Problem 25LL** | 7,17 | 7 7 7 7 7 7 7 7 7 7 7 7 7 7 7 17 17 17 17 17 17 17 17 17 17 |
| **Problem 25LT** | 8,15,24 | 8 8 8 8 8 15 8 8 8 8 15 15 8 8 8 15 15 24 24 24 15 15 24 24 24 |
| **Problem 25TL** | 8,22 | 8 8 8 8 8 22 8 8 8 8 22 22 8 8 8 22 22 22 22 22 22 22 22 22 22 |
| **Problem 25TT** | 8,15,24 | 8 8 8 8 8 15 8 8 8 8 15 15 8 8 8 15 15 24 24 24 15 15 24 24 24 |

**Table 2.** Comparison of results.

| Problem | Ant Colony Optimization Algorithm | | Hybrid simulated annealing algorithm | | Lagrange relaxation algorithm | |
|---|---|---|---|---|---|---|
| | calculation time (s) | average deviation (%) | calculation time (s) | average deviation (%) | calculation time (s) | average deviation (%) |
| **Problem 10LL** | 0.03 | 0.00 | 0.05 | 0.00 | 0.04 | 0.00 |
| **Problem 10LT** | 0.03 | 0.00 | 0.06 | 0.00 | 0.05 | 0.00 |
| **Problem 10TL** | 0.03 | 0.00 | 0.06 | 0.00 | 0.06 | 0.00 |
| **Problem 10TT** | 0.03 | 0.00 | 0.07 | 0.00 | 0.07 | 0.00 |
| **Problem 20LL** | 0.06 | 0.00 | 0.20 | 0.00 | 0.42 | 0.00 |
| **Problem 20LT** | 0.08 | 0.00 | 0.13 | 0.00 | 1.51 | 0.51 |
| **Problem 20TL** | 0.08 | 0.00 | 0.12 | 0.00 | 0.19 | 0.00 |
| **Problem 20TT** | 0.09 | 0.00 | 0.21 | 0.00 | 0.21 | 0.00 |
| **Problem 25LL** | 0.35 | 0.00 | 0.36 | 0.00 | 1.95 | 0.01 |
| **Problem 25LT** | 0.43 | 0.00 | 0.42 | 0.01 | 2.34 | 0.04 |
| **Problem 25TL** | 0.50 | 0.00 | 0.43 | 0.02 | 1.85 | 0.03 |
| **Problem 25TT** | 1.02 | 0.01 | 0.44 | 0.03 | 2.43 | 0.31 |

## 6. Conclusion

This paper takes the advantage of ant colony optimization algorithm in solving combinatorial optimization problems. The final solutions are built in the form of solution pairs and six kinds of local search algorithms are inserted into parallel computing ant colony groups to enhance the search ability of ant colony algorithm on optimal solutions. Example simulation experiment is conducted according to the AP database as well. The experimental result shows that: ant colony optimization algorithm can be better used in CSAHLP indeed, which solves a lot of complex location problems that are hard to calculate. Ant colony optimization algorithm itself is a probability selection algorithm that has the speed and convenience that other fixed algorithms don't have. Combined with some other mature algorithms, it will be of wide use in the near future.

## References

[1]. Randall M., Solution approaches for the capacitated single a location hub location problem using ant colony optimization, *Computational Optimization Applications*, Vol. 39, 2008, pp. 239–261.

[2]. Qiao Yan-Ping, Zhang Jun, Traveling Salesman Problem Solving Based on an Improved Genetic Simulated Annealing Algorithm, *Computer Simulation*, Vol. 26, Issue 5, 2009, pp. 205–208.

[3]. Li Yang, Research on hub and spoke network theory and its application, *Fudan University*, Shanghai, 2006 (in Chinese).

[4]. Liu Hong, Reactive power optimization based on improved particle swarm optimization algorithm with hard restriction regulation, *Journal of Tianjin University*, Vol. 42, Issue 9, 2009, pp. 796–801.

[5]. Alumur S., Kara B. Y., Network hub location problem: the state of the art, *European Journal of Operational Research*, Vol. 190, Issue 1, 2008, pp. 1- 21.

[6]. Der-Horng Lee, Meng Dong, A Heuristic Approach to Logistics Network Design for End–of–lease Computer Products Recovery, *Transportation Research Part E*, Vol. 44, Issue 3, 2008, pp. 455–474.

[7]. Besasley J., http: //people.brune.lac.uk /~mastjjb /jeb /info.html [DB]. OR- Library. 2005

[8]. Galski Roberto, Application of a GEO + SA hybrid optimization algorithm to the solution of an inverse radiative transfer problem, *Inverse Problems in Science & Engineering,* Vol. 17, Issue 3, 2009, pp. 321-334.

[9]. Zhang Ya-Ming, Shi Hao-Shan, Liu Yan, A Better Itinerary Analysis for Mobile Agent (MA) through Using ACA-SAA Algorithm in Wireless Sensor

Networks, *Journal of Northwestern Polytechnical University*, Vol. 30, Issue 5, 2012.

[10]. Srivastava S. K., Network Design for Reverse Logistics, *The International Journal of Management Science*, Vol. 36, Issue 4, 2008, pp. 535–548.

[11]. Wang Bao-Hua, He Shi-Wei, Robust Optimization Model and Algorithm for Logistics Center Location and Allocation under Uncertain Environment, *Journal of Transportation Systems Engineering and Information Technology*, Vol. 9, Issue 2, 2009, pp. 69–74.

[12]. Yu Hong-Tao, Xue Jing-Ling, Level by level: making flow-and context-sensitive pointer analysis scalable for millions of lines of code, *in Proceedings of the 8th Annual IEEE/ACM International Symposium on Code Generation and Optimization*, 2010, pp. 218-229.

[13]. Pearcedj, Kellyphj, Hankinc, Efficient field-sensitive pointer analysis for C, *ACM Trans on Programming Languages and Systems*, 2007, Vol. 30, Issue 1, pp. 37–42.

[14]. Qin Jin, Shi Feng, Bi-level Simulated Annealing Algorithm for Facility Location, *Systems Engineering*, Vol. 25, Issue 2, 2007, pp. 36–40.

[15]. Costa M. D. G., Capacitated single allocation hub location problem - A bi-criteria approach, *Computers and Operations Research*, Vol. 35, Issue 11, 2008, pp. 3671-3695.

[16]. Ge Chun- Jing, Wang Xia, Guan Xian-Jun, Robust optimization of emergent service facilities hub-and-spoke network response for large-scale emergency, *Industrial Engineering and Management*, 2010, Vol. 15, Issue 6, pp. 45-50, 57.

[17]. Liu Chen-Qi, Li Mei-Juan, Chen Xue-Bo, Order picking problem based on ant colony algorithm, *Systems Engineering - Theory and Practice*, 2009, Vol. 29, Issue 3, pp. 179- 185.

[18]. Hansen P., Mladenovic N., Perez JAM., Variable neighborhood search: methods and applications, 4OR A *Quarterly Journal of Operations Research*, 2008, Vol. 6, Issue 4, pp. 319- 360.

———————————————

# Design and Implementation of Dual-Mode Wireless Video Monitoring System

## BAO Song-Jian, YANG Shou-Liang

ChongQing University of Arts and Sciences College of Electronic and Electrical Engineering,
Chong Qing 402160, China
Tel.: 15223220951
E-mail: bsj126@126.com

**Abstract:** Dual-mode wireless video transmission has two major problems. Firstly, one is time delay difference bringing about asynchronous reception decoding frame error phenomenon; secondly, dual-mode network bandwidth inconformity causes scheduling problem. In order to solve above two problems, a kind of TD-SCDMA/CDMA20001x dual-mode wireless video transmission design method is proposed. For the solution of decoding frame error phenomenon, the design puts forward adding frame identification and packet preprocessing at the sending and synchronizing combination at the receiving end. For the solution of scheduling problem, the wireless communication channel cooperative work and video data transmission scheduling management algorithm is proposed in the design. *Copyright © 2014 IFSA Publishing, S. L.*

**Keywords:** Dual-mode transmission, Time delay, Scheduling, Video monitoring, Frame identification.

## 1. Introduction

Video monitoring has been widely used in all walks of life. With the emergency monitoring, mobile monitoring demand growth and the limitation of the cable video monitoring system in the wiring (factors such as geographical environment and project cycle), the demand for wireless video monitoring system has become more and more urgent.

Comparing with the traditional video monitoring system based on wireless transmission technology, dual-mode wireless video monitoring system made up for the shortcomings of single mode video transmission. It has high transmission speed, small dependence on a single network and high stability, and can be trace monitoring for mobile observation. But it also brings some problems: using two different networks with time delay is different, this led to

receive asynchronous, so it must be conducted frame synchronization at the receiving end , and which can correctly display video frames; Rate of wireless channel network also brings problems: due to the performance of the mobile communication network and wireless resources and environment change over time, so the monitoring terminal need according to the data transmission effect, increase the wireless resource environment good amount of data transmission, and improve the performance of the system. This paper thus put forward an effective improvement of TD-SCDMA and CDMA20001x dual-mode video transmission effect of the method. The algorithm is to solve the TD-SCDMA and CDMA20001x dual mode of video transmission video frame synchronization of combination and scheduling problem. The method is based on the current wireless video monitoring system, using the new protocol standards and transmission way to

realize the dual-mode wireless network video surveillance, the performance of video transmission system is better. The method includes video data adding frame identification and packet preprocessing when sending, using the receive buffer to realize synchronization combination and efficient scheduling algorithms when receiving. The former can solve the problem of dual mode of asynchronous receive, which greatly improved the availability of the network. The former can solve the problem of dual-mode asynchronous receive. The latter greatly improved the availability of the network.

## 2. System Structure and Function

### 2.1. System Overall Composition

Terminal system overall architecture is shown in Fig. 1, the system consists of OMAP3530 embedded chip and its peripheral chips. It mainly can be divided into five parts: network, a video capture, video compression, local storage and peripheral control [2].

Network part consists of 1 block of CDMA module and 1 block of TD-SCDMA. When system is working, it can use routing load balancing strategy in the Linux system and dual-mode scheduling algorithm control sending rate of two modules.

Local storage part consists of 1 piece of mobile hard disk. Responsible for uncompressed video data or compressed video data is stored locally, and it stores uncompressed video data or compressed video data according to the determined by the users themselves.

Peripheral control part consists of 1 piece of CPLD. It can control the external set of power supply, camera, and light.

The thread synchronization is initialized by Rendezvous program module. The module using POSIX condition realizes synchronizing threads initialized. Each thread performs its initialization, since the end of the object to be notified of Rendezvous. All the threads after initialization, unlock at the same time, and began to implement the main loop [3].
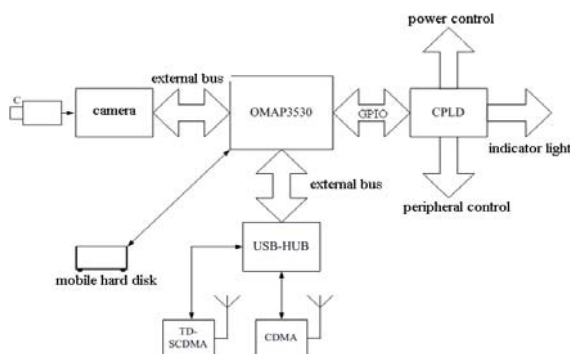


**Fig. 1.** Dual-mode video terminal system hardware structure.

### 2.2. System Main Function

The system main function is image acquisition, its compression and real-time transmission to the monitoring center. On this basis, it also can realize video parameters modification, the modification of network transmission parameters, local storage, as well as the local power supply control.

### 2.3. System Working Process

The System overall flow is shown in Fig. 2. After powered on, firstly, the system is initialized, including hardware initialization, software initialization and interacts with the server process information, etc.
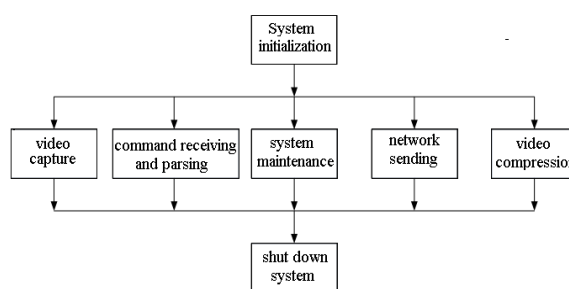


**Fig. 2.** System software overall flow chart.

Normal initialization is completed, the main thread will create video capture thread, video compression thread, command receiving and parsing thread, the network sending thread, system debugging thread. Video compression thread will create local storage thread, a total of five kinds of six threads (because of having 1 CDMA module and 1 TD-SCDMA module, so a total of 2 command receiving and parsing thread). Then the main thread blocking, waiting for the end of each thread, finally shutdown operation.

## 3. Dual Mode Video Transmission Scheduling Algorithm

### 3.1. System Sender Data Preprocessing

### 3.1.1. Packet Synchronization Combination Algorithm Target

Video transmission use TD-SCDMA and CDMA20001x 2 modules, and use the serial port using UDP protocol to send under Linux. With two different networks, delay differences lead to receive signal asynchronously, so the signal will be synchronously managed. For the monitoring center, it need to check every frame length parameters, determine whether within the normal range, then determine received correctly or not. If receiving is

normal, according to the data frame length, frame the order, the system repeated receiving video frame, and then each complete frame is decoded. Once errors, lost the front receiving incomplete frame data, and then set the frame in a check in the new received data, until it receives the fixed frame identification. At the same time, the monitoring center needs frame synchronization based on different channel transmission frame tagging, and completes the data combination [4].

### 3.1.2. Basic Principle of the Algorithm

The monitoring center receives the two modules of UDP packets, and deposited in the receive buffer, the receive buffer can adopt the circular queue data structure to achieve. Each data received frame of fixed frame marks is checked, if received fixed frame marks is the finishing marks of the each video complete frame, the video complete frames are searched in the receive buffer. Search method is to search the receive buffer frame of marks for the end frame, according to the frame to search the other parts of the entire frame, in order to improve the search efficiency. Here considering the same network may take a different route to send data, even if it is a module to send data, the order of receive data and the order of send data is always a possibility inconsistencies, the probability of the problem is not big, so not every receives a data frame to search, take the search algorithms mentioned above. If searching a complete frame, then each part of the complete frame will be deleted in the receive buffer; If it can't search complete the frame and the receive buffer is full, it will receive the packet to cyclic covering the original packet. It is necessary to reasonably set the receive buffer size, too long, the receive buffer will inevitably reduce search efficiency; Too short, the receive buffer may not receive a complete video frames because of the time delay difference bigger.

### 3.1.3. Synchronous Combination Algorithm Implementation

The sender increased frame identifier when sending, consider to use 4 bytes the type to identify TD-SCDMA module and CDMA20001x modules send data, and the position in the whole frame, whether for the end frame, etc.

Implementation of the algorithm and flow chart is shown in Fig. 3.

### 3.2. Dual Mode Video Transmission Scheduling Algorithm

### 3.2.1. Scheduling Algorithm Target

For wireless video transmission, due to the limited bandwidth of wireless channel has very instability, using a single module for video

transmission prone to serious lost frames and time delay, and cannot achieve the ideal real-time monitoring effect. This project adopts multiple terminal modules for video transmission based on UDP/IP protocol, including a CDMA module and a TD-SCDMA module, but during transport multiple modules to prevent competition it is necessary to take effective scheduling algorithms, at the same time the scheduling algorithm can effectively utilize the limited wireless channel resources. On the basis of maximized data transmission, it achieves video data efficient and orderly sending in the sending end, and can complete real-time and correct receiving and broadcasting at the receiving end [5].
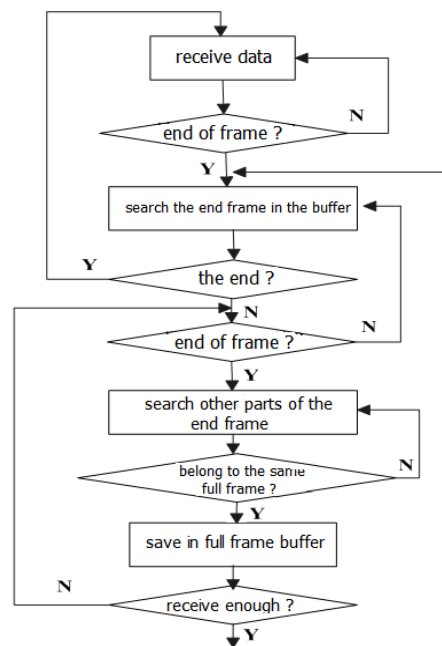


**Fig. 3.** Synchronous combination algorithm flow chart.

### 3.2.2. Basic Principles of Scheduling Algorithm

The monitoring center feedbacks two modules transmission rate to terminal in real time. The sender according to the feedback of the two modules of transmission rate in real time distribute the packets of two modules, bandwidth broad module sends more data, bandwidth small sends a small amount of data, set of TD module (hereinafter referred to as the T module) rate is $R_T$, the rate of CDMA module (hereinafter referred to as C module) rate is $R_C$, distribution ratio principle is $n=R_T: R_C$.

About packet retransmission, the monitoring center according to the received data packets feedback receives the information to the sender, too much feedback message increases the complexity of the system also increases the cost of the system. In order to reduce channel costs, on the premise of guarantee the quality of transmission, try to simplify the feedback information of the monitoring center.

Before image play in the receiving end, only to play image but there is no complete received frame retransmission packets.

### 3.2.3. Implementation of Scheduling Algorithm

The sender selects delivery module according to the monitoring center received feedback information: according to the feedback information, video packet sequence is divided; Monitoring center is statistics integrity of data packets received image frames, if there are packets of image frames are not complete, then send feedback to inform the sender to resend the lost packets. Specific solution flow chart is shown in Fig. 4.
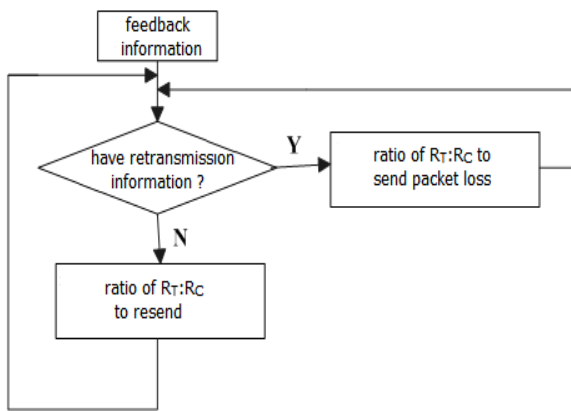


**Fig. 4.** Scheduling algorithm program flow chart.

Setting collection of data packets is M, M={D1,D2,D3...DN}.The ratio of 2 module of transmission rate is n=$R_T/R_C$. The algorithm steps are as follows.

1) According to the feedback information of 2 module transmission rate $R_T,R_C$ calculate the n, the packet sequence M={D1,D2,D3...DN} is divided (T module) n:1(C module) proportion dividing group，

$$M = \{(D_1,D_2\cdots D_n),D_{n+1},(D_{n+2},D_{n+3}\cdots D_{2n+1}),D_{2(n+1)},\cdots,$$
$$(D_{(k-1)(n+1)+1},D_{(k-1)(n+1)+2}\cdots D_{(k-1)(n+1)+n}),D_{k(n+1)})\}$$

After redistribution the queue T module is to send packet queues:

$$M_T = \{(D_1,D_2\cdots D_n),(D_{n+2},D_{n+3}\cdots D_{2n+1})$$
$$\cdots(D_{(k-1)(n+1)+1},D_{(k-1)(n+1)+2}\cdots D_{(k-1)(n+1)+n})\}$$

the queue C module is to send packet queues:

$$M_C = \left\{D_{n+1},D_{2(n+1)},\cdots,D_{k(n+1)}\right\}.$$

2) First of all determine whether receive the monitoring center the retransmission packets of information feedback. If resent the information, the sender need resend packet; If does not resend the information, data packets in the queue are sent according to the module (T) n:1 module (C) the proportion.

The algorithm flow chart is shown in Fig. 5.
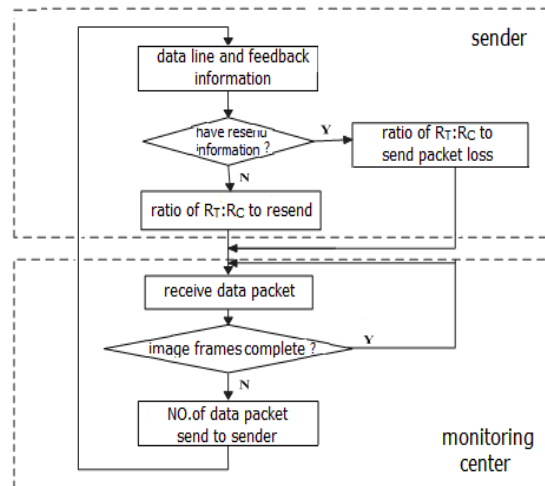


**Fig. 5.** Data send flow diagram.

## 4. Realization of Dual Mode Communication under Linux

### 4.1. TDM230 Module user Space Virtual Serial Port Communication Program

Virtual serial port to read and write program flow diagram is shown in Fig. 6.
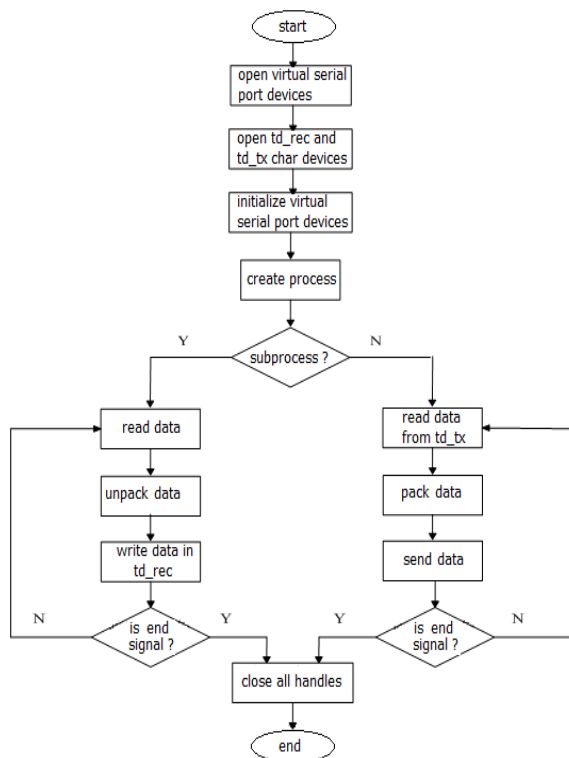


**Fig. 6.** User space virtual serial port communication program.

## 5. Transmission Effect Test and Analysis of Dual Mode Video Scheduling Algorithm

After testing, performance results are shown in Table 1. Through it, you can see that under the condition of monitoring terminal video image acquisition frame rate same, TD-SCDMA and CDMA20001x modules than single CDMA module transmission video data is much faster.

**Table 1.** Single mode and dual mode video comparison.

|  | Single mode CDMA | Dual mode before optimize | Dual mode after optimize |
|---|---|---|---|
| Acquisition frame rate after compression/fps | 25 | 25 | 25 |
| Server display frame rate/fps | 6-10 | 6-25 | 15-25 |
| Correctness of frame/fps | 90 | 40 | 90 |
| Available bandwidth of network/kb | 64 | 64+128 | 64+128 |
| System time delay/s | 5 | 7 | 7 |

Dual-mode system makes full use of the TD-SCDMA and CDMA20001x transmission bandwidth, compared with the single mode video transmission system effectively improve the video transmission bandwidth. This is because in the monitoring terminal through the scheduling algorithm, make full use of the two modules of the wireless channel resources, make the data transfer rate maximize. Before without using optimization algorithm, dual mode of video transmission system receives the frame it is difficult to form a complete video frame, frame rate only a few, after using optimization algorithm, dual mode video transmission system can already close to the ideal level. Dual-mode terminal video monitoring system which using dual mode video transmission algorithm sends video signal, the monitoring center receives signal as shown in Fig. 7.

## 6. Conclusions

We put forward a kind of effective two-mode video transmission algorithm. In wireless video data transmission, comprehensive utilization synchronous combination and effective scheduling algorithm solved video transmission delay difference and two-mode receive asynchronous solution frame errors occur. The algorithm can make full use of network resources and improved the quality of video transmission.

Completed the software overall architecture of the dual-mode video transmission system, the system main function is image acquisition, compression and real-time transmission to the monitoring center, also can realize the modification of video parameters , the modification of network transmission parameters, local storage, as well as the local power supply control.
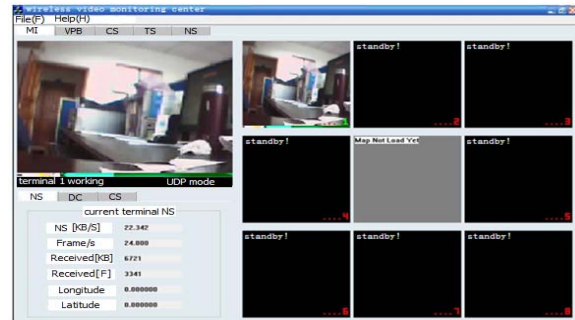


**Fig. 7.** Wireless video monitoring center.

## Acknowledgements

## References

[1]. F. F. Yan, S. F. Gao, and X. L. Liu, Safety and Reliability Research of the Remote Video Monitoring System, *Computer Engineering and Design*, Vol. 26, Issue 9, 2007, pp. 2494-2496.

[2]. Z. S. Tian, Q. J. Li, and W. He, An Improvement Approach of TD - SCDMACDMA20001x Dual-Mode Video Transmission Effective, *Journal of Chongqing University of Posts and Telecommunications*, Vol. 22, Issue 1, 2010, pp. 37-40.

[3]. J. M. Sohn, S. H. Baek, and J. D. Huh, Design Issues towards a High Performance Wireless USB Device, *IEEE International Conference on ICUWB 2008*, Ultra- Wideband, 10-14 March 2008, pp. 109-112.

[4]. M. F. Liao, L. Zhao, and J. W. Mo, The Design of Embedded Video Acquisition System Based on CMOS Image Sensor, *Computer System Application*, Vol. 5, Issue 18, 2009, pp. 194-197.

[5]. Y. Y. Xu, S. J. Bao, Dual-Mode Wireless Video Monitoring System Design and Implementation Based on OMAP3530, *Video Engineering*, Vol. 35, Issue 1, 2011, pp. 115-118.

_____

# Sensors & Transducers

# A Method for Query and Display Massive Time-series Data

**[1] Zhongwen Li, [2] Guoxin Li, [1] Yan Li**

[1] College of Engineering and Design, Hunan Normal University, Changsha, 410081, China
[2] Computer Lab. of China University of Political Science and Law, Beijing, 100088, China
E-mail: lee_zw@163.com

**Abstract:** A method for querying and displaying time series data based on extreme value of periods is proposed. By which the range of time to be queried and analyzed is divided into periods, and then determine the number of sampling points within a time period according to extreme value of the each time period's data and the total number of points to be taken. Uniformly take the sampling points through a database query mechanism, combined with multi-threading mechanism to achieve parallel query and curve drawing of each time period data. The experimental results show that compared with traditional methods, the number of points needed for sampling can be assigned, and the drawn curve has a good approximation of the original curve in the case that the number of access points has been pre-determined; it is able to greatly shorten the time of curve query and drawing, with good engineering practicality. *Copyright © 2014 IFSA Publishing, S. L.*

**Keywords:** Time-series, Database query, Time series database, Curve drawing, Multi-thread.

## 1. Introduction

Time-series data universally exists in medical science, finance, sensor networks, mobile objects, automated testing [1] and other fields, and is successfully applied in biological sequence analysis, financial data analysis, sensor network monitoring and other fields.

Current researches on time-series data are basically focused on similarity search [1, 2], time-series segmentation and pattern discovery[3], and time-series prediction [4], etc., where a lot of research results are achieved. But as a research field with promising application prospects [5-8], research on time-series visualization is relatively less. Now there are some researches, and in addition, corresponding visualization tools are developed, such as time series on spirals [9], time searcher [10], vizTree [11], timeseries bitmaps [12] and so on. Domestic research in this field is less.

Time series is defined as:
Time-series R is a finite set $\{ (t_1,\sigma_1),(t_2,\sigma_2),...,(t_n,\sigma_n) \}$, where $t_i < t_{i+1}$.

Database that consists of time-series data is called time-series databases. When the data is stored, how to query and analyze the existing data becomes difficult and important. In order to facilitate analysis, a more commonly used method is to retrieve data from the database, and show the data in form of curves, enabling data analysts to intuitively analyze trends of retrieved data and local data. However, due to the high time density of data, in some applications, if calculated on basis of one record per second, the daily amount of data is 86400, and the total data amount is 604800 per week as an analysis cycle. To retrieve so much data all at once for curve drawing is not possible: on the one hand, retrieving data from the database takes a lot of time, and such a long time waiting for response is unacceptable for the user; on

the other hand, such a huge data amount will consume a lot of memory space of analysis software, and drawing all the data is not feasible when the amount of data becomes larger.

Traditional solution is to process the large amount of data page by page, which means to retrieve a fixed amount data at a time for curve drawing. When the user clicks on the next page, retrieve out data of the next time period in a same amount and draw. Here comes the following shortcomings: suppose showing 2000 data records per page, if calculated on basis of one record per second, only about 33 minutes of data is involved, far too short for one week of analysis cycle, so that analysts cannot determine the general growing trend of data for one week, nor does the time interval where abnormal data exists can be quickly located.

Another solution is the common curve compression algorithms such as Douglas-Poiker method, line segment filter method, vertical distance limit method, to compress the data for curve drawing. The advantage of these algorithms is that they can extract feature points rather represent the curve, so that the drawn curves of characteristic points better approximate the original curve. However, two problems exist in applying such these algorithms in environment of extremely great amount of data:

1) These algorithms need to iterate through all the data, and calculate between them, in order to extract the feature points. If, as mentioned above, the data is checked on basis of one record per second, only the query of a week's data from the database without any operation already needs a long time, plus the time needed for data processing, the time consumed for curve drawing is clearly unacceptable.

2) Although these algorithms can compress the amount of data, the degree of compression is dependent on a certain threshold value. For instance, in Douglas-Poiker and vertical distance limit value method, a certain vertical distance needs to be specified as filtering threshold for data filtering, in line segment filtering method, the length of the line segment needs to be specified as data filter threshold. For different data require different thresholds are needed, which analysts often cannot directly provide.

At present, there is no better solution to one time off curve query and display of data of such large amount.

In this paper, a method for querying and displaying time series data based on extreme value of periods is proposed. It can specify the total number of points, show trends in data according to fewer data points, and improve the response speed with multi thread mechanism.

## 2. Method Description

The basic idea of the proposed method in this paper is: to divide the whole time interval that needs query analysis into segments, acquire different number of data points respectively in each segment according to a certain strategy, the data point collection obtained by each section is treated as a point collection of trend of change of the whole time interval; in addition, in order to speed up response to query rendering of the whole curve, time interval of each segment opens a separate thread for data query and analysis and curve view update.

Point extraction and method execution are discussed separately below.

### 2.1. Basic Assumption

If total number of points needed for extraction is pcount, which can be set by the user or automatically by the program according to the user's display screen resolution. The total time is divided into n sections.

### 2.2. Number of Points in Each Time Section

According to the general statistical law, for any two time periods with the same span, the one with bigger extreme value difference will accommodate more data change information, namely, hidden with more curve changes, therefore, more data points should be collected; and for the time period with smaller extreme value difference, data change smoothly in its range, and less data points may be selected. Therefore, taking more points from the section with larger changes and fewer points from that with gentle changes can reflect the general data changes in a better way when the overall number of point is fixed.

In order to describe the degree of data change, in this paper we use absolute distance $d_i$ between values to reflect value change in i time section, i.e.:

$$d_i = max_i - min_i, \qquad (1)$$

where $max_i$ is the maximum data of the $i$ period, $min_i$ is the minimum data of the $i$ time period.

According to equation (1), the sum of absolute distances of all segments is

$$sum = \sum_{i=1}^{i=n} d_i, \qquad (2)$$

The number of points taken in section $i$ is determined according to the ratio of absolute distance $d_i$ of each time period in the $sum$ of absolute distances, i.e.

$$p_i = d_i / sum \times pcount, \qquad (3)$$

For equation (3), the determination of $p_i$ is applicable for when $d_i$ is not 0, when $d_i$ is 0, indicating that the time section has no value change, then take $p_i = 2$, so seen from the two circumstances, the value of $p_i$ is:

$$
\begin{cases}
d_i \,/\, sum \times pcount & when\, d_i\, is\, not\, 0 \\
p_i = 2 & when\, d_i = 0
\end{cases}
, \qquad (4)
$$

In the above formula (1) (2) (3) (4), the range of i is $0 < i \le n$. When calculating pi according to formula (3) the results are round up to integer.

## 2.3. Sampling Strategy

The strategies are as follows:

1) When $d_i$=0, $p_i$ =2, which indicates that data in the *i* time period has no change, therefore, the selection of the two points at both ends of this period will represent the curve of this time period.

2) In order to speed up the response to data query and curve drawing and to avoid the need of all-data query for calculation and the default of time waste by such method as Douglas-Poiker, this paper uses the uniform sampling strategy that samples from all data points according to the sequence numbers on basis of uniform intervals. This not only enables effective control of the total number of sampling points according to total data amount and even intervals, but also obtains direct database support due to its uniform sampling. The mainstream large databases such as Oracle, DB2, can realize uniform point extraction through SQL statement. The points accessed by database query being the target points, greatly shorten the time consumption of sampling points query.

3) For each time period, both the maximum and minimum values are taken as the target points for query and curve drawing.

## 2.4. Number of Segment

Let the total data number of the time region that needs query and analysis be *total*, when the extracted number *pcount* is fixed, it obvious that the more segments are divided the more likely that the extracted points can reflect the change trend of original data, therefore we have

$$n=total/pcount, \qquad (5)$$

However, due to the fact that the more *n* is, the more parallel processing threads are open, the more system resources are consumed. Therefore, according to experience the value of *n* should generally not beyond 50.

## 2.5. Specific Process

Process of the method is as follows:

**Step 1**: get database query conditions from user input, and the number of data points that need to be extracted i.e. the number of drawn points *pcount*, which can be specified by user input, with a default value set to 3000, can be specifically set according to screen resolution;
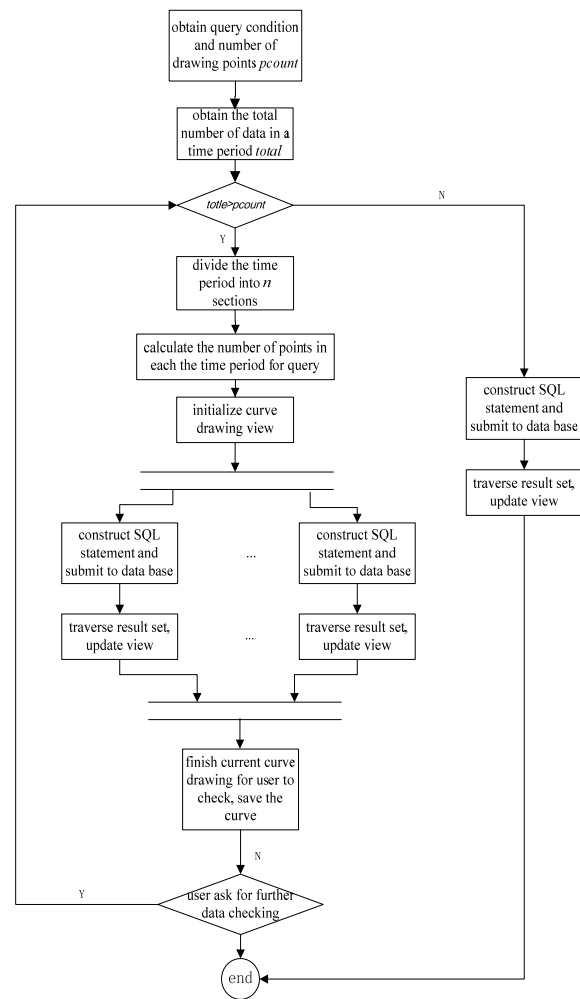


**Fig. 1.** Process for query and display method.

**Step 2**: Obtain the total number of data total from the database in the time period that the user wants to query. If the total is greater than pcount, go to step 3; otherwise directly construct SQL statement according to the query condition, submit the query request to the database, and get the result set for curve drawing and display for the user to check and analyze, and then save the drawn curve, finish the curve drawing;

**Step 3**: Divide the time interval into n sections by equal data amount according to equation (5);

**Step 4**: Query corresponding time points to the maximum and minimum values of each time period. Calculate the number of points to be obtained of each time period respectively according to equation (4);

**Step 5**: Initialize curve drawing view, put the maximum and minimum value of each time period obtained in step 4 into the view for drawn curve display, then open n threads, the number i thread processes curve query and view update of i time period according to the number of points pi to be obtained in i time period that is get in step 4, including construction of SQL statements and result set returned from traverse through the database, and when traversing, updating curve display view each time a data point is taken, until traversal of the current result set is finished.

**Step 6**: When the n threads finish processing, curve drawing completes, the user view, analyze and save the drawn curve;

**Step 7**: If the user wants to further see data of a certain time interval, select the time interval from drawn curve display view, and then go to step 2; if the user does not need to further see the data, finish curve drawing this time. When the user mark a certain time interval in the drawn curve display view by the mouse, then the time range of the interval's abscissa is treated as a new time interval for query.

## 2.6. Pseudo-code

The pseudo-code of the time-series query process is as Fig. 2.

```
Process name：drawTendencyCurve
Input 1: pcount (means the number of data points that need to be extracted)
Input 2: timeSE (means time period that the user wants to query)
Output：tendency curve of time-series
Code：
    // Obtain the total number of data total from the database in the time period that the user wants to query
    total=getAllPointCount(timeSE);
  if(total<=pcount)
            drawAll(); // directly query all the time-series, draw curve for the user to check and analyze
  else { // otherwise get point by follow strategy
            n=getSegmentCount(total, pcount); // divide the time interval into n sections by equal data amount according to equation (5)
            scount= total/n；  //get point number of each time period
    // query start and end time of each segment, then store them in data structure segTimeSet
            segTimeSet=querySegmentTimeSet(scount, timeSE);
      //query the maximun and minimun value of each segment, then store them in data structure minMaxSet
            minMaxSet=queryMinMaxSet(segTimeSet);
            drawMinMax(minMaxSet); // draw curve with the data structure minMaxSet
            for(i=0; i<n; i++){
            pᵢ=getPointCountOfSegment(pcount,minMaxSet); //get the number of points of each segment
            drawThreadi.start(); //according the number of points and the time of segment period, start thread for curve drawing
        }
    }
  END
```

**Fig. 2.** Pseudo-code.

## 3. Experiment and Analysis

Presently there is a test data management application system for spacecraft. The main functions provided by the application system including the storage, query and analysis of spacecraft mass test data. As for the application system, fields of main data tables in its database are time, [parameters 1], [parameter 2], [parameter 3]..., wherein the time is the primary key, with accuracy of millisecond, and the time column stored in the database is long integer data type. The database system is Oracle9i database. The data query and analysis subsystem of the application system makes query and curve drawing on test data on basis of the method proposed in this paper. Running on ordinary PC, the subsystem is programmed in JAVA language, open-source Jfreechart toolkit is used for curve drawing. The experimental environment is shown in Table 1.

**Table 1.** Experimental Environment.

| Experimental machine | Hardware configuration | Software |
|---|---|---|
| PC | CPU: Intel Core Duo 2.6 GHz RAM:2 GB | Windows XP JDK1.6 |
| Database server | HP E4440 server RAM:8 G | HP UNIX 11.0 Oracle9i |

In the database there is spacecraft test data for a year. The experimental process is to take 3000 points for curve drawing as proposed in this paper. And then extract all data points in the time period for curve drawing. Compare time consumption and curve shapes of the two process.

Query parameter in this experiment is A01, and the query time range is a total of 10 days from October 17, 2006 to October 27, with data quantity 405300. In the curve view, the abscissa represents time, and longitudinal coordinate represents numerical value in parameter numbered as A01.

Following is the detailed analysis of data query and curve drawing in the experiment:

1) The value of n obtained from formula (5) is much larger than 50, so the n is made 50, which means the time range is divided into 50 time periods, each contains data with an amount of pavg=405300/50=8106.

2) Find the starting and ending time points of each time period's data respectively, the SQL statement being SELECT time FROM (SELECT time, ROWNUM from tb_name WHERE time BETWEEN 1161043100000 AND 1161935558000 AND (A01 IS NOT NULL)) WHERE MOD (ROWNUM-1, pavg) =0, wherein tb_name is the name of corresponding table, ROWNUM is the oracle system's ordinal allocation number of a

returned row of the query, 1161043100000 is the long integer representation of the query starting time October 17, 2006 07:58:20 of the experiment, while 1161935558000 is the long integer representation of the query ending time October 27, 2006 15:52:38.

3) Query and get the maximum and minimum values and corresponding time points of each time period point according to starting and ending time of each segment. Then calculate the sumof absolute distance, in this experiment $sum = \sum_{i=1}^{i=50} di = 16.44$.

According to value setting method of formula (4), in the 50 time periods, the number of sampling points obtained respectively are: 878, 2, 2, 2841, 2, 2, 2, 9, 2, 2126, 27, 2, 2, 2, 2, 2, 2, 2, 2, 2, 2129363, 2, 9, 9, 2246, 2, 2, 2, 2, 2, 2, 2, 2, 2239, 2, 2, 2, 2, 2, 2, 2, 2, 2 and 27.

4) Initialize curve drawing view. Put all obtained maximum and minimum values of each time period into the curve display view. In the present experiment the maximum and minimum values of the 50 time segments are in total 100 data points, which will be connected in the form of a line in the curve display view, as shown in Fig. 3.
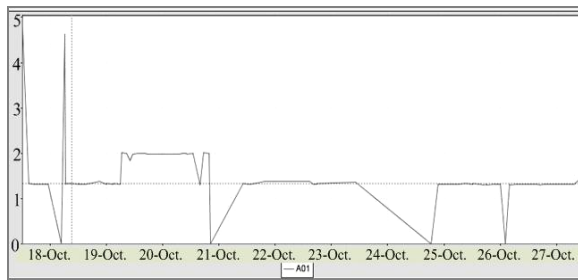


**Fig. 3.** Graph of maximum and minimum values curve.

5) Open 50 threads, each thread deals with curve query and view update of one time period. Let the starting and ending time of each time segment of the 50 time segments be $(t1,t2)…(ti, ti+1)…(t50,t51)$ respectively, and the number of points to be taken in the corresponding time period be pi, then the SQL query statement constructed by thread i is SELECT time,A01 FROM (SELECT time,A01,ROWNUM FROM tb_name WHERE time BETWEEN ti AND ti+1 AND A01 IS NOT NULL ) WHERE MOD(ROWNUM-1, tvi)=0, where tb_name is the name of the corresponding table, parameter tvi =pavg/pi, where tvi represents the number of intervals that are needed for even-interval-sampling, and ti,, ti+1 represent the starting and ending time value of the time period i.

6) when all the 50 threads are processed, the curve drawing is finished. The user can view the drawn curve and analyze the curve trend, to see whether there is anything abnormal, and save the curve data for later reference or analysis.

Upon finishing curving drawing of the present experiment, the curve displayed in curve display view is as shown in Fig. 4.
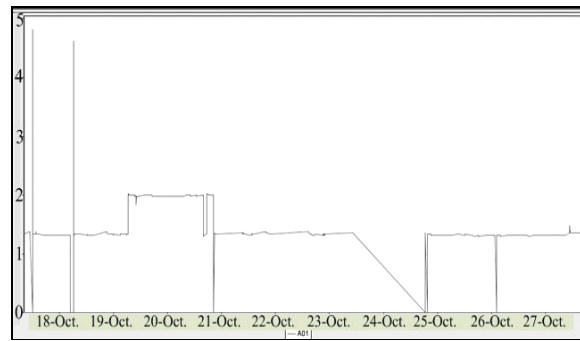


**Fig. 4.** Graph of sectional extreme values curve.

The total number of data points drawn is 3010, because pi is calculated by round up, and tvi is calculated by integer, the number of total points taken will only approximate to pcount. By contrasting, Fig. 5 shows a curve drawn without using this method. We can see that they look quite the same, with much less data points, Fig. 4 gives perfect character of Fig. 5, and by using the method hereby proposed, its time consumption is only 5 seconds, far less than 572 seconds for full data extraction.
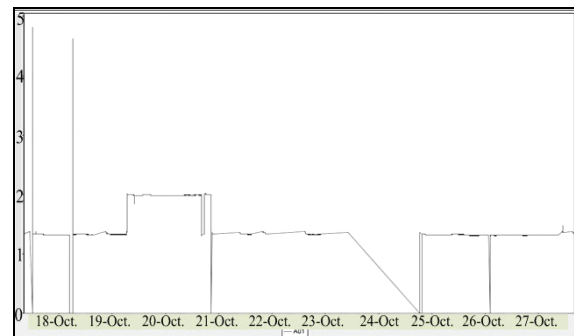


**Fig. 5.** Graph of all data points query curve.

When using the Douglas-Poiker method or the vertical distance limit value method, which requires data process, its time consumption will be more than 572 seconds.

From the above experiment we can see that the method proposed here is better both time wise and space wise than other curve thinning algorithms, and with good curve character extraction effect. It can be better used in engineering practice. In the spacecraft testing field, changes in most parameters should follow certain rules or be within ranges, and data analysts can easily find these features by drawn curve, and locate abnormal data. The method raised in this paper gives an easy way for the analysis of the spacecraft to see whether there is any thing abnormal. It facilitates data analysts to check long time curve trend of data in a short time, and find anything abnormal readily, as well as spot its location quickly, and further find out the abnormal position in the aircraft accordingly.

146

## 4. Conclusions

This paper presents a query and display method for data of time series based on segmented extreme value. First the time range for query and analysis is to be segmented, and then decide the number of sampling points of the time period according to absolute distance of data of each time period and the total number of sampling points, to achieve uniformly sampling of points through the query mechanism of database itself, combined with multi-threading mechanism to achieve parallel query and curve drawing of each time period data. The experimental results show that compared with traditional methods, it can better display changes in the curve under specified number of feature points, greatly shorten the query and drawing time, with good practicability in engineering. The method has been successfully applied to a spacecraft test data analysis system.

## Acknowledgements

## References

[1]. Yang Y., Papadopoulos S., Papadias D., Kollios G., Authenticated indexing for outsourced spatial databases, *VLDB Journal*, 2008, pp. 1-18.

[2]. Bueno R., Traina A. J. M., Traina Jr C., Genetic algorithms for approximate similarity queries, *Data and Knowledge Engineering*, Vol. 62, Issue 3, 2007, pp. 459-482.

[3]. Qisong Chen, Xiaowei Chen, Yun Wu, Optimization Algorithm with Kernel PCA to Support Vector Machines for Time Series Prediction, *Journal of Computers*, Vol. 5, Issue 3, 2010, pp. 380-387.

[4]. Claudio Ribeiro, Ronaldo Goldschmidt, Ricardo Choren, A Reuse-based Environment to Build Ensembles for Time Series Forecasting, *Journal of Software*, Vol. 7, Issue 11, 2012, pp. 2450-2459.

[5]. Yu J., Hunter J., Reiter E., et al., Recognising visual patterns to communicate gas turbine time-series data, *Applications and Innovations in Intelligent Systems*, 2002, pp. 105-108.

[6]. Hochheiser H., Shneiderman B., Visual queries for finding patterns in time series data, *University of Maryland,* Maryland, 2002.

[7]. Hochheiser H., Shneiderman B., Visual specification of queries for finding patterns in time-series data, *University of Maryland,* Maryland, 2001.

[8]. Hochheiser H., Interactive graphical querying of time series and linear sequence data sets, *University of Maryland,* Maryland, 2003.

[9]. Weber M., Alexa M., Muller W., Visualizing Time-Series on Spirals, in *Proceedings of the IEEE Symposium on Information Visualization (INFOVIS'01)*, CA, USA, 2001.

[10]. Hochheiser H., Shneiderman B., Dynamic Query Tools for Time Series Data Sets: Timebox Widgets for Interactive Exploration, *Information Visualization*, Vol. 3, Issue 1, 2004, pp. 1-18.

[10]. Jessica Lin, Eamonn Keogh, Stefano Lonardi, Visualizing and discovering non-trivial patterns in large time series databases, *Information Visualization*, Vol. 4, Issue 2, 2005, pp. 61-82.

[11]. Nitin Kumar, Nishanth Lolla, Eamonn Keogh, Time-series bitmaps: a practical visualization tool for working with large time series databases, in *Proceedings of the 5th SIAM International Conference on Data Mining,* Newport Beach, 2005, pp. 531-535.

# CTM-Based Traffic Signal Multi-Objective Dynamic Optimization under the Uncertain Traffic Demand

## Dongxia YANG, Yongfeng JU

School of Electronic and Control Engineering, Chang'an University, Xi'an 710064, Shaanxi, China
Tel.: +8613572279628
E-mail: dxyang@chd.edu.cn

**Abstract:** In this paper, the traffic signal dynamic control and optimization problems of urban isolated intersection are studied under the traffic demand uncertainty. A multi-objective dynamic optimization model based on the cell transmission model (CTM) for isolated intersection traffic signal control is presented under uncertain traffic demand, in which the cycle time and the durations of each green signal phase are taken as decision variables, and the intersection total delay and total capacity are taken as comprehensive optimization objective function. The authors describe running status of intersection traffic flow with CTM, and also adopt genetic algorithm to optimize the solution of traffic signal. The simulation results show that the model can effectively reflect the uncertainty of traffic demand on the signal timing, traffic delays and capacity calculation in a variety of traffic conditions, and can also realize the optimization for the intersection traffic signal settings. *Copyright © 2014 IFSA Publishing, S. L.*

**Keywords:** Traffic signal settings, Dynamic optimization, Multi-objective, Uncertain traffic demand, Cell transmission model.

## 1. Introduction

In traffic signal settings, the optimal signal timing planning is usually determined according to the traffic demand so as to obtain the best performance index reflecting the traffic benefit, such as minimum vehicle delay, maximum capacity, and minimum vehicle queue length, etc. In real life, traffic demand is constantly fluctuating, but due to the difficulty in collecting data, when calculating the fixed signal settings, most of the research literatures [1-2] adopt the average traffic demand, considering the traffic demand to be relatively consistent at the same period of ordinary days(known as day to day ). However, the actual traffic demand is fluctuating, especially in the intersection or crowded conditions, and the traffic

demand change is significant at the same period of each day in a week [3].Therefore, in order to make the optimal settings of signal timing planning with certain adaptability and stability in the uncertain traffic demand cases, relatively smaller amounts of the literatures [3-4] consider the uncertainty (fluctuation) of traffic demand when setting up the traffic signal. Ref. [4] proposes a novel method to consider the uncertainty of traffic flow, that is: traffic demand flow with uncertainty is taken as a TRANSYT input and is simultaneously input, and then an optimized signal timing planning suitable for every day in a week is determined. This is a kind of static fixed signal timing control method. On this basis, Ref. [3] further puts forward three models to determine the robust optimal fixed signal timing planning, which is not sensitive to the

fluctuation of traffic demand flow, minimizes the average delay per vehicle and maintains fairly stable performance. In this paper, on the basis of the above research literatures, the authors do not only consider the uncertainty of traffic demand flow at some time period of everyday, but also its dynamic change in this period. And the authors apply CTM model to simulate the traffic flow propagation process, which can reflect traffic flow dynamic characteristics. At the same time, in order to apply to over-saturated traffic conditions, the authors take not only the intersection total delay, but also total capacity as comprehensive optimization objective function. Thus, the authors present a multi-objective dynamic optimization model based on CTM for isolated intersection traffic signal control in order to determine the signal timing planning. The genetic algorithm is used for the solution of the model.

## 2. CTM-Based Traffic Signal Control Optimization Model

Fig. 1 shows a four-phase isolated signalized intersection. The arrow in Fig. 1 represents the traffic flow and its direction. Each source lane of the intersection is divided into three traffic flows, they are the left-turning, the through and the right-turning movements; and each exit lane of the intersection has only one traffic flow. Each traffic flow is numbered according to the following rules: the left-turning movements in the four directions from north clockwise are represented respectively by 1, 3, 5 and 7, and the through-running and right-turning movements of the four directions from south clockwise are represented respectively by 2, 4, 6 and 8, and the exit traffic flows in the four directions from east clockwise are represented respectively by 9, 10, 11 and 12.
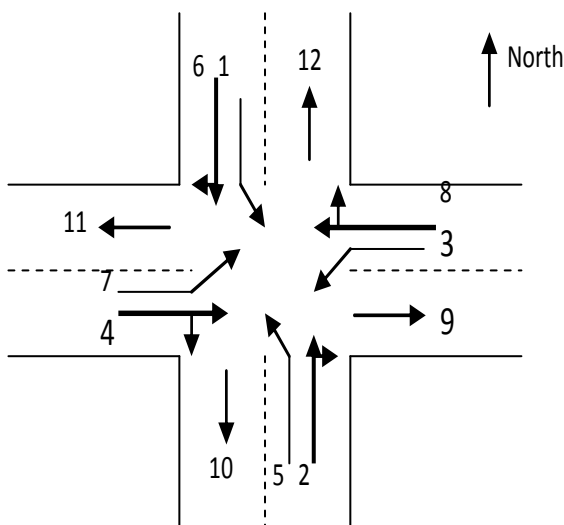


**Fig. 1.** The traffic flow distribution diagram of an isolated intersection.

### 2.1. Cell Transmission Model (CTM)

The literatures [5-6] put forward a traffic model, shortly, LWR model, which can be stated by the following two conditions:

$$\frac{\partial f}{\partial x} + \frac{\partial \rho}{\partial t} = 0, \qquad (1)$$

$$f = F(\rho, x, t), \qquad (2)$$

where Eq. (1) states the traffic flow conservation condition, $f$ is the traffic flow, $\rho$ is the traffic density, $x$ and $t$, are the space and time variables respectively, and $F$ is the function relating $f$ and $\rho$. The relation $F$ between flow $f$ and density $\rho$ is also a fundamental relationship in traffic flow theory. Given a set of suitable initial conditions and boundary conditions, one can determine $f$ and $\rho$ at any $(x, t)$ by solving Eqs. (1) and (2). The literatures [7-8] simplified the solution scheme by adopting the following relationship between traffic flow, $f$, and density, $\rho$:

$$f = \min\left\{v_f \cdot \rho, \ Q, \ \omega/v_f \cdot (\rho_{jam} - \rho)\right\}, \quad (3)$$

where $\rho_{jam}$ denotes the jam density, $Q$ is the maximum allowable inflow, $v_f$ is the free-flow speed, and $\omega$ denotes the backward propagation speed of disturbances in congested traffic. Essentially, Eq. (3) approximates the flow-density relationship by a piece-wise linear model as shown in Fig. 2.
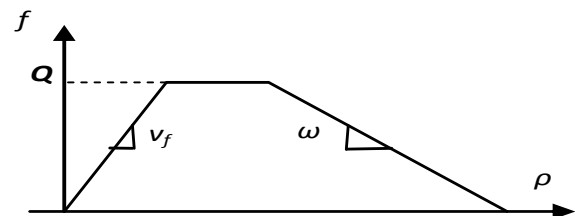


**Fig. 2.** The flow-density relationship used in CTM.

The CTM method is to discredit the road into smaller sections with the same characteristics (or cells), and also divide the time into interval (or time step), $k$, with the same length, $T_s$, so that the cell length is equal to the distance by free-flowing traffic in one time interval, Here, the vehicles entering the cell in a short period of time cannot leave the cell at the same period of time, so, the LWR model is approximated by this set of recursive equations [7-8]:

$$n_j(k+1) = n_j(k) + f_j(k) - f_{j+1}(k), \qquad (4)$$

$$f_j(k) = \min\left\{n_{j-1}(k), Q_j(k), (\omega/v_f)\left[N_j(k) - n_j(k)\right]\right\}, \quad (5)$$

where the subscript $j$ refers to a cell $j$, and $j + 1$ ($j-1$) represents the cell downstream (upstream) of $j$. The variables $n_j(k), f_j(k), N_j(k)$ denote the number of vehicles, the actual inflow, and the maximum number of vehicles allowable in cell $j$ at time $k$. The variables $Q_j(k)$ denote the maximum allowable inflow in cell $j$ at time $k$. Eq. (4) describes the conservation of traffic in cell $j$, and determines the time-varying traffic condition: the number of vehicles in cell $j$ at time $k+1$ is equal to the number of vehicles that was in that cell at time $k$ plus the number of vehicles that entered, and minus the number of vehicles that left. Eq. (5) shows that the number of vehicles entering cell $j$ at time $k$ is the minimum of three terms: vehicles at the upstream cell waiting to enter $j$, the inflow capacity of $j$, and a function of the available space in $j$. This equation covers automatically the whole range of congested and non-congested region as shown in Fig. 2. After the actual inflow is determined, traffic flow in the network can be updated by Eq. (4).

The model only describes the intercellular traffic flow propagation in a single section, but the research literature [8] further extends it to the network:

1) Ordinary links (as shown in Fig. 3.)
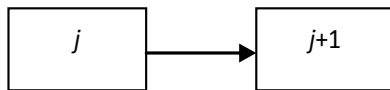


**Fig. 3.** Ordinary links.

We define $S_j(k) = \min\{Q_j(k), n_j(k)\}$ as the maximum flows that can be sent by cell $j$ in the interval between $k$ and $k + 1$ and $R_{j+1}(k) = \min\{Q_{j+1}(k), \delta[N_{j+1}(k) - n_{j+1}(k)]\}$ as the maximum flows that can be received by cell $j + 1$ in the interval between $k$ and $k + 1$, where $\delta = \omega/v_f$. Then the actual inflow in cell $j+1$ at time $k$ is: $f_{j+1}(k) = \min\{S_j(k), R_{j+1}(k)\}$.

2) Merges (as shown in Fig. 4):
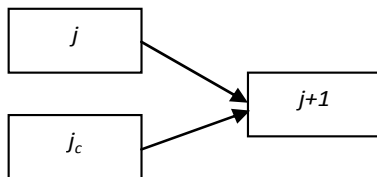


**Fig. 4.** Representation of a merge.

If

$$R_{j+1}(k) < S_j(k) + S_{j_c}(k),$$

then

$$f_{j,j+1}(k) = \min\left\{S_j(k), \ R_{j+1}(k) - S_{j_c}(k), \ p_j R_{j+1}(k)\right\}$$

$$f_{j_c,j+1}(k) = \min\left\{S_{j_c}(k), \ R_{j+1}(k) - S_j(k), \ p_{j_c} R_{j+1}(k)\right\}$$

It is assumed that a fraction $(p_j(k))$ of the vehicles come from $j$ and the remainder $(p_{jc}(k))$ from $j_c$, where $p_j(k) + p_{j_c}(k) = 1$, For the sake of simplicity, they are determined according to maximum input flow $Q(k)$ at time $k$, namely,

$$p_j(k) = \frac{Q_j(k)}{Q_j(k) + Q_{j_c}(k)}, p_{j_c}(k) = \frac{Q_{j_c}(k)}{Q_j(k) + Q_{j_c}(k)}.$$

If $R_{j+1}(k) > S_j(k) + S_{j_c}(k)$,

then $f_{j,j+1}(k) = S_j(k), \ f_{j_c,j+1}(k) = S_{j_c}(k)$.

3) Diverges (as shown in Fig. 5):
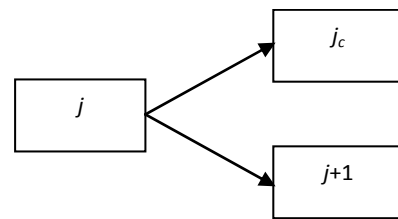


**Fig. 5.** Representation of a diverge.

Thus,

$$f_j(k) = \min\left\{S_j(k), \ R_{j+1}(k)\Big/\beta_{j+1}(k), \ R_{j_c}(k)\Big/\beta_{j_c}(k)\right\},$$

where $\beta_{j+1}(k) + \beta_{j_c}(k) = 1$, the $\beta_{j+1}(k)$ and $\beta_{jc}(k)$ denote the proportions of $S_j(k)$ going each way respectively:

$$\beta_{j+1}(k) = \frac{f_{j+1}(k)}{f_j(k)}, \ \beta_{j_c}(k) = \frac{f_{j_c}(k)}{f_j(k)}.$$

As the CTM provides a numerical approximation to the LWR equations, all the traffic phenomena demonstrated in the LWR model can be fully replicated in CTM. On the basis of LWR model, CTM can also cover the full range of the fundamental density-flow-speed relationships diagram. So the traffic dynamics model based on CTM can be applied to traffic signal optimal control problem in a variety of traffic condition.

## 2.2. CTM-Based Intersection Traffic Dynamics Model

Traffic flow distribution based on CTM of an isolated intersection is shown in Fig. 6.

The traffic flow in Fig. 6 can be divided into two independent types [9]:

1) The set of source link—where exogenous traffic demand is introduced to the intersection, such as links 1, 2… 8 in Fig. 6.
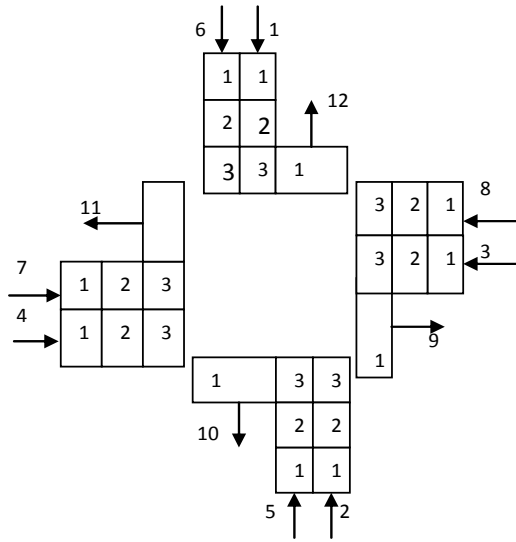
**Fig. 6.** CTM-based traffic flow distribution of an isolated intersection.

2) The set of exit link—where all the traffic flow terminates and exits the intersection, such as links 9, 10, 11, 12 in Fig. 6.

Each link of the isolated intersection can be subdivided into a number of cells. The cells can be named consecutively from the upstream direction of traffic flow as follows: cell $(i, j)$ represents the *j*-th cell in link *i*, and the first cell of link *i* is named as cell $(i, 1)$. For instance, cell $(1, 1)$ means the first cell of link 1.

There are the cells with special characteristics as discussed below [9]:

1) The first cell in a source link at time $k=1$ stores the total demand that intends to enter the intersection—the effect of a big parking lot. The inflow capacity of the second cell, $Q_{i2}(k)$, $i=1$, 2…8, of a source link is set to the exogenous dynamic demand, $D_i(k)$. Vehicles will enter the intersection according to the dynamic demand if space is available in the second cell. Otherwise, vehicles will wait in the big parking lot. As $Q_{i2}(k)$, $i=1, 2…8$ is time variant, one can model dynamic demand readily from this formulation. Mathematically:

$$n_{i1}(1) = \sum_k D_i(k), \; i=1, 2…8, \qquad (6)$$

$$Q_{i2}(k) = D_i(k), \; i=1, 2…8, \qquad (7)$$

where $n_{i1}(1)$ denotes the number of vehicles in cell $(i, 1)$ at time $k = 1$; $Q_{i2}(k)$ the inflow capacity of cell $(i, 2)$ at time $k$; and $D_i(k)$ the exogenous demand into source link *i* at time *k*.

2) The third cell in a source link simulates the action of a signal. Its inflow capacity is set to the saturation flow when $k$ is in a green phase; zero otherwise. That is

$$\begin{cases} Q_{i3}(k) = S_i \; if \; k \in green \; phase, i = 1, 2…8 \\ Q_{i3}(k) = 0 \; if \; k \in red \; phase, i = 1, 2…8 \end{cases} \qquad (8)$$

where $S_i$ is the saturation flow and $Q_{i3}(k)$ is the inflow capacity of cell $(i,3)$, $i=1, 2…8$.

3) The exit links have only one cell. It serves as a reservoir to store the vehicles that exit from the intersection. The cell's holding capacity is set to infinity in order not to restrict the arrival of vehicles.

In Fig. 6, by carefully relating the neighboring cells, and the difference equations Eqs, (4) - (5) can be written for each cell in the intersection. And the cell in an exit link is the equal of a merge cell, and the through and left-turning traffic flows from the upstream direction of the intersection enter this merge cell as shown in Fig. 7:
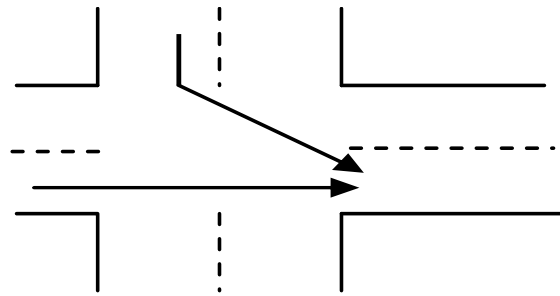


**Fig. 7.** Intersection schematic diagram of a merge.

As the storage of a cell in exit link is set to infinity, the through and left-turning traffic flow into the merge cell is calculated by the following:

$$f_{i3}(k) = \min\{n_{i3}(k), Q_{i3}(k)\}, \; i=1,2…8.$$

where $n_{i3}(k)$ denotes the number of vehicles in the third cell of a source link (signalized cell), $Q_{i3}(k)$ the outflow capacity of signalized cell. And the number of vehicles in the merge cell is updated according to the following formula (cell $(9, 1)$ in Fig. 6 as an example):

$$n_{91}(k+1) = n_{91}(k) + f_{43}(k) + f_{13}(k).$$

So the model based on CTM can simulate traffic flow running state and signal control condition of the intersection.

### 2.3. CTM-based Intersection Traffic Signal Optimization Model

The vehicle delay and the total capacity of traffic flow of an isolated intersection in Fig. 6 are taken as comprehensive optimization objective function and cycle time and duration of each green signal phase as decision variables, and a multi-objective optimization model based on CTM for urban traffic signal dynamic control is presented under uncertain traffic demand so as to find the

151

optimal signal timing planning. To represent the uncertainty of traffic flow of each source link to the intersection, a set of random events $\Omega_i = \{1, 2, 3\ldots Y\}$ is introduced. For each random event $y \in \Omega_i$, the occurrence probability is $p^y$, and the traffic flow at link $i$ is $q_i^y$, $i=1, 2\ldots 8$.

### 2.3.1. Total Vehicle Delay Calculation

As mentioned above, when a random event $y$ for the traffic flow $i$ happens, the corresponding traffic flow is $q_i^y$, thus, the total delay under traffic flow event $y$, $D^y$, can be determined. CTM provides a convenient way to determine the delay in a cell. This delay is defined to be the additional time beyond the nominal or free-flow travel time a vehicle stays in a cell [9]. At the cell level, the delay is determined as:

$$d_{i,j}(k) = n_{i,j}(k) - f_{i,j+1}(k).$$

Basically, if the exit flow from cell $(i, j)$ at time $k$ is less than its current occupancy, those that cannot leave the cell will incur a delay of one time step. Then, at the intersection level, which can be expressed as:

$$D^y = \sum_k \sum_i \sum_j d_{i,j}(k), \qquad (9)$$

### 2.3.2. Total Vehicle Capacity Calculation

The total capacity of traffic flow of an isolated intersection can be obtained by calculating the number of all vehicles through the intersection, which is all the vehicle number in all exit cells at the end of the entire study period in Fig. 6 [10]. Thus, under traffic flow event $y$, the computation formula of the total capacity of traffic flow of an isolated intersection is as follows:

$$Pa^y(k) = n_{9,1}(k) + n_{10,1}(k) + n_{11,1}(k) + n_{12,1}(k), \quad (10)$$

where $n_{9,1}(k)$, $n_{10,1}(k)$, $n_{11,1}(k)$ and $n_{12,1}(k)$ denote the number of vehicles in exit cells (9,1), (10,1), (11,1) and (12,1) at time $k$ under traffic flow event $y$, respectively.

### 2.3.3. Constraint Condition

The duration of each green signal phase $g_1(l)$, $g_2(l)$, $g_3(l)$ and $g_4(l)$ in the $l$ cycle and cycle time $C(l)$ of per cycle within the study period can be determined dynamically through certain optimization method, and which meets the needs of constraints:
1) Uncertain exogenous dynamic demand:

$$Q_{i2}^y(k) = D_i^y(k), \ i=1,2\ldots 8, y \in \Omega_i, \qquad (11)$$

where $D_i^y(k)$ is the exogenous uncertain demand into source link $i$ at time $k$ under traffic flow event $y$, and $Q_{i2}^y(k)$ is the inflow capacity of cell $(i, 2)$ in source link $i$ at time $k$ under traffic flow event $y$.

2) In order to avoid the traffic jams caused by the too short duration of green signal phase, each green phase time in per cycle should meet the following constraints:

$$C(l) = g_1(l) + g_2(l) + g_3(l) + g_4(l), l=1,\ldots L$$
$$g_{min} \le g_p(l) \le g_{max}, p=1,2,3,4 \qquad (12)$$
$$C_{min} \le C(l) \le C_{max},$$

where $C(l)$ is a cycle time of the four-phase total time in a cycle $l$, $g_p(l)$ is a green time of $p$ phase in a cycle $l$; $g_{min}$ and $g_{max}$ are the minimum and maximum green time respectively; and $C_{min}$ and $C_{max}$ are the minimum and maximum cycle length respectively. The authors assume that the total loss of time is not considered, and the study period is $L$ cycles.

### 2.3.4. Optimization Model

Minimum vehicle delay and maximum capacity of traffic flow of an isolated intersection are taken as evaluation index. As they have the different dimensions, they should first be done through linear normalization process and then through linear weighted sum: $\dfrac{D^y}{D_0} - \mu \cdot \dfrac{Pa^y}{Pa_0}$, where $D_0$ and $Pa_0$ are the initial value of the total delay and capacity. In this paper, the authors hope to minimize the comprehensive evaluation index, so the second item in the above formula will be negative, which will maximize the total capacity; where $\mu$ is a weight coefficient of a multi-objective optimization problem converted into a single objective optimization problem.

When the uncertainty and dynamic change of traffic flow are considered, to determine the optimal cycle time and duration of each green signal phase per cycle, the optimization model can be represented as:

$$\min J = \min \sum_y p^y \cdot (\dfrac{D^y}{D_0} - \mu \cdot \dfrac{Pa^y}{Pa_0}) \ \ y \in \Omega_i, \qquad (13)$$

$$s.t. \quad C(l) = g_1(l) + g_2(l) + g_3(l) + g_4(l), l=1,\ldots L$$

$$g_{min} \le g_p(l) \le g_{max}, p=1,2,3,4$$

$$C_{min} \le C(l) \le C_{max}$$

where $\sum_y p^y \cdot (\dfrac{D^y}{D_0} - \mu \cdot \dfrac{Pa^y}{Pa_0})$ is the weighted sum with the occurrence probability $p^y$ of traffic flow events $y$.

When cycle time $C(l)$ and duration of each green signal phase $g_1(l)$, $g_2(l)$, $g_3(l)$ and $g_4(l)$ are taken as decision variables, the relationship between them with objective function $J$ need to be built. And as the mentioned above, the influence of signal timing planning on the objective function based on CTM is produced through their effect on the value of the outflow capacity of signalized cells (i.e. the cell $(i, 3)$), $Q_{i3}(k)$. Therefore, the relationship between timing planning with output capacity of the corresponding signalized cells should be firstly set up and then establish the relationship with the objective function $J$. The specific circumstances can be illustrated by signal phase diagrams as shown in Fig. 8.

For the $l$-th cycle:

The first phase: the start and end times of that phase, $Sp_1(l)$, $Ep_1(l)$, are, respectively,

$$Sp_1(l) = \sum_{x=1}^{l} C(x-1) \text{ (given } C(0)=0) \text{ and}$$

$$Ep_1(l) = Sp_1(l) + g_1(l), \text{ if } Sp_1(l) \le k \le Ep_1(l),$$

then

$$\begin{cases} Q^y_{23}(k) = S_2, \ Q^y_{63}(k) = S_6 \\ Q^y_{13}(k) = Q^y_{33}(k) = Q^y_{43}(k) = Q^y_{53}(k) = Q^y_{73}(k) = Q^y_{83}(k) = 0 \end{cases}$$
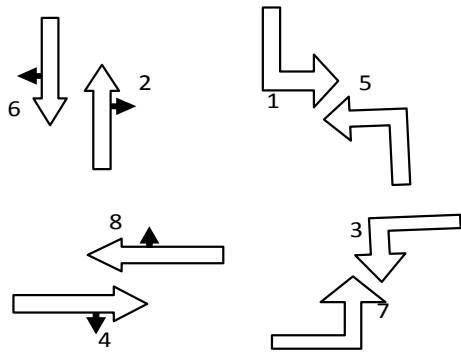


**Fig. 8.** The signal phase diagram of a four phase.

The second phase: the start and end times of that phase, $Sp_2(l)$, $Ep_2(l)$, are, respectively,

$$Sp_2(l) = \sum_{x=1}^{l} C(x-1) + g_1(l) \text{ and}$$

$$Ep_2(l) = Sp_2(l) + g_2(l), \text{ if } Sp_2(l) \le k \le Ep_2(l), \text{ then}$$

$$\begin{cases} Q^y_{13}(k) = S_1, \ Q^y_{53}(k) = S_5 \\ Q^y_{23}(k) = Q^y_{33}(k) = Q^y_{43}(k) = Q^y_{63}(k) = Q^y_{73}(k) = Q^y_{83}(k) = 0 \end{cases}$$

The third phase: the start and end times of that phase, $Sp_3(l)$, $Ep_3(l)$, are, respectively,

$$Sp_3(l) = \sum_{x=1}^{l} C(x-1) + g_1(l) + g_2(l) \text{ and}$$

$$Ep_3(l) = Sp_3(l) + g_3(l), \text{ if } Sp_3(l) \le k \le Ep_3(l), \text{ then}$$

$$\begin{cases} Q^y_{43}(k) = S_4, \ Q^y_{83}(k) = S_8 \\ Q^y_{13}(k) = Q^y_{23}(k) = Q^y_{33}(k) = Q^y_{53}(k) = Q^y_{63}(k) = Q^y_{73}(k) = 0 \end{cases}$$

The fourth phase: the start and end times of that phase, $Sp_4(l)$, $Ep_4(l)$, are, respectively,

$$Sp_4(l) = \sum_{x=1}^{l} C(x-1) + g_1(l) + g_2(l) + g_3(l) \text{ and}$$

$$Ep_4(l) = Sp_4(l) + g_4(l), \text{ if } Sp_4(l) \le k \le Ep_4(l), \text{ then}$$

$$\begin{cases} Q^y_{33}(k) = S_3, \ Q^y_{73}(k) = S_7 \\ Q^y_{13}(k) = Q^y_{23}(k) = Q^y_{43}(k) = Q^y_{53}(k) = Q^y_{63}(k) = Q^y_{83}(k) = 0 \end{cases}$$

## 3. Optimization Methods

In this paper, as there is much the complexity of traffic signal control problem, the genetic algorithm is adopted for the solution of the model. Genetic algorithm provides a generic framework for solving complex system optimization problems. It does not depend on the specific areas of the problem. The genetic algorithm simulates the phenomenon occurring in the natural selection, the reproduction, the crossover and the mutation. It starts from any initial population by random selection, crossover and mutation operation to produce a group of individuals better-adapted to the environment, making the population evolve to better and better area in the search space. In this way, population reproduces and evolves from generation to generation, finally convergences to a group of individuals most-adapted to the environment, and the optimal solution of problem can be got [11]. Main optimization calculation process is described below:

1) Determine the individual coding way: The floating-point encoding is used here. The floating-point coding means that the individual gene value is expressed in a range of a floating point number and the individual coding length is equal to the number of decision variables in optimization problems. This coding way uses real value of decision variables as an individual's genes, and it is also known as the true value coding method. The true value coding method is direct and natural description of continuous optimization problems, and there is no encoding and decoding process, and will improve solution accuracy and computing speed [11].In this paper, the authors express an individual with $[g_1(1) \ g_2(1) \ g_3(1) \ g_4(1) \ \dots \ g_1(L) \ g_2(L) \ g_3(L) \ g_4(L)]$, where $g_1(l)$, $g_2(l)$, $g_3(l)$ and $g_4(l)$ represent duration of each green signal phase of four phases in 1 cycle, which are the decision variables of optimization problems (since $C(l)$ can be determined by $C(l) = g_1(l) + g_2(l) + g_3(l) + g_4(l)$).

2) Generate the initial population: Set the size of the population between 10 to 200 according to the actual situation [11]. In this paper, the authors randomly generate 100 individuals to meet the constraint conditions (12) to form an initial population, and set the maximum number of generations and other genetic algorithm parameters.

3) Determine the fitness function: Determine it according to the objective function of optimization

problem *J*. In this paper, the authors calculate the fitness value with fitness distribution method based on sorting. The corresponding objective function values of all the individuals in a population will be sorted firstly in descending order. As the minimum problem in this paper is considered, the maximum objective function value will be placed in the first position in the ranking list of the objective function value, and the minimum objective function value is placed in the last position on the list, Then the fitness value of each individual can be calculated according to its position in the ordered list, that is: the direct use of the objective function as fitness function.

4) Genetic operations: This includes selection, recombination and mutation process to create the next generation. The chromosome in a generation of "offspring" is removed if it is not subject to the constraints (12).

5) Judge whether the process has run to the maximum number of generations: if "yes", to perform the next step; or jump to step (3).

6) Give the Pareto best solution according to minimum objective function value, i.e., the best effective green time of the four phases and cycle time.

# 4. Numerical Simulations

The effectiveness of the above model is verified by four-phase signal intersection in Fig. 6.

## 4.1. The Input Parameters Configurations

The traffic demands in the traffic flow direction $i$, $i$= 1, 2... 8, are dynamic change throughout the study period T = 1000 s (about eight timing cycles): Assuming that the traffic demand is unsaturated in 0 ~ 300 s time segment, oversaturated in 301 ~ 600 s time segment and unsaturated in 601 ~ 1000 s time segment; there were vehicles on network in advance, which accounts for 75 % of the jam density; And the traffic demands are also fluctuating at the same study period of each day. This uncertainty can be represented by a set of traffic flow samples following normal distribution. The distribution parameters are traffic flow means and SDs as shown in Table 1.

And these traffic flow samples are a set of traffic flow events with equal occurrence probability. Other parameters of the intersection are set as follows: the minimum green time $g_{min}$ = 10 s, the maximum green time $g_{max}$= 90 s, the minimum cycle length $C_{min}$ = 40 s, the maximum cycle length $C_{max}$= 120 s, and the study period is divided into K=100 time intervals to yield every time interval

$T_s$ = 10 s. In the second column in Table 1 the saturation flow of all links $i$ =1, 2… 8 are given.

**Table 1.** The input data.

| Link number | Saturation flow (veh/h) | Non-saturated | | Over-saturated | |
|---|---|---|---|---|---|
| | | means | SDs | means | SDs |
| 1 | 3800 | 400 | 100 | 525 | 140 |
| 2 | 1900 | 225 | 65 | 275 | 90 |
| 3 | 1900 | 275 | 65 | 275 | 60 |
| 4 | 3800 | 650 | 125 | 875 | 160 |
| 5 | 1900 | 250 | 25 | 350 | 75 |
| 6 | 3800 | 500 | 100 | 650 | 175 |
| 7 | 3800 | 650 | 75 | 900 | 150 |
| 8 | 1900 | 170 | 25 | 250 | 65 |

## 4.2. Simulation Result Analysis

The traffic flow samples produced according to the input data in Table 1 can be taken as the uncertain traffic demand of all source links, and then are loaded to the network, and the traffic flow propagation in intersection is simulated by CTM model.

Simulation results are shown in Table 2 and 3. On the first column in Table 2, "Fluctuation1, Fluctuation2, Fluctuation3 and Fluctuation4" represent four kinds of traffic flow situations, in which the fluctuation extent of the traffic flow increases gradually. On the fourth, fifth…and the last columns in Tables 2 and 3, they are the effective green durations of four phases in all cycles. Due to the limitation of space, only the effective green durations of four phases in the first and eighth cycle are listed. On the first column in Table 3, "Average" represents the average traffic flow situation.

The simulation results in Table 2 show that the corresponding vehicle delays of traffic flow are on the increase with the increase of traffic demand fluctuations, hence, the decrease of the capacity. Thus, even in the conditions of the dynamic change of traffic demand flow, the proposed CTM-based multi-objective model can effectively reflect the impact of the uncertainty of traffic demand for signal timing, vehicle delays and capacity calculation, and can achieve the optimal traffic signal setting for an isolated intersection. The simulation results in Table 3 show that compared the vehicle delay and capacity with the consideration of traffic demand fluctuation with those without consideration of it, the vehicle delay decreases while the capacity obviously increases so that the overall performance of the intersection and the adaptability of traffic signal control system can be improved.

**Table 2.** The delay and capacity calculation and signal settings under different fluctuations.

| | Delay value (s/ veh) | Capacity (veh) | Cycle 1 | | | | ... | Cycle 8 | | | |
|---|---|---|---|---|---|---|---|---|---|---|---|
| | | | $g_1(1)$ (s) | $g_2(1)$ (s) | $g_3(1)$ (s) | $g_4(1)$ (s) | ... | $g_1(8)$ (s) | $g_2(8)$ (s) | $g_3(8)$ (s) | $g_4(8)$ (s) |
| Fluctuation 1 | 68.46 | 1190 | 40 | 30 | 30 | 20 | | 40 | 20 | 30 | 30 |
| Fluctuation 2 | 75.89 | 1186 | 20 | 30 | 30 | 40 | | 40 | 30 | 20 | 30 |
| Fluctuation 3 | 77.56 | 1170 | 30 | 30 | 40 | 10 | | 30 | 20 | 40 | 30 |
| Fluctuation 4 | 83.20 | 1161 | 50 | 40 | 20 | 10 | | 30 | 30 | 30 | 30 |

**Table 3.** Comparison in both cases of considering and non considering traffic flow fluctuation.

| | Delay value (s/veh) | Capacity (veh) | Cycle 1 | | | | ... | Cycle 8 | | | |
|---|---|---|---|---|---|---|---|---|---|---|---|
| | | | $g_1(1)$ (s) | $g_2(1)$ (s) | $g_3(1)$ (s) | $g_4(1)$ (s) | ... | $g_1(8)$ (s) | $g_2(8)$ (s) | $g_3(8)$ (s) | $g_4(8)$ (s) |
| Average | 80.03 | 1148 | 40 | 40 | 30 | 10 | | 30 | 20 | 20 | 20 |
| Fluctuation | 79.48 | 1182 | 30 | 40 | 30 | 20 | | 30 | 30 | 30 | 30 |

# 5. Conclusions

A dynamic multi-objective traffic signal optimal control model based on CTM is established. The optimal timing planning is generated through optimizing the total delay and total capacity of the system in which the dynamic change and uncertainty of traffic demand are taken into account. The GA method is adopted. The simulation results show that the model can effectively display the influence of traffic flow fluctuation on the signal settings, vehicle delay and total capacity calculation under the dynamic change conditions from the non-saturated traffic flow to over-saturated traffic flow, and the optimized traffic signal timing planning and corresponding optimization performance index are got, which further illustrates the validity and practicability of the model. Although this model is aimed at an isolated intersection, its theory and method can also be extended to multi-intersection and network.

# Acknowledgements

# References

[1]. Webster F. V., Traffic Signal Settings, Road Research Technical Paper No. 39, Department of Scientific and Industrial Road Research Laboratory, Her Majesty's Stationery Office, London, England, 1958.

[2]. Wallace C. E., Courage K. G., Hadi M. A., et al., TRANSYT-7F User's Guide, *University of Florida*, Gainesville, FL, 1998.

[3]. Yin Ya-Feng, Robust optimal traffic signal timing, *Transportation Research Part B,* Vol. 42, 2008, pp. 911–924.

[4]. Ribeiro P. C. M., Handling traffic fluctuation with fixed-time plans calculated by TRANSYT, *Traffic Engineering and Control,* Vol. 35, Issue 6, 1994, pp. 362-366.

[5]. Lighthill M. J., Whitham G. B., On kinematic waves: a theory of traffic flow on long crowded roads, *Proceedings of Royal Society Series A*, Vol. 22, 1955, pp. 317-345.

[6]. Richards P. I., Shock waves on the highway, *Operations Research*, Vol. 4, 1956, pp. 42-51.

[7]. Daganzo C. F., The cell transmission model part I: a simple dynamic representation of highway traffic, *Transportation Research Part B: Methodological,* Vol. 28, Issue 4, 1994, pp. 269-287.

[8]. Daganzo C. F., The cell transmission model part II: network traffic, *Transportation Research Part B: Methodological*, Vol. 29, Issue 2, 1995, pp. 79-93.

[9]. Lo H. K., A Cell-Based Traffic Signal Control Formulation: Strategies and Benefits of Dynamic Timing Plans, *Transportation Science*, Vol. 35, Issue 2, 2001, pp. 148-164.

[10]. Zeng Jian-Qin, Wang Jia-Jie, et al., CTM-MOGA Based Crossroad Traffic Signal Control, *Journal of University of Science and Technology of China*, Vol. 35, Issue 2, 2005, pp. 284-290.

[11]. Lei Ying-Jie, Zhang Shan-Wen, Li Xu-Wu, etc., The MATLAB genetic algorithm toolbox and its application, *Xi'an University of Electronic Science and Technology Press,* Xi'an, 2005.

---

# A Case Study of the Seasonal Underground Variation Contributions to the gPhone Gravimeter Observations Based on Fourier Analysis

**[1, 2, 3] Wei Jin, [2, 3] Li Hui, [1] Shen Wenbin**

[1] School of Geodesy and Geomatics, Wuhan University, Wuhan 430079, China
[2] Institute of Seismology, CEA, Wuhan 430071, China
[3] Crustal Movement Laboratory, Wuhan 430071, China
[1] Tel.: 15927365563
E-mail: pierce212@163.com

**Abstract:** In this paper, the seasonal gravity variation rules of gPh040 continuous gravity visualizer in Wujiahe seismic station caused by underground water variation was obtained with the Fourier series analysis method and polynomial fitting method using the continuous gravity observation data of this kind of gravimeter within the period of two and a half years. The result shows that the observation accuracy of gPh040 can reach up to 50 % of the accuracy of superconductive gravimeter in the noise level of approximately $\pm 0.3 \times 10^{-8}$ ms$^{-2}$/cm. The seasonal underground water contributions can be well obtained by both of the two methods compared with the actual measurement of underground water variation and the global water model (the correlation coefficient of above 80 %). And the correlation coefficient between drift correction method of Fourier analysis and actual measurement of underground water level is as high as 95 %. The impact factor ($0.153 \times 10^{-8}$ ms$^{-2}$/cm) of underground water level variation to gravity calculated by this method is near the theoretical result of physical ground measurement. Therefore, comparing with the polynomial fitting method, the Fourier analysis method can not only fit a better continuous drift of spring gravimeter but also provide a new analysis way to contrast the contribution of seasonal underground variation to the gPhone type continuous gravity observation. *Copyright © 2014 IFSA Publishing, S. L.*

**Keywords:** gPhone040, GLDAS, CPC, Underground water, Fourier analysis.

## 1. Introduction

Continuous gravity observation is able to detect the long-term (years) and short-term (seasons) variation of superposed gravity change effects, which is caused by the migration of various materials in earth system [1]. The gravity change effects mainly consist of self-changes of hydrology, atmosphere, earth and ocean tides, etc, and the materials migration process of earth crust deformation in earth system and structure changes caused by its loads [1-5]. To collect long-term signals, spring and superconductive

gravimeter must face the interference of drift in effective signal. Van Camp and Francis (2007) [6] studied the drift characteristic of superconductive gravimeter with absolute gravimeter, and they pointed out that the drift of gravimeter could be confirmed by the same site observation of absolute gravimeter and superconductive gravity gravimeter. Riccardi et al (2011) [7] researched the drift characteristic of gPhone gravimeter using polynomial fitting method by comparison and measurement of gPhone054 spring gravimeter and GWRC026, although the observation data of gravimeter

especially the spring gravimeter could be interrupted in the actual observation by the interference of external factors such as power failure and lighting stroke, eventually the complexity of segmentation fitting would be increased and the observation data could not be used at all. The research team of Institute of Seismology in China Seismological Bureau [8] studied the observation data of seven gPhone gravimeters in the digital earthquake observation network using segmentation fitting drift method, and proposed the contribution of underground water variation to gravity field.

This work is based on the observation data of gPhone gravimeter in Wujiahe seismic station during the years of 2008~2011 in the digital earthquake observation network. The spring gravimeter drift is confirmed and the gravity variation signals caused by seasonal variation of underground water are quantitatively contrasted using a new analysis method with comprehensive consideration of air pressure and underground water level monitor tools of this station, with constraint of global land water model, and with combination of spring type gravimeter drift continuity and the continuity characteristics of gravity variation.

## 2. Fourier Analysis of Solid Earth Tides Observation Data

Although there is a lot of complexity as to the spring gravimeter drift, the drift is a continuous process without the obvious interference of external factors (measurement break down, serous lighting stroke, long term failure due to power cut, etc.) to spring [9]. The superimposed gravity variation caused by external factors should also be a continuous process. Therefore, considering that any of continuous periodic function could be unfolded as Fourier series, this work simulated and observed the complex and continuous drift using the Fourier analysis method. The non-tidal analysis model and drift error function simulated by Fourier series are as follows:

$$g_{gPhone} = g_{tide+ocean} + g_{nontidel} + g_{drift} + \varepsilon , \quad (1)$$

$$g_{nontide} = g_{air} + g_{pol} + g_{waterload} + \varepsilon_1 , \quad (2)$$

$$g_{drift}(t_i) = a_0 + \sum_{j=1}^{n}(a_j \cos \omega_0 n t_i + b_j \sin \omega_0 n t_i) + \varepsilon_2 \quad (3)$$

In equation (1), the gravity observation data $g_{gPhone}$ is mainly consist of tidal part $g_{tide}$, non-tidal part $g_{nontide}$, the drift $g_{drift}$, and the error $\varepsilon$. In equation (2), the non-tidal part $g_{nontide}$ is mainly resulted from the pole-shift tide $g_{pol}$ and the migration contribution of seasonal materials, such as air pressure load $g_{air}$, water load $g_{waterload}$, and non-tidal noise $\varepsilon_1$. Equation

(3) adopts the truncated form of infinite series (up to n order), where $g_{drift}$ is the drift of meter, $a_j$ and $b_j$ $(j = 1,2,3...,n)$ are the fitting parameter of Fourier series, n is the order of Fourier series, $t_i$ $(i = 0,1,2,3,...,m)$ is the observation time, the subscript $i$ represents for the observation time counted as $i$, m is the total observation data numbers, and $\omega_0$ is the angular speed which is usually calculated by $\pi/(m-1)$.

Given a drift time sequence, the Fourier series fitting parameter $a_j$, $b_j$ $(j = 1,2,3...,n)$ can be resolved using error function equation (3) and the least squares principle, thus the drift rules of observation time sequence can be confirmed.

## 3. Handling and Analyzing of Observation Data in Wujiahe Seismic Station

### 3.1. Station and Observation Data

In the year of 2007, 17 gPhone type of spring gravimeter was induced from LRC Corporation U.S.A. by China Seismological Bureau. The continuous observation and measurement was performed in Joufeng seismic station in Wuhan Hubei Province. The gravimeter was calibrated using the $M_2$ wave tidal factor measured by the superconducting gravimeter SGC053 in this station in 2010. The calibration factor of gPhone040 (gPh040 for short below) spring gravimeter was $1.0024\times10^{-8}$ ms$^{-2}$/V. After the measurement, the gPh040 spring gravimeter was installed in the cave of Wujiahe seismic station in Nei Monggol Autonomous Region in 2007. The north of this cave was Yin Mountain, and the south was wide Hetao impact plain. It had drought in nine years out of tem. The station provided not only the assistant observation of air and water pressure and rainfall, but also the observation station of underground water level in the mountain 800 miles away far from the seismic station. After the test run, gPh040 has been working regularly since Sep. 2008. Although a small time of power cut and failure happened during the observation process, the meter could work stable on the whole. The data sample interval of gPh040 is 1 Hz.

### 3.2. Data Pre-processing

It is shown in Fig. 1 that the main factor which influents the spring gravimeter is the irregular drift of spring beside the solid earth tide. At the same time, the anisotropy of the spring itself leads to the difficulty of accurate simulation of spring drift using fixed mathematical function. Finally, the micro-gal level effect caused by external factors would be covered up of by solid earth tide, and what's more, flooded by the spring gravimeter drift.
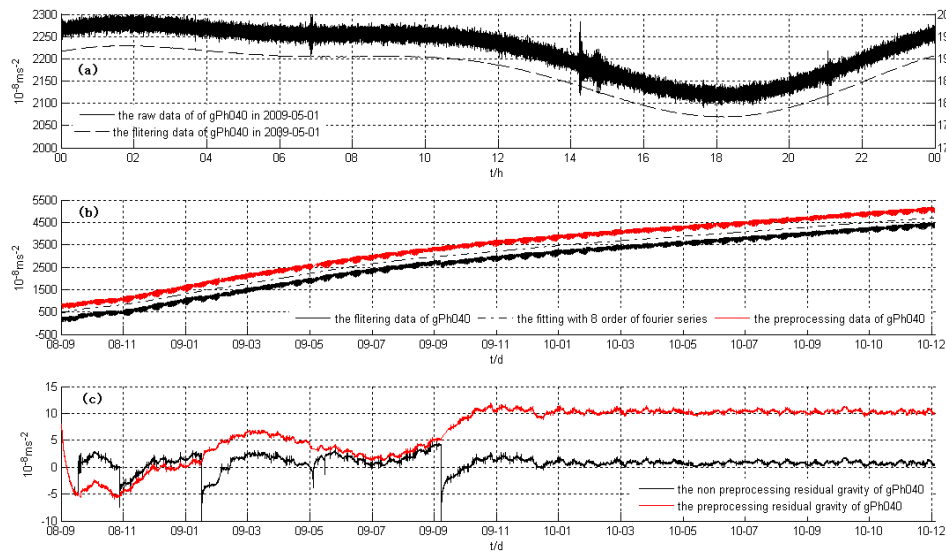
**Fig. 1.** The data preprocessing of gPh040 with Fourier analysis.
a) The raw data of gPh040 with 1 Hz (solid line), and the filtering data of gPh040 with 1 circle per minute (dotted line) at 2009-05-01; b) The filtering data (black line), the preprocessing data (red line) and the drift fitting by 8 order of Fourier series; c) The non preprocessing residual (black line) and preprocessing residual gravity (red line) of gPh040.

Based on the continuous drift of spring gravimeter and the gravity variation caused by natural environment, this work firstly filtered the sampling data at 1 Hz of gPh040 using ideal low pass filter [10]. Then the minute sampling gravity observation data were obtained by calibrating transformation. High order Fourier series were utilized to simulate the spring gravimeter drift after amendment of tides (see tides included). The tide amendment of observation data and their drift amendment by Fourier series fitting were performed. The residual should also be a continuous function and the variation could not exceed $100 \times 10^{-8}$ ms$^{-2}$. The pre-processing experience of superconducting gravimeter was used for reference again [11], the accuracy and efficiency of data pre-processing would be improved by time sequence amendment of the residual after drift amendment. The dash lines in Fig. 1 (b) shows the eight order Fourier series fitting drift in this work.

In the continuous gravity observation from Sep. 2008 to Jan. 2011, the gradual recovering drift which was resulted from the external factors such as power cut, lightning stroke, and strong shock and exceeded $5\text{-}10 \times 10^{-8}$ ms$^{-2}$ was hardly to distinguish by eyes because of the cover up of drift and solid earth tides under the original observation data. This work could distinguish well and further modify these errors due to the non-environment factors during observation process by Fourier analysis method.

### 3.3. Analysis and Amendment of Tides

Based on the observation data pre-processing of gPh040, the international two reconcile and analysis software VAV03 and ETERNA34 were used to do the tidal analysis [12], obtain the main tidal parameter, and confirm the air press admittance value and white noise level in meter observation environment with combination of observation air pressure data at the same station in this work. The gPh040 observation accuracy and stability were weighed by the time variation of meter drift rate and the time variation consequence of the highest accuracy wave tidal factor M2. The analysis results are shown as Table 1 and Table 2.

**Table 1.** Harmonic analytical results and their comparison of 8 waves with VAV03 and ETERNA34.

| Wave group name | VAV reconcile and analysis results | | | | ETERNA reconcile and analysis results | | | |
|---|---|---|---|---|---|---|---|---|
| | Tidal factor | Mean square error | Phase position | Mean square error | Tidal factor | Mean square error | Phase position | Mean square error |
| Q1 | 1.17007 | 0.00079 | 0.350 | 0.039 | 1.16928 | 0.00173 | 0.314 | 0.085 |
| O1 | 1.16725 | 0.00016 | 0.190 | 0.008 | 1.16705 | 0.00036 | 0.180 | 0.018 |
| P1 | 1.16090 | 0.00039 | -0.099 | 0.018 | 1.15943 | 0.00088 | -0.039 | 0.046 |
| K1 | 1.14639 | 0.00011 | 0.071 | 0.006 | 1.14655 | 0.00028 | 0.086 | 0.014 |
| N2 | 1.16529 | 0.00039 | 0.041 | 0.019 | 1.16598 | 0.00063 | 0.025 | 0.031 |
| M2 | 1.16374 | 0.00008 | 0.086 | 0.004 | 1.16375 | 0.00013 | 0.088 | 0.006 |
| S2 | 1.16328 | 0.00025 | -0.024 | 0.016 | 1.16311 | 0.00028 | -0.038 | 0.015 |
| K2 | 1.16421 | 0.00058 | 0.140 | 0.028 | 1.16468 | 0.00085 | 0.190 | 0.042 |

The reconciling and analysis results of the former air pressure observation at the same station indicate that the errors of tidal factors of eight main tides are all better than ±0.8 ‰. And the mean square error order of the most accurate M2 tide is only 1/10 of the total level. Compared with the analysis result of high accurate superconducting gravimeter SGC053 [13], the mean square error is only twice than that of SGC053. Its phase position hysteresis varies at around 0° and the mean square error totally better than ±0.08°. This is revealing that although the observation accuracy of gPh040 is slightly lower than that of superconducting gravimeter, the gPh040 spring gravimeter could still provide excellent observation of gravity solid earth tide. What's more, the environment white noise level of gPh040 located in the cave is only ±0.3×10$^{-8}$ ms$^{-2}$.This cave provides good observation environment for observing the impact of external factors such as air pressure on the gravity.

At the same time, it can be seen from the drift rate time variation and M2 tidal factor time sequence variation that the total drift rate of gPh040 is not only about 300×10$^{-8}$ ms$^{-2}$/M, but also decreases gradually. But the tidal factor time sequence variation range is only 0.003 (relative variation of tidal factor is about

0.2 %), indicating the data of gPh040 gravimeter is stable in the former period and highly reliable.

The time series of the drift rate and the $\delta_{M2}$ on gPh040 are shown in Fig.2.

**Table 2.** The atmospheric pressure admittance and white noise level.

| Analysis method | Air pressure admittance value (10$^{-8}$ms$^{-2}$/mbar) | White noise Level (10$^{-8}$ms$^-$) |
|---|---|---|
| VAV analysis | -0.269±0.0107 | ±0.28 |
| ETERNA analysis | -0.265±0.0035 | ±0.35 |

Considering the Wujiahe seismic station is located inland, VAV03 tidal analysis was adopted in the tidal amendment to obtain the resultant tide. The tide-generating potential containing 1200 tidal wave component inferred by Tamura was used and the gravity variation caused by the resultant tide (solid earth tide and sea tide) in the pre-processing observation of gPh040 gravimeter was taken out. The gravity residual time sequence of Wujiahe seismic station is shown in Fig. 3 (a).
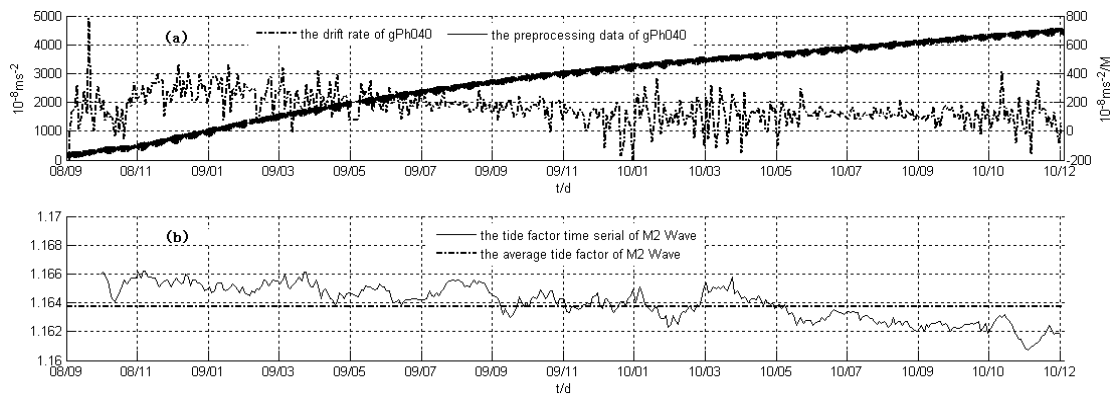


**Fig. 2.** The time series of the drift rate and the $\delta_{M2}$ on gPh040. (a) The time series of the preprocessed data and the drift rate on gPh040.(b) The average of $\delta_{M2}$ and the time series of the $\delta_{M2}$ on gPh040.
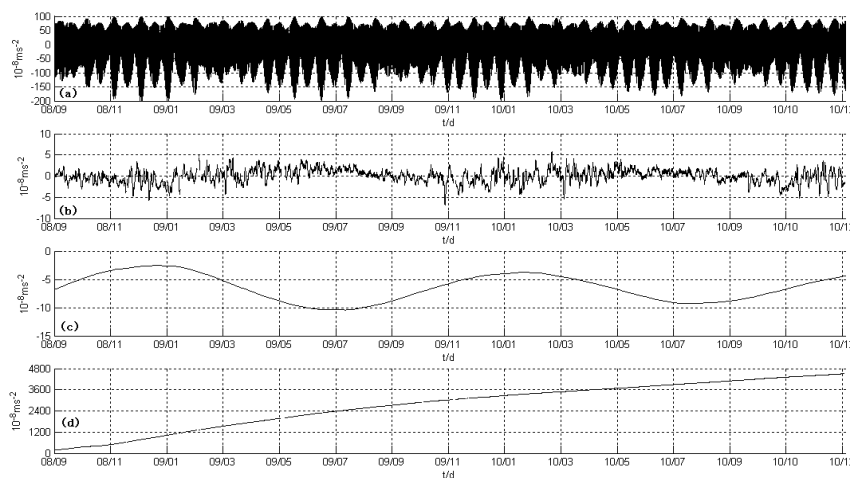


**Fig. 3.** Some correction and the residual of gPh040. (a) The synthetic gravity tides by VAV03 model;
(b) The time series after air pressure correction; (c) The time series after polar correction;
(d) The gravity residual series after correction of (a–c).

## 3.4. Polar Motion Amendment

The day sampling data are downloaded from International Earth Rotation Serve (IERS) website and used for observation data of calculating polar motion gravity effect. Then the linear function is used as interpolating hour value and the following equations are adopted for amendment of polar gravity effect [14]:

$$\Delta g_{pol} = -\delta_{pol}\omega^2 r \sin 2\theta[\cos(m_1\lambda) - \sin(m_2\lambda)] \quad (4)$$

where $m_1$ and $m_2$ are two parameters describing polar motion, $m_1$ points to meridian line direction which is east longitude 90°, $(\theta, \lambda)$ is the longitude and latitude of the station. The gravity effect is caused by the polar motion calculated by the equation. The gravity residual amendment value is $-\delta_g$. In this equation, tidal factor $\delta_{pol}$ is 1.16, the earth rotation angular speed $\omega$ is $7.292115\times10^{-5}$ rad/s, and the radius of earth $r$ is 6378137 m. The calculated results are shown in Fig. 3 (c).

## 3.5. Air Pressure Amendment

The gravity variation caused by atmosphere substances variation could be divided into the direct attraction impact of atmosphere load and the indirect impact generated from the atmosphere load caused by the earth's crust and sea level variation. The main parameter of measuring the effect of air pressure on a station is air pressure admittance value (shown as Table 1). In this work, the weighed mean air pressure admittance value $\alpha = -0.267 \pm 0.002 \times 10^{-8}$ ms$^{-2}$/mbar at this station is used, which is calculated by the two reconcile and analysis methods. The air pressure amendment equation is as follows:

$$\Delta g_{air} = -\alpha(p - p_n), \quad (5)$$

where $P$ is the time observation air pressure observation value (unit: mbar), $P_n$ is the normal air pressure value, which equals to 900.065 mbar. The air pressure data and their amendment values are shown in Fig. 3(b).

The amendment using the resultant tide confirmed by observation data, air pressure data observed at the same station, and the polar motion data published by IERS has shown that, beside the influence of resultant tide ($\pm150\times10^{-8}$ ms$^{-2}$), air pressure ($\pm5\times10^{-8}$ ms$^{-2}$) and polar motion amendment ($\pm8\times10^{-8}$ ms$^{-2}$), the biggest impact factor is still the spring drift. Therefore, the drift amendment must be done before extracting the influence of seasonal factors.

## 4. Comparison between Drift Amendment and Residual Time Sequence

The elastic system of gPhone gravimeter is composed of low drift metalized zero-length spring system. The factors such as elastic hysteresis, creep, after elastic effect, the decade, the temperature, and the pressure load of spring in gravimeter elastic system must be considered if simulating the spring gravity drift. Although there are lots of factors influences the spring, the drift of spring is continuous. In this work, two methods were chosen to simulate the spring drift, and the global water load model and the underground water data were used to check the seasonal variation of residual time sequence.

## 4.1. Global Earth and Water Model (CPC and GLDAS)

CPC (Climate Prediction Center) is a global land water model provided by Climatic Prediction Center of NOAA U. S. A., which is the 0.5o ×0.5o soil humidity network data formed by considering the factors of soil humidity, temperature, and water fall. The temporal resolution is 1 month. Their data reflect the soil humidity data of the global land. GLDAS (global land data assimilation systems) is a global land data fusion system provided by CSR laboratory of NASA U. S. A., which constrain and simulate the ground water condition using new generation ground and space observation data. The spatial resolution of this modal is 1°×1°, and the temporal resolution is 1 month. The land water is consisting of soil water, underground water, and snow water, but without the perpetual water content variation under ice.

When calculating the influence of global water on gPh040, the equivalent water height of each grid point in the global land water model is h, the load gravity influence Lg(θ, λ) can be calculated by Green's function integral formula. θ, λ are correspondingly the earth latitude and longitude. The calculating formula is as follows [15]:

$$Lg(\theta,\lambda) = R^2\rho\iint_s G(\psi)h(\theta',\lambda')\sin\theta' d\theta' d\lambda', \quad (6)$$

where R is the mean radius of earth, $\theta', \lambda'$ are the integral grid point coordinates, $\psi$ is the spherical angle distance between the station and grid point, $S$ is the entire land area.

## 4.2. Relative Analysis of Two Types of Drift Fitting Method

The first method is provided by Riccardi et al (2011) [3], the observation data are firstly drift amended linearly by one order, and then the residual are drift amended by high order polynomial fitting. The second method is the direct fitting drift (see section 2) using the Fourier analysis method proposed by our work. Considered the above amendments, the residual time consequence is mainly consisting of the influence of drift and water load. After analysis of the underground water level data of Wujiahe seismic station and the gPh040 gravimeter data after deduct of the residual time consequence, and the results are as Table 3 and Table 4.
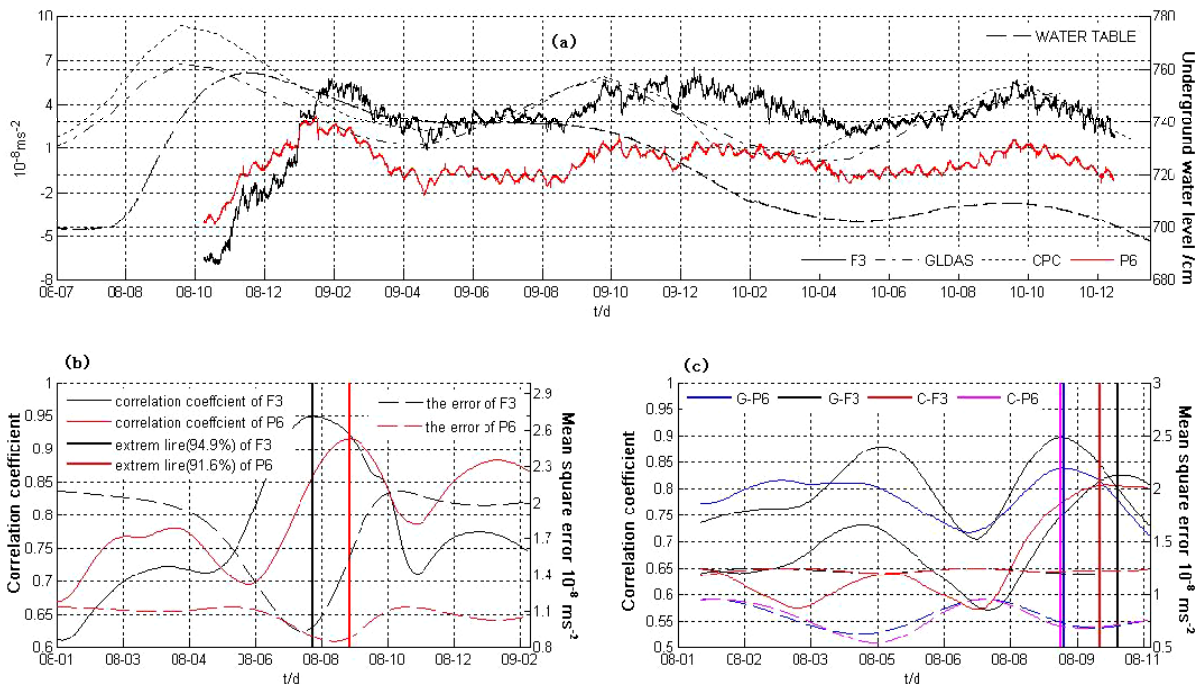
**Fig. 4.** The time series and correlated analysis between the residual of gPh040 with 3 order Fourier series and 6 order polynomial and the gravity change with CPC and GLDAS. (a) the time series of the table ground and the gravity effect by the global model of GLDAS and CPC; (b) The time series of the middle error and correlation coefficient between the ground table and F3, P6. The start point is 2008-01-01. The windows length is the length of F3 and F6. The step is 1 day. (c) The time series of the middle error and correlation coefficient between GLDAS, CPC, F3 and P6 by (b). The solid line in (b) and (c) represents the correlation coefficient. The dotted line indicates that the associated error analysis. Vertical lines represent extreme line.

**Table 3.** The table of the correlation analysis (hourly).

| Model | Proportionality coefficient | Correlation coefficient | Mean square error | Phase potion days |
|---|---|---|---|---|
| W-F1 | 1.911 | 0.952 | 11.873 | 34 |
| W-F2 | 0.151 | 0.927 | 1.277 | 91 |
| W-F3 | 0.155 | 0.949 | 0.972 | 77 |
| W-F4 | 0.097 | 0.892 | 1.039 | 82 |
| W-F5 | 0.093 | 0.891 | 1.085 | 82 |
| W-P4 | 0.191 | 0.868 | 2.127 | -79 |
| W-P5 | 0.079 | 0.897 | 0.929 | 66 |
| W-P6 | 0.094 | 0.916 | 0.874 | 45 |
| W-P7 | 0.055 | 0.865 | 0.708 | 37 |
| W-P8 | 0.038 | 0.855 | 0.557 | 48 |

**Table 4.** The correlation analysis between the residual and the global model (daily statistical results) *

| Model | Proportionality coefficient | Correlation coefficient | Mean square error | Phase delay |
|---|---|---|---|---|
| C-F3 | 0.126 | 0.806 | 1.225 | 81 |
| C-P6 | 0.350 | 0.896 | 0.701 | 107 |
| G-F3 | 0.237 | 0.825 | 1.184 | 68 |
| G-P6 | 0.376 | 0.838 | 0.729 | 105 |

*Notes: The table only considers the results that have the smallest mean square of phase delay and the biggest coefficient of association in the 2-3 months. In the column of model, W is water table, F is Fourier series, P is polynomial, C is CPC global land water model and G is GLDAS global land water model. CPC and GLDAS used the month water load model and linearly interpolating each day's gravity effect, and analysis the whole day residual time sequence value and global model interpolating value.

The statistical results (Table 3 and Table 4) show that beside the Fourier one order and fore order polynomial fitting method, the other phase position of drift amendment methods are all delayed by 2-3 months. When the Fourier series is fixed as 3-order or the polynomial fitting is fixed as 6-order, the

dependency of the two amendment methods exceeds 90 %. This analysis result is basically the same as the global model analysis results (the dependency exceeds 80 %). At the same time, the correlation coefficients calculated by Fourier series drift amendment method are all larger than those of polynomial fitting. Therefore, the 3-order Fourier series (F3 for short) and 6-order polynomial fitting (P6 for short) could eliminate the influence of drift on the spring gravimeter and extract the gravity signal variation caused by underground water level variation (fitting equations are shown in Table 5).

**Table 5.** The Fitting Function of 3-order Fourier series and 6-order Polynomial [*]

| Fitting method | Fitting times | Fitting equations |
|:---:|:---:|:---:|
| F3 | 1 | $g_{drift}=a_0+a_1 cos(\omega_0 t_i)+a_2 cos(2\omega_0 t_i)+a_3 cos(3\omega_0 t_i)$ $+ b_1 sin(\omega_0 t_i)+b_2 sin(2\omega_0 t_i)+b_3 sin(3\omega_0 t_i)$ $\omega_0=0.00015839; a_1=2775.5746; a_2=-476.0818; a_3=36.1102;$ $b_1=-181.1816; b_2=555.6707; b_3=115.3710;$ |
| P6 | 1 | $g_{drift}=kt_i+b; k=0.2122; b=591.38;$ |
| | 2 | $g_{drift}=a_0+a_1 t+a_2 t^2+ a_3 t^3+a_4 t^4+a_5 t^5+a_5 t^6;$ $a_0=-408.97; a_1=-0.0523; a_2=7.16\times10^{-5}; a_3=-1.156\times10^{-8};$ $a_4=7.79\times10^{-13}; a_5=-2.488\times10^{-17}; a_6=3.1095\times10^{-22};$ |

*Notes: Fourier series can calculated the drift curve in one time, while polynomial fitting method firstly uses 1-order polynomial to fit, and then use 6-order polynomial to fit again for the residual time consequence.

It can be seen from the time consequence curves in Table 4 (a) that the residual time consequence of the two drift amendment methods shows obvious fluctuate phenomenon. Compared with the time consequence of underground water level, the underground water level raised up for more than 60 mm in the four months started at Aug. 2008. And the gravity residual was lifted as well from Nov. 2008 to Mar. 2009. Compared with the global water load model, the variation of underground water level is seasonal, and the gravity residual time consequence of gPh040 after drift amendment has an obvious the same variation rules.

It is shown in the time consequence of correlation coefficient and mean square error that the three water models express the seasonal variation of water migration, and the gravity hysteresis variation caused by this water seasonal variation. Moreover, the mean square error reaches its lowest value when the correlation coefficient is the largest, and the correlation of local water level variation is superior obvirously than the global load model. This indicates that the global water load model can be used to restrain the seasonal factors impact of gravity variation. But the local water level variation can be used to amend the contribution of the gravity variation in this area more accurately.

### 4.3. Calculation and Comparison of Gravity Impact factor of Underground Water

Based on the equations proposed by Torge et al. (1989) [16-20], Bouguer plate model could be used to describe the influence of underground water level and the soil gap water content time variation on the gravity:

$$\delta_{gw} = 2\pi G\rho_w P\delta H = 0.42P\delta H , \qquad (7)$$

where the unit of underground water level gravity variation $\delta_{gw}$ is $10^{-8}ms^{-2}$, G is the gravitation constant, $\rho_w$ is the water density $1\times10^3$ kgm$^{-3}$, the unit of soil gap water content P is %, and the unit of water level variation $\delta H$ is cm. Considering the drill strain gap water pressure is used in this underground water observation, the soil gap water content is about 10%-15 %. The theoretical impact factor of Wujiahe area underground water to gravity calculated by equation (7) is $0.21\sim0.04\times10^{-8}$ ms$^{-2}$/cm. This theoretical range is basically the same as the real observation result (the gap water content using underground water level estimated to be 25 %-35 %). Fourier analysis method is more reliable because of consideration of fitting correlation.

## 5. Conclusions

In this work, the continuous gravity observation data in Wujiahe seismic station during two and a half years were used, and Fourier series and polynomial fitting methods were adopted. The seasonal variation of gravity has been extracted with utilizing air pressure and underground water level observation at the same station, and GLDAS, CPC global land water model. The result shows that the gPhone has been working stably during the period from Sep. 2008 to Jan. 2011 after data pre-processing using Fourier analysis assisted by conducting gravimeter pro-processing method. The observation accuracy of this meter could reach half of that of the conducting gravimeter under the white noise level of $0.3\times10^{-8}$ms$^{-2}$. The pressure admittance value is $-0.267\pm0.002\times10^{-8}$ ms$^{-2}$/mbar.
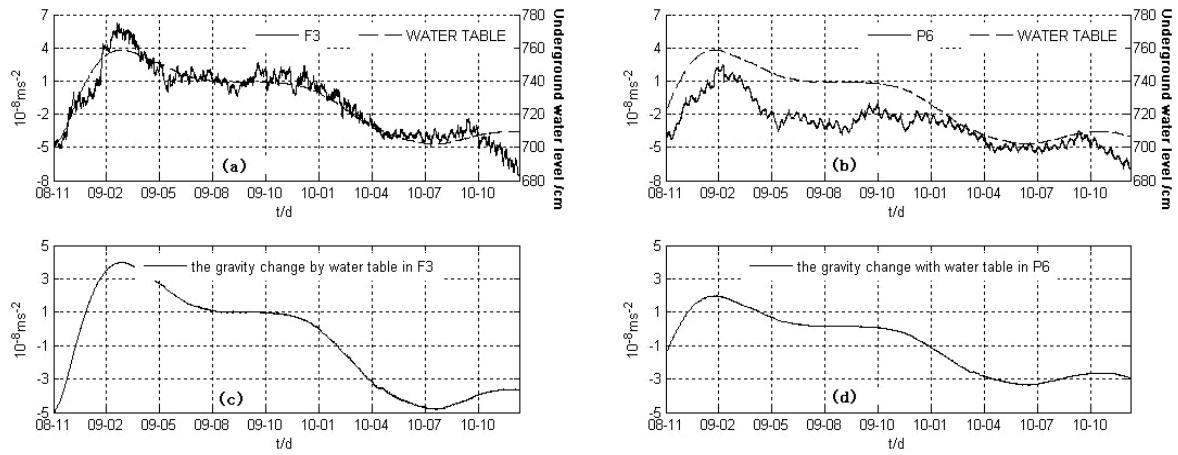
**Fig. 5.** The relationship between the residual gravity and water table and the gravity change by water table.
(a) The residual gravity corrected by F3 and the water table corrected by phase lag; (b) the residual gravity corrected by P6 and the water corrected by phase lag; (c) the water table correction with $0.153 \times 10^{-8} ms^{-2}/mm$; (d) the water table correction with $0.093 \times 10^{-8} ms^{-2}/mm$.

The amendment using resultant tide from observation data, air pressure data at the same station, and the polar motion data has shown that, beside the effect of resultant tide ($\pm 300 \times 10^{-8} ms^{-2}$), air pressure ($\pm 5 \times 10^{-8} ms^{-2}$) and polar motion ($\pm 7 \times 10^{-8} ms^{-2}$), the most dominant influence factor is the spring continuous drift. It has been analyzed that the positive direction rate of Wujiahe seismic station spring is approximately $300 \times 10^{-8} ms^{-2}/M$.

In the premise of hypothesis that the drift of spring gravimeter and the gravity non-tidal variation should be a continuous process, the polynomial fitting method was used for comparison in this work. The efficiency of Fourier series fitting drift has been verified by using hill and underground water level data in Wujiahe seismic station and the two global land water models (GLDAS and CPC). The result shows an obvious seasonal rule could be reflected by polynomial and Fourier series fitting drift amendment methods, when comparing with the global land water model or the underground water level observation. The relative analysis indicates the correlation between them is more than 80 %. The underground water level amendment residual time consequence shows that the underground water level gravity influence impact factors obtained by two kinds of methods are almost the same as theoretical value. But the correlation of 95 % between Fourier analysis result and underground water level observation indicates that the spring gravimeter continuous drift fitted and the seasonal variation extracted by Fourier series are more reliable than those of polynomial analysis. The gravity influence of Wujiahe seismic station underground water level is approximately $\pm 5 \times 10^{-8} ms^{-2}$, and the gap water content of Wujiahe area is approximately 25 %-35 %.

Compared with polynomial fitting, the Fourier analysis could also fit the continuous drift of spring gravimeter. The advantage of this method is not only once time molding, but the effect is also superior to those of polynomial fitting. The former method and underground water data could be used not only to extract the gravity variation caused by seasonal underground water level variation, but also to extract the gravity variation caused by non-seasonal factors. This method provides a new method and way to extract the contribution of seasonal underground water from the gPhone continuous observation data and the influence of non-seasonal factors.

## Acknowledgements
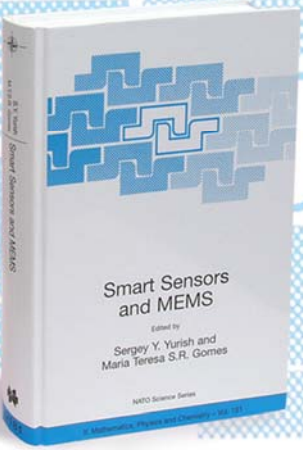
## References

[1]. Tapley B. D., Bettadpur S., Ries J. C., Thompson P. F., Watkins M. M., GRACE measurements of mass variability in the Earth system, *Science*, Vol. 305, Issue 23, 2004, pp. 503-505.

[2]. Imanishi Y., Sato T., Higashi T., Sun W. K, Okubo S., A network of superconducting gravimeters detects submicrogal coseismic gravity changes, *Science*, Vol. 306, Issue 5695, 2006, pp. 476-478.

[3]. Sun W., Wang Q., Li H., Wang Y., Okubo S., Shao D. S., Fu G. Y., Gravity and GPS measurements reveal mass loss beneath the Tibetan Plateau Geodetic evidence of increasing crustal thickness, *Geophysical Research Letters*, 2009, Vol. 36, L02303.

[4]. Sun W., Wang Q., Li H., Wang Y., Okubo S., A reinvestigation of crustal thickness in the Tibetan Plateau using absolute gravity, GPS and GRACE data, *Terr Atmos Ocean*, Vol. 22, Issue 2, 2011, pp. 109-119.

[5]. He Ping Sun, Takemoto S., Hsu H.-T., Higashi T., Mukai A., Precise tidal gravity recorded with

superconducting gravimeters at stations Wuhan (China) and Kyoto (Japan), *Journal of Geodesy*, Vol. 74, Issue 10, 2001, pp. 720-729.

[6]. Camp M. V., Francis O., Is the instrumental drift of superconducting gravimeters a linear or exponential function of time, *Journal of Geodynamics,* Vol. 81, 2007, pp. 337-344.

[7]. Riccardi U., Rosat S., Hinderer J., Comparison of the Micro-g LaCoste gPhone-054 spring gravimeter and the GWR-C026 superconducting gravimeter in Strashourg (France) using a 300-day time series, *Metrologia*, Vol. 48, 2011, pp. 28-39.

[8]. Kang K. X., Li H., Peng P., Hao H. T., Wei J., Seasonal variations in hydrological influences on gravity measurements using gPhone, *Terr. Atmos. Ocean*, Vol. 22, 2011, pp. 157-168.

[9]. Xing Lelin, Li Hui, Xia Zhengchao, Hao Xinghua, Hao Hongtao, Liu Ziwei, Study on zero drift characteristics of CG-5 gravimeter, *Acta Seismologica Sinica*, Vol. 32, Issue 3, 2010, pp. 369-373.

[10]. Liu Ziwei, Li Hui, Hao Hongtao, Wei Jin, Xing Lelin, Analysis of observations of superconducting gravimeter SG-053, *Journal of Geodesy and Geodynamics*, Vol. 30, Issue 6, 2010, pp. 157-160.

[11]. Xu Jianqiao, Theory and analysis method of gravity solid tidal - analysis and dispose of Wuhan station superconducting gravimeter observation data, Doctor's Thesis, *Institute of Geodesy and Geophysics*, China, 1997.

[12]. Tian Guie, Chen Xiaodongm Sun Heping, Chen Guang, Song Lijie, Liu Nannan, Comparison and investigation of VAV and ETERNA tidal analysis methods, *Journal of Geodesy and Geodynamics*, Vol. 29, Issue 2, 2009, pp. 96-99.

[13]. Wei Jin, Li Hui, Liu Ziwei, Kang Kaixuan, Noise level measurement of SG-053 with MLE, *Journal of Geodesy and Geodynamics*, Vol. 31, Issue 3, 2011, pp. 69-74.

[14]. Chen X. D., Kroner C., Sun H. P., Abe M., Zhou J. C., Yan H. M., Wziontek H., Determination of gravimetric parameters of the gravity pole tide using observations recorded with superconducting gravimeters, *Journal of Geodynamics*, Vol. 48, 2009, pp. 348-353.

[15]. Zhou Jiangcun, Sun Heping, Xu Jianqiao, Validating global hydrological models by ground and space gravimetry, *Chinese Sci. Bull*., Vol. 54, Issue 9, 2009, pp. 1534-1542.

[16]. Torge W., Gravimetry, *Walter de Gruyter,* Berlin, New York, 1989.

[17]. Zerbini S., Raicich F., Richter B., Gorini V., Errico M., Hydrological signals in height and gravity in northeastern Italy inferred from principal components analysis, *Journal of Geodynamics*, Vol. 49, 2010, pp. 190-204.

[18]. Hasan S., Peter A. T., Boll J., Kroner C., Modeling the hydrological effect on local gravity at Moxa, *Journal of Hydrometeorology*, Vol. 7, 2005, pp. 346-354.

[19]. Abe M., Takemoto S., Fukuda Y., Higashi T., Imanishi Y., Iwano S., Ogasawara S., Kobayashi Y., Dwipa S., Kusuma D., Hydrological effects on the superconducting gravimeter observation in Banding, *Journal of Geodynamics*, Vol. 41, 2006, pp. 288-295.

[20]. Neumeyer J., Barthelmes F., Dierks O., Flechtner F., Harnisch M., Harnisch G., Hinderer J., Imanishi Y., Kroner C., Meurers B., Petrovic S., Reigber Ch., Schmidt R., Schwintzer P., Heping Sun, Virtanen H., Combination of temporal gravity variations resulting from superconducting gravimeter (SG) recordings, GRACE satellite observations and global hydrology models, *Journal of Geodesy*, Vol. 79, Issue 10-11, 2006, pp. 573-585.

---

IEEE  AESS  I&M IEEE instrumentation & measurement society

# IEEE International Workshop on
# Metrology for Aerospace

## Benevento, Italy, June 4 - 5, 2015

**HONORARY CHAIR**
Marina Ruggieri, Italy

**GENERAL CHAIRS**
Pasquale Daponte, Italy
Robert Rassa, US

**TECHNICAL PROGRAM CO-CHAIRS**
Stephen Dyer, US
Alfonso Farina, Italy

**PUBLICATION CHAIR**
Ernestina Cianca, Italy

**TREASURY CHAIR**
Cosimo Stallo, Italy

**INTERNATIONAL PROGRAM COMMITTEE**
Domenico Acierno, Italy
Carlo Albanese, Italy
Giovanni Betta, Italy
Erik P. Blasch, US
Paolo Carbone, Italy
Luigi Carrino, Italy
Goutam Chattopadhyay, US
Stefano Debei, Italy
Murat Efe, Turkey
Pietro Ferraro, Italy
Jesus Garcia, Spain
Domenico Giunta, Netherlands
Maria S. Greco, Italy
Richard Hochberg, US
Satoshi Ikezawa, Japan
Stephen Johnson, US
Karel Kudela, Slovak Rep.
Chin E. Lin, Taiwan
Walter Matta, Italy
Daniele Mortari, US
Aldo Napoli, France
Pavel Paces, Czech
Jacek Pieniazek, Poland
Vasily Popovich, Russia
Helena G. Ramos, Portugal
Artur L. Ribeiro, Portugal
Roberto Sabatini, Australia
Nicolas Sklavos, Greece
Patrizia Tavella, Italy
Fabrizio Francesco Vinaccia, Italy
Graham Wild, Australia
Ho-Soon Yang, Republic of Korea
Mark Yeary, University of Oklahoma, US
David Zucconi, Italy

**LOCAL COMMITTEE**
Pasquale Arpaia, Italy
Luca De Vito, Italy
Gianluca Mazzilli, Italy
Francesco Picariello, Italy
Sergio Rapuano, Italy
Silvia Ullo, Italy
Judy Scharmann (IEEE AESS Executive Assistant)

**LOCAL ARRANGEMENTS**

ATHENA SRL

## ABOUT THE WORKSHOP

MetroAeroSpace aims to gather people who work in developing instrumentation and measurement methods for aerospace. Attention is paid, but not limited to, new technology for metrology-assisted production in aerospace industry, aircraft component measurement, sensors and associated signal conditioning for aerospace, and calibration methods for electronic test and measurement for aerospace.

## WORKSHOP TOPICS

The main topics include, but are not limited to:

- Electronic instrumentation for aerospace
- Automatic test equipment for aerospace
- Sensors and sensor systems for aerospace applications
- Wireless sensor networks in aerospace
- Attitude - and heading - reference systems
- Monitoring systems in aerospace
- Metrology for navigation and precise positioning

## PAPER SUBMISSION

Paper submission will be handled electronically, through the submission page set up on the conference web page: **www.metroaerospace.org**

The best contributions will be awarded, including the Best Student Paper Award and the Best Paper authored and presented by a woman.

Special sessions will be organized on specific topics, see online at:

www.metroaerospace.org/index.php/program/special-session

## IMPORTANT DATES

➤ **January 11, 2015** – Submission of Extended Abstract

➤ **March 1, 2015** – Notification of Acceptance

➤ **April 19, 2015** – Submission of Final Paper

## BENEVENTO

Benevento, due to the Santa Sofia's Church with its Cloister, has been part of UNESCO World Heritage Sites as "*Longobards in Italy. Places of the power*".

## CONTACT US

www.metroaerospace.org

info@metroaerospace.org

## With the endorsement of

Università degli Studi del Sannio

DAC Distretto Aerospaziale della Campania

# A Half-duplex Synchronous Serial Fieldbus S²CAN with Multi-host Structure

**Xu-Fei SUN**

College of Physics and Information Engineering, Fuzhou University, Fuzhou, 350108, China
E-mail: sunxffd@fzu.edu.cn, 2545721075@qq.com

**Abstract:** This paper describes a field bus of which the physical layer using CAN (Controller Area Network) transmission line and the data link layer using SPI (Serial Peripheral Interface) interface protocol. It uses half-duplex transmission mode, which can be used to build a LAN (Local Area Network) control system with multi-host structure. The bus takes advantage of the electrical characteristics of CAN transmission line, inheriting its anti-interference ability and the advantage of long transmission distance. Also, it inherits the merits of SPI bus in fast communication, simple use and low cost. The paper describes the communication protocol and hardware and software implementation of the novel fieldbus and gives the experimental data and test results to verify the feasibility of the novel fieldbus and excellent communication characteristics. *Copyright © 2014 IFSA Publishing, S. L.*

## 1. Introduction

The high development of measurement and control technology, communication network technology, computer technology and silicon chip technology leads to profound changes in the equipment manufacturing, control method and system integration of the automation field. It builds up a fieldbus control system based on the fieldbus, changing the traditional control system fundamentally. Currently, there are over 50 kinds of influential fieldbus protocols, which are protocol standards formed after applying special provisions to meet the needs of some industrial applications. The typical example is the CAN bus (Controller Area Network). CAN bus is a serial data communication protocol which was originally developed by BOSCH Company in Germany to solve many controls of modern cars and data exchange between the test equipment. Now, it has been used and promoted more frequently to more and more different areas. It

is a multi-host bus, whose communication medium can be twisted pair, coaxial cable or optical fiber, with the advantages of simple connection, stable and reliable situation, long-distance transmission and low cost [3]. These are mainly due to the electrical characteristics of the CAN transmission line. However, its communication protocols and interface hardware is complex and its cost is high, the procedure of use is also complicated and the communication rate is not too high. Other types of fieldbus have similar characteristics. For electronics engineers, UART (Universal Asynchronous Receiver /Transmitter), SPI (Serial Peripheral Interface), I2C (Inter-Integrated Circuit) bus are the most well-known as well as the standard interfaces for many embedded processors. If a fieldbus using these interfaces can be built, both the hardware or labor costs are very favorable. However, all these three types of serial bus use unbalanced single-ended transmission that the communication distance is too short and it cannot build fieldbus directly. Therefore,

developing the advantage above and avoiding the disadvantage as well, the paper puts forward a fieldbus S$^2$CAN (Synchronous Serial Controller Area Network) whose physical layer uses CAN transmission line and data link layer uses SPI interface. It also describes the interface circuit structure and communication protocols that connect with common processor SPI interface.

## 2. Electrical Characteristics of CAN Transmission

A CAN transmission line has two signal lines CANH and CANL, using NRZ coding method. Level is expressed as Dominant and Recessive, as shown in Fig. 1. "Dominant" represents a logical value "0" while " Recessive " represents the logical value "1". The differential voltage between CANH and CANL is rather large when it is dominant, while rather small when it is recessive. CAN transceiver determines the logic "0" and "1" of the bit code by detecting the magnitude of the differential voltage. Therefore, CAN transmission line has a strong resistance to common mode interference. As long as the transmission line impedance matches well, the transmission distance can be very far away. Further, the bus level can be obtained by the "wired-AND" mechanism based on the level of each node. When the node transmits Recessive bit, it is actually isolated from the bus. Only when the node transmits Dominant bit can the level of bus be changed [1-2].
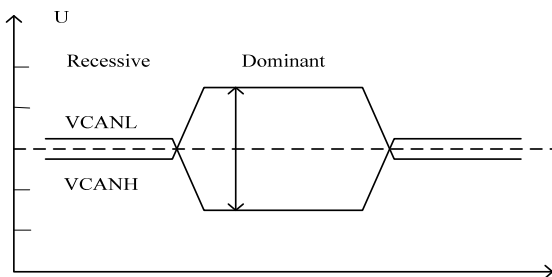


**Fig. 1.** The electrical feature of CAN bus.

## 3. Interface Hardware Structure of Novel Fieldbus

Based on the electrical characteristics of CAN transmission lines described above, the data transmitted from the SPI interface are transmitted through CAN transmission lines after level switch by which it can improve reliability and extend communication distance. The fieldbus system, which uses two sets of signal channels, presented in this paper is multi-host structure, and the signal channel consists of CAN transceivers and CAN transmission lines. The structure of the interface circuit is shown in Fig. 2, in which the BUSY and the M/S are user-

defined common I/O ports of the MCU (Micro Controller Unit), Channel A transmits data stream and Channel B transmits synchronization clock. When the bus is free, each node is in slave mode, the M/S port of the MCU outputs low level which controls the on and off states of the relevant tri-gates. In Channel A, the MISO port of the MCU is connected to the TXD input of the CAN transceiver and the MOSI port is connected to the RXD output. In Channel B, the CLK port of the MCU is connected to the RXD output of the CAN transceiver. When one of the nodes starts the communication, it should switch to master mode. The M/S port of the MCU outputs high level which controls the on and off states of the relevant tri-gates. In Channel A, the MISO port of the MCU is connected to the RXD output of the CAN transceiver and the MOSI port is connected to the TXD input. In Channel B, the CLK port of the MCU is connected to the TXD input of the CAN transceiver. In this novel fieldbus, the master addresses the slave by transmitting the address code instead of using the chip select line, so the chip select port SSEL of the SPI slave inputs low level by M/S port.
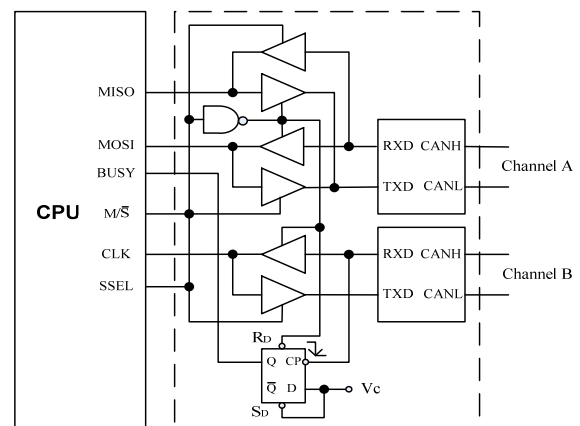


**Fig. 2.** Novel fieldbus interface hardware structure.

The output of the D-flip flop which is shown in Fig. 2, is connected to BUSY port. The BUSY port is used to monitor the state of the bus. When the node is in master mode, the D-flip flop is in reset state. So when the system is initialized, the node needs to switch to master mode, and then back to slave mode. Based on the electrical characteristics of CAN transmission lines, the protocol dictates that when the bus is free, the clock lines and the data lines are in high level, which is in recessive level state. In the bus, when one of the nodes switches the mode from slave to master and starts transmitting the data, the clock lines drop to low level so that a level negative jump generates. At this point, the RXD port of Channel B of all communication nodes outputs a level negative jump except the master in the bus, the state of the D-flip flop of every slave is put to logic 1 so that the BUSY port of the MCU rises to high level.

So, in order to prevent the transmission conflict, it needs to check the level of BUSY port before a node switches its mode from slave to master. When BUSY port is in low level, it illustrates there is not any communication competitors in the bus, so it allows the node to switch to master mode, otherwise it needs to wait for the communication of other nodes to finish. After a round of the communication ends, since BUSY port of the slave is still in high level, to make it return to initial state, all of the slave must switch to master mode to make the D-flip flop reset, and then switch back to slave mode without any further processing.

Since the physical layer of the novel fieldbus adopts the CAN transmission lines, its network topology can inherit from all forms of the network topology of the CAN bus, the exemplary structure is shown in Fig. 3.



**Fig. 3.** Normal way of composition of novel fieldbus network.

## 4. Communication Protocol

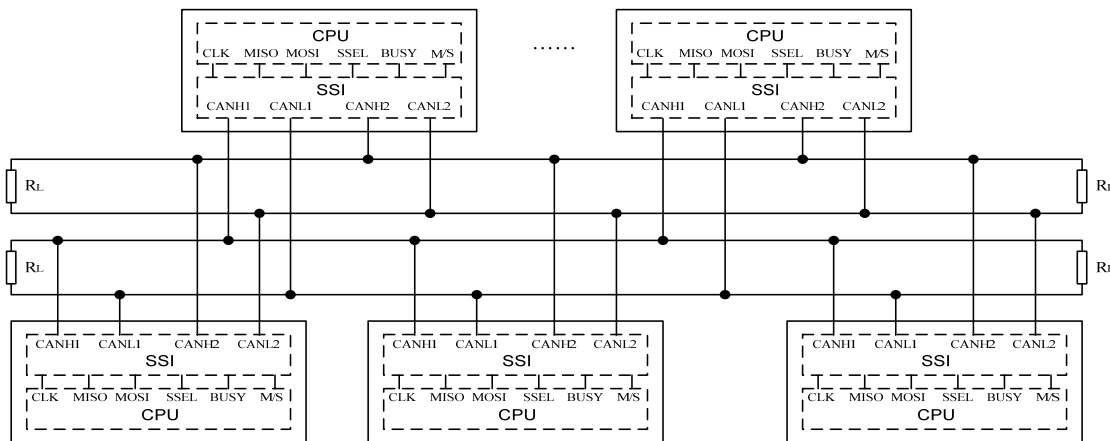SPI bus protocol is full-duplex, a byte of data is transmitted and received simultaneously. Master as the communication initiator completes transmitting a byte of data, and receives a byte of data as well. Slave as a passive recipient completes receiving a byte of data, and transmits a byte of data [4]. Since the reception and transmission of a novel fieldbus share a data channel, it must be half-duplex communication. In order to achieve half-duplex communication, the protocol dictates that the message recipient should transmit recessive code (0xFF) when the message sender transmits a message. This is equivalent to the transmitting port of the information recipient to separate from the bus electrically, so as not to affect the sender transmitting the message. In order to give a simple illustration, the narration of transmitting recessive code (0xFF) when the recipient receives the information is omitted in the following part.

This paper presents a designed S2CAN bus communication protocol. When a node initiates a round of communication, all the other nodes on the bus must operate according to this communication protocol. If any step fails, all the slaves must be reset to the free state. The protocol specifies two states for master, which are starting state and communicating state, and four states for slave, which are free state, waiting state, connected state and non-connected state. In the process of communication, states of masters and slaves will migrate.

In addition, the protocol adopts six characters in ASCII table as function symbols in the process of communication. Codes and functions of these six characters are shown in Table 1 [5].

**Table 1.** Encoding of the Functional characters.

| Characters | DLE | STX | ETX | EOT | ETB | CAN |
|---|---|---|---|---|---|---|
| **Coding** | 0x10 | 0x02 | 0x03 | 0x04 | 0x17 | 0x18 |
| **Function** | Escape | Start of Text | End of Text | End of Transmission | End of Trans. Block | Cancel |

### 4.1. Obtaining Control of Bus

The node which initiates communication detects the level of the interface port BUSY at first. If the level is low, which means all the nodes on the bus are in the free state, then the initiating node is allowed to switch to the master mode, or otherwise, the initiating node fails to obtain the control of the bus and is forbidden to switch to the master mode. After being into the master mode, the initiating node transmits one byte of the source address code, with high bit in front. The source address refers to the

identical address of the master node, of which the code value also represents the communication priority of the node, with smaller value corresponding with higher priority. When one of the nodes (Master A) starts the communication and detects that the bus is free, it's likely to have a situation that one of the other nodes (Master B) has just started the communication, because there is a delay in signal propagation, Master A doesn't detect Master B yet. Then both of them transmit their respective source address code to the bus at approximately the same time, so the data signals and clock signals both are in conflict. But, when the time difference between Master A and Master B which initiate communication is less than half synchronous clock cycle, as shown in Fig. 4, the clock signal CLKa of Master A and the clock signal CLKb of Master B have a behavior called "wired-AND" in the CAN transmission lines of Channel B which will generate the clock signal CLK. Similarly, the address code ADRa of Master A and the address code ADRb of Master B have a behavior called "wired-AND" in the CAN transmission lines of Channel A which will generate the address code signal ADDR. As can be seen in the figure of time sequence wave, the address code ADDR is the same as ADRb, and the code value of ADRb is less than ADRa, this illustrates that when the communication initiates at the same time, only the node of higher priority can receive its own address code. Therefore, when the communication initiates, the master which receives the address code of local node can get the control of bus and the other master which receives the address code of other node must avoid and wait. Obviously, to ensure this function works, the maximum time delay between the nodes should be controlled in less than half synchronous clock cycle, when the physical length and the communicating rate of the bus are planned. If high transmission rate is needed which leads to not reaching the limitation of time delay mentioned above, the rate of transmission can be decreased at the stage of getting the control of bus, and is increased after getting the control of bus.
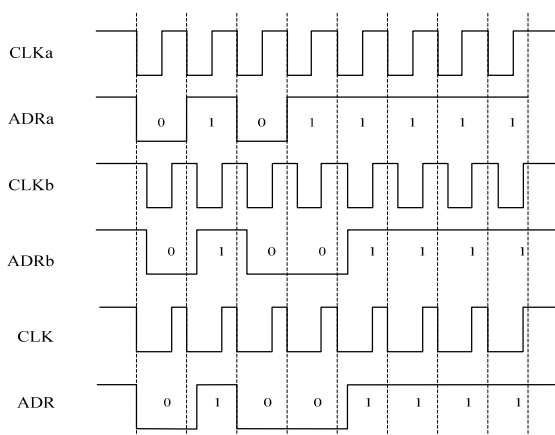


**Fig. 4.** Waveform of two address signal "wired-AND" and two clock signal "wired-AND".

After obtaining the control of the bus, the master migrates to the starting state. Once a salve in the free state receives one byte of data, which will always be regarded as the source address code transmitted by master, it will migrate to the waiting state.

### 4.2. Establishing Connection

After being into the starting state, the master transmits one byte of the target address (the identical address of the communication target node), and waits for responses. After receiving one byte of data in the waiting state, a slave will regard it as the target address transmitted by master. If the target address code match with the local address code, the slave will transmit one byte of dominant code (0x00) as ACK response and then migrate to the connected state, or otherwise, the slave will transmit one byte of recessive code (0xFF) as NAK response and migrate to the non-connected state.

What needs to be pointed out is that the master may not receive the dominant code (0x00) when it is transmitted as the slave needs to respond ACK. This is generated by the phase difference between the synchronization signal and data signal. Because the delay of the received data transmission for the master occurs, it generates the phase difference between local synchronization signals. When the phase difference is large, the sampling misalignment occurs and master data will be wrong. If the misalignment is less than 4, the low 4 bits reply code received from the master will not be misaligned. Therefore, as long as the 4 bits are logic 0, it can be judged that the slave answers the ACK.

If the master judges the received response as ACK, which means the communication target is connected, it will migrate to the communicating state. If the master receives NAK, which means the communication target cannot be connected, it should transmit the characters DLE-CAN (1 byte of escape character DLE and 1 byte of cancel character CAN), which represents request for cancel, and then retransmit the target address.

If the master does not receive an ACK response for twice consecutively after transmitting the target address, it will transmit the characters DLE-EOT (1 byte of escape character DLE and 1 byte of ending transmission character EOT), which represents termination of communication, and gives up the control of the bus temporarily.

### 4.3. Transmitting Data Frames by Master

After being into the communicating state successfully, the master will transmit messages, which can be consecutive data packets, in the format shown in Fig. 5a and 5b. The two characters DLE-STX in both two figures represent the start of the message. The two characters DLE-ETX in Fig. 5a represent that this data frame is in the middle of the

message. The two characters DLE-ETB in Fig. 5b represent that this data frame is the last one of the message. BCS is the 2-byte CRC (Cyclic Redundancy Check) check code. After finishing transmitting a data frame, the master turns into receiving responses from slaves. If the response is NAK, the master needs to retransmit data packets. If the retransmission fails or the response is ACK, the master will transmit the characters DLE-EOT, which represent termination of communication, and reset to

the slave's free state, ending this round of communication.

Each time a data byte is transmitted in the process of transmitting data frames, the master will compare this transmitted byte with the data byte received at the same time. If they equal to each other, that means the transmission is normal, or otherwise, the transmission is abnormal. If the abnormality occurs, the current data frame should be retransmitted.

| DLE STX | Data area (Max1024 bytes) | DLE ETX | BCS (2 bytes) |
|---------|---------------------------|---------|---------------|

**Fig. 5a.** The middle data frame format.

| DLE STX | Data area (Max 1024 bytes) | DLE ETB | BCS (2 bytes) |
|---------|----------------------------|---------|---------------|

**Fig. 5b.** The ending data frame format.

To avoid that the master with a higher priority occupies the bus for long while transmitting consecutive data frames, which leads to that the data of the node with a lower priority cannot be transmitted in time, this protocol specifies that after one round of communication, a master can transmit again only after a 10-byte communication time interval, during which other nodes can switch to master mode immediately and initiate communication. In this way, nodes with lower priorities also have chances to transmit data in time.

### 4.4. Receiving Data Frames by Slave

If the slave is in the non-connected state, it will not operate any process on the received data or make any response. Instead, it will just wait for the DLE-EOT characters transmitted by master. When the slave receives the DLE-EOT characters, it returns to the free state.

If the slave is in the connected state, when a DLE character is received, the slave will always regard it as a non-data and non-command blank. If the following character is still DLE, then this following DLE is data 0x10. If the following character is not DLE, then it is a function character, which should be processed according to its definition shown in Table 1. When the function character is CAN, the slave cancels current receiving operation and reinitializes its reception. If the function character is EOT, the slave returns to the free state. In order to make BUSY return to low level, it is necessary that the slave switches into master and then switch back to the slave mode.

In the receiving process of data frames, if the start characters of a data frame is found not to be DLE-STX, or an undefined function character is

received (it means the data length that the DLE character is excluded in data area), or the length of a data field exceeds 1024 bytes, The received data is judged as abnormal. At this time, the slave does not transmit recessive code (0xFF), but changes to transmit one byte of dominant code (0x00) as abnormal notice when it receives the next byte. If after the slave transmits abnormal notice, the next 2 bytes received are DEL-STX character and it resets the receiving. Otherwise, it retransmits the abnormal notice as mentioned above repeatedly, until the next 2 bytes received are DLE-STX character and reset the receiving.

A data field starts from the third character of a frame. The slave will put received data into the receive buffer successively. The reception of a data field ends after receiving the end character or the message end character (DLE-ETX or DLE-DTB), followed by 2 bytes of data received as the CRC check code. After receiving the 2-byte CRC check code, the CRC value of the received data will be calculated. If they are equal to each other (check is correct), an ACK (dominant code 0x00) response will be transmitted, otherwise, an NAK (recessive code 0xFF) response will be transmitted.

### 4.5. Monitoring Timeout

To avoid that the state of a node is not reset when communication fails, this protocol requires monitoring the communication time of each round. No matter whether a node is in the master mode or the slave mode, when its state breaks away from free state, it will be monitored. If a node does not return to the free state in a predetermined overtime period, it will be forced back into the free state and get its state initialized. The length of the overtime period can be specified according to data

transmission rate, of which the minimum length can be specified as twice as the time needed to transmit a data frame.

## 5. Communication Process

When two nodes communicate, they often transmit data packets interactively in which the master is not fixed, mode switching will occur in the communication process. As shown in Fig. 6a, Node A needs to switch to master before it starts the communication, and transmits the data after getting the control of bus. Then Node B receives the data by slave mode. As shown in the figure, SADR is the source address code characters transmitted by master, TADR is the destination address code characters transmitted by master, ACK is the a dominance code (0x00) replied by slave, DATA BLOCK is the data packets transmitted by master, DLE-EOT is the end character of communication transmitted by master. Node A switches back to slave mode after a round of the communication ends. When the Node B responds to the transmitting data of Node A, it switches to master mode and follows the processing method of the master above to transmit the response data, the communication process is shown in Fig. 6b. At the same time, Node A follows the processing method of the slave mentioned above to receive data.
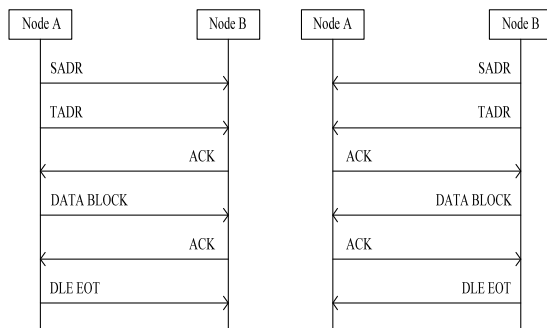


**Fig. 6a.** a) Node A initiates communication;
b) Node B responds to the communication.

## 6. Realization and Test of the Communication

In order to verify the characteristics of the S2CAN bus, two sets of CAN transmission lines in the test use the 30m long twisted pair with the load resistance of standard 150 ohm. The bus accesses three communication nodes. CLK is set at high level when the bus is free and sampling data by all nodes is set at the first jumping edge of the clock signal. In the initial stages, the clock polarity of each node is set with requirements above and the relevant data is initialized.

When the communication nodes are in the master mode or slave mode, it follows the processing method of the protocol above. But when the node receives data, using the SPI interrupt mode or query mode will make the process flow different. In this paper, the communication program of the master is realized by the process module, which is one C language function. When the master initiates the communication to some nodes in the bus, the certain C function is called only once and the communication objective is realized. According to the characteristics of the SPI interface, only the query mode is suitable for transmitting process of the master in this situation. The flow chart is shown as Fig. 7, "Get the control of bus" and "Master initiates the connection" within the process are both working in accordance with the protocol, the detail process of which is not discussed here. The "transmitting data frame" is to transmit the data which has set to follow the frame format. In order to distinguish between data 0x10 and character DLE, the DLE character should be inserted in front of the every one byte of data 0x10 in data area to show that the latter 0x10 is data instead of character DLE. Transmitting data frame is a finite cyclical process, when the master detects an error, exiting the loop.
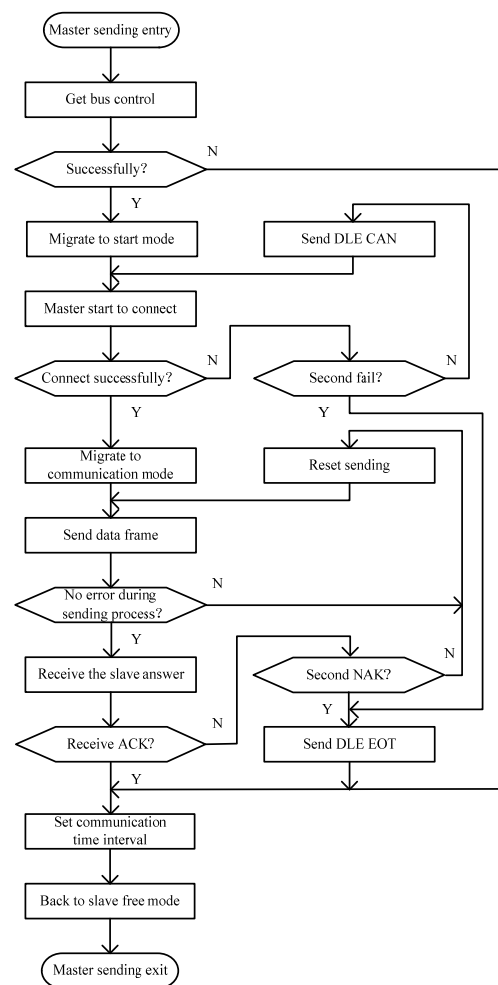


**Fig. 7.** The process flow chart of master.

The communication program of the slave is also realized by a process module. The receiving process in the communication adopts the method combining one byte of receiving data with the current state. Interrupt mode can also be used as query mode in receiving, but the process method is different from the one of the master. Although the process module is also one C language function, it is called when the slave receives every byte of data. The flow diagram for data process is shown in Fig. 8. What is needed to point out is that the mode switch to let the BUSY return to low level is not listed here and it is included in the process of "migrate to free state" instead.
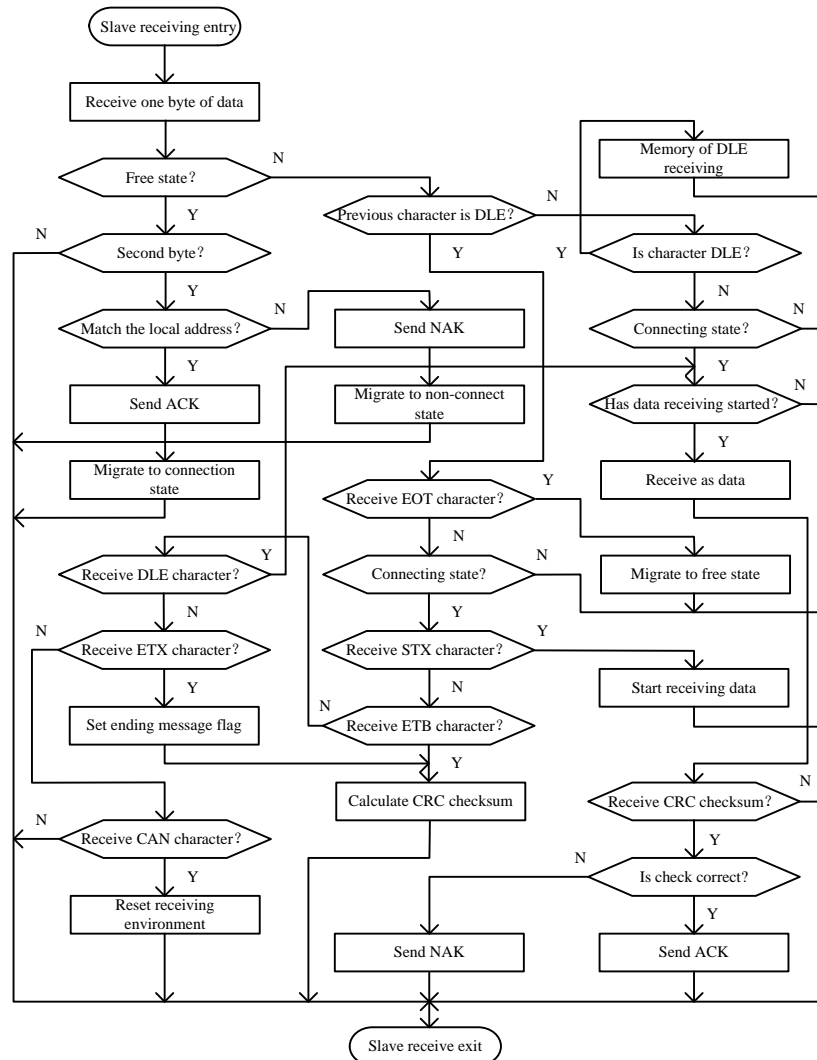


**Fig. 8.** The process flow chart of slave.

The timeout monitor process is to count events in the condition in which the node is broken away from free state by using timing events in the application program. When the count value is over the determined time, it forces the node to reset, making it return to free state. This is a simple independent process, and the flow chat will not be given here.

## 7. Conclusions

The test results show that the novel bus as the fieldbus is applicable and effective in a suitable rate range. It can be found that the highest data transmission rate is 2.25 Mbps which is higher than the data transmission rate of CAN bus. In addition, when transmitting the data by CAN bus, the data field is only 60 percent of the frame data, but S2CAN bus is almost 100 percent. Therefore, the transmitting efficiency of S2CAN bus is higher than CAN bus at the same rate. As a result, S2CAN bus has the simplicity, high rate and low cost that CAN bus cannot compare, it is very suitable for the measurement and control system with multi-host structure. The bus communication reliability is heavily dependent on the one of software processing. In this regard, the test is not sufficient, which needs continuous improvement and perfection in the future.

## References

[1]. F. D. Zhang, Fieldbus technology and application, *Technology Press*, 2008.

[2]. K. M. Wu, CAN bus principle and application system design, *Publishing House of Beijing University Aeronautics and Astronautics*, 1996.

[3]. M. Farsi, K. Ratcliff, M. Barbosa, An overview of controller area network, *Computing & Control Engineering Journal*, Vol. 10, 1999, pp. 113–120.

[4]. F. Leens, An introduction to I$^2$C and SPI protocols, IEEE *Instrumentation & Measurement Magazine*, Vol. 12, 2009, pp. 8-13.

[5]. V. G. Cerf, ASCII format for network interchange, *UCLA*, 1969.

---

# The System Developing of Intelligent and High-precision Power Parameter Measurement in Power System Based on Power Spectral Density Algorithm

**Huimin ZHANG**

Department of Communication, Chongqing College of Electronic Engineering,
Chongqing 401331, China
Tel.: +8613206006614
E-mail: Zhuomi99@126.com

**Abstract:** In modern power systems, high-precision power parameter measurement has occupied an important position for power quality in power grids. This paper presents a high-precision intelligent power parameter measurement device, which can collect parallel alternative current parameter values among 0 to 250 V in 3-channel easily and quickly, and improve the measurement accuracy by using the power spectral correction algorithm for sample parameters. The ATT7022B chip is used as the front-end of the data acquisition, and we use STM32 chip as the processor, which is easy to implement the algorithm on this platform. Results obtained from test application of the entire system show that the system has advantages of stable performance, small size, high reliability, and excellent accuracy. *Copyright © 2014 IFSA Publishing, S. L.*

**Keywords:** Power parameters, Power spectral density, High-precision, Measurement, ATT7022B.

## 1. Introduction

Electrical energy has become a part of our life; therefore, and power quality is related to all aspects of our social life. The measurements of these parameters are directly reflected in the power quality of the power supply, therefore monitoring power parameters in power grids has important practical significance [2]. Due to the wide coverage of power grids, there is a considerable number of disperse nodes need to detect. Therefore that how to monitor the power parameters in real-time effectively is still required to be continually studied. According to this situation, we designed a high-precision intelligent power parameter measurement device which can quickly and easily achieve a single system of parallel acquiring parameter values from 0 to 250 V in 3-channel; the power parameter measurement in this paper mainly discusses the measurements of voltage RMS (URMS), the current RMS (IRMS), the apparent power (S), the active power (P), the power factor ($\sigma$) and other parameters of alternative current working at 50 Hz, then correct the sampled parameters by using power spectral algorithm to improve the electric parameter measurement accuracy. The results show that the system has advantages of stable performance, small size, high reliability, and excellent accuracy.

## 2. Hardware Design

### 2.1. System Design

According to the demand for measuring power parameter, we build a wireless network monitoring system. The structure is shown in Fig. 1.
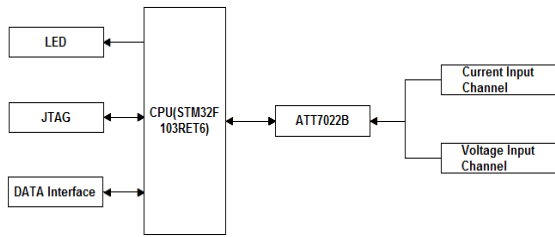
**Fig. 1.** Measurement error characteristics of sensor.

As is shown in Fig. 1, the system uses STM32F103RET6 as the main module, which has rich on-chip resources of peripheral module, to expand trunk RS232 (UART), Power Measurement Module (SPI) and other functions. The main function of the system is to complete the parameter measurement of power equipment in operation in real-time and reach the target of real time monitoring. Therefore, the module of power parameter measurement is an important part of the system. In order to getting more comprehensive parameters of power equipment operation, we decided to use specific single-chip solution, with digital signal processing methods simultaneously capture three-wire power line voltage, current and other parameters [5].

We choose STM32F103RET chip as the processor, which based on the ARM®Cortex™-M3 32-bit RISC core operating at a 72 MHz frequency, high-speed embedded memories (Flash memory up to 512 Kbytes and SRAM up to 64 Kbytes), and an extensive range of enhanced I/Os and peripherals connected to two APB buses. All devices offer three 12-bit ADCs, four general-purpose 16-bit timers plus two PWM timers [8], as well as standard and advanced communication interfaces: up to two I2Cs, three SPIs, two I2Ss, one SDIO, five USARTs, an USB and a CAN. These properties can meet the

control, acquisition, processing algorithms design requirements. Besides, its high performance to price ratio also is the one of reasons why we choose it.

ATT7022B chip is used to acquire power parameter data in our system. ATT7022B is highly accurate three-phase power metering chip, for three-phase three-wire and three-phase four-wire applications; integration of six second-order sigma-delta ADC, voltage reference circuit and all the digital signal processing circuits of power, energy, voltage and current RMS, power factor and frequency measurement. This chip provides an SPI interface, which can easily transmit the data of measurement parameters and table parameters between the external MCU and itself. Besides, its internal voltage monitoring circuit can guarantee it working properly when the chip power on and off. The chip can directly measure the power parameters, but accuracy is not ideal. Therefore, we must use power spectral density algorithm to correct acquisition parameters [9].

### 2.2. Power Parameter Acquisition Circuit Design

ATT7022B is a semiconductor integrated chip so that it cannot directly connect high voltage or high current signal for power parameters. In order to measure these parameters, we isolate the signal from power grid, at the same time, the strong signal is converted to small one, and then put these converted signal into ATT7022B for measuring. ATT7022B peripheral circuit is referred to the chip manual, we can see it in Fig. 2. Avoiding unnecessary interference, we let part of unused pins disconnect or connect ground; the chip SPI communication interface connect to the STM32 I/O ports for transmitting command or data.
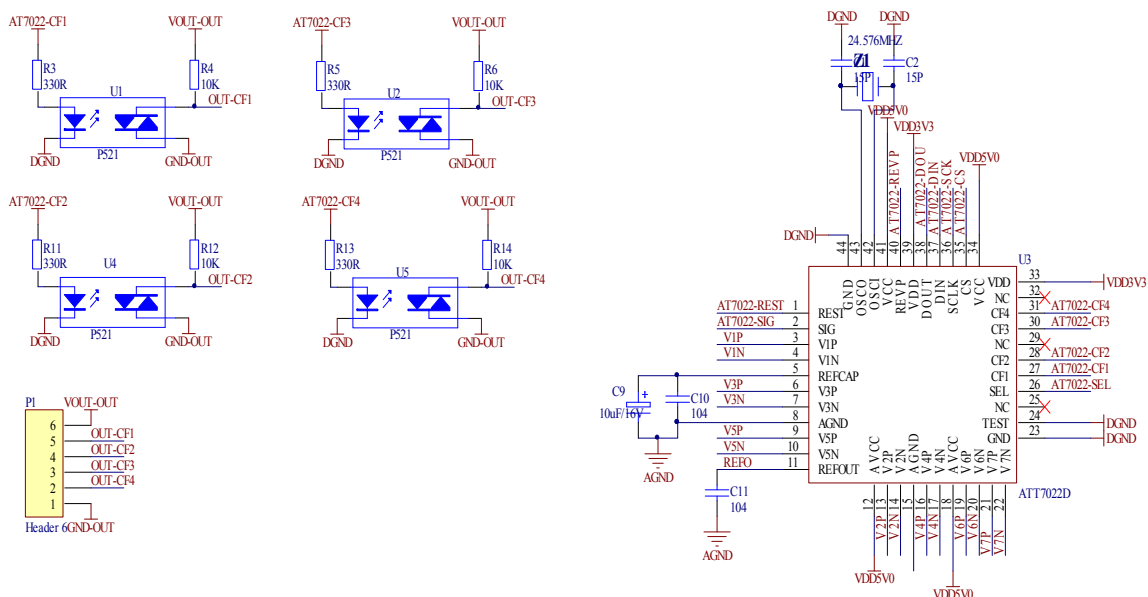


**Fig. 2.** ATT7022B peripheral circuit.

ATT7022B analog input circuit shown in Fig. 3. Firstly, the voltage directly access into circuit, through the voltage divider, and then superimposed on a reference voltage signal. Finally, this signal will be transmit into A/D converter for sampling.
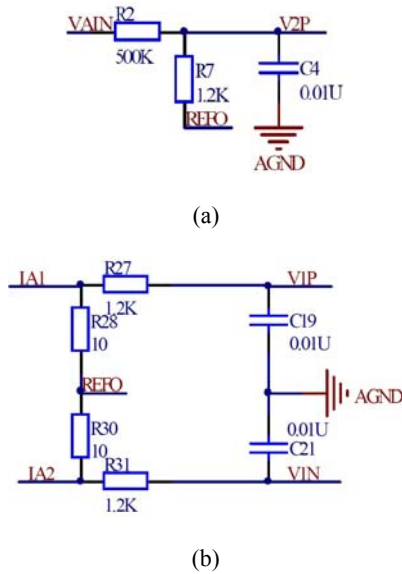


(a)



(b)

**Fig. 3.** (a) The measured voltage input interface; (b) current detection input interface.

From ATT7022B chip manual, we know that ATT7022B voltage channel input range from 0 V to 1 V, the current channel input range from 2 mV to 1 V. And its sampling rate is 3.2 kHz, therefore, the input frequency greater than 1.6 kHz will form aliasing frequency at low frequency band; we usually choose a simple RC filter to filter these high frequency components. For power chip, the useful signal only near by the sampling frequency of the signal, so the bandwidth is generally from 0 to 2 KHz. The filter cutoff frequency is $fL$=1.3$k$, by the formula are:

$$fL = \frac{1}{2\pi RC},\tag{1}$$

where $R$=12$k$.

In ATT7022B, each of the AC input channel requires a superposition of a DC bias voltage, as shown in Fig. 4. The REFO resistor is used to provide the DC bias voltage, and the DC bias voltage can be obtained by the chip voltage reference voltage output, or can be provided from an external reference voltage.

ATT7022B has a SPI serial communication interface, which communicates in slave mode having two control lines and two data lines: CS, SCLK, DIN, and DOUT. Considering the SPI transmission signal line may be disturbed or jitter, so we put a small resistor (10Ω) in series with the signal line. This

resistor and IC input parasitic capacitance C can be combined to become a low-pass filter to eliminate any oscillation of SPI interface signals.
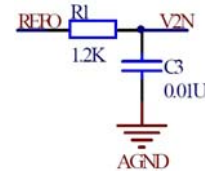


**Fig. 4.** Reference voltage input interface.

### 2.3. Processor Circuit Design

Fig. 5 illustrates the mini-system circuit design of STM32, which includes a reset circuit, clock circuit, and STM32 processor circuit. As we can see, STM32 not only controls logic controller to send the data, but also communicate with the PC via RS232 or RS485 interface.

### 2.4. PCB Layout Design

We design two-layers PCB board for our system by using Altium Designer, the PCB board size is supposed to meet the size requirements of external mechanical structure, the system board layout shown in Fig. 6. System board layout, the minimum line width of 8mil, the minimum line spacing 8mil, smallest hole is 16mil, is a high wiring density on the PCB board.

## 3. Power Spectral Density Correction Algorithm

According to electrical theory, valid values of periodically changing voltage and current signals:

$$U = \sqrt{\frac{1}{T}\int_0^T u^2(t)dt},\tag{2}$$

$$I = \sqrt{\frac{1}{T}\int_0^T i^2(t)dt},\tag{3}$$

where $T$ is the period of the signals.

We discretize Equation (2) and Equation (3), we have

$$U = \sqrt{\frac{1}{N}\sum_{n=0}^{N-1} u^2(n)},\tag{4}$$

$$I = \sqrt{\frac{1}{N}\sum_{n=0}^{N-1} i^2(n)},\tag{5}$$

**Fig. 5.** Mini-system circuit design of STM32.



**Fig. 6.** System board layout.

where $u(n)$ and $i(n)$ are the discrete sequences, which is transformed from measured voltage and current signals respectively by the sampling, holding and A/D conversion. $N$ is a frequency period of sampling points. Single-phase active power is:

$$P = UI \cos \phi, \qquad (6)$$

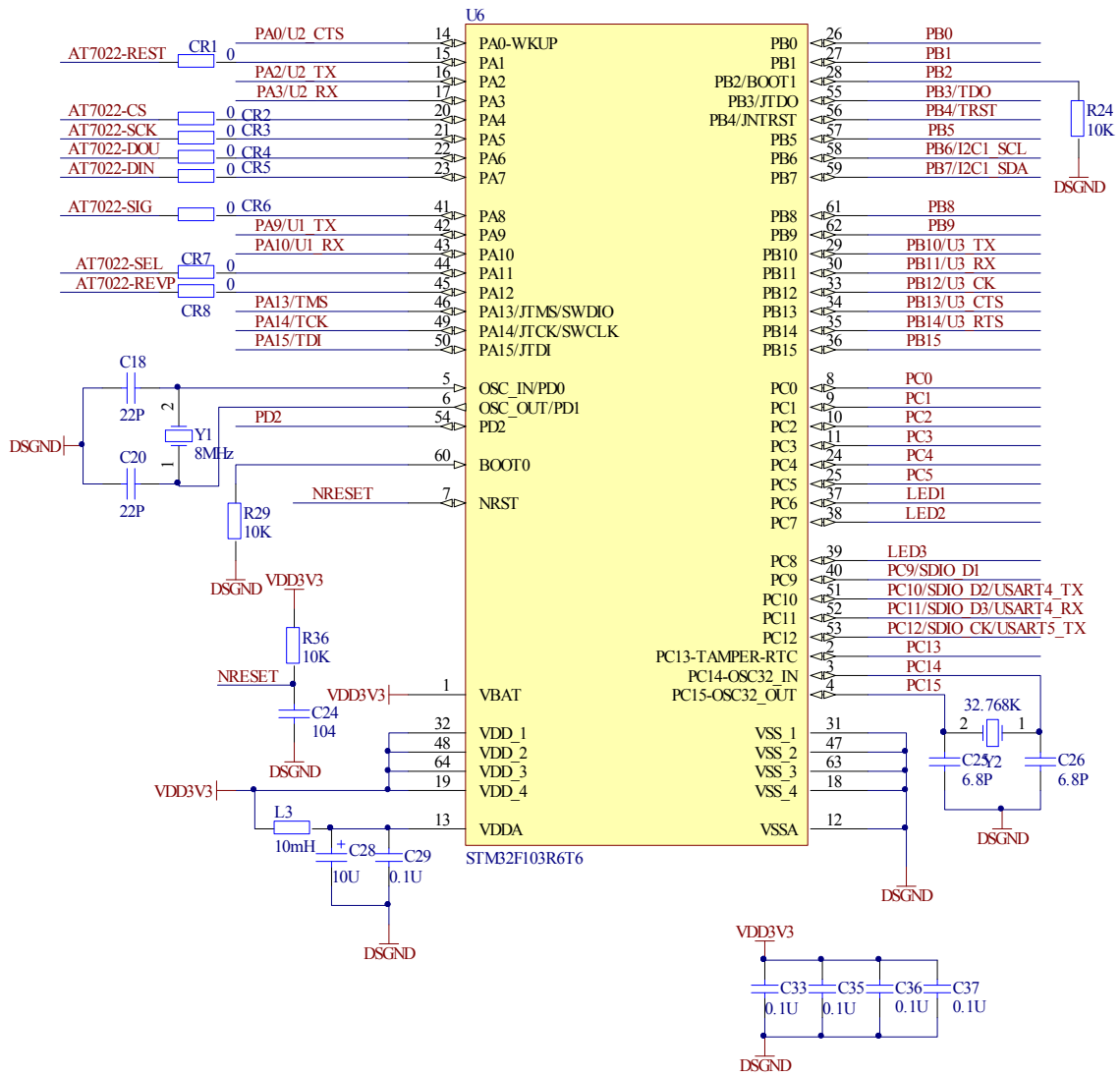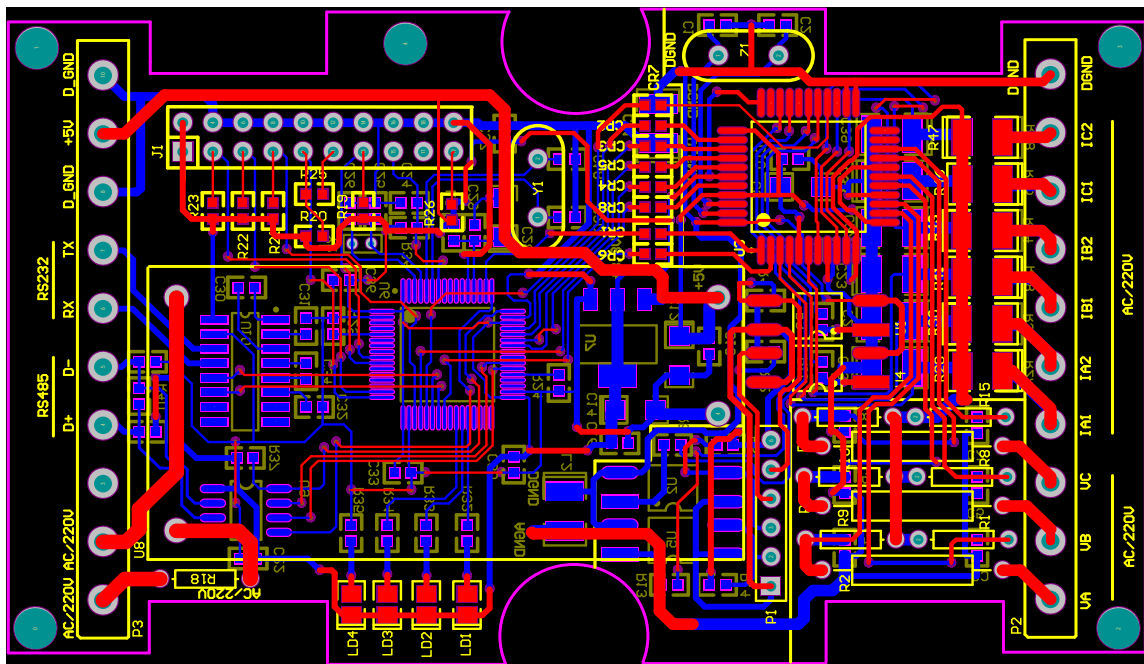where $U$ and $I$ are the voltage and current RMS, $\cos\phi$ is the power factor of the load. Besides, active power can also be calculated by the following formula:

$$P = \frac{1}{T} \int_0^T u(t)i(t)dt, \qquad (7)$$

Discretizing Equation (7), we have

$$P = \frac{1}{N} \sum_{n=0}^{N-1} u(n)i(n), \qquad (8)$$

In the three-phase four-wire circuit, the total active power equal to sum of each phase of active power, can be written as:

$$P = P_A + P_B + P_C, \qquad (9)$$

In three-phase three-wire circuit, the total active power can be measured by two-Wattmeter method:

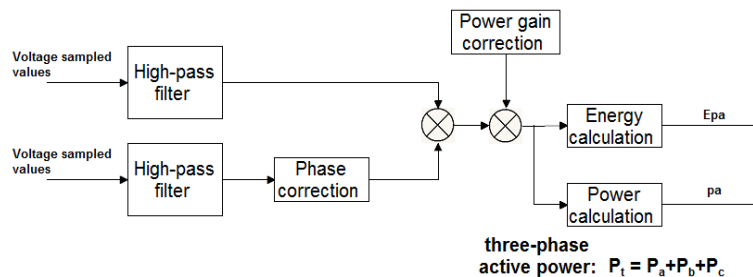$$P = P_{AC} + P_{BC}, \qquad (10)$$

Power parameters of the sampling system can provide fundamental, harmonics and voltage of each phase and three-phase full-wave RMS voltage vector, and a full-wave current RMS, and RMS phase current vector. Grid voltage signal is converted to the sampling values by ADC of ATT7022B chip; and then, it can be sent to the STM32 processor family unit operation; finally, we can get its RMS value. After reading the corresponding value of the register, we right 13 bit to obtain the required measurements. Measurement block diagram shown in Fig. 7:
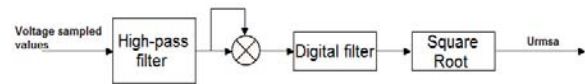


**Fig. 7.** RMS measurement block diagram.

When we remove the DC component from the voltage or current signals, after a series of multiplications, additions, and digital filtering; we can get the active power of each phase. Voltage and current sampling data contains 21-order harmonic, and based formula is:

$$P = \frac{1}{N} \sum_{n=0}^{N} U(n) I(n), \qquad (11)$$

Calculating active power contains at least 21-order harmonic information. Active power measurement block diagram shown in Fig. 8, is

$$P_t = P_a + P_b + P_c.$$



**Fig. 8.** Active power measurement block diagram.

## 4. Testing

When we calibrate the power meter of power parameter measurement, we must provide a standard meter. Compared with standard meter, only the active should be calibrated and reactive power does not require calibration. After calibrated, accuracy of active power measurement can achieve up to 0.5s. Power correction is divided into ratio error correction and phase error correction. Ratio error correction removes the ratio error in transformer. Nonlinear of transformer ratio error cannot be ignored when it needs precision measurement. ATT7022B offers

register Iregchg, compensation can be set based on the current size of the staging area. Besides, phase error correction also can be corrected segmentally. In applications, the segments do not need to separate too small. Phase error correction should do after completing ratio error correction. Ratio error correction should be performed when power factor equal to 1.0, and phase error correction should be performed at 0.5 L [10].

We can read register HFConst directly from ATT7022B to know the pulse frequency of output CF, which is selected to calibrate the meter. HF Const cannot be written more than 0x000D00 of

parameter values. The constant frequency pulse is EC, rated input voltage is Un, rated input current is Ib, voltage of sampling voltage channel is Vu, voltage of sampling current channel is Vi, ATT7022B gain is G. Therefore, we calculate the value of HF Const:

$$HF_{Const} = INT\left[5760000000 \times \frac{G^2 \times V_u \times V_I}{U_n \times I_b \times EC}\right], \quad (12)$$

where *INT[]* means to take the integer part.

When $U_{gain}=0$, voltage correction register can be read directly from ATT7022B by SPI interface, the value is *DataU*. Then, we can read the actual input voltage RMS $U_r$ from standard meter. We know actual input voltage RMS is $U_r$, measuring voltage RMS is

$$U_{rms} = DataU \times 2^{10}/2^{23}, \text{ so we have}$$

$$U_{gain} = U_r/U_{rms} -1, \quad (13)$$

If

$$U_{gain} \geq 0, \; U_{gain} = INT\left[U_{gain} \times 2^{23}\right],$$

$$U_{gain} < 0, \; U_{gain} = INT\left[2^{24} + U_{gain} \times 2^{23}\right].$$

The RMS output register of ATT7022B is supplementary code, the highest bit is the sign bit; RMS is always greater than or equal to 0, so the maximum sign bit is always equal to 0. The 24-bit data $V_{rms}$ convert to actual voltage RMS is

$$U_{rms} = V_{rms} \times 2^{10}/2^{23}, \quad (14)$$

The reference power spectral density correction algorithm to correct for acquisition parameters, the main process of calibration: Parameter settings, A phase correction, B phase correction, C phase correction. Where the parameter set is divided into: the voltage channel ADC gain select, high-frequency pulse output setting, ratio error compensated area setting, phase compensation area setting, loss of pressure threshold setting, the starting current setting, energy accumulation mode setting, and the other parameters of the phase correction steps: Power gain correction ($P_f$=1.0), phase error correction ($P_f$=0.5 L), voltage correction (rated voltage), current correction (rated current). Test environment: Laboratory temperature Test objects: 220 V/25 W incandescent, 220 V/60 W incandescent, transformers power supply.

As we can see from the Table 1, the power parameters, which correct by power spectral density power correction algorithm, differ from the nominal value. But the result is same with the test values of standard correction meter, indicating that the system is able to achieve high-precision measurement of power parameters [11].

**Table 1.** Test Results.

| Test object | Voltage RMS | Current RMS | Power |
|---|---|---|---|
| 220 V/25 W incandescent | 213.3 V | 0.12 A | 25 W |
| 220 V/60 W incandescent | 212.5 V | 0.27 A | 57 W |
| 9 W transformers power supply | 217.6 V | 0.04 A | 9 W |

## 5. Conclusion

This paper presents a developing method of high-precision power parameter measurement equipment based on power spectral density correction. This method can correct power parameter error, and has high precision in correction. Besides, the algorithm is simple and is very suitable for high-precision measurement of power parameters. However, because the power parameter measurement device itself can only collect three voltage and current values, the accuracy of the data must be referred to standard measuring instruments and it cannot achieve self-correcting, which leads to the range of application of high-precision power parameter measurement devices in some extent will be restricted.

## Acknowledgements

## Reference

[1]. SUN He-lin, Lu Yuan-long, TIAN Yue-jun, Remote power quality monitoring system based on GPRS and virtual instruments, *Relay*, Vol. 35, Issue 1, 2007, pp. 59-62.

[2]. Sun Guo-dong, Lei Zai-shuan, Zhou Yu-guo, et al., Design of Comprehensive Electrical Power Monitoring Device, *Electrical Measureme Instrumentation*, Vol. 44, Issue 7, 2007, pp. 37-40.

[3]. Lei,Yang, Guang-ming, Huang, et al., The realization of automatic correction table platform, *Electrical Measurement & Instrumentation*, Vol. 44, Issue 5, 2007, pp. 58-60.

[4]. Chen Tao, He Wei, Liu Xiao-Ming, et al., An on-line ultraviolet detecting system of EHV transmission lines, *Automation of Electric Power Systems*, Vol. 29, Issue 7, 2005, pp. 88-92.

[5]. Liu Hai-Chang, Liu Hao, Wang Jiao-Xia, et al., Design and implementing of remote power quality monitoring system, *Power System Protection and Control*, Vol. 37, Issue 1, 2009, pp. 109-111.

[6]. Intel Corporation. Intel MCS-51 microcontroller family user's manual. http://www.intel.com, 2006-05-20.

[7]. Li Xia, Sun Hui, A novel divider based on dual-bit algorithm, *Chinese Journal of Semiconductors*, Vol. 25, Issue 6, 2004, pp. 645- 649.

[8]. Wei J. D., Sun C. T., Constructing hysteresis memory in neural networks, *IEEE Transactions Systems Man Cybernetics*, Vol. 30 Issue 4, 2000, pp. 601-609.

[9]. Jang X. G., A CCD driver based on programmable logic device, *J. Foreign Electronic Elements*, Vol. 11, 1996, pp. 41-43.

[10]. Ai L. L., Yuan F., Ding ZH. L., Measurement of spatial object. s exterior attitude based on linear CCD, *Chinese Optics Letters*, 2008, Vol. 6, Issue 7, pp. 505-509.

[11]. Texas Instrument, CC2430 Datasheet, 200715.

---

# The Automation Control System Design of Walking Beam Heating Furnace

**[1] Hong-Yu LIU, [2] Jun-Qing LIU, [3] Jun-Jie XI**

[1] School of Mechanical Engineering and Automation,
University of Science and Technology Liaoning, Anshan, Liaoning Province, 114051, China
[2] School of Automation, Shenyang Institute of Engineering,
Shenyang, Liaoning Province, 110136, China
[3] School of Mechatronics Engineering, Zhengzhou Institute of Aeronautical Industry Management,
Zhengzhou, Henan Province, 450015, China
E-mail: junqing_liu@126.com

**Abstract:** Combining the transformation project of certain strip steel rolling production line, the techniques process of walking beam heating furnace was elaborated in this paper. The practical application of LOS-T18-2ZC1 laser detector was elaborated. The network communication model of walking beam heating furnace control system was designed. The realization method of production process automation control was elaborated. The entire automation control system allocation picture and PLC power distribution system picture of walking beam heating furnace were designed. Charge machine movement process was elaborated. Walking beam movement process was elaborated. Extractor movement process was elaborated. The hydraulic station of walking mechanism was elaborated. Relative control circuit diagram was designed. The control function of parallel shift motor, uplifted and degressive motor was elaborated. The control circuit diagram of parallel shift motor of charge machine and extractor of first heating furnace was designed. The control circuit diagram of uplifted and degressive motor of charge machine and extractor of first heating furnace was designed. The realization method of steel blank length test function was elaborated. The realization method of tracking and sequence control function of heating furnace field roller were elaborated. The design provides important reference base for enhancing walking beam heating furnace control level. *Copyright © 2014 IFSA Publishing, S. L.*

## 1. Introduction

Hot treatment must be done on steel blank before rolling so as to ensure rolling temperature and refining steel blank inner grain crystal structure. Heating furnace is the hot treatment equipment must be equipped in steel rolling industry. With the development of industry automation technology, large and highly autchnical walking beam heating furnace should be equipped in modern steel rolling mill so as to enhance the quality and market competition power of product.

Walking beam heating furnace was designed by American Surface Combustion Corporation. It was imported by Japan Abroad Furnace Corporation before long. From that time, walking beam heating furnace was adopted generally on many steel rolling mills all over the world. It becomes key equipment

on steel rolling line [1]. Walking beam heating furnace is the heat treatment equipment designed to satisfy steel rolling techniques. Walking beam heating furnace is a kind of continuous heating furnace. Steel blank can be moved and advanced by the movement of ascending, advancing, descending and retreating of walking beam. The meaning of walking is transporting steel blank from furnace inlet to furnace exit periodically. Steel blank can be heated to rolling techniques requirement temperature at furnace exit. Relative control system is the key to ensure reliable production of walking beam heating furnace. Two walking beam heating furnaces were researched in this paper. The heating capability of each heating furnace is 260 ton an hour. The furnace inner steel blank temperature is about 1450 °C.

## 2. The Techniques Process of Walking Beam Heating Furnace

Firstly, steel blank enters front furnace roller. The check and centering of steel blank were completed in this stage. Front furnace roller contains adjacence roller and loading roller. Adjacence roller was named as A roller. It contains four set rollers that are A1 to A4 respectively. Loading roller was named as B roller. It contains five set rollers that are B1 to B5 respectively. A roller is the opening roller heating furnace field. The length test and check of steel blank were completed in A roller. The centering of steel blank before heating furnace was completed in B roller so as to transport steel blank to heating furnace front accurately. Then charge machine and loading steel furnace gate coordinating move to put steel blank on the appointed position of fixed beam of heating furnace. Last, steel blank was transported forward according to certain step distance that is 500 mm by walking beam cycle movement.

There are two LOS-T18-2ZC1 laser detectors. They were equipped on every heating furnace. One laser detector was used to realize location and length test of steel blank during loading. Another laser detector was used to realize steel blank location on heating furnace exit. When steel blank was detected by laser detector on heating furnace exit and also required from rough rolling field at the same time, extractor and extracting steel furnace gate coordinating move to transport heated steel blank on blank exit roller. Blank exit roller was named as C roller. It contains seven set rollers that are C1 to C7 respectively. Then steel blank was transported to rough rolling field by C roller movement.

## 3. LOS-T18-2ZC1 Laser Detector

LOS-T18-2ZC1 laser detector is high power laser detector. It was mainly used to detect whether steel blank was located on special heating furnace position or not. Meanwhile switch quantity control signal was outputted so as to realize control function. It is suitable for metallurgy industry heating furnace work environment. Big power semiconductor infrared laser was adopted as emitter. After modulating, a beam strong laser was emitted. The emitted laser was received by phototube. After amplification processing, a control signal was outputted. Emitter has the characteristics of big transmitting power, penetrating high temperature heating furnace, far function distance and strong capacity of resisting disturbance. The optical lenses of emitter and receptor were all made of thermostability quartz glass.

Installation picture of LOS-T18-2ZC1 laser detector was shown as Fig. 1. Electronic part of emitter was shown as Fig. 2. Emitter optics lenses was shown as Fig. 3. Receptor optics lenses were shown as Fig. 4. Electronic part of receptor was shown as Fig. 5. Relative emitting mode was adopted on this laser detector. Firstly, the optics lenses and electronic parts of emitter and receptor were installed well. Then optical fibers were used to connect optics lenses and relevant electronic parts. After connecting electric source, optics lenses of emitter and receptor were adjusted so as to realize accurate collimation. 300 Hz infrared laser was modulated and emitted by electronic part of emitter. Electronic part of receptor was modulated to 300 Hz so as to receive. When steel blank has not entered detection area, normal signal can be received by receptor. Reception energy pilot lamp was lit. Output status is normal. When steel blank has entered detection area, normal signal can not be received by receptor. Reception energy pilot lamp was not lit. Output status is abnormal. Owing to infrared modulated high frequency laser, this laser detector has good capacity of resisting disturbance. Relevant movement is reliable.
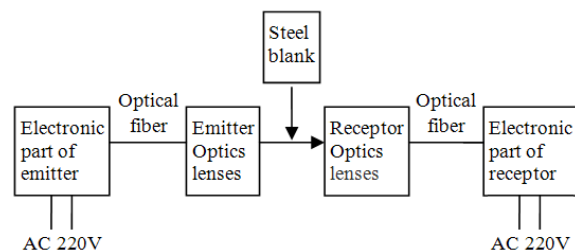


**Fig. 1.** Installation picture of LOS-T18-2ZC1 laser detector.



**Fig. 2.** Electronic part of emitter.

**Fig. 3.** Emitter optics lenses.



**Fig. 4.** Receptor optics lenses.



**Fig. 5.** Electronic part of receptor.

The main performance parameters of LOS-T18-2ZC1 laser detector are as follows. Detection area is no more than 50 meters. Emitter is infrared semiconductor laser. Laser wavelength is 95 nm. Emitter peak value output power is 150 Watts. Laser security classification is CLASS IIIb. Level signal response time is no more than 15 milliseconds. Node signal response time is no more than 100 milliseconds. Supply voltage is

AC 220 V. Environmental temperature range is -25 °C to 70 °C.

## 4. The Entire Automation Control System and PLC Power Distribution System of Walking Beam Heating Furnace

The key of walking beam heating furnace control system are series PLC provided by America GE Corporation. There are three kinds of network communication models. They are internal memory reflection network, Ethernet and GENIUS network. The communications among heating, rough rolling and finish rolling were realized by internal memory reflection network. The communications among heating furnace inner PLC were realized by Ethernet. The communications between PLC and HMI were realized by Ethernet. The communications between PLC and long distance station were realized by GENIUS.

There are six computers in heating furnace field. They were used on the operation of instrument, electrical device and vaporization respectively. The CIMPLICITY system of America GE Corporation was adopted on exploiting function menu. All kinds of production process parameters of temperature, pressure and flux and so on can be monitored by relative function menu in operation station. The production process automation control can be realized by equipment instrument monitoring system, electrical device monitoring system and vaporization monitoring system of heating furnace field. The entire automation control system allocation picture of walking beam heating furnace was shown as Fig. 6. The power supply of all PLC systems in heating furnace field was realized by a USP. The entire PLC power distribution system picture of walking beam heating furnace was shown as Fig. 7.
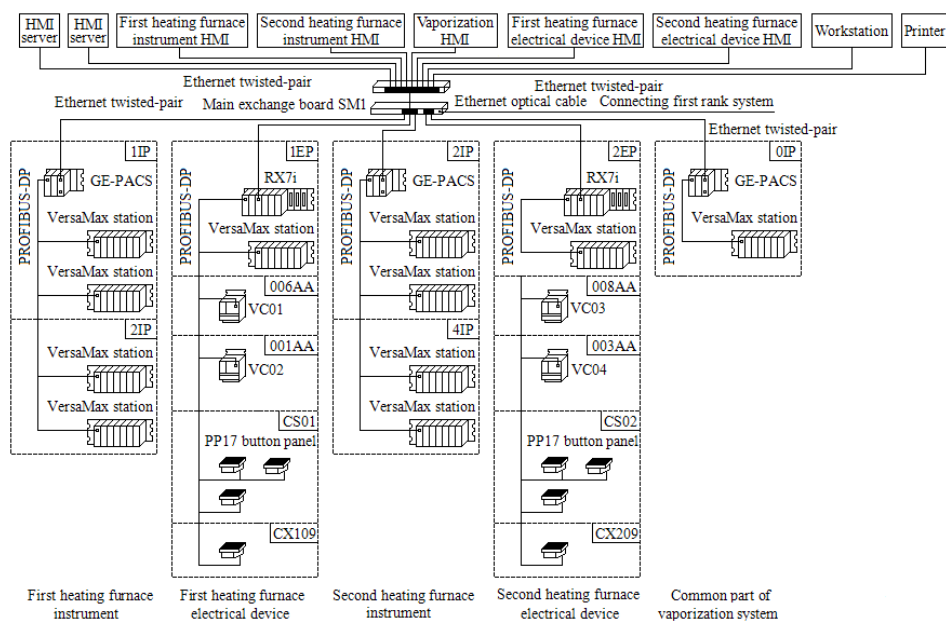


**Fig. 6.** The entire automation control system allocation picture of walking beam heating furnace.
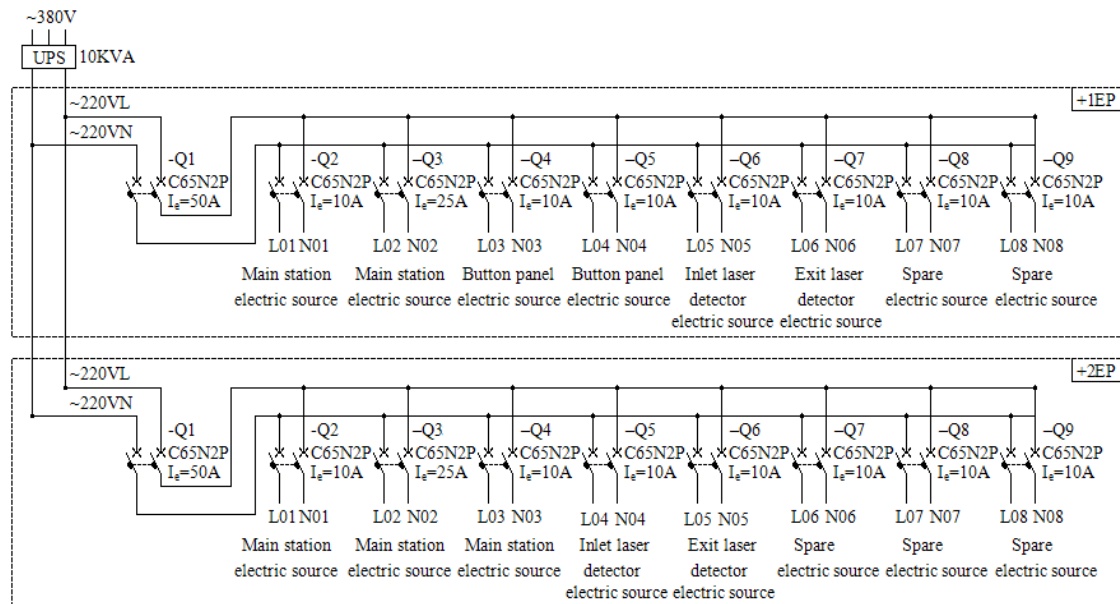
**Fig. 7.** The entire PLC power distribution system picture of walking beam heating furnace.

## 5. Charge Machine Movement Process

The movement distance of front charge machine of walking beam heating furnace is 10 meters. Charge machine was shown as Fig. 8.



**Fig. 8.** Charge machine.

Charge machine movement mechanism contains parallel shift, uplifted and degressive mechanism. Charge machine movement contains five parts. They are pushing steel, uplifting steel, transporting steel, putting steel and return. In pushing steel process, after obtained centering finish signal of steel blank on loading roller, charge machine begin to move parallel and push steel blank. When charge machine front overstepping loading roller 50 mm, charge machine stops. It can ensure that steel blank was transported to an accurate position. Relative charge machine movement distance $S_p$ was shown as formula (1).

$$S_p = 1925 - B, \qquad (1)$$

where $B$ is the steel blank width, $S_p$ is the parallel movement distance.

In uplifting steel process, the uplifted and degressive mechanism of charge machine moves. Steel was uplifted and left roller certain distance. The uplifting steel order and opening loading gate order were emitted by PLC simultaneously. In transporting steel process, the parallel shift mechanism of charge machine moves. Steel blank was transported to heating furnace inner. When the distance between current steel blank and previous steel blank is 50 mm, charge machine stops. Relative charge machine movement distance $S_c$ was shown as formula (2).

$$S_c = 3915 + X_{m+1}, \qquad (2)$$

where $X_{m+1}$ is the distance between the m+1 steel blank end and fixed beam end.

In putting steel process, the uplifted and degressive mechanism of charge machine moves. Steel was put on walking beam and descended to inferior limit position. In return process, the parallel shift mechanism of charge machine returns its original position with maximum speed. When the distance to original parallel shift mechanism position is 1.8 meter, the closing loading gate order was emitted by PLC.

## 6. Walking Beam Movement Process

According to techniques requirement, hydraulic inclined double wheel rail drive mode was adopted by walking mechanism. The uplifted and degressive movement of kinetic beam was driven by double fluid cylinder synchronously. The horizontal shift of horizontal beam was driven by horizontal fluid cylinder. The uplifted and degressive movement of uplifted and degressive beam was driven by vertical fluid cylinder. The structure lateral picture of walking mechanism was shown as Fig. 9.
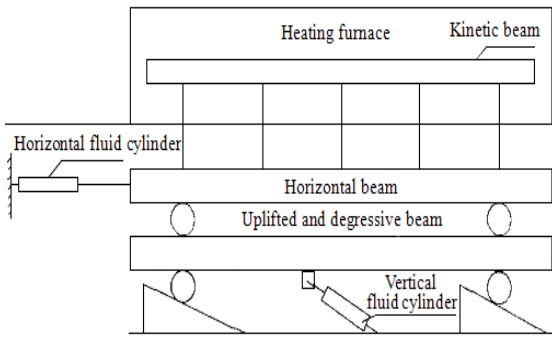
**Fig. 9.** Structure lateral picture of walking mechanism.

During running process, walking mechanism speed control was realized by adjusting oil flux in fluid cylinder [2]. Owing to the big flux and high pressure of oil in hydraulic system, electro-hydraulic proportional valve was adopted. The power was provided by a set of separate hydraulic station. The hydraulic station can satisfy relative requirements of step distance, speed and impact load during all kinds of walking beam cycle movements. The control circuit diagrams of the first main pump to the third main pump of hydraulic station were shown as Fig. 10, Fig. 11 and Fig. 12 respectively. The control circuit diagram of the first cycle pump of hydraulic station was shown as Fig. 13.



**Fig. 11.** The control circuit diagram of the second main pump of hydraulic station.



**Fig. 10.** The control circuit diagram of the first main pump of hydraulic station.



**Fig. 12.** The control circuit diagram of the third main pump of hydraulic station.

**Fig. 13.** The control circuit diagram of the first cycle pump of hydraulic station.

After charge machine loading finish, according to actual condition, one of the follow movements may be chosen by walking beam to begin cycle movement from its original position. Positive cycle movement was chosen usually. It contains the movements of ascending, advancing, descending and retreating. A step distance that is 500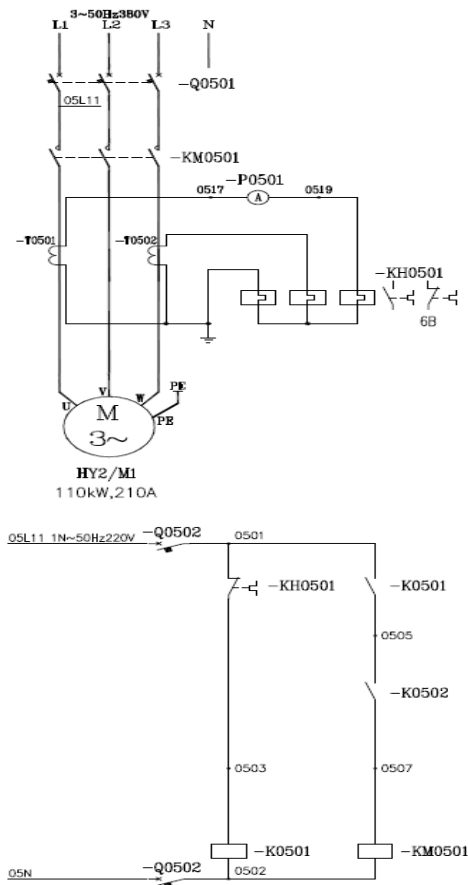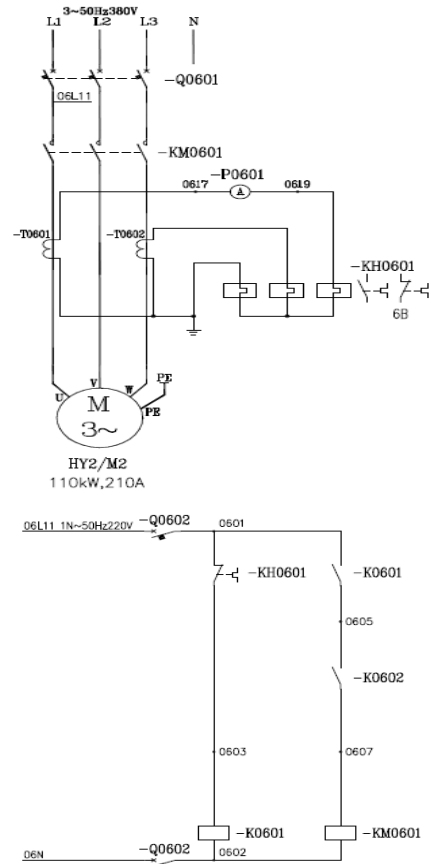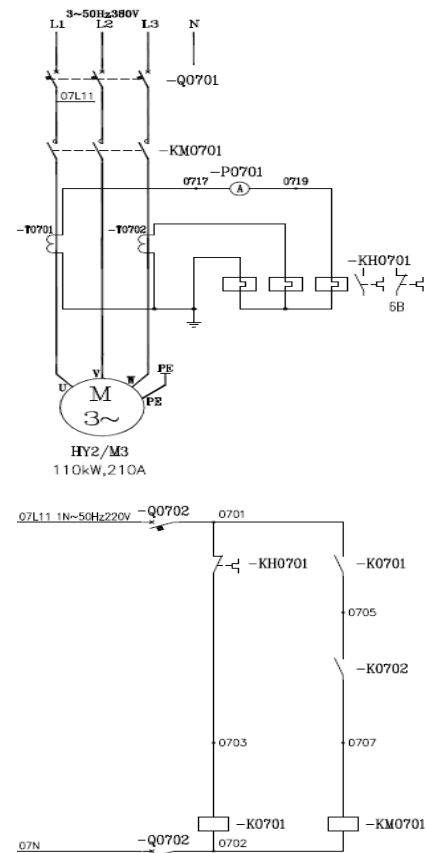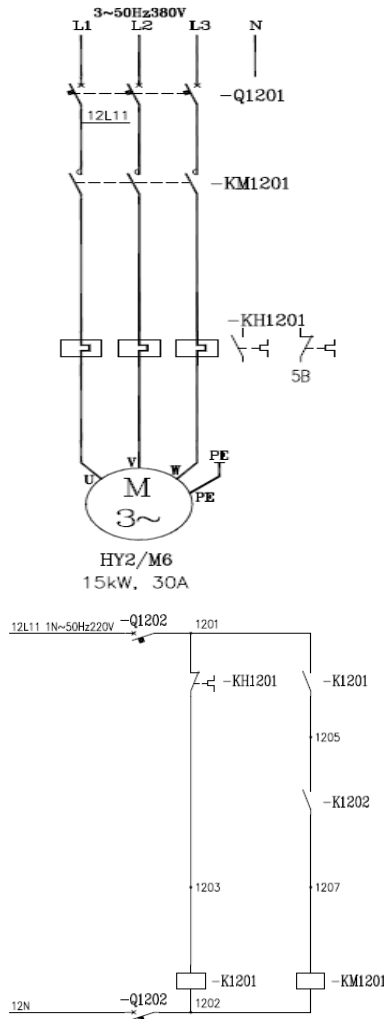 mm was advanced on steel blank in heating furnace by positive cycle movement. Manual reverse cycle movement was chosen during fault. It contains the movements of advancing, ascending, descending and retreating. A step distance that is 500 mm was retreated on steel blank in heating furnace by reverse cycle movement. When waiting rolling time is less than one hour, stepping movement was adopted. It contains the movements of ascending to limit position, postponing and descending. In heating furnace, steel blank was stepped on its original position by stepping movement. When waiting rolling time is more than one hour, accordant stepping movement was adopted. It contains the movements of ascending to fixed beam height, postponing and descending. In heating furnace, steel blank was stepped on its original position by accordant stepping movement.

## 7. Extractor Movement Process

Front extractor of heating furnace was shown as Fig. 14.



**Fig. 14.** Front extractor of heating furnace.

Extractor motion mechanism contains parallel shift mechanism and uplifted and degressive mechanism. When forward command was sent by PLC, quick parallel shift of extractor lever from original position to heating furnace was implemented. When lever is near to steel blank, parallel shift motor decelerates and stops at target position. When forward command was sent by PLC, heating furnace gate opening command was also sent by PLC. When up command was sent by PLC, extractor uplifted and degressive motor work. Lever and steel blank were uplifted. When backward command was sent by PLC, steel blank was extracted and moved parallel from heating furnace by extractor lever. Extractor lever returns to original position. When the distance between extractor lever and its original position reaches set value, heating furnace gate shut command was sent by PLC. When fall command was sent by PLC, extractor uplifted and degressive motor work. Lever and steel blank were dropped. Steel blank was put on table roller [3-8]. The whole tapping process can be accomplished by above operations.

## 8. The Control of Parallel Shift, Uplifted and Degressive Motors of Charge Machine and Extractor

The parallel shift motor control circuitry of charge machine and extractor of first heating furnace was shown as Fig. 15. The controls of corotation startup, corotation stop, reversal startup, reversal stop, overload protection, frequency conversion and banding brake of parallel shift motor can be realized by relative control circuitry. Inverter wiring diagram was shown as Fig. 16. The uplifted and degressive motor control circuitry of charge machine and extractor of first heating furnace was shown as Fig. 17. The controls of corotation startup, corotation stop, reversal startup, reversal stop, overload protection and banding brake of uplifted and degressive motor can be realized by relative control circuitry.
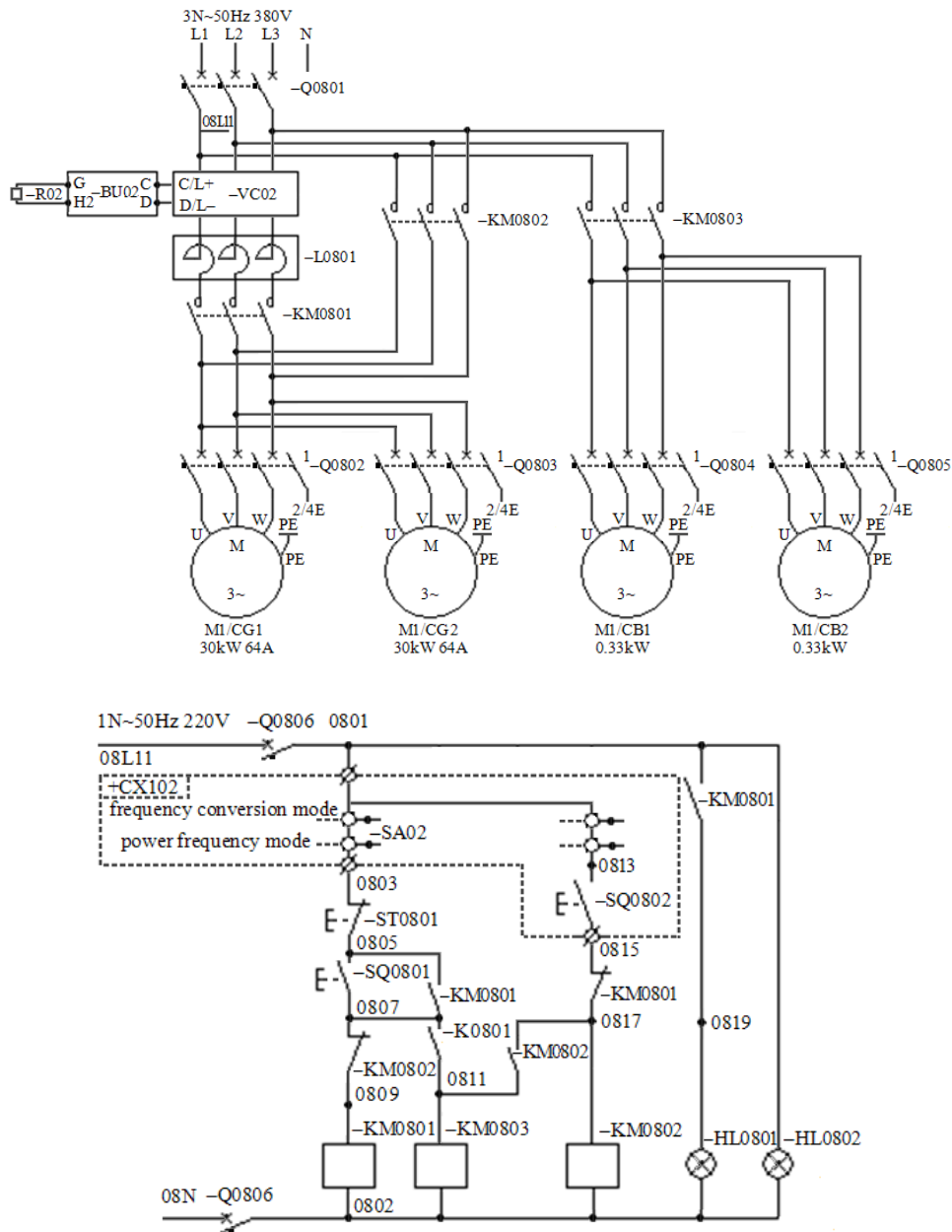
**Fig. 15.** The parallel shift motor control circuitry of charge machine and extractor of first heating furnace.
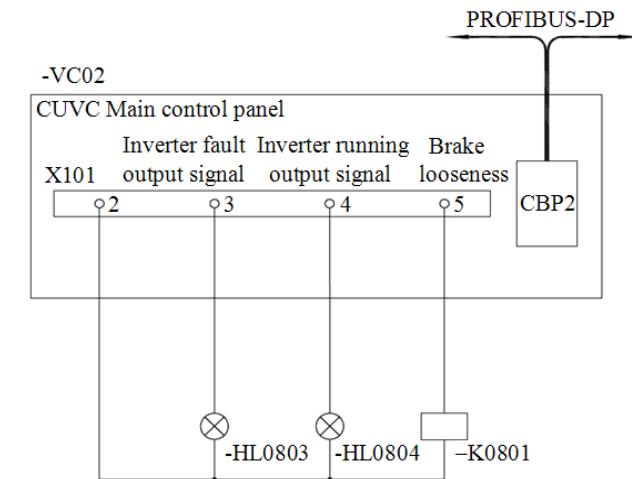


**Fig. 16.** Inverter wiring diagram.
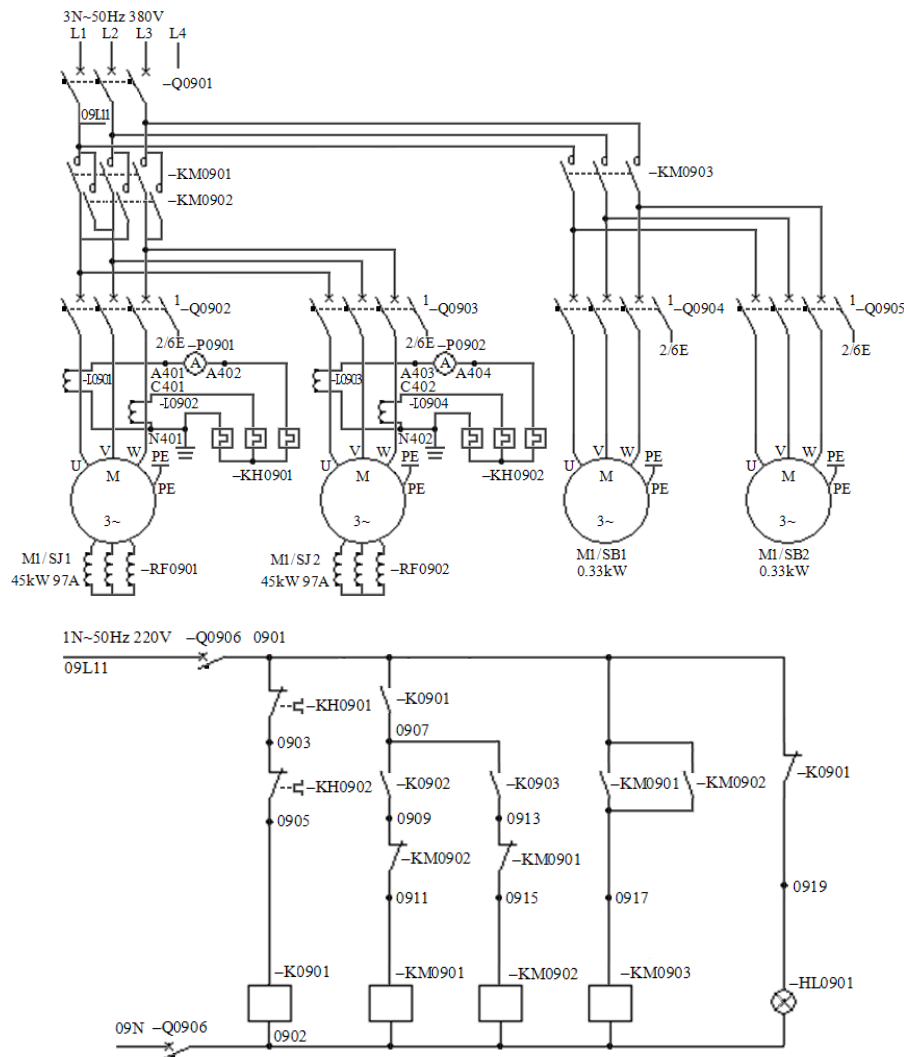
**Fig. 17.** The uplifted and degressive motor control circuitry of charge machine and extractor of first heating furnace.

## 9. The Tracking and Sequence Control of Heating Furnace Field Roller

### 9.1. The Realization Method of Steel Blank Length Test

Pulser and laser detector were installed on A1, A2, A3 and A4 adjacence rollers. Pulser was used as record steel blank movement distance. Laser detector was used as check the top and end positions of steel blank. When the top position of steel blank was checked, the impulse number collected by high speed counting template was reset. The collected impulse number increases with steel blank passing distance simultaneously. When the end position of steel blank was checked, steel blank length can be calculated by impulse number and impulse increment.

### 9.2. The Realization Method of Heating Furnace Field roller Tracking Function

When steel blank enters certain roller, detector was covered. Then steel existence signal was produced. Steel blank data were entered into relative roller data flow. When steel blank leaves certain roller, detector was not covered. Then steel inexistence signal was produced. Steel blank data were dislodged from relative roller data flow. Steel blank data in PLC were changed with continuous running of steel blank among rollers accordingly. By this way, the tracking function of heating furnace field roller can be realized.

### 9.3. The Realization Method of Heating Furnace Field Roller Sequence Control Function

When steel blank movement distance from current roller to next roller reaches definite distance, next rollers were started. When steel blank enters next rollers, it can ensure the same speed of current rollers and next rollers. This can avoid unnecessary roller empty running. So energy was saved. Roller working life was lengthened. By this way, the sequence control function of heating furnace field roller can be realized.

## 10. Conclusions

The practical application of LOS-T18-2ZC1 laser detector was elaborated in this paper. The network communication model of walking beam heating furnace control system was designed. The realization method of production process automation control was elaborated. The entire automation control system allocation picture and PLC power distribution system picture of walking beam heating furnace were designed. Charge machine movement process was elaborated. Walking beam movement process was elaborated. Extractor movement process was elaborated. The hydraulic station of walking mechanism was elaborated. Relative control circuit diagram was designed. The control function of parallel shift motor, uplifted and degressive motor was elaborated. The control circuit diagram of parallel shift motor of charge machine and extractor of first heating furnace was designed. The control circuit diagram of uplifted and degressive motor of charge machine and extractor of first heating furnace was designed. The realization method of steel blank length test function was elaborated. The realization method of tracking and sequence control function of heating furnace field roller were elaborated. After practice test, the design can satisfy the walking beam heating furnace field automation control requirement. The design enhances continuous strip steel rolling productivity obviously.

## Acknowledgements

## References

[1]. X. Z. Tang, L. Tang, The development and technology progress of walking heating furnace, *Metallurgical Equipment Management and Maintenance*, Vol. 20, Issue 1, 2002, pp. 19-20.

[2]. F. Li, L. C. Zeng, G. C. Luo, Research on speed control system of walking beam heating furnace, *Chinese Hydraulics & Pneumatics*, Vol. 28, Issue 9, 2004, pp. 15-16.

[3]. J. D. You, PLC control of walking beam heating furnace, *Electric Engineering*, Vol. 32, Issue 12, 2011, pp. 24-25.

[4]. L. M. Zhang, The application of ACS800 transducer on heating furnace extractor control system, *Electric Engineering*, Vol. 32, Issue 1, 2011, pp. 45-46.

[5]. X. P. Sheng, Z. D. Xu, The optimal design of heating furnace extractor, *Journal of Qingyuan Polytechnic*, Vol. 3, Issue 6, 2010, pp. 64-67.

[6]. F. X. Han, L. X. Wu, Application of PLC controlling transducer of heater stove tapping machine, *The World of Inverters*, Vol. 10, Issue 5, 2006, pp. 102-104.

[7]. L. Han, G. M. Fan, Summarization of electrical control system within heating furnace region of ANGAN 1700 mm hot continuous rolling mills, *ANGANG Technology*, Vol. 42, Issue 6, 2005, pp. 8-11.

[8]. H. Liang, G. M. Fan, Optimization control of walking beam heating furnace of AISC 1780 hot continuous rolling mill, *ANGANG Technology*, Vol. 38, Issue 5, 2001, pp. 42-45.

---

# Wire Finishing Mill Rolling Bearing Fault Diagnosis Based on Feature Extraction and BP Neural Network

**[1] Hong-Yu LIU, [1] Ze-Ning XU, [2] Jun-Jie XI**

[1] School of Mechanical Engineering and Automation,
University of Science and Technology Liaoning, Anshan, Liaoning Province, 114051, China
[2] School of Mechatronics Engineering, Zhengzhou Institute of Aeronautical Industry Management,
Zhengzhou, Henan Province, 450015, China
E-mail: lhy_12@126.com

**Abstract:** Rolling bearing is main part of rotary machine. It is frail section of rotary machine. Its running status affects entire mechanical equipment system performance directly. Vibration acceleration signals of the third finishing mill of Anshan Steel and Iron Group wire plant were collected in this paper. Fourier analysis, power spectrum analysis and wavelet transform were made on collected signals. Frequency domain feature extraction and wavelet transform feature extraction were made on collected signals. BP neural network fault diagnosis model was adopted. Frequency domain feature values and wavelet transform feature values were treated as neural network input values. Various typical fault models were treated as neural network output values. Corresponding relations between feature vector and fault omen were utilized. BP neural network model of typical wire plant finishing mill rolling bearing fault was constructed by training many groups sample data. After inputting sample needed to be diagnosed, wire plant finishing mill rolling bearing fault can be diagnosed. This research has important practical significance on enhancing rolling bearing fault diagnosis precision, repairing rolling bearing duly, decreasing stop time, enhancing equipment running efficiency and enhancing economic benefits. *Copyright © 2014 IFSA Publishing, S. L.*

**Keywords:** Feature extraction, BP neural network, Wire finishing mill, Rolling bearing fault diagnosis, Wavelet transform.

## 1. Introduction

With the development of wire finishing rolling technology, finishing mill develops toward the direction of large, continuous and automated. After finishing mill drive system arising faults, entire production line will stop. It will cause huge economic loss. The ratio of rolling bearing fault is big in finishing mill drive system faults. The ratio of rolling bearing fault causing Anshan Steel and Iron Group wire plant stop is big in entire equipment faults.

The abnormal work of rolling bearing can cause many rotary machine faults. So, rolling bearing loss plays a decisive role in the normal work of entire equipment. After rolling bearing loss, equipment vibrations were caused. Massive noises were caused. Machine equipment paralysis was caused [1]. Rolling bearing is the commonest part in machine field. Its application is very universal. It is the easiest worn part. Relevant statistical data show that thirty percent existing machine faults were caused by rolling bearing faults. So, relevant fault analysis diagnosis on rolling bearing is an important research task in equipment fault diagnosis all the time [2]. Rolling bearing is main part in rotary machine. It is feeble section in rotary machine. Its outstanding feature is

big life discreteness. The life difference is big within a batch rolling bearings with same material, processing technique and equipment. Rolling bearing running status affects entire mechanical equipment system performance directly. Suitable quantities rolling bearings were all equipped with modern industrial equipment. Generally speaking, rolling bearing is the most accurate part in machine. Many rolling bearings in industry field lose efficacy because of abrasion. So, detecting rolling bearing early symptom and estimating fault severity extent are very important [3].

The method of combining feature extraction and BP neural network was adopted on Anshan Steel and Iron Group wire plant finishing mill rolling bearing fault diagnosis.

## 2. Frequency Domain Feature Extraction and Wavelet Transform Feature Extraction of Rolling Bearing

### 2.1. Finishing Mill Vibration Signal Collection

Various anomalies and losses were caused during rolling bearing work. Most faults will aggravate rolling bearing vibration. So, vibration signal becomes main information on rolling bearing fault diagnosis. There are many methods on rolling bearing fault diagnosis currently. Vibration diagnosis method was discussed in this paper mainly.

The influences on rolling bearing vibration information caused by different fault type are different. So, rolling bearing fault status can be obtained by detecting vibration information [4]. In the periodical detection of Anshan Steel and Iron Group wire plant, vibration acceleration signals of the third finishing mill drive device were regarded as research object. Acceleration sensors were adopted on collecting relative vibration acceleration signals. Sampling frequency is 1280 Hz. Anshan Steel Iron and Steel Group wire plant finishing mills is shown as Fig. 1. Collection channel is shown as Fig. 2. The third finishing mill drive device is shown as Fig. 3.



**Fig. 2.** Collection channel.
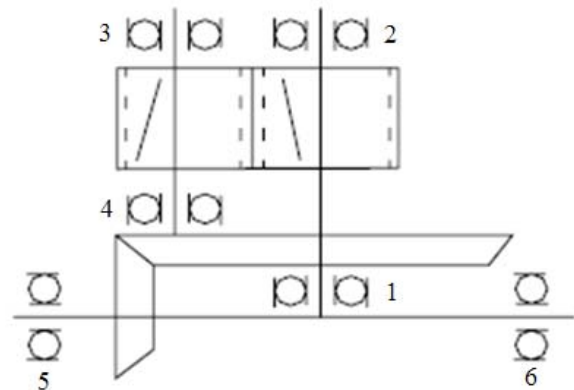


**Fig. 3.** The third finishing mill drive device.

Four kinds of fault feature frequencies of six running rolling bearings in the third finishing mill drive device is shown as Table 1. Four kinds of faults of six rolling bearings are inner ring roller path fault, outer ring roller path fault, rolling element fault and retainer fault separately. Axis rotation frequency of rolling bearing 1 and rolling bearing 2 is 78.0 Hz. Axis rotation frequency of rolling bearing 3 and rolling bearing 4 is 30.9 Hz. Axis rotation frequency of rolling bearing 5 and rolling bearing 6 is 26.6 Hz.

**Table 1.** Four kinds of fault feature frequencies of six running rolling bearings.

| Rolling number | Inner ring roller path fault (Hz) | Outer ring roller path fault (Hz) | Rolling element fault (Hz) | Retainer fault (Hz) |
|---|---|---|---|---|
| 1 | 313.2 | 242.2 | 238.7 | 13.5 |
| 2 | 158.0 | 107.4 | 115.8 | 10.7 |
| 3 | 201.5 | 137.9 | 121.7 | 12.6 |
| 4 | 226.1 | 144.2 | 132.9 | 12.4 |
| 5 | 795.9 | 608.5 | 574.8 | 33.9 |
| 6 | 863.6 | 695.9 | 623.4 | 34.8 |



**Fig. 1.** Anshan Steel and Iron Group wire plant finishing mills.

### 2.2. Frequency Domain Analysis Frequency Domain Feature Extraction of Finishing Mill Vibration Signal

Collected vibration acceleration signals of the third finishing mill drive device is shown as Fig. 4. Fourier analysis and power spectrum analysis were made on relative signals. Fourier analysis of collected vibration acceleration signals is shown as Fig. 5.

Power spectrum analysis of collected vibration acceleration signals is shown as Fig. 6. Relative frequency spectrum feature values on feature frequency were extracted.

Frequency spectrum feature value on feature frequency of Fourier analysis is shown as Fig. 7. Frequency spectrum feature value on feature frequency of power spectrum analysis is shown as Fig. 8.



**Fig. 4.** Collected vibration acceleration signals of the third finishing mill drive device.



**Fig. 5.** Fourier analysis of collected vibration acceleration signals.



**Fig. 6.** Power spectrum analysis of collected vibration acceleration signals.



**Fig. 7.** Frequency spectrum feature value on feature frequency of Fourier analysis.



**Fig. 8.** Frequency spectrum feature value on feature frequency of power spectrum analysis.

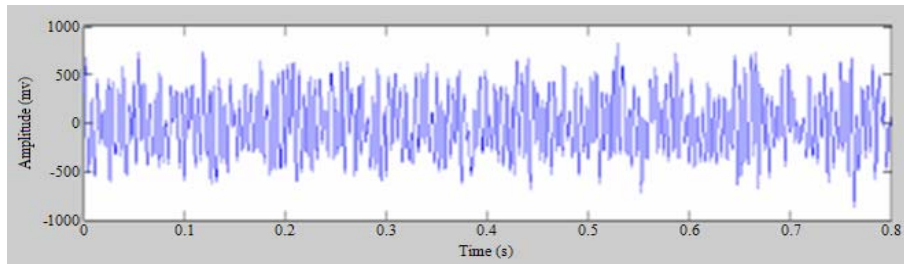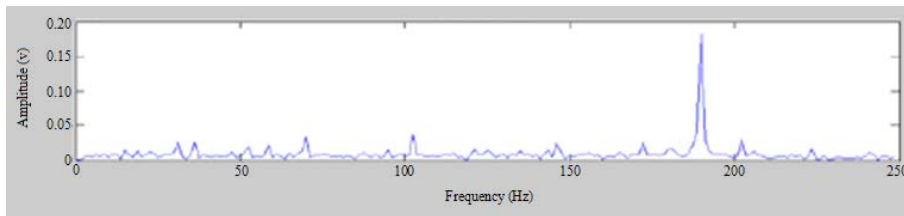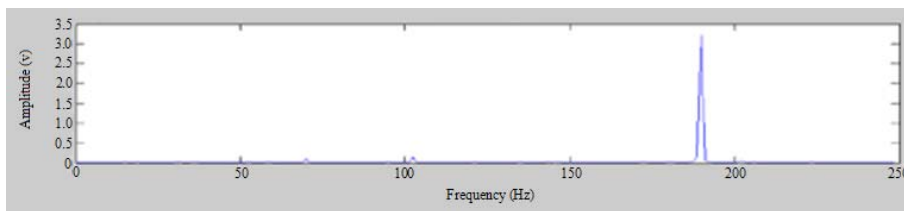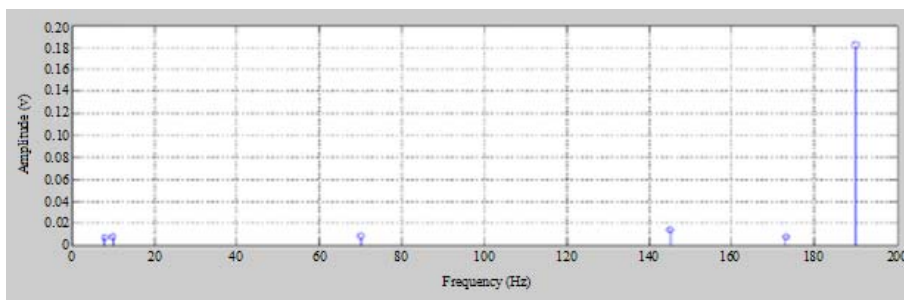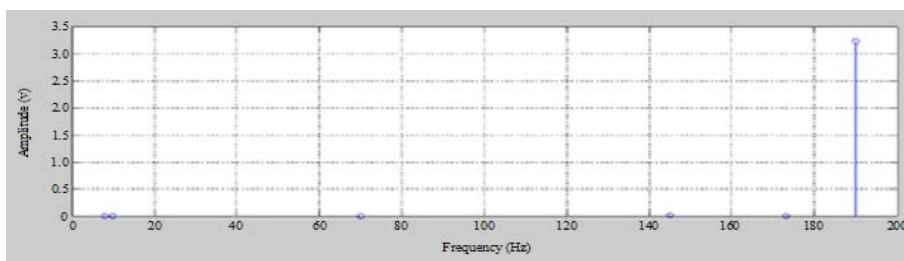Fig. 7 and Fig. 8 show that the most typical frequency of vibration signal is 190 Hz. The feature value related to the most typical frequency is maximal. Above frequency relates and approaches rolling bearing 3 inner ring roller path fault 201.5 Hz in Table 1. So, the fault type related to vibration signal was judged as rolling bearing 3 inner ring roller path fault. The feature values extracted from Fourier analysis and power spectrum analysis were treated as input that is training sample data of BP neural network model.

### 2.3. Wavelet Transform and Relative Feature Extraction of Finishing Mill Vibration Signal

At present wavelet analysis method is the most effective method on rolling bearing status monitoring and fault diagnosis. It has good localization feature on time domain and frequency domain. It can peel and resolve vibration signal at different extent. Different scale detail signals and outline information can be obtained. It benefits to distinguish fault features and relative interference signals [5]. Wavelet transform as a time and frequency analysis method has multiresolution feature. It has the capability of representing local signal feature on time domain and frequency domain. It has been described as math microscope [6]. It is the development and continuation of Fourier transformation thought method. It has good time and frequency analysis feature. It suits nonstationary signal treatment especially. Wavelet transform provides good technical support for feature extraction of rolling bearing fault diagnosis.

After signal orthogonality wavelet transform, every layer coefficient corresponds to some section frequency component of original signal. The sum of every layer high frequency coefficient energy and N layers low frequency coefficient energy is equal to original signal energy. Original signal energy is unchanged with wavelet decomposition from start to finish. When system fault occurrence, relative change of energy space distribution will take place between fault system output signal and normal system output signal. Energy change of respective output signal frequency component represents damage extent of some mechanical equipment components. Based on this point, rolling bearing faults were diagnosed by utilizing respective frequency component energy change.

Wavelet transform was made on the collected vibration signals of the third finishing mill drive device. Five layers wavelet decomposition were made on relative vibration signals. Six wavelet decomposition coefficients were obtained. They are a5, d5, d4, d3, d2 and d1 respectively. Six wavelet decomposition coefficients and relative frequency ranges are shown as Table 2. Restructuring graph of respective layer wavelet decomposition coefficients is shown as Fig. 9. Vibration signal energy distribution graph of respective layer wavelet decomposition coefficients is shown as Fig. 10.

Fig. 10 shows that within relative frequency range of wavelet decomposition coefficient d2 vibration signal energy amplitude is maximal. It can be checked from Table 2 that relative frequency range of wavelet decomposition coefficient d2 is from 160 Hz to 320 Hz. Above frequency relates and approaches rolling bearing 3 inner ring roller path fault 201.5 Hz in Table 1. So, the fault type related to vibration signal was judged as rolling bearing 3 inner ring roller path fault. The feature values extracted from wavelet transform were treated as input that is training sample data of BP Neural Network model.
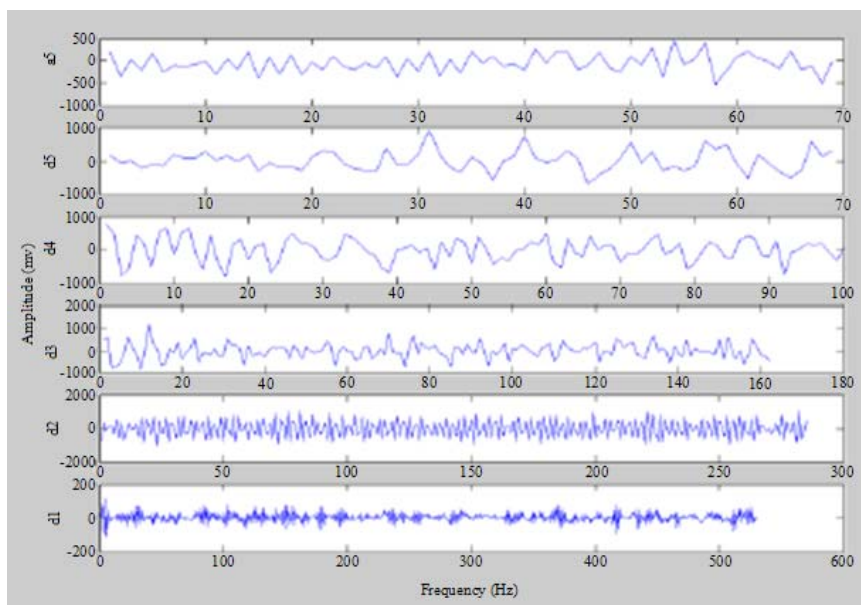


**Fig. 9.** Restructuring graph of respective layer wavelet decomposition coefficients.
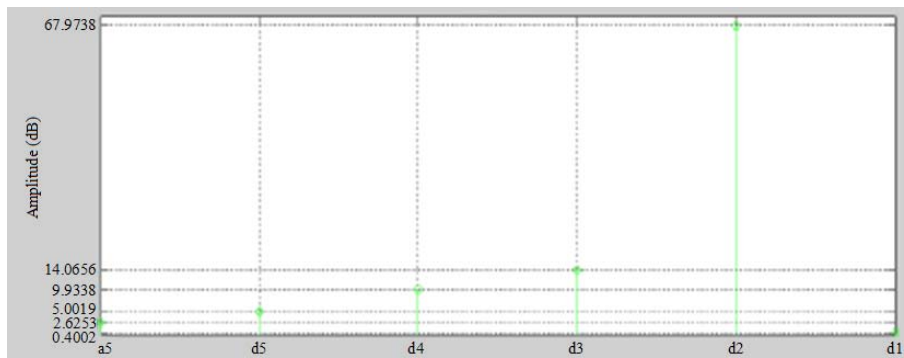
**Fig. 10.** Vibration signal energy distribution graph of respective layer wavelet decomposition coefficients.

**Table 2.** Six wavelet decomposition coefficients and relative frequency ranges.

| Wavelet decomposition coefficients | Frequency ranges (Hz) |
|---|---|
| a5 | 0-20 |
| d5 | 20-40 |
| d4 | 40-80 |
| d3 | 80-160 |
| d2 | 160-320 |
| d1 | 320-640 |

According to diagnosis results of Fig. 5, Fig. 6 and Fig. 10, rolling bearing 3 was checked by spot maintainer. Rolling bearing 3 is shown as Fig. 11. Actual condition is that inner ring roller path of rolling bearing 3 was worn badly. Rolling bearing 3 with bad inner ring roller path abrasion is shown as Fig. 12.



**Fig. 11.** Rolling bearing 3.



**Fig. 12.** Rolling bearing 3 with bad inner ring roller path abrasion.

## 3. The Construction and Application of BP Neural Network Model of Rolling Bearing

Neural network is a very large scale continuation time power system with high nonlinearity. It has the features of nonlinear mapping, quickly parallel distribution processing, autonomic organization, autonomic study and robustness. It was applied on nonlinear control and fault diagnosis. Artificial neural network was abbreviated named as neural network. It is a hot interdiscipline developed in recent years. Applying neural network technology to solve various practical problems was concerned highly and widely. It has the functions of complicated multimodal treatment, association, supposition and memory. It is suit for fault diagnosis system specially. Neural network is a kind of intelligent method with the advantages of strong nonlinear mapping, autonomic study, autonomic organization and autonomic adaptability. It is suit for fault diagnosis rolling bearing specially [7]. Neural network is a new intelligent information calculation treatment system. It can imitate human brain information, associate, remember and obtain entire information from partial information. Although system was disturbed in some extent with big feature information change, neural network can also distinguish and dispose information with optimized work status. It has important significance on on-line real time monitoring and diagnosis of system. It can train satisfied sample requirement decision region under the conditions of big data, incomplete data and noise data.

Multilevel perceptron network with BP algorithm was abbreviated named as BP neural network. It is a kind of artificial neural network with the broadest application. It has important application on various subject areas. BP algorithm applied by multilevel perceptron neural network is a kind of study algorithm wit instructor [8]. The study process of BP algorithm contains forward propagation and backward propagation. In forward propagation process, after hidden layer neures treatment, input model was transferred from input layer to output layer. Every layer neures status only affects next layer neures status. If expected output can not be

obtained, propagation was transferred to backward propagation. Error signals were transferred from output layer to input layer simultaneously. Connection weight values and threshold values were adjusted during backward propagation. It can decrease system error continuously so as to satisfy precision requirement. This algorithm is to calculate error function minimal value. Weight values were changed along negative error function gradient direction and converged minimal point by repeatedly training multiple samples with fastest descent method.

### 3.1. Structure Determination of BP Neural Network

Three layer BP neural networks were adopted in this paper. M input points are $x_1$, $x_2$, …, $x_M$ respectively. L input points are $y_1$, $y_2$, …, $y_L$ respectively. Hidden network layer contains q units. BP neural network topology structure is shown as Fig. 13.

Fourier analysis, power spectrum analysis and wavelet transform can reflect signal frequency feature accurately. Incompact combination type was adopted in this paper to realize the combination of Fourier analysis, power spectrum analysis, wavelet transform and BP neural network. Fourier analysis, power spectrum analysis and wavelet transform were treated as proposed treatment means of BP neural network. Fourier analysis, power spectrum analysis and wavelet transform provide input feature vectors for BP neural network.

Every weight value change produced by cycle training was decided by study efficiency. Big study efficiency can cause system instability. Small study efficiency can cause long training time and slow convergence. So, in general condition, small study efficiency was selected so as to ensure system stability. The study efficiency selections range is between 0.01 and 0.8. Several different study efficiencies were selected in advance in order to train in the network design process of this paper. Best study efficiency was selected by comparing the system errors from all training. Study efficiency selections and system errors are shown as Table 3.
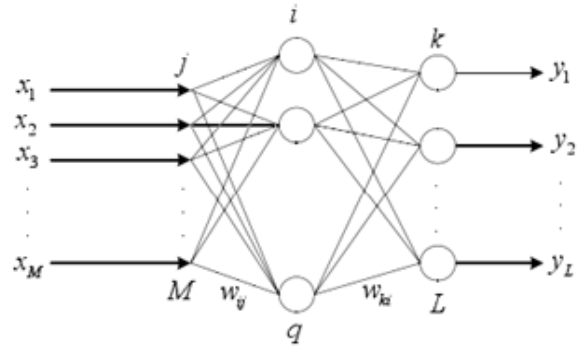


**Fig. 13.** BP neural network topology structure.

Table 3 shows that system error is the smallest with relative study efficiency 0.01. So, study efficiency was selected as 0.01 in this paper. Sigmoid function with abbreviated name S type function was selected as transfer function in this paper according to BP neural network requirement and requisite output purpose. The initial weight value was intercalated within 0 and 1.

**Table 3.** Study efficiency selections and system errors.

| Serial number | Input layer node number | Hidden layer node number | Output layer node number | Study efficiencies | Study step length | System errors |
|---|---|---|---|---|---|---|
| 1 | 4 | 4 | 4 | 0.01 | 5000 | $4.59 \times 10^{-6}$ |
| 2 | 4 | 4 | 4 | 0.03 | 5000 | $4.45 \times 10^{-4}$ |
| 3 | 4 | 4 | 4 | 0.05 | 5000 | $4.28 \times 10^{-5}$ |
| 4 | 4 | 4 | 4 | 0.07 | 5000 | $1.93 \times 10^{-4}$ |
| 5 | 4 | 4 | 4 | 0.09 | 5000 | $2.18 \times 10^{-4}$ |
| 6 | 4 | 4 | 4 | 0.1 | 5000 | $5.38 \times 10^{-4}$ |
| 7 | 4 | 4 | 4 | 0.3 | 5000 | $1.95 \times 10^{-5}$ |
| 8 | 4 | 4 | 4 | 0.5 | 5000 | $2.5 \times 10^{-4}$ |

Relative process knowledge was saved in trained BP neural network. Study can be made in trained BP neural network from quantitative fault information direct. BP neural network can be trained by various object status information. Current tested information can be distinguished by trained BP neural network so as to ascertain fault.

Too many BP neural network input nodes can cause too large BP neural network structure. More noise information will be inputted unavoidably. Too less BP neural network input nodes can not ensure necessary network information quantity. So, the network input node selection is important task of BP neural network mode construction. In this paper, four kinds of rolling bearing fault models are inner ring roller path fault, rolling element fault, retainer fault and outer ring roller path fault separately. Relative ideal output vectors are $Y_1$, $Y_2$, $Y_3$ and $Y_4$. They are

treated as BP neural network model output vectors. Four kinds of rolling bearing fault models and relative ideal output vectors are shown as Table 4.

**Table 4.** Four kinds of rolling bearing fault models and relative ideal output vectors.

| Fault model | Ideal output vector |
|---|---|
| Inner ring roller path fault | $Y_1 = [0\ 0\ 0\ 1]$ |
| Rolling element fault | $Y_2 = [0\ 0\ 1\ 0]$ |
| Retainer fault | $Y_3 = [0\ 1\ 0\ 0]$ |
| Outer ring roller path fault | $Y_4 = [1\ 0\ 0\ 0]$ |

### 3.2. Rolling Bearing Fault Diagnosis Based on BP Neural Network

During finishing mill rolling bearing fault diagnosis process, the fault feature values extracted by frequency domain analysis and wavelet transform analysis were treated as input vectors of BP neural network that is training sample data in this paper. The input layer unit number of BP neural network adopted in this paper is 4. Four input vectors are corresponding with four units. They are inner ring roller path fault feature value $X_1$, rolling element fault feature value $X_2$, retainer fault feature value $X_3$ and outer ring roller path fault feature value $X_4$

separately. The output layer unit number of BP neural network adopted in this paper is 4. Four output vectors are corresponding with four units. They are inner ring roller path fault $Y_1$, rolling element fault $Y_2$, retainer fault $Y_3$ and outer ring roller path fault $Y_4$ separately. The hidden layer unit number of BP neural network adopted in this paper is 4. Training sample data under four kinds of rolling bearing fault models are shown as Table 5.

Before BP neural network training, standardization treatments were made on original data. Treated data were applied as BP neural network input sample. System error was stipulated as 0.001. Study efficiency was stipulated as 0.01. Training number was stipulated as 5000.

Initial weight value and threshold value were produced by uniform distribution random algorithm program. The treatment can satisfy precision requirement. Trained BP neural network model was saved to diagnose finishing mill fault. Standardization treatments were made on training sample data of Table 5. Relative treated data are shown as Table 6.

After standardization treatments, relative training sample data were inputted into trained BP neural network model. The output vectors of training sample data after standardization treatments and ideal output vectors are shown as Table 7.

**Table 5.** Training sample data under four kinds of rolling bearing fault models.

| Fault model | Training sample serial number | Training sample data | | | |
|---|---|---|---|---|---|
| | | $X_1$ | $X_2$ | $X_3$ | $X_4$ |
| Inner ring roller path fault | 1 | 5.2104 | 7.0904 | 9.0185 | 98.2035 |
| Rolling element fault | 2 | 5.6845 | 8.3625 | 15.8705 | 70.2541 |
| Retainer fault | 3 | 4.5681 | 15.5002 | 8.9560 | 67.2540 |
| Outer ring roller path fault | 4 | 12.7410 | 8.0021 | 9.68452 | 69.3251 |

**Table 6.** Training sample data under four kinds of rolling bearing fault models after standardization treatments.

| Fault model | Training sample serial number | Training sample data after standardization treatments | | | |
|---|---|---|---|---|---|
| | | $X_1$ | $X_2$ | $X_3$ | $X_4$ |
| Inner ring roller path fault | 1 | 0.0786 | 0.1366 | 0 | 1.0000 |
| Rolling element fault | 2 | 0 | 0.1513 | 1.0000 | 0.1084 |
| Retainer fault | 3 | 0.0090 | 1.0000 | 0 | 0.1054 |
| Outer ring roller path fault | 4 | 1.0000 | 0.0969 | 0 | 0.0669 |

**Table 7.** The output vectors of training sample data after standardization treatments and ideal output vectors.

| Training sample serial number | Training sample output vectors | Ideal output vectors |
|---|---|---|
| 1 | $Y_1 = [-0.0001\ 0.0000\ 0.0005\ 0.9993]$ | $Y_1 = [0\ 0\ 0\ 1]$ |
| 2 | $Y_2 = [0.0003\ -0.0000\ 1.0003\ 0.0046]$ | $Y_2 = [0\ 0\ 1\ 0]$ |
| 3 | $Y_3 = [0.0003\ 1.0000\ 0.0000\ 0.0037]$ | $Y_3 = [0\ 1\ 0\ 0]$ |
| 4 | $Y_4 = [1.0000\ -0.0000\ -0.0004\ -0.0001]$ | $Y_4 = [1\ 0\ 0\ 0]$ |

Frequency domain analysis and wavelet analysis were made on practical test vibration signals of finishing mill rolling bearing under rolling element fault. Relative fault feature values were extracted and

inputted into BP neural network model. Relative output result is [ 0.0051 0.1980 1.0024 0.0089] . It is very close to relative training sample output vector that is [0.0003 -0.0000 1.0003 0.0046]. It shows that

the method of combining feature extraction and BP neural network has high fault recognition precision on rolling bearing fault diagnosis.

## 4. Conclusions

Vibration acceleration signals of the third finishing mill of Anshan Steel and Iron Group wire plant were collected in this paper. Fourier analysis, power spectrum analysis and wavelet transform were made on collected signals. Frequency domain feature extraction and wavelet transform feature extraction were made on collected signals. BP neural network fault diagnosis model was adopted. Frequency domain feature values and wavelet transform feature values were treated as neural network input values. Various typical fault models were treated as neural network output values. Corresponding relations between feature vector and fault omen were utilized. BP neural network model of typical wire plant finishing mill rolling bearing fault was constructed by training many groups sample data. After inputting sample needed to be diagnosed, wire plant finishing mill rolling bearing fault can be diagnosed. Relative experiment was made. The outputted vector errors under various typical rolling bearing faults are small between diagnosis outputted results and ideal outputted results. It shows that the BP neural network model of typical wire plant finishing mill rolling bearing fault has high identification precision on rolling bearing fault. The model can satisfy the fault diagnosis requirement of Anshan Steel and Iron Group wire plant finishing mill rolling bearing.

## References

[1]. W. L. Hu, Rolling bearing fault diagnosis based on wavelet analysis, *East China Science & Technology*, Vol. 29, Issue 11, 2013, pp. 369.
[2]. Q. Gu, C. Z. Chen, H. Zhou, Research on new rolling bearing fault diagnosis method, *Machinery Design & Manufacture*, Vol. 51, Issue 9, 2013, pp. 117-119.
[3]. C. S. Gou, Y. Zhang, Application of modern diagnosis technology on rolling bearing fault diagnosis, *Chongqing Steel and Iron Motorized Energy*, Vol. 26, Issue 3, 2013, pp. 35-40.
[4]. J. Huang, Y. H. Wang, Research on rolling bearing fault model and vibration test technology, *Quality and Reliability*, Vol. 24, Issue 2, 2012, pp. 30-32.
[5]. C. S. Gou, Y. Zhang, Fault diagnosis of rolling bearing based on wavelet analysis, *Mechanical Engineer*, Vol. 24, Issue 2, 2012, pp. 30-32.
[6]. T. Peng, X. Ma, Application of wavelet neural network on rolling element bearings fault diagnosis, *Computer Engineering and Applications*, Vol. 46, Issue 4, 2010, pp. 213-215.
[7]. Y. B. Hu, S. Y. Li, L. B. Hu, Fault diagnosis of rolling bearing based on neural network, *Machinery Design & Manufacture*, Vol. 50, Issue 2, 2012, pp. 187-189.
[8]. Z. F. Zhang, L. M. Xia, Intelligent method of fault diagnosis of rolling bearing based on neural network, *Information Technology*, Vol. 32, Issue 8, 2008, pp. 53-55.

_____

# Intelligent Test Mechanism Design of Worn Big Gear

**[1] Hong-Yu LIU, [1] Ze-Ning XU, [2] Jun-Jie XI**

[1] School of Mechanical Engineering and Automation,
University of Science and Technology Liaoning, Anshan, Liaoning Province, 114051, China
[2] School of Mechatronics Engineering, Zhengzhou Institute of Aeronautical Industry Management,
Zhengzhou, Henan Province, 450015, China
E-mail: lhy_12@126.com

**Abstract:** With the continuous development of national economy, big gear was widely applied in metallurgy and mine domains. So, big gear plays an important role in above domains. In practical production, big gear abrasion and breach take place often. It affects normal production and causes unnecessary economic loss. A kind of intelligent test method was put forward on worn big gear mainly aimed at the big gear restriction conditions of high production cost, long production cycle and high-intensity artificial repair welding work. The measure equations transformations were made on involute straight gear. Original polar coordinate equations were transformed into rectangular coordinate equations. Big gear abrasion measure principle was introduced. Detection principle diagram was given. Detection route realization method was introduced. OADM12 laser sensor was selected. Detection on big gear abrasion area was realized by detection mechanism. Tested data of unworn gear and worn gear were led in designed calculation program written by Visual Basic language. Big gear abrasion quantity can be obtained. It provides a feasible method for intelligent test and intelligent repair welding on worn big gear. *Copyright © 2014 IFSA Publishing, S. L.*

**Keywords:** Big gear, Intelligent test mechanism, Polar coordinate equation, Rectangular coordinate equation, Laser sensor.

## 1. Introduction

When gear surface was worn, gear can not work normally. Gear work precision was affected. Vibrations and noises may be caused [1]. With the continuous development of science and technology, how to decrease gear abrasion and prolong gear service life is an important problem in industrial production [2]. Generally speaking, during gear transmission process, the material loss phenomenon of gear teeth contact surface belongs to abrasion research. For gear abrasion type, different country has different partition standard, for example German DIN3979 standard, American ANSI1010-E95 standard, International Standardization Organization

ISO10825 standard and Chinese GB3481-83 standard. Generally speaking, main gear abrasion research contents contain gear abrasion influence factor, gear abrasion change law, wear resistance method and gear abrasion repair method. In these fields, lots of works were made by native and foreign scholars.

In gear abrasion test, under the invariable load and gear width ratio condition on some contact point, the pressures on every tooth profile contact point are nearly equal. Gear abrasion thicknesses are nearly equal. It was obtained by Huseyin Imrek [3]. The influences of rigidity and lubricant film thicknesses on gear surface abrasion were tested by mode detection method. Gear surface abrasion was

estimated by vibration signal detection method. It was obtained by M. Amarnath [4]. Gear surface abrasion status was researched by testing lubricant oil temperature. The influence of lubricant oil temperature on gear surface abrasion status was estimated again. It was obtained by B. R. Hohn [5]. Gear surface point corrosion and gear vibration were researched. It can be known from vibration and ferrography technology that the more gear point corrosion, the more gear breach, the more gear vibration and the more gear abrasion. It was obtained by Wei Feng [6]. The relation between gear dynamic property and gear surface abrasion were researched. Finite element plasmodium method, simplified dispersed body method and worn gear surface model method were combined to accomplish above researches. The relation between gear surface abrasion and nonlinear dynamics of gear work was demonstrated based on multiple simulation results. It was obtained by Huali Ding [7]. Hypoid gear contact model was constructed. Abrasion simulation was made on hypoid gear by Archard abrasion model. Analyses were made by finite element method. Slither distance and contact pressure were calculated on every position of meshing surface according to simulation model. Slither distance calculation formula of gear surface meshing contact area was summarized. It was obtained by D. Paek [8]. The popularization and application of simulation technology decreases abrasion analysis complexity, saves research time, enhances work efficiency. It provides reference for deeper gear abrasion research.

In this paper, measure equations of straight involute gear under rectangular coordinates were derived. Gear abrasion test mechanism was designed. Gear abrasion quantity calculation program was written.

## 2. The Measure Equations Derivation of Straight Involute Gear under Rectangular Coordinates

Gear involute equations were expressed by polar coordinate equations in most data. Its derivation process is simple. It is accessible by reader. It is the base of other derivation and calculation. But it is inconvenient to gear abrasion test. The gear abrasion test in this paper needs to be made under rectangular coordinates. So, derivation and transformation of gear involute equations under polar coordinates were made. Gear involute equations under polar coordinates are shown as formula (1).

$$r_A = \frac{r_B}{\cos \alpha_A} \quad ,$$
$$\theta_A = tg\,\alpha_A - \alpha_A \tag{1}$$

where $r_A$ is the radius vector from A point to circle center. $r_B$ is the gear base circle radius. $\alpha_A$ is the A point pressure angle. A point is an arbitrary point on

gear involute under polar coordinates. Gear involute profile under rectangular coordinates is shown as Fig. 1. In Fig. 1, the connection straight line from base circle center to the intersection point of involute and base circle is $x$ axis. The vertical upward straight line from base circle center is $y$ axis. E point is an arbitrary point on gear involute. Curve EA represents a part of gear profile. Gear involute equations under polar coordinates can be transformed gear involute equations under rectangular coordinates. They are shown as formula (2).
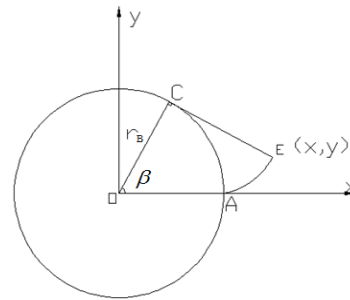


**Fig. 1.** Gear involute profile under rectangular coordinates.

$$x = r_B \cos \beta + r_B \sin \beta$$
$$y = r_B \sin \beta - r_B \cos \beta \tag{2}$$

where $r_B$ is the base circle. $\beta$ is the included angle of straight line OC and straight line OA in Fig. 1. Its unit is degree.

Rectangular coordinates with gear tooth groove centre line as its X axis was requisite in practical test. So, $\varphi$ angle was revolved on above rectangular coordinates in a clockwise direction. X axis and Y axis correspond to new rectangular coordinates. It is shown as Fig. 2. After angle rotation, gear involute equations under new rectangular coordinates are shown as formula (3). After substituting formula (2) into formula (3), gear involute equations are shown as formula (4).
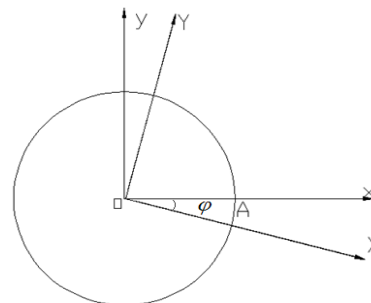


**Fig. 2.** New rectangular coordinates after revolving $\varphi$ angle.

$$X = x \sin \varphi + y \cos \varphi$$
$$Y = x \cos \varphi - y \sin \varphi \tag{3}$$

$$X = r_B(\cos\beta + \beta\sin\beta)\sin\varphi + r_B(\sin\beta - \beta\cos\beta)\cos\varphi,$$
$$Y = r_B(\cos\beta + \beta\sin\beta)\cos\varphi - r_B(\sin\beta - \beta\cos\beta)\sin\varphi \qquad (4)$$

where $r_B$ is the base circle. Its calculation formula is shown as formula (5).

$$r_B = \frac{mz\cos\alpha}{2}, \qquad (5)$$

In formula (4), $\varphi$ is the rotation angle of original rectangular coordinates. Its unit is radian. It equals to gear tooth groove angle half. Its calculation formula is shown as formula (6).

$$\varphi = \frac{s}{2r_B}, \qquad (6)$$

where $s$ is gear base circle tooth width. Its calculation formula is shown as formula (7).

$$s = m(\pi/2 - 2xtg\alpha - zinv\alpha)\cos\alpha, \qquad (7)$$

where $m$ is gear modulus. $x$ is modification coefficient. $\alpha$ is gear reference circle pressure angle. Its unit is degree. After substituting formula (5) and formula (6) into formula (7), formula (8) can be obtained.

$$\varphi = \frac{\pi}{2z} - \frac{2x\,tg\,\alpha}{z} - inv\alpha, \qquad (8)$$

After substituting formula (8) into formula (4), formula (9) can be obtained.

$$X = \frac{mz\cos\alpha}{2}\left[(\cos\beta + \beta\sin\beta)\sin\left(\frac{\pi}{2z} - \frac{2xtg\alpha}{z} - inv\alpha\right) + (\sin\beta - \beta\cos\beta)\cos\left(\frac{\pi}{2z} - \frac{2xtg\alpha}{z} - inv\alpha\right)\right]$$
$$Y = \frac{mz\cos\alpha}{2}\left[(\cos\beta + \beta\sin\beta)\cos\left(\frac{\pi}{2z} - \frac{2xtg\alpha}{z} - inv\alpha\right) - (\sin\beta - \beta\cos\beta)\sin\left(\frac{\pi}{2z} - \frac{2xtg\alpha}{z} - inv\alpha\right)\right], \qquad (9)$$

Radian system is inconvenient than angle system. So, in order to convenient calculation, formula (9) was transformed into angle system. It is shown as formula (10).

$$X = \frac{mz\cos\alpha}{2}\left[\left(\cos\beta + \frac{\pi\beta}{180^0}\sin\beta\right)\sin\frac{180^0}{\pi}\left(\frac{\pi}{2z} - \frac{2xtg\alpha}{z} - inv\alpha\right)\right.$$
$$\left. + \left(\sin\beta - \frac{\pi\beta}{180^0}\cos\beta\right)\cos\frac{180^0}{\pi}\left(\frac{\pi}{2z} - \frac{2xtg\alpha}{z} - inv\alpha\right)\right]$$
$$Y = \frac{mz\cos\alpha}{2}\left[\left(\cos\beta + \frac{\pi\beta}{180^0}\sin\beta\right)\cos\frac{180^0}{\pi}\left(\frac{\pi}{2z} - \frac{2xtg\alpha}{z} - inv\alpha\right)\right.$$
$$\left. - \left(\sin\beta - \frac{\pi\beta}{180^0}\cos\beta\right)\sin\frac{180^0}{\pi}\left(\frac{\pi}{2z} - \frac{2xtg\alpha}{z} - inv\alpha\right)\right], \qquad (10)$$

Formula (11) and formula (12) can be obtained from Fig. 1.

$$\beta = \alpha_i + \theta, \qquad (11)$$

$$\theta = tg\alpha_i - \alpha_i, \qquad (12)$$

After substituting formula (11) into formula (12), formula (13) can be obtained.

$$\beta = tg\alpha_i, \qquad (13)$$

After transforming radian into angle, formula (14) can be obtained.

$$\beta = \frac{180^0}{\pi}tg\alpha_i, \qquad (14)$$

After substituting formula (14) into formula (10), formula (15) can be obtained.

$$X = \frac{mz\cos\alpha}{2}\left[\left(\cos\frac{180^0}{\pi}tg\alpha_i + tg\alpha_i\sin\frac{180}{\pi}tg\alpha_i\right)\times\sin\frac{180^0}{\pi}\left(\frac{\pi}{2z} - \frac{2xtg\alpha}{z} - inv\alpha\right)\right.$$
$$\left. + \left(\sin\frac{180^0}{\pi}tg\alpha_i - tg\alpha_i\cos\frac{180^0}{\pi}tg\alpha_i\right)\times\cos\frac{180^0}{\pi}\left(\frac{\pi}{2z} - \frac{2xtg\alpha}{z} - inv\alpha\right)\right]$$
$$Y = \frac{mz\cos\alpha}{2}\left[\left(\cos\frac{180^0}{\pi}tg\alpha_i + tg\alpha_i\sin\frac{180}{\pi}tg\alpha_i\right)\times\cos\frac{180^0}{\pi}\left(\frac{\pi}{2z} - \frac{2xtg\alpha}{z} - inv\alpha\right)\right.$$
$$\left. - \left(\sin\frac{180^0}{\pi}tg\alpha_i - tg\alpha_i\cos\frac{180^0}{\pi}tg\alpha_i\right)\times\sin\frac{180^0}{\pi}\left(\frac{\pi}{2z} - \frac{2xtg\alpha}{z} - inv\alpha\right)\right], \qquad (15)$$

Modulus and modification coefficient of standard involute straight gear can be known easily.

Modification coefficient $x$ is 0. It was substituted into formula (15), formula (16) can be obtained.

$$X = \frac{mz\cos\alpha}{2}\left[\left(\cos\frac{180^0}{\pi}tg\alpha_i + tg\alpha_i\sin\frac{180}{\pi}tg\alpha_i\right)\times\sin\frac{180^0}{\pi}\left(\frac{\pi}{2z}-inv\alpha\right)\right.$$
$$\left.+\left(\sin\frac{180^0}{\pi}tg\alpha_i - tg\alpha_i\cos\frac{180^0}{\pi}tg\alpha_i\right)\times\cos\frac{180^0}{\pi}\left(\frac{\pi}{2z}-inv\alpha\right)\right]$$
$$Y = \frac{mz\cos\alpha}{2}\left[\left(\cos\frac{180^0}{\pi}tg\alpha_i + tg\alpha_i\sin\frac{180}{\pi}tg\alpha_i\right)\times\cos\frac{180^0}{\pi}\left(\frac{\pi}{2z}-inv\alpha\right)\right.$$
$$\left.-\left(\sin\frac{180^0}{\pi}tg\alpha_i - tg\alpha_i\cos\frac{180^0}{\pi}tg\alpha_i\right)\times\sin\frac{180^0}{\pi}\left(\frac{\pi}{2z}-inv\alpha\right)\right],\qquad(16)$$

## 3. Gear Abrasion Test Principle

The test principle diagram of gear abrasion surface drawn on gear cross section is shown as Fig. 3. In Fig. 3, straight line $L_2$ is the near tooth groove centre line of worn gear. The tooth groove was divided equally by straight line $L_2$. Two near gears are symmetrical about straight line $L_2$. Straight line $L_1$ is the centre line of worn gear. Worn gear was divided equally by straight line $L_1$. The distance straight line $L_1$ from and straight line $L_2$ is H. Laser sensor is on D point of straight line $L_2$. Laser sensor test route is a straight line perpendicular to straight line $L_2$. The straight line intersects straight line $L_1$ at C point. The straight line intersects unworn gear tooth involute at A point. The straight line intersects worn gear tooth involute at B point.

In worn gear surface test process, Laser sensor moves along straight line $L_2$ back and forth to realize gear abrasion test. The motion covers entire gear surface abrasion area. Laser sensor can test the distance from D point to B point. C point position can be obtained by calculated gear parameters. A point position can be obtained by substituting tested A point data into derived standard involute straight gear equations that is formula (16). Straight line DA distance is the difference between H and straight line AC. Gear surface abrasion quantity AB is the difference between straight line DB and straight line DA. Other point positions on gear cross section can be obtained in the same way. Gear worn surface test can be realized by this method.
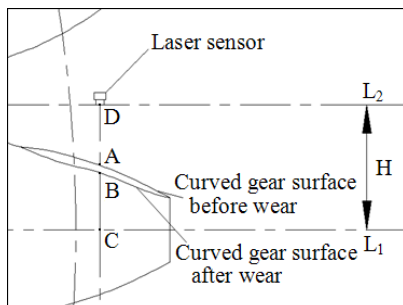


**Fig. 3.** The test principle diagram of gear abrasion surface.

In practical production, there is not law on gear surface abrasion. Gear surface abrasion is different with different working conditions. In order to dispose data conveniently, relative regular division was made on tested gear surface in this paper. The straight lines along gear width direction that is parallels with gear axis hole centre line and the curves along gear surface direction that is parallels with gear involute profile were used on division. n straight lines with same distance along gear width direction were selected. m straight lines with same distance along gear surface direction were selected. The distances between straight lines are equal to the distances between curves. Gear surface was divided n×m grids. It is shown as Fig. 4. In test, Laser sensor moves and tests along straight line and curves successively. Tested data are related to divided grids density. After test, n×m groups data can be obtained.
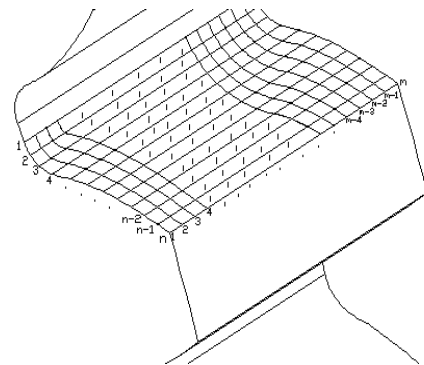


**Fig. 4.** Gear surface grids division diagram.

Tested data were given on rectangular coordinate form. $X_{11}$ was named as X axis coordinate of grid test point on first row first column. $Y_{11}$ was named as Y axis coordinate of grid test point on first row first column. Grid test point coordinate on first row first column was named as $(X_{11}, Y_{11})$. Other test point coordinates can be obtained by above method. Entire gear surface abrasion area can be tested and expressed with discrete points form. It provides theory base for intelligent gear surface test and intelligent gear surface repair welding.

## 4. Gear Test Localization

### 4.1. Gear Test Circle Center Localization

In order to realize test process, gear axis hole center need to be localized. It is very important to test

coordinates localization, test mechanism localization and repair welding mechanism localization. At present there are two kinds of circle center localization methods. One is three points circle center localization. Another is least square method circle center localization. In three points circle center localization, arbitrary three points were selected on circle. Their coordinates are $(x_1, y_1)$, $(x_2, y_2)$ and $(x_3, y_3)$ respectively. Circle center coordinate is $(x_0, y_0)$. Circle radius is R. By this method, formula (17) can be obtained.

$$\begin{aligned}(x_1 - x_0)^2 + (y_1 - y_0)^2 &= R^2 \\ (x_2 - x_0)^2 + (y_2 - y_0)^2 &= R^2 \\ (x_3 - x_0)^2 + (y_3 - y_0)^2 &= R^2\end{aligned} \quad (17)$$

After solving formula (17), relative circle center coordinate can be obtained. But obtained result by this method is inexact because of the big errors of gear coordinate point selections. In order to realize the approach between result and circle center position, least square method was adopted in this paper. Gear circle center coordinate was intercalated as (M, N). Then formula (18) can be obtained.

$$\left(x - M\right)^2 + \left(y - N\right)^2 = R^2 , \quad (18)$$

After spreading and arranging formula (18), formula (19) can be obtained.

$$x^2 - 2Mx + M^2 + y^2 - 2Ny + N^2 = R^2 , \quad (19)$$

It was intercalated that *m* is equal to *-2M*. *n* is equal to *-2N*. *p* is equal to the sum of $M^2$, $N^2$ and $-R^2$. Then formula (19) can be written as formula (20).

$$x^2 + y^2 + mx + ny + p = 0 , \quad (20)$$

In this paper, gear tooth number is z. So, z points were selected on selected circle. The coordinate of the *i* point is intercalated as $(x_i, y_i)$. $d_i$ is the distance from the *i* point to circle center. Then formula (21) can be obtained.

$$d_i^2 = \left(x_i - M\right)^2 + \left(y_i - N\right)^2 = x_i^2 + y_i^2 + mx_i + ny_i + p , \quad (21)$$

It was intercalated that $\delta_i$ is equal to $d_i^2$. Then formula (22) can be obtained.

$$\delta_i = x_i^2 + y_i^2 + mx_i + ny_i + p , \quad (22)$$

Then formula (23) can be obtained.

$$\sum \delta_i^2 = \sum \left[ \left( x_i^2 + y_i^2 + mx_i + ny_i + p \right) \right]^2 , \quad (23)$$

When the value of $\sum \delta_i^2$ was taken as minimum value, $x_i$ and $y_i$ will illimitably approach the *i* point

coordinate value on selected circle. After calculating parameters value of *m*, *n* and *p*, selected circle center coordinate that is gear circle center coordinate related the *i* point coordinate value can be obtained by formula (24).

$$\begin{aligned}X = M = -\frac{m}{2} , \\ Y = N = -\frac{n}{2}\end{aligned} \quad (24)$$

## 4.2. Gear Surface Test Mechanism Design

Gear surface test mechanism was designed in this paper. The three dimensional mode of gear surface test mechanism was constructed by Pro/E three dimensional design software. The assembly diagram of gear surface test mechanism and gear is shown as Fig. 5.
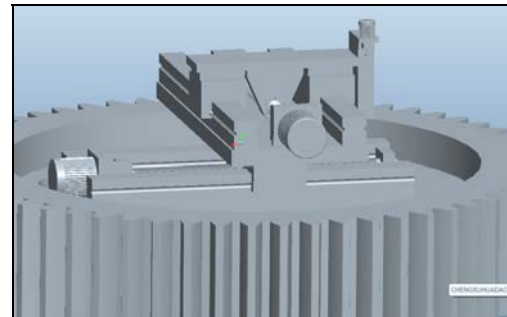


**Fig. 5.** The assembly diagram of gear surface test mechanism and gear.

The under part of gear surface test mechanism contains a ball screw, a lead rail, a motor and a work platform 1. Another set of ball screw, lead rail, motor and work platform was placed horizontally on work platform 1. Work platform 2 is perpendicular to work platform 1. Another set of ball screw, lead rail, motor and work platform was placed horizontally on work platform 2. Work platform 3 is vertical to work platform 2. The left and right motions of work platform 1 can be realized by adjusting work platform 1. The forward and backward motions of work platform 2 can be realized by adjusting work platform 2. The up and down motions of work platform 3 can be realized by adjusting work platform 3. The localization of entire test mechanism can be realized by this method. Sensor was adjusted to worn gear surface by adjusting the motors on work platform 1 and work platform 2. Sensor was localized on start test position according to divided grids. Then the motor on work platform 3 was opened. Test was made by sensor along gear width direction. Worn gear surface and unworn gear surface were all tested by the same method. The abrasion quantity of worn gear surface can be obtained by subtracting tested worn gear surface data from unworn gear surface data.

## 5. Sensor Selection

The tested information by sensor can be transformed to electrical signal form or other recognizable signal form. They were output to satisfy the requirements of transmission, processing, storage, record and show. Laser sensor was selected in this paper. Laser sensor is a kind of sensor testing by laser technology. Laser sensor can realize remote and contactless test. Its response speed is quick. Its precision is high. When laser sensor works, impulse was emitted by diode toward tested object. Impulse was reflected by tested object to laser sensor. Laser signal received by laser sensor was emitted to photoelectricity diode. The weak laser signal was amplified and transformed into relative electrical signal in photoelectricity diode. After processing relative electrical signal by computer, data test was accomplished. OADM 12 laser distance test sensor produced by Shanghai Peng Cheng Electronic Technology Limited Company was selected in this

paper as gear surface test mechanism sensor. It is shown as Fig. 6.



**Fig. 6.** OADM 12 laser distance test sensor.

The basic parameters, electrical parameters, mechanical parameters, test precision and environment conditions of OADM 12 laser distance test sensor are shown as Table 1 ~ Table 5 respectively.

**Table 1.** Basic parameters.

| Response element | Tuning | Start pilot lamp | Camera lens polluted pilot lamp | Light source | Wave length (nm) | Laser grade | Light beam type | Light beam diameter (mm) | Interference suppression (ms) |
|---|---|---|---|---|---|---|---|---|---|
| Direct row optical array | Button /outside | LED green | LED red /LED red quick flashing | Impulse red laser diode | 675 | 2 | Dot | 0.2~0.5 | <30 |

**Table 2.** Electrical parameters.

| Response time /Release time (ms) | Work voltage range (VDC) | Electricity attrition maximum (mA) | Output signal (mA) | Output circuit | Short circuit protection | Reversed polarity protection |
|---|---|---|---|---|---|---|
| <0.9 | 12~28 | 100 | 4~20 | Analog quantity | Yes | Yes |

**Table 3.** Mechanical parameters.

| Width/Diameter (mm) | Height/Length (mm) | Depth (mm) | Type | Hull material | Front panel | Connector type |
|---|---|---|---|---|---|---|
| 12.4 | 37 | 34.5 | rectangle | die casting zinc | glass | Union joint M8 4 needle |

**Table 4.** Test precision.

| Test distance (mm) | Resolution (mm) | Linear error (mm) | Minimum self learning range (mm) |
|---|---|---|---|
| 16~26 | 0.002~0.005 | ±0.006~±0.015 | > 1 |

**Table 5.** Environment conditions.

| Operation temperature (°C) | Protection grade |
|---|---|
| 0~50 | IP67 |

## 6. Calculation Program Design

In order to enhance data processing efficiency and decrease personal error, Visual Basic programming language was adopted in this paper to design two calculation programs. By one calculation program, rectangle coordinate values of points on gear surface can be calculated according to variational pressure angle. Tested data of unworn gear and worn gear were led in another designed calculation program. Then big gear abrasion quantity can be obtained.

### 6.1. Rectangle Coordinate Calculation Program of Standard Involute Straight Gear

Formula (12) shows that rectangle coordinate values of points on gear tooth profile are relate to pressure angle of relative point, gear modulus, gear tooth number and gear pressure angle. The modulus, tooth number and pressure angle of tested gear are known variables. They can be inputted into program directly. The pressure angle of relative point is unknown variable. Four textboxes were designed on program main interface to input data in this paper. Input data are gear modulus, gear tooth number, gear pressure angle and tested point pressure angle separately. Another two textboxes were designed on program main interface to output calculation results. After inputting relative data, calculation button was pressed down. Relative X value and Y value under rectangle coordinates can be shown in two result output textboxes separately. After pressing down delete button, calculated data and improper input data can be deleted so as to input data again. After pressing down finish button, calculation program running was accomplished. The main interface of rectangle coordinate calculation program of standard involute straight gear is shown as Fig. 7.



**Fig. 7.** The main interface of rectangle coordinate calculation program of standard involute straight gear.

### 6.2. Gear Abrasion Quantity Calculation Program

Two rows textboxes, two rows command keys and a row picture boxes were designed on gear abrasion quantity calculation program main interface. By pressing down five command keys on the third row, a set of tested worn gear data can be inputted into first row textboxes. By pressing down five command keys on the fourth row, a set of tested unworn gear data can be inputted into second row textboxes. The differences of inputted data between first row textboxes and second row textboxes can be shown in five picture boxes of the fifth row. The differences can be outputted with matrix form. By pressing down calculation key in the last row, above differences calculation results can be shown in five picture boxes of the fifth row. Big gear abrasion quantity calculation program main interface is shown as Fig. 8.



**Fig. 8.** Big gear abrasion quantity calculation program main interface.

## 7. Conclusions

A kind of intelligent test method was put forward on worn big gear. The measure equations transformations were made on involute straight gear. Original polar coordinates equations were transformed into rectangular coordinates equations. Transformed rectangular coordinates equations calculation program were written by Visual Basic language. According to big gear abrasion measure principle, big gear abrasion test mechanism was designed. After adjustment and positioning of big gear abrasion test mechanism, data collection on worn big gear surface can be realized by laser sensor. Tested data of unworn gear and worn gear were led in designed calculation program written by Visual Basic language. Big gear abrasion quantity can be obtained.

## Acknowledgements

## References

[1]. Y. H. Mo, L. M. Zhang, S. B. Wang, Self-repairment of wearing in gear transmission, *Journal of Shanghai University Natural Science*, Vol. 17, Issue 1, 2011, pp. 90-93.

[2]. L. J. Zhao, H. Shi, Overview on gear transmission wear and its repair, *China Construction Machinery*, Vol. 5, Issue 2, 2007, pp. 243-247.

[3]. H. Imrek, H. Duzcukoglu, Relation between wear and tooth width modification in spur gears, *Wear*, Vol. 262, Issue 3-4, 2007, pp. 390-394.

[4]. M. Amarnath, C. Sujatha, S. Swarnamani, Experimental studies on the effects of reduction in gear tooth stiffness and lubricant film thickness in a spur feared system, *Tribology International*, Vol. 42, Issue 2, 2009, pp. 340-352.

[5]. B. R. Hohn, K. Michaelis, Influence of oil temperature on gear failures, *Tribology International*, Vol. 37, Issue 2, 2004, pp. 103-109.

[6]. W. Feng, X. P. Xie, Q. S. Liao, Experimental study of relation of wear and vibration in gear pitting failure, *Lubrication Engineering*, Vol. 32, Issue 11, 2007, pp. 69-73.

[7]. H. Ding, A. Kahraman, Interactions between nonlinear spur gear dynamics and surface wear, *Journal of Sound and Vibration*, Vol. 307, Issue 3-5, 2007, pp. 662-679.

[8]. D. Park, A. Kahraman, A surface wear mode for hypoid gear pairs, *Wear*, Vol. 267, Issue 9-10, 2009, pp. 1595-1604.

_____

# Research on the Simulation and Application of a Universal Model of Airborne Electronic Countermeasure System

### [1] LIU Xiaoli, [2] PAN Dingqi, [1] ZHOU Xiaomin, [1,*] HE Ketai

[1] University of Science and Technology Beijing, Beijing, 100083, China
[2] Air Force Military Training Device Research Institute, Beijing, 100195, China
[1] Tel.: 86-10-62334511
E-mail: heketai@hotmail.com

**Abstract:** According to the requirements of the electronic countermeasure (ECM) integrated simulation training used in flight simulator, the tasks, missions, structure and function of ECM system are analyzed and a universal model of airborne ECM equipment which is applicable to a variety of aircraft simulators is proposed. Then the key technologies on how to design the data interfaces and configuration files and the simulation method of operational process are described. This universal model is conductive to the construction, management, maintenance and upgrade of the airborne ECM system. *Copyright © 2014 IFSA Publishing, S. L.*

**Keywords:** Electronic countermeasures, Simulation, Universal model.

## 1. Introduction

As wireless communication technology is widely used in military activities, the integrated electronic countermeasures capability of both sides has become one of the key factors influencing the result of war [1]. The integrated simulation training system of electronic countermeasures is used to build a lifelike electromagnetic environment of battlefield by using simulation techniques. That will enable trainees to complete ECM training in complex electromagnetic environment in the laboratory simulation environment instead of the training with real weapons and ammunition, which may cause security problems and high expense.

To date, certain achievements on the application of ECM simulation system in flight simulators have been obtained. But most ECM simulation systems are especially for some specific types of fighter. In other words, little research working on universal simulation model has been done [2]. According to the requirements of network based ECM training, this paper proposes a simulation method that can be applied to the simulation in multiple ECM systems. This method is used in building the input/output interfaces of each module, designing universal model configuration files and packaging internal process of ECM. With this method, ECM of multiple airplanes can be realized and the simulation granularity of all nodes in the network can be well controlled, which is beneficial to the fidelity of the simulation system. What's more, taking the comprehensiveness, versatility, expandability and other characteristics of the simulation system into account, this method is convenient for the construction and management of ECM simulation system. That will reliably support the design optimization and the performance improvement of the system in the future. With the above advantages, the system development cost and debugging time can be significantly reduced.

## 2. Modules of ECM Simulation System

According to the analysis of the actual ECM equipment, the airborne electronic warfare simulation system is designed, which includes four modules, RWR (Radar Warning Receiving), MWR (Missile approximating Warning Receiving), JAM (active jamming) and CFDS (passive jamming).

For simulating network based airborne ECM system, the mathematical model of RWR and MWR system should be established in accordance with the working process and service behavior of RWR and MWR equipment.

This model will receive signals from threat sources in the network and analyze their identity, and create a warning signal which will guide JAM and CFDS system to dispense jamming.

### 2.1. RWR Module

RWR simulation system receives radiation source data and power status data from the nodes in the network. The received signal parameters include carrier frequency, arrival angle and arrival time. Then the radar data is loaded and the system sorts the radar signals according to signal features. With the model the system can calculate whether the carrier aircraft can be scanned by the radar on hostile plane and whether the threat is in detecting-range of the system. Related alarming information, incorporating picture and sound will be shown to the pilots.

Whether RWR simulation system gives alarms depends on conditions of frequency domain and space domain and energy condition. RWR system should check the operating parameters of the working radiation source and get rid of the radiation sources from the list which cannot meet the conditions. After that, the system judges whether the source can be detected according to the location and power status of the radiation source and the sensitivity of RWR system.

Frequency condition refers to the radar alarm's frequency band. The target hostile aircraft frequency should be within the band, that is to say, $f_{\min} \leq f \leq f_{\max}$. Space domain condition refers to RWR's angle coverage in azimuth and pitching angle. The azimuth α and the pitching angle β of the target hostile aircraft in the coordinate system of carrier aircraft can be calculated based on the position of target hostile aircraft and the location and attitude of carrier aircraft. α and β should meet the following inequations:

$$\alpha_{\min} \leq \alpha \leq \alpha_{\max}, \ \beta_{\min} \leq \beta \leq \beta_{\max}, \quad (1)$$

Energy condition restricts the biggest warning distance by one-way link equation.

$$P_R + G_R \leq P_t + G_t - 32 - 20\lg(F) - 20\lg(d), \quad (2)$$

where $P_R + G_R$ is the system sensitivity, $P_t$ is the transmitter radiation power, $G_t$ is the radar antenna maximum gain, $F$ is the radar frequency and $D$ is the target distance.

### 2.2. MWR Module

MWR simulation system receives data from missile sources in the network. With the model the system estimates whether coming missiles are approaching the carrier aircraft according to their motion state and calculates whether the threat is in alarm range. Related alarm information will be shown to the pilots.

The alarming conditions include two aspects, airspace condition and energy condition. Airspace condition means that the system should judge whether the target is in the warning range according to its azimuth and pitching angle. The azimuth and the pitch angle should meet the following inequations:

$$\alpha_{\min} \leq \alpha \leq \alpha_{\max}, \beta_{\min} \leq \beta \leq \beta_{\max}, \quad (3)$$

The biggest warning distance can be calculated by the following equation.

$$E_r = \frac{1}{R^2} I \exp(-kR) + L_c, \quad (4)$$

where $I$ is the radiation intensity of target, $R$ is the target distance, $k$ is the extinction coefficient and $L_c$ is the irradiancy of noise.

### 2.3. JAM and CFDS Module

JAM and CFDS system receives information of threat sources and warning data from RWR and MWR system. It will distribute and manage the interference resources in time domain, airspace and frequency domain in accordance with the principle of power management [3]. The system disturbs the radars on hostile aircraft artificially or automatically to perturb its detection results. In such way, the carrier aircraft is much safer.

The constraint conditions that make the JAM simulation system effective include several aspects such as conditions in frequency domain, in airspace domain, in time domain, energy conditions and the interference ability of JAM system.

Frequency condition refers that the center of the jamming signal's frequency range should be near to the frequency of the radar on hostile aircraft to ensure that the signal can be captured by it. Time condition refers that interference signals are only emitted when the carrier aircraft is in danger. Interference ability refers to the number of threat sources that the system could disturb at the same time.

Different interference methods should be used for different patterns of radar in hostile aircrafts. Different interference models should be designed for JAM and CFDS. During the implementation, to get the best jamming effect, appropriate interference pattern or combined pattern should be chosen from the system.

## 3. Universal Model of Electronic Countermeasures

To build ECM universal model, the main aim is to realize versatility and pertinence. During the development of the system, the establishment of the model is based on actual equipment system. After the composition, technical index and operation process of various types of airborne self-defense ECM equipments are analyzed, then the structures of input data and output data should be summarized. After that, a kind of ECM framework with general parameter database is constructed. With the structure, the universal applicability can be realized. And the customization can be implemented by setting parameters. In this way, a realistic ECM simulation system can work well.

### 3.1. Defining Interface

In order to use and manage the model modularly, the interfaces for all the modules should be defined.

(1) RWR interface.

RWR module communicates with avionics system. The input data of RWR system is from aircrafts and radars in the network, mainly including aircraft position data, posture data, location of radiation sources, type of radiation sources, signal feature of radiation sources and operating characteristic of radiation sources, etc. The RWR module parses and calculates the information from the targets and then exports warning list. The detailed data of the list includes name, number, azimuth, pitching, distance, working state, type and danger level of the radiation sources. Structure of interfaces is shown in Fig. 1.

(2) MWR interface.

The input data of MWR system comes from aircrafts and pills in the network, mainly including radiation intensity of the targets and identification-friend-foe-neutral data.

After parsing and calculating the information from the targets, the MWR module exports warning list. The specific data of the list includes name, number, azimuth, pitching, distance, working state, type and danger level of the radiation sources. Structure of interfaces is shown in Fig. 2.

(3) JAM interface.

The input data of JAM system contains manual operation data and warning list data which includes name, ID, location, work status, antenna main lobe gain, antenna minor lobe gain, main lobe wave band, antenna scanning frequency, type, frequency, power, pulse repetition frequency (PRI), pulse width (PW) of the radiation sources, etc. The JAM module rank all the targets according to their danger level. The module's interference ability depends on the type of selected jamming pod. Structure of interfaces is shown in Fig. 3.
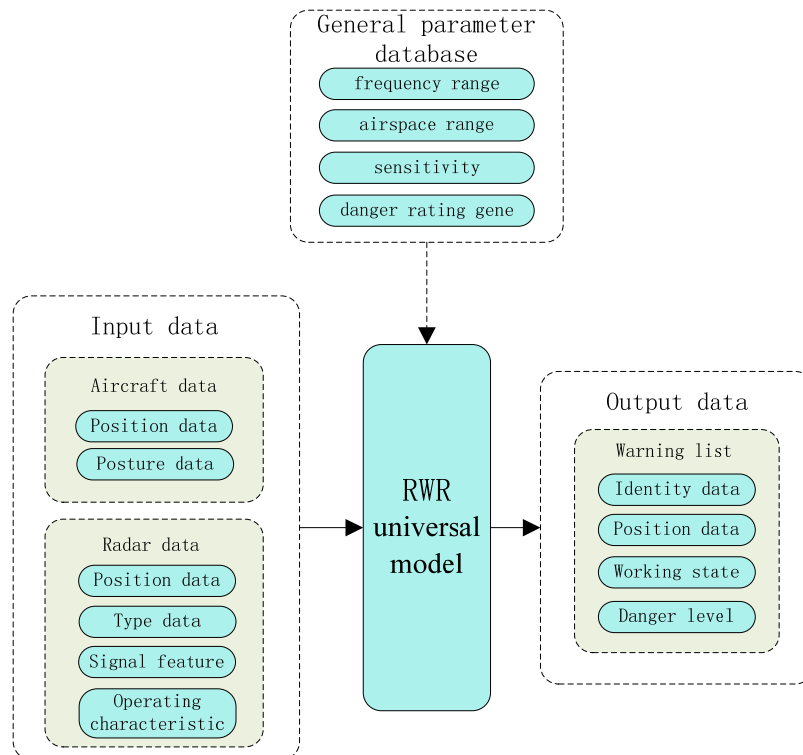


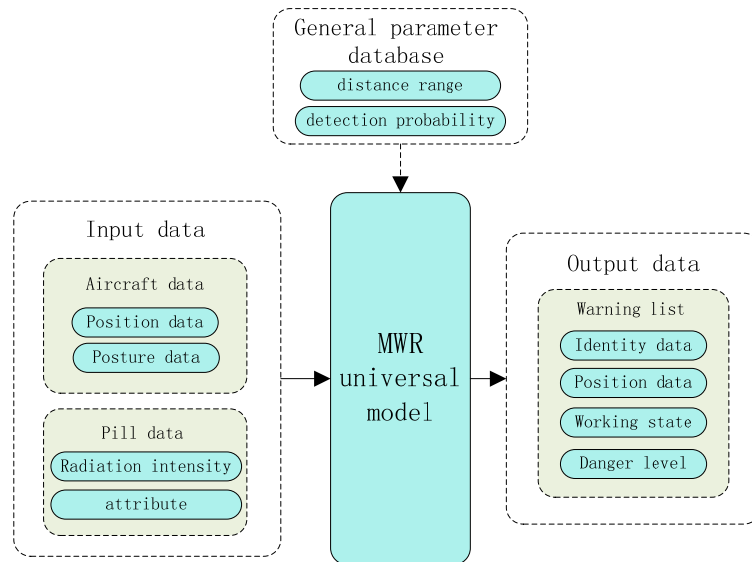**Fig. 1.** RWR universal model interface.

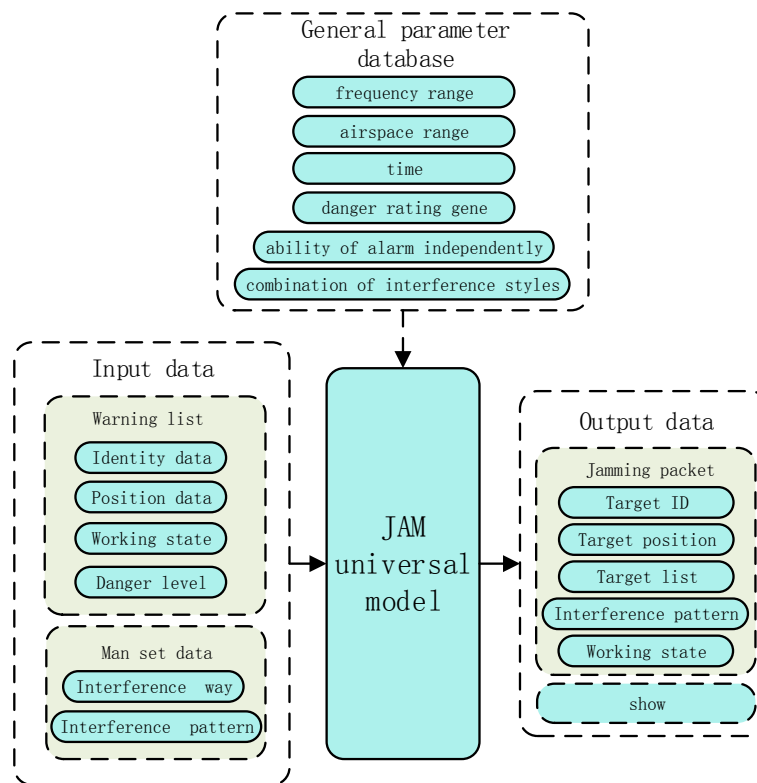**Fig. 2.** MWR universal model interface.



**Fig. 3.** JAM universal model interface.

As for aircraft without alarm, its jamming pod has independent alarm function. The input data of JAM system contains data of aircrafts and radars in the network and manual operation data. The JAM system will give an alarm independently first and then implement interference. The output is jamming packet, which includes the target ID, interference pattern, target position, interference noise power, interference bandwidth, antenna gain, polarization way and target list, etc. Structure of interfaces is shown in Fig. 4.

(4) CFDS interface.

The input data of CFDS system contains manual operation data and warning list data which include radar's name, ID and position, kind of pills, quantity of pills, delivery time interval, etc. The CFDS module exports ballistic packets. For example, the output parameters of CChaff or IR decoy include the location and speed of the pill. Structure of interfaces is shown in Fig. 5.
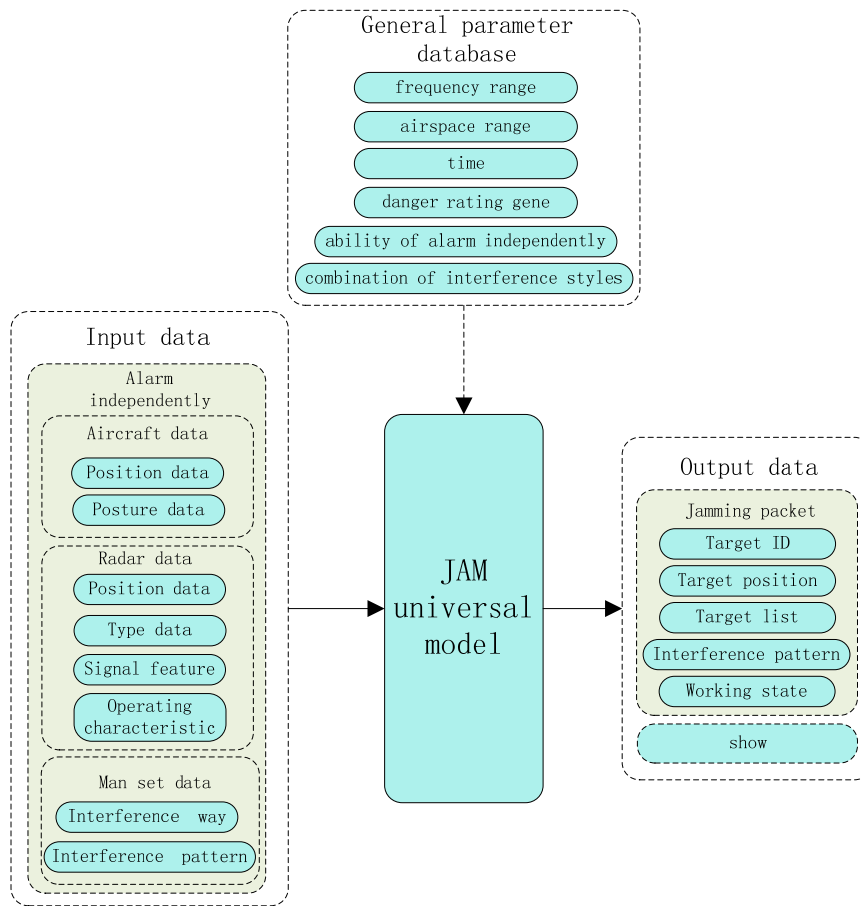
**Fig. 4.** JAM universal model interface
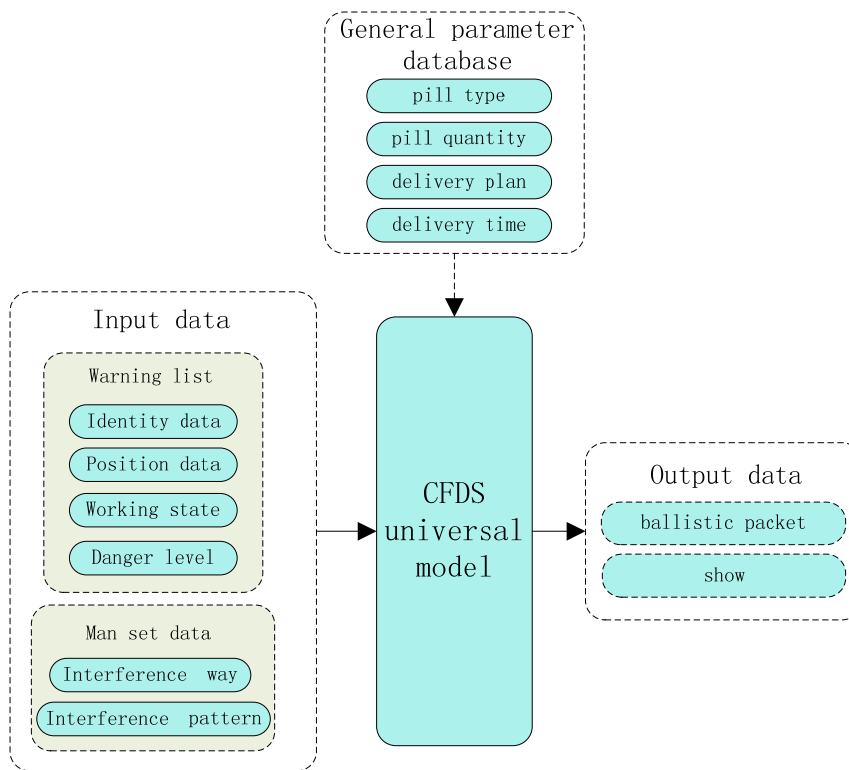(Warning independently).



**Fig. 5.** CFDS universal model interface.

### 3.2. General Model Parameter Database

In order to realize the model's generalization, a method to establish universal model parameter database is proposed. The first step is to extract model parameters of different types of the modules. And then the configuration files are designed respectively with the parameters. When the program is running, performance parameters in configuration files will be read out and assigned to variables of the alarm and jammer system. Thus the simulation for certain type ECM equipment can be executed by adjusting the parameters. So the reusability of the codes can be promoted and the development cycle and maintenance cost can be reduced.

(1) RWR.

The ability of radar alarm is constrained by conditions of frequency, airspace and energy. Different RWR devices have different properties in these aspects. The following is an example for a radar alarm.

a. Frequency domain condition.

Signal frequency range of the RWR is 4~18 GHz (band I: 4~8 GHz, band II: 8~18 GHz).

b. Space domain condition.

There are six receiving antennae on this RWR device. The directional patterns in horizontal and vertical are shown in Fig. 6.
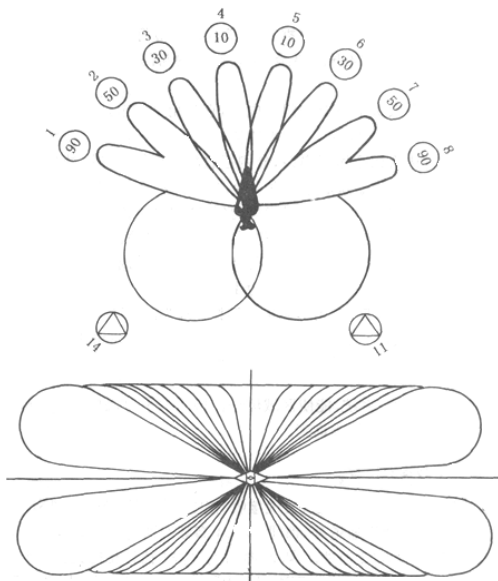


**Fig. 6.** RWR antenna scans direction.

According to the position of target hostile aircraft and the location and attitude of carrier aircraft, the target's azimuth $\alpha$ and angle of pitch $\beta$ in the coordinate system of carrier aircraft can be calculated. Then the direction of the target can be made out. The signal whose azimuth and pitching angle does not match the condition can not be exported.

c. Energy condition.

For a radiation source, according to the one-way link equation, the system can judge whether its distance meets the energy condition or not. In this equation, the receiver's sensitivity varies with different types [4].

According to the analysis of the forementioned special case, we can extract the autonomous configuration parameters of RWR including frequency range, airspace range, sensitivity and danger factor.

When the module is activated, it reads related parameters and puts them to the buffer. These parameters are written in fixed format in the configuration files with the No. of band being used as the key field [5].

(2) MWR.

The ability of MWR is constrained by conditions of airspace and energy. The properties of different MWR devices are different in these aspects. According to the analysis of real equipment, the autonomous configuration parameters of MWR including distance range and detection probability can be extracted.

(3) JAM.

The ability of JAM is constrained by conditions of frequency, airspace, time and energy. Different JAM devices have different interference patterns. According to the analysis of real equipment, the autonomous configuration parameters of JAM including frequency range, airspace range, time, danger rating gene, ability of alarm independently and combination of interference styles can be extracted.

(4) CFDS.

CFDS equipment drops CChaff and IR decoy to interfere the hostile aircrafts. According to the analysis of real equipment, the autonomous configuration parameters of CFDS include pill type, pill quantity, delivery plan and delivery time can be extracted.

### 3.3. System Software Design

(1) RWR and MWR module.

The main function of RWR and MWR module is to provide pilots with warning information and provide guidance for active and passive jamming. The workflow of RWR is shown in Fig. 7. The workflow of MWR is shown in Fig. 8.

(2) JAM and CFDS module.

There are two kinds of electronic jamming, active jamming and passive jamming. JAM module can interfere with multiple threat sources at the same time and adjust the jamming project automatically according to the variation of threat information. For jammer that can search risk sources autonomously, it will take alarm action, rank the threats independently and interfere them. CChaffs and IR decoys are dropped according to the instruction. Workflow of JAM is shown in Fig. 9. Workflow of CFDS is shown in Fig. 10.
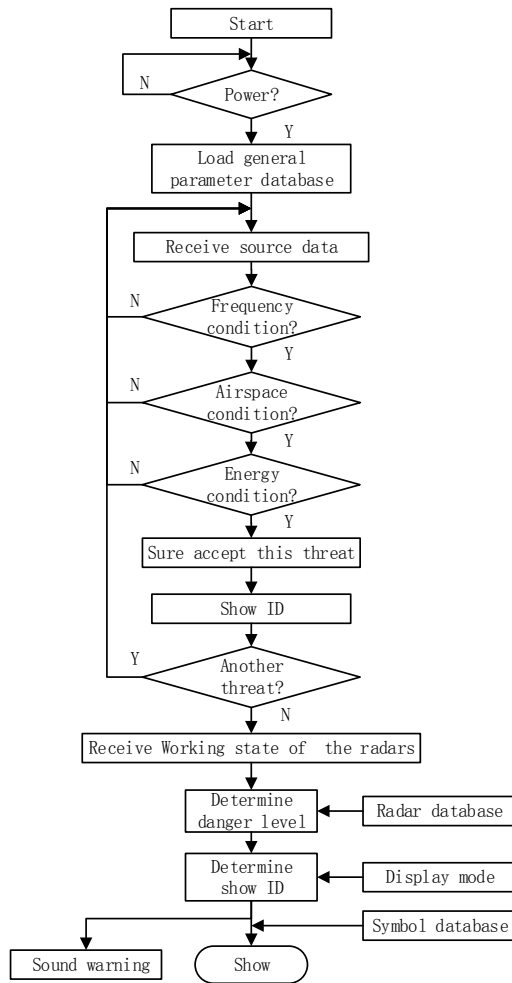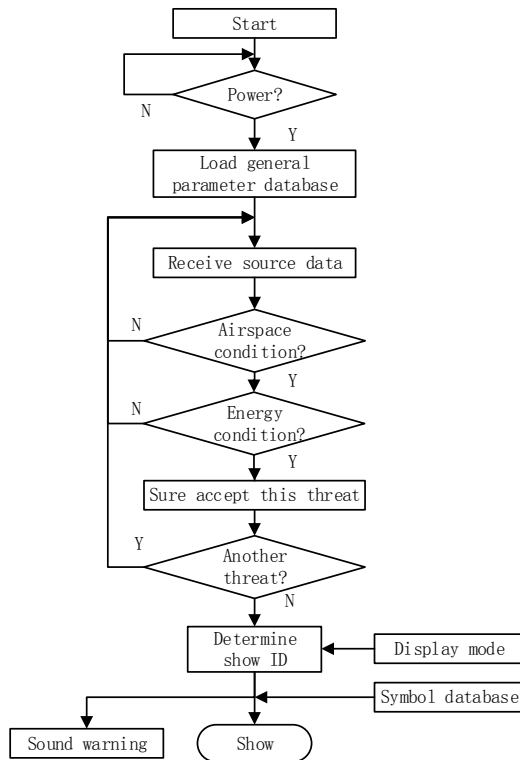
**Fig. 7.** RWR workflow.
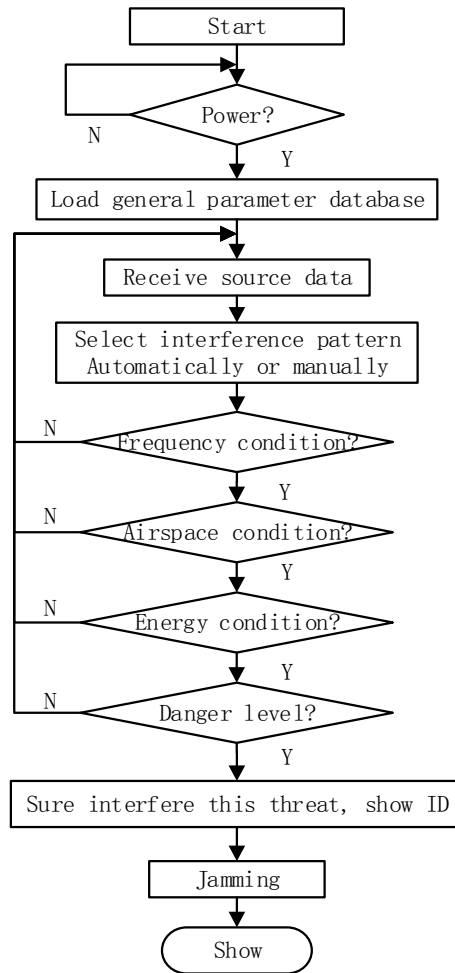


**Fig. 8.** MWR workflow.
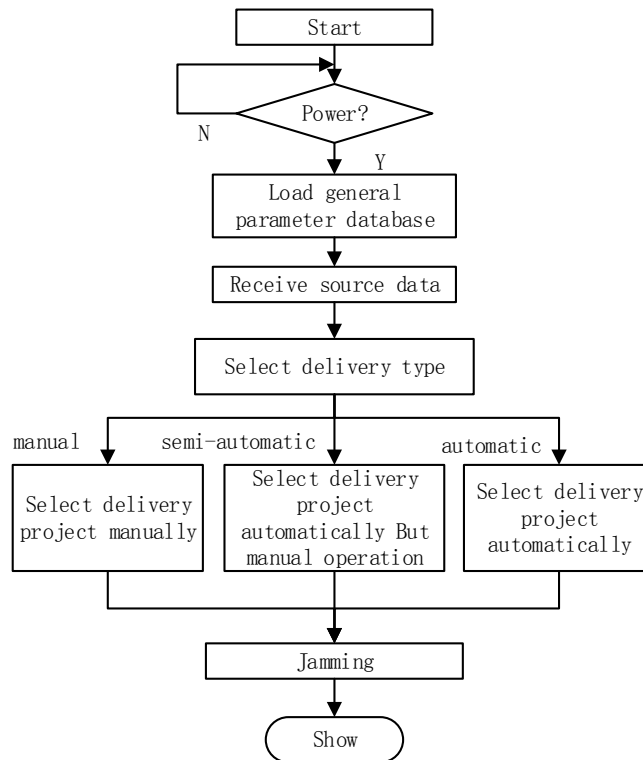
**Fig. 9.** JAM workflow.



**Fig. 10.** CFDS workflow.

## 4. Pilot Study

The proposed ECM model has been used on different types of aircraft simulators. Their effects are shown in Fig. 11, Fig. 12 and Fig. 13.
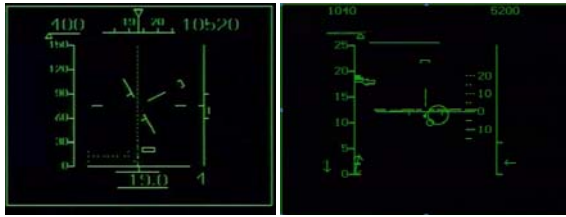


**Fig. 11.** Electrical interference effect of model 1.



**Fig. 12.** Electrical interference effect of model 2.



**Fig. 13.** Electrical interference effect of model 3.

The simulation results show that the model works well. What's more, in the training of network based multi-simulator, the simulation granularity of all the nodes insure the fidelity of the system. The optimization design principles, modulization, standardization and structuralization, are used in modeling [6], which is of great benefit to maintain, using, and upgrade of the model.

Technical performance in the pilot practices is described as follows:

Simulation cycle: 10 ms;

Network bandwidth: 100 M;

Node: 20 in local, 20 in allopatry, the length of every Node packet are not more than 5 k;

Electromagnetic environment: Radiation sources of ground and air.

## 5. Conclusion

The ECM model built in this paper is able to simulate the real countermeasure training process. The input and output data interface and model configuration files of RWR module, MWR module, JAMMER module and CFDS module are designed according to the functional requirements. It is designed to make the model applicable to countermeasure simulation of a variety of airplane types. This model has been applied to kinds of simulators and the results are satisfied. This method is beneficial to unification construction and management of ECM simulation system.

## References

[1]. Fan Xian-De, Yao Jia-Ling, Study of formation way on integrated simulation training system – self-defensive electric counterwork in complex electromagnetic environment, *Journal of CAEIT*, Vol. 6, Issue 5, 2011, pp. 506-510.

[2]. Lu Yang, Xiao Qiu-Fen, Zhang Jian-Qiang, Study of key technology for general purpose ECM jamming pod, *Journal of CAEIT*, Vol. 3, Issue 5, 2008, pp. 451-454.

[3]. Jiang Nan, Simulation techniques of electronic countermeasures training and applications, *Aerospace Electronic Warfare*, Vol. 24, Issue 3, 2008, pp. 59-61.

[4]. Li Yu-Qi, Ma Jun-Chao, Electronic countermeasure simulation system modeling and its operational effectiveness assessment method, *Shipboard Electronic Countermeasure*, Vol. 31, Issue 1, 2008, pp. 61-66.

[5]. Xie Jun, Research on networking simulation technology for electronic countermeasure, *Radio Engineering*, Vol. 41, Issue 4, 2011, pp. 56-61.

[6]. Li Bo, Li Xiao-Di, Gao Xiao-Guang, Zheng Jing-Song, The simulation and evaluation system of the airborne electronic countermeasure, *Fire Control & Command Control*, Vol. 37, Issue 6, 2012, pp. 134-143.

_____

# A Novel Sub-pixel Measurement Algorithm Based on Mixed the Fractal and Digital Speckle Correlation in Frequency Domain

**[1] Zhangfang Hu, [1] Dongdong Huang, [1] Yuan Luo, [2] Yi Zhang, [1] Bing Xi**

[1] Key Laboratory of Optical Fiber Communication Technology, Chongqing University of Posts and Telecommunications, No. 2, Chongwen Road, Nan'an District, Chongqing, 400065, China
[2] Research Center of Intelligent System and Robot, Chongqing University of Posts and Telecommunications, No. 2, Chongwen Road, Nan'an District, Chongqing, 400065, China
[1] Tel.: +86-18725875566
E-mail: huzf@cqupt.edu.cn

**Abstract:** The digital speckle correlation is a non-contact in-plane displacement measurement method based on machine vision. Motivated by the facts that the low accuracy and large amount of calculation produced by the traditional digital speckle correlation method in spatial domain, we introduce a sub-pixel displacement measurement algorithm which employs a fast interpolation method based on fractal theory and digital speckle correlation in frequency domain. This algorithm can overcome either the blocking effect or the blurring caused by the traditional interpolation methods, and the frequency domain processing also avoids the repeated searching in the correlation recognition of the spatial domain, thus the operation quantity is largely reduced and the information extracting speed is improved. The comparative experiment is given to verify that the proposed algorithm in this paper is effective. *Copyright © 2014 IFSA Publishing, S. L.*

**Keywords:** Digital speckle correlation, Sub-pixel displacement, Interpolation algorithm, Fractal, Frequency domain.

## 1. Introduction

It is well-known that the digital speckle correlation method (DSCM) has nowadays become one of the most commonly adopted optical metrology techniques to quantify surface deformation in a variety of practical fields, since it was originally proposed in the early 1980s [1-5]. The fundamental principle of DSCM lies in comparing gray scale images of an object capture before and after displacement, usually referred to as reference and target images, respectively, based on some specific correlation criterion to get the information on displacements of some points sampled beforehand on the reference image [6, 7]. But this algorithm has a large amount of calculation because of the utilizing of repeated searching, and the accuracy of the measurement can only reach pixel level. To achieve displacement measurement with sub-pixel accuracy, several classes of subset-based sub-pixel registration algorithm [2, 8-10] have been put forward over the past three decades, some of which, e.g., the gradient-based method [2] and the Newton-Raphson (NR) iteration method [8] and the other interpolation methods [11], have already been widely used in a variety of application fields.

Based on an optical flow method developed by Davis and Freeman [12], the gradient-based algorithm that considered the effect of intensity gradients of both images before and after displacement was presented [9]. In practical application, the error is introduced by abandoning the higher order term due to the use of Taylor formula. The coarse-fine (pyramid) search method, iteration and second-order Taylor formula are used to reduce the error, but distinctly increase the computation [13].

Interpolations used in the sub-pixel registration usually include phase correlation interpolation [14], intensity interpolation [15] and correlation function interpolation [16]. The phase correlation interpolation method is suitable for the images seriously distorted, however, the accuracy of which is the lowest among the three [17]. While the intensity interpolation has been less adopted for its immense computation consumption, the correlation function interpolation is generally considered due to its lower computation and better noise-proof feature, nevertheless, an obvious weakness is that the sensitivity is limited by the interpolation step because of the systematic error of the algorithm [18, 19].

Iterative algorithm often requires the calculation of second-order spatial derivatives of the digital images, which further increases computation complexity.

However, the traditional digital speckle correlation method in spatial domain does not avoid the problem of large amount of calculation caused by repeated searching. In this paper, the DSCM is converted into the frequency domain by Fourier transform, so avoids a large number of calculations. Meanwhile, a fast interpolation method based on fractal theory is proposed to improve the measurement accuracy.

## 2. Fast Sub-pixel Interpolation Based on Fractal

### 2.1. Fractal and Random Midpoint Method

Fractal theory is a discipline for describing the irregular things and phenomena in the nature. The researching object is a class fractal object of self-similarity and self-affine. Because of many things have explicitly or implicitly fractal characteristics, the fractal can be divided into rules fractal and random fractal. Rules fractal is iteration formation based on certain rules and functions. While random fractal is randomness, it can be better description of natural phenomena.

Mandelbrot applied fractal dimension to quantitative describe the image's similarity between the whole and partial, proposed the concept of Fractional Brownian Motion (FBM). Random midpoint displacement method can use a simple equation to express the interpolation point ($x_{mi}, y_{mi}$)

$$x_{mi} = (x_i + x_{i+1}) / 2 + s \cdot w \cdot rand(), \qquad (1)$$

$$y_{mi} = (y_i + y_{i+1}) / 2 + s \cdot w \cdot rand(), \qquad (2)$$

where $s$ and $w$ are the parameters indicating the moving direction and the moving distance respectively, $rand()$ is the random variable.

### 2.2. Fractal Interpolation Algorithm

For an image obtained from nature, the geometrical image follow the variation of fractal geometry, and the distribution of brightness also has the characteristics of fractal. According to the fractal nature of the image, image and the actual scene have the same fractal dimension stayed unchanged even with the different transformation ratios, so fractal interpolation can be used to achieve sub-pixel measurement. The image interpolated usually loses the texture features with using the traditional methods, because of the principle of which based on the fact that it is uniformly continuous change between the data point. A basic feature of fractal is able to demonstrate the fine structure of the object, so fractal interpolation can achieve the better effect in the processing of extracting the sub-pixel displacement.

According to the fractal geometric feature, the new pixel's information is increased between the known pixels. In order to calculate the gray of the new pixel, recursive random midpoint displacement method is adopted as shown in Fig. 1.
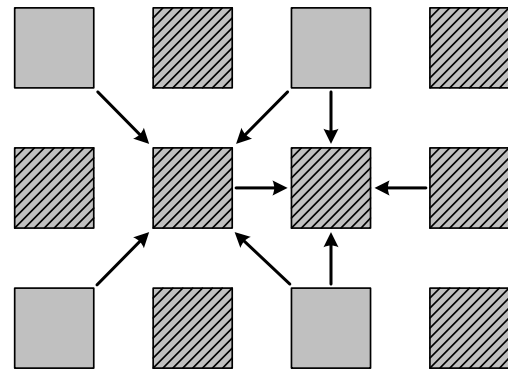


**Fig. 1.** Schematic of the fractal interpolation.

The recursive formula of the fractal interpolation can be expressed as follows. $(i, j)$ represent the location of the original pixels. Obviously $I(i, j)$ is known when $i$ and $j$ are odd. When $i$ and $j$ are even, the gray of new pixel can be written as

$$I(x, y) = [I(i-1, j-1) + I(i+1, j+1) + I(i-1, j+1) + I(i+1, j-1)] / 4 + \Delta I \qquad (3)$$

When $i$ is an odd and $j$ is even, or $i$ is even and $j$ is an odd, then

$$I(x,y) = [I(i-1,j) + I(i,j+1) + $$
$$I(i,j-1) + I(i+1,j)] / 4 + \Delta I \qquad (4)$$

$$\Delta I = \sqrt{1 - 2^{2H-2}} H \sigma G \times \left(1/2^{H/2}\right)^{n-1}, \qquad (5)$$

where $x, y \subset k + 1/2^n$ ($k$ is the positive integer), $n$ is the number of interpolation, $H$ is the fractal parameter, $\sigma$ is the mean-square deviation of pixels' brightness and $G$ is Gaussian random variable following $N(0,1)$. Traversing image, $\Delta I$ multiplied by the factor $2^{-H/2}$ each cycle, and repeating the iteration until achieves the desired spatial resolution. From the theoretical analysis, the measurement accuracy can be achieved $1/2^n$ after $n$ times interpolation.

## 3. Principle of DSCM in Frequency Domain

The frequency domain processing avoids the repeated searching in the correlation recognition of the spatial domain, thus the operation quantity is largely reduced and the information extracting speed is improved.

First of all, $p(x,y)$ is considered to the sample sub-region of the original digital speckle image, and $p_-(x,y)$ is the other region, so the reference image can be written as

$$I_1(x,y) = p(x,y) + p_-(x,y), \qquad (6)$$

Similarly, the image after moving is expressed as

$$I_2(x,y) = q(x,y) + q_-(x,y), \qquad (7)$$

where $q(x,y)$ is the target sub-region. In this paper, the motion follows the horizontal or vertical direction in the plane coordinate system. And the gray value of anyone pixel remains the same in reference image and the moved image, because of the displacement is very small compared with the lighting area. So we can acquire the following expression:

$$q(x,y) = p(x+u, y+v), \qquad (8)$$

where $u$ and $v$ are the displacement vector in $x$ direction and $y$ direction respectively.

On the one hand, the sample sub-region is converted to frequency domain by Fourier transform, and $(w_x, w_y)$ is used as the coordinate parameters.

$$f(w_x, w_y) = FFT\{p(x,y)\}$$
$$= |f(w_x, w_y)| \exp\left[j\varphi(w_x, w_y)\right] \qquad (9)$$

We can easily find the conjugate expression:

$$f^*(w_x, w_y) = |f(w_x, w_y)| \exp\left[-j\varphi(w_x, w_y)\right] \qquad (10)$$

Eq. (10) can be seen as the conjugate filter, $|f(w_x, w_y)|$ and $\varphi(w_x, w_y)$, respectively, represent the amplitude and the phase.

On the other hand, we can readily acquire the following expression similar to the Eq. (9):

$$g(w_x, w_y) = FFT\{I_2(x,y)\} = FFT\{q(x,y) + q_-(x,y)\}$$
$$= FFT\{p(x+u, y+v) + q_-(x,y)\} \qquad (11)$$
$$= |f(w_x, w_y)| \exp\left[j2\pi(uw_x + vw_y)\right] + k(w_x, w_y)$$

with

$$k(w_x, w_y) = FFT\{q_-(x,y)\}, \qquad (12)$$

The frequency spectrum of the target image filtered with the conjugate filter, that is, Eq. (11) multiplied by Eq. (10).

$$h(w_x, w_y) = f^*(w_x, w_y) g(w_x, w_y)$$
$$= |f(w_x, w_y)|^2 \exp\left[j2\pi(uw_x + vw_y)\right] \qquad (13)$$
$$+ f^*(w_x, w_y) k(w_x, w_y)$$

Finally, Eq. (13) is analyzed by using the Fourier transformation. That is

$$H(\varepsilon,\eta) = FFT\{h(w_x, w_y)\}$$
$$= G(\varepsilon,\eta)\delta(\varepsilon-u,\eta-v) + F(-\varepsilon,-\eta) * K(\varepsilon,\eta) \qquad (14)$$

in which, $*$ represents the convolution and

$$K(\varepsilon,\eta) = FFT\{k(w_x, w_y)\}, \qquad (15)$$

We may equivalently rewrite Eq. (14) as

$$H(\varepsilon,\eta) = G(\varepsilon-u,\eta-v) + F(-\varepsilon,-\eta) * K(\varepsilon,\eta), \qquad (16)$$

The first item of Eq. (16) shows up as a correlation light spot, and the magnitude and direction of displacement can be extracted according to the location of the light spot. And the second one represents fuzzy convolution. But in the actual experiment, the two sub-regions have the same size and the location are acquired, respectively, from the reference image and the target image because of the fact that the sub-pixel displacement is tiny compared with the size of the sub-region. Additionally, fractal interpolation is used to ensure the sub-pixel precision. For clarity, Table 1 presented a simple step to illustrate how the newly proposed algorithm works.

**Table 1.** The steps of this algorithm.

| | |
|---|---|
| **Step. 1** | Collect sub-region images, respectively, from reference image and target image |
| **Step. 2** | Fractal interpolation on the two sub-regions |
| **Step. 3** | Make the filter |
| **Step. 4** | Filtering the frequency spectrum of the target sub-region with the filter |
| **Step. 5** | Acquire the Fourier transformation of the output obtained in Step. 4 |
| **Step. 6** | Obtain the light spot and extract the displacement according to the location of the light spot |

## 4. Results and Discussion

To verify the feasibility and effectiveness of the proposed algorithm, synthetic speckle images are created. It was hypothesized that the simulated reference image of size $512 \times 512$ pixels, and the target image is assumed to undergo in-plane displacement along horizontal and vertical direction, and the value, respectively, is 0.5 and 0.8 pixel, as shown in Fig. 2.
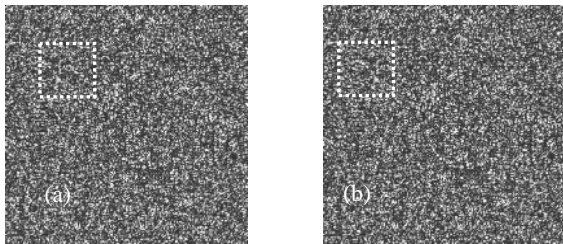


**Fig. 2.** (a) Simulated reference image, (b) the corresponding deformed image with the motion following horizontal and vertical direction in-plane.

In the Fig. 2, the dotted box part is used as the subsets have the same size and the location in our experiment, Fig. 3 exhibited the influence on the choice of the subset size.
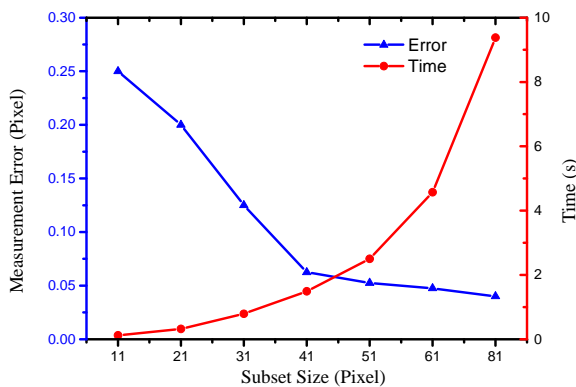


**Fig. 3.** The choice of the subset size.

In Fig. 3, the true displacement is 0.5 pixels only following the horizontal direction. It could be easily learned that the measurement error decreases along with the increscent subset size, inversely, the elapsed time is proportional to the size of the sub-region. In this paper, the experimental environment as follows: Windows 7, 64-bit operating system, Intel(R) Celeron(R)CPU 2.60 GHz, MATLAB 2012a. Considering the measurement error and the run-time, synthetically, $41 \times 41$ is the desired size of the subset, so the size of subset is set to $41 \times 41$ pixel. The experimental result of Fig. 2 without taking fractal interpolation as shown in Fig. 4.
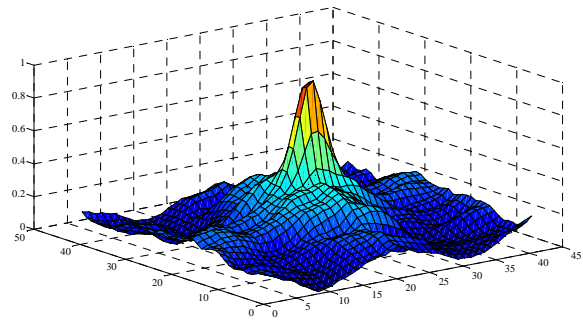


**Fig. 4.** Measurement result without using fractal interpolation.

It could be learned from Fig. 4 that the peak seems very wide. And finally, the actual measured value is 1 pixel and 1 pixel according to the location of the peak, respectively, in the $x$ direction and $y$ direction. Obviously, the measurement error is unacceptable, so the fractal interpolation algorithm described above is employed to improve the measurement accuracy as shown in Fig. 5.
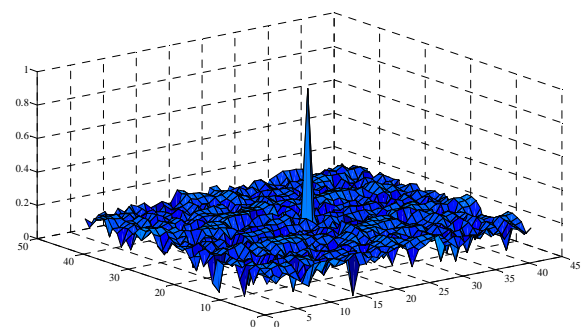


**Fig. 5.** Measurement result after using fractal interpolation.

Compared with Fig. 4, the peak in Fig. 5 seems more exquisite and sharp. And the actual measured value is 0.4375 pixels and 0.8125 pixels in horizontal direction and vertical direction, meanwhile the measurement error is in the acceptable range.

Another set of experiments indicate the effectiveness of the proposed algorithm via detecting

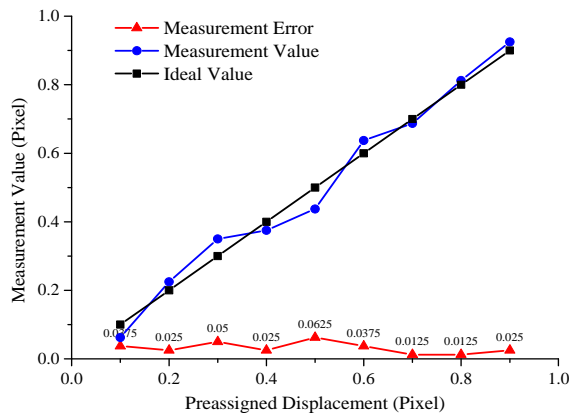displacement of different sizes as shown in Fig. 6 and Fig. 7.



**Fig. 6.** The measurement results and error curve presented by the proposed algorithm.
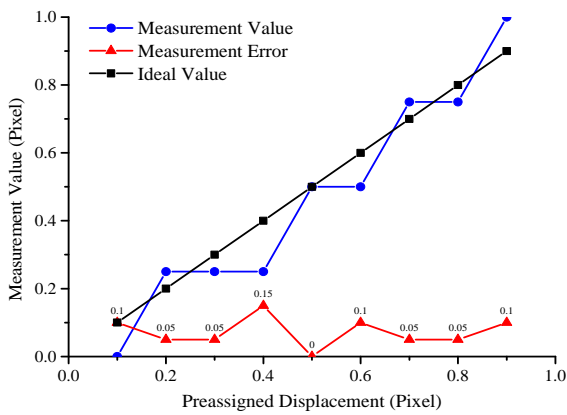


**Fig. 7.** The measurement results and error curve presented by the bicubic interpolation with the DSCM in spatial domain.

Obviously, in the same coordinate system, the dot line seems smooth in Fig. 6 compared with that in Fig. 7, and overall, the triangle curve in Fig. 6 is more close to the horizontal axis. Data also show that the maximum absolute error is 0.0625 pixels by using the proposed algorithm less than 0.15 extracted by the traditional method in spatial domain. In this paper, the stability of algorithm can be represented by the uncertainty, and the standard deviation of the absolute error indicates the uncertainly. After calculation, the uncertainly of former is 0.034 less than 0.075 calculated by another algorithm. Summary it can be concluded that the stability and effectiveness of the proposed algorithm is superior to the traditional digital speckle correlation method in spatial domain.

## 5. Conclusions

In this paper, a novel sub-pixel measurement algorithm combining fractal interpolation in frequency domain is proposed. The traditional digital speckle correlation method is converted to the frequency domain via the Fourier transform, and avoids the repeating search in spatial domain. Meanwhile, the fractal interpolation is utilized to ensure the sub-pixel accuracy. Finally, comparative experiments verify the fact that the effectiveness and stability of proposed algorithm is superior to the traditional method.

## Acknowledgements

## References

[1]. M. A. Sutton, J. J. Orteu, H. W. Schreier, Image correlation for shape, motion and deformation measurements, *Springer*, 2009.

[2]. Zhang Jun, Jin Guanchang, Ma Shaopeng, Me Libo, Application of an improved subpixel registration algorithm on digital speckle correlation measurement, *Optics & Laser Technology*, Vol. 35, Issue 7, 2003, pp. 533-542.

[3]. M. Fazzini, S. Mistou, O. Dalverny, L. Robert, Study of image characteristics on digital image correlation error assessment, *Optics and Lasers in Engineering*, Vol. 48, Issue 3, 2010, pp. 335-339.

[4]. T. C. Chu, W. F. Ranson, M. A. Sutton, Applications of digital-image-correlation techniques to experimental mechanics, *Experimental Mechanics*, Vol. 25, Issue 3, 1985, pp. 232-244.

[5]. Chen Jinlong, Zhang Xiaochuan, Zhan Nan, Hu Xiaoyan, Deformation measurement across crack using two-step extended digital image correlation method, *Optics and Lasers in Engineering*, Vol. 48, Issue 11, 2010, pp. 1126-1131.

[6]. F. Hild, S. Roux, Digital image correlation: from displacement measurement to identification of elastic properties – a review, *Strain*, Vol. 42, Issue 2, 2006, pp. 69-80.

[7]. Huang Jianyong, Pan Xiaochang, Peng Xiaoling, et al, High-efficiency cell-substrate displacement acquisition via digital image correlation method using basis functions, *Optics and Lasers in Engineering*, Vol. 48, Issue 11, 2010, pp. 1058-1066.

[8]. C. Cofaru, W. Philips, W. Van Paepegem, Improved Newton-Raphson digital image correlation method for full-field displacement and strain calculation, *Applied Optics*, Vol. 49, Issue 33, 2010, pp. 6472-6484.

[9]. Zhou Peng, K. E. Goodson, Subpixel displacement and deformation gradient measurement using digital image/speckle correlation (DISC), *Optical Engineering*, Vol. 40, Issue 8, 2001, pp. 1613-1620.

[10]. Hu Zhenxing, Xie Huimin, Lu Jian, et al, Study of the performance of different subpixel image correlation methods in 3D digital image correlation, *Applied Optics*, Vol. 49, Issue 21, 2010, pp. 4044-4051.

[11]. Luo Yuan, Liu Yuan, A fast interpolation algorithm based on the fractal in the digital speckle sub-pixel

displacement measurement, *Applied Mechanics and Materials*, Vol. 344, 2013, pp. 238-241.

[12]. C. Q. Davis, D. M. Freeman, Statistics of subpixel registration algorithms based on spatiotemporal gradients or block matching. *Optical Engineering*, Vol. 37, Issue 4, 1998, pp. 1290-1298.

[13]. Hu Zhangfang, Huang Dongdong, Luo Yuan, et al, Research on a novel compensation algorithm for MEMS sub-pixel displacement measurement, *Advanced Materials Research*, Vol. 901, 2014, pp. 81-86.

[14]. L. Luu, Z. Wang, M. Vo, et al, Accuracy enhancement of digital image correlation with B-spline interpolation, *Optics Letters*, Vol. 36, Issue 16, 2011, pp. 3070-3072.

[15]. P. Lava, S. Cooreman, S. Coppieters, M. De Strycker, D. Debruyne, Assessment of measuring errors in DIC

using deformation fields generated by plastic FEA, *Optics and Lasers in Engineering*, Vol. 47, Issue 7, 2009, pp. 747-753.

[16]. V. N. Dvornychenko, Bounds on (deterministic) correlation functions with application to registration, *IEEE Transactions on Pattern Analysis and Machine Intelligenc*e, Vol. 5, Issue 2, 1983, pp. 206-213.

[17]. Tian Qi, Michael N. Huhns, Algorithms for subpixel registration, *Computer Vision, Graphics, and Image Processing*, Vol. 35, Issue 2, 1986, pp. 220-233.

[18]. Yu Qifeng, Lu Hongwei, X. Liu, Image based precise measurement and motion measurement, *Beijing Science Press*, Beijing, 2002.

[19]. H. W. Schreier, J. R. Braasch, M. A. Sutton, Systematic errors in digital image correlation caused by intensity interpolation, *Optical Engineering*, Vol. 39, Issue 11, 2000, pp. 2915-2921.

_____

## Aims and Scope

*Sensors & Transducers* is a peer reviewed international, interdisciplinary journal that provides an advanced forum for the science and technology of physical, chemical sensors and biosensors. It publishes original research articles, timely state-of-the-art reviews and application specific articles with the following devices areas:

- Physical, chemical and biosensors;
- Digital, frequency, period, duty-cycle, time interval, PWM, pulse number output sensors and transducers;
- Theory, principles, effects, design, standardization and modeling;
- Smart sensors and systems;
- Sensor instrumentation;
- Virtual instruments;
- Sensors interfaces, buses and networks;
- Signal processing and interfacing;
- Frequency (period, duty-cycle)-to-code converters, ADC;
- Technologies and materials;
- Nanosensors;
- Microsystems;
- Applications.

Further information on this journal is available from the Publisher's web site:
http://www.sensorsportal.com/HTML/DIGEST/Submission.htm

## Subscriptions

An annual subscription includes 12 regular issues and some special issues. Annual subscription rates for 2014 are the following:

Electronic version (in printable pdf format): 590.00 EUR
Printed with b/w illustrations: 950.00 EUR

25 % discount is available for IFSA Members.

Prices include shipping costs by mail. Further information about subscription is available through IFSA Publishing's web site: http://www.sensorsportal.com/HTML/DIGEST/Journal_Subscription.htm

## Advertising Information

If you are interested in advertising or other commercial opportunities please e-mail sales@sensorsportal.com and your enquiry will be passed to the correct person who will respond to you within 24 hours. Please download also our Media Planner 2014: http://www.sensorsportal.com/DOWNLOADS/Media_Planner_2014.pdf

## Books for Review

Publications should be sent to the IFSA Publishing, S.L. office: Parc UPC-PMT, Edifici RDIT-K2M, c/ Esteve Terradas, 1, Room 113, 08860, Castelldefels, Barcelona, Spain.

## Abstracting Services

This journal is cited, indexed and abstracted by Chemical Abstracts, EBSCO Publishing, IndexCopernicus Journals Master List, ProQuest Science Journals, CAS Source Index (CASSI), Ulrich's Periodicals Directory, Scirus, Google Scholar, etc. Since 2011 *Sensors & Transducers* journal is covered and indexed by EI Compendex index (including a Scopus, Embase, Engineering Village and Reaxys) in *Elsevier* products.

## Instructions for Authors

Please visit the journal web page http://www.sensorsportal.com/HTML/DIGEST/Submission.htm Authors must follow the instructions very carefully when submitting their manuscripts. Manuscript must be send electronically in both: MS Word for Windows and Acrobat (pdf) formats by e-mail: editor@sensorsportal.com

**IFSA**

# ADVANCES IN SENSORS: REVIEWS

## 2

**Sergey Y. Yurish**

**Editor**

# Sensors and Biosensors, MEMS Technologies and its Applications
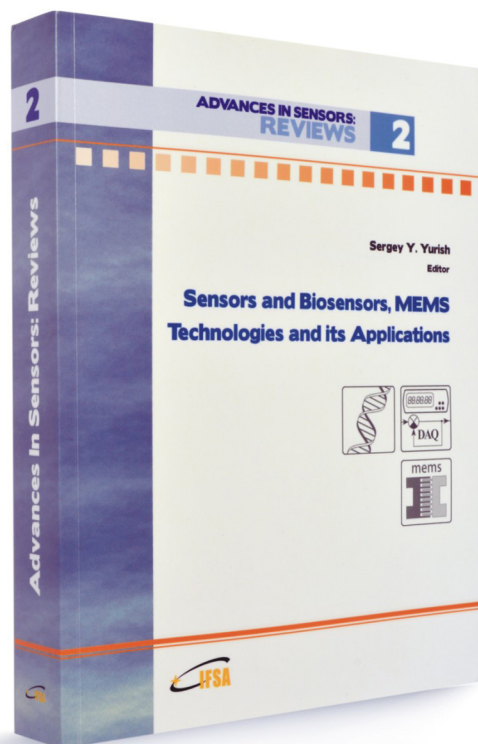
The second volume titled *'Sensors and Biosensors, MEMS Technologies and its Applications'* from the *'Advances in Sensors: Review'* Book Series contains eighteen chapters with sensor related state-of-the-art reviews and descriptions of the latest achievements written by experts from academia and industry from 12 countries: China, India, Iran, Malaysia, Poland, Singapore, Spain, Taiwan, Thailand, UK, Ukraine and USA.

This book ensures that our readers will stay at the cutting edge of the field and get the right and effective start point and road map for the further researches and developments. By this way, they will be able to save more time for productive research activity and eliminate routine work.

Built upon the series *Advances in Sensors: Reviews* - a premier sensor review source, it presents an overview of highlights in the field and becomes. This volume is divided into three main parts: physical sensors, biosensors, nanoparticles, MEMS technologies and applications. With this unique combination of information in each volume, the *Advances in Sensors: Reviews* Book Series will be of value for scientists and engineers in industry and at universities, to sensors developers, distributors, and users.

Like the first volume of this Book Series, the second volume also has been organized by topics of high interest. In order to offer a fast and easy reading of the state of the art of each topic, every chapter in this book is independent and self-contained. The eighteen chapters have the similar structure: first an introduction to specific topic under study; second particular field description including sensing applications.

**Order online:**
http://sensorsportal.com/HTML/BOOKSTORE/Advance_in_Sensors_Vol_2.htm